PROCEEDINGS
SIXTEENTH WORKSHOP
GEOTHERMAL RESERVOIR ENGINEERING

January 23–25, 1991

Henry J. Ramey, Jr., Roland N. Horne,
Paul Kruger, Frank G. Miller,
William E. Brigham, Jean W. Cook
Stanford Geothermal Program
Workshop Report SGP-TR-134

Library of Congress Catalog Card No. 86-643338
ISSN 1058-2525

TABLE OF CONTENTS

PREFACE vii

INTRODUCTION

The California Energy Commission's Geothermal Activities
B. Crowley, Vice Chair 1

DOE'S Geothermal Program- New Emphasis on Industrial Participation
J. E. "Ted" Mock and G. Beeland 3

GEOCHEMISTRY

Quality Control of Chemical and Isotopic Analyses of Geothermal Water Samples
M.J. Reed and R.H. Mariner 9

The Origin of High-Temperature Zones in Vapor-Dominated Geothermal Systems
A. Truesdell 15

HOT DRY ROCK

A Coupled Model of Fluid Flow in Jointed Rock
D. Swenson, R. Martineau, M. James, and D. Brown 21

A Review of the UK Geothermal Hot Dry Rock R&D Program
G.D. Symons and J.H. Clarke 29

The Economics of Heat Mining- An Analysis of Design Options and Performance Requirements of Hot Dry Rock (HDR) Geothermal Power Systems
J.W. Tester and H.J. Herzog 35

Civil Litigation and the Geothermal Industry
G.M. Moore 53

TRACER INJECTION

Preliminary Assessment of Halogenated Alkanes as Vapor-Phase Tracers
M.C. Adams, J.N. Moore, and P. Hirtz 57

The Use of Air as a Natural Tracer in Fractured Hydrothermal Systems, Los Azufres, Mexico, Case Study
M.C. Suarez, H. Gutierrez, J.M. Ochoa 63

An Investigation of Radial Tracer Flow in Naturally Fractured Reservoirs
J. Ramirez-Sabag, F. Samaniego V., J. Rivera R., and F. Rodriguez 67

FIELD PERFORMANCE - I

Reservoir Response to Injection in the Southeast Geysers
S. Enedy, K. Enedy, and J. Manney 75

Current Techniques in Acid-Chloride Corrosion Control and Monitoring at The Geysers
P. Hirtz, C. Buck, R. Kunzman 83

Analysis of Reinjection Strategies for The Geysers
M. Shook and D.D. Faulder 97

FIELD PERFORMANCE - II

Fracture Patterns in Graywacke Outcrops at The Geysers Geothermal Field
C.G. Sammis, J.A. Lin, and I.Ershaghi 107

One-Dimensional Steam Flow in Porous Media under Desorption
C.P. Nghiem and H.J. Ramey, Jr. 113

FIELD PERFORMANCE - III

A Preliminary Assessment of a Medium-Enthalpy Geothermal Resource in Nagqu (Tibet) People's Republic of China
A. Battistelli, R.J. Rivera, F. D'Amore, et al 117

Conceptual Geologic Model and Native State Model of the Roosevelt Hot Springs Hydrothermal System
D.D. Faulder 131

Reservoir Engineering Studies of Small Low-Temperature Hydrothermal Systems in Iceland
G. Axelsson 143

MODELLING - I

Numerical Simulation of the Sumikawa Geothermal Field in the Natural State
J.W. Pritchett, S.K. Garg, K. Ariki,and Y. Kawano 151

Comparison of Thermal Cooldown Estimates in the Russkie Komarovtsy Petrogeothermal Reservoir
P. Kruger, Y. Dyadkin, S. Gendler, E. Artemieva, and N. Smirnova 159

Prediction and Prevention of Silica Scaling at Low Levels of OverSaturation - Case Studies, and Calculations for Uenotai Geothermal Field, Akita Prefecture, Japan
C.W. Klein, S. Iwata, R. Takeuchi, and T. Naka 165

Heat Deliverability of Homogeneous Geothermal Reservoirs
E.R. Iglesias and S.L. Moya 177

MODELLING - II

Simulating a Challenging Water Dominated Geothermal System - The Cerro Prieto Field, Baja California, Mexico
E.U. Antunez, A.J. Menzies, and S.K. Sanyal 183

Numerical Modeling of the Initial State and Matching of Well Test Data from The Zunil Geothermal Field, Guatemala
A.J. Menzies, E.E. Granados, S.K. Sanyal, L. Merida-I, and A. Caicedo-A 193

Two-Phase Flow Visualization and Relative Permeability Measurement in Transparent Replicas of Rough-Walled Rock Fractures
P. Persoff, K. Pruess, and L. Myer 203

Grid Orientation Effects in the Simulation of Cold Water Injection into Depleted Vapor Zones
K. Pruess 211

MODELLING - III

Pressure Interference Testing of the Sumikawa Geothermal Field
S.K. Garg, J.W. Pritchett, K. Ariki, and Y. Kawano 221

Optimizing Reinjection Strategy at Palinpinon, Philippines, Based on Chloride Data
M.E.G. Urbino and R.N. Horne 231

Modifications to TOUGH and Analysis of Build-up Data of PTS (Pressure/Temperature/Spinner) Logging in a Two-phase Condition
T. Okabe, K. Osato, and S. Takasugi 241

CHEMISTRY/GAS

Variations in Dissolved Gas Compositions of Reservoir Fluids from the Coso Geothermal Field
A.E. Williams and J.F. Copp 247

Geysering Discharge of a Geothermal Wellbore at Zunil, Guatemala
D.E. Michels 255

Hydrochemical Features of a Geothermal Test Well in a Volcanic Caldera, Mt. Pinatubo, Philippines
D.E. Michels, V.C. Clemente, M.N. Ramos 261

Geochemical Characteristics of Acid Fluids in Mt. Pinatubo, Philippines
M.M. Buenviaje 267

PAPERS NOT PRESENTED

Simulating Wellflow of High-Noncondensable-Gas Geofluids Using Laboratory Measurements on Secondary Fluids
R.N. Laoulache and R. Dipippo 275

Some Approaches to Rock Mass Hydrofracture Theory
Y.D. Dyadkin 283

LATE PAPERS AND PAPERS NOT RECEIVED

A Study of Steady-State Steam-Water Counterflow in Porous Media
C. Satik, M. Parlar, and Y.C. Yortsos 291

Enthalpy Determination Using Flowing Pressure-Temperature Surveys in Two-Phase Wellbores in the Coso Geothermal Field
D.H. Kaspereit 293

LIST OF PARTICIPANTS 295

SUBJECT INDEX 303

AUTHOR INDEX 309

PREFACE

The Sixteenth Workshop on Geothermal Reservoir Engineering was held at Stanford University on January 23-25, 1991. The Workshop Banquet Speaker was Dr. Mohinder Gulati of UNOCAL Geothermal. Dr. Gulati gave an inspiring talk on the impact of numerical simulation on development of geothermal energy both in The Geysers and the Philippines. Dr. Gulati was the first recipient of The Stanford Geothermal Program Reservoir Engineering Award for Excellence in Development of Geothermal Energy. Dr. Frank Miller presented the award.

The registered attendance figure of one hundred fifteen participants was up slightly from last year. There were seven foreign countries represented: Iceland, Italy, Philippines, Kenya, the United Kingdom, Mexico, and Japan. As last year, papers on about a dozen geothermal fields outside the United States were presented.

There were thiry-six papers presented at the Workshop, and two papers were submitted for publication only. Attendees were welcomed by Dr. Khalid Aziz, Chairman of the Petroleum Engineering Department at Stanford. Opening remarks were presented by Dr. Roland Horne, followed by a discussion of the California Energy Commission's Geothermal Activities by Barbara Crowley, Vice Chairman; and J.E. "Ted" Mock's presentation of the DOE Geothermal Program: New Emphasis on Industrial Participation.

Technical papers were organized in twelve sessions concerning: hot dry rock, geochemistry, tracer injection, field performance, modelling, and chemistry/gas. As in previous workshops, session chairpersons made major contributions to the program. Special thanks are due to Joel Renner, Jeff Tester, Jim Combs, Kathy Enedy, Elwood Baldwin, Sabodh Garg, Marcelo Lippman, John Counsil, and Eduardo Iglesias.

The Workshop was organized by the Stanford Geothermal Program faculty, staff, and graduate students. We wish to thank Pat Ota, Angharad Jones, Rosalee Benelli, Jeanne Mankinen, Ted Sumida, and Terri A. Ramey who also produces the Proceedings Volumes for publication. We owe a great deal of thanks to our students who operate the audiovisual equipment and to Michael Riley who coordinated the meeting arrangements for a second year.

Henry J. Ramey, Jr.
Roland N. Horne
Frank G. Miller
Paul Kruger
William E. Brigham
Jean W. Cook

PROCEEDINGS, Sixteenth Workshop on Geothermal Reservoir Engineering
Stanford University, Stanford, California, January 23-25, 1991
SGP-TR-134

THE CALIFORNIA ENERGY COMMISSION'S GEOTHERMAL ACTIVITIES

Barbara Crowley

California Energy Commission
1516 Ninth Street
Sacramento, CA 95814

Thank you for the invitation to participate in this distinguished gathering. I would like to briefly relate the interests of the California Energy Commission in geothermal energy. Geothermal energy is a basic component of many of our primary activities, and is expressly cited in our statutory authority, the Warren-Alquist Act (1974).

Our mandates affect the geothermal industry both directly and indirectly. The Commission is responsible for 5-, 12-, and 20-year forecasts of California electricity supply and demand. These forecasts are reported in our biennial Electricity Report. These forecasts are used in various official regulatory proceedings. The primary use is in the Commission's power plant siting authority. The forecasts establish the base used to determine the need for new capacity and energy in the current planning period. The forecasts are also used in other Commission activities as well as in proceedings at the Public Utilities Commission.

The 1990 Electricity Report represents a dramatic change in the way this agency balances the relative importance of price competition, environmental quality, demand management as a system resource, and the implications of continued reliance on natural gas. Generally, the Commission is grappling with the elusive and complex problems of quantifying the appropriate value to assign to external (i. e., non-market) environmental attributes of competing technologies. While we have not decisively established such values, we do believe that they do exist and that we are moving in the right direction. The adopted policies have positive long term implications for geothermal and the other renewable technologies.

The Commission has been in existence since 1975 and during that time has seen the development of geothermal energy in several areas of the state. As a regulatory agency, we have authority over the construction of thermal electric plants over 50 megawatts (MW). To date the Commission has certified the construction of more than 1200 MW in the Geysers. This area is now experiencing a dramatic loss in productivity.

The Commission is engaged in a cooperative effort with the parties operating in the Geysers to address the problem of resource productivity. We held a hearing to examine the causes of the decline of the geothermal steam resources and its affect on electric energy supply. An outcome of the hearing was the establishment of a Technical Advisory Committee with the responsibility of providing the Commission projections of capacity and energy under the current rates of steam decline. The Committee was also charged with examining options on efficient resource management, including research and development, testing, and analyses regarding reservoir and power plant operations.

In addition to sharing Committee costs, the Commission is funding two county studies on the physical, economic, legal, and environmental constraints of developing new water sources for increased injection. The Commission has also joined with industry and the Department of Energy

in funding projects to ameliorate the problems at the Geysers.

Projects less than 50 MW are the jurisdiction of local authorities. For such projects, we have assisted local jurisdictions develop siting guidelines that are consistent with our certification in affordability, availability, reliability, and environmental acceptability.

Since 1981, the Commission has also offered grants and loans as well as technical assistance to cities, counties, special districts, Native American tribes, and municipal utilities. Two to three million dollars is available annually for this program. The funds can be used for geothermal related local planning and policy development, identification and mitigation of geothermal development impact, or resource exploration and development. The bulk of funding has been for resource assessment, exploration, and project development. Until recently, these efforts have focused on low temperature resource for direct application. The most prominent examples include district heating. Municipal projects in exploratory drilling for low temperature resources are in development stages.

The Commission is also interested in expanding the long term potential of geothermal resources. We are working with the Department of Energy on two research projects. A hot dry rock project conducted by Los Alamos National Laboratory is under way in the Geysers area, and a deep well project to extract heat from a magma body is being developed by Sandia National Laboratory in the North Eastern Sierra.

California has a strong geothermal industry. The Commission supports increasing the efficiency and competitiveness of the technology by cofunding innovative projects through the Energy Technology Advancement Program.

Further, the Commission serves as a liaison between industry and foreign governments which dominate overseas energy markets. We provide project opportunity information to California businesses and offer matching grants for feasibility studies. The Commission sponsors tours of geothermal areas for foreign visitors and provides opportunities to meet California vendors. These services are provided as part of a broader program which assists energy related businesses, the Energy Technology Export Program.

The State has the honor of being selected as the site of the headquarters of the next International Geothermal Association Secretariat. The Commission actively supported the effort to bring the IGA to California. The Commission encouraged and coordinated the Legislature's and the Governor's formal invitation. We look forward to this opportunity as a valuable focus for your Association. The Secretariat will provide facilities and resources at universities and the Commission for all IGA members.

The Commission has a commitment and continuing interest in this valuable and environmentally preferable indigenous resource. Thank you for inviting me and the Commission to participate in your prestigious activities.

PROCEEDINGS, Sixteenth Workshop on Geothermal Reservoir Engineering
Stanford University, Stanford, California, January 23-25, 1991
SGP-TR-134

DOE's GEOTHERMAL PROGRAM: NEW EMPHASIS ON INDUSTRIAL PARTICIPATION

John E. Mock, Director
Geothermal Division
U.S. Department of Energy

Gene Beeland
Meridian Corporation
Alexandria, Virginia

ABSTRACT

In line with industry's traditional strong role in targeting research priorities for the Department of Energy's geothermal program, the new policy thrust toward industry-driven R&D will complement our existing planning processes. Cost-sharing and leveraging of DOE's limited research resources remain critical elements, especially at The Geysers where DOE-funded research must have a very strong potential for yielding early industrial application.

Upcoming geothermal reservoir engineering program initiatives respond to industry's expressed need for new exploration technologies to find undiscovered geothermal resources where there are little or no surface manifestations and for drilling innovations to reduce the costs of exploration for such resources. In accord with the Department's policy of focusing on research supported by industry, long-term research on geopressured and hot dry rock resources has been reduced in scope or deferred.

INTRODUCTION

As the geothermal community gathers once again here at Stanford, we are supporting a new Department of Energy policy emphasis on industrial participation in renewable energy technology development. We have, in fact, been the vanguard of governmental/industry cooperation in technology development since the early 1970's, with industry playing a strong traditional role in targeting research priorities for the Department's geothermal program. Thus, the new focus on industry-driven R&D will complement our existing planning process. Cost-sharing and leveraging of DOE's limited research resources remain critical elements, and my remarks this morning will address these aspects of our program implementation with respect to the elements with which this audience is primarily concerned -- reservoir technology, with special emphasis on research at The Geysers and the potential commercial benefits to be derived.

FAVORABLE TRENDS FOR GEOTHERMAL DEVELOPMENT

First, however, I would like to review briefly trends in energy supply and demand and emerging environmental principles that appear to be healthy for geothermal development for the present, and optimistic and promising for the future. While all of you are no doubt generally aware of these trends, they bear repeating as a boost to our determination to continue to develop needed cost-effective hydrothermal technology.

I use the term "healthy" to describe both DOE's geothermal R&D program and industry's posture at the moment. California Energy Co., for example, has announced record third quarter 1990 revenue and earnings at the Coso installation that surpassed over 85 percent of its entire earnings for fiscal year 1989. Electricity output rose nearly 80 percent over the same period in 1989, and the Coso facility operated at 91.5 percent of capacity in the third quarter of 1990, compared to 83.5 percent for the first half of the year.

Magma Power continues to report quarter after quarter of record earnings generated by its plants at the Salton Sea and royalty payments from other plants. Its 1989 net income increased 140 percent over 1988, even before the last Salton Sea plant was completed in January 1990.

Richard J. Stegemeier, president of Unocal, has called Unocal's new Salton Sea geothermal facility the company's "crown jewels," and announced that Unocal's geothermal sales reached $188 million in 1990. Unocal is planning, he said, "to spend several hundred million dollars over the next several years for further exploration and development along the Pacific Rim's geologic 'ring of fire.' Currently the company is constructing a 110 MWe plant in Indonesia which culminates nearly a decade of exploration, field development, and negotiations with the Indonesian government.

I salute all of these industry successes as well as the many others that have come to fruition in recent years. Each of them has been reached via unique developmental pathways and with varying sources and amounts of financial support, but always with the vision

that geothermal energy is a highly efficient and cost-effective resource that, properly managed, can reap profits for industry's stockholders.

I believe that DOE's geothermal program is "healthy" for several reasons. Renewable energy technologies received a great deal of visibility and acceptance during the National Energy Strategy process. As a result, while the Department continued throughout 1990 to analyze and evaluate the many other energy options proposed, Secretary Watkins early in the year designated renewable energy for "fast track" consideration among the policy choices available. This action, combined with greater budgetary support from Congress, indicates an enhanced emphasis on renewable energy programs.

The direction of the geothermal R&D budget has been reversed for the first time in recent years. As shown in Table 1, appropriated funds for FY 1989 were $23.7 million, $17.8 million for FY 1990, and $27.9 million for this year, or FY 1991. I am pleased with this improvement, and feel that it is more than justified by the proven attributes of geothermal energy and the continuing participatory performance of industry in the R&D program.

The Department's leadership in establishing the concept of Integrated Resource Planning, or IRP, also supports a healthy climate for geothermal development. As you know, this utility planning process -- also known as Least Cost Utility Planning or LCUP -- includes the consideration of demand reduction and alternative energy sources in planning for the supply of future energy sources. This concept not only offers geothermal power a brighter future among supply-side alternatives, but can rapidly increase the market for direct use applications of this resource, as both a supply- and demand-side alternative. Utilities in this country and abroad are recognizing this phenomenon, or have already done so, primarily through the demonstrated benefits of geothermal heat pumps. By replacing electric resistance heating as the primary heat source for thousands of residences and commercial establishments, this technology has the potential to eliminate or postpone construction of costly power plants. In addition, the load leveling potential of geothermal heat pumps complements the base load strength of geothermal power, significantly reducing the seasonal demands on utilities. While the Geothermal Division has no mandate to support improvement in heat pump technology, we are looking at relatively quick and inexpensive methods for drilling shallow vertical (and horizontal) heat exchanger wells.

Another exciting prospect for geothermal's future is inherent in projections of increased power demand in regions where geothermal energy is available to pursue these markets along with competing fuels. According to a forecast adopted by the California Energy Commission last year, the peak demand for electricity by California's consumers, businesses, and industries will grow over the next 20 years by more than 23,000 MWe, the equivalent of providing energy to power 23 million additional homes. This represents a growth rate of 2.7 percent per year and is approximately a 50 percent increase over peak 1989 demand. The forecast shows a demand increase of more than 2,000 MWe compared to the Commission's 1988 projection.

Similarly, the highest of the annual power demand growth rate projections for the Pacific Northwest is placed at 2.5 percent. This forecast contrasts to a period of substantial electricity surplus at the lowest costs in the nation, a period in which new energy technologies had little, or no, opportunity to develop. According to the 1990 Annual Report of the Northwest Power Planning Council, the joint interim forecast of the Council and the Bonneville Power Administration indicated that, with very high economic growth, the region's need for power could climb by 13,000 MWe by the year 2010, up from the 16,620 MWe consumed in 1988. A more likely medium-low to medium-high economic growth would translate into a 2,400 MWe to 7,800 MWe increase in regional demand compared with 1988.

These statistics relate to <u>overall</u> power demand in key geothermal regions, but I believe the most exciting prospect inherent in these numbers is the potential for <u>specific</u> geothermal power demand. In California, according to CEC, the largest bulk of the additional demand will occur in areas served by Pacific Gas and Electric Co., Southern California Edison, and San Diego Gas and Electric. Untapped geothermal resources are available to all of these utilities, and all of them have substantial experience and expertise in geothermal operations. And, significantly, these utility service areas are populated by the world's most knowledgeable and capable independent geothermal power producers!

In the Pacific Northwest, the power surplus provided a grace period in which those responsible for the region's power needs -- both in planning and providing power -- could learn how to deal with uncertainty and evaluate and select resources in a manner that would be the least costly to the regional electrical power system. As a result of comprehensive studies of various scenarios critiqued by technical advisory committees and energy and environmental organizations, the NPPC decided to include 350 MWe of geothermal power in its resource portfolios analysis and evaluate another 1,000 MWe to determine its role in the Power Plan. Specifically, for the near term, the Council is recommending the acquisition of three geothermal demonstration projects at separate sites in the Cascades, producing at least 10 MWe each. Who would have thought,

even two years ago, that this market would soon be opened this fully to geothermal development.

The geothermal industry's ability to respond expeditiously to this challenge in the Northwest is enhanced greatly by the results of the DOE/industry cost-shared drilling projects at promising prospect areas in the Cascades. This is but one more example of the commercial benefits that derive when government and industry pool their limited resources to reach a common goal.

To me, however, of equal importance to the opportunities opened to geothermal operations through increased demand is the shift toward incorporating "external" costs and benefits -- or externalities -- into the energy decision making process by using least-cost or integrated resource planning as described above. The Northwest Power Planning Council, for example, in preparing its 1991 power plan defines "least-cost" and "cost-effective," to refer "to total costs to society, including environmental, labor, and other capital costs." In California, CEC's adopted demand forecast "for the first time explicitly takes into account the impacts of air quality rules adopted by the South Coast Air Quality Management District." The rules adopted include measures for reducing emissions from fuel combustion, some of which would require the use of electricity instead of other fuels in industrial facilities. In its evaluation of ways that utilities can meet future power demands, the Commission has announced that it will determine the best mix of these alternatives balancing environmental, energy security, and economic concerns and goals. How can geothermal lose under this set of criteria?

The outlook abroad is also promising. A compilation of statistics provided to the World Bank indicate that developing countries plan to more than double their geothermal power capacities during the 1990's from 2 GW to 5 GW. Our U.S. geothermal industry, with the assistance and support of DOE, has established an Export Trading Company to enhance its ability to tap this large overseas market. We wish the companies every success in their venture. With each successful geothermal project, wherever it is located, the perception of geothermal energy as a reliable and desirable fuel grows in those places where its reputation counts -- at the energy policy- and decision-making level, whether local, regional, national, or international.

CURRENT R&D PROGRAM

To answer my rhetorical question above, geothermal energy can "lose" even under very favorable circumstances if technology development does not advance sufficiently rapidly to help find new resources to support long-term industry growth and to facilitate economic definition of known resources. These objectives are the focus of this workshop and DOE's Reservoir Technology Task. The Department's current budget for reservoir R&D has increased over allocations for recent years; I wish to emphasize, however, that while the trends are healthy, the funds committed remain "limited" in light of today's costs and the broad needs in terms of technology innovations, improvements, and remedial measures needed for geothermal energy to achieve its full potential. Thus, the continued commitment of industry support to various R&D projects is essential, first, to DOE approval of specific projects, and, second, to the successful conclusion of approved projects. Nowhere is this participation more necessary than at The Geysers where both federal and private interests are at stake.

I am happy to report this morning that industry is not only supporting DOE-sponsored research at The Geysers, its contributions are quite substantial. Estimates are that industry spent $3.5 million in FY 1990 and that it has committed $4.5 million this year. Most of last year's expenditures were for the injection tests performed jointly by the Northern California Power Agency and Calpine Corp., with instrumentation assistance from Unocal. The data developed are being provided to DOE for use in additional research, a major milestone in government/industry cooperation. DOE's expenditures at The Geysers for the same two years are $1.2 million and $2.5 million, respectively.

Proposals for DOE-supported research are reviewed by a "Steering Committee for Geysers Research" consisting of representatives of the Unocal Geothermal Division, Calpine Corporation, Northern California Power Agency, and Coldwater Creek Operator Company, with Marcelo Lippmann of the Lawrence Berkeley Laboratory (LBL) acting as coordinator. At this writing, 41 proposals have been reviewed for FY 1991 funding. Contract awards are expected this month after some proposers provide more information on specific milestones and deliverables. In the case of the proposals that did not meet the requirements of the Steering Committee, it was suggested that their authors communicate with industry to better discern industry's needs. This approach is in line with the policy that research funded at The Geysers must have a very strong potential for yielding results that have early industrial application and will benefit industry. In addition to DOE, the major non-industry participants in The Geysers research are:

- Idaho National Engineering Laboratory
- Lawrence Berkeley Laboratory
- Lawrence Livermore Laboratory
- Oak Ridge National Laboratory
- Stanford University Geothermal Program
- University of Utah Research Institute

In addition, the Brookhaven National Laboratory is participating in corrosion mitigation, the U.S. Geological Survey is working with others to investigate the buildup of hydrochloric acid in the field, and the specialties of other widely diverse institutions are being tapped for specific research needs.

During FY 1990 significant progress was made on Geysers projects, but results are not yet quantifiable in all cases. The achievements are summarized in Table 2. Preliminary results indicate, for example, that the research correlating seismic velocity and attenuation images to geological and reservoir conditions demonstrated a methodology that can be used to locate steam and 2-phase zones. This in turn will lead to improved well siting and to better reservoir management policies.

Geysers projects for this year are summarized in Table 3 along with reservoir-oriented projects for wider application. The number of geophysical activities aimed toward improving this technology for geothermal application is too numerous to describe in detail here, but I want to point up one project that we expect to advance the exploration for as yet undiscovered resources. Numerical analysis will be performed to determine theoretical geophysical responses from fluid-filled fractures, and field tests of surface geophysical techniques will be designed and conducted to verify the responses to be expected. The use of new interpretation methods for these advanced geophysical techniques for locating fractured hydrothermal systems will be investigated, concentrating on electromagnetic and passive seismic exploration methods. The observed geophysical data will be combined with laboratory measurement of physical properties and existing geologic data to provide exploration plans for regions such as the Cascades volcanic province for which data sets are available. I feel sure that other speakers will provide the details of other on-going and anticipated geophysical projects.

In other R&D areas, work is continuing on improvements in technology to identify the location and extent of lost circulation zones and methods for plugging; advanced drilling and coring concepts are being explored with emphasis on high-temperature drilling systems for operation above 300°C; and downhole electronic memory tools for use in very harsh geothermal environments are in development.

The heat cycle research is continuing efforts to increase the net fluid effectiveness of binary technology and to reduce the consumptive cooling water requirements for geothermal power plants and still maintain heat rejection performance comparable to that of a conventional wet cooling system.

Corrosion mitigation at The Geysers involves development and testing of material for lining casing and installation of a lined casing string for downhole evaluation. Other materials developments include lightweight cements resistant to carbon dioxide, thermally conductive polymer concrete liners for heat exchangers, chemical systems for lost circulation control, and high-temperature chemical coupling systems. The equilibrium model of complex brine chemistry is being prepared for use with personal computers to enhance its usefulness in the field, and analysis of the first generation of modified bioreactors for the treatment of waste sludges will be completed.

In accordance with the Department policy of focusing on research supported by industry, long-term research on geopressured and hot dry rock resources has been reduced or deferred. However, industry and the State of California are now expressing interest in using geopressured brines for such purposes as thermal enhancement of oil recovery (TEOR) and supercritical waste treatment, and the Department is considering participation in these efforts. Where geopressured fluids are collocated with fields of medium and heavy oils, TEOR with the naturally heated fluid would provide an environmentally clean method of recovery and add millions of barrels of oil to the country's recoverable resources. Supercritical water oxidation (SCWO) of hazardous organic chemical wastes is an emerging self-sustaining technology. It is a low-temperature chemical reaction effective for contaminated water, concentrated organics, and complex mixtures in which the effluent is fully controlled.

The experimental hot dry rock reservoir at Fenton Hill, New Mexico, will be subjected to a long-term flow test beginning next year which will provide a basis for future commercial exploitation of hot dry rock resources worldwide. A generalized economic model recently developed by researchers at the Massachusetts Institute of Technology, Drs. Jefferson W. Tester and Howard J. Herzog, indicates that high-grade HDR resources (i.e., an average gradient of 80°C/km) are competitive with $18/barrel oil, and that mid-grade (50°C) would be competitive with oil at more than $30/barrel, and/or if environmental costs associated with fossil-fuel systems -- e.g., an acid rain or carbon tax -- were included. Thus the hot dry rock research performed over nearly 20 years has established the potential commercial viability of yet another form of geothermal energy.

CONCLUSION

In concluding these remarks I would like to quote a former U.S. senator from Nevada -- Senator Alan Bible. As early as 1973, the Senator wrote:

"What are the prospects for geothermal power? The answer depends on the willingness of the federal government and the willingness and capacity of private industry and the scientific community to get on with the task of ascertaining the technical and economic feasibility and environmental acceptability of the development of geothermal resources."

All three of the entities he charged with the responsibility for determining the course of the development of this "ageless phenomenon and challenging new frontier" are represented here, and we have met our responsibilities. The sessions this week will further our cooperative efforts to pursue even greater horizons for geothermal energy.

TABLE 1

DOE GEOTHERMAL PROGRAM BUDGET
($1,000)

	FY 1989	FY 1990	FY 1991
HYDROTHERMAL			
Hard Rock Penetration	2,250	2,205	2,385
Reservoir Technology	2,450	2,074	5,500
Conversion Technology	1,935	1,527	1,943
Other	0	0	7,800**
TOTAL	6,635	5,806	17,628
GEOPRESSURED	10,380	5,755	6,000
HOT DRY ROCK	1,635	5,039*	4,967***
MAGMA	3,500	*	***
OTHER			
Capital Equipment	795	444	405
Program Direction	826	814	900
TOTAL	**23,771**	**17,858**	**27,900**

* New category designation; "Advanced Systems" includes $3,390 for hot dry rock and $1,649 for magma.
** Includes activities in Hawaii, Boise, Oregon Institute of Technology, and other low-temperature projects.
*** Advanced Systems includes $3,967 for hot dry rock and $1,000 for magma.

TABLE 2

SIGNIFICANT FY 1990 ACCOMPLISHMENTS OF GEYSERS RESEARCH

- Preparation of a major subset as "MULKOM" modules for release of "TOUGH2"; documentation of code futures.
- Analysis of microseismic signals to produce seismic and attenuation images and their relationship to geological and reservoir conditions.
- Development of laboratory equipment for measuring HC between liquid and vapor phases.
- Expansion of existing algorithms to include calculations of trapping pressures from estimates of the CO_2 contents of inclusion fluids and to calculate pressure corrections for NaCl concentrations up to 26 weight percent.
- Numerical simulation of injection into superheated zones vs. injection into 2-phase vapor-dominated zones.
- Identification of hydrochlorofluorocarbons as suitable tracers for a vapor-phase environment and methodologies for injecting, sampling, and analyzing tracers in vapor-dominated reservoirs.

TABLE 3

SUMMARY OF FY 1991 RESERVOIR TECHNOLOGY RESEARCH AREAS FOR SPECIFIC APPLICATION AT THE GEYSERS AND/OR OTHER HYDROTHERMAL RESERVOIRS

- Development and testing of new advanced geophysical equipment and interpretive methods for locating fractures and permeable zones, determining fluid concentrations, and estimating reservoir generating capacity and longevity for use in exploration and field development.
- Refinement of predictive models and investigation of the applicability of existing numerical simulations to Geysers problems.
- Development of conceptual models for geothermal exploration.
- Development of cryogenic gravimeters to detect minute changes in mass within the earth.
- Development and testing of tracer materials and techniques for tracer injection, sampling, and interpretation.
- Analysis of the strength of seismic signals produced by fluid injection and production.
- Investigation of HCl formation at The Geysers.
- Incorporation of experimental data into brine chemistry equilibrium model.
- Investigation of relationship of adsorbed water on fracture surfaces to Geysers development.
- Evaluation of remote sensing and biogeochemistry as geothermal exploration tools.

PROCEEDINGS, Sixteenth Workshop on Geothermal Reservoir Engineering
Stanford University, Stanford, California, January 23-25, 1991
SGP-TR-134

QUALITY CONTROL OF CHEMICAL AND ISOTOPIC ANALYSES OF GEOTHERMAL WATER SAMPLES

Marshall J. Reed[1] and Robert H. Mariner[2]

1. Geothermal Division, U.S. Dept. of Energy, Washington, DC 20585
2. Water Resources Division, U.S. Geological Survey, Menlo Park, CA 94025

ABSTRACT

Chemical and isotopic analyses of geothermal water samples must meet certain levels of accuracy and reliability to be useful for identifying geochemical processes in hydrothermal systems. Quality control is largely a concern for the analytical laboratory, but the geochemist or reservoir engineer using the chemical data must also be concerned with analytical quality. To test accuracy and reliability of analyses available from laboratories, splits of seven water samples were sent to four stable-isotope laboratories, and splits of five water samples were sent to four chemical laboratories. The analyses of each sample were compared among laboratories, and the differences in analyses were evaluated using criteria developed for this comparison. Isotopic compositions were considered reliable if they deviated from mean values by less than 2‰ for hydrogen and by less than 0.15‰ for oxygen. Concentrations of each chemical component were considered reliable if they differed from mean values by less than 10%. Chemical analyses were examined for internal consistency by calculating the error in ionic charge balance and the error between ionic charge and electrical conductivity. To be considered internally consistent, chemical analyses must have less than 5% error in charge balance and less than 10% error in conductivity balance. Three isotope laboratories gave consistent compositions of all samples. No chemical laboratory gave consistent analyses of all samples. Recommendations are made that provide the user of isotopic and chemical data with the ability to better evaluate the quality of analyses.

INTRODUCTION

The examination and interpretation of geochemical data can provide powerful tools for characterizing newly discovered geothermal systems and for monitoring the production and injection of developed geothermal reservoirs. Chemical analyses have long been used to estimate subsurface temperatures, and computer simulations of multiple geochemical equilibria provide the means for predicting scaling and corrosion, for estimating loss of reservoir permeability from mineral precipitation, and for detecting breakthrough of injected water. Isotopic analyses may provide qualitative indications of source areas and volumes for recharge to hydrothermal systems and are used to calculate additional estimates of reservoir temperatures. Isotopic analyses have also been used to determine the contribution of injected water to the total fluid produced from developed geothermal fields. Increasing sophistication of geochemical modeling programs now possible on larger computers makes it imperative to question the quality of isotopic and chemical data. More complex geochemical calculations are not meaningful if the accuracy and precision of the analytical data used in those calculations are questionable.

It is common in studies of aqueous geochemistry to assume that chemical analyses report concentrations that are within ±10% of the actual concentration of any constituent. It is worth noting the limitations that a 10% error places on the most common geochemical calculations, the chemical geothermometers. For a reservoir temperature of 275°C, a 10% error in silica or sodium concentration will change the calculated temperature by about 10°C; and, for a reservoir temperature of 85°C, a 10% error in silica or sodium will change the temperature by 3 to 4°C. In order to evaluate the validity of this often-assumed error limit and to determine the reliability of isotopic data, a test was conducted to compare analyses from several laboratories which analyze geothermal water samples on a routine basis.

Many inter-laboratory comparisons have been conducted in the past, and two recent comparisons dealt with hydrothermal waters. Ellis (1976) sent seven waters to 48 laboratories in 18 countries, and he concluded "the standard of water analysis for many common constituents still leaves much to be desired." Giggenbach and others (1986) sent three waters to 22 laboratories in 19 countries, and they concluded "that there is ample room for improvement." Due to the large number of laboratories used in both of these previous studies, extensive statistical analysis of reported concentrations was possible. In both reports, concentrations of several chemical constituents varied by more than 10% from the mean value.

Many geothermal researchers performing geochemical calculations depend on analyses of samples collected and analyzed by others. This report first discusses methods used to evaluate reported analyses, and then makes suggestions for collection and

analysis of new samples. As more geothermal researchers develop and apply geochemical tools to interpret reservoir conditions, it is expected that many will want more control over the collection and analyses of samples.

EVALUATION CRITERIA

Isotopic compositions for hydrogen and oxygen are reported as the difference (δ) between the ratio of isotopes in a sample and the ratio in the standard (equation 1):

$$[1] \quad \delta = \frac{R(\text{sample}) - R(\text{standard})}{R(\text{standard})} \; 10^3$$

$$\text{where } R = \frac{^{18}O}{^{16}O} \text{ or } R = \frac{D}{H}$$

All ratios (R) are of the heavier isotope to the lighter isotope. This small difference in ratios is reported in per mil (‰) relative to V-SMOW (Vienna standard mean ocean water, Gonfiantini, 1978). Isotopic compositions of geothermal fluids vary widely, and individual analyses contain little intrinsic information that can be used to check their validity. To evaluate the isotopic analysis of an aqueous fluid sample (water or steam), both hydrogen and oxygen isotopic ratios must be determined. Isotopic compositions for water samples can easily be plotted against the global meteoric water line (Craig, 1961) to rapidly identify unusual analyses. The meteoric water line, derived from values for precipitation (rain and snow), rivers, and lakes world wide, is represented by the following expression (2):

$$[2] \quad \delta D = 8 \, (\delta^{18}O) + 10$$

where δD and $\delta^{18}O$ are the differences calculated from equation 1. Geothermal water samples usually plot at some distance to the right of the meteoric water line, depending on the amount of oxygen-isotope exchange that has occurred at high temperature between the water and rocks (which typically have more ^{18}O). There is limited possibility for hydrogen-isotope exchange in hydrothermal systems, and the hydrogen isotopic composition of a fluid sample is usually very close to that of the meteoric water which recharges the system. Fluid samples plotting to the left of the meteoric water line are rare and may be suspect.

The evaluation of a chemical analysis depends on the degree to which the analysis reflects the complete composition of the water sample. Many reports include only partial analyses used for a specific purpose, and the quality of partial analyses can rarely be evaluated. Chemical analyses can best be evaluated if they include the field measurement of pH, a complete suite of the major ions (Li, Na, K, Ca, Mg, F, Cl, SO_4, and HCO_3), and the laboratory measurements of pH and conductivity. The chemical species of considerable geothermal interest (SiO_2, B, and Fe) should be added to the basic analyses. From the concentrations of the major ions, it is possible to calculate charge balance and conductivity balance of the sample.

Some general relations are common in geothermal water samples. The concentrations of the cations usually follow a trend with Na > K > Li and Ca > Mg. Among samples from a single system, SiO_2 increases with increasing temperature. The occurrence of other major ions in the analysis, such as phosphate or nitrate, is normally an indication of contamination from surface water.

A few simple calculations were used to determine the reliability of the chemical analyses performed for this inter-laboratory comparison. The ionic species were expressed as equivalent concentrations from the following calculation (equation 3):

$$[3] \quad \text{Equiv. Conc.} = \frac{(\text{concentration})\,(\text{ionic charge})}{\text{molecular weight}}$$

where molecular weight is in grams/mole, concentration is in milligrams per liter (mg/L), and equivalent concentration is in milliequivalents per liter (meq/L). Using equivalent concentrations of the ions, the error in charge balance was calculated from the absolute difference between the sums of cations and of anions divided by the average of the total cations and anions (equation 4):

$$[4] \quad \text{Error (\%)} = \frac{200 \, |\Sigma\text{Cations} - \Sigma\text{Anions}|}{(\Sigma\text{Cations} + \Sigma\text{Anions})}$$

The water can have no net electrical charge, so an error greater than 5% in the ionic charge balance is indicative of a problem and the analysis should be repeated. This limit is based on the experience of the authors, and there must be a compromise between a restrictive limit that few samples would pass and a permissive limit that would ignore a significant error in a major ion.

If the electrical conductivity of a water is measured, a comparison can be made between the ionic charge and the electrical conductivity (referred to here as the conductivity balance). The calculation of error is based on an empirical relation for the conductivity of sodium chloride solutions at 25°C. Different ions in solution act to increase or decrease the conductivity from that of sodium chloride, but the relation holds well for many natural waters (Hem, 1970, p. 235). The error in conductivity balance was calculated using the following expression (5):

$$[5] \quad \text{Error (\%)} = \frac{100 \, |\text{conductivity} - (100 \; \Sigma\text{Cations})|}{\text{conductivity}}$$

where the conductivity is in standard units of microsiemens per centimeter (μS/cm), and the sum of equivalent concentrations of cations (or anions) is first multiplied by 100. The error in electrical conductivity balance should be less than 10% for either anions or cations.

Errors in charge balance of more than 5% or in conductivity balance of more than 10% usually result from three main sources: 1) an important ion was not analyzed, 2) a mistake was made in an analysis of a major ion, and 3) a decimal point was misplaced. If the conductivity balance error is low for cations and high for anions, the anion analyses are the likely source of error. Calculations of error in charge balance and in conductivity balance only consider the ionic species. Some waters with high concentrations of unusual ions may repeatedly fail these tests. Friedman and Erdmann (1982) describe the quality assurance program of the USGS National Water Quality Laboratory and give further discussion of ways to identify analytical errors.

If the same water samples were analyzed by several laboratories, the concentrations of each constituent may be compared among laboratories by calculation of the means and deviations from the means. If the concentrations from one laboratory are significantly different (greater than 15%) than those from other laboratories, the anomalous concentrations are suspect. Geochemical calculations made in the examination of a geothermal water are only valid if the constituent concentrations used in the calculations are from one analysis at a time. Many geothermal researchers have averaged concentrations of a constituent (such as silica) from several different samples and suggested that calculations using these averages are more significant in evaluating reservoir conditions. By using averages, these researchers have actually ignored the possible errors in individual analyses and have presented a concentration that is not directly related to the reservoir or to the conditions during sample collection or analysis.

ISOTOPIC ANALYSES

Sample Collection

Based on the discussion above, several procedures are available to judge the reliability of geochemical data received from a laboratory. Evaluation of reported analyses is limited to calculations and comparisons that examine internal consistency. Much greater control of analytical quality is available if new samples are submitted for analysis. In submitting new samples, there is the possibility for interaction between the collector and the analyst that may result in more meaningful analyses. Water samples for isotopic analysis should be collected and shipped in 60-ml glass bottles with air-tight (polyseal) caps, and every effort should be made to prevent evaporation. This volume of sample will allow repeat analyses if necessary. If an error is suspected in sample preparation or in mass spectrometric analysis, the analyst should attempt to measure a duplicate preparation.

Suggestions for Isotopic Analyses

It is not cost effective for most researchers to request isotopic analyses from more than one laboratory, so the laboratory to be used should be chosen carefully. Most stable-isotope laboratories will have a quality control manual, and a copy of the manual should be requested when a laboratory is being considered for analytical work. Requests for isotopic analyses should include differently labeled duplicates of about 10% of the samples to provide an internal check of analytical consistency. It is useful to resubmit a water sample that has been analyzed for isotopic ratios at some previous time and to compare the results. The USGS Water Resources Division isotope laboratory (Reston, VA) routinely divides incoming waters into two samples, and each is analyzed on a different day to identify any instrumental or procedural errors. This procedure of dividing samples is not common to all laboratories, and duplicate samples submitted at different times will provide a check on time dependent errors. It is reasonable to request the isotope values obtained for the standards used to calibrate the analyses of a set of your samples as well as the established values for those standards. This request becomes more important if a laboratory is used repeatedly with the same standards.

Analytical Methods

All isotopic ratios were determined by mass spectrometry, but equipment and analytical methods differed among laboratories. The standard methods used to exchange oxygen isotopes of water with carbon dioxide, to separate and measure the carbon dioxide isotopic composition, and to calculate the composition of the water are described by Epstein and Mayeda (1953). Two different methods were used to prepare hydrogen from water samples for isotopic analysis. The older method involves conversion of water to hydrogen gas through reaction with uranium metal at temperatures from 400 to 700°C (Bigeleisen and others, 1952). More recently, many laboratories have used zinc shot to convert water to hydrogen gas, and Tanweer and others (1988) suggested zinc reaction at temperatures over 460°C and a ten-fold excess of zinc over the stoichiometric amount required. Only the USGS Geologic Division isotope laboratory (Menlo Park, CA) used the older uranium method. The USGS Water Resources Division isotope laboratory (Reston, VA) now uses the Japanese Hokko (trademark) beads (3% platinum) to equilibrate isotopes between water and hydrogen, but this method was not used for analyses in this report.

Test Results

Splits of seven water samples were sent to three isotope laboratories within the USGS and to a laboratory which preforms commercial analyses. Interlaboratory comparison of isotope compositions of hydrogen and oxygen in each sample was limited to calculation of the deviation from the mean of the measurements. The limited number of analyses did not warrant further statistical calculations. Isotope compositions determined by the various laboratories are generally very similar. Significant differences

exist in the age of the mass spectrometers and in the methods of sample preparation. Based on the limits of reproducibility, analyses were considered anomalous if the measurements deviated from the mean value by more than 2‰ for hydrogen or by more than 0.15‰ for oxygen. The USGS Geologic Division laboratory (Menlo Park, CA) has the oldest mass spectrometer of the laboratories in this comparison, and analyses slightly exceeded our acceptable error limits on two hydrogen isotope measurements and three oxygen isotope measurements. The remaining analyses were within acceptable limits.

CHEMICAL ANALYSES

Sample Collection

At the time of collection, the temperature and pH should be measured, and the total alkalinity of the water determined by titration with 0.05N sulfuric acid to the inflection point of the titration curve (Barnes, 1964). Most chemical species should be preserved during collection to stabilize concentrations for later analysis in the laboratory. Water samples should be prepared for laboratory analysis as follows: 1) for anion analysis, a portion of the water should be filtered through 0.45-μm pore size membrane filter to remove particles and biological material, and 2) a portion of the water should be filtered and acidified to pH 2 with concentrated, high-purity hydrochloric acid to stabilize the cations, particularly magnesium, calcium, and iron, by preventing precipitation of carbonates, sulfates, or hydroxides. Samples should be shipped in 500-ml polypropylene bottles with tightly fitting caps. Blanks of distilled, deionized water, should be treated in the field with the same procedures and preservatives as the samples to test for contamination in sampling and processing.

Suggestions for Chemical Analyses

As suggested for isotopic analyses, sets of samples submitted for chemical analyses should include differently identified (blind) duplicates of some samples to provide an internal check of analytical consistency. It is also useful to resubmit water samples that have been analyzed at some previous time and to compare the results. Duplicates of some water samples can be spiked with known additions of specific ions to test the analytical ability of a laboratory to determine the increase in concentration.

Analytical Methods

The chemical laboratories chosen for this comparison used different methods for preparation and analysis of the samples. Each laboratory used similar methods for chloride (Mohr - argentometric titration), fluoride (ion-selective electrode), alkalinity (acid titration), and conductivity (electrical cell) analysis. The atomic absorption method was used to determine cation concentrations (Na, K, Li, Ca, Mg, Fe) by three laboratories; but one used inductively-coupled argon plasma (ICP) spectrophotometry. Silica concentration was determined by the molybdate-blue method in two laboratories or by ICP in two laboratories. Three laboratories determined boron by ICP (one also checked the boron with vis-UV), but one lab used the dianthrimide method. Sulfate was determined gravimetrically by two laboratories, one used a turbidimetric titration, and one used ion chromatography. Each analytical method has a concentration range for optimum measurement. As the lower limit of detection is approached, the percent error could become very large. To properly evaluate the analyses, laboratories must report their limits of detection for each chemical species.

Test Results

One USGS Laboratory and three commercial laboratories were selected for this analytical comparison because they performed many analyses on geothermal water samples. This inter-laboratory comparison produced some interesting and surprising results. Correspondence among the chemical analyses of the five water samples was worse than expected. None of the four laboratories provided completely acceptable analyses of all samples, and one laboratory reported significantly anomalous concentrations of major solutes in all five samples. We conclude that it would be poor judgment to rely on chemical analyses from only one laboratory without a thorough understanding of the quality assurance procedures of that laboratory. From calculations of charge balance and conductivity balance, many of the worst analyses were easily identified, and repeat analyses could be requested. These calculations should have been performed routinely by the analytical laboratories to avoid reporting obvious errors. The concentrations of lithium, magnesium, iron, fluoride, and sulfate in some samples were below the limits of detection for the analytical methods used. One laboratory did not report an acceptable value for chloride in any of the five samples (three were low and two were high), and, as a result, calculated errors in charge balance and conductivity balance were also unacceptably high. This difficulty with all of the chloride concentrations reported, strongly suggests instrumental or procedural errors. It must be remembered that we are comparing the values reported by individual labs against the average of selected values. With the exception of silica, where ICP gives higher concentrations than molybdate blue, the use of different analytical methods does not seem to be responsible for the inter-laboratory differences.

ACKNOWLEDGEMENTS

The authors greatly appreciate the cooperation and information provided by the analysts about their analytical methods and their routine error checking. Suggested changes by several reviewers have enhanced this report. The review of Cathy Janik (USGS) is especially appreciated. Funding for this project was provided by the Geothermal Division of the U.S. Department of Energy and by the Geothermal Research Program of the U.S. Geological Survey.

REFERENCES

Barnes, I., 1964, Field measurement of alkalinity and pH: U.S. Geol. Survey Water-Supply Paper 1535-H, p. 1-17.

Bigeleisen, J., Perlman, M. L., and Prosser, H. C., 1952, Conversion of hydrogenic materials to hydrogen for isotopic analysis: Anal. Chem., v. 24, n. 8, p. 1356-1357.

Craig, H. 1961, Isotopic variations in meteoric waters: Science, v. 133, p. 1702-1703.

Ellis, A. J., 1976, The IAGC interlaboratory water analysis comparison programme: Geochim. Cosmochim. Acta, v. 40, p. 1359-1374.

Epstein, S. and Mayeda, T., 1953, Variation of O18 content of water from natural sources: Geochim. Cosmochim. Acta, v. 4, p. 213-224.

Friedman, L. C. and Erdmann, D. E., 1982, Quality assurance practices for the chemical and biological analyses of water and fluvial sediments: U.S. Geol. Survey, Techniques of Water-Resources Investigations, Bk. 5, Chap. A6, 181 p.

Giggenbach, W. F., Goguel, R. L., and Singers, W. A., 1986, Immediate report on interlaboratory comparative geothermal water analysis program: Vienna, Austria, International Atomic Energy Agency, unpublished), 20 p.

Gonfiantini, R., 1978, Standards for stable isotope measurements in natural compounds: Nature, v.271, p. 534-536.

Hem, J. D., 1970, Study and interpretation of the chemical characteristics of natural water; Second edition: U.S. Geological Survey Water-Supply Paper 1473, 363 p.

Tanweer, A., Hut, G., and Burgman, J. O., 1988, Optimal conditions for the reduction of water to hydrogen by zinc for mass spectrometric analysis of the deuterium content: Chem. Geol. (Isotope Sec.), v. 73, p. 199-203.

PROCEEDINGS, Sixteenth Workshop on Geothermal Reservoir Engineering
Stanford University, Stanford, California, January 23-25, 1991
SGP-TR-134

THE ORIGIN OF HIGH-TEMPERATURE ZONES IN VAPOR-DOMINATED GEOTHERMAL SYSTEMS

Alfred H. Truesdell

700 Hermosa Way,
Menlo Park, California 94025

ABSTRACT

Vapor-dominated geothermal systems are proposed to originate by downward extension (by the "heat pipe" mechanism) into hot dry fractured rock above a large cooling igneous intrusion. High temperature zones found by drilling are shallow parts of the original hot dry rock where the penetration of the vapor reservoir was limited, and hot dry rock may extend under much of these reservoirs. An earlier hot water geothermal system may have formed during an early phase of the heating episode.

INTRODUCTION

Intensive drilling at The Geysers and Larderello has shown that these large geothermal fields have vapor-dominated reservoirs over most explored areas and depths. Recent deep drilling at Larderello and exploration of the northern edges of The Geysers have encountered zones with temperatures substantially higher than those extrapolated from the temperature gradient of the vapor-dominated reservoirs, suggesting a different type of reservoir. Although available drilling data and physical measurements from Larderello are limited (Cappetti et al., 1985), a high-temperature zone in the northern Geysers is well documented (Drenick, 1986; Walters et al., 1988). The presence of these high-temperature zones should be accommodated in existing models of vapor-dominated systems or new models should be formulated. This paper discusses this problem and suggests a conceptual model based in part on earlier published work but with some individual features. This model is being studied by numerical simulation at the Lawrence Berkeley Laboratory.

OBSERVATIONS

In major and minor vapor-dominated geothermal systems, pressures and temperatures in the reservoir increase slowly with depth, and high heat flow with little fluid flow is observed at the surface. Wells drilled into these systems produce saturated or superheated steam often with some initial liquid. The top of these reservoirs tend to be at 235°C and 32 bars abs, although exceptions are observed. Since the early 1970's there has been general agreement that in the natural state these reservoirs contain counterflows of rising steam and descending condensate that constitute "heat pipes" (White et al., 1971). Observed condensation of steam at the top of the reservoir contributes high heat flow to overlying rocks, but the origin of the steam (and the fate of the condensate) has never been observed. Boiling liquid below a liquid-vapor interface has been assumed by most workers and lateral transport of liquid below such an interface is necessary to explain gas concentration patterns due to steady-state Rayleigh condensation. Salts leached by descending condensate have been assumed to accumulate in the boiling liquid forming a brine.

Recent detailed observations of dry high-temperature zones at The Geysers (Drenick, 1986; Walters et al., 1988) and observations of deep high temperatures at Larderello (Bertini et al., 1955; Batini et al., 1985; Cappetti et al., 1985; Pruess et al., 1987) provide the first direct evidence of the character of these systems below the vapor-dominated reservoirs. The Larderello observations are not very detailed but show that some deep wells (VC-11, PC-29, Sasso 22, and San Pompeo 2) have bottom-hole temperatures of 350-400°C that lie well above the depth-temperature relation for the normal vapor-dominated reservoir (fig. 1 modified from Pruess et al., 1987). An analytical and numerical study by Pruess et al. (1987) concluded that the temperatures measured were originally those of a liquid-dominated heat pipe below the vapor-dominated reservoir. The highest temperatures (383°C at 4000 m depth and 394°C at 2560 m) reported by Cappetti et al. (1985) are above the critical point of pure water.

The high-temperature zone(s) of the NW Geysers have been encountered by wells drilled by several companies. Evidence for the existence of high temperatures and distinct fluids in wells owned by Geothermal Resources International-GEO Operator Corp. (now Coldwater Creek Operator Corp.) has been published by Drenick (1986) and Walters et al. (1988). These accounts are highly detailed and only the observations of most importance to this paper are summarized.

The GEO wells penetrated the normal vapor-dominated reservoir with temperatures near 245°C and entered an underlying high-temperature reservoir at depths between 1700 m and 2000 m. Flowing steam temperatures measured in the well exceeded 335°C in some instances and bottom-hole temperatures measured during drilling may have exceeded 347°C. The high-temperature steam was distinctive chemically with 2 to 10 times higher gas than steam from the normal reservoir, about 200 ppm HCl (normal steam has < 1 ppm), and was enriched in hydrogen and oxygen isotopes. The transition from the normal to the high-temperature reservoir is very sharp. In figure 6 of Walters et al. (1988), the transition from bottom-hole temperatures (cooled by drilling air) of about 200°C to (cooled) bottom-hole temperatures greater than 300°C occurs within 150 to 200 m, and the transition of return air temperatures from 210°C to 260°C was even more abrupt (< 100 m?). Measured pressures

were essentially identical in the two reservoirs,and there was no mineralogical or drilling evidence of a low permiability barrier. Models based on these observations were proposed by Drenick (1986) and Walters et al. (1988) and will be discussed later.

MODELS OF VAPOR-DOMINATED SYSTEMS

General agreement concerning the structure and properties (origin of superheat, etc.) of vapor-dominated reservoirs has existed since the early 1970's when White et al. (1971) suggested that the exploited reservoir in the natural state contains counter-flowing steam and condensate functioning as a heat pipe. About the genesis of this reservoir there is less agreement, although the formation of vapor-dominated reservoirs from hot-water reservoirs has been simulated in several studies (Pruess and Truesdell, 1981; Pruess, 1985; Ingebritsen and Sorey, 1988). The high-temperature zones observed in the field were not produced in these simulations and are not consistent with the White et al. (1971) model. For this reason it will be useful to reexamine other models to see if they hold any clues.

ORIGINAL VAPOR MODELS

Goguel (1953) hypothesized that at Larderello an igneous intrusion at ~5000 m depth heated meteoric water and generated a current of supercritical steam rising along large fissures that eventually cooled below the critical point and condensed in the reservoir to heat the rock and augment a downflowing current of cold water. When produced to a well, the steam flow was increased by liquid evaporated by heat transfer from the rock. Since the downflowing current of cold water started outside the reservoir, the limit on production was the store of heat, not fluid. The origin of the upflowing steam was evaporation of the downflowing current of water, so there was no water-saturated zone at the bottom of the vapor reservoir. Sestini (1970) modified this model to allow condensed water to initially circulate within the reservoir itself. As this water was evaporated and produced it was replaced by deep superheated steam, so that steam temperatures increased and production rates stabilized to equal those of the deep recharge.

ORIGINAL LIQUID MODELS

These models by Facca and Tonani (1964), Ferrara et al. (1970), and Weres et al. (1977) assert that in the natural state the reservoir was water filled and only became steam filled as a result of exploitation. The problems of producing dry steam from an initially water-saturated reservoir are discussed by Truesdell and White (1973). In these models vapor systems are considered identical in origin to hot-water systems. This is also true of theories related to steam formed above boiling water that ascends to a water table and after losing steam, flows away laterally (steaming ground models). As originally proposed by Elder (1966) and followed by James (1968), vaporization was entirely at the interface of the vapor reservoir (containing no liquid) and the boiling water table. This process occurs on a small scale in hot-spring areas. The supply of steam is constant because water after boiling flows away along the water table. Scaling up this process to form a major vapor reservoir is not possible.

HEAT PIPE MODELS

These models have won general acceptance from scientists concerned with vapor-dominated systems (see earlier references). Upward flowing vapor, condensation at the top of the reservoir, and downward percolating condensate can produce essentially all observed phenomena in these systems, including high surface heat flow, low-pressure gradients, and changes in gas chemistry with time. These models have been tested by numerical simulation and found workable.

The deep end of the heat pipe, where condensate boils to form steam, was originally considered to be brine-saturated rock heated from below by fluid convection and ultimately by conduction from an igneous source (White et al., 1971). This part of the heat pipe has not been intersected by drilling except possibly by the few high-temperature wells described earlier. No samples of the deep brine have been recovered; the high-Cl steam that appeared in the 1960's at Larderello was attributed to evaporation of this brine (D'Amore and Truesdell, 1979), but it now appears more likely that general drying out of the reservoir allowed Cl to reach well bottoms at that time (Truesdell et al., 1989).

The only clear evidence for a liquid-saturated layer at the bottom of at least some parts of the Larderello reservoir is the distribution of gases and isotopes around centers of high temperature and production, which follow a Rayleigh condensation pattern. In a steady-state process this condensation implies centrifugal lateral steam flow that must be balanced by a centripetal liquid flow only possible in saturated rock (D'Amore and Truesdell, 1979). Such a deep, sloping water table was found at Larderello from levels in nonproducing wells (Calore et al., 1980).

FORMATION OF HIGH TEMPERATURE ZONES

Although the evidence for high-temperature zones at Larderello is incomplete, a numerical model by Pruess et al. (1987) has shown that most of the observations may be explained by the presence of a liquid-dominated heat pipe below the vapor-dominated reservoir. The liquid-dominated heat pipe consists of a column of boiling water in which hydrostatic pressure increases downward and temperatures increase along a "boiling-point-to-depth" curve referred to the temperature and pressure at the bottom of the vapor-dominated reservoir at 2500 m. The measured temperature of 394 °C at 2960 m in the San Pompeo 2 well (fig. 1) is not consistent with a liquid-dominated heat pipe and must indicate superheated vapor or the absence of fluid.

Models of relatively shallow high-temperature zones based on experience by GEO in the NW Geysers have been proposed by Drenick (1986) and elaborated on by Walters et al. (1988). Drenick proposed three models: (1) An active liquid-dominated reservoir at high temperature and pressure was separated from the vapor-dominated reservoir by an impermeable barrier. There was no evidence for high pressure or impermeable rocks so Drenick rejected this hypothesis. (2) Local heating by an igneous intrusion left hot dry rock within the vapor-dominated reservoir. Steam from the normal reservoir passed through the hot rock on the way to the wells.

Although this idea has considerable merit, Drenick (and Walters et al.) preferred his third model (3) in which a liquid-dominated reservoir below a vapor-dominated reservoir has boiled dry leaving hot rock containing vapor and adsorbed water at temperatures above those in the vapor-dominated reservoir. The situation before the final boildown would be similar to that found in simulations of the development of vapor-dominated reservoirs from water-filled systems (e.g., Pruess, 1985; Ingebritsen and Sorey, 1988). Drying out a high-temperature liquid without disrupting an overlying, cooler vapor-liquid reservoir seems difficult.

This "fossil liquid-system" model is consistent with the observed pressure continuity and lack of an impermeable boundary, but does not agree with the sharp temperature gradient observed. If liquid in saturated rock had boiled dry, the temperature of the rock should be reduced by the heat required to convert liquid to vapor and the final temperatures would fall below the boiling-point curve. A water-saturated rock with 5% porosity at 240°C would cool by 40°C if it boiled dry (data in Truesdell and White, 1973). The amount of cooling would be greater with higher porosity and less at higher temperatures as the latent heat of vaporization decreases. The presence of dissolved salts raises boiling temperatures, so boiling temperatures in boiling brine increase more rapidly with depth than those of pure water.

Figure 2 shows boiling points to depth calculated for pure water and for 25% NaCl solutions using data from Haas (1971) and Nathenson (1980). The boiling curves are shown for a hot-water system and for a vapor-dominated system underlain by boiling liquid. The vapor-dominated system was assumed to have a liquid-saturated layer from ground surface to 400 m depth, a vapor-dominated reservoir from 350 m (and 236°C, the enthalpy maximum of saturated steam) to 2000 m and a boiling liquid at greater depths. If this deep liquid boiled dry without any external heat added, then the original boiling-point-to-depth curve would represent the maximum temperatures of the remaining dry rock. If heat in the rock was required to vaporize the original liquid, then temperatures would be lower as discussed above.

It can be seen that the minimum distance from bottom of the vapor-dominated reservoir at 242°C to a point in the underlying dry rock at 342°C (100°C higher) is about 1500 m for pure water and 900 m for 25% NaCl solution. If heat required to vaporize liquid is included, these distances are increased. The observed distance in the northern Geysers from normal vapor reservoir temperatures of 246°C to high-temperature zone temperatures of 345°C was less than 200 m (Walters et al., 1988). This is not consistent with the high-temperature zone being a fossil hot-water reservoir. Of the models proposed by Drenick (1986), the "local heat source" appears the most reasonable.

PROPOSED MODEL

Given the difficulties of the earlier models in explaining observations of a high-temperature zone (to 345°C) immediately beneath the normal vapor-dominated reservoir at the NW Geysers and of near 400°C temperatures at 2900 m at Larderello, I propose a somewhat different model that may apply to much of The Geysers and perhaps Larderello. This model has features adopted from earlier proposals, in particular by Goguel (1953) and Drenick (1986). It differs from their models particularly in the timing of events and in the assumed generality of its application.

Almost all models with the exception of that of Goguel (1953) and Sestini (1970) have assumed that a boiling-liquid layer existed at the base of the vapor reservoir. This boiling liquid was assumed necessary to feed steam to the vapor reservoir and accept condensate, consistent with the generally accepted heat pipe mechanism. In fact, the observations do not require a deep liquid layer except in those areas (chiefly at Larderello) where lateral steam flow and Rayleigh condensation is found. Evaporation of condensate and generation of steam can occur equally well on hot dry rock surfaces as in a liquid layer. Temperatures of hot dry rocks, unlike a boiling-liquid layer, are not limited by boiling-point-to-depth and, because of the moderate thermal conductivities of dry rock, can tolerate steep gradients. Thus, in Drenick's "local heat source" model, 350°C temperatures could exist very close to the normal 245°C reservoir.

The new model involves drying out the deeper parts of a preexisting geothermal system over a broad area, possibly the entire Geysers. This drying could have been accomplished by an increase in conductive heating over numerous igneous intrusions at depths of greater than 2000 m (in the southern Geysers) to greater than 4000 m (in the northern Geysers). After drying we propose that a vapor-dominated reservoir establishes itself by the heat pipe mechanism.

Simulations of the formation of vapor reservoirs from liquid reservoirs have shown that the vapor reservoir extends to greater depths with greater heat input, greater discharge relative to recharge, and longer times (Pruess, 1985; Ingebritsen and Sorey, 1988). None of these simulations has reached such extreme conditions that the vapor-dominated liquid-vapor reservoir was replaced by a vapor-only reservoir at the bottom of the simulated system but such a process is almost certainly possible. Near active volcanoes, subsurface temperatures increase rapidly with depth until liquid water disappears and only superheated steam or a supercritical fluid is found. This process would be expected in a geothermal system intruded at depth by an igneous body of sufficient size.

Formation of a vapor-dominated reservoir underlain by a high-temperature zone would occur in three phases (figs. 2-4). In the first stage, moderate heating might establish a hot-water system (fig. 2) that would deposit hydrothermal minerals, seal some small fractures, and produce brittle rock more likely to sustain open fractures in later stages. If a vapor-dominated reservoir were produced in this stage, NaCl leached from the rock would accumulate in a deep brine (fig. 2). However, the lack of intense fracturing may not provide the dual porosity required for the formation of a vapor-dominated reservoir at this stage.

Increased igneous activity in the second stage would increase temperatures until the geothermal system dried out from the bottom. This stage would involve fracturing and vigorous boiling, possibly that described by Moore et al. (1989) which occurred at temperatures as much as 50°C above boiling-point-to-depth for present topography. Depending on the intensity of heating, the dried zone may extend to the near surface as shown in figure 3. An idealized conductive gradient would be linear as shown,

but the real gradient is complex and depends on the heating history, rock conductivities, the heating effect of steam formed at greater depths, and other factors. Fluid inclusions from Larderello containing hypersaline brine trapped at 300 to 350°C (Belkin et al., 1985) may have been formed from an earlier deep brine or from boiling during the heating stages. Higher temperature inclusions and mineral assemblages at 400°C to >550°C (Cathelineau et al., 1989) may be related to the heating maximum.

The third stage (fig. 4) represents a cooling of the top high-temperature dry rock by the formation of the modern vapor-dominated reservoir. The intense fracturing of the earlier heating episode in addition to tectonic fracturing allows surface waters to penetrate the heated rock. At the surface the rocks are saturated and altered with decrease in permeability, but at slightly greater depths a vapor-dominated heat pipe formed and cooled the hot rock by evaporation of descending water. Cooling produced by this mechanism would be much greater than that of cooling by conduction so the temperature gradient below the vapor-dominated reservoir would be very steep (idealized in fig. 4) in agreement with measured temperatures in GEO drill holes (Walters et al., 1988).

The rate of cooling and therefore the thickness of the vapor-dominated reservoir depend on the supply of surface water and the rate of conductive heat transfer from the top of the reservoir to the surface. Both water supply and conduction would be greater if the top of the reservoir was closer to the surface. At The Geysers this effect may have observable consequences. Where the reservoir top is shallowest, it is also thickest, and where its top is deep, the reservoir is relatively thin (Ken Williamson, pers. commun., 1990). By this mechanism the reservoir may have become lenticular as observed at Larderello (Calore et al.,1980). At the sides of the reservoir, particularly in the north, the high-temperature zone occurs at shallow depths under a relatively thin vapor-dominated reservoir. In the center of the field the top of the reservoir is nearer the surface and the high-temperature zone has been pushed below 3000 to 4000 m.

The felsite intrusions found in the central and southern Geysers could represent some of the intrusions producing the heating and drying. Because these rocks were near the surface they were probably cooled and solidified at an early stage so that they fractured along with the greywacke during further heating. In the last stage the vapor-dominated system extended into these rocks but fractures were more limited than in the greywacke. The lesser degree of fracturing may have caused the heat-pipe-driven vapor-dominated system to extend only a short distance into the intrusion. Thus, the high-temperature zone in the southern Geysers may exist in solidified igneous rocks with little porosity so that the amount of high-temperature steam is limited.

The distinctive chemistry of the steam contained in the dry rock of the high-temperature zone could have resulted from intense reactions with rock at high temperatures with possibly some magmatic contribution. High CO2 concentrations are typical of igneous gases and could be generated by metamorphism of calcite; exchange with rock at high temperatures would produce high O-18 steam; and high concentrations of HCl could be generated by reaction with rock containing halite and aluminosilicates (D'Amore et al., 1990). Halite could have been formed in the drying phase when brine from continued boiling below the vapor zone was finally dried. Steam and gases in the high-temperature rock would not tend to mix with those in the normal vapor reservoir because pressures would be equal until disturbed by exploitation. Gases that entered the vapor-dominated reservoir would be removed by reaction with rock minerals (HCl and other acid gases) or diluted by steam produced from evaporation of meteoric water (CO2, O-18). Dilution would be greater where the vapor-dominated reservoir is thicker and less where it is thinner.

SUMMARY

Observed temperatures in normal and high-temperature reservoirs of the northern Geysers can best be explained by recent downward extension of the vapor-dominated reservoir into dry rock heated by igneous intrusion. The igneous episode was probably preceded by a hot-water geothermal system. The modern vapor-dominated reservoir lies above the remaining hot rock with a thickness depending on the amount of heat removed and water added at the surface.

This model suggests that a high-temperature zone may exist under much of The Geysers. This high-temperature zone may contain steam with high HCl and gas in parts of the field where it is shallow enough to be fractured and particularly where it is developed in greywacke. If this is true, then continued production may lower pressures sufficiently to cause steam from high-temperature zones to enter wells even in the central and possibly southern areas.

ACKNOWLEDGMENTS

I wish to thank my many colleagues who have discussed this paper with me before and after its presentation at the Stanford workshop -- in particular Mark Walters of CCOC, Karsten Pruess, Bo Bodvarsson, and Marcelo Lippmann of LBL, Joe Moore of UURI, Steve Ingebritson and Don White of the USGS, Jill Haizlip of Dames and Moore and Franco D'Amore of CNR (Pisa). I also thank Jean Goguel and Andy Drenick who had most of the ideas first.

REFERENCES

Batini, F., G. Bertini, G. Gianelli, E. Pandeli, M. Puxeddu, and I.M. Villa, 1985, Deep structure, age and evolution of the Larderello-Travale geothermal field, Geotherm. Resourc. Counc. Trans., v. 9, part 1, p. 253-259.

Belkin, H., B. DiVivo, G. Gianelli, and P. Lattanzi, 1985, Fluid inclusions in minerals from the geothermal fields of Tuscany, Italy, Geothermics, v. 14, p. 59-72.

Bertini, G., G. Gianelli, E. Pandeli, and M. Puxeddu, 1985, Distribution of hydrothermal minerals in Larderello-Travale and Mt. Amiata geothermal fields, Geotherm. Resourc. Counc. Trans., v. 9, part 1, p. 261-266.

Calore, C., R. Celati, F. D'Amore, P. Squarci, and A.H. Truesdell, 1980, A geologic, hydrologic and geochemical model of the Serrazzano zone of the Larderello geothermal field, Proceedings, 6th Workshop on Geothermal Reservoir Eng., Stanford, p. 21-27.

Cappetti, G., R. Celati, U. Cigni, P. Squarci, G. Stefani, and L. Taffi, 1985, Development of deep exploration in the geothermal areas of Tuscany, Italy, *in* 1985

International Symposium on Geothermal Energy, International Volume, Geotherm. Resourc. Counc. Trans., v. 9, p. 303-309.
Cathelineau, M., J. Dubessy, C. Marignac, A. Valori, G. Gianelli, and M. Puxeddu, 1989, Pressure-temperature fluid composition changes from magmatic to present day stages in the Larderello geothermal field (Italy), Proceedings, 6th Water-Rock Interaction Symposium, p. 137-140.
D'Amore, F. and A.H. Truesdell, 1979, Models for steam chemistry at Larderello and The Geysers, Proceedings, 5th Workshop on Geothermal Reservoir Eng., Stanford, p. 283-297.
D'Amore, F., A.H. Truesdell, and J.R. Haizlip, 1990, Production of HCl by mineral reactions in high-temperature geotrhermal systems, Proceedings, 15th Workshop on Geothermal Reservoir Eng., Stanford (in press).
Drenick, A., 1986, Pressure-temperature-spinner survey in a well at The Geysers, Proceedings, 11th Workshop on Geothermal Reservoir Eng., Stanford, p. 197-205.
Elder, J.W., 1966, Heat and mass transfer in the Earth: hydrothermal systems, New Zealand Dept. Scientific and Industrial Research Bull. 169, 115 p.
Facca, G. and F. Tonani, 1964, Natural steam geology and geochemistry, in Proceedings, U.N. Conference on New Sources of Energy, Rome, 1961, v. 2, Geothermal Energy, p. 219-228.
Ferrara, G.C., C. Panichi, and G. Stefani, 1970, Remarks on the geothermal phenomenon in an intensively exploited field: results of an experimental well: Geothermics Special Issue 2, v. 2, pt. 1, p. 578-586.
Goguel, J., 1953, Le regime thermique de l'eau souterraine, Annales des Mines, 142 anne, no. x, p. 3Å29.
Haas, J.L., Jr., 1971, The effect of salinity on the maximum thermal gradient of a hydrothermal system of hydrostatic pressure and near boiling, Econ. Geol., v. 66, p. 940-946.
Ingebritsen, S.E. and M.L. Sorey, 1988, Vapor-dominated zones within hydrothermal systems: evolution and natural state, J. Geophys. Res., v. 93, p. 13635-13655.
James, R., 1968, Wairakei and Larderello; geothermal power systems compared, New Zealand J. Sci., v. 11, no. 4, p. 706-719.
Moore, J.N., J.B. Hulen, M.M. Lemieux, J.N. Sternfeld, and M.A. Walters, 1989, Petrographic and fluid inclusion evidence for past boiling brecciation and associated hydrothermal alteration above the NW Geysers steam field, California, Geotherm. Resourc. Counc. Trans., v. 13, p. 467-472.
Nathenson, Manuel, 1980, Boiling-point-to-depth for pure water with depth, temperature and pressure (unpublished data).
Pruess, Karsten, 1985, A quantitative model of vapor-dominated geothermal reservoirs as heat pipes in fractured porous rock, Geotherm. Resourc. Counc. Trans., v. 9, part 2, p. 353-361.
Pruess, K., Celati, R., Calore, C., and Cappetti, G., 1987, On fluid and heat transfer in deep zones of vapor-dominated geothermal reservoirs, Proceedings 12th Workshop Geothermal Reservoir Eng., Stanford, CA, 89-96.
Pruess, K. and A.H. Truesdell, 1981, A numerical simulation of the natural evolution of vapor-dominated hydrothermal systems, Proceedings, 6th Workshop on Geothermal Reservoir Eng., Stanford, p. 94-103.
Sestini, G., 1970, Superheating of geothermal steam, Geothermics Special Issue 2, v. 2, part 1, p. 622-648.
Truesdell, A.H. and D.E. White, 1973, Production of superheated steam from vapor-dominated geothermal reservoirs, Geothermics, v. 2, no. 3-4, p. 154-173.
Truesdell, A.H., F. D'Amore, and J.R. Haizlip, 1989, The rise and fall of chloride in Larderello steam, Proceedings, 14th Workshop on Geothermal Reservoir Eng., Stanford, p. 131-137.
Weres, O., K. Tsao, and B. Wood, 1977, Resource, technology and environment at The Geysers, Lawrence Berkeley Lab. Rept. LBL-5231.
Walters, M.A., J.N. Sternfeld, J.R. Haizlip, A.F. Drenick, and J. Combs, 1988, A vapor-dominated reservoir exceeding 600 °F at The Geysers, Sonoma County, California, Proceedings 13th Workshop on Geothermal Reservoir Eng., Stanford, p. 73-81.
White, D.E., L.J.P. Muffler, and A.H. Truesdell, 1971, Vapor-dominated hydrothermal systems compared with hot-water systems, Econ. Geol., v. 66 no. 1, p. 75-97.

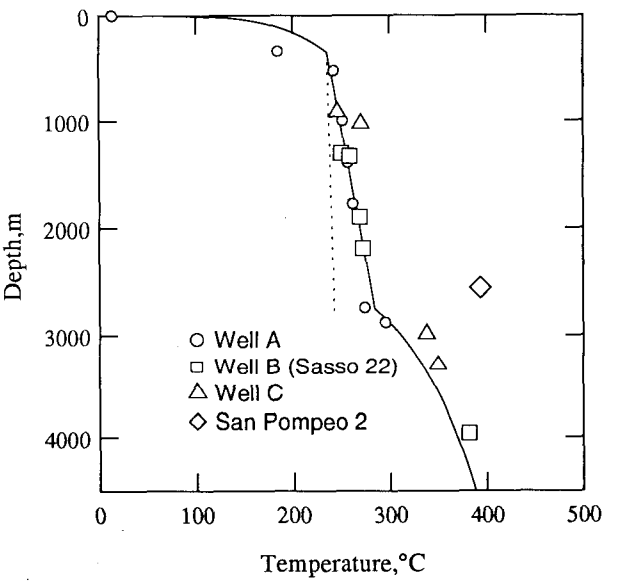

Figure 1. Measured temperatures for three deep wells in the central area of Larderello from Pruess et al. (1987), with an additional temperature from the San Pompeo 2 well. Solid lines show a hypothetical vapor-dominated system with boiling water below 3000 m. Dotted line is for a static vapor column.

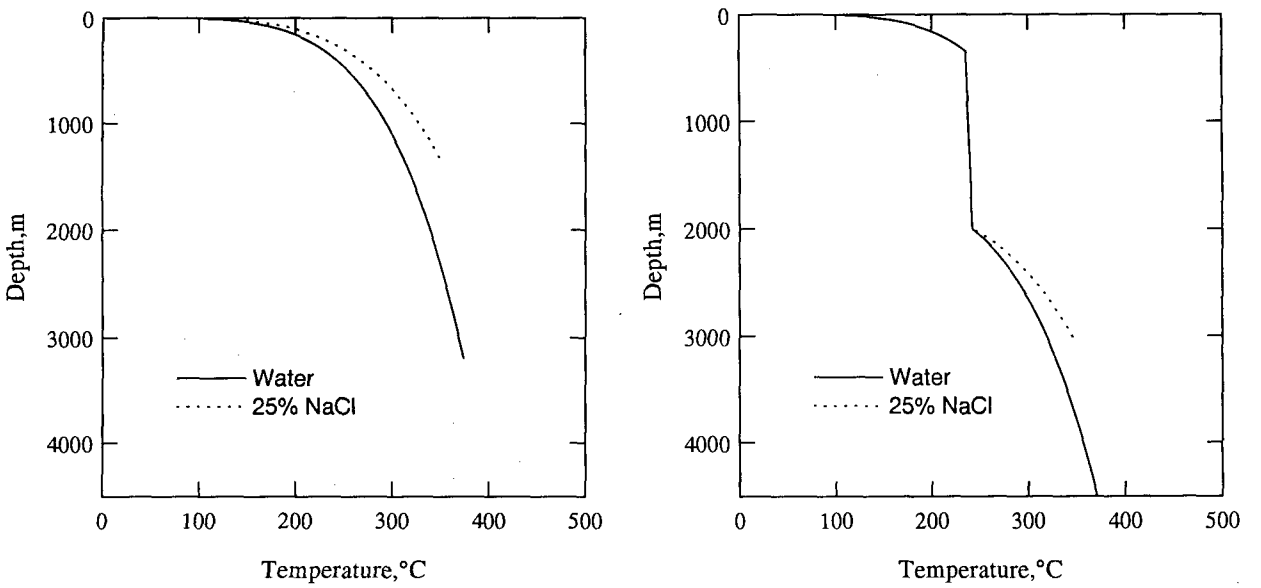

Figure 2. Calculated static boiling-point-to-depth curves for pure water (solid line) and 25% NaCl solution (dots). The left figure shows a hot-water system and the right figure shows a vapor-dominated system with boiling water or salt solution below 2000 m.

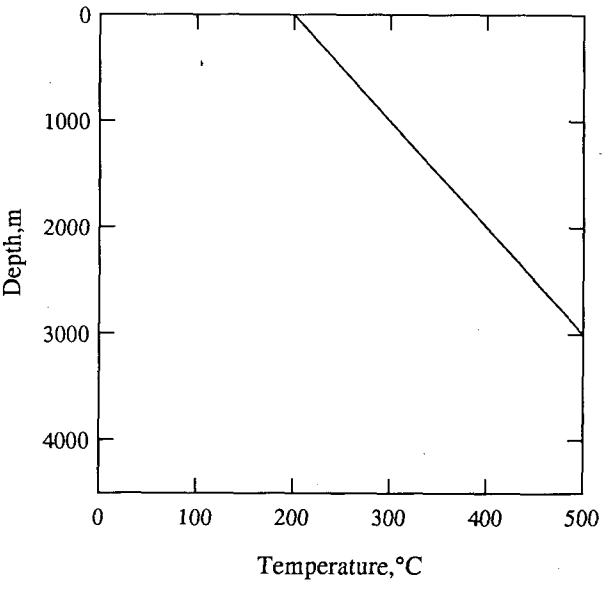

Figure 3. Hypothetical temperature profile for heat conduction in dry rock between an igneous intrusion at 6000 m and 800°C to a near surface temperature of 200°C.

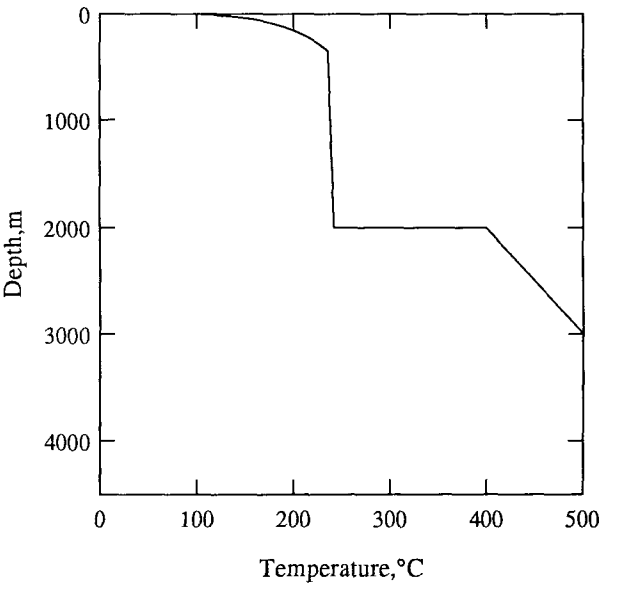

Figure 4. Hypothetical temperature profile of a vapor-dominated heat pipe removing heat and cooling hot rock originally with the temperatures shown in figure 3. Temperatures are for static conditions.

PROCEEDINGS, Sixteenth Workshop on Geothermal Reservoir Engineering
Stanford University, Stanford, California, January 23-25, 1991
SGP-TR-134

A Coupled Model of Fluid Flow in Jointed Rock

Daniel Swenson
Mechanical Engineering Dept., Kansas State University, Manhattan, KS 66506

Rick Martineau
Los Alamos National Laboratory, Los Alamos, NM 87545

Mark James
Fracture Analysis Consultants, Inc., Ithaca, NY 14853

Don Brown
Los Alamos National Laboratory, Los Alamos, NM 87545

ABSTRACT

We present a fully coupled model of fluid flow in jointed rock, where the fluid flow depends on the joint openings and the joint openings depend on the fluid pressure. The joints and rock blocks are modeled discretely using the finite element method. Solutions for the fluid and rock are obtained and iteration is performed until both solutions converge. Example applications include an examination of the effects of back-pressure on flow in a geothermal reservoir and transient fluid injection into a reservoir.

INTRODUCTION

Geothermal energy is produced within the earth's crust by slowly decaying, naturally occurring, radioactive isotopes. Hot dry rock (HDR) is naturally heated rock that does not produce natural steam or hot water at commercially useful rates. Energy can be extracted from a region of hot rock by circulating pressurized water in a closed loop through a man-made fracture system (Figure 1). The useful heat is recovered at the surface through heat exchangers; the cooled water is reinjected to recirculate through the underground loop. Economic analysis and feasibility studies of commercial HDR energy production sites requires both experimental verification and analytic models of the reservoir. In this paper, we describe a fully coupled stress/fluid model of a reservoir based on a discrete model of rock joints.

Our model extends previous models of fluid flow in discrete joints (Noorishad et al., 1982; Hilber and Taylor, 1976; Cundall, 1982; and Asgian, 1988) to be directly applicable to reservoir analysis. The model complements the work of Kelkar and Zyvoloski (1990) in their development of a three dimensional model of multiphase flow in porous and permeable media, and the work of Robinson (1990) in modeling fluid flow in discrete fractures.

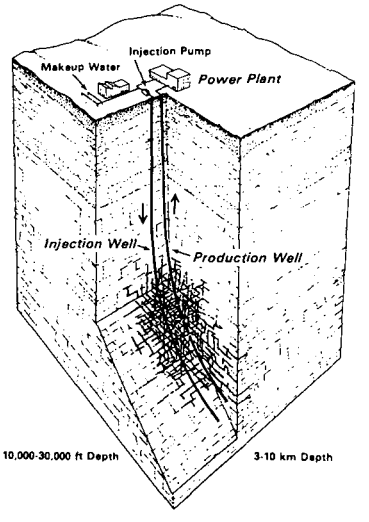

Figure 1: Hot dry rock concept (Tester et al., 1989)

FINITE ELEMENT DERIVATIONS

Our goal is to solve for a set of nodal unknowns (displacements and pressures) that interact with each other through a highly nonlinear relationship. The joint displacements are a function of joint fluid pressures, and joint flow rates are a cubic function of joint displacements.

Two separate models are developed, one for the structural solution and one for the fluid solution. The separate models can be solved using either dynamic relaxation or Newton-Raphson iteration. Information is then transferred between the two calculations and iteration is continued until global convergence is reached.

Rock Deformation Model

The equation of equilibrium for a body in three dimensional Euclidean space is:

$$\sigma_{ij,j} + b_i = \rho \ddot{u}_i \quad (1)$$

where σ_{ij} is the stress tensor, b_i is the body force, ρ is the density, and $\ddot{u}_i$ is the acceleration.

We assume small displacements and small strains and use the standard Galerkin approach to obtain the finite element approximation:

$$\sum_{e=1}^{numel} \{ \int_{S_e} \mathbf{N}^T \mathbf{N} dS \mathbf{t} - \int_{V_e} \mathbf{B}^T \mathbf{D} \mathbf{B} dV \mathbf{u} - \int_{V_e} \rho \mathbf{N}^T \mathbf{N} dV \ddot{\mathbf{u}} \} = \mathbf{0} \quad (2)$$

where **N** and **B** are the shape function and shape function derivative matrices, **D** is a material matrix, ρ is the density, **t** is the nodal traction vector, and **u** is the nodal displacement vector.

The assembled element contributions are the global structural stiffness matrix $\mathbf{K}_S$, the global mass matrix **M**, and the global force vector **f**, or:

$$\mathbf{K}_S \mathbf{u} + \mathbf{M} \ddot{\mathbf{u}} = \mathbf{f} \ . \quad (3)$$

The above equations including inertia terms. When solving using Newton-Raphson iteration, the acceleration term is not included. When solving using dynamic relaxation, we solve for the accelerations and integrate the accelerations through time. In this case, we do not actually assemble the stiffness matrix but do an element by element evaluation. Also, we scale the element masses for faster convergence.

Fluid Flow Model

For one-dimensional fluid flow in a rock joint, conservation of mass is given by

$$-\frac{\partial q}{\partial x} = \dot{a} \quad (4)$$

where q is the volumetric flow rate and $\dot{a}$ is the joint opening velocity. We assume that the flow is proportional to the pressure gradient and the joint permeability,

$$q = -k_p \frac{\partial p}{\partial x} \quad (5)$$

The joint permeability, k_p, is given by the cubic law,

$$k_p = \frac{a^3}{12 \mu f} \quad (6)$$

where a is the joint opening, μ is the dynamic viscosity, and f is a frictional loss factor. Combining equations 4, 5, and 6 and then proceeding as before, we obtain the final set of global equations for the fluid flow model (see James, 1988, for details),

$$\mathbf{K}_p \mathbf{p} = \mathbf{q} + \mathbf{S} \dot{\mathbf{a}} \ , \quad (7)$$

where $\mathbf{K}_p$ is the permeability matrix, **p** is the nodal pressure vector, **q** is the external flow load vector, **S** is the joint opening storage matrix, and $\dot{\mathbf{a}}$ is the joint opening velocity vector. The storage term allows us to solve for quasi-static transient problems, where we neglect the inertia of the fluid, but store fluid in the opening joints. The storage term is required for reservoir inflation analyses, but makes convergence much more difficult.

Finite Element Types

In the model, we use three different types of elements: continuum, interface, and fluid. The continuum elements are used to model the rock blocks between the joints. These are standard six-noded triangle elements with quadratic shape functions.

The interface elements represent the joint response between the rock blocks. Line elements with quadratic shape functions are used. The joint displacement/stress relation for the interface elements can be linear or nonlinear. One nonlinear option is the "Bed-of-Nails" model (Gangi, 1978). In this model, the joints become more stiff as they close; as they open they become softer.

The final element type is the fluid flow element. Again, quadratic shape functions are used for the pressures in the element. In the geometry description, the fluid element is identified by six nodes corresponding to the structural nodes. However, the actual solution is calculated using three nodes along the element length. The program internally assigns node numbers to the pressure nodes and uses these nodes for the solution. Pointers are then maintained from the pressure nodes to the structural nodes and from the structural nodes to the pressure nodes.

In an analysis, the pressure and joint elements are superimposed to form a pressurized rock joint. The surface tractions due to the fluid pressure are added to the loads due to the interface element. This is consistent with the concept of effective stress. If there is no fluid pressure, the rock joint carries all the load. As the fluid pressure increases, the load carried by the rock joint decreases.

SOLUTION PROCEDURE

We are faced with two sets of simultaneous equations, both possibly nonlinear, that are coupled in a highly nonlinear manner:

$$\mathbf{K_S u} = \mathbf{f} \qquad \text{(for the structure)} \qquad (8)$$

$$\mathbf{K_P p} = \mathbf{q} - \mathbf{S\dot{a}} \quad \text{(for the fluid)} \qquad (9)$$

Nonlinearities can occur in $\mathbf{K_S}$ due to the nonlinear joint behavior, and in $\mathbf{K_P}$ due to possible nonlinear far-field leakage terms (not included in the present calculations). The nonlinear coupling between the sets of equations arises as follows:

- **f**, the load on the structure, includes loads on the rock blocks due to the fluid pressures in the joints, **p**.
- $\mathbf{K_P}$, the fluid permeability matrix of the joints, depends on the cubic of the joint openings, which are functions of **u**.
- $\dot{\mathbf{a}}$, the joint opening velocity, depends on the displacements, **u**, and the time step.

This means that the joint displacements change the fluid solution and the fluid solution then applies different loads on the structure. The goal of the solution procedure is to find solutions for the simultaneous equations that also satisfy the coupling between the sets of equations.

A simple iterative scheme is used to reach convergence between the coupled structure and fluid equations. We first solve the fluid equations, then pass this information to the structure, where the pressures become part of the loads on the structure. After solving the structure, we pass the information on joint openings back to the fluid solution. We continue iterating between the two solutions until global convergence is reached.

Experience has shown that for steady-state problems, global convergence is reached rapidly, typically in less than five iterations. However, convergence is much more difficult when solving transient problems (where storage is included in the solution). In this case, it is necessary to control the iteration procedure to prevent instability.

We use two methods to control the iteration procedure and guide it to convergence: ensuring that the initial pressure solutions are reasonable and damping the joint opening velocity term used in the fluid solution. Damping the calculated joint opening velocities is most important to ensure convergence. Damping is done using the following equation,

$$\dot{\mathbf{a}}_{new} = \dot{\mathbf{a}}_{old} + f(\dot{\mathbf{a}} - \dot{\mathbf{a}}_{old}) \qquad (10)$$

where f is a factor less than 1.0 and a is the joint opening velocity calculated from the actual joint displacements. Equation 10 damps the calculation of the new joint opening velocities, however, when convergence is reached the full joint opening velocities are being used in the solution. Experience has shown that the value of the factor depends on the problem size (assuming joint properties are held constant). For small problems a value of 0.25 performs well. However, for large problems, it is necessary to reduce the factor to a value of 0.001 to 0.01. In this case 100's of iterations are required before convergence is reached.

APPLICATIONS

In this section we demonstrate initial calculations for the Phase II HDR reservoir at Fenton Hill, New Mexico. Two of the calculations assume steady state conditions. They are used to examine the effect on flow rate of changing back pressure in the reservoir. The third calculation is a transient analysis of test 2070, an experiment in which a constant flow rate was injected into the reservoir and the resulting pressure transient was monitored at the recovery well (which was shut in).

It is believed that the Phase II reservoir consists of interconnected joints with low and high opening stresses (Brown, 1988). The low opening stress fractures are called "tensile" fractures, and the high opening stress fractures are called "shear" fractures. Although the true geometry is a complicated three dimensional geometry, as a first approximation the Phase II reservoir will be modelled as a horizontal plane with unit depth. We look at the horizontal plane in plan view, with flow occurring only in the fractures in this plane. In this model, there is an in-situ stress of 22.5 MPa in the X (horizontal) direction, and a lower value of 15 MPa in the Y (vertical) direction. This means that the vertically oriented joints are closed more tightly than the horizontally oriented joints. The vertically oriented joints restrict flow more than the horizontal joints.

Finite Element Model

Figure 2 shows the overall finite element model used to represent the reservoir, and Figure 3 shows details of the mesh around the injection point. The model consists of three types of elements: six-noded triangular elements representing the rock blocks, six-noded joint (interface) elements representing the joints, and three-noded fluid elements superimposed on the joint elements. The dimensions are 450 x 300 meters with the left boundary treated as an axis of symmetry. The reservoir is assumed to be 1000 meters deep.

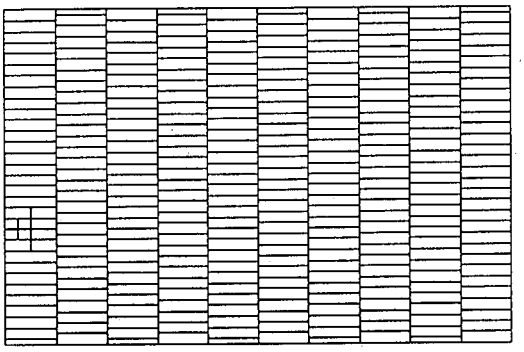

Figure 2: Reservoir discretization

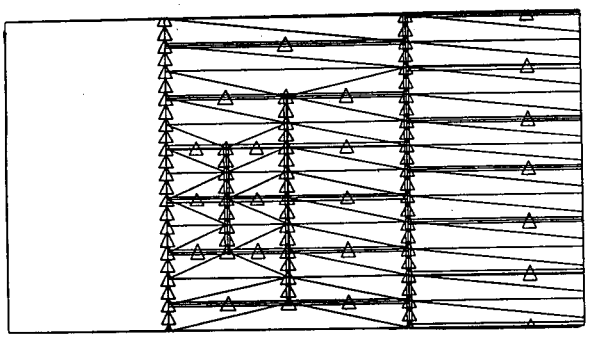

Figure 3: Details of mesh around injection point

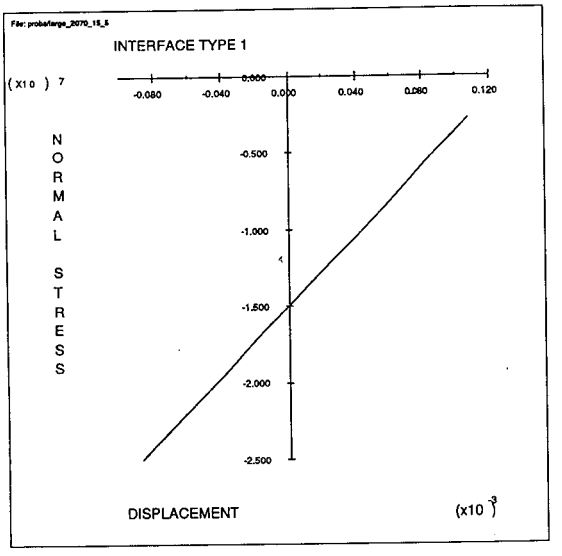

Figure 4: Joint displacement/stress relation (horizontal joints)

A linear joint displacement/stress relation is used. As shown in Figure 4, the initial stresses in the joints are chosen to be in equilibrium with the in-situ stresses. Around the reservoir, far-field joints are used to represent the deformation of the bounding rock. The stiffness of these joints is calculated by assuming that deformation would only occur within 300 meters of the reservoir. Table 1 summarizes the reservoir properties.

Young's Modulus	25.0 GPa
Poisson's Ration	0.1
In-situ X Stress	22.5 MPa
In-situ Y Stress	15 MPa
Initial Vert. Joint Opening	2.50×10^{-5} m
Initial Horiz. Joint Opening	4.16×10^{-5} m
Fluid Dynamic Viscosity	1.166×10^{-4} Ns/m^2
Factor of Roughness	1.5

Table 1: Reservoir properties

Flow Sensitivity to Back Pressure

Our first calculations examine the effect of back pressure on the flow in the reservoir. Because the flow rate is a nonlinear function of the joint opening, it may be possible to increase the flow in the reservoir by increasing pressure at the extraction well while maintaining a constant injection pressure. This could reduce the pumping energy required to operate the reservoir.

To examine this effect, we solve two steady state problems. In both problems the injection pressure is kept constant at 15 MPa, while in the first the extraction pressure is 5 MPa and in the second the extraction pressure is 10 MPa. Approximately 350 meters separate the injection and extraction wells. Also, because of symmetry, the problem represents two extraction wells on either side of the injection well.

As expected, the higher back pressure opens the joints more than with a low back pressure. The calculated total injection flow rates for the two cases are 0.265×10^{-3} m^3/s for 10 MPa back pressure and 0.348×10^{-3} m^3/s for 5 MPa back pressure. For this calculation, the flow rate did not increase with increased back pressure, but the pumping energy per unit volume decreased. That is, a 50% reduction in pressure drop across the reservoir gave only a 24% reduction in flow. Further studies would be necessary to find an optimum operating point, but this calculation demonstrates a possible design parameter for the reservoir. One possible problem with using a high back-pressure could be reservoir growth during operation.

Transient Analysis of Test 2070

Test 2070 was a constant flow rate, shut-in test conducted in the Phase II reservoir at Fenton Hill. Water was pumped into the HDR reservoir at a flow rate of 8.39×10^{-3} m³/s (133 gpm). The pressure was monitored at both the injection well and the shut-in extraction well. Figure 5 shows the measured pressure history at the injection and extraction wells for the first two hours of experiment 2070. There is a significant delay from the time at which injection is started until the pressure increase is noted at the extraction well, and the pressures at the extraction well only increase slightly.

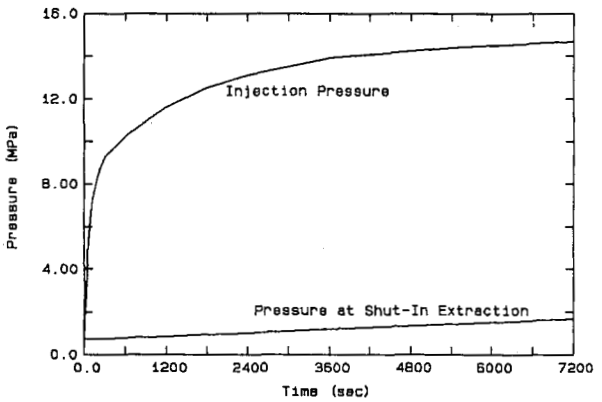

Figure 5: Measured pressures

The analysis was performed by first solving a steady state problem with a pressure of 0.724 MPa at the injection well (corresponding to the measured pressures at the beginning of the experiment). We then performed a transient analysis in which the measured injection pressures were specified at the injection well. The flow rates were not specified, but were calculated by the model as part of the solution. The time step used in this problem was 5 minutes.

Results are presented as a series of displacement and pressure plots. Figure 6 shows the calculated displacements and Figure 7 shows the pressures in the reservoir. The results show the injected fluid opening the joints around the injection point and beginning to fill the reservoir. This pressure pattern is completely different from a steady state problem and demonstrates the effect of the storage term in equation 9. The injected fluid is stored in the joints as they open and the fluid gradually spreads into the mesh.

Figure 8 gives a comparison of the calculated and measured extraction pressures. The curve labeled Flow Rate BC uses the present results, but with time scaled by the total injected fluid. The fact that the flow rate solution is relatively close to the experimental data indicates that approximately the correct amount of storage is available in the present model. If we had

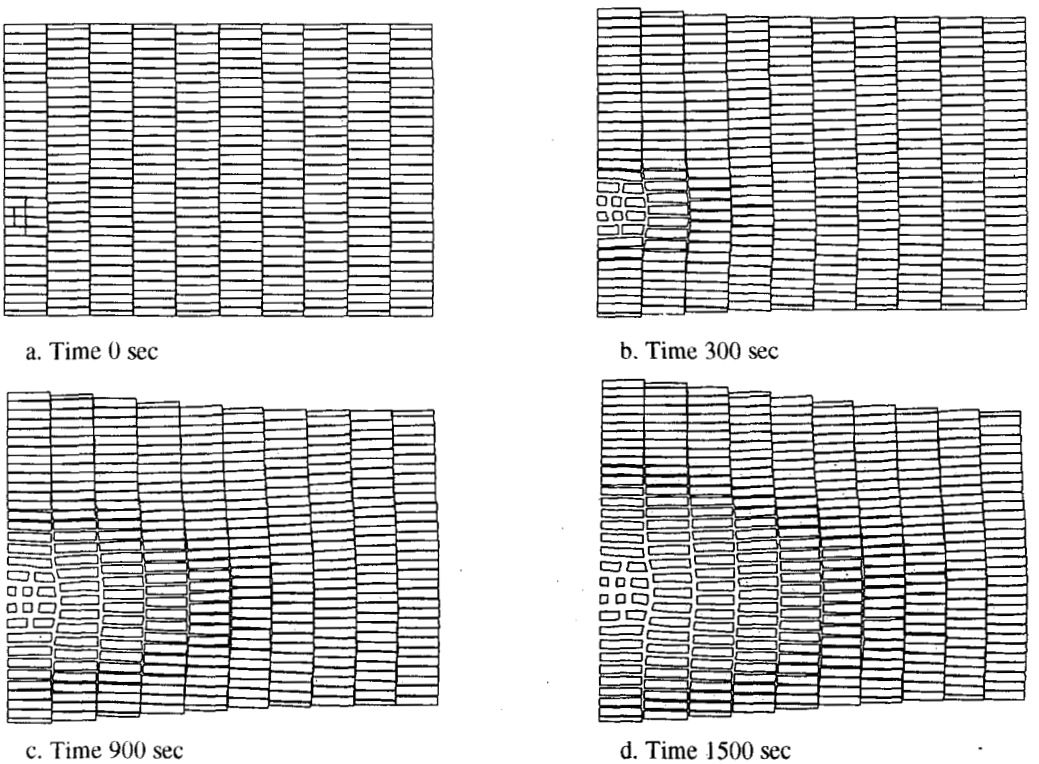

a. Time 0 sec

b. Time 300 sec

c. Time 900 sec

d. Time 1500 sec

Figure 6: Calculated displacements during transient

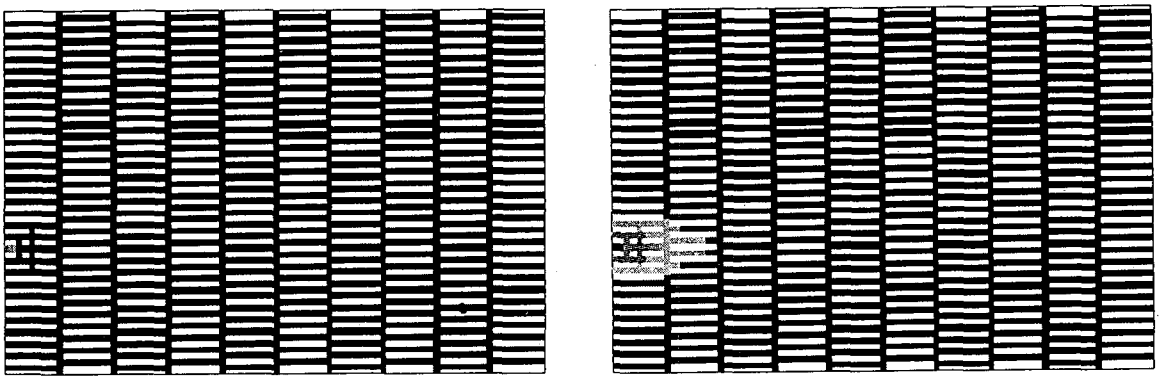

a. Time 300 sec

b. Time 1500 sec

Figure 7: Pressures during transient (Contours 0.7 MPa to 12 MPa)

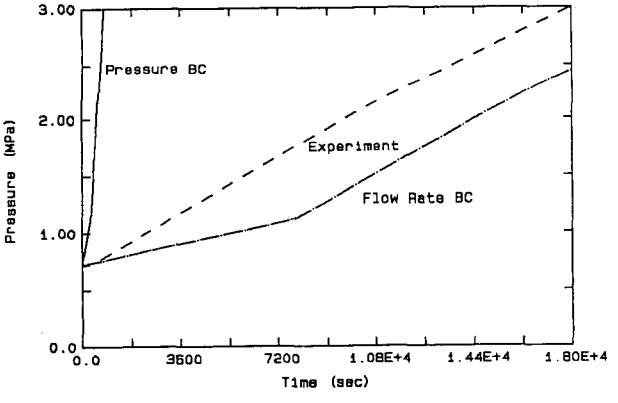

Figure 8: Comparison of calculated and measured extraction pressures

insufficient storage, the pressure would have risen too rapidly even with the scaled time. Clearly, the model could be adjusted so the there was more resistance to flow around the injection well. The would reduce the flow rate and bring the solution close to that for the flow rate boundary condition. There is experimental evidence that flow is restricted around the borehole.

CONCLUSIONS

In this paper, we have described a fully coupled model of fluid flow in jointed rock. The derivation results in two sets of nonlinear equations, representing fluid flow and rock deformation, that are coupled in a nonlinear manner. Fluid pressures in the joints tend to open the joints, and the joint opening changes the joint permeability. The solution of the simultaneous equations is especially difficult in the transient case where highly local joint opening (and corresponding storage of fluid) occurs.

Solutions are obtained by iteratively solving the fluid and rock models, passing information between the two models in each iteration. In transient analyses, solutions were obtained by damping the joint storage terms as the solution iterated between the fluid and rock model. This scheme appears reliable, however it may require 100's of iterations between the models for complete convergence.

Application of the model to an analysis of sensitivity to back pressure showed that using a higher back pressure could open the joints and decrease the required pumping energy in the reservoir. This seems to be an attractive design option.

The transient analysis demonstrated the inflation of the reservoir for a shut-in condition at the extraction well. This analysis capability makes it possible to examine the effects of operating the reservoir in a cyclic mode as compared to a steady state mode.

In summary, significant progress has been made in developing a tool for the HDR designer. Future work should proceed in several areas:

- Increasing solution speed by implementing a formulation where displacements and pressures are solved simultaneously. This should significantly reduce the need for iteration and help convergence when using nonlinear joints.
- the addition of rock porosity to the analysis.
- the addition of heat transfer capability to the model.

ACKNOWLEDGEMENTS

This work was supported by Los Alamos National Laboratory, contract 9-XA9-3643Y-1. We thank Don Brown for his encouragement and guidance during the project and appreciate the discussions we have had with Bruce Robinson, Sharad Kelkar, and George Zyvoloski.

REFERENCES

Asgian, M.I., 1988, "A Numerical study of Fluid Flow in Deformable, Naturally Fractured Rock Masses," Submitted to *Int. J. Rock Mech. Mining Sci. & Geomech. Abstr*

Brown, Don, 1988, personal discussion.

Cundall, Peter A., 1982, "Fluid-Rock Interaction Program (FRIP) Manual," Internal report - University of Minnesota, Dept. of Civil and Mineral Engineering.

Gangi, Anthony F., 1978, "Variation of Whole and Fractured Porous Rock Permeability with Confining Pressure," *Int. J. Rock Mech. Min. Sci. & Geomech Abstr.*, Vol 15, pp 249-257.

Hilber, Hans M. and Robert L. Taylor, 1976, "A Finite Element Model of Fluid Flow in Systems of Deformable Fractured Rock," Department of Civil Engineering, Division of Structural Engineering and Structural Mechanics, University of California, Berkeley, CA.

James, Mark, 1988, "A Finite Element Model of Fluid Flow in Jointed Rock," M.S. Thesis, Kansas State University, Manhattan, KS.

Kelkar, Sharad, and Zyvoloski, George, 1990, "Hydro-Thermo-Mechanical Response of a Fractured Rock Block," 31st U.S. Symposium on Rock Mechanics, June 18-20, 1990, Colorado School of Mines, Golden, Colorado.

Noorishad, J., M.S. Ayatollahi, and P.A. Witherspoon, 1982, "A Finite Element Method for Coupled Stress and Fluid Flow Analysis in Fractured Rock Masses," *Int J. Rock Mech. Min. Sci. & Geomech. Abstr.*, Vol 19, pp 185-193.

Robinson, Bruce A., 1989, "A Discrete Fracture Model of a Hot Dry Rock Geothermal Reservoir," International HDR Geothermal Energy Conference, Camborne, U.K., June 27-30.

Tester, J. W., Brown, D. W., and Potter, R. M., 1989, "Hot Dry Rock Geothermal Energy - A New Energy Agenda for the 21st Century," LA-11514-MS, Los Alamos National Laboratory, Los Alamos, New Mexico, 87545.

PROCEEDINGS, Sixteenth Workshop on Geothermal Reservoir Engineering
Stanford University, Stanford, California, January 23-25, 1991
SGP-TR-134

A REVIEW OF THE UK GEOTHERMAL HOT DRY ROCK R&D PROGRAMME

Geoff D Symons and John H Clarke

Energy Technology Support Unit
Harwell Laboratory
Oxfordshire OX11 0RA
United Kingdom

ABSTRACT

The UK Department of Energy's Geothermal Hot Dry Rock (HDR) Programme was last reviewed in 1987/88, when a number of technical problems were identified. These related to the size of reservoir (heat exchanger), its thermal behaviour (short circuits) and water losses.

A programme of work to address these problems was subsequently set up. This work has recently been reviewed. The main conclusions are:

- a satisfactory procedure for creating a commercial-scale HDR reservoir has yet to be demonstrated;
- there is a dearth of information on rock properties at the 6–7 km depths needed for a commercial reservoir;
- a satisfactory method of sealing short circuits has not yet been demonstrated;
- although it is difficult to determine accurately the economics of HDR because of these technical uncertainties, it is believed that electricity from a commercial HDR power station is unlikely to be competitive with conventional means of generation in the short to medium term;
- despite the earlier promise of the technology, HDR has been shown over the past two years to be still at an early stage of development and it is unlikely to attract private sector funding in the short term;
- participation in a joint European programme offers the opportunity of resolving some of the technical uncertainties.

INTRODUCTION

At depths of several kilometres below the Earth's surface, the temperature of the rock is sufficiently high to allow steam to be raised for electricity generation. However the heat is not readily accessible in the UK because the rock is usually dry and has low permeability. The UK Department of Energy's Hot Dry Rock R&D Programme aims to remove these restrictions by developing techniques to introduce water into the rock from the surface, circulate it through an artificially created heat exchanger in the rock, and bring it back to the surface. However, translation of this simple principle into practice represents a formidable technical challenge. With no technical or economic constraints it was thought that it might be possible to site local power stations widely across the UK, providing a pollution-free supply of heat and electricity. This was the appealing target in 1974 when the Department first became involved in hot dry rock research.

HDR TECHNOLOGY

The UK Department of Energy's R&D Programme is attempting to extract heat from rocks which are hot but which do not contain water or steam capable of being circulated to the surface. This resource has become known as hot dry rock (HDR). In the UK, the granite formations of south west England are the most attractive in this respect since their temperature rises more rapidly with depth than other rocks because of radiogenic decay of natural isotopes. The temperature gradient in Cornwall (UK) is 30–35°C per kilometre of depth and it would be necessary to drill to 6 km to reach 200°C, a temperature suitable for generating electricity.

The basis of the technology for extracting this heat is to pump water down an injection borehole drilled from the surface, circulate it through enlarged or 'stimulated' pre-existing fractures (or joints) in the rock and bring it back to the surface via a second, production, borehole. The joints behave as the conduits of a subsurface heat exchanger.

In Cornwall the pattern of jointing can be seen in the rock where it outcrops on the surface. Two jointing planes, nearly vertical and at right angles to each other, are known to extend to a depth of at least 3.5 km. They are expected to go deeper still although, as depth increases, the joints are likely to become 'tighter', with less width between the faces.

In a commercial system, the initial sections of the two boreholes would be drilled vertically but they would be deviated at depth to intersect the maximum number of joints. See Figure 1. In practice, the deviation is currently limited by drilling constraints to about 35° from the vertical. The diameter of the lower part of the borehole would be about 180 mm. The vertical sections would be drilled using technology based on standard

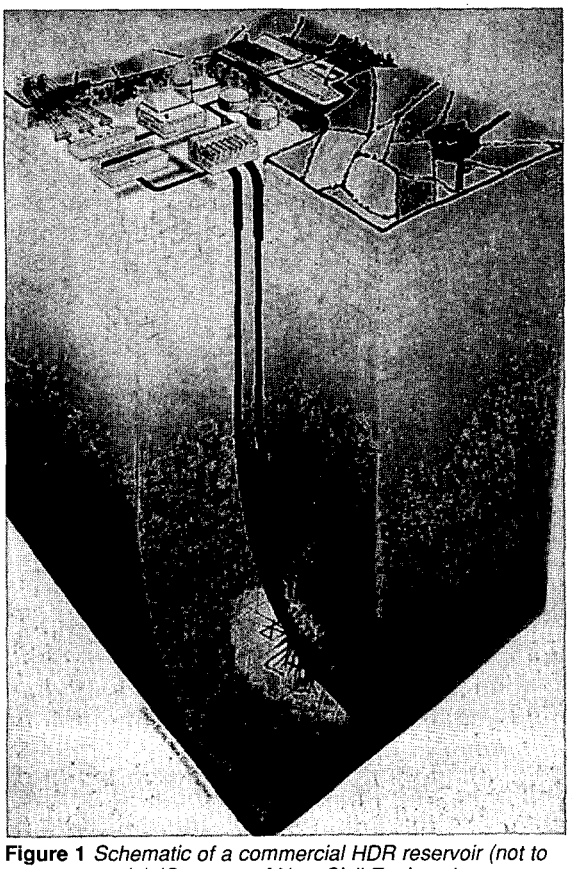

Figure 1 *Schematic of a commercial HDR reservoir (not to scale) (Courtesy of New Civil Engineer)*

oilfield practice, but HDR experiments to date have shown that the deviated sections would be best drilled using an hydraulically driven downhole motor to turn the drilling bit rather than turning the whole drill assembly from the surface. Although HDR drilling to depths of about 6 km in the hostile environment of hard, hot, crystalline rock is currently difficult, it does not present a major technological problem – apart from its cost.

The major problem with HDR technology lies in the creation of the subsurface heat exchanger, usually referred to as a 'reservoir'. Use of the word reservoir has developed by analogy with reservoirs found in oil-bearing rocks and geothermal aquifers. In the HDR context, the use of the term is not so clear and is not strictly justifiable since an HDR reservoir neither has a well-defined boundary nor contains a significant amount of fluid. However, the term has been used for a number of years and is retained here.

The permeability of a rock such as granite is determined by the aperture and frequency of its natural joints; the joint apertures in the undisturbed state are likely to be 0.01 to 0.1 mm at the depths of interest in Cornwall, and the joint frequency is about one in 20 m. To enable sufficient volumes of water to circulate at acceptable pumping pressures the rock must be 'stimulated' to increase the joint widths. Hydraulic fracturing is a procedure that has been developed in oilfields to encourage flow of hydrocarbons from reservoir rocks to wellbores. In HDR terminology this process is usually referred to as 'rock stimulation'.

For the initial stimulation of an HDR reservoir, large volumes of water or low-viscosity gel would be pumped into the rock via the lower section of the first borehole to be drilled, at a high enough pressure to open up or dilate the natural joints in the rock. The pattern of reservoir growth from this stimulation would depend on the pre-existing joint pattern and the magnitude and direction of the rock stresses.

Experience gained[1, 2, 3] in the UK Programme to date suggests that, in a commercial system, repeated major stimulations would need to be made from a borehole, spread over the lower 2 km or so, and that the second borehole would be drilled obliquely to make the most effective intersection with the joints of the stimulated rock volume. See Figure 2.

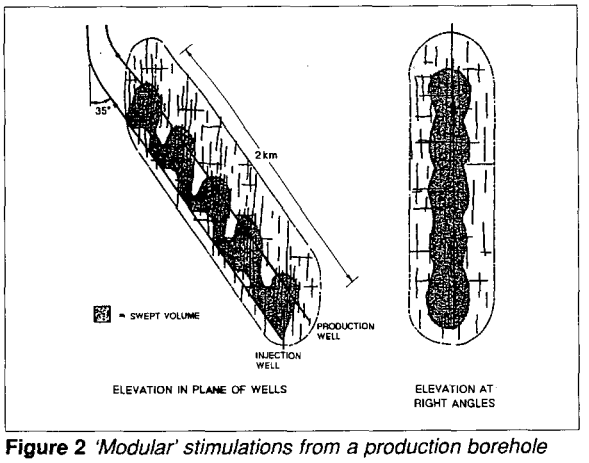

Figure 2 *'Modular' stimulations from a production borehole*

The current targets for the hydraulic performance of a complete commercial system are an impedance of 0.1 MPa per l/s and a total flow from the production borehole of 75 l/s. Impedance is defined as the pressure differential across the two boreholes divided by the flow out of the production borehole. Given these commercial targets, a differential pumping pressure of 7.5 MPa (about 1100 lb/in^2) would be required for water circulation through the reservoir itself; in addition there will be substantial friction losses in the well casings. Power for this pumping represents a severe parasitic load which must be subtracted from the output of the HDR power station.

For a reasonably long lifetime (about 15 years) a commercial reservoir of a few MW electrical output would have to act as an effective heat exchanger of sufficient size for the temperature drop (at the production

well) from cooling of the rock to be less than 1°C per year. To ensure this, the reservoir would need to have a stimulated rock volume of 300 million cubic metres with a heat transfer area of 10 million square metres spread evenly over a multiplicity of flow paths of comparable impedances.

Immediately after the stimulations, or at some later time during the life of the reservoir, it is quite possible that the flow pattern in the reservoir between the two boreholes would prove to be unsatisfactory:

- the reservoir impedance might be too high, requiring excessive pumping pressures for the required flow;
- one or two preferential flow paths (short circuits) might be established between the boreholes giving in effect a smaller reservoir than intended and leading to a rapid decline in the temperature of water reaching the production borehole;
- water losses between the two boreholes might be unacceptably high;
- geochemical effects might adversely affect reservoir characteristics.

For all these reasons the geothermal engineer will need to have at his disposal a selection of techniques to determine whether the HDR reservoir has the necessary thermal and hydraulic properties to operate as an effective heat exchanger over the required lifetime. If not, he must be able to diagnose the shortcomings and carry out repairs to rectify any problems. Development and testing of these repair or manipulation techniques has been an important part of the UK HDR R&D Programme to date.

The energy release associated with the displacement of joints during stimulation causes microshocks which can be detected by a suitable network of sensors located at depth and near the surface around the stimulation site. Measurement of this 'microseismicity' has been used to infer the shape and extent of the experimental reservoirs created in the Programme. By recording and processing the microseismic data associated with the microshocks, the location of each one can be calculated. With suitable graphics software, a 3-D map can be built up showing the extent of the microshocks – and this has been interpreted as the envelope of the reservoir. It has been claimed that areas of dense microseismic activity (the blackest areas in Figure 3) represent regions of significantly enhanced permeability through which water can be expected to flow once circulation starts in the reservoir. However, more recent work has suggested that this hypothesis is open to question.

One large-scale correction technique which has been used attempts to prevent reservoir joints being squeezed shut near to the production borehole after the stimulation is complete. The technique involves injecting sand (referred to in this context as a 'proppant') into the joints. This would be done as part of a secondary

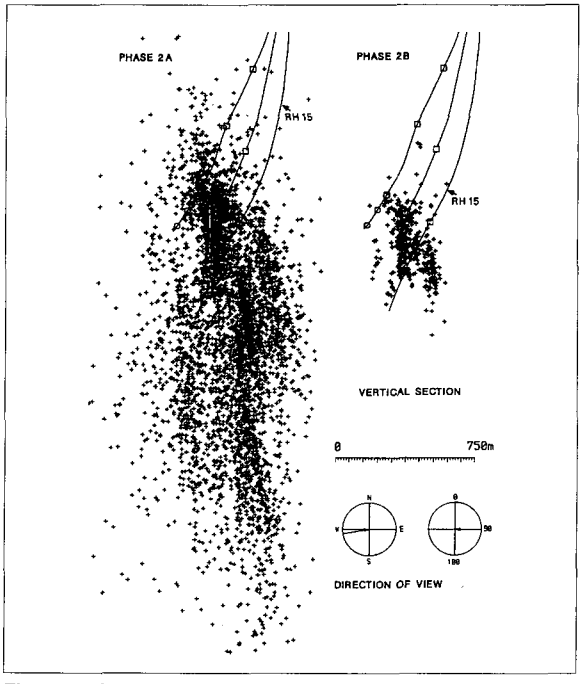

Figure 3 *Comparison of microseismicities from the Phase 2A (bulk water) and the Phase 2B (viscous gel) stimulations at Rosemanowes*

stimulation, by injecting a gel into the production borehole under pressure to open the joints and carry the proppant. If successful, the joints would remain propped open as the stimulation pressure was reduced.

A treatment would also be needed for short circuits, which would need to be sealed off to force the circulating water to take alternative, more effective, routes if the temperature of the production water were to be maintained. The ideal treatment would be to seal the short circuits within the reservoir using a temperature-sensitive gel, to congeal and block cold flow paths. But such gels are not yet available. The wall of the well could be sealed using conventional oilfield techniques, including cement, liners or packers.

When reservoir creation is complete and a reliable supply of hot water is available, there will still remain the task of converting it to electricity. A conventional condensing turbine has been considered but is unlikely to be used; power plants based on the organic Rankine cycle or the flash steam cycle are more efficient. This technology is well proven and electricity generation units are commercially available now for future HDR use.

THE UK PROGRAMME

The heart of the HDR R&D Programme in the UK has been a series of drilling and circulation experiments[1, 2, 3] carried out by the Camborne School of Mines at a disused granite quarry at Rosemanowes, near Falmouth in Cornwall. See Figure 4. Phase 1 work started in 1977

with a demonstration of the feasibility of establishing subsurface hydraulic connections between shallow (300 m) boreholes drilled into the granite. This was sufficiently successful to allow progress to Phase 2.

Phase 2 was an eight year project attempting to create an experimental commercial-scale HDR reservoir. In order to avoid high drilling costs and also the peripheral materials-related problems associated with the temperatures expected at 6 km depth, the project has been carried out at depths between 2 and 3 km, where maximum temperatures have been a more manageable 80°C. The rock jointing and stress régimes have been assumed to be similar to those at 6 km.

Two deviated boreholes spaced 300 m apart at depth were drilled to 2 km and a water stimulation made from the lower borehole to create a reservoir in the near-vertical joints rising to and intersecting the upper borehole. When circulation started, the reservoir did not behave as expected: water losses were too great for a commercially viable operation and the impedance and pumping pressures for circulation were too high. It was not possible to get within a factor of ten of the sustainable target production flow of 75 l/s. Detailed examination of the available microseismic evidence and findings from pumping and tracer tests suggested that each borehole had a large vertical reservoir beneath it, but that the interconnection between them was poor. To improve this connection by further hydraulic stimulation would have risked continuing reservoir growth and even greater water losses.

Measurements made after these two boreholes had been drilled showed that the direction of the maximum principal stress in the ground was aligned almost exactly with the borehole deviation – believed to be the worst possible alignment for HDR purposes. Consequently, a new borehole was drilled to a depth of 2600 m along a helical path crossing the original stimulated region at right angles to the vertical plane of the first two boreholes to try to get the maximum number of intersections. A medium-viscosity gel was used to stimulate a reservoir between this new borehole and the deeper of the original boreholes.

From the evidence of extensive circulation experiments, this new reservoir has proved to have substantially lower impedance and lower water losses than the original one, but its better hydraulic performance has been at the expense of thermal performance. The temperature of water at the top of the production borehole dropped from 80°C to 55°C over a three year period from 1985 to 1988. This is due to a short-circuit route that has been identified through the reservoir and which has significantly reduced its effectiveness as a heat exchanger. The rock surrounding the short circuit has cooled more rapidly than the rest of the reservoir. This has introduced colder water to the production borehole, thus lowering the final production water temperature. Efforts to date to seal the short circuit temporarily by mechanically closing off its entry to the production borehole using a steel pipe have been successful. Experiments are currently planned to seal off the short circuit permanently by non-mechanical methods.

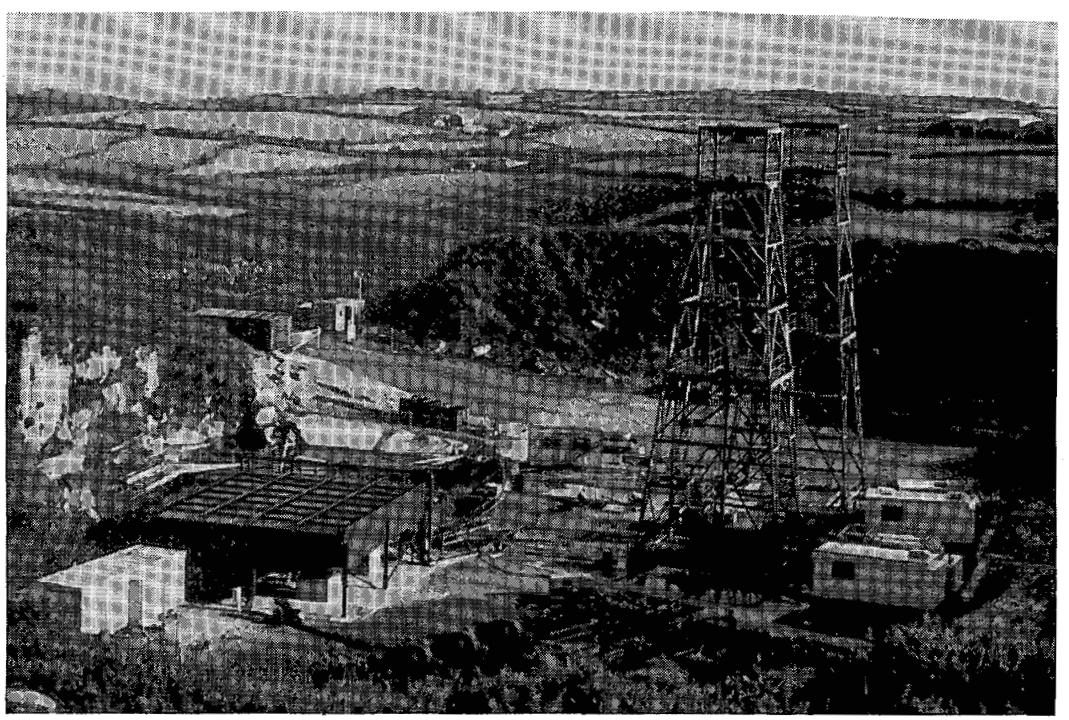

Figure 4 *Production and injection boreholes at Rosemanowes Quarry, Camborne School of Mines, located in Cornwall (UK) (Photo courtesy CSM)*

An experiment to place proppant particles in the joints close to the production borehole (as part of a secondary stimulation using high-viscosity gel) was successful in reducing water losses and reservoir impedance even further – but also served to worsen the short circuit; the reasons for this are unclear.

Throughout the period of the project, the experiments at Rosemanowes have been supported by other research including the development of modelling programs. The research has also included development of high-temperature downhole instrumentation (an example is illustrated in Figure 5) and data acquisition systems, investigation of geochemical effects in HDR systems and a continuous monitoring programme for possible seismic implications of HDR exploitation. The modelling has encompassed HDR costs, the dependence of temperature on depth, the size of the nationwide resource, and reservoir creation, manipulation and operation techniques (hydraulic, thermal and geochemical).

Since late 1988 when Phase 3 of the UK R&D Programme started, more emphasis has been placed on the commercial prospects for a viable HDR technology. RTZ Consultants Limited, assisted by the Camborne School of Mines, have carried out a conceptual design for a 6 km deep, commercial, HDR prototype.

Although this summary concentrates on UK research, other countries – notably the United States, France, Germany, Japan and Sweden – are also involved in HDR drilling, stimulation and circulation experiments. The main HDR work abroad is being carried out at Fenton Hill, New Mexico, USA, at Hijiori, Japan, and near Soultz, 50 km north of Strasbourg, France. None of this work is as advanced as that in the UK. The work at Soultz is funded by the French and German Governments, and by the Commission of the European Communities. An experimental hole is being drilled to 3 km .

The proposed European geothermal research programme includes a possible experimental prototype, and a first task is to carry out feasibility studies on sites in France, Germany and the UK with the intention of selecting a suitable site by about 1992.

THE RESOURCE

A simple analysis shows that there is a large amount of heat contained in the rocks at depth. A cubic kilometre of granite at 200°C contains approximately 4 x 10^{17} joules of heat and the cooling of this rock with a temperature reduction of 10% over a lifetime of 15 years would be equivalent to a thermal power transfer of 90 MW. However, the thermodynamics of the conversion of heat to electricity involves inevitable inefficiencies, and the maximum available electric power from the cubic kilometre is likely to be only about 12 MW. The size of the target reservoir described earlier

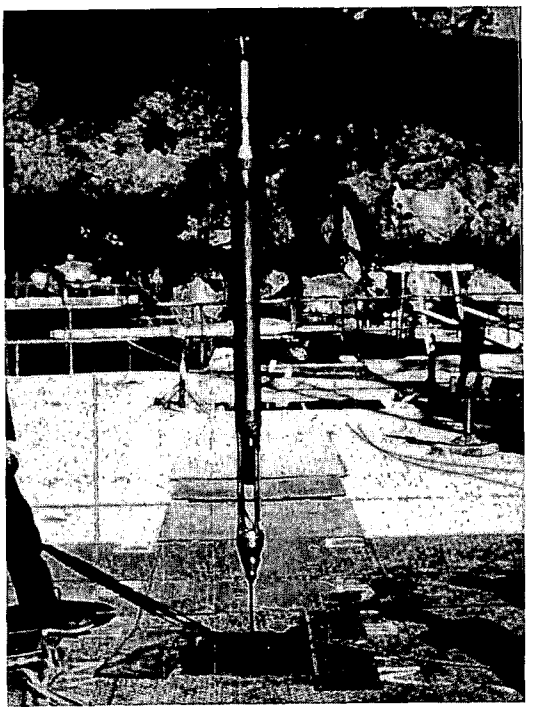

Figure 5 *Downhole 'hydrophones' developed by the Camborne School of Mines (Photo courtesy CSM)*

is about one-third of a cubic kilometre with a corresponding electric power of about 4 MW. Pumping requirements could halve this figure, resulting in a final net output of about 2 MW.

In practice the geothermal resource in the UK is limited to depths that can be reached by reasonably economic drilling. The economics of HDR and the size of the resource are thus inextricably linked. UK measurements[4] by the British Geological Survey carried out as part of the R&D Programme have established that only the south west peninsula of England and the Weardale area in north east England are likely to yield worthwhile temperatures at accessible depths.

HDR is for all practical purposes a non-renewable resource, available for extraction once only. Any subsequent reheating of the granite after HDR exploitation at a site would require thousands of years. For this reason, HDR is not a 'renewable' energy source like wind or wave power; but it offers an environmentally clean alternative to conventional fuels.

PRESENT STATUS

After a decade of funding by the UK Department of Energy in support of theoretical and experimental research into HDR technology in the UK, progress has been made in understanding the important factors controlling reservoir development and economics.

Nevertheless it is now concluded that:

- a satisfactory procedure for creating a commercial-scale HDR reservoir has yet to be demonstrated;
- no effective method of sealing reservoir short circuits has yet been demonstrated;
- there is little information available on the properties of rocks at the 6 km depths needed for commercial HDR reservoirs;
- although it is difficult to determine the economics of HDR accurately because of these technical uncertainties, electricity from a commercial-size HDR power station built in the short to medium term could be an order of magnitude more expensive than electricity generated by conventional means.

FUTURE PROSPECTS

Despite the promise of the technology in the early 1980s and an expenditure of £40M in the UK, HDR is still at an early stage of development. It is unlikely to attract private sector funding in the short term. Collaborative research within a European programme could however resolve some of the technical and economic uncertainties.

REFERENCES

1. Camborne School of Mines (1989), 'Camborne Geothermal Energy Project 2C-5: Final Report of Phase 2C (1986–1988)', Energy Technology Support Unit Report G 137F, Harwell Laboratory, UK

2. Taylor, R J (1988), 'The 1987/88 Geothermal HDR Programme Review', Energy Technology Support Unit Report R 46, Harwell Laboratory, UK

3. Camborne School of Mines (1990), 'Progress in Hot Dry Rock Geothermal Energy Technology for Application in South West England (1987–1989)', Energy Technology Support Unit Report G 151P1, Harwell Laboratory, UK

4. British Geological Survey (1988), 'Geothermal Energy in the UK: Review of the BGS Programme (1984–1987)', Energy Technology Support Unit Report G 131F, Harwell Laboratory, UK

PROCEEDINGS, Sixteenth Workshop on Geothermal Reservoir Engineering
Stanford University, Stanford, California, January 23-25, 1991
SGP-TR-134

The Economics of Heat Mining: An Analysis of Design Options and Performance Requirements of Hot Dry Rock (HDR) Geothermal Power Systems

Jefferson W. Tester and Howard J. Herzog
Massachusetts Institute of Technology
Energy Laboratory, Room E40-455
Cambridge, MA 02139

Abstract

A generalized economic model was developed to predict the breakeven price of HDR generated electricity. Important parameters include: (1) resource quality-- average geothermal gradient (°C/km) and well depth, (2) reservoir performance-- effective productivity, flow impedance, and lifetime (thermal drawdown rate), (3) cost components-- drilling, reservoir formation, and power plant costs and (4) economic factors-- discount and interest rates, taxes, etc. Detailed cost correlations based on historical data and results of other studies are presented for drilling, stimulation, and power plant costs. Results of the generalized model are compared to the results of several published economic assessments.

Critical parameters affecting economic viability are drilling costs and reservoir performance. For example, high gradient areas are attractive because shallower well depths and/or lower reservoir production rates are permissible. Under a reasonable set of assumptions regarding reservoir impedance, accessible rock volumes and surface areas, and mass flow rates (to limit thermal drawdown rates to about 10°C per year), predictions for HDR-produced electricity result in competitive breakeven prices in the range of 5 to 9 cents/kWh for resources having average gradients above 50°C/km. Lower gradient areas require improved reservoir performance and/or lower well drilling costs.

Introduction

The HDR geothermal energy resource is associated with accessible regions of hot rock beneath the earth's surface that do not contain sufficient natural porosity or permeability. Energy can be extracted by creating artificial permeability using hydraulic stimulation techniques to propagate and open joints or fractures. The resulting fracture network is connected to a set of injection and production wells where heat is removed by circulating water under pressure from the surface, down one well, through the fractured zone, and up a second well (see Figure 1). Electricity and/or process steam would then be generated using the heated water in an appropriately designed plant. This *heat mining* concept is closed-loop on the geothermal side so there are no effluents, thus minimizing the environmental impact of the entire HDR "fuel cycle" to site preparation, well drilling, and other land use issues.

Because HDR systems do not require natural, indigenous hot fluids and high permeability, the HDR resource itself can be defined by the accessible thermal energy in the earth's crust above some minimum temperature level. Thus the size of the HDR resource is very large and more widely distributed than natural geothermal systems. For example, in the U.S., to a 10 km depth assuming an average geothermal temperature gradient of 25°C/km and a minimum initial rock temperature of 150°C (deg C), the amount of thermal energy in place is about 10 million quads (Tester, Brown, and Potter (1989)). The worldwide HDR resource base is estimated at over 100 million quads (Armstead and Tester (1987)). Based on the enormous size and ubiquitous distribution of the resource and its positive environmental characteristics, HDR could provide an acceptable alternative to the fossil and nuclear options for meeting a substantial fraction of worldwide electric power and space and process heat demand.

The main objectives of this study were first, to review and analyze several economic assessments of Hot Dry Rock (HDR) geothermal energy systems, and second, to reformulate an economic model for HDR with revised cost components. This paper in large part is an extension of our earlier work on HDR economic forecasting (see Tester and Herzog (1990) for a detailed discussion of the methodology used). The economic models reviewed include the following studies sponsored by:

- Electric Power Research Institute (EPRI)-- Cummings and Morris (1979)
- Los Alamos National Laboratory (LANL)-- Murphy, et al. (1982)

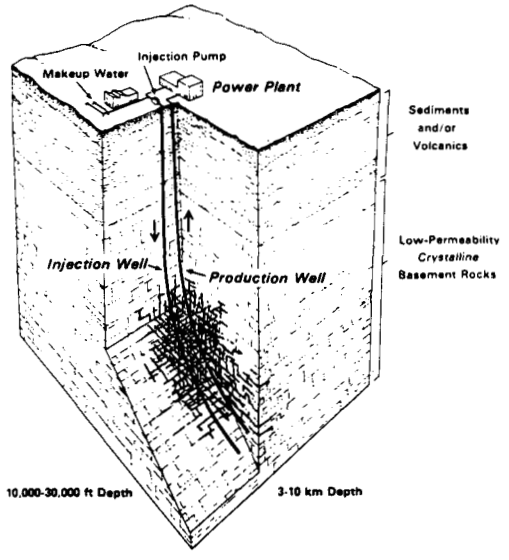

Figure 1. HDR reservoir concept for an interconnected network of fractures stimulated in a low-permeability formation (from Tester, Brown, and Potter (1989)).

- United Kingdom (UK)--Shock (1986) with an update by Harrison, et al. (1989)
- Japan--Hori, et al. (1986)
- Meridian--Entingh (1987)
- Bechtel (1988)
- Geothermik--Smolka and Kappelmeyer (1990)

Before discusssing the predictions of these models, HDR resource and performance parameters are reviewed.

Key Resource and Performance Parameters

The development of the HDR resource at a particular location depends largely on being able to gain access to high rock temperatures which will lead to acceptable fluid temperatures for generating electric power. Although some exploration for locating high quality HDR resources is required, the difficulty and costs associated with locating a suitable HDR site are far less than for hydrothermal or fossil fuel resource development. In fact, the more or less ubiquitous nature of the HDR resource suggests that its *grade* in terms of average geothermal gradient will be the single key factor influencing the "commercial-quality" of a particular site. In *Heat Mining*, Armstead and Tester (1987) subdivide the grade of HDR resources in the U.S. into two categories, *thermal* with above average gradients ≥38°C/km and *non-thermal* with gradients of about 20 to 25°C/km. About 16% of the land area in the U.S. can be categorized as a thermal area with a significant fraction existing in hyperthermal regions near or within active hydrothermal systems. A typical range for average gradients in such hyperthermal systems would be from 60 to 80°C/km. Fenton Hill, NM and Roosevelt Hot Springs, UT fall into this latter category.

Although HDR reservoir temperatures are selected as a design choice, an acceptable range can easily be bracketed for electric power applications. In any situation, one balances the cost of producing the fluid against the cost of converting its thermal energy into electric power. Effectively, this is equivalent to balancing drilling costs against power plant capital costs to reach a minimal total cost corresponding to optimal design temperature or reservoir depth for a particular HDR site. These effects are illustrated in Figure 2. Using the dashed line for reference, one can see that reservoir design temperature range from about 140°C for low gradient areas (20°C/km) to about 250°C or more for high gradient areas (>80°C/km) with a fairly flat minimum. Strictly speaking, the actual values of these reservoir design temperature optima depend on the capital costs and system performance assumptions used. These points are revisited again later in the paper.

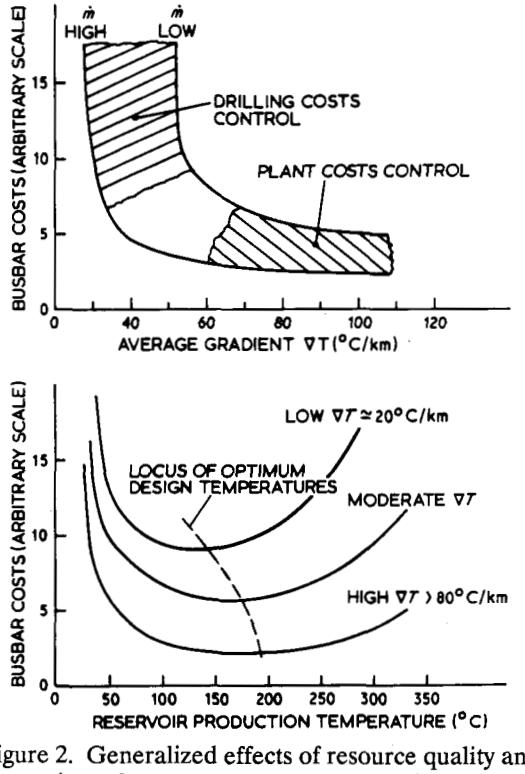

Figure 2. Generalized effects of resource quality and reservoir performance on busbar generating costs for HDR-produced electricity (from Armstead and Tester (1987)).

The temperature changes that may occur in the reservoir output fluid, as well as the rate of power production over the 20 to 40 year lifetime of an HDR system, are crucial in determining economic viability and in developing an optimal strategy for reservoir management. The most desirable approach is to maintain a constant output temperature while maximizing the mass flow rate of fluid through the reservoir. This will not be possible because any finite-sized HDR system will have a finite rate of temperature decline or drawdown. The energy drawdown rate for a fractured HDR reservoir with low formation permeability will depend on the following factors:

- Accessible fracture surface area and rock volume
- Mass flow rate of produced fluid
- Reservoir temperature distribution
- Distribution of fluid across the factured surface, and through the fractured region
- Thermal properties of the rock (density, heat capacity, and conductivity)
- Net impedance to flow and allowable pressure drop
- Water loss rates

High reservoir temperatures, low reservoir flow impedances, and large reservoir surface areas and volumes are desirable--leading to lower rates of thermal drawdown at specified fluid production rates. A key design objective is to maximize the rate of fluid throughput and energy production while minimizing the rate of drawdown. How closely this is achieved is the primary measure of energy extraction effectiveness. Furthermore with low impedance to flow, parasitic pumping losses will be minimized and in the optimal situation, "*self-pumped*" systems are possible as a result of buoyancy drive.

The issue of water loss raises some speculation about induced seismic effects and the possible economic impact of a large makeup supply of water in arid regions of the U.S. It should be emphasized that proper pressure management of the HDR system, which in extreme cases may require downhole pumping from the production well, can control or eliminate all water losses should they become a critical issue. Furthermore, in all testing to date, no measurable seismic risk has occurred.

The production of electricity from HDR geothermal resources can be accomplished in several ways. Technologies developed for low temperature energy sources such as solar, geothermal, and process waste heat are easily adaptable to the HDR system. Because pressurized hot water ranging in temperatures from about 150 to 300°C will be produced from HDR reservoirs, the following conversion options are possible (see Kestin, et al. (1980) and Tester (1982) for details):

- Single and multi-stage flash cycles
- Binary Rankine cycles employing organic working fluids (ORC)
- Trilateral Wet Vapor Cycle (TWVC) (Smith (1981))
- Total flow concepts such as the helical screw expander or the biphase turbine

Because HDR-produced fluids will most likely have low concentrations of dissolved salts and non-condensible gases, any of the four options cited above are technically acceptable in terms of performance -- economic factors will eventually determine what specific design selections are best suited to a particular HDR system and its heat rejection conditions.

HDR systems are flexible in their application to a variety of end uses. For example, they could be retrofitted to improve fossil conversion plants using cogeneration and feed water heating concepts. In some new design concepts under development, peaking with cyclic energy storage as well as the more traditional, base load applications are possible for HDR systems. A key point to remember is that HDR fluid/rock temperatures are selected by choice depending on end use requirements and the economic "grade" of a specific resource which is largely expressed by its average thermal gradient.

For all HDR applications that are envisioned, "off-the-shelf," commercial power plant systems are available. Further development of newer conversion technology such as the TWVC and total flow systems will undoubtedly increase the attractiveness of HDR by permitting operation at higher conversion efficiencies.

Comparison of HDR Economic Models

Key parameters and results for the seven analyzed studies have been tabulated in Tables 1 and 2 where one can easily see the extremely wide range of resource, reservoir, and economic parameters and assumptions. Therefore, any agreement in predicted breakeven electricity price must be regarded with

TABLE 1. COMPARISON OF KEY RESOURCE AND POWER PLANT PARAMETERS

PARAMETER	HDR ECONOMIC STUDY						
	EPRI (1979)	LANL (1982)	Japan (1986)	UK TWVC (1986)	Meridian III (1987)	Bechtel (1988)	Geothermik (1990)
Site Grade	low	high	high	low	high	high	low
Average Gradient (deg C/km)	40	55	120	35	62	78	41
Average Well Depth (km)	4	4.5	3	6	3	3.6	5.5
Initial Ave Reservoir Temp (C)	175	260	300	220	200	270	240
Flowrate per Well Pair (kg/s)	75	46	74	75	78	120	75
Water Loss Rate (%)	5	5	13	2	-	10	20
Reservoir Impedance (GPa-s/cum)	-	0.09	0.14	0.1	-	0.08	0.01
Drawdown (a)	low	moderate	moderate	low	moderate	high	moderate
Net Installed Capacity (MWe)	50	75	68.7	35.275	112	70	-
Reservoir Pumping Power (MWe)	-	0	9.2	2.275	7	20	-
Average Net Power Output (MWe)	50	75	59.5	33	105	50	-
Project Lifetime (yrs)	30	10/30	15	25	20	30	25

(a) Low corresponds to a drawdown parameter <0.0001 kg/sqm-s; moderate 0.0001-0.0002 kg/sqm-s; and high >0.0002 kg/sqm-s.

TABLE 2. COMPARISON OF NORMALIZED CAPITAL COST COMPONENTS AND PREDICTED ELECTRICITY PRICES (1989 $ BASIS)

PARAMETER	HDR ECONOMIC STUDY						
	EPRI (1979)	LANL (1982)	Japan (1986)	UK TWVC (1986) (d)	Meridian III (1987)	Bechtel (1988)	Geothermik (1990) (e)
Net Installed Capacity (MWe)	50	75	68.7	35.275	112	70	-
Individual Well Cost (M$)	-	6.3	5.8	8.2	3.0	4.0	-
($/kWe installed)	-	84.2	85.1	232.6	26.5	57.2	-
Total Well Costs (M$)	(b)	57.2	74.0	82.1	110.0	32.0	-
($/kWe installed)	-	762.9	1077.7	2326.4	982.2	457.8	-
Exploration Costs (M$)	7.9	3.6	44.2	8.1	49.6	-	-
($/kWe installed)	158.1	48.5	643.8	229.2	442.4	-	-
Stimulation Costs (M$)	(b)	7.4	22.4	8.2	54.5	15.2	-
($/kWe installed)	-	99.1	326.1	232.6	486.7	216.5	-
Fluid Distribution Costs (M$)	1.8	9.6	30.3	-	26.1	10.1	-
($/kWe installed)	37.0	128.6	336.7 (c)	-	233.1	144.4	-
Power Plant Costs (M$)	72.6	70.7	85.3	67.3	107.3	61.4	-
($/kWe installed)	1452.2	943.1	947.7 (c)	1908.8	957.8	877.3	-
Total Capital Cost (M$) (excl. AFDC)	137.1	148.7	256.3	165.7	347.4	118.7	-
($/kWe)	2741.3	1982.2	3730.1	4697.1	3102.2	1696.0	-
Average Net Power Output (MWe)	50	75	59.5	33	105	50	-
Total Capital Cost ($/kWe output)	2741.3	1982.2	4306.9	5020.9	3309.0	2374.4	-
Redrilling/Restimulation Costs (M$)	14.9	-	45.4	-	-	94.4	-
(M$/yr)	0.50	-	3.03	-	-	3.15	-
Other O & M Costs (M$/yr)	0.81	3.02	-	4.66	5.68	4.24	-
Electricity Breakeven Price (cents/kWh)	6.46	4.56	11.03	6.67	7.74	5.62	12.2

Notes: (a) All costs normalized to 1989$ using cost indexes in Figure 3 for drilling and plant construction costs.
Stimulation and exploration cost normalization based on drilling cost index.
Electricity breakeven price normalized on a hybrid, weighted cost index.
(b) Total well and stimulation costs are $55.8M or $1117/kWe installed.
(c) Based on 90 MWe installed.
(d) Conversion rates: $1 per pound for wellfield; $1.6 per pound for power plant.
(e) Conversion rate: 1.64 Dm/$. Individual component costs not available in this paper.

caution. Nonetheless, one can see why certain studies predict high prices and others lower ones or where particular cost components are out of line. We will discuss these predictions again later in the context of our generalized HDR economic model.

A major purpose of analyzing each study was to extract component cost information in order to guide us in developing a set of composite conditions. In addition, by reviewing the other assumptions regarding reservoir and power plant performance used in each study, we can construct a reasonable model that brackets the range of values assumed. Furthermore, by studying the range of costs and other factors, we have developed suitable intervals for parameter sensitivity studies.

HDR Component Costs

Drilling and Completion Costs

To establish base case costs and a cost range for HDR drilling, we reviewed all available drilling and completion cost data for geothermal (hydrothermal and HDR) and oil and gas wells for the period 1972-1988. The geothermal well costs came from a number of sources including Carson and Lin (1981), Entingh (1989), Batchelor (1989a), and Armstead and Tester (1987) as well as from the seven case studies being examined. Joint Association Survey (JAS) data for drilling and completing oil and gas wells in the continental U.S. in a particular year were used as a reference point to compare actual HDR well costs against.

In order to normalize well costs to a common year dollar, a drilling cost index was established as shown in Figure 3. To develop this index, JAS average oil and gas well costs based on total footage for depths ranging from 1250 ft (0.38 km) to 20,000 ft (6.1 km) were used from 1977 to 1988. In addition, Energy Information Administration (EIA) costs for 1976 to 1977 (Anderson and Funk (1986)) was used to supplement the JAS data base. For wells drilled before 1976, a 17% annual inflation factor was assumed.

Table 3 gives actual and predicted drilling and completion costs for individual wells for HDR and hydrothermal systems. 1988 JAS composite costs for completed oil and gas wells are also included in Table 3. Dry well costs were not included in deriving the JAS composite. Costs for average well depths are shown. Figure 4 presents a composite of actual and predicted well costs normalized to 1989 $. The collection of individual well cost data from a number of hydrothermal sites in the U.S. compiled by Carson and Lin (1981) was normalized to 1989 $ and plotted in Figure 5. The straight line plotted in Figures 4 and 5 corresponds to a least squares fit of the 1988 JAS oil and gas composite well cost data extrapolated to 1989 $. One immediately sees that without exception, all hydrothermal and HDR well costs are higher than a typical, average oil and gas well drilled to the same depth. Furthermore, the *bandwidth* of costs for HDR wells lies somewhat above the scatter of hydrothermal wells.

Following the methodology described earlier by Milora and Tester (1976) and later updated by Armstead and Tester (1987), we chose to establish a range of expected drilling costs for HDR wells drilled to 10 km depths. In Figure 4, an HDR base case curve has been plotted with an upper bound (HDR problem burdened) and a lower bound (HDR commercially mature) shown.

Stimulation Costs

Developing and perfecting HDR stimulation methods have been a major focus of the U.S. and UK R&D programs during the past 15 years (see Armstead and Tester (1987), Batchelor (1984 (a,b), 1987, 1989b), Tester et al. (1989) and Brown et al. (1990) for details). Although the field efforts have made considerable progress, there is not yet sufficient knowledge regarding rock fracturing characteristics to absolutely guarantee that a fractured network of sufficient size and viability can be created and connected to an appropriately designed injection and production well system. Given this inherent uncertainty, we must make several assumptions regarding the formation of such a reservoir system in order to proceed with an economic assessment of HDR.

All studies have assumed that current fracturing technology (or some modest extension of it) is sufficient to create a viable HDR reservoir at depths of interest. In addition, they have estimated the costs associated with these stimulation methods. These include the costs of pumping at high pressures and rates, costs for fluids with special rheological properties, and the costs of diagnostic geophysical testing. Figure 6 provides an estimate of stimulation costs per kWe of net installed capacity for different temperature reservoirs. Also plotted on the same figure are specific estimates for stimulation costs taken from the economic assessment studies. Note that we have tried to account for the effect of resource grade on the stimulation costs by plotting costs as a function of initial reservoir temperature. Lower gradient regions will in general require deeper wells and/or higher well flow rates and therefore proportionately higher stimulation costs will result.

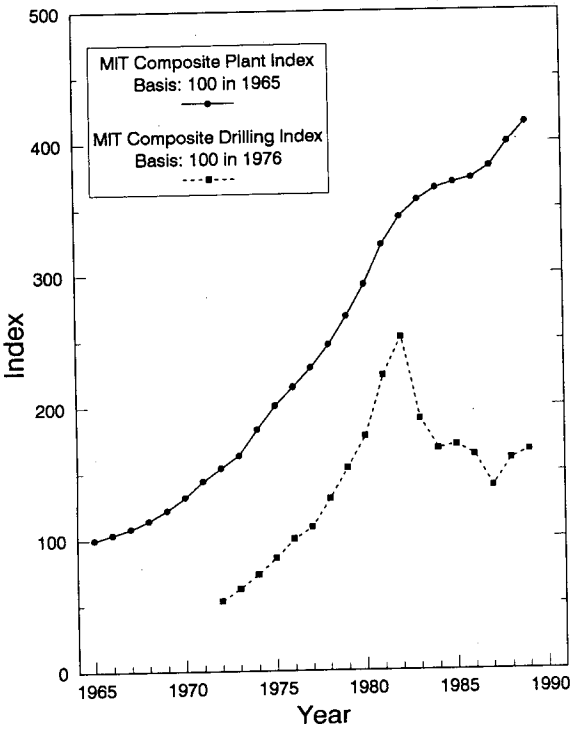

Figure 3. Estimated plant construction and drilling cost inflation indexes.

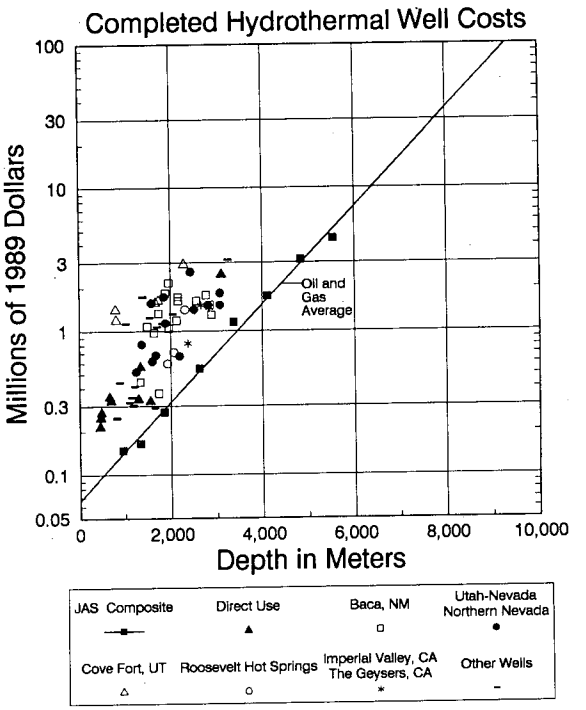

Figure 5. Actual hydrothermal completed well costs as a function of depth (adapted from Carson and Lin (1981), Batchelor (1989a), and the Joint Association Survey (1988)).

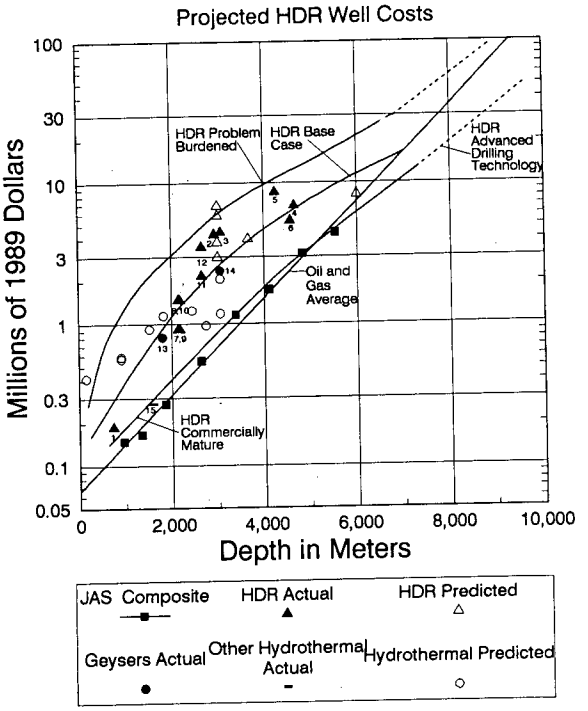

Figure 4. Projected HDR well drilling and completion costs for the base case with limits for problem-burdened, commercially mature, and advanced drilling technology shown.

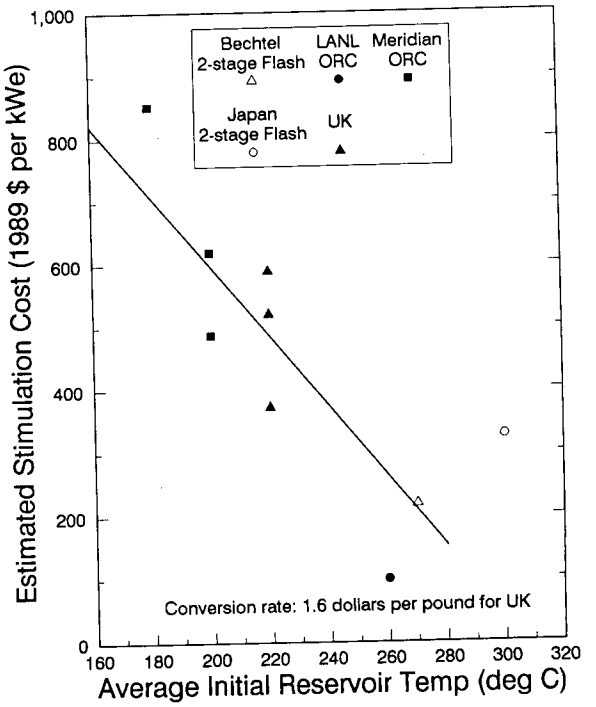

Figure 6. Estimated HDR reservoir stimulations costs in $ per kWe installed as a function of average initial reservoir temperature. Note that ORC (Organic Rankine Cycle) and 2-stage flash refer to power plant choices.

TABLE 3. ACTUAL AND PREDICTED DRILLING AND COMPLETION COSTS (1989$)

Plot #	Well ID	Depth Meters	Cost M$	Year Com-pleted	Cost 1989 M$	Comments
1	GT-1	732	0.060	1972	0.187	Fenton Hill Site, New Mexico, USA.
2	GT-2	2,932	1.900	1974	4.315	Actual costs.
3	EE-1	3,064	2.300	1975	4.465	
4	EE-2	4,660	7.300	1980	6.827	
5	EE-3	4,250	11.500	1981	8.545	
6	EE-3A	4,572	5.160	1988	5.364	
7	RH-11 (low)	2,175	1.240	1981	0.921	Rosemanowes Site, Cornwall, UK.
8	RH-11 (high)	2,175	1.984	1981	1.474	Actual costs.
9	RH-12 (low)	2,143	1.240	1981	0.921	Conversion rates:
10	RH-12 (high)	2,143	1.984	1981	1.474	low = $1 per pound.
11	RH-15 (low)	2,652	2.250	1985	2.192	high = $1.6 per pound.
12	RH-15 (high)	2,652	3.600	1985	3.507	as recommended by A.S. Batchelor (1989a).
	UK (Shock, 1987)	6,000	8.424	1985	8.206	From Camborne School of Mines ($1 per pound).
	Bechtel (1988)	3,657	3.359	1987	4.006	Predictions for Roosevelt Hot Springs, UT Site.
	Japan (1986)	3,000	6.000	1985	5.845	Predicted costs.
	Meridian (1987) I	3,000	6.900	1984	6.838	Predicted costs based on Heat Mining.
	Meridian (1987) II	3,000	3.800	1984	3.766	
	Meridian (1987) III	3,000	3.000	1984	2.973	
	Heat Mining (1987)	3,000	3.000	1984	2.973	Predicted costs.
13	Geysers	1,800	0.486	1976	0.807	Actual costs cited in Milora and Tester (1976).
14	Geysers	3,048	2.275	1989	2.275	Actual costs from A.S. Batchelor (1989a).
15	Other Hydrothermal	1,600	0.165	1976	0.274	Actual costs cited in Milora and Tester (1976).
	IM-GEO IV-FL	1,829	1.123	1986	1.146	Meridian predictions of hydrothermal wells
	IM-GEO IV-BI	2,743	0.956	1986	0.975	from their IM-GEO data base (Entingh, 1989).
	IM-GEO BR-FL	2,438	1.217	1986	1.242	Only base well costs shown.
	IM-GEO BR-BI	914	0.556	1986	0.567	See key below for hole details.
	IM-GEO CS-FL	3,048	2.032	1986	2.073	
	IM-GEO CS-BI	914	0.576	1986	0.588	
	IM-GEO YV-FL	1,524	0.906	1986	0.924	
	IM-GEO YV-BI	152	0.406	1986	0.414	
	IM-GEO GY-DS	3,048	1.155	1986	1.178	
	JAS	954	0.142	1988	0.148	Actual costs for oil and gas wells
	JAS	1,340	0.160	1988	0.166	from Joint Association Survey (1988).
	JAS	1,859	0.263	1988	0.273	
	JAS	2,628	0.528	1988	0.549	
	JAS	3,376	1.111	1988	1.155	
	JAS	4,108	1.682	1988	1.748	
	JAS	4,834	3.019	1988	3.138	
	JAS	5,539	4.236	1988	4.403	

Plot #'s refer to Figure 4.

M$ = Millions of US Dollars.

Key:

IV-FL - Imperial Valley Flash, Salton Sea, CA field.

IV-BI - Imperial Valley Binary, Heber, CA field.

BR-FL - Basin and Range Flash, Dixie Valley, NV field.

BR-BI - Basin and Range Binary, generic NV field.

CS-FL - Cascades Flash, Newberry, OR field.

CS-BI - Cascades Binary, generic OR, WA field.

YV-FL - Young Volcanics Flash, Coso, CA field.

YV-BI - Young Volcanics Binary, Mammoth, CA field.

GY-DS - Dry Steam, The Geysers, CA field (Costs from B.J. Livesay).

This methodology for estimating stimulation costs falls short of providing a clear dependence of costs on the size of the reservoir. Consequently, we examined an alternate approach. In Figure 7, the estimated cost of stimulating an HDR doublet system is plotted as a function total effective reservoir surface area in m^2 per kWe of installed capacity. By using the installed capacity to normalize costs and reservoir size, the effect of fluid temperature (and hence gradient and depth) on conversion efficiency is accounted for. Data from the Bechtel, LANL, Meridian, Japan, and UK HDR economic studies are plotted along a regressed line (solid) for the composite base case that will be used in the economic projections described later in this paper. One should note that the Meridian Organic Rankine Cycle (ORC) estimates were not used in the regression. The dotted lines shown represent twice (200%) and one half (50%) of the composite base case stimulation costs to illustrate the range of estimates.

Following the Shock (1987) study, Mortimer and Minett (1990) reexamined drilling and stimulation costs for HDR development in the UK. For a doublet well system 6 km in depth, they estimate a drilling and completion cost of 10.314 million £ ($16.5 million per doublet or $8.25 million per well at $1.6/£). This is essentially identical to the normalized Shock (1987) estimate of $8.42 million per well. Nonetheless, Mortimer and Minett's stimulation costs are considerably different than those from the Shock study and from this study's projections. For the same 6 km doublet, Mortimer and Minett estimate a cost for 3 stimulations of 6.004 million £ ($9.6 million) or 37% of the total subsurface system costs. Shock used 10% of the well costs ($1.68 million for a 6 km doublet system), which lies on our base case line in Figure 7. We feel that Mortimer and Minett's approach of using large volumes of expensive rheologic gelled fluids is too pessimistic based primarily on U.S. fracturing experience at Fenton Hill. However, in all cases, stimulation cost estimates should be regarded as only approximate in that the technology for creating commercial-sized HDR reservoirs is still under development. In the discussion that follows, we perform sensitivity analyses to further quantify the uncertainties associated with the stimulation cost component.

Power Plant Costs

Estimated costs in 1989 $/kWe installed for HDR power plants are shown in Figure 8 as a function of the fluid production temperature that would enter the plant. An upper limit of 300°C was chosen to avoid problems of mineral transport and deposition with the HDR reservoir/power plant system. A nominal 50 MWe sized plant has been selected with costs shown for an appropriate range of conditions that would be expected for applications in the U.S. A median or base case line is shown, but some variations are anticipated for different sites, geologic and ambient conditions, and plant designs. For example, heat rejection using wet cooling with ocean or river water would result in more efficient cycles, in general, with lower costs. Dry cooling or wet/dry cooling in regions of high ambient temperature and/or limited water availability would have lower efficiencies and somewhat higher costs on a $/kWe basis.

In order to achieve a common 1989 $ cost basis for plant costs, a composite cost index was developed. The data used to develop the composite came from several sources including the Chemical Engineering (CE) Plant Cost Index, Marshall and Swift (M & S) Equipment Cost Index, Nelson Refinery Construction Cost Index, and the Engineering News-Record (ENR) General Construction Cost Index. All cost indexes were normalized to 100 in 1965 and a linear average for each year was used to estimate the MIT composite index as shown in Figure 3. The composite index was then used to convert all plant costs from the studies to a 1989 $ basis. The generic cost curve from *Heat Mining* (Armstead and Tester (1987)) was also normalized and plotted for reference, and as can be seen from Figure 8, the base case line selected is approximately the same as the generic example from *Heat Mining* at a condensing temperature of 37°C. It is important to emphasize that these cost estimates are only to be used for HDR resources in the temperature range shown from 125 to 300°C; extrapolation outside the range could lead to serious errors.

Also plotted in Figure 8 are estimated power plant installed costs for the specific designs selected in the HDR economic studies. No total flow plant costs, other than the TWVC, were provided in the seven studies. Based on the observed agreement among U.S. cost estimates, we would anticipate that estimated installed HDR power plant costs would be accurate to ±20%. At any rate, the uncertainty in plant costs is significantly lower than for HDR drilling and stimulation costs as discussed above.

Generalized HDR Economic Model for Electricity Production

Building on the models and correlations presented above, a generalized HDR economic model was developed. To distinguish it from other treatments, we have labelled it the *MIT HDR* economic model, with no Institute endorsement implied. For a given

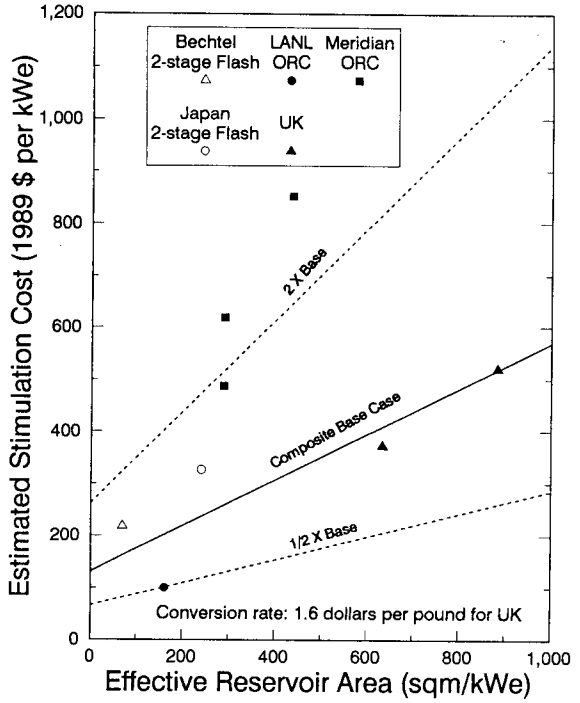

Figure 7. Estimated HDR reservoir stimulation costs in $ per kWe installed as a function of normalized effective reservoir surface area in m^2/kWe installed.

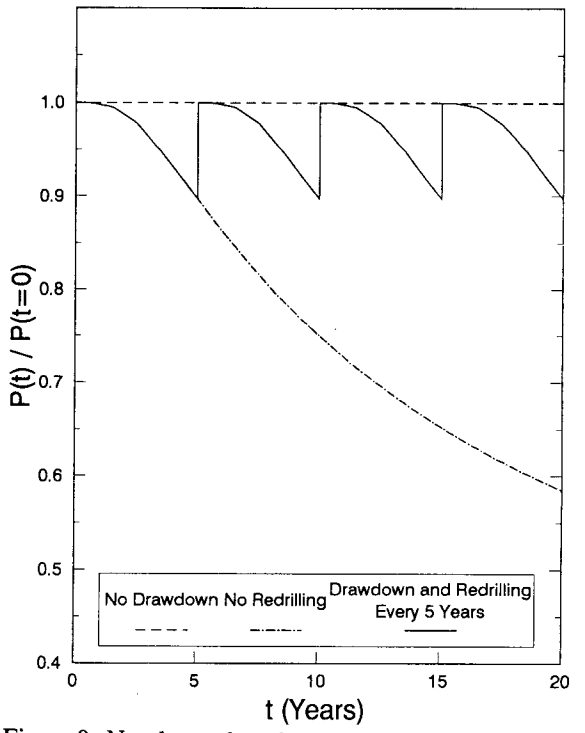

Figure 9. Net thermal performance levels as a result of thermal drawdown and redrilling/restimulation. For comparison, the cases of no drawdown and drawdown with no redrilling are shown. P(t) is the thermal power extracted at time t.

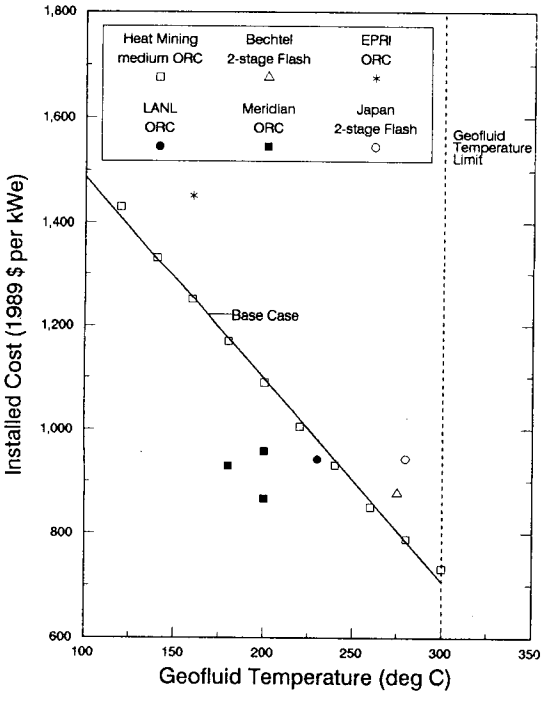

Figure 8. Estimated HDR power plant construction costs for the U.S. Base case cost estimates should only be used in the geofluid temperature range from 100° to 300°C.

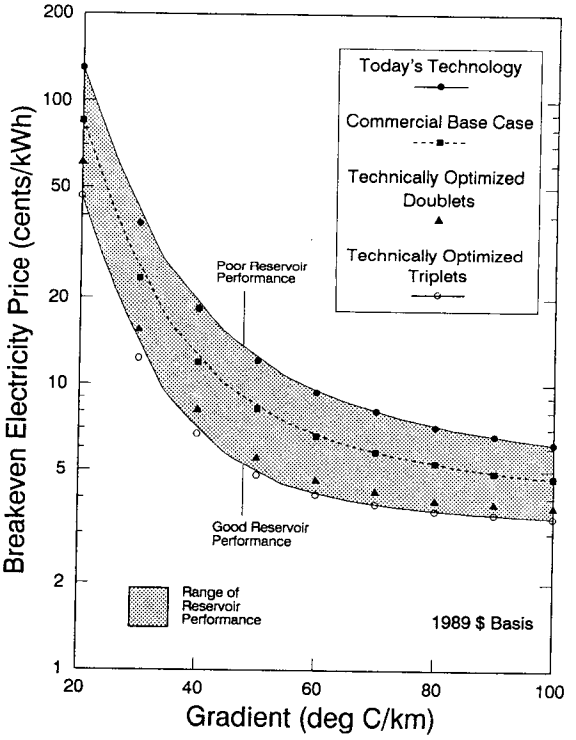

Figure 10. *MIT HDR* economic model results for electricity breakeven price as a function of gradient and reservoir performance.

set of parameters which define a technology case, the model calculates breakeven electricity price as a function of gradient. To cover a range of reservoir performances and costs, the following four technology cases were considered:

- **Today's Technology (TODAY) Case** - Reflects today's relatively high drilling and completion costs (see Figure 4, HDR Base Case line) with poor reservoir performance at a level comparable to the Fenton Hill System.

- **Commercial Base (BASE) Case** - Keeps same drilling and completion costs as the TODAY case, but reflects the improved reservoir performance required for commercial operation.

- **Technically Optimized Doublet (DOUBLET) Case** - Combines good reservoir performance with optimized drilling and completion costs (see Figure 4, HDR Commercially Mature line).

- **Technically Optimized Triplet (TRIPLET) Case** - Maintains same optimized drilling costs as DOUBLET case, but improves reservoir performance with a configuration of 1 injector and 2 producer wells per reservoir.

The specific parameters used to define these cases are detailed in Table 4. A thermal drawdown rate of 2% per year was selected. This corresponds to an effective drawdown parameter of 1.4×10^{-4} kg/m^2•s. Redrilling and restimulation are done at 5 year intervals to restore reservoir temperatures to their initial values. This is shown in Figure 9. For comparison, the cases of no drawdown and drawdown with no redrilling are also shown. For the cases with drawdown, the thermal power levels (P(t)) follow an error function dependence on effective reservoir heat transfer area ($<A>$), mass flow rate ($\dot{m}$) and time (t) as given by equation A-5 in Appendix A.

The model calculates several important engineering parameters, including average well depth, initial reservoir temperature, geothermal fluid temperature and availability, utilization efficiencies, effective reservoir area, overall pressure drop, and pumping power. Costs are calculated on a per kWe installed basis. This has the advantage of eliminating plant size as a model parameter. However, results will be most accurate for facilities in the 25-100 MWe installed capacity range, since this is the range upon which most of the correlations are based. This capacity range also corresponds to the most probable size of HDR plants to be built.

A fixed annual charge rate approach is employed because it is easy to implement and use. A 15.34% annual charge rate suggested by Entingh (1987) was incorporated. In our preliminary analyses, we used both a fixed annual charge rate and a levelized lifecycle approach. Our results showed both methods give the same trends, with the fixed charge rate yielding about 15% higher electricity breakeven prices.

The drilling and completion, stimulation, and power plant costs used were estimated from the base cases shown in Figures 4, 7, and 8, respectively. Redrilling and restimulation costs were averaged over the plant lifetime and treated as increments to the operating and maintenance (O&M) costs. All results are presented in 1989 dollars.

The key results of the *MIT HDR* economic model are given in Figure 10 and Table 5. To get a better feel for the results, compare Figure 10 to Figure 2. (Note: Figure 10 has a logarithmic y-axis compared to a linear one for Figure 2). These graphs have the same form and the discussion of Figure 2 applies equally to Figure 10. As the gradient decreases, drilling and completion costs become more dominant and drive the busbar costs up exponentially. Much of the range in costs at a given gradient is a result of reservoir performance. Poor performance translates into low geothermal fluid flowrates per well pair or per reservoir, which drive up the costs.

One place the model results differ with the earlier discussion is in optimum reservoir production temperatures (i.e., drilling depths). Figure 11 summarizes the model results. At 40°C/km and above, the model suggests drilling to a depth associated with the maximum allowable reservoir temperature (300°C). Only at lower gradients is an optimum found at lower reservoir temperatures (180-200°C for 20°C/km and 220-245°C for 30°C/km). The optimization of other reservoir and power plant design parameters are discussed in a general treatment outlined in Appendix A.

Figure 12 compares the *MIT HDR* economic model results to the breakeven electricity price reported in the seven other economic studies analyzed. Predictions using the generalized HDR economic model are in general agreement with the normalized results of the several of seven previous HDR economic studies. This agreement, however, is fortuitous unless the individual component costs for each model are close to one another. Most of the time, there was only minimal agreement on specific component costs such as drilling, stimulation, or power plant costs. But to the extent that the studies agreed on their methodology, we were able to use their data to justify and specify critical cost components in the revised composite model.

On another note, we recently received a copy of a

TABLE 4. MIT HDR ECONOMIC MODEL - CASE DEFINITIONS

TECHNOLOGY CASE	TODAY	BASE	DOUBLET	TRIPLET
ENGINEERING PARAMETERS				
Water Loss Rate (%)	5	5	5	2.5
Capacity Factor (%)	86	86	86	90
Redrilled Wells / Initial Wells	0.5	0.5	0.5	0.17
# Injectors / # Producers	1.0	1.0	1.0	0.5
Pump Efficiency (%)	80.0	80.0	80.0	80.0
Drawdown Parameter (kg/sqm-s)	0.00014	0.00014	0.00014	0.00007
T Reservoir - T Geofluid (deg C)	15.0	15.0	15.0	15.0
Maximum Reservoir T (deg C)	300.0	300.0	300.0	300.0
Production Well Flowrate (kg/s)	40.0	75.0	75.0	75.0
Reservoir Impedance (GPa-s/cum)	0.30	0.10	0.08	0.08
Injector Well Casing ID (in)	7	7	7	8.681
Producer Well Casing ID (in)	7	7	7	7
ECONOMIC PARAMETERS				
Fixed Charge Rate (%)	15.34	15.34	15.34	15.34
AFDC Rate (%)	9.0	9.0	9.0	9.0
Project Lifetime (yrs)	20.0	20.0	20.0	20.0
COST CORRELATIONS				
Drilling and Completion (Figure 4)	Base	Base	Mature	Mature
Stimulation (Figure 7)	2X Base	Base	0.5X Base	0.5X Base
Power Plant (Figure 8)	Base	Base	0.9X Base	0.9X Base

TABLE 5. MIT HDR ECONOMIC MODEL - RESULTS

GRADIENT deg C/km	BREAKEVEN ELECTRICITY PRICE (1989 $ basis) cents/kWh			
	TODAY	BASE	DOUBLET	TRIPLET
20	129.8	85.3	60.9	46.6
30	37.5	23.5	15.5	12.3
40	18.4	11.9	8.1	6.7
50	12.1	8.2	5.5	4.8
60	9.4	6.6	4.6	4.1
70	8.1	5.8	4.2	3.8
80	7.1	5.3	3.9	3.6
90	6.6	4.9	3.8	3.5
100	6.2	4.7	3.7	3.4

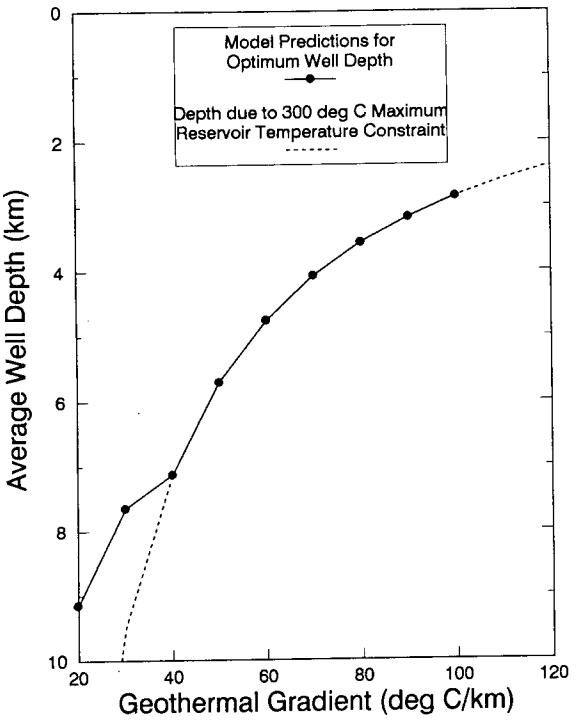

Figure 11. *MIT HDR* economic model predictions for optimum well depth as a function of gradient for the commercial base case.

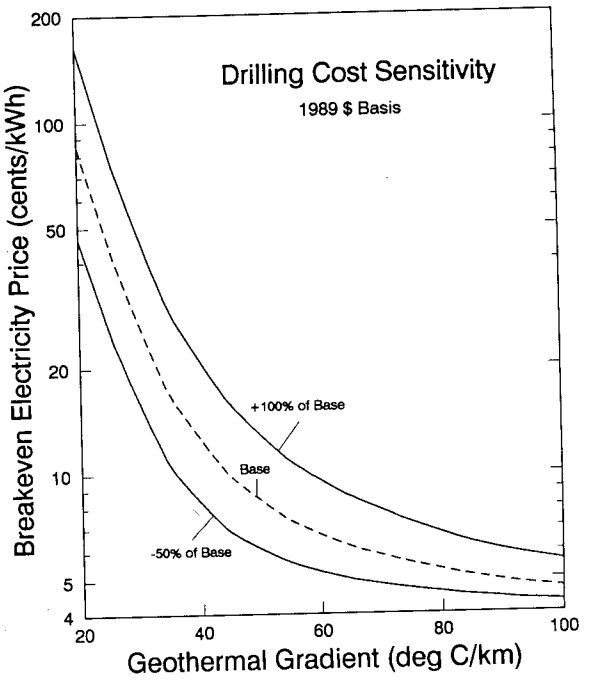

Figure 13. Sensitivity of the *MIT HDR* economic model base case to doubling and halving the drilling and completion costs.

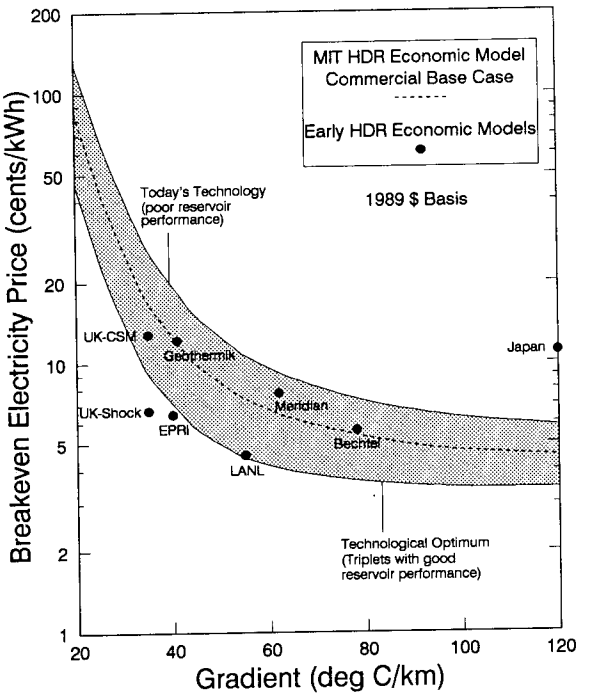

Figure 12. Comparison of *MIT HDR* economic model results to those of the seven economic studies analyzed for this report. UK estimates based on Harrison, et al. (1989) study (UK-CSM point) added at a conversion rate of $1.6/£.

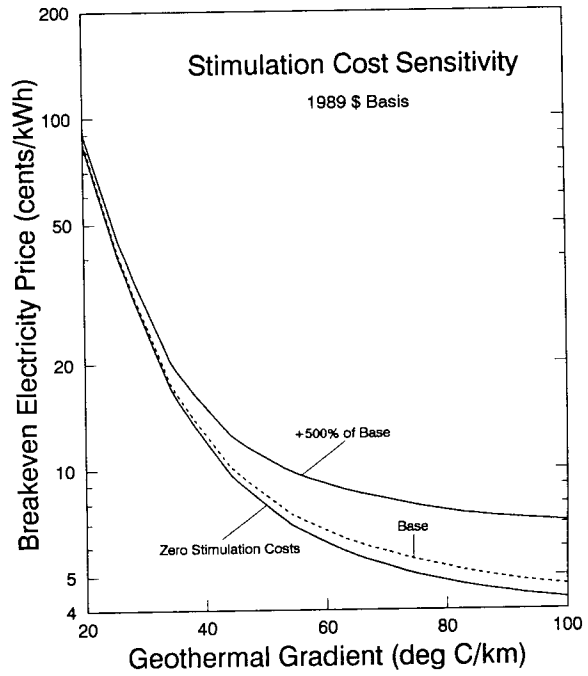

Figure 14. Sensitivity of the *MIT HDR* economic model base case to stimulation costs. The two sensitivity cases considered are zero stimulation costs and six times the base case stimulation costs (+500% of base).

paper by Harrison, Doherty, and Coulson (1989) that updates the Shock (1986) study of HDR economics in the UK. The resource and reservoir performance parameters used by Harrison, et al. are identical to those used by Shock (see Table 1). However, Harrison and coworkers based their power plant design on a two stage-flash system. Although their results are not presented in detail, their estimate of 8 pence/kWh (approximately 12.8¢/kWh) is very consistent with our projections for mid- to low-grade HDR resources.

Case studies were performed with the *MIT HDR* economic model to determine breakeven price sensitivity to certain model parameters. This phase of the investigation focused on areas with the greatest uncertainty, specifically optimum well depth, drilling and completion costs, stimulation costs, and thermal drawdown rates. Our analysis showed:

1. The price versus depth curve is fairly flat near the optimum (see Figure 2). This leads to some uncertainty as to optimum drilling depth.

2. Price is highly sensitive to drilling and completion costs (see Figure 13). At low and mid-gradients, this sensitivity is an order of magnitude greater than sensitivity to stimulation costs (see Figure 14) or to power plant costs.

3. The MIT HDR model is much more sensitive to production flowrate than drawdown. Thus, maximizing flowrate per reservoir is desirable, even at the expense of increasing drawdown rate. Of course, this principle cannot be carried to the extreme limit of an unacceptably high rate of drawdown that would not permit an adequate payback of the capital investment in drilling and stimulation.

Conclusions and Recommendations

Several general conclusions can be drawn from our projections assuming base case performance and costs:

1. High-grade (80°C/km) HDR resources are competitive at today's energy prices.

2. Mid-grade (50°C/km) HDR resources are only marginally competitive at today's energy prices. With higher oil prices >30$/bbl and/or environmental costs associated with fossil-fuel fixed systems, e.g., an acid rain or carbon tax, mid-grade HDR systems would be competitive.

3. Low-grade (30°C/km) HDR resources would not be competitive for electricity production until significantly higher energy prices exist. Although it should be noted for direct heat (space or process heating) or for cogeneration applications, low-grade HDR resources would compete much more favorably because Second Law efficiencies for conversion of HDR thermal energy into electricity are not relevant.

As a result of our economic analysis, we can identify where research should be focussed to improve the commercial viability of lower grade HDR resources (<50°C/km). The technologically optimized cases are first guesses of how far advanced drilling and reservoir stimulation technology might go with a sustained R&D effort. An R&D effort should be sustained in order to continue the development of the following crucial elements of HDR technology:

- Improved drilling technology to lower drilling and completion costs. This will open up the low- to mid-grade HDR resource for commercial development.

- Reservoir formation and stimulation technique development to improve reservoir performance, including flow impedance reduction. This will lower costs proportionately.

- Reservoir diagnostic technique development using seismic, tracer, and other geophysical methods for geometry characterization and system design optimization to reduce risk.

- Modeling of the thermal-hydraulic and geochemical behavior of fractured HDR reservoirs to reduce risk.

- Evaluation of untested concepts such as operation with multiple production wells (e.g. triplet arrangement); cyclic operation with pumped storage for peaking power supply or hybrid/cogeneration applications to demonstrate flexibility of HDR systems.

Acknowledgement

The authors would like to express their appreciation to those individuals who provided important data and comments. Although it would be impossible to name them all, J.N. Albright, H.C.H. Armstead, A.S. Batchelor, D.W. Brown, F. Cochrane, R.E. Cummings, D. Duchane, R.B. Duffield, J. Dunn, D. Entingh, S. Fleming, R. Grieder, C.O. Grigsby, R. Hendron, A. Jelacic, J.E. Livesay, J.E. Mock, G. Morris, H.D. Murphy, C.W. Myers, R. Nicholson, J. Owen, R.M. Potter, J.E. Rannels, F. Roach, B.A. Robinson, I. Smith, M.C. Smith, C. Tosaya, R. Traeger, and J. Whetten were

especially helpful. A. Carbone and J. Hale are gratefully acknowledged for their help in preparing the paper. The Geothermal Technology Division of the U.S. Department of Energy, Sandia National Laboratories and the MIT Energy Laboratory provided partial support for this project. The views and opinions presented in this report are solely those of the authors, and as such, do not necessarily reflect an endorsement by the U.S. Government, its agencies or laboratories.

References

Anderson, T.C. and V.T. Funk, "Indexes and Estimates of Domestic Well Drilling Costs 1984 and 1985," Energy Information Administration report DOE/EIA-0347 (84-85), Washington, D.C. (1986).

Armstead, H.C.H. and J.W. Tester, *Heat Mining*, E.F. Spon, London (1987).

Batchelor, A.S., "Hot Dry Rock Geothermal Exploitation in the United Kingdom," *Modern Geology*, Vol. 9, pp. 1-41 (1984a).

Batchelor, A.S., "Hot Dry Rock Reservoir Stimulation in the UK--an Extended Summary," and "An Overview of Hot Dry Rock Technology," 4th Int. Conf. on Energy Options, The State of Alternatives in the World Energy Scene, IEE Papers, London (1984b).

Batchelor, A.S., "Development of Hot Dry Rock Systems in the UK," IEE Proc. A, Vol. 134(5), London pp. 371-380 (1987).

Batchelor, A.S., GeoScience Ltd., Falmouth, UK, personal communication, 12 Dec 1989 (1989a).

Batchelor, A.S., "Hot Dry Rock and Its Relationship to Existing Geothermal Systems," Camborne School of Mines International Hot Dry Rock Conference, Camborne, Cornwall, England, July 1989, 20 pages (1989b).

Bechtel National, Inc., "Hot Dry Rock Venture Risks Investigation," Final report for the USDOE, under contract DE-AC03-86SF16385, San Francisco, CA (1988).

Brown, D.W., R.M. Potter, and C.W. Myers, "Hot Dry Rock Geothermal Energy - An Emerging Energy Resource with Large Worldwide Potential," in *Energy and Environment in the 21st Century*, MIT Press, Cambridge, MA (1990).

Carson, C.C. and Y.T. Lin, "Geothermal Well Costs and Their Sensitivity to Changes in Drilling and Completion Operations," Proc. Int. Conf. on Geothermal Drilling and Completive Technology, Albuquerque, NM, pp. 21-23 (1981).

Cummings, R.G. and G.E. Morris, "Economic Modeling of Electricity Production from Hot Dry Rock Geothermal Reservoirs: Methodology and Analyses," EPRI report EPRI EA-630, Palo Alto, CA (1979).

Entingh, D., "Historical and Future Cost of Electricity from Hydrothermal Binary and Hot Dry Rock Reservoirs, 1975-2000," Meridian Corp. report 240-GG, Alexandria, VA (1987).

Entingh, D., personal communication, Meridian Corp., Alexandria, VA (1990).

Harrison, R., P. Doherty, and I. Coulson, "Hot Dry Rock Cost Modeling," Camborne School of Mines International Hot Dry Rock Conference, Camborne, Cornwall, England (1989).

Hori, Y. et al., "On Economics of Hot Dry Rock Geothermal Power Station" and related documents. Corporate Foundation Central Research Institute for Electric Power, Hot Dry Rock Geothermal Power Station Cost Study Committee report 385001, Japan (1986).

Joint Association Survey on Drilling Costs for Years 1978-1988, American Petroleum Institute, Washington, D.C. (1978-1988).

Kestin, J. et al. (eds.), *A Sourcebook on the Production of Electricity from Geothermal Energy*, U.S. Government Printing Office, Washington, D.C. (1980).

Milora, S.L. and J.W. Tester, *Geothermal Energy as a Source of Electric Power*, MIT Press, Cambridge, MA (1976).

Mortimer, N.D. and S.T. Minett, "Hot Dry Rock Geothermal Energy Cost Modeling: Drilling and Stimulation Results," in R. Baria (ed), *Hot Dry Rock Geothermal Energy. Proceedings of the International Hot Dry Rock Geothermal Energy Conference, Camborne School of Mines, 27-30 June 1989*, Robertson Scientific Publications, London (1990).

Murphy, H.D., R. Drake, J.W. Tester, and G.A. Zyvoloski, "Economics of a 75-MWe Hot Dry Rock Geothermal Power Station Based upon the Design of the Phase II Reservoir at Fenton Hill," Los Alamos National Laboratory report LA-9241-MS, Los Alamos, NM (1982).

Shock, R.A.W., "An Economic Assessment of Hot Dry Rocks as an Energy Source for the U.K.," Energy Technology Support Unit report ETSU-R-34, UKDOE, Oxfordshire, UK (1986).

Smith, I., "The Trilateral Wet Vapor Cycle," City College of London, London, UK, working paper (1981).

Smolka, K. and O. Kappelmeyer, "Economic Cost Evaluation of HDR Power Plants" *Hot Dry Rock Geothermal Energy. Proceedings of the International Hot Dry Rock Geothermal Energy Conference, Camborne School of Mines, 27-30 June 1989*, R. Baria (ed.), Robertson Scientific Publications, London (1990).

Tester, J.W., "Energy Conversion and Economic Issues for Geothermal Energy," *Handbook of Geothermal Energy*, Ch. 10, L.M. Edwards et al. (Eds.), Gulf Publishing, Houston, TX (1982).

Tester, J.W., D.W. Brown, and R.M. Potter, "Hot Dry Rock Geothermal Energy--a New Energy Agenda for the 21st Century," Los Alamos National Laboratory report LA-11514-MS, Los Alamos, NM (1989).

Tester, J.W. and H.J. Herzog, "Economic Predictions for Heat Mining: A Review and Analysis of Hot Dry Rock (HDR) Geothermal Energy Technology," MIT Energy Laboratory report MIT-EL 90-001, Cambridge, MA (1990).

Appendix A A general approach to optimizing the performance of an HDR system

In our earlier work (Milora and Tester, 1976; Tester, 1982; and Armstead and Tester, 1987) we considered how several control variables affected the breakeven price of HDR-generated electricity. These included well depth (Z), gradient (∇T), and mass flow rate ($\dot{m}$). Given that we have constructed an analytical representation of system performance in terms of thermal or electrical power output, it is possible, at least conceptually within a somewhat idealized framework, to describe a general multiparameter optimization to include the effects of all important input and control variables relating to resource and reservoir properties. The set of variables includes:

Input Variables

1. gradient (∇T)
2. initial flow impedance (I(t=0))
3. rock and water thermophysical properties (ρ,C_p,λ,...)
4. ambient heat rejection condition (T_o)

Control Variables

1. mass flow rate ($\dot{m}$)
2. reservoir size (<A>)
3. reinjection temperature (T_{inj})
4. well depth (Z)
5. redrilling strategy

The total electrical output over the production period of the reservoir (t_f) can be expressed in integral form as:

$$E_e(t_f) = \int_0^{t_f} [\dot{m}\,\eta_u(T(t))\,\Delta B(T(t),T_{inj},T_o) - P_{pump}(\dot{m},t)]\,dt \qquad \text{(A-1)}$$

where

$\dot{m}$ = mass flow rate

η_u = utilization efficiency

ΔB = availability = $\Delta H - T_o \Delta S$ over $\{T(t),T_{inj}\}$

P_{pump} = pumping power required to circulate fluid at a flow rate $\dot{m}$ and time t

$T(t)$ = reservoir fluid production temperature

T_{inj} = reinjection temperature

T_o = ambient temperature

In turn, we can express the dependence of η_u on T(t) as:

$$\eta_u = 0.21 + 0.41\left[\frac{1}{1 + \exp\left[-\dfrac{T(t)+\beta}{\alpha}\right]}\right] \qquad \text{(A-2)}$$

to empirically match plant performance data where α and β are adjustable parameters (see Armstead and Tester (1987), Figure 14.3, p. 404). The availability, in turn, can be calculated rigorously as:

$$\Delta B = \int_{T_{inj}}^{T(t)} C_p(T)[1 - T_o/T]\,dt \qquad \text{(A-3)}$$

where $C_p(T)$ is the heat capacity of saturated liquid water which can be approximated as:

$$C_p(T) = A + BT + CT2 \qquad \text{(A-4)}$$

where A, B, C are empirically fit parameters to steam table data. The outlet reservoir fluid production temperature T(t) will, in general, be a complex function of the geometry, flow characteristics, and thermophysical properties of the reservoir. For conceptual sensitivity studies, a simple idealized model involving 1-D flow and 1-D rock conduction can be used. (Armstead and Tester (1987) and Tester and Herzog (1990)). In this case,

$$T(t) = T_{inj} + (T_r^{\infty} - T_{inj}) * erf\left[\frac{\lambda_r <A>}{\dot{m} C_p \sqrt{\alpha_r t}}\right] \quad \text{(A-5)}$$

where

T_r^{∞} = initial rock temperature at depth

λ_r = rock thermal conductivity

α_r = rock thermal diffusivity

C_p = fluid heat capacity

$<A>$ = effective reservoir heat transfer area

Redrilling and restimulating the reservoir at some time $t < t_f$ will, of course, change the formulation of equation (A-5).

The pumping power required to circulate fluid through the reservoir/well bore system is dependent on frictional losses in the well bore and reservoir. Bouyancy effects caused primarily by the density difference between the hot and cold legs of the system reduce the pumping requirement. Reservoir losses are typically expressed in the form of an impedance term (I) which must be specified while well bore losses can be estimated for given hole and casing diameters, well depth, and mass flow rate.

For a complete economic analysis, the capital and operating costs for creating and maintaining the well bore/reservoir system and for constructing and running the power plant must be incorporated. Nonetheless, much can be learned by examining how the net electrical output over a specified production period depends on the control variables. Electrical power is the commodity that is priced to meet capital and operating cost burdens to establish a so-called breakeven price.

In our earlier work, we have optimized performance with respect to only one control parameter at a time, such as geothermal gradient and optimal well depth as shown in Figure 11. Each point on that figure was established by varying depth at a fixed gradient to establish a minimum breakeven cost for electricity. (see Tester and Herzog (1990) for details). Above a gradient of 40°C/km the cost versus depth curve had a very shallow minimum or was still decreasing when the maximum 300°C reservoir temperature boundary was reached. This result was contingent on specifying all other parameters, including flow impedance, thermal drawdown rate, and well flow rate at their base case conditions as given in Table 4.

With the general model described above, we can begin to study how performance is affected by other important control variables from a fundamental perspective. For example, how does drawdown rate expressed by $\dot{m}/<A>$ influence the net electrical output from an HDR system over its lifetime or how does reinjection temperature affect output. Equation (A-1) can be modified to more clearly show this effect by setting the parasitic pumping power to zero and dividing by $<A>$:

$$\frac{E_e(t_f)}{<A>} = \int_0^{t_f} \left[\frac{\dot{m}}{<A>} \eta_u(T(t)) \Delta B(T(t), T_{inj}, T_o)\right] dt \quad \text{(A-6)}$$

Figures A-1 and A-2 illustrate the effect of drawdown on net output per unit reservoir area for a HDR system at 50°C/km and 5.7 km depth with a reinjection temperature of 55°C with no redrilling or pumping losses. The four graphs corresponding to points A, B, C and D show the power output versus time over a 20 year production period at particular values of $\dot{m}/<A>$. Note that maximum electrical output is achieved as the production rate $\dot{m}$ is balanced with reservoir size $<A>$ at a drawdown parameter $\dot{m}/<A>$ of about 0.5×10^{-4} kg/m^{2}s.

Higher values of $\dot{m}/<A>$ result in too rapid production temperature decline reducing performance by lowering η_u and ΔB while lower values result in suboptimal output controlled by the $\dot{m}/<A>$ term in equation (A-6).

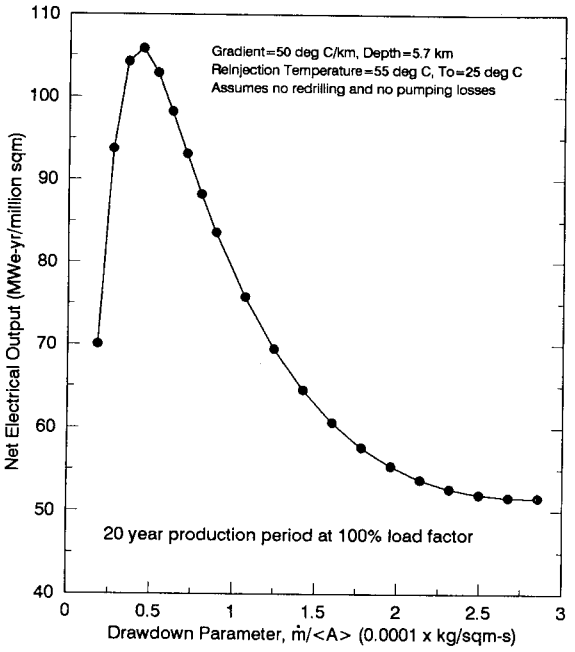

Figure A-1. Effect of reservoir thermal performance on electrical output.

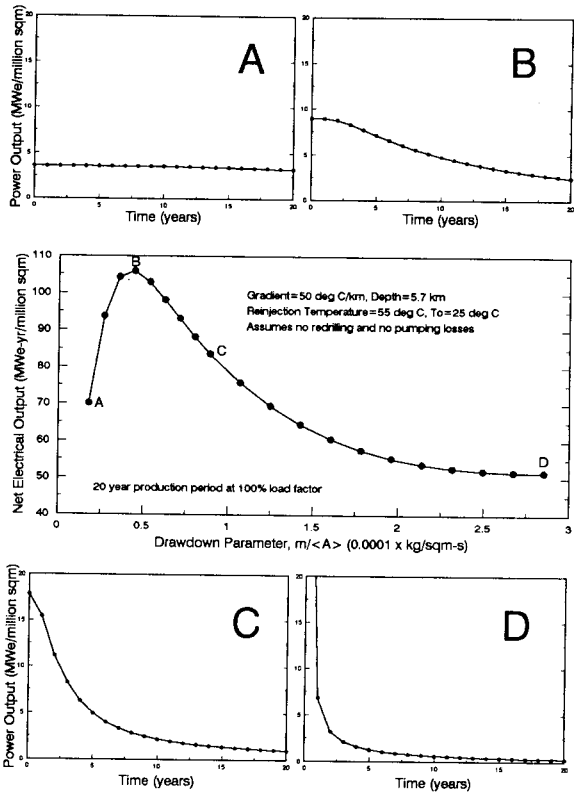

Figure A-2. Time histories of electrical power output for representative values of drawdown parameters ($\dot{m}/<A>$).

PROCEEDINGS, Sixteenth Workshop on Geothermal Reservoir Engineering
Stanford University, Stanford, California, January 23-25, 1991
SGP-TR-134

CIVIL LITIGATION AND THE GEOTHERMAL INDUSTRY

George M. Moore

Kenny, Burd, Knutson & Markowitz
(415) 397-3100
Four Embarcadero Center, 25th Floor
San Francisco, CA 94111

ABSTRACT

This paper offers some reflections on the interactions between the legal profession and the realm of the geothermal scientist and engineer. The author, now a litigation attorney, became an attorney after about fifteen years as an engineer and physicist. Over the past several years the author was involved in litigation related to geothermal contracts.

THE CIVIL LITIGATION PROCESS

Our system of justice, deriving from the English legal system, has always made provision for civil enterprise to approach a court with a request for a determination of the rights of the parties regarding a disagreement. The parties can then obtain from the court a judgment, ultimately enforceable by the force of a police agency involved, determining the rights of the parties before the court. This the civil justice system runs in parallel with, and competes for resources with, the criminal justice system-a system in which the "state" prosecutes actions on behalf of the citizens of the state.

There is a civil justice system at both the federal and state court levels. However, for the purposes of this brief discussion, both federal and state courts will be considered the same, unless otherwise indicated.

It should be noted that the right of a jury trial in a civil case is somewhat a matter of grace, although the practical effect is that if one of the parties to a case makes the request, a jury trial will be granted. Further, it should be noted that there are a number of alternative methods of dispute resolution (non court methods such as arbitration in its various forms, rental of commercial judges, etc.). Many of these alternatives to the conventional civil justice system are encouraged, if not actively supported, by an overloaded civil justice system.

Those who follow the news have probably heard of the impact on the civil justice system caused by the "flood" of criminal cases (primarily drug related cases) that have saturated the court systems at all levels. To those in the legal profession, however, a disturbing, and to some extent related problem, has been the failure of the court systems to follow general legal salary trends. Failure of judicial salaries to keep pace with the legal community salaries, coupled with some of the increased workload requirements has created what some think is a situation that is pointing toward a terrible future problem for the civil justice system in this country. In addition to the disincentive to become a judge initially, the low salaries, combined with a demand for private juding created by court overloading, has created a situation that has resulted in a recent exodus of many of what have been considered the better civil justice minds from the state trial bench. The impact of these trends will be discussed later.

A LEGAL PERSPECTIVE OF THE GEOTHERMAL COMMUNITY

From a legal viewpoint the geothermal community (an admittedly imprecise term) has some distinctly unique

aspects. In the general legal framework, the basis of laws relating to geothermal energy and exploration comes from the field of oil and gas law. Interactions with regulatory bodies (i.e. California Energy Commission, CPUC, FERC, etc.) are similar to other power supply entities. However, as a practical matter the legal problems of the geothermal community are somewhat unique. First, the geothermal operation itself is almost anti-competitive by its nature. The fuel supply can't be transported over significant distances. Therefore, supplier and user are either the same or are locked into a longterm relationship from which there is no recourse but to deal with the other party. Some of the normal leverage in negotiations (i.e. I'll go somewhere else for my business) is not a part of the geothermal scene.

Second, the industry is, to a great extent, in its infancy and the supplier and user to some extent must "share the risk" regarding significant capital investments in some situations. This results in a situation (when two or more parties are involved) where contract development and ongoing contract monitoring and renegotiation are of greater importance than in other areas. There is generally no ability for one party to mitigate the damages caused by a breach of contract by the other party.

Third, the size of the geothermal community is small and there are very few "experts" outside the staff of the companies participating in the community or who do not have some significant allegiances to the major companies participating in the community. From a litigation point of view this sometimes makes it hard to get an "unbiased" opinion. Here "unbiased" refers to the appearance of bias rather than to actual bias.

Finally, the geothermal community enjoys a unique position in the energy domain. Like solar,wind, and other alternative energy sources, it enjoys a "favored" status in government and regulatory circles. Associated with this is a visionary aura that attaches to the geothermal community.

WHEN WORLDS COLLIDE, LEGAL VIEWPOINT vs. SCIENTIFIC VIEWPOINT

When litigation touches any scientific community (the geothermal community not being unique in this aspect) the philosophical difference between the world of the attorney and that of the scientist regarding the meaning of truth becomes apparent. The difference in the perception and practical significance of the difference is something that the scientist, engineer, and business manager of a scientific company should be aware of and consider carefully.

Scientists are trained to seek the truth through experimentation and the rigorous testing of a hypothesis. To an attorney, truth is what a court will allow into evidence and therefore what the attorney can convince a jury or judge to believe. The attorney's view is not necessarily as cynical as it sounds. There is an inherent belief underlying our judicial system that the adversarial system is best suited for determination of the "truth" and therefore the outcome of a question brought to a court.

As a result of the structure of our legal system and the exclusive use of the adversarial system, there is serious doubt as to whether the legal system can function adequately in the context of complex litigation with complex technical issues.

Whenever the technical person or manager has to give thought to the issue of litigation, either to address a wrong (e.g. the delivery of purchased equipment not meeting specification, the failure of a contractor to perform, etc.), or as an alternative in negotiation, the fundamental difficulty of the legal system in dealing with such issues should be considered -- long before litigation is entered into.

THE IMPACT OF LITIGATION

Litigation, as viewed by the attorneys involved, is a war. The other participants are, by and large, the casualties whether or not their "side" ultimately prevails or loses. Because 95% of civil cases never reach the trial stage, prevailing in the sense of winning is generally a self-imposed criteria.

There are, fortunately, some fundamental understandings and preemptive policies that the scientific manager and individual engineer or scientist can do to minimize the impact of involvement in litigation. Unfortunately, these are lessons and policies that must be invoked prior to the onset of litigation in order to be of benefit. A few items will certainly be available from corporate or retained counsel, although sometimes the scientific side must ask.

Contrary to the impressions left by popular examples of courtroom drama, litigation is not done on the fly, or "trial by ambush." It is now a well established concept in civil proceedings that what will go on at trial should be known to the participants long before the trial. This is called civil discovery and is strictly enforced by courts. As a practical matter, if a company is involved in litigation, it can be forced to "open" its files (from larger files to the contents of an individual's desk or computer) to other parties in a case. The opening may be ordered without regard to prior confidentiality agreements by which the holder has acquired the information. The cost of this opening can be enormous in the loss of manpower as well as the actual cost. In the legal community there are large companies with hundreds of employees totally devoted to the copying, microfilming, categorizing, and indexing of documents produced in discovery.

In addition, prior to trial, the taking of testimony from various individuals will be done under court mandate. Employees, former employees, etc. may be subpoenaed and spend significant periods of time testifying, or preparing to testify, before a case can go to trial.

Although these are necessary "evils of a litigation system, the cost can be minimized and the potential harm minimized as well by the adoption of policy guidelines, and use of the guidelines regarding document retention, storage, and marking. At both a corporate and individual level adequate policies can minimize the impact of litigation.

Further, an understanding, and appropriate use of the attorney-client privilege can protect the confidentiality of information that might be damaging to the corporation if it were not adequately protected. Once again, consideration of these items with corporate counsel should come at the initiative of the scientific community.

Finally, the use by scientific manager of contracted for methods of alternative dispute resolution (e.g. binding arbitration clauses in contracts) should always be a consideration to minimize the impact of litigation on the company.

MODIFYING THE LEGAL COMMUNITY

Groups such as the geothermal community are in a unique position to lobby to modify the manner in which civil litigation is done in complex cases. The recognition of the need for such changes should come from outside the legal community as well as inside. Recent changes in the patent appeal process are examples that indicate that changes can be made, albeit slowly, but there are numerous reminders of the problems still inherent in the patent system.

Anything that can be done to strengthen the legislative process and decrease the apparent current willingness of the legislative bodies to default to the courts for decision making would be ultimately helpful. This, however, merely avoids the problem of the lack of suitability of the legal process for technical decision making.

In summary, there are no apparent solutions to these problems, but the active interest of the scientific community, and various subgroups such as the geothermal community are essential if fundamental changes are to be made.

PROCEEDINGS, Sixteenth Workshop on Geothermal Reservoir Engineering
Stanford University, Stanford, California, January 23-25, 1991
SGP-TR-134

PRELIMINARY ASSESSMENT OF HALOGENATED ALKANES AS VAPOR-PHASE TRACERS

Michael C. Adams[1], Joseph N. Moore[1], and Paul Hirtz[2]

1. University of Utah Research Institute
Salt Lake City, UT 84108

2. Thermochem, Inc.
Santa Rosa, CA 95403

ABSTRACT

New tracers are needed to evaluate the efficiency of injection strategies in vapor-dominated environments. One group of compounds that seems to meet the requirements for vapor-phase tracing are the halogenated alkanes (HCFCs). HCFCs are generally nontoxic, and extrapolation of tabulated thermodynamic data indicate that they will be thermally stable and nonreactive in a geothermal environment. The solubilities and stabilities of these compounds, which form several homologous series, vary according to the substituent ratios of fluorine, chlorine, and hydrogen. Laboratory and field tests that will further define the suitability of HCFCs as vapor-phase tracers are under way.

INTRODUCTION

Tracers that can quantify the behavior of injected fluids in vapor-dominated geothermal systems are needed for reservoir management. In order to evaluate the mass recovery of the injectate, an ideal vapor-phase tracer should have the same concentration in the steam and liquid, regardless of the mass fraction of steam produced from the injected liquid. Unfortunately, only the isotopes of the elements of water even approach this behavior. Of these, deuterium and O-18 have multiple injection sources whose compositions vary with time. Thus, these are qualitative tracers. Tritium, which has been used frequently as a tracer at The Geysers, can be used to document breakthrough but cannot be used to differentiate multiple injection sources in a single tracer test. Consequently, there is a need for several new tracers that can be used to quantify the mass recovery of injected fluids on a field-wide basis. One such approach, which uses multiple tracers to tag each of several injection wells, was employed successfully at the Dixie Valley geothermal system (Adams et al., 1989).

In addition to the characteristics desired in a liquid-phase tracer such as inertness, detectability, and low toxicity, vapor-phase tracers are subject to potential degradation by the high oxygen content of the injection fluid and to more stringent environmental considerations because the steam may be released to the atmosphere. Thus, even if the high oxygen content of the injectate did not degrade the majority of organic compounds, their release into the atmosphere could still be prohibited.

Halogenated alkanes (HCFCs) provide an initial solution to the problem of effective vapor-phase tracers (Table 1). These compounds are completely nontoxic and chemically inert. However, the atmospheric interactions of the most stable, least expensive, and best-characterized of these compounds with ozone has caused some uncertainty regarding their long-term use and availability. Although there are environmentally benign HCFCs known and more are under development, their availability will be low until some consensus is reached on which are the most acceptable to the manufacturing industries. We are currently investigating a variety of HCFCs in order to be ready to use those that will eventually become available. These compounds include the chlorofluorocarbons, the hydrofluorochlorocarbons, the hydrofluorocarbons, and the fluorocarbons. In this paper we discuss the extent of the HCFC thermochemical data set and present estimates of thermal stabilities and solubilities at reservoir conditions.

HISTORICAL DEVELOPMENT OF HCFCS

Although it seems unlikely, the criteria for refrigerants are similar to those for vapor-phase tracers. Refrigerants must be volatile at low temperatures, withstand cycling through a variety of temperatures in the presence of potentially degrading chemicals, and they must have very low toxicities because of their common household usage. Prior to the introduction of HCFCs, toxic, flammable, or unstable compounds such as methyl chloride, sulfur dioxide, ammonia, propane, or butane were used as refrigerants. In 1928, Thomas Midgley of Frigedaire Inc. was asked to develop nonflammable refrigerants with boiling points between -40° and 0°C, and with low toxicities, high thermal stabilities, and low chemical reactivities. Although this task was considered next to impossible, within three days Midgley had considered the elements of the periodic table that made up the individually unsatisfactory refrigerants and synthesized the first HCFC refrigerant. Using the same methodology, he developed the antiknock agent tetraethyl lead within a similar time period (Midgley, 1937).

TOXICITY

In general, the toxicity of a halogenated compound decreases rapidly with increasing fluoride content and slowly with decreasing molecular weight. The HCFCs currently in use have been tested by Underwriters Laboratory and were shown to be nontoxic at air concentrations greater than 20 volume percent for times of at least two hours (Downing, 1988). They are classified as noncarcenogenic and nonmutegenic, with extremely low acute and chronic toxicities.

Table 1. Status, ozone-depletion potential (ODP), and molecular formula of currently available and future HCFCs. The ODP is an arbitrary scale referenced to the compound R-11. Compounds that will be phased out under the Montreal Protocol (Mont. Prot.) are noted. The brominated compounds have not been considered as tracers because of their excessively high ODPs. na = not available.

Current Choices	ODP	Mont. Prot.	Molecular Formula
R-11	1	yes	CCl_3F
R-12	1.9	yes	CCl_2F_2
R-13	na	no	$CClF_3$
R-13B1	na	no	$CBrF_3$
R-14	na	no	CF_4
R-21	na	no	$CHCl_2F$
R-22	na	no	$CHClF_2$
R-23	na	no	CHF_3
R-112	na	no	$CCl_2F\text{-}CCl_2F$
R-113	0.8	yes	$CCl_2F\text{-}CClF_2$
R-114	1	yes	$CClF_2\text{-}CClF_2$
R-114B2	na	no	$CBrF_2\text{-}CBrF_2$
R-115	0.6	yes	$CClF_2\text{-}CF_3$
R-116	na	no	$CF_3\text{-}CF_3$
R-C318	na	no	$c\text{-}C_4F_8$
1211	3.0	yes	$CBrClF_2$
1301	10.0	yes	$CBrF_3$
2402	6.0	yes	$C_2Br_2F_4$

Future Choices	ODP	Molecular Formula
R-141b	0.081	$CH_3\text{-}CCl_2F$
R-142b	na	$C_2H_3ClF_2$
R-134a	0.000	$CH_2F\text{-}CF_3$
R-22	0.053	$CHClF_2$
R-123	0.016	$CHCl_2\text{-}CF_3$
R-124	na	C_2HClF_4
R-125	0.000	C_2HF_5
R-152a	0.000	$C_2H_4F_2$

Table 2. Critical constants of HCFCs. Data taken from Reid, Prausnitz, and Poling (1987). Tb = boiling point (K) at one atmosphere, Tc = critical temperature (K), Pc critical pressure (Bars), Vc = critical volume (cc/mole), Zc = critical compressibility factor (PcVc/RTc), Ω = Pitzer's acentric factor, Dipm = dipole moment (Debyes), and na = not available.

Compound	Tb	Tc	Pc	Vc	Zc	Ω	Dipm
R-11	296.9	471.2	44.1	247.8	0.279	0.189	0.5
R-12	245.2	385.0	41.4	216.7	0.280	0.204	0.5
R-13	193.2	302.0	38.7	180.4	0.278	0.198	0.5
R-14	145.1	227.6	37.4	139.6	0.276	0.177	0.0
R-22	232.4	369.3	49.7	165.6	0.268	0.221	1.4
R-23	191.0	299.3	48.6	132.7	0.259	0.260	1.6
R-114	276.2	418.9	32.6	293.8	0.275	0.246	na
R-115	235.2	353.2	32.3	251.8	0.277	0.279	0.3
R-116	164.9	293.0	30.6	222.0	0.279	na	0.0
R-C318	267.2	388.5	27.8	324.0	0.279	0.356	na
R-218	236.5	345.1	26.8	299.8	0.280	0.325	na
SF6	209.6	318.7	37.6	198.8	0.282	0.286	0.0
R-141b	263.4	409.6	43.3	231.0	0.294	0.251	2.1
R-124	263.0	399.9	37.2	244.0	0.273	0.281	na
R-152a	248.2	386.7	45.0	181.0	0.253	0.256	2.3

HCFCS AS HYDROLOGIC TRACERS

The use of HCFCs as hydrologic tracers was first proposed by Thompson et al. (1974). The thesis of this study was that HCFCs had been used extensively and released to the atmosphere for at least 15 years, and therefore could be used to date groundwater qualitatively. Subsequent studies (Thompson, 1976; Thompson and Hayes, 1979) demonstrated a general correspondence of tritium ages with R-11 contents. However, in at least one instance in Texas complete drying of soil caused adsorption/desorption cycles which resulted in spurious enrichments and calculated ages that were too young (Russell and Thompson, 1983). Other uses of HCFCs as anthropogenic tracers include the evaluation of oceanic water-column ventilation rates (Wallace and Moore, 1985; Hammer and Hayes, 1978). HCFCs have also been used as purposefully introduced tracers to evaluate the diffusion parameters, tortuosity, and sorption-affected porosity of the unsaturated zone (Weeks et al., 1982; Kreamer et al., 1988), open-ocean dispersion and air-sea exchange properties (Watson and Ledwell, 1988), and the determination of true groundwater velocities (Ciccioli et al., 1980). These studies were possible because of the extremely low detection limits of one part per trillion that can be achieved with an electron-capture detector (Lovelock and Watson, 1978; Thompson, 1976).

PROPERTIES OF AVAILABLE HCFCs AND THEIR ALTERNATIVES

Although there is a broad base of thermodynamic data for HCFCs, these data primarily relate to refrigerant conditions. Thus, the data base is restricted to the pressure-temperature-volume relationships and heat capacities of the anhydrous liquid or gas (Martin, 1959). However, the critical constants of a majority of the compounds are known (Table 2), allowing the estimation of compressibility factors and fugacity coefficients. Because of the corrosion potential of water in a refrigeration system, some data also exist on their solubility in water to temperatures of 100°C (Table 3). The solubility data were extrapolated to higher temperatures by transforming the Henry's Law constants (Kh) to volatility ratios (VR), which represent the ratio of the molal concentration in the gas to that in the liquid. It has been shown empirically that log(VR) is an approximately linear function of temperature (Drummond, 1981). The compressibility factors required for the transformation of Kh to VR were calculated from the critical constants listed in Table 2 using the three-parameter corresponding states correlation of Lee and Kesler (1975).

The solubilities of HCFCs in water, extrapolated to geothermal conditions, are shown in Fig. 1. The measured solubilities of hydrogen and carbon dioxide, which are common geothermal gases, are shown for reference. The solubility behavior of the HCFCs follow a consistent trend with composition. Those containing hydrogen (R-22, -23, and -31) are the most soluble. Compounds that contain only chlorine and fluorine (i.e., R-12 and -13) are intermediate in solubility, with the solubility being proportional to the number of chlorine atoms in the molecule. Gases that contain only fluorine (i.e., R-14, -116, -218, -C318, and SF_6) are sparingly soluble, with the solubility decreasing as the molecular weight increases.

Table 3. Literature sources for solubility data of HCFCs.

Compound	Formula	Literature Sources
R-11	CCl_3F	3, 4
R-12	CCl_2F_2	2, 3, 4
R-13	$CClF_3$	2, 3, 4
R-14	CF_4	1, 2, 3
R-22	$CHClF_2$	2, 4
R-23	CHF_3	2, 4
R-31	CH_2ClF	4
R-114	$C_2Cl_2F_4$	5
R-115	C_2ClF_5	2, 4
R-116	C_2F_6	1, 3
R-C318	c-C_4F_8	3
R-218	C_3F_8	1
-	SF_6	3

1. Wen and Muccitelli (1973)
2. Parmelee (1953)
3. Park et al. (1982)
4. Numerous sources listed in the compilation of Wilhelm et al. (1977)
5. Stepakoff and Modica (1973)

The stabilities of HCFCs have been tested under various conditions, some of which were similar to those found in geothermal environments. The test conditions ranged from repeated flow cycles through a high-temperature (up to 700°C) compartment (Snider, 1967; Callighan, 1969) to static experiments in sealed quartz vials containing oils, metals, metal oxides, water, or oxygen (Norton, 1957; Parmelee, 1965; Kvalnes and Parmelee, 1957). The experiments with oxygen and water are particularly pertinent because oxygen is absorbed from the atmosphere in the cooling tower and has the potential to degrade many organic compounds.

The stabilities of HCFCs also vary as a function of their compositions. In general, the stability of these compounds is directly proportional to fluorine saturation and inversely proportional to hydrogen saturation. For example, temperatures that will induce 1% decay per year in substituted methanes with one, two, and three fluorines are 298°, 498°, and 538°C, respectively. In contrast, a compound that contains two fluorines but also one hydrogen will decay 1% per year at 250°C. A comparison of decay rates for a substituted methane that contains two fluorines and either two chlorines (R-12) or one chlorine and one hydrogen (R-22) is shown in Fig. 2. These decay curves are based on the experimental data of Norton (1957). In these experiments, oxygen and water had little effect and were grouped with data for the pure compound, indicating that these HCFCs are not likely to be affected adversely by oxygenated injectate.

APPLICATION OF HCFCS AS GEOTHERMAL TRACERS

Although the HCFCs appear to have excellent potential as vapor-phase geothermal tracers, little data exist for these compounds under actual geothermal injection and

reservoir conditions. Two separate approaches are currently being used to produce these data.

The first approach involves the laboratory simulation of a geothermal environment. Strict control of variables in the laboratory will allow the determination of specific properties of the HCFCs, such as their thermal stabilities and solubilities. These tests are currently being conducted at UURI in a laboratory specifically designed for this purpose.

The second approach is to perform field tests. Field tests address the variables inherent in the practical application of HCFCs as tracers, which include the injection of the tracers and the sampling and analysis of production fluids. A field test that will take place in early 1991 is planned for the underpressured region of the Southeast Geysers. This test will inject R-12 and -13 simultaneously into NCPA well C-11. At least 10 production wells will be monitored.

The tracers will be injected from pressurized cylinders at a constant rate. The production well fluids will be sampled using evacuated flasks that contain cadmium chloride, a method that is similar to conventional gas sampling. No special equipment or ports are needed. The purpose of the cadmium chloride is to precipitate hydrogen sulfide, which can interfere with the analysis. The analytic method, developed at Thermochem, is performed on a gas chromatograph equipped with an electron capture detector. Detection limits as low as 0.1 parts per billion can be achieved using this method.

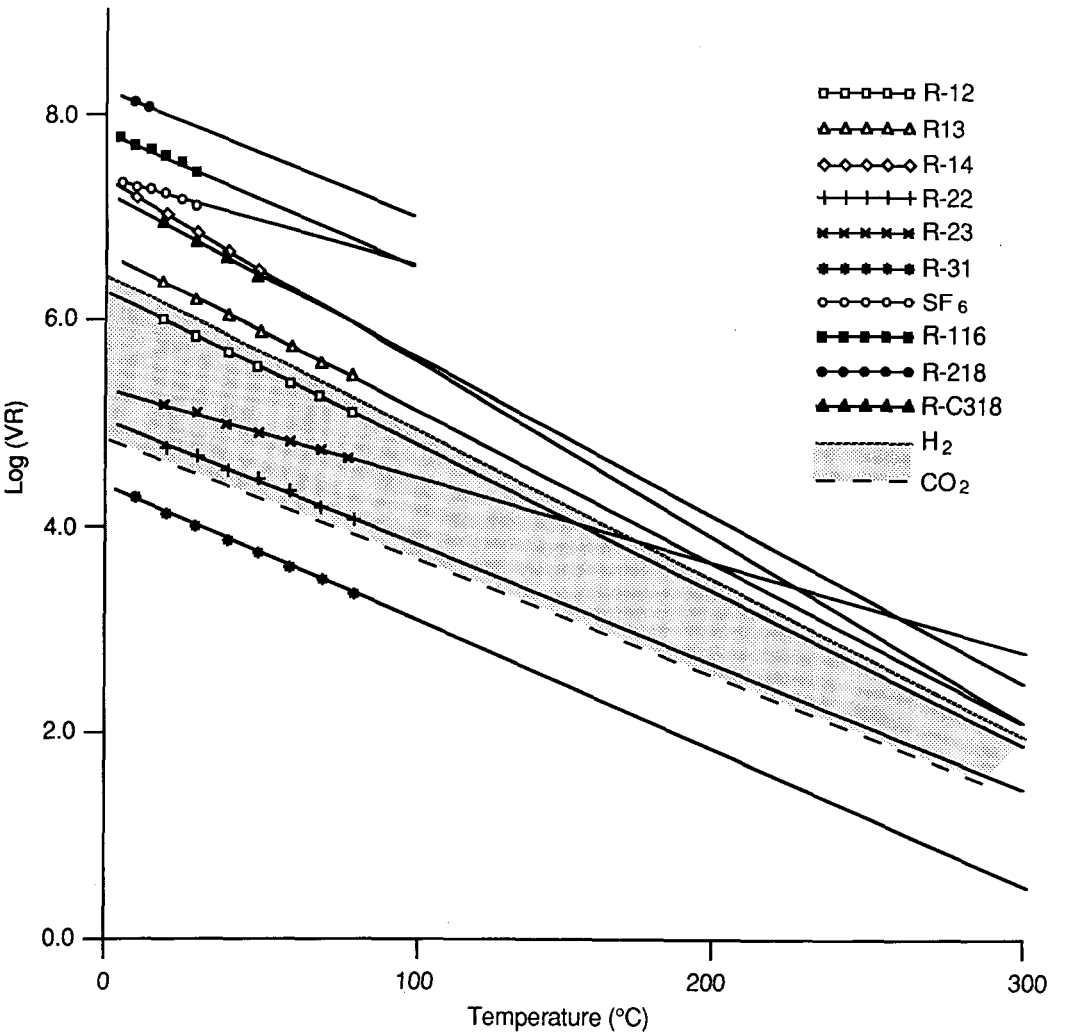

Figure 1. Temperature variations of the volatility ratios (VR) of the HCFCs. VR is defined as the ratio of the molal concentrations in the steam and liquid phases. The shaded area represents the VR region of common geothermal gases (Drummond, 1981). The data sources for the HCFCs are listed in Table 3. The symbols represent measured values, while the solid lines are extrapolations. The lines for H_2 and CO_2 represent measured values throughout the temperature range. Note that the shallow slopes of R-23 and SF_6 will not converge to zero at the critical point of water, indicating that the solubility data for these compounds may be of poor quality.

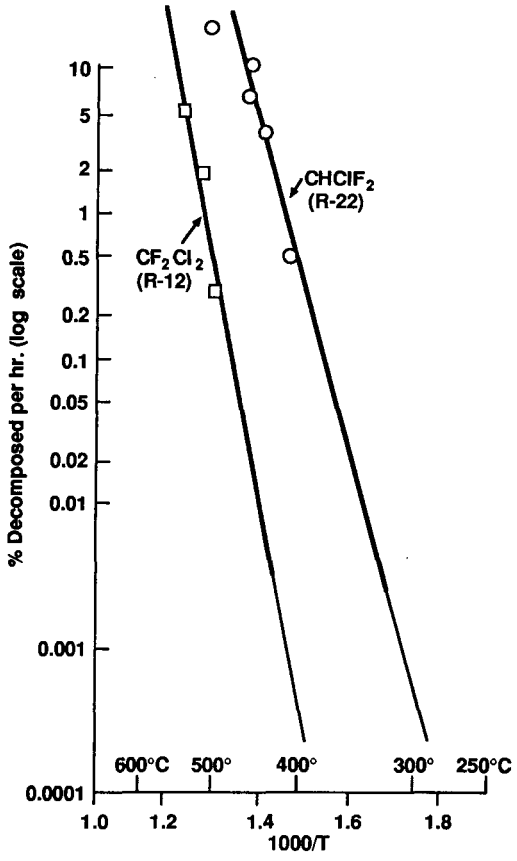

Figure 2. Decay rates of two HCFCs, R-12 and -22. The hydrogen-containing compound, R-22, is representative of the new generation of HCFCs. Up to one percent each of water and oxygen were included in the experiments that produced these data. Data from Norton (1957).

Several chromatographic scans of steam from The Geysers were performed in late 1989 to measure the background levels the HCFCs that are commonly found in the atmosphere, which include R-12 and -13. Background concentrations in these samples were below detection.

CURRENT AND FUTURE AVAILABILITY OF HCFCS

Although HCFCs are nearly ideal for use as vapor-phase tracers, their use as industrial chemicals has been criticized because they influence the steady-state concentration of ozone in the stratosphere. This effect is due to the presence of chlorine or bromine in the molecule. For example, R-11, which contains 3 atoms of chlorine per molecule, has been assigned an ozone-depletion potential (ODP) of 1.0. Brominated compounds, which are widely used as fire extinguishing agents, have ODPs which range from 3 to 10 (Table 1). In contrast, compounds with similar properties, but which contain hydrogen in addition to chlorine and fluorine, have ODPs as low as 0.016. Compounds on only hydrogen and fluorine pose no threat to the ozone layer and have an ODP of zero.

Because of the suspected ozone degradation from the HCFCs currently in use, new compounds with similar properties are being developed for use as refrigerants at breakneck speed. The candidates that can perform as replacements are listed in Table 1 under the heading of future choices. Of these, R-123 and -134a are on the EPA inventory of existing chemicals (i.e., grandfather clause) and can be produced without extensive toxicity testing. The others are not grandfathered and production will be delayed until testing is completed. Most of the new compounds have passed preliminary toxicity tests, but the complete tests are still in progress and won't be finished until the mid-1990's. Despite these potential delays, plants are already being built to produce many of the new compounds on the assumption that they will pass the toxicity tests.

SUMMARY

Halogenated alkanes (HCFCs) possess many of the characteristics required for vapor-phase tracers. These compounds are very stable and nontoxic, and are available in a wide variety of compositions. HCFCs consist of various combinations of hydrogen, chlorine, and fluorine on a saturated carbon skeleton. In general, the stabilities of HCFCs are increased by the addition of fluorine atoms to the molecule, while solubilities are increased in proportion to the number of chlorine or hydrogen atoms. The ozone-depletion potential decreases with decreasing chlorine content and is zero for compounds with no chlorine.

Stability data exist for some HCFCs in environments similar, but not identical, to those believed to occur in vapor-dominated geothermal systems. These data indicate that HCFCs may be sufficiently stable for use as tracers. Tests are currently under way to determine their stabilities under simulated and actual geothermal conditions. The results of our analytic development for field tests indicate that a detection limit as low as 0.1 parts per billion can be achieved.

The costs of HCFCs vary as a function of their use by the manufacturing and refrigeration industries. Cost and availability will vary during the next few years as new HCFCs are developed to replace those with high ozone-depletion potentials. We expect that many of the new compounds will be useful as vapor-phase tracers.

ACKNOWLEDGEMENTS

This work was supported by the U.S. Department of Energy under contract number DE-AC07-85ID12489. Such support does not constitute an endorsement by the U.S. Department of Energy of the views expressed in this publication.

REFERENCES

Adams, M. C., Benoit, W. R., Bodvarsson, G. S., and Moore, J. N., 1989, The Dixie Valley, Nevada, tracer test: Trans. Geothermal Resources Council, v.13, pp. 215-220.

Callighan, J. A., 1969, The thermal stability of fluorocarbons 114 and 216: ASHRAE J., v. 11, pp. 65-69.

Ciccioli, P., Cooper, W. T., Hammer, P. M., and Hayes, J. M., 1980, Organic solute-mineral interactions: a new method for the determination of groundwater velocities: Water Resources Res., v. 16, pp. 217-223.

Downing, R. C., 1988, Fluorocarbon refrigerants handbook: Prentice-Hall, Englewood Cliffs, New Jersey.

Drummond, S. E., Jr., 1981, Boiling and mixing of hydrothermal fluids: chemical effects on mineral precipitation: Ph. D. thesis, The Pennsylvania State University.

Hammer, P. M., and Hayes, J. M., 1978, Exploratory analyses of trichlorofluoromethane (F-11) in North Atlantic water columns: Geophys. Res. Letters, v. 5, pp. 645-648.

Kreamer, D. K., Weeks, E. P., and Thompson, G. M., 1988, A field technique to measure the tortuosity and sorption affected-porosity for gaseous diffusion of materials in the unsaturated zone with experimental results from near Barnwell, South Carolina: Water Resources Res., v. 24, pp. 331-341.

Kvalnes, D. E., and Parmelee, H. M., 1957, Behavior of refrigerants 12 and 22 in sealed-tube tests: Refrig. Eng., v. 65, pp. 40-86.

Lee, B. I., and Kesler, M. G., 1975, A generalized thermodynamic correlation based on three-parameter corresponding states: AIChE Journal, v. 21, pp. 510-527.

Lovelock, J. E., and Watson, A. J., 1978, Electron-capture detector, theory and practice: Jour. Chromatography, v. 158, pp. 123-138.

Martin, J. J., 1959, Correlations and equations used in calculating thermodynamic properties of Freon refrigerants: in Thermodynamic and Transport Properties of Gases, Liquids, and Solids, American Society of Mechanical Engineers, New York, N.Y., pp. 110.

Midgley, T., Jr., 1937, From the periodic table to production: Ind. Eng. Chem., v. 29, pp. 239.

Norton, F. J., 1957, Rates of thermal decomposition of $CHClF_2$ and CF_2Cl_2: Refrig. Eng., v. 65, pp. 33-35.

Park, T., Rettich, T. R., Battino, R., Peterson, D., and Wilhelm, E., 1982, Solubility of gases in liquids. 14. bunsen coefficients for several fluorine-containing gases (Freons) dissolved in water at 298.15 K: Jour. Chem. Eng. Data, v. 27, pp. 324-326.

Parmelee, H. M., 1953, Water solubility of Freon refrigerants: Refrig. Eng., v. 61, pp. 1341-1345.

Parmelee, H. M., 1965, Sealed-tube stability tests on refrigeration materials: ASHRAE Trans., v. 71, pp. 154-169.

Reid, R. C., Prausnitz, J. M., and Poling, B. E., 1987, The properties of gases and liquids: R. R. Donnelley & Sons Co., 742 p.

Russell, A. D., and Thompson, G. M., 1983, Mechanisms leading to enrichment of the atmospheric fluorocarbons CCl_3F and CCl_2F_2 in groundwater: Water Resources Res., v. 19, pp 57-60.

Snider, K. L., 1967, Thermal stability of several fluorocarbons: ASHRAE J., v. 9, pp. 54-58.

Stepakoff, G. L., and Modica, A. P., 1973, The hydrolysis of halocarbon refrigerants in freeze desalination processes: Part I. solubility and hydrolysis rates of Freon 114 ($CClF_2CClF_2$): Desalination, v. 12, p. 85.

Thompson, G. M., Hayes, J. M., and Davis, S. N., 1974, Fluorocarbon tracers in hydrology: Geophys. Res. Letters, v. 1, pp. 177-180.

Thompson, G. M., 1976, Trichlorofluoromethane, a new hydrologic tool for tracing and dating ground water: Ph. D. thesis, Indiana University.

Thompson, G. M., and Hayes, J. M., 1979, Trichlorofluoromethane in groundwater - a possible tracer and indicator of groundwater age: Water Resources Res., v. 15, pp. 546-554.

Wallace, D. W. R., and Moore, R. M., 1985, Vertical profiles of CCl_3F (F-11) and CCl_2F_2 (F-12) in the central Arctic Ocean basin: Jour. Geophys. Res., v. 90, pp. 1155-1166.

Watson, A. J., and Ledwell, J. R., 1988, Purposefully released tracers: Phil. Trans. R. Soc. Lond. A, v. 325, pp. 189-200.

Weeks, E. P., Earp, D. E., and Thompson, G. M., 1982, Use of atmospheric fluorocarbons F-11 and F-12 to determine the diffusion parameters of the unsaturated zone in the southern high plains of Texas: Water Resources Res., v. 18, pp. 1365-1378.

Wen, W. Y., and Muccitelli, J. A., 1979, Thermodynamics of some perfluorocarbon gases in water: J. Solution Chemistry, v. 3, pp. 225-245.

Wilhelm, E., Battino, R., and Wilcock, R. J., 1977, Low-pressure solubility of gases in liquid water: Jour Chem. Rev., v. 77, pp. 219-262.

PROCEEDINGS, Sixteenth Workshop on Geothermal Reservoir Engineering
Stanford University, Stanford, California, January 23-25, 1991
SGP-TR-134

THE USE OF AIR AS A NATURAL TRACER IN FRACTURED HYDROTHERMAL SYSTEMS. LOS AZUFRES, MEXICO, CASE STUDY

Mario César Suárez Arriaga, Héctor Gutiérrez Puente, Josefina Moreno Ochoa

COMISION FEDERAL DE ELECTRICIDAD
A.P. 31-C, Morelia, Michoacán, 58290 MEXICO.

ABSTRACT

Injection of atmospheric air mixed with cold water has been occurring since 1982 at the Los Azufres geothermal field. Several chemical and thermodynamical evidences show that air injection into this fractured hydrothermal system could be considered as a long term natural tracer test. Nitrogen and Argon separated from the air mixture migrate, under the action of the induced injection-extraction gradient, from reinjection sectors to production zones following preferential paths closely related to high permeability conduits. A coarse numerical estimation of the average permeability tensor existing at Tejamaniles, the southern sector, explains the unsuccessful recovery of the artificial tracer tests performed in past years: the anisotropic nature of the fractured volcanic rock would demand considerably quantities of tracer in order to be detected at the producing wells, especially when fluid extraction was low. At the same time concentrations of calcium, cesium, chloride, potassium, rubidium and sodium, are increasing in the liquid produced by the oldest wells of this field's sector.

INTRODUCTION.

Los Azufres is a fractured volcanic hydrothermal system, located in the western part of the Mexican Neo-Volcanic Axis at an elevation of about 2800 masl. With about 60 wells completed, Los Azufres generates up to date, 90 MWe. Some general descriptions of this field have been previously published elsewhere (Gutiérrez et al,1982; Cathelineau et al,1985; Suárez et al, 1990). Tejamaniles, the field's southern sector, has been in exploitation since August 1982 subjecting the reservoir gradually to mass and heat extraction. To avoid the environmental impact of liquid waste disposal from the Tejamaniles geothermal field, the only alternative has been to inject the waste liquid back into the formation by gravity, without pumping. Besides this need, a well done injection may produce a higher recovery of heat stored in the reservoir. Fluid extraction takes place at the center of the field, while reinjection is performed to the west of the production zone (Fig. 1). During the past years, there were some tracer studies about the fluid transport in this reservoir but they had null responses all of them (Horne and Puente 1989).

Simultaneously with geothermal water reinjection, an important amount of air has been continuously inflowing to the reservoir through the open wellheads of the injection wells; also, atmospheric air is 'dragged' from the open surface of the collection boxes (Fig. 2). There are several evidences that the incidental injection of air into this intensely fractured system could be considered as a long term natural tracer test because the Nitrogen separated from the air mixture is transported by the extraction-injection gradient through the high permeability conduits to the producing wells, by means of a hydrodynamic dispersion mechanism. The undesirable aspects of reinjection such as serious interference of the lower enthalpy of this water with the energy outflow of the producing wells, or decreasing formation permeability by chemical deposition, or contamination of groundwater have never been noticed either at this field.

TEJAMANILES SUBJECT TO EXPLOITATION

Since August 1982, two wellhead non-condensing units, generating 5 MW_e each, were installed at Tejamaniles: Unit 1 connected to wells Az-6 and Az-16D, and Unit 2 connected to well Az-17. In September 1987 Unit 6 has been connected to well Az-18 in order to generate 5 additional MW_e. In November 1988 a 50 MW_e unit was installed in Tejamaniles, feeding with steam coming from wells Az-22, Az-33, Az-34, Az-35, Az-36, Az-37, Az-38 y Az-46 (Fig.1). These plants have been in continuous operation with a total extraction mass of about 780 T/h.

As we have explained, the exploitation of Tejamaniles occurs parallel to the injection of "cold" fluid and air. The temperature of injection varies between 40 to 50 °C at atmospheric pressure (0.73 bar). Figure 1 shows the areal disposition of reinjection lines and figure 2, exhibits the details of the injection system at well Az-8. The rates of mass extraction and of fluid injection are illustrated for wells Az-16D (2-phase), Az-17 (steam) and Az-7 (injector) in figures 3 and 4. For the rate of air injection we have a measured value at well Az-8: 274 Kg/h of air in 231 T/h of water.

In the southern sector, the extracted fluid is two-phase in natural state, with a non homogeneous steam saturation, which ranges between 0 to 70 %. Pressure and temperature profiles (Suárez et al 1990) show that between 1600 and 2500 masl, a nearly vaporstatic distribution of thermodynamic conditions exists and between 0 and 1550 masl the thermodynamic profiles correspond to hydrostatic conditions. The present pressure and temperature profiles of the production wells exhibit changes, indicating that the system as a whole, has started to abandon its natural steady state.

TRACER STUDIES

Between August 1983 and July 1987 six tracer tests were performed at Los Azufres. In three of these tests some amount of tracer (Potassium Iodide and Iridium-192) was injected into wells Az-7 and Az-8 in order to know where the reinjected water could go. Those investigations had very low effectiveness in the understanding of the real phenomena as has been reported by Horne and

FIGURE 1.- AREAL DISTRIBUTION OF REINJECTION LINES AT THE TEJAMANILES RESERVOIR

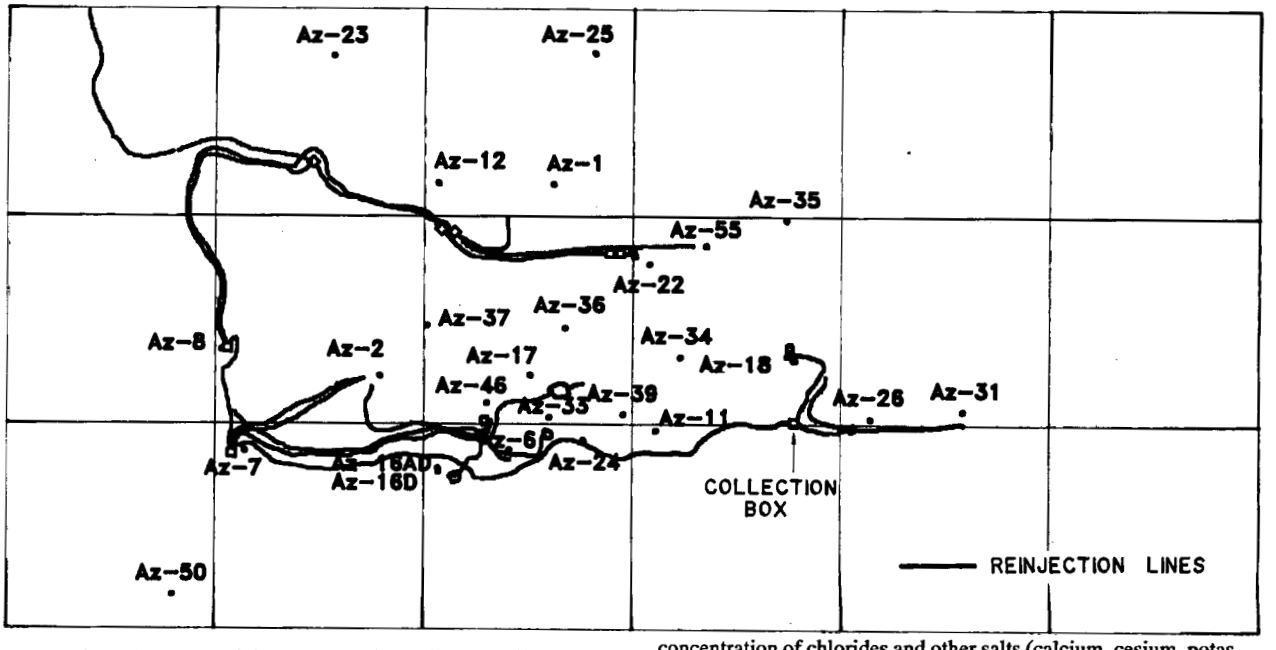

Puente in 1989. Tracer injection into the wells was effectively achived yet no return of the tracer was detected at the two closest wells Az-2 and Az-16D. The authors concluded either: the tracer was retained within the reservoir by some mechanism, or the return occurred after the monitoring was terminated, or was at such low concentration as to escape detection. The general conclusion was that tracer return times could be longer than expected at this portion of the reservoir. At that time, the effect of global production could not be taken into account. Roland Horne (*ibidem*) was one of the first investigators to notice that N_2 concentration at well Az-16D was higher than the normal N_2 solubility of the reservoir's fluid, suggesting that the intake of atmospheric air was important.

THE EFFECT OF AIR INJECTION

Reinjection of nearly 15 million tons of water since 1982 up until December 1990, has been accomplished mainly through wells Az-7 and Az-8. Today, the maximum amount of waste water accepted by well Az-7 is about 260 T/h and about 250 T/h by well Az-8 (nevertheless, well Az-7 could accept more than 325 T/h in 1985). The horizontal distances of the reinjection wells from the nearest production wells ranges from 1000 to 2000 m.; the injection wells being 500 to 1000 m. deeper. The total vectorial distance between producing and injection wells is a critical parameter because reinjection too close to the producing zone would sooner or later provoke a drop in the temperature of the fluid produced. Apparently fluid is reinjected at an adequate distance from the production zones at Tejamaniles, with the only exception of well Az-33 (after data in Suárez et al., 1990). If it is so, the thermodynamical effect of reinjection could increase the production and longevity of this geothermal field.

In the other hand, the rich chemical history of wells Az-6, Az-16D and Az-17 shows interesting evolutions. This information together with data coming from another group of younger productors (Az-2,33,37 and 46) show that Argon and Nitrogen in steam, concentration of chlorides and other salts (calcium, cesium, potassium, rubidium, sodium, etc.) in liquid, have been growing since June 1986 (Figs. 5, 6 and 7). This effect has a close relation with the injection of fluids into the reservoir by inducing successive evaporation of the injected water within the production zones. Molar ratio N_2/Ar has been decreasing with time reaching, in some cases, the same value as in the atmosphere (83.6); this is also a consequence of the continuous injection of fluid into wells Az-7 and Az-8. The air mixed with the fluid could flow through the fractures and high conductivity faults finally arriving to the production zones. This effect extends to wells Az-16D, Az-33, Az-37 and Az-46. Wells Az-22, producing vapor and liquid and well Az-6 producing superheated steam, do not show any important trend on their chemical behavior, suggesting the existance of some kind of impervious boundaries around the zones where these wells are located.

FIG. 2.- DETERMINATION OF THE RATE OF AIR INJECTED IN WELL Az-8

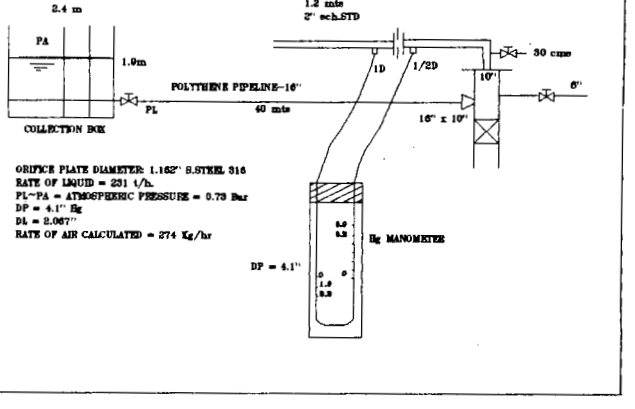

Oxygen coming together with Nitrogen into the reservoir is not taken into account beacause it does not appear in any production well; it must be "consumed" by chemical reducing agents present in the reservoir, probably within the neighborhood of the injection wells. The influence of all the other gases forming the air mixture is neglected.

EXTRACTION/REINJECTION MODELING

We have performed numerical simulations in order to investigate some particularly important aspects of this phenomenon. The calculations were performed using MULKOM-TOUGH, a powerful multicomponent simulator, with a water-air equation of state (Pruess, 1988). The simulation consisted in numerical experiments concerning a 3-D simplified porous model representing Tejamaniles, which included production and reinjection of geothermal water and air with heat inflow at the bottom of the reservoir. The idealized physical processes involved anisotropic flow of heat, liquid, vapor and air within a saturated porous media.

The numerical results have been reported in Suárez and Mañón (1990). Some resumed results are as follows: We could partially match the production/injection history of the field as well as the observed behaviour of Nitrogen and fluid enthalpy. We could estimate, by trial and error, average values for the absolute permeability tensor existing between injection and production zones; for the region between well Az-7 and well Az-16D the figures are:

$$K_x = 1 \times 10^{-16}\ m^2;$$
$$K_y = 15 \times 10^{-15}\ m^2;$$
$$K_z = 8 \times 10^{-12}\ m^2$$

These roughly numbers correspond to some preferential dispersion paths followed by Nitrogen during its rapid migration from reinjection to extraction zones. We estimated as well that the air injected in well Az-7 and/or in well Az-8 takes about 50 days to arrive at well Az-16D, corresponding to an average velocity equal to 22 m/day, and about 35 days to arrive at well Az-17, meaning an average velocity equal to 46 m/day. The total amount of air injected into the Tejamaniles reservoir up until December 1990, is about 24,000 tons, for an average rate of 13.2 T/day.

CONCLUSIONS

- Air is a good and cheap natural tracer.

- Reinjection of liquid and air at Los Azufres geothermal field, could be considered as a long term injection test using the Nitrogen of the air as a natural tracer that migrates following non-isotropic paths from injection sectors to production zones.

- When extraction starts simultaneously with reinjection, the Nitrogen of the air mixed to the injected water propagates very fast through the fractures network and arrives to the producing regions with negligible thermal interference.

- No Oxygen effects have been noticed up to date.

Fig. 3.- RATE OF FLUID EXTRACTION AT TEJAMANILES

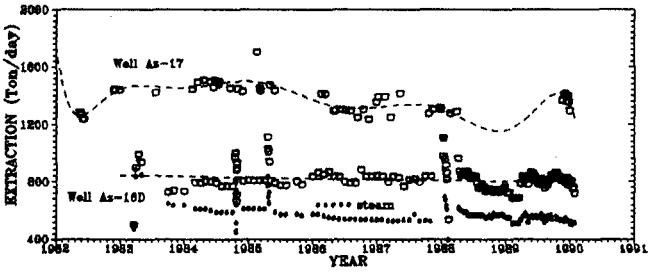

Fig. 4.- RATE OF FLUID INJECTION AT WELL Az-7

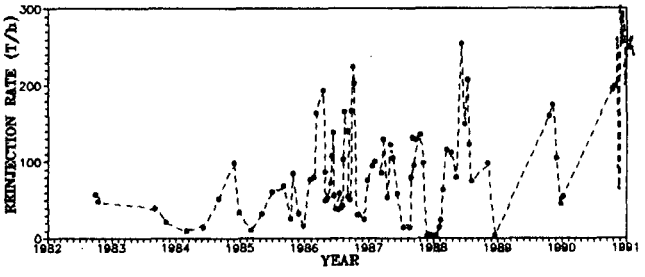

Fig. 5.- NITROGEN EVOLUTION AT WELL Az-16D

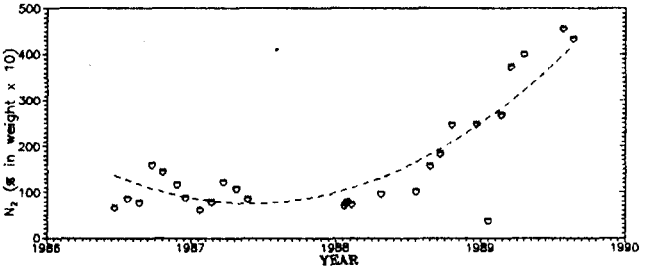

Fig. 6.- NITROGEN EVOLUTION AT WELL Az-17

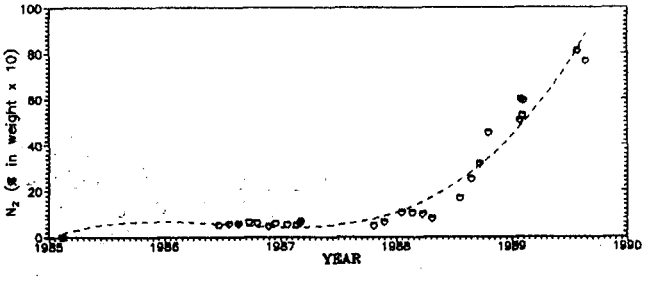

Fig. 7.- EVOLUTION OF SALTS AT WELL Az-16AD

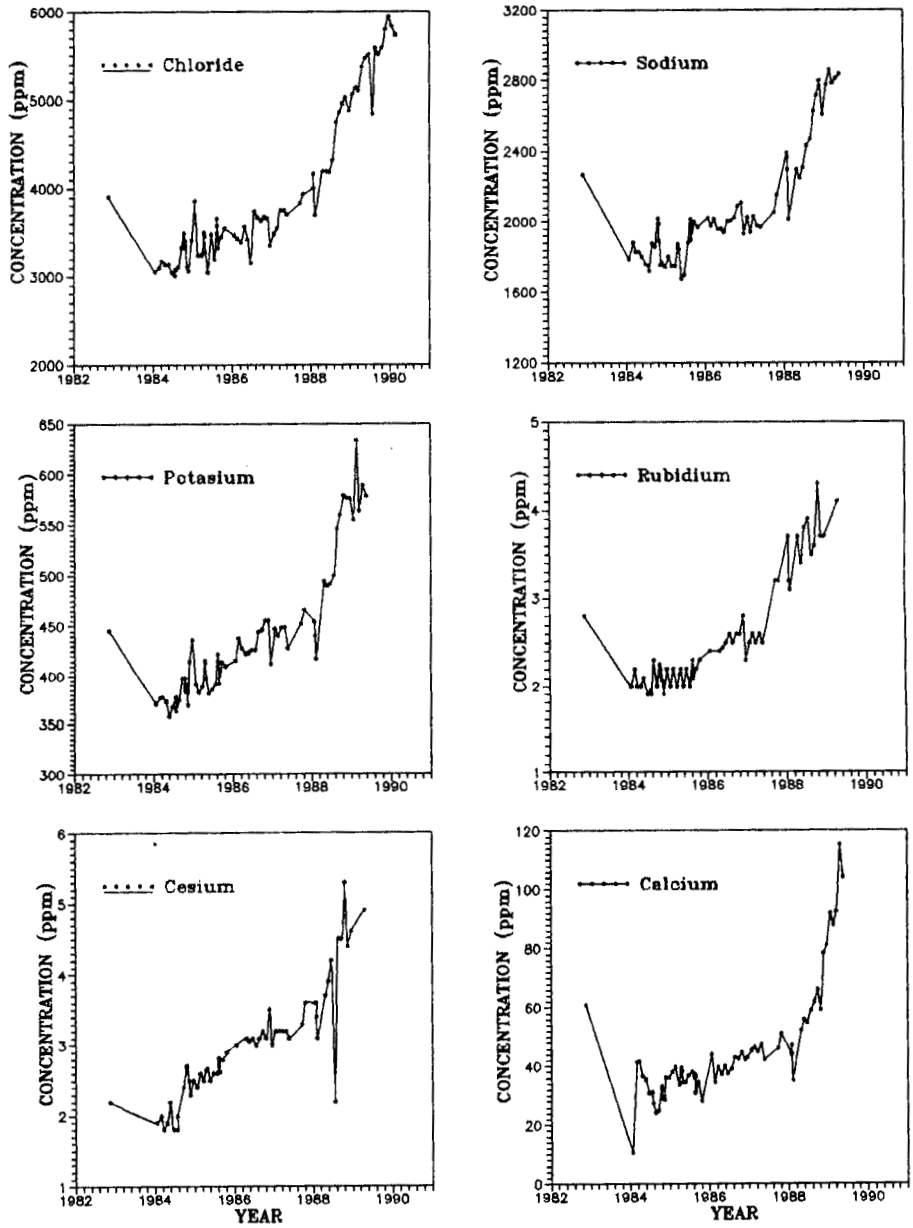

REFERENCES.

CATHELINEAU M., OLIVER R., NIEVA D., GARFIAS A.,1985. 'Mineralogy and distribution of Hydrothermal Mineral Zones in Los Azufres (Mexico) Geothermal Field'. Geothermics, Vol. 14 No.1, pp. 49-57.

GUTIERREZ N.,AUMENTO F. 1982.'The Los Azufres (Mich.,Mexico) Geothermal Field'. 26th Inter. Geological Congress, J. Hydrology 56, pp.137-162.PRUESS K., 1988. 'SHAFT, MULKOM, THOUGH: A Set of Numerical Simulators for Multiphase Fluid and Heat Flow.' Geotermia-Revista Mexicana de Geoenergia, Vol.4, No.1, pp. 185-202.

HORNE,R.N. and H.G.PUENTE, 1989. 'Tracer Testing at Los Azufres'. Proceedings, 14th Workshop on Geothermal Reservoir Engineering, pp.197-199. Stanford University, Stanford, California.

SUAREZ C.,NARANJO S.,MORENO J.,ESTRADA R., 1990. 'Los Azufres: The Initial Response of a Fractured Hydrothermal System to Exploitation'. Preprints of the 15th Workshop on Geothermal Reservoir Engineering, Stanford, California.

SUAREZ C. and MAÑON A., 1990. 'Injection of Cold Water and Air in a Two-Phase Volcanic Hydrothermal System'. TOUGH Workshop Proceedings. Lawrence Berkeley Laboratory. September 13-14. Berkeley, California.

PROCEEDINGS, Sixteenth Workshop on Geothermal Reservoir Engineering
Stanford University, Stanford, California, January 23-25, 1991
SGP-TR-134

AN INVESTIGATION OF RADIAL TRACER FLOW IN NATURALLY FRACTURED RESERVOIRS

Jetzabeth Ramírez-Sabag[1], Fernando Samaniego V.[1,2],

Jesús Rivera R.[1,2], and Fernando Rodríguez[3]

Universidad Nacional Autónoma de México,
Facultad de Ingeniería, 04510 México, D.F.

ABSTRACT

This study presents a general solution for the radial flow of tracers in naturally fractured reservoirs. Continuous and finite step injection of chemical and radioactive tracers are considered. The reservoir is treated as being composed of two regions: a mobile region where longitudinal dispersion and convection take place and a stagnant region where only diffusion and adsorption are allowed. Radioactive decay is considered in both regions. The model of this study is thoroughly compared to those previously presented in literature by Moench and Ogata, Tang et al., Chen et al., and Hsieh et al. The solution is numerically inverted by means of the Crump algorithm. A detailed validation of the model with respect to solutions previously presented and/or simplified physical conditions solutions (i.e., homogeneous case) or limit solutions (i.e., for short times) was carried out.
The influence of various dimensionless parameters that enter into the solution was investigated. A discussion of results obtained through the Crump and Stehfest algorithm is presented, concluding that the Crump method provides more reliable tracer concentrations.

INTRODUCTION

Reservoir characterization plays a very important role in the optimization plan of a reservoir. Among the tools available to acomplish this task, the injection of tracers and proper analysis has shown through the years to be a useful mean. Naturally fractured reservoirs are complex systems that require careful studies for optimal exploitation conditions. In aiming toward this goal, tracer flow test provide estimation of basic reservoir parameters, in addition to the connectivity of the reservoir and the transit time of injected fluids. This latter information is very important in fluid reinjection projects.

There are several papers that deal with the flow of tracers in naturally fractured reservoirs (for a review, see the paper by Ramírez et al., 1990). The existing literature with regard to the radial flow of tracers appears to be mostly oriented to the homogeneous case (Bailey and Gogarty, 1961; Brigham and Smith, 1966; Moench and Ogata, 1981; Pickens, et al., 1981; Güven, et al., 1985; Hsieh, 1986; Guvansen and Guvansen, 1987; Chen, 1987; Falade and Brigham, 1989). A review indicates only a few papers that discuss the radial flow of tracers in naturally fractured systems (Chen, 1985 and 1986; Stephenson et al., 1989). The purpose of this study is to present a general solution for the radial flow of tracers in naturally fractured reservoirs. Continuous and finite step injection of chemical and radioactive tracers are considered. This solution considers all the important mechanisms that affect tracer flow: diffussion, convection, adsorption, and radioactive decay.

MATHEMATICAL MODEL

The model considered in this study is shown in Fig. 1. The naturally fractured medium is represented by means of a system of horizontal equally spaced parallel fractures, alternated with matrix blocks. The system shown in this figure consists of two flow regions: a) a mobile

1. Universidad Nacional Autónoma de México
2. Pemex
3. Petrobrás/Unicamp

region constituted by the fracture network and b) a stagnant or immobile region. Both regions are interconnected by means of a thin fluid layer contained within the immobile region, which controls the fluid and mass transfer between the regions. This type of visualization of the problem by means of two regions has been used by other authors in the past (Deans, 1963; Walkup and Horne, 1985; Maloszewski and Zuber, 1985; Chen, 1986; Rivera et al., 1987; Ramírez et al., 1988 and 1990).

In the mobile region the following effects are considered:

a) Longitudinal dispersion that includes molecular difussion:

$$D_r = \alpha v + D_{mr} \qquad (1)$$

The Z direction is not considered because it is assumed that fracture with 2w is small and, consequently there is no concentration gradient in this direction.

b) Convection. Based upon the discussion presented in a), flow velocity in the Z direction is assumed to be uniform and only its variation is considered along the r direction. For the case of this study of radial flow under constant rate injection, velocity is defined as

$$v = \frac{a}{r} \qquad (2)$$

where

$$a = \frac{Q}{4\pi(w-\delta)} \qquad (3)$$

c) Decay. This condition is considered for the case of a radioactive tracer of decay time less than the transit (travel) time.

For the immobile region the following effects are considered:

a) Difussion. This effect is only considered in the Z direction, because the longitudinal component is assumed to be negligible.
b) Adsorption
c) Decay

Based upon the above mentioned assumptions, considering an incompressible fluid, the governing equations for tracer concentrations in the fracture and in the porous matrix can be stated as follows:

a) Fractures:

$$\frac{\partial C_{1D}}{\partial t_D} = \frac{1}{r_D}\frac{\partial^2 C_{1D}}{\partial r_D^2} - \frac{1}{r_D}\frac{\partial C_{1D}}{\partial r_D} - \gamma C_{1D} + \frac{D_{2D}}{Z_{oD}}\frac{\partial C_{2D}}{\partial Z_D}\bigg|_{Z_{oD}} \qquad (4)$$

b) Matrix

$$\frac{\partial C_{2D}}{\partial t_D} - RD_{2D}\frac{\partial^2 C_{2D}}{\partial Z_D^2} + \gamma C_{2D} = 0 \qquad (5)$$

where the definitions for the dimensionless groups that enter into these equations are

$$t_D = \frac{at}{\alpha^2} \qquad (6)$$

$$C_{1D} = \frac{C_1 - C_i}{C_o - C_i} \qquad (7)$$

$$C_{2D} = \frac{C_2 - C_i}{C_o - C_i} \qquad (8)$$

$$Z_D = \frac{Z}{\alpha} \qquad (9)$$

$$r_D = \frac{r}{\alpha} \qquad (10)$$

$$D_{2D} = \frac{D_2}{a} \qquad (11)$$

$$\gamma = \frac{\lambda\alpha^2}{a} \qquad (12)$$

$$R = \frac{\phi_2}{\phi_2 + \rho K(1-\phi_2)} \qquad (13)$$

The last term of Eq. 4 considers the interaction between the fractures and matrix systems, representing a difussion mass transfer from the fractures to the matrix at $Z_{OD} = (w-\delta)/\alpha$.

The equations that complete the model are given by Eqs. 14-19.

Boundary conditions

$$C_{1D}(r_{oD}, t_D) = 1 \qquad (14)$$

$$C_{2D}(r_D, Z_{oD}, t_D) = C_{1D}(r_D, t_D) \qquad (15)$$

$$C_{1D}(\ , t_D) = 0 \qquad (16)$$

$$\frac{\partial C_{2D}}{\partial Z_D}\bigg|_{(r_D, E/2\alpha, t_D)} = 0 \qquad (17)$$

Initial conditions

$$C_{1D}(r_D,0) = 0 \qquad (18)$$

$$C_{2D}(r_D,Z_D,0) = 0 \qquad (19)$$

To find the solution to this problem, the Laplace transformation method was used. The resulting equations after the application of this method to Eqs. 4 and 5 were coupled, yielding:

$$\frac{d^2\bar{C}_{1D}}{dr_D^2} - \frac{d\bar{C}_{1D}}{dr_D} - \xi r_D \bar{C}_{1D} = 0 \qquad (20)$$

where

$$\xi = S+\gamma+\frac{D_{2D}}{Z_{0D}}\sqrt{\beta}\,\tanh\left\{\sqrt{\beta}\left(\frac{E}{\alpha}-2Z_{0D}\right)\right\} \qquad (21)$$

$$\beta = \frac{S+\gamma}{RD_{2D}} \qquad (22)$$

with the following boundary conditions:

$$\bar{C}_{1D}(r_{0D},S) = \frac{1}{S} \qquad (23)$$

$$\bar{C}_{1D}(\ ,S) = 0 \qquad (24)$$

To express Eq. 20 in an easier form, the following expressions can be used (Tang and Babu, 1979):

$$y = r_D + \frac{1}{4\xi} \qquad (25)$$

$$\bar{C} = \bar{C}_{1D}\ \exp(-y/2) \qquad (26)$$

$$x = \xi^{1/3}\ y \qquad (27)$$

The result is the standard Airy equation (Abramowitz and Stegun, 1970):

$$\frac{d^2\bar{C}}{dx^2} = x\bar{C} \qquad (28)$$

The general solution of Eqs. 20 and 21-28 is

$$\bar{C}_{1D} = \frac{1}{S}\exp\left(\frac{y-y_0}{2}\right)\frac{A_i(\xi^{1/3}\ y)}{A_i(\xi^{1/3}\ y_0)} \qquad (29)$$

where

$$y_0 = r_{0D} + \frac{1}{4\xi}$$

Eq. 29 gives the tracer concentration, chemical or radioactive, in the fractured region for the case of continuous injection.

A solution for the finite step injection case, may be obtained through the use of Eq. 29 and the principle of superposition.

METHOD OF SOLUTION

The Airy functions $A_i(x)$ that enter into Eq. 29 were computed according to (Abramowitz and Stegun, 1970, p. 448, Eq. 10.4.59).

For small times, Z>4.8:

$$A_i(Z) = \frac{1}{2}\pi^{-1/2} Z^{-1/4} e^{-\xi}\sum_{k=1}(-1)^k C_k \xi^{-k} \qquad (30)$$

where

$$\xi = \frac{2}{3} Z^{3/2}$$

$$C_0 = 1$$

$$C_k = \frac{\Gamma(3K+1/2)}{54^k K!\,\Gamma(K+1/2)}$$

For $-5.0 \le Z \le 4.8$, $A_i(x)$ can be computed according to (Abramowitz and Stegun, 1970, p. 446, Eq. 10.4.2)

$$A_i(Z) = C_1 f(Z) - C_2 g(Z) \qquad (31)$$

where

$$f(Z) = \sum_{K=0} 3^K \left(\frac{1}{3}\right)_K \frac{Z^{3K}}{(3K)!}$$

$$g(Z) = \sum_{K=0} 3^K \left(\frac{2}{3}\right)_K \frac{Z^{3K+1}}{(3K+1)!}$$

$$(\alpha+1/3)_0 = 1$$

$$3^K(\alpha+1/3)_K = (3\alpha+1)(3\alpha+4)\ldots(3\alpha+3K-2)$$

and $C_1 = 3^{-2/3}/\Gamma(2/3) = 0.3550280538$,

$C_2 = 3^{-1/3}\,\Gamma(1/3) = 0.2588194037$

where α for this problems is equal to 0.

An excellent comparison with the tabulated values of the Airy function of Abramowitz and Stegun (1970, p.475, Table 10.11) was observed keeping 20 terms each of f(Z) and g(Z).

For the inversion of Eq. 29 the algorithm of Crump (1976) was used, obtaining excellent results for the range of parameters used; this will be discussed later in this paper. The Stehfest numerical inverter algorithm (1970) was also used for the inversion of Eq. 29, finding important numerical dispersion problems for large t_D's or large r_D's .

VALIDATION OF MODEL

The solution of the model of this study was compared in its homogeneous porous media version with those of Moench and Ogata (1981) and Hsieh (1986). It is important to keep in mind that the differential equation that describes the tracer flow problem of these two papers and the one used in this work are the same, the only change being the method of solution. The continuous tracer concentration solutions of these authors are expressed in the Laplace space by means of Airy functions. Moench and Ogata numerically invert their solution using the Stehfest algorithm and Hsieh's solution is of integral type. It can be demonstrated that these solutions correspond to particular cases of the model of this study. For the case of small diffusion coefficient and porosity of the matrix (Stagnant) region, $(D_{2D}/Z_o)\sqrt{(S+\gamma)/(RD_2)} \cong 0$, the naturally fractured porous media approaches homogeneous behavior and, the proposed model simplifies to a homogeneous model. In other words, for these conditions Eq. 21 reduces to $= S$.

Table 1 shows a comparison of the results presented by Hsieh and those of this study, for dimensionless times t_D equal to 50 and 100, r_{wD}= 10 and different dimensionless radial distances r_D. It can be observed, in light of a comparison with the analytical solution of Hsieh that the accuracy of the results of this model is very good.

With regard to the naturally fractured case, the solution of this study will correspond to that of Chen (1985), provided that the matrix region behaves under transient conditions (the matrix region be of infinite extent for the times of interest). For these conditions, Eq. 21 becomes,

$$\xi = S + \left(\frac{SD_{2D}}{Z_{oD}^2 R} \right)^{1/2}$$

Fig. 2 presents a comparison of results obtained by means of the continuous tracer concentration analytic and approximate solutions of Chen and those of this study. It can be observed that agreement is excellent.

DISCUSSION OF RESULTS

Next, a presentation of results for the continuous tracer concentration solution will follow. The data used to get the results are those of Chen (1986), where the constant injection rate Q is equal to 0.01 m^3/d.

Fig. 3 shows results of tracer concentration versus radial distance for dimensionless times of 1, 5 and 10. The concentration level gradually decreases with radial distance.

Fig. 4 presents results of tracer concentration versus radial distance, for values of the dimensionless well radius of 0.5, 1.0, 1.5, and 2.0, for a dimensionless time of 1. These results are similar to those presented by Hsieh (1986) for the homogeneous case, showing that tracer concentration response is strongly affected by the wellbore radius.

Fig. 5 shows a graph of tracer concentration versus time for a wellbore radius of 0 and for a radial distance of 1. This graph can be compared to the tracer concentration results of Ramírez et al. (1990) for linear flow, not shown in this paper, concluding that a uniqueness problem may arise if the test interpretation were to be conducted without additional information coming from other sources (i.e., geological, core analysis, well logs, etc.).

Fig. 6 presents results of tracer concentration for the finite-step case, for injection times of 0.3 and 0.5. As expected, it is observed from results of this figure that as the injection time increases, so does the maximum tracer concentration and, that the time at which this maximum is attained is larger than the injection period, due to the dispersion effects. Again, as previously discussed with regard to Fig. 5, a uniqueness problem may arise if the test interpretation were to be conducted without additional information coming from other sources (i.e., geological, core

analysis, well logs, etc.).

CONCLUSIONS

The main objective of this work has been to present a solution for the radial flow of a tracer in a naturally fractured reservoir.

The main conclusions of this study are as follows:

1. A model is presented for the radial flow of a tracer in naturally fractured reservoirs. It considers the following mechanisms: diffusion, convection, adsorption, and radioactive decay.

2. The Crump algorithm was found to be superior for the numerical inversion of the solution of this study to that provided by the Stehfest algorithm.

3. A thorough validation of the model against simplified and similar solutions published in the literature was carried out.

4. Solutions are presented for the continuous and finite step injection cases.

5. A comparison of radial and linear tracer flow continuous and finite-step injection solutions indicates that a uniqueness problem may arise in the interpretation of a test.

NOMENCLATURE

a = advection parameter, Eq. 3
$A_1(x)$ = Airy function

C = tracer concentration
$\overline{C}$ = parameter, Eq. 26
C_D = dimensionless tracer concentration Eqs. 7 and 8
D_{mr} = molecular diffusion coefficient, L^2/T
D_r = longitudinal dispersion coefficient, Eq. 1, L^2/T
E = thickness of the symmetry element, L
K = adsorption constant, L^3/M
Q = constant injection rate, L^3/T
r = radial distance, L

R = dimensionless parameter, Eq. 13
t = time, T
v = fluid velocity, L/T
w = fracture half-width, L
x = parameter, Eq. 27
y = parameter, Eq. 25
Z = vertical coordinate, L
Z_{OD} = dimensionless effective fracture half-width

Greek simbols

α = dispersivity of fracture, L
β = parameter, Eq. 22
γ = dimensionless parameter, Eq. 12
δ = Stagnant fluid film thickness, L
= parameter, Eq. 21

Subscripts

D = dimensionless
i = initial
1 = mobile or fractured region
2 = immobile (fluid layer and porous matrix) region.

REFERENCES

Abramowitz, M. and Stegun, I.A., 1970. Handbook of Mathematical Functions with Formulas, Graphs, and Mathematical Tables. National Bureau of Standards, Washington, D.C.

Bailey, H.R. and Gogarty, W.B., 1963. Diffusion Coefficients from Capillary Flow. Soc. Pet. Eng. J. (Sept.) 256-266.

Brigham, W.E. and Smith, D.H., Jr., 1966. Prediction of Tracer Performance on a Five-Spot Pattern. J. Pet. Tech. (April) 513-517.

Chen, C-S., 1985. Analytical and Approximate Solutions to Radial Dispersion from an Injection Well to a Geological Unit with Simultaneous Diffusion into Adjacent Strata. Water Resources Research, Vol. 21, No. 8 (August) 1069-1076.

Chen, C-S., 1986. Solutions for Radionuclide Transport from an Injection Well into a Single Fracture in a Porous Medium. Water Resources Research, Vol. 22, No. 4 (April) 508-518.

Chen, C-S., 1987. Analytical Solutions for Radial Dispersion with Cauchy Boundary at Injection Well. Water Resources Research, Vol. 23, No. 7 (August) 1217-1224.

Crump, K.S., 1976. Numerical Inversion of Laplace Transforms Using a Fourier Series Approximation. J. of the Association of Computing Machinery, Vol. 23, No. 1 (January) 89-96.

Deans, H.A., 1963. A Mathematical Model for Dispersion in the Direction of Flow in Porous Media, Soc. Pet. Eng. Jour. 3(1):49-52.

Falade, G.K. and Brigham, W.E., 1989. Analysis of Radial Transport of Reactive Tracer in Porous Media. SPE Reservoir Engineering (Feb.) 85-90.

Guvansen, V. and Guvansen, V.M., 1987. An Approximate Semianalytical Solution for Tracer Injection Tests in a Confined Aquifer with Radially Converging Flow Field and Finite Volume of Tracer and Chase Fluid. Water Resources Research, Vol. 23, No. 8 (August) 1607-1619.

Güven, O., Falta, R.W., Molz, F.J. and Melville, J.G., 1985. Analysis and Interpretation of Single-Well Tracer Tests in Stratified Aquifers. Water Resources Research, Vol. 21, No. 5 (May) 676-684.

Hsieh, P.A., 1986. A New Formula for the Analytical Solution of the Radial Dispersion Problem. Water Resources Research, Vol. 22, No. 11 (Oct.) 1597-1605.

Maloszewski, P. and Zuber, A., 1985. On the Theory of Tracer Experiments in Fissured Rock with Porous Matrix. J. Hydrol. 79, 333-358.

Moench, A.F. and Ogata, A., 1981. A numerical Inversion of the Laplace Transform Solution to Radial Dispersion in a Porous Medium. Water Resources Research, Vol. 17, No. 1 (Feb.) 250-252.

Pickens, J.F., Jackson, R.E., Inch, K.J., and Merrit, W.F., 1981. Measurement of Distribution Coefficients Using a Radial Injection Dual-Tracer Test. Water Resources Research, Vol. 17, No. 3 (June) 529-544.

Ramírez, J., Rivera, J., and Rodríguez F., 1988. Tracer Flow Model for Naturally Fractured Geothermal Reservoirs. Proceeding, Thirteenth Workshop on Geothermal Reservoir Engineering, Stanford University, Stanford, Ca., January 19-21, SGP-TR-113.

Ramírez,S.J., Rivera,R.J., Samaniego, V.F., and Rodríguez, F., 1990. A Semianalytical Solution for Tracer Flow in Naturally Fractured Reservoirs. Proceedings, Fifteenth Workshop on Geothermal Reservoir Engineering, Stanford University, Stanford, Ca., January 23-25, 1990.

Rivera, R.J., Ramírez, J., and Rodríguez, F., 1987. Parallel Fractures Model for Tracer Flow Through Geothermal Reservoirs-Preliminary Results. Proceedings, Twelfth Workshop on Geothermal Reservoir Engineering, Stanford University, Stanford, Ca., January 20-22, SGP-TR-109.

Stehfest, H., 1970. Numerical Inversion of Laplace Transforms. Commun. ACM, Vol. 13, No. 1, p. 47-49.

Stephenson, D., Paling, W.A.J., and de Jesus, A.S.M., 1989. Radioatracer Dispersion Tests in a Fissured Aquifer.J. of Hydrol.,110,p.253-164.

Tang, D.H. and Babu, D.K., 1979. Analytical Solution of a Velocity Dependent Dispersion Problem. Water Resources Research, Vol. 15, No. 6 (Dec.) 1471-1478.

Walkup, G.W. and Horne, R.N., 1985. Characterization of Tracer Retention Processes and Their Effect on Tracer Transport in Fractured Geothermal Reservoirs. California Regional Meeting, Bakersfield, Ca., March 27-29. SPE paper 13610.

TABLE 1. COMPARISON OF THE HOMOGENEOUS RESULTS OF HSIEH (1986), G. AND THOSE OF THIS STUDY, C_D.

$t_D = 50$			$t_D = 100$		
r_D	G	C_D	r_D	G	C_D
11.0	0.964	0.96412	11.0	0.993	0.99301
12.0	0.892	0.89231	13.0	0.949	0.94875
13.0	0.775	0.77523	14.0	0.900	0.90010
14.0	0.617	0.61714	16.0	0.724	0.72402
15.0	0.439	0.43925	18.0	0.463	0.46298
16.0	0.273	0.27294	20.0	0.213	0.21295
17.0	0.145	0.14493	22.0	0.065	0.06501
18.0	0.645	0.64501	23.0	0.030	0.03005
19.0	0.023	0.02207	25.0	0.004	0.00397

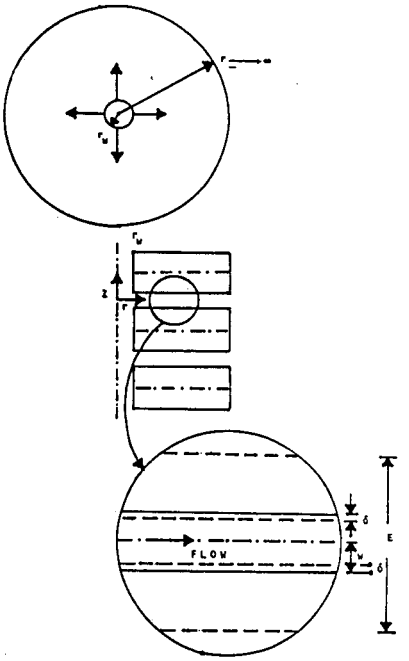

Fig. 1. Proposed Model for representation of the naturally fractured medium.

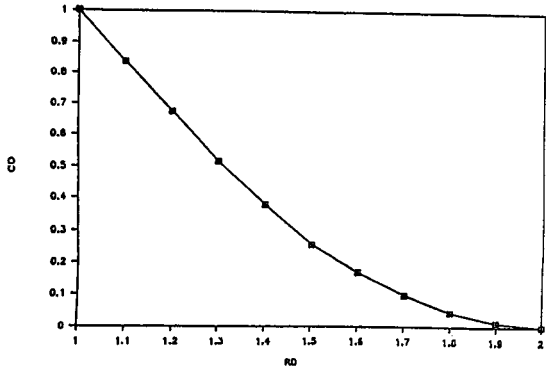

Fig. 2. Comparison of the continuous tracer concentration solutions, for naturally fractured reservoirs, of Chen (1986) and of this study.

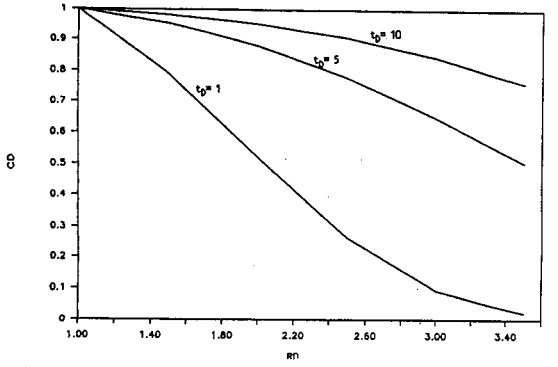

Fig. 3. Continuous injection tracer concentration vs radial distance for various values of t_D.

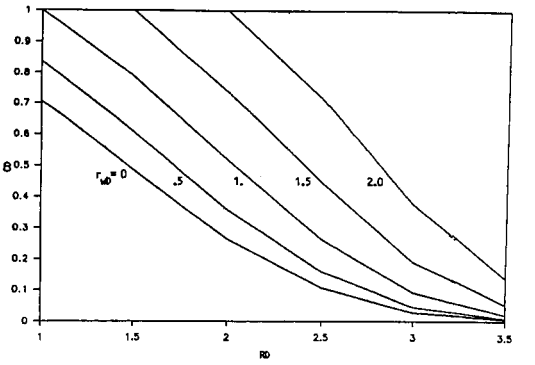

Fig. 4. Continuous injection tracer concentration vs radial distance for various values of the dimensionless wellbore radius, for t_D=1.

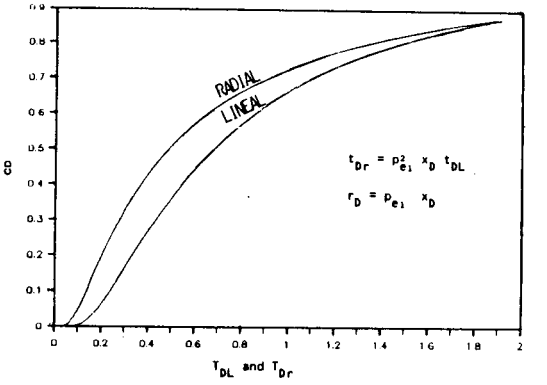

Fig. 5. Comparison of the radial and linear continuous tracer concentration responses for equivalent matrix-fracture system characteristics.

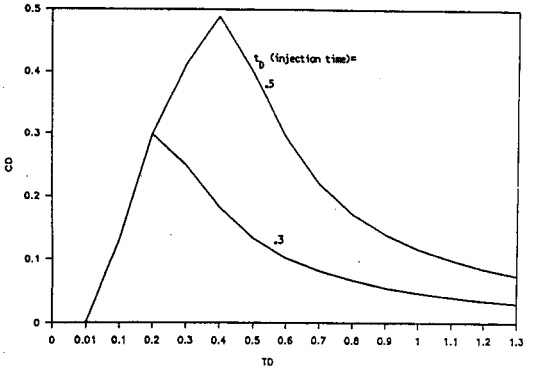

Fig. 6. Influence of the injection period on the finite-step injection tracer concentration.

PROCEEDINGS, Sixteenth Workshop on Geothermal Reservoir Engineering
Stanford University, Stanford, California, January 23-25, 1991
SGP-TR-134

RESERVOIR RESPONSE TO INJECTION IN THE SOUTHEAST GEYSERS

Steve Enedy[1], Kathy Enedy[2], John Maney[3]

1. Northern California Power Agency
2. Calpine Corporation
3. Unocal Geothermal

ABSTRACT

A 20 megawatt (MW) increase in steam flow potential resulted within five months of the start-up of new injection wells in the Southeast Geysers. Flow rate increases were observed in 25 wells offset to the injectors, C-11 and 956A-1. This increased flowrate was sustained during nine months of continuous injection with no measurable decrease in offset well temperature until C-11 was shut-in due to wellbore bridging. The responding steam wells are located in an area of reduced reservoir steam pressure known as the Low Pressure Area (LPA). The cause of the flowrate increases was twofold 1) an increase in static reservoir pressure and 2) a decrease in interwell communication.

Thermodynamic and microseismic evidence suggests that most of the water is boiling near the injector and migrating to offset wells located "down" the static pressure gradient. However, wells showing the largest increase in steam flowrate are not located at the heart of the pressure sink. This indicates that localized fracture distribution controls the preferred path of fluid migration from the injection well. A decrease in non-condensible gas concentrations was also observed in certain wells producing injection derived steam within the LPA.

The LPA project has proven that steam suppliers can work together and benefit economically from joint efforts with the goal of optimizing the use of heat from The Geysers' reservoir. The sharing of costs and information led directly to the success of the project and introduces a new era of increased cooperation at The Geysers.

BACKGROUND

Water injection into The Geysers geothermal field first began in 1969 with the start-up of well SB-1 in the Pacific Gas and Electric (PG&E) Units 1-6 area. Since 1982 throughout the Geyser field, approximately 450 billion pounds of water or 28% of the mass of steam produced has been reinjected with the remainder being evaporated in the power plant cooling process. Overall, injection has proven to be an environmentally safe method of disposing of the plant effluent since the injectate is contained in the reservoir and does not contaminate surface water (Crockett and Enedy 1990). The steamfield operators have experienced both positive and negative results with water injection (Barker et. al. 1989). Experience shows that water injection can lessen the rate of steam flow decline at The Geysers.

There are few examples in the literature of beneficial long-term reservoir response to injection at The Geysers due to the often subtle or delayed effects of injection on offset steam well flowrate. However, through the use of advanced decline curve analysis techniques, decreased rates of steam flow decline have been determined. For example, Ripperda and Bodvarsson (1987) found a slowing of the rate of steam decline on selected Geysers' wells "probably" due to injection which began in the "immediate vicinity" just prior to the change in flow behavior. In the Southeast Geysers, K. Enedy (1989) found lower flowrate declines on producers located offset to an injector which were in part attributable to "water injection support". In both studies, type curves were used to aid in the decline curve analysis.

Further evidence that water injection can supplement steam production is based on tracer tests. Deuterium and tritium are two tracers used at The Geysers to estimate the injection derived component of steam production and to track fluid movement across the reservoir. In a 1975 tritium tracer test in well SB-1, approximately 18% of the injected tritium was recovered from 20 offset steam wells demonstrating that the injectate is boiling and being produced as steam within a few weeks of injection (Gulati, 1978). In the Southeast Geysers, a 1989 tritium test of NCPA's well Y-5 showed tritium recovery within one day of injection. Also, a total of 27% of the tritium was recovered within seven months from 33 steam wells. Beall, Enedy and Box (1989) demonstrated that injectate recovery as steam peaked between 35% and 50% in the Southeast Geysers. These calculations were based on the elevated deuterium content of the injection derived steam. In a similar study for the Unocal-NEC-Thermal (U-N-T) joint venture, Gambill (1990) stated that the mass of injectate produced as steam in 1988 was roughly equivalent to 65% to 80% of the mass of liquid injected during that year.

LOW PRESSURE AREA INJECTION PROJECT

High flowrate declines in the Southeast Geysers, starting in 1986, led to studies to augment

condensate injection with excess fresh water as a means to improve reservoir performance. In order to better understand the role of water injection in the Southeast Geysers, a joint injection project was conceived to quantify the ability of the reservoir to support and benefit from augmented water injection.

An agreem ıt between NCPA, Calpine, and U-N-T delineated general study area and called for the exchange of specific reservoir, geochemical, and geologic data within the Low Pressure Area (LPA) in August, 1989. In addition, U-N-T's microseismic monitoring system was expanded into the NCPA and Calpine leaseholds. The joint study area (Southeast Geysers Study Area) encompasses approximately 2,000 acres, and includes parts of PG&E's Units 13, 16, 18 and NCPA's Plants 1 and 2 (Figure 1). The LPA was defined as the area enclosed by the 220 psig (wellhead) contour based on the January, 1989, isobaric map. It contains approximately 790 acres. Figure 2 shows the outline of the LPA, the wellhead location of the data trade production wells, the mid-point of steam entries on the six injection wells, and the new microseismic stations within the study area.

NCPA and Calpine Corporation agreed to jointly deliver condensate to NCPA's C-Site. Well C-11 was chosen as the joint injector due to both its location within the heart of the low pressure area near the common lease line and its reservoir characteristics which were considered ideal to maximize the return of injectate as steam. A schematic of the joint injection system is shown in Figure 3. Note that there are currently eight wells available for injection of condensate from the combined NCPA and Unit 13 plant areas with two additional wells proposed for conversion to injection. This reflects the philosophy that water needs to be distributed throughout the reservoir and injected at relatively low rates.

STUDY AREA RESERVOIR DESCRIPTION

The two primary formations which host the geothermal reservoir within the Southeast Geysers Study Area are 1) the Franciscan Greywacke, which is a metamorphosed sandstone and 2) a silicic intrusive known as the Felsite, which underlies the entire study area. Greenstone segments within the

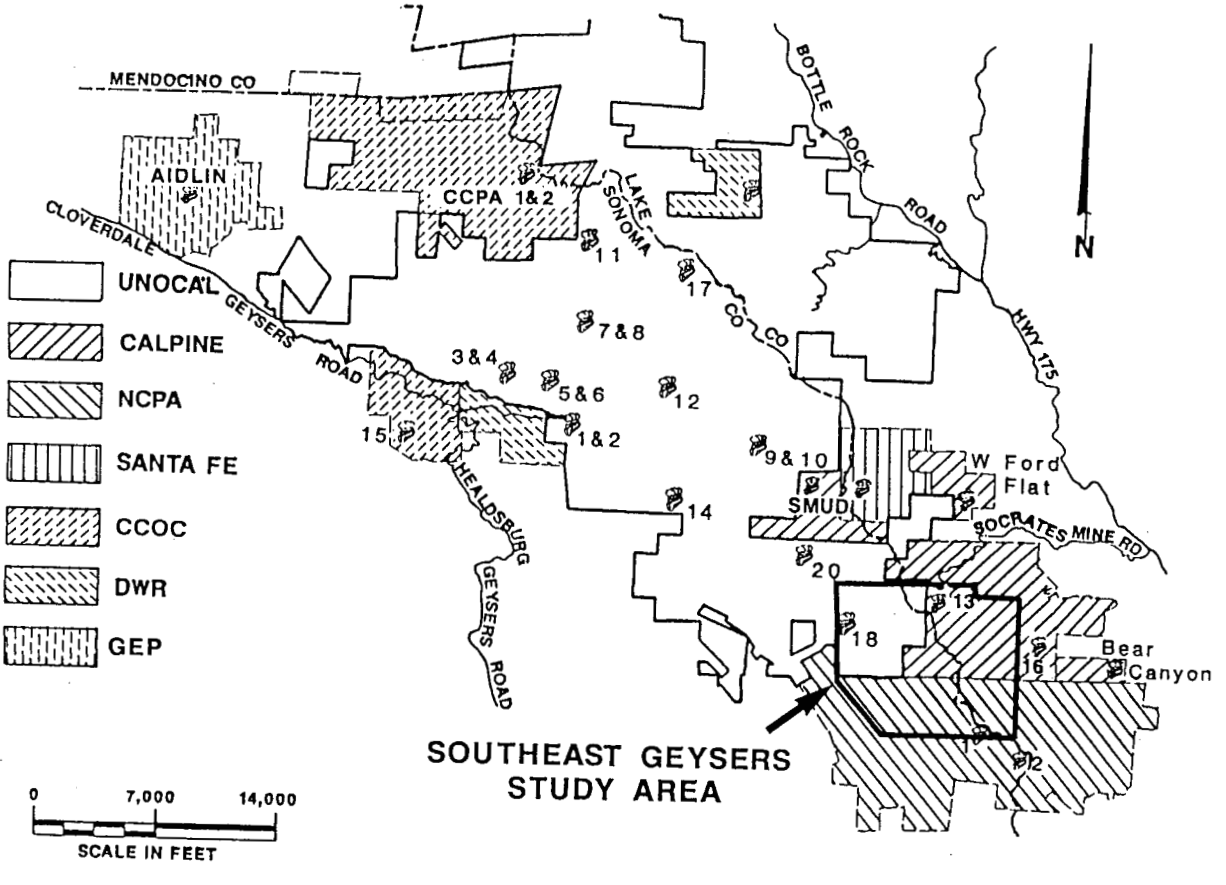

FIGURE 1: Geysers Development map.

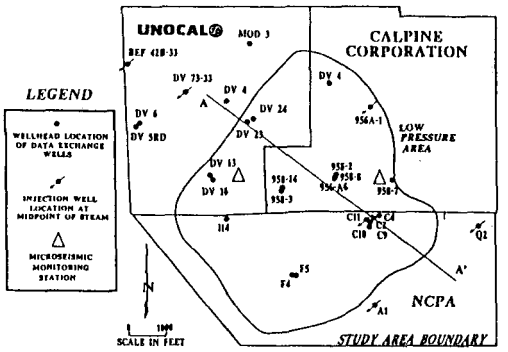

FIGURE 2: Southeast Geysers Study Area.

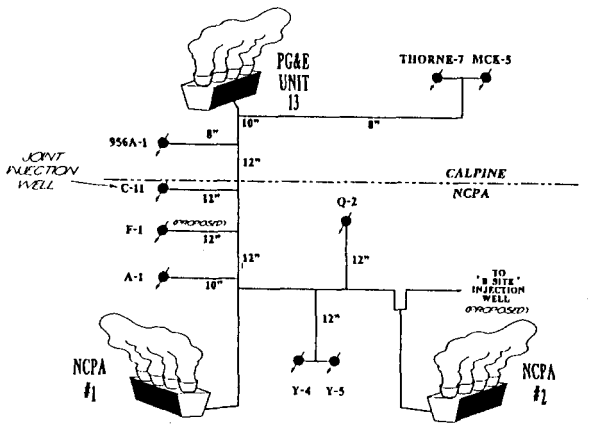

FIGURE 3: Injection schematic.

greywacke are a secondary host rock and can be of importance in specific areas. The main reservoir greywacke is overlain by a heterogeneous mixture of rock types which are normally set behind casing. Matrix permeability in these rocks is very low and extensive fracturing of these rocks has resulted in a high secondary permeability. Reservoir permeability-thickness product is a direct function of the size and distribution of fractures and faults open to steam flow and ranges between 20,000 and 200,000 md-ft. Although fracturing is extensive throughout the study area (especially within the LPA), the distribution is relatively random with large blocks of the formation containing no major steam-bearing fractures. The lower reservoir boundary appears to be gradational in nature, with fractures becoming more widely spaced with increasing depth. Producing wells offset the study area in all directions except to the southwest which is bounded by a fault zone. (Thompson and Gunderson 1989, Beall and Box 1989, Thompson 1989, Smith 1990, Bodvarsson et. al. 1989, Maney et. al. 1990)

The reservoir geology of the study area is distinguished from other portions of The Geysers by the relatively shallow depth of the felsite and the felsite's role as a major reservoir rock especially in the northwest (Unit 18) area. The NW-SE trending felsite intrusion is shallowest within the study area where it reaches sea-level in the middle of Unit 18, and deepens to approximately 4300 feet below sea-level near injection well C-11 (Figure 12). The felsite and greywacke are in hydraulic communication due to their similar static pressure gradient.

SELECTION CRITERIA

Through an ongoing reservoir testing and monitoring program, sufficient data were gathered to evaluate the spatial distribution of reservoir and fluid properties which led to the eventual selection of the LPA as an ideal target for water injection. C-11 was chosen as a joint injector due to both its location along the common lease boundary and the reservoir parameters listed in Table 1. These parameters are documented in a series of technical papers presented at the 1989 GRC Annual Meeting (See References).

TABLE 1

Parameters Used To Select Injection Targets

Parameter	Source	Value
Reservoir Pressure	Based on PBU tests and P/T/S surveys	< 220 psig-Feb89
Reservoir Temperature	Based on P/T/S surveys and geothermometers	> 450 °F
Reservoir Enthalpy	Based on P/T/S surveys	> 1220 Btu/lbm
Fracture Distribution (Permeability)	Drilling history and P/T/S surveys	multiple entries (> 5 per well)
Amount of Injection Derived Steam	Based on Deuterium concentration	< 10 %

The most important criteria for selecting the LPA as an injection target was evidence of reduced or absent liquid saturation while substantial heat remained trapped in the reservoir rock. This data was supplied by a Pressure-Temperature-Spinner (P/T/S) logging program conducted over a three year period, which supplied a spatial and temporal evolution of both enthalpy and superheat within the LPA. (Enedy, K.L. 1989).

Downhole superheat (SH) of up to 80°F was measured on well 956A-2 (Figure 4) in May, 1988, after eight years of production. As this well is completed in the LPA, the elevated SH indicates that the high rate of mass withdrawal is causing this portion of the reservoir to dry-out. Additional evidence of reduced water saturation within the LPA was the increasing trend of downhole enthalpy with time. A modified Mollier diagram, shown in Figure 5, traces the progression of the calculated enthalpy and shows that the LPA wells range between 1220 and 1250 Btu/lbm which is higher than the undisturbed portions of the reservoir (≅1205 Btu/lbm). Also, measured downhole temperatures of 450°F or greater indicate little or no temperature depletion. Other factors such as high flowrate

decline and elevated boron concentrations also confirmed that the LPA was a prime target for liquid injection.

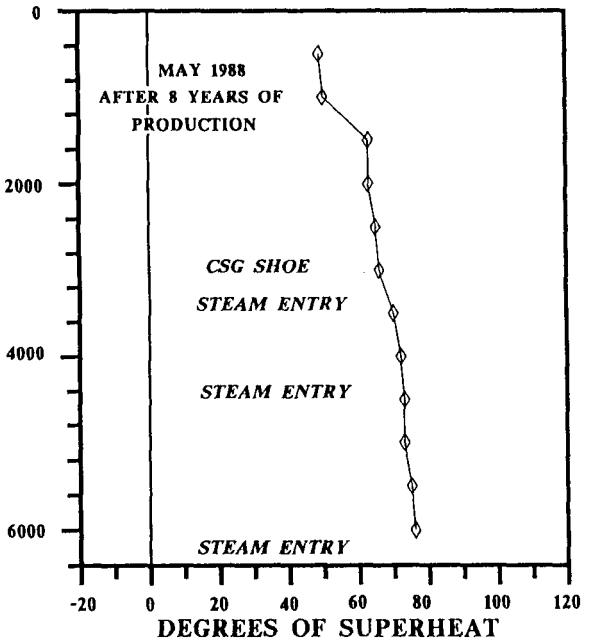

FIGURE 4: Superheat vs. Depth Calpine Well 956A-2.

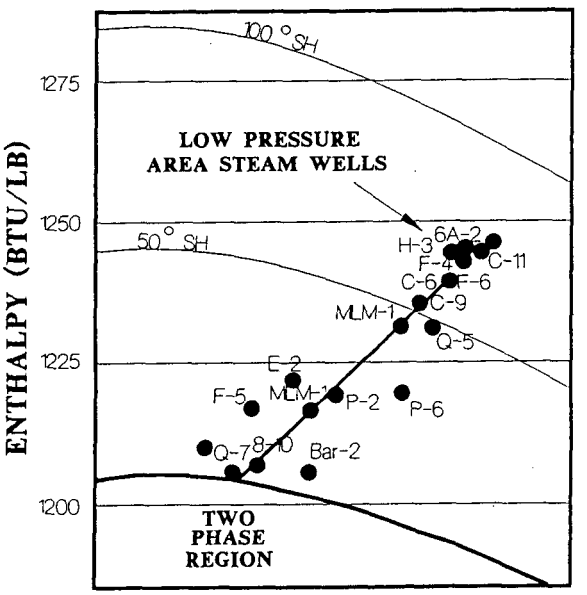

FIGURE 5: Modified Mollier Diagram Flowing steam enthalpy Southeast Geysers steam wells.

OPERATIONAL EXPERIENCE

During the next nine months subsequent to September 20, 1989, approximately two billion pounds of condensate were injected at a nominal rate of 800 GPM (Figure 6). However, C-11 was shut-in on June 4, 1990 due to thermal breakthrough with

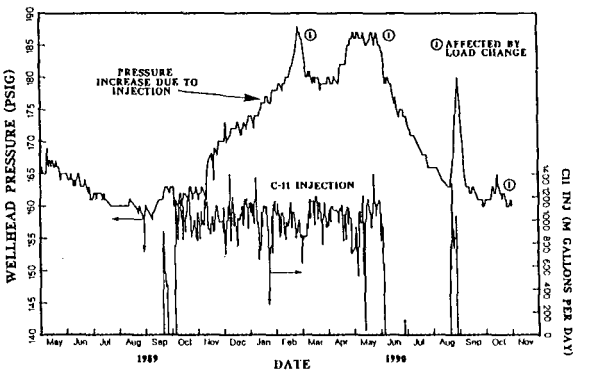

FIGURE 6: F-4 observation Well pressures with C-11 injection Rate.

production well C-8. It was later found that a shallow bridge had formed in the C-11 wellbore causing condensate to flow through a shallow fracture system to the offset production well. The injector remained shut-in until a drilling rig cleaned out the well and a casing liner was installed. Injection resumed on August 21, 1990. However, the casing liner hanger failed nine days later and the well remained shut-in until a second workover was successfully completed. Injection resumed at a nominal rate of 800 GPM on November 19, 1990.

C-11, the first joint injection well utilized at The Geysers, experienced no unusual operational problems due to its combined use by both Calpine and NCPA. Injection rates were held fairly constant thanks to the cooperation of both the NCPA and Calpine field operators (Figure 6). Liquid level surveys indicated that at moderate rates of 800 GPM or less, injection was confined to fractures located in the greywacke-greenstone reservoir between depths of 3800 and 5600 feet. Injection below that depth was limited by a bridge in the wellbore. The installation of the casing liner solved the thermal breakthrough problem with offset steam well C-8.

RESERVOIR RESPONSE

The reservoir responses to the start-up of injection into the LPA consisted of changes in various reservoir properties including static pressures, flowrates, microearthquake response, geochemical changes, and rock temperatures.

Static Pressure Increase

The observed reservoir pressures within the LPA increased in many of the offset NCPA and Calpine production wells due to injection into C-11 and 956A-1. Reservoir pressure on observation well F-4, which is located 2400 feet to the southwest of C-11, increased from 158 to 163 psig (+5 psi) within ten days and to 180 psig (+22 psi or 14%) within five months (Figure 6). This higher pressure level was sustained until C-11 was shut-in on June 4, 1990. The wellhead pressure then gradually declined to near the pre-injection level. Despite the five month

shut-in of injector C-11, F-4's shut-in pressure of 162 psig in October 1990, was 15 psi higher than the extrapolated decline without injection. The sustained pressure support is a long-term benefit obtained from injection.

Finally, during August 1990, after only eight days of injection, F-4's pressure increased from 165 psig to the previously observed maximum of 180 psig. The August pressure response was accelerated when contrasted with the initial pressure response. This effect most likely occurred because of a higher starting water saturation due to previous injection.

A second reservoir pressure response due to injection into C-11 was a decrease in interwell communication between the NCPA and Calpine steamfields. Specifically, during a seven week overhaul of Unit 13, prior to LPA injection, the shut-in pressure of F-4 increased from 168 to 191 psig or 23 psi (Figure 7). Immediately following plant start-up, the well's pressure started to decline and within five weeks returned to the original level. In contrast after seven months of continuous injection, only a 6 psi increase was measured following a four week Unit 13 curtailment associated with a plant cycling test. The elevated pressure level was maintained approximately two weeks following the unit's start-up. Also, the pre-injection outage response of 23 psi is similar to the 22 psi increase due to injection into C-11.

Analysis of the static pressure data indicates that water injection causes a change in the local reservoir boundary condition. Prior to injection, this area behaved like a closed, depleting system. Over short time periods, the post-injection behavior is like that of a constant pressure source system. The pressure support is supplied by the volumetric expansion of flashed injection water.

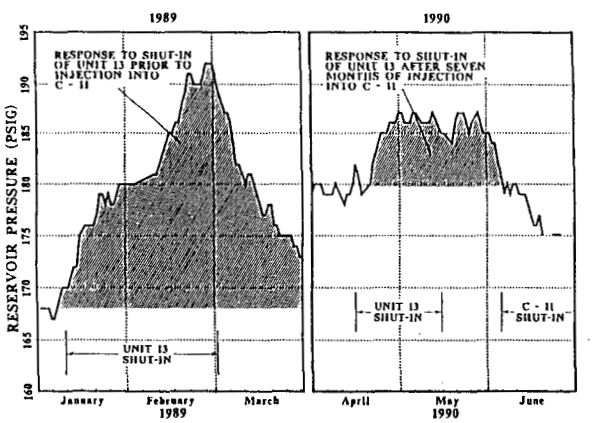

FIGURE 7: F-4 observation well pressure during offset unit shutdown.

Individual Well Flowrate Response

Increases in individual well steam flowrate potentials ranging between 5,000 and 30,000 lbm/hr were observed from 25 wells located within the LPA after five months of injection. The well mid-points of steam and magnitude of the increases are shown on Figure 8. Although all the wells are within the pressure sink, those showing the largest increases are not in the center of the sink but are northwest and southwest of C-11. This indicates that the flow of flashed steam is controlled regionally by the static pressure distribution and locally by fracture orientation.

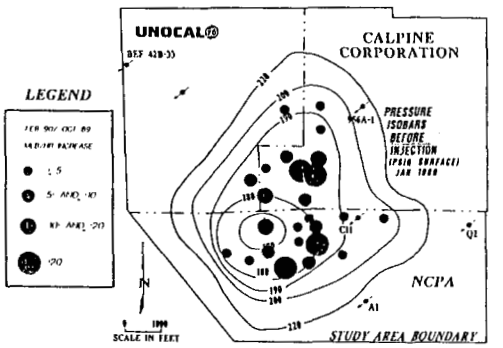

FIGURE 8: Location of wells with flowrate - increases due to injection.

A typical flowrate decline curve for a responding well located on each of the three leases is shown on Figure 9. Calpine's 958-14 and NCPA's F-7 are both located roughly 1,800 feet from C-11, to the northwest and southwest respectively. Both wells started to increase in flowrate by late October, only one month after the start of injection into C-11 and continued to increase for the next five months at similar incline rates of 58 and 61% respectively. Calpine's 958-14 increased from 95,000 to 125,000 lbm/hr or 30,000 lbm/hr. NCPA's F-7 increased from 22,000 to 30,000 lbm/hr or 8,000 lbm/hr.

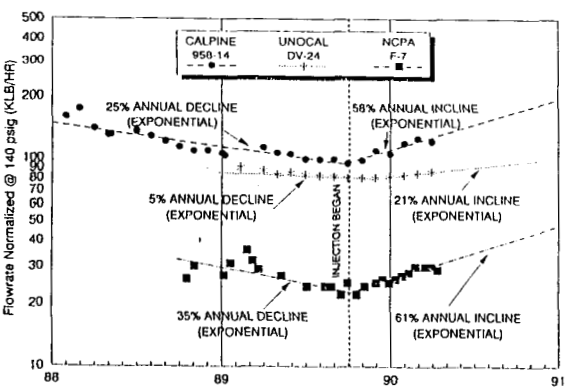

FIGURE 9: Historical monthly flowrate

U-N-T's DV-24 is located in the southeast corner of Unit 18 approximately 3200 feet northwest of C-11. In late November 1989, DV-24 production flowrates began responding favorably to injection from C-11

(Figure 9). For six months prior, the production history of the well indicated a steady decline rate of 5% per year. From December, 1989, through April, 1990, production flowrates in DV-24 increased 7% from 81,000 lbm/hr to approximately 87,000 lbm/hr.

Total Flowrate Response

An increase in total steam flowrate potential equivalent to 20 MW or 360,000 lbm/hr was measured from 23 NCPA and Calpine producers offset to the new injection wells after five months. Figure 10 shows a plot of the combined flowrate potential increase at 140 psig for 14 NCPA wells along with the monthly production from those wells and injection into C-11. Flowrate inclined at an annual exponential rate of 56% for five months. In comparison, the combined flowrate potential of seven responding Calpine wells inclined at a similar 54% annual exponential rate (Figure 11). The overall reservoir benefit obtained from injection into C-11 and 956A-1 has been split almost evenly between the NCPA and Calpine steamfields. U-N-T has observed less injection response due to the greater distance between C-11 and U-N-T producers.

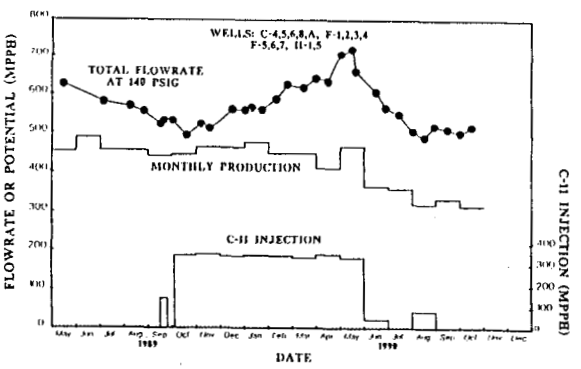

FIGURE 10: Total flowrate of NCPA wells, offset to injector C-11.

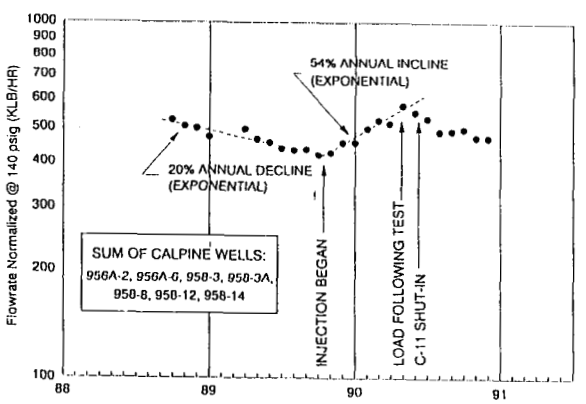

FIGURE 11: Total flowrate of Calpine wells offset to injector C-11.

The material balance of LPA incremental injection and production indicates that injection into both C-11 and 956A-1 brought about the observed flow response. The percent contribution from each injector is not clear at this time. An increase of 2.4 billion pounds of steam was measured during the first year of injection. This was greater than the mass injected into either well and approximately 54% of the total injected mass into both. Following the shut-in of C-11, 956A-1's continued injection induced relatively lower production declines from offset wells (Figure 11). According to geochemical studies, these offset wells also continued to produce injection derived steam.

Microearthquake Response To C-11

The microearthquake (MEQ) cross-section shown in Figure 12 was constructed on azimuth N 53° W through C-11 to show the seismic response to injection at C-11. All the MEQ's located horizontally within 1,000 feet of the section line were included. The data indicate that there were very few events in the area prior to the start of extended injection in early October 1989. After the start of injection, however, a MEQ cluster formed in an area close to the wellbore of C-11 between approximately 2,600 and 4,600 feet below sea level. Stark (1990) interpreted similar injection-related MEQ clusters on U-N-T leases as rough images of the presence of injected liquid. Therefore, Figure 12 would suggest that the injected fluids boil a short distance from the wellbore. In contrast, Stark's U-N-T examples showed MEQ clusters deeper and further away from the associated injection wellbore.

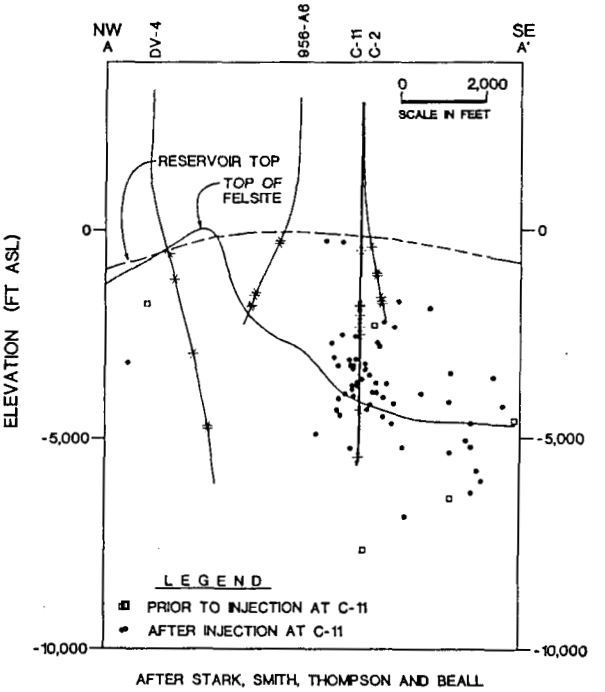

FIGURE 12: Microearthquake cross-section, Azimuth N 53° W through C-11, September, 1989 - April 1990.

Based on the distribution of microseismicity, the majority of the liquid injected into the greywacke appears not to migrate deep into the felsite. Lower fracture density within the felsite may be the limiting factor. Although boiling appears to be primarily in the greywacke, wells completed in both zones produce injection derived steam.

Geochemical Response

Additional evidence that injectate was boiling and being produced as steam is provided by shifts in both deuterium and non-condensible gas concentration. Figure 13 plots the deuterium values for two LPA wells and the injectate composition for C-11. NCPA's well H-4, near the edge of the LPA approximately 3,500 feet from C-11, continued to produce steam without an injection derived steam (IDS) component throughout the injection period. However, NCPA's well F-6, located approximately 1,500 feet from C-11, produced an IDS component within two months of injection start-up to C-11. The IDS component ranged between 65 and 88% during the injection period. After the shut-in of C-11 in June 1990, IDS component returned to near pre-injection levels.

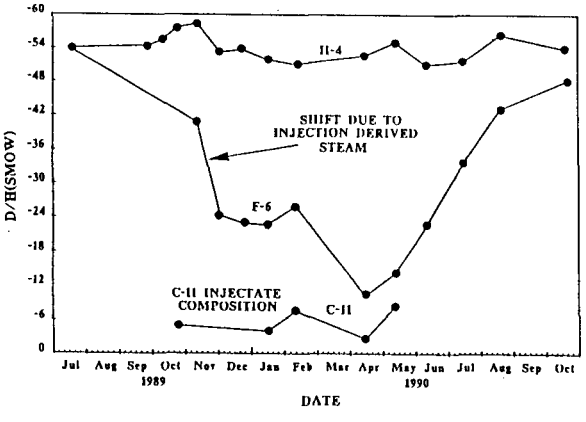

FIGURE 13: Deuterium shifts selected wells in low pressure area.

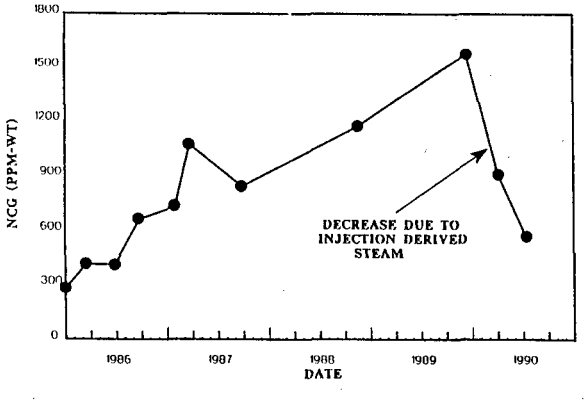

FIGURE 14: Well F-5, non-condensible gases vs. time.

Selected wells which produced injection derived steam within the LPA showed a decrease in non-condensible gas (NCG) concentrations. NCG concentrations had been increasing throughout the Southeast Geysers since 1986 (Maney et al., 1990). Figure 14 shows this increasing NCG trend in NCPA's well F-5 since 1986 through the start-up of C-11 in late 1989 which peaked at 1550 ppm. Soon after injection began, NCG concentrations returned to a mid-1986 value of 590 ppm.

Steam Temperatures

No decrease in reservoir temperatures were measured on steam wells offset to the injectors during the nine month injection period. This indicates that only a fraction of the total available heat capacity of the rock has been extracted. Figure 15 compares the downhole temperature profiles for well F-6 from pre- and post- injection P/T/S surveys. F-6 was stated in the previous section to have produced up to 88% IDS. The 1990 downhole temperatures measured seven months after injection are essentially the same as the 1986 pre-injection temperatures.

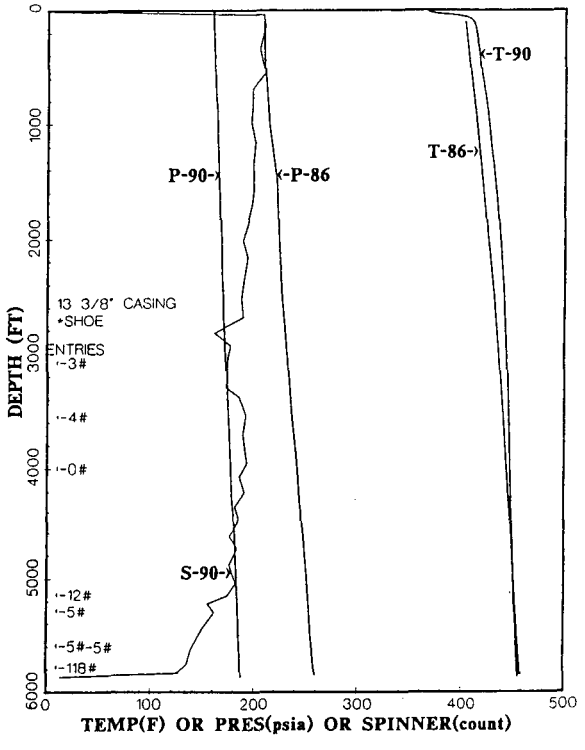

FIGURE 15: Pressure and temperature comparison, well F-6 1986 and 1990

The only measured decrease in downhole temperature occurred in the injector, C-11. Figure 16 contrasts the temperature profiles for C-11 just prior to the start of injection and ten weeks following the C-11 shut-in. A 60°F decrease was measured at the primary greywacke injection zone between 3,800 and 6,000 feet.

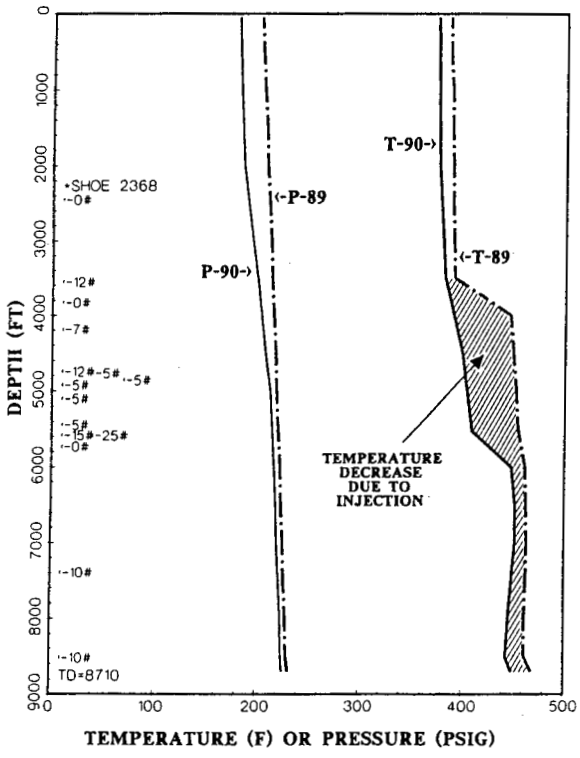

FIGURE 16: C-11 temperature and pressure survey on 9/20/89 - 1/2" vent, survey on 8/17/90 - 3" vent.

CONCLUSIONS

The start-up of new injection wells in the Southeast Geysers resulted in a 20 MW increase in steam flow potential within five months from 25 wells offset to the injectors. These wells behave as if a constant pressure source has been introduced into the reservoir.

The Low Pressure Area Injection Project demonstrated that a properly planned injection project can "mine" or extract additional heat from the rock and positively impact both reservoir pressure and flowrate while minimizing thermal breakthrough to offset wells. These results suggest that further development of fresh water sources to enhance injection may well extend the life of the resource. Those injection projects found to be economically favorable would benefit the electrical consumer by increasing and extending power plant generating capacity.

ACKNOWLEDGEMENTS

The authors would like to thank the members of the Southeast Geysers Study Committee who added both their insight to the data analysis and support for the concept of data sharing including: Unocal's Ben Barker, Mitch Stark, Ken Riedel, Kim Legg, Phil Molling, Debbie Wheeler; NCPA's Dick Yarter, Bill Smith, Steve Jones; Calpine's Tom Box, Joe Beall, Chris Dunkle. Graphics by Bud Schroeder, Ed Keppel. Manuscript was prepared by Judy Hathorn.

REFERENCES

Barker, B.J., M.A. Bryan, K.L. Riedel,,(1989),"Geysers Reservoir Performance", GRC Meeting trans., Vol.13.

Beall, J.J., S.L. Enedy, , W.T. Box, (1989), "Recovery of Injected Condensate as Steam in the South Geysers Field," GRC Meeting trans., Vol.13 pg 351-358.

Beall, J.J., W.T. Box, (1989), "The Nature of Steam Bearing Fractures in the South Geysers Reservoir", GRC Meeting trans., Vol.13 pg 441-448.

Crockett, C.L., K.L. Enedy, (1990), "A Walk Through Time: Injection In The Southeast Geysers," paper presented at Underground Injection Practices Council Meeting, October 29, 1990, Santa Rosa, California.

Enedy, K.L, (1989), "Downhole Enthalpy and Superheat Evolution in Geysers Steam Wells," GRC Meeting trans., Vol.13, pg 377-382.

Enedy, K.L., (1989), "The Role of Decline Curve Analysis at the Geysers," GRC Meeting trans., Vol.13, pg 383-392.

Enedy, S.L., M.A. Grande, J.L.Smith, (1990),"A Case History of Steamfield Development, Reservoir Evaluation and Power Generation in the Southeast Geysers,"GRC Bulletin, October 1990, pg 232-248.

Gambill, D.T., (1990) "The Recovery of Injected Water as Steam at The Geysers," GRC Meeting trans., Vol.14, pg 1655-1660.

Gulati, M.S., S.C. Lipman, C.J. Stroebel, (1978), "Tritium Tracer Test at The Geysers," GRC Meeting trans., Vol. 2, pg 237-239.

Kline, C., S.L. Enedy, (1989), "Effect of Condensate Reinjection on Steam Chemistry at The Geysers Field," GRC Meeting trans., Vol.13, pg 409-414.

Maney,J.J., R.C. Thompson, B.A. Koenig, (1990), "The Geysers Unit 18, A Case History, GRC Geysers Monograph Proposed.

Ripperda, M., G.S. Bodvarsson, (1987), "Decline Curve Analysis of Production Data From The Geysers Geothermal Field," Proceedings, Twelfth Workshop on Geothermal Reservoir Engineering, Stanford University, pg 23-27.

Stark, M.A., (1990), "Imaging Injected Water in The Geysers Reservoir Using Microearthquake Data," GRC Meeting trans., Vol.14. pg 1697-1703.

Thompson, R.C., (1989), "Structural Stratigraphy and Intrusive Rocks At The Geysers Geothermal Field," GRC Meeting trans., Vol.13, pg 481-485.

Thompson, R.C., R.P. Gunderson, (1989), "The Orientation Of Steam-Bearing fractures at the Geysers Geothermal Field", GRC Meeting trans., Vol.13 pg 487-490.

PROCEEDINGS, Sixteenth Workshop on Geothermal Reservoir Engineering
Stanford University, Stanford, California, January 23-25, 1991
SGP-TR-134

Current Techniques in Acid-Chloride Corrosion Control and Monitoring at The Geysers

Paul Hirtz, Cliff Buck and Russell Kunzman

Thermochem, Inc., 5347 Skylane Blvd., Santa Rosa, California 95403

ABSTRACT

Acid chloride corrosion of geothermal well casings, production piping and power plant equipment has resulted in costly corrosion damage, frequent curtailments of power plants and the permanent shut-in of wells in certain areas of The Geysers. Techniques have been developed to mitigate these corrosion problems, allowing continued production of steam from high chloride wells with minimal impact on production and power generation facilities. The optimization of water and caustic steam scrubbing, steam/liquid separation and process fluid chemistry has led to effective and reliable corrosion mitigation systems currently in routine use at The Geysers. When properly operated, these systems can yield steam purities equal to or greater than those encountered in areas of The Geysers where chloride corrosion is not a problem. Developments in corrosion monitoring techniques, steam sampling and analytical methodologies for trace impurities, and computer modeling of the fluid chemistry has been instrumental in the success of this technology.

INTRODUCTION

The production of volatile chloride from Geysers wells was not recognized to be a problem until as late as 1986, after severe production piping corrosion/erosion damage and a wellhead failure had occurred in the Northeast Geysers. Previous corrosion damage, including turbine blade and piping failures, may have been caused by chloride, but monitoring techniques had not been established that could identify acid-chloride as the primary cause. Accurate measurements of chloride in steam produced at The Geysers were not performed before 1986, when specific sampling and analysis methods were developed. Therefore, little data is available to determine trends in produced chloride concentrations from Geysers wells, although it is generally assumed that concentrations are increasing in certain areas. The range of chloride concentrations measured in dry, superheated steam produced by wells at The Geysers is currently from <0.010 ppm_w to 200 ppm_w.

Corrosion damage due to acid-chloride at The Geysers includes extensive well casing corrosion, casing head perforation, well surface piping failures, and gathering system piping perforations or extreme wall loss. The corrosion products exfoliated from wellbores and gathering systems have had a severe impact on power plant equipment, such as the plugging of steam strainers and erosion of turbine blades. Corrosion within the power plants due to residual acid-chloride has resulted in perforations of steam piping, the freezing of stop valves and turbine damage.

The first full-scale corrosion mitigation system at The Geysers was implemented at the Aidlin project by Mission Power Engineering during start-up of the two 10 megawatt (net) units in mid-1989[1]. This system involves water and caustic (NaOH) injection at each production wellhead with subsequent liquid removal by vertical separators and a final two-stage steam washing/separator combination at the plant inlet. This project is unique to The Geysers in that all production wells produce significant levels of chloride in steam and require treatment. The corrosion mitigation system has been very successful in preventing corrosion damage to the steam gathering system and power plant, with surface piping corrosion rates typically below 10 mil/year and turbine inlet steam below 0.05 ppm_w chloride. After the first nine months of operation, a full turbine inspection was performed, including non-destructive testing and scale deposit analysis, which revealed no corrosion damage or evidence of acid-chloride or caustic deposits within the turbine. The operating results for this system encouraged the application of acid-chloride corrosion mitigation technology throughout The Geysers.

This paper outlines the design basis of acid-chloride corrosion mitigation systems currently in use at The Geysers. Details of the process chemistry are discussed, including chemical computer modeling of the vapor-liquid chemical dynamics, and mechanical equipment considerations in maintaining high mass transfer and separation efficiencies. Procedures for corrosion monitoring, fluid sampling and analytical techniques, and mass/heat balance calculations are presented. Initially, the volatile chloride phenomenon, acid-chloride corrosion and dewpoint corrosion are reviewed with analogies to corrosion problems in other industries.

BACKGROUND

The Occurrence of Volatile Chloride in Steam

Geothermal steam containing volatile chloride has been reported in steam fields throughout the world, such as Larderello, Italy; Tatun, Taiwan; Krafla, Iceland; Saint Lucia, Windward Islands, and The Geysers, USA[2,3,4]. These geothermal systems vary greatly in reservoir characteristics, including vapor-dominated, liquid-dominated and volcanic-related fields, but all have produced measurable levels of chloride in dry steam from certain wells without the associated quantities of alkali metals or alkaline earth metals (Na, K, Ca, Mg). Only a few reported cases exist for geothermal systems where it can be conclusively stated that the volatile chloride species is hydrogen chloride (HCl), although the presence of HCl has been well documented for high-temperature volcanic gases[5]. Recently, volatile chloride produced from the two vapor-dominated systems, Larderello and The Geysers, has been considered HCl, although historically chloride produced in steam from Larderello was referred to as ammonium chloride (NH_4Cl)[2,6].

In the condensate of chloride-bearing steam at The Geysers, ammonium ions (NH_4^+) are usually present in excess relative to chloride, making it unclear whether the chloride was initially HCl that reacted with NH_3 in solution, or was transported as NH_4Cl in the vapor phase. Often ferrous iron (Fe^{+2}) is present in quantities much greater than ammonium, as a result of the corrosion of carbon steel piping. This occurrence has been interpreted as proof that the original chloride species was HCl due to the apparent lack of ammonium relative to

chloride[7]. However, this argument is not convincing since ammonium chloride would also corrode carbon steel, resulting in a pH increase and the loss of ammonia to the vapor phase. The presence of dissolved ferrous iron (as a corrosion product) has frequently confounded the interpretation of chloride-enriched condensates by also drastically lowering the pH as ferrous iron oxidizes to ferric upon exposure of a sample to air. Typically, the excess of ammonia relative to chloride in most chloride-bearing steam condensates results in pH values above 5.0 units at 20°C, although systems without excess ammonia may produce condensates below 2.0 pH units at 20°C.

The presence of volatile chloride in steam is a common problem related to conventional steam turbine power plants utilizing subcritical high-pressure boilers. Chloride deposited within steam turbines can cause pitting corrosion and stress-corrosion cracking of the turbine blades. The vapor phase chloride species in this industry is frequently referred to as ammonium chloride, although extensive research has also been conducted on the volatility of NaCl at high temperatures (>300°C). Ammonia is considered a possible aid in the transport of chloride and sulfate from boilers where it is added as ammonium hydroxide for pH control. However, research on the actual transport mechanism has been inconclusive and it appears that ammonium chloride will decompose to HCl and NH_3 at temperatures of 200°C to 250°C, and possibly lower under certain conditions. Experiments performed for the Electric Power Research Institute (EPRI) showed that consistent 1:1 mole ratios, within analytical error, of NH_4^+ and Cl^- could be generated in superheated steam exposed to a saturated NH_4Cl solution at temperatures of 143°C to 190°C. But measurements of pH on the condensed steam shifted erratically between 3.2 and 8.0 units during the tests, indicating that some NH_4Cl decomposed to NH_3 and HCl, which volatilized at slightly varying ratios[8,9].

Most geothermal researchers agree that volatile chloride in geothermal steam is transported as hydrogen chloride. However, there is a considerable debate over the mechanism of HCl generation in the reservoirs. Haizlip, et al.[10], presented a model attempting to account for the chloride levels found at The Geysers and Larderello based on moderate to high saline fluids (10,000 to 100,000 ppm_w NaCl) at depth within a range of temperatures and pH values expected for these reservoirs. Unfortunately, these calculations were based on extrapolated HCl vapor pressure data and HCl dissociation constants which are highly uncertain due to the wide disparities among literature values. Anderson[11] presented a more rigorous thermodynamic model of HCl volatility in high temperature saline brines and concluded that HCl would not partition to the steam phase at the higher concentrations found in The Geysers by this process (10 - 100 ppm_w Cl^-).

Research on equilibrium distributions of strong electrolytes between concentrated salt solutions and dry saturated steam has been performed in the U.S.S.R., including studies of molecular NaCl, NaOH, HCl and hydrated ion solubilities in steam at temperatures of 320°C to 350°C[12,13,14,15]. Comparison of the recent modeling data to this experimental work indicates that the volatile chloride produced at The Geysers could not be the result of direct partitioning from high temperature NaCl solutions alone. Based on experimental data of Tatarinov, the total chloride (HCl + NaCl species) in equilibrium steam over water containing 24 g/Kg chloride at pH 5.5 (calculated) is only 4 ppm Cl^-, while Haizlip's calculations yield 70 ppm Cl^- (HCl only) and Anderson's calculations yield 1 ppm Cl^- (HCl only) at the same conditions. Diagram 1 compares the vapor phase Cl^- concentrations obtained from modeling to the experimentally measured values at 350°C as a function of liquid phase chloride content.

Another possible mechanism for HCl generation is through the complete evaporation of NaCl solutions at high temperature, as demonstrated by Fournier[16]. D'Amore, et al., has presented several mineral-halite reactions as possible sources of HCl[17]. Given the wide range of geothermal reservoir conditions associated with volatile chloride production, it may be possible that more than one mechanism is responsible for its generation and transport.

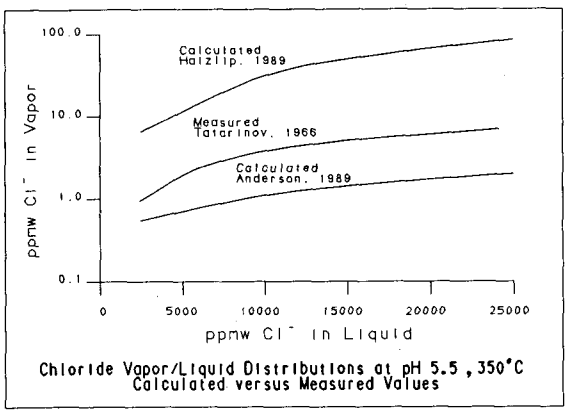

Diagram 1

Chloride Induced Corrosion

Severe corrosion problems in geothermal power systems related to volatile acid-chloride species have been reported worldwide[2,3]. In Larderello, Italy, low ppm levels (1-10 ppm_w) of chloride in steam has resulted in etching of turbine components, mostly at the base of stationary and moving blades in the wet stages of the machines. Severe corrosion of carbon steel steam lines was caused by tens to hundreds of ppm_w vapor phase chloride in contact with condensate.

In Krafla, Iceland, the Well No. 12 produced 20-100 ppm_w chloride in dry superheated steam resulting in corrosion rates over 800 mils/yr for carbon steel. Excessive corrosion of 13% chromium steel turbine blade test coupons exposed to this steam was observed. Severe corrosion and erosion of the first and second stage turbine blades and damage to the main stop valves was revealed upon inspection of the unit and attributed to the steam from Well No. 12.

In conventional steam turbine power plants, chloride-induced stress corrosion cracking is considered to be one of the major problems in turbine reliability[18]. These units operate at much higher inlet pressures and superheat than geothermal units, generating greater stresses on the machines and increasing the likelihood of salt deposition upstream of the Wilson line (condensation zone). Sodium chloride is often found in the turbine deposits of conventional units and linked with stress corrosion cracking. Hydrochloric acid and ammonium chloride have also been identified in these turbine deposits and are considered highly undesirable due to their extreme corrosivity in addition to their tendency to cause stress corrosion cracking[8,9].

The turbines in use at the Cerro Prieto geothermal field (Mexico) are exposed to mechanically-entrained sodium chloride, rather than volatile chloride, and have experienced negligible corrosion[19]. The turbine blade material in use at these units is 12% chromium steel, similar to The Geysers units. The caustic scrubbing process for volatile chloride removal described in this paper generates sodium chloride, which is entrained in the turbine steam at trace levels, but would be expected to have similar turbine impacts as experienced at Cerro Prieto.

Sodium chloride is the primary component dissolved in moderate salinity geothermal brines, which are universally produced through low-carbon steel piping. Corrosion rates in

these systems are typically 1 to 12 mils/yr when the pH is greater than 6 units, the chloride concentration is under 20,000 ppm_w and no oxygen is present[20]. These fluids contain substantial quantities of dissolved silica and often other scale-forming minerals that tend to form stable, protective films on carbon steel surfaces, inhibiting corrosion. The caustic scrubbing process for volatile chloride removal generates similar water chemistry to these geothermal brines, except that scale-forming minerals are absent, requiring higher pH values to limit the corrosion of carbon steel.

Acid-chloride corrosion of carbon steel proceeds by the hydrogen ion reduction reaction:

$$Fe + 2H^{+} \rightarrow Fe^{+2} + H_2$$

Chloride ions do not participate directly in the electrochemical reaction, but play an important role in the corrosion process[21]. Pitting corrosion, which is the primary mode of failure under these conditions, is largely the result of chloride ions which accelerate the localized dissolution of metal by electrically balancing the rapid build-up of positively charged metal ions and increase their solubility through complexation. This process is in contrast to oxygen reduction, in neutral or basic aerated solutions ($2Fe + O_2 + 2 H_2O \rightarrow 2Fe^{+2} + 4OH^{-}$) which generates hydroxide ions that migrate more slowly than chloride to the newly formed metal ions and precipitate metal hydroxides that tend to inhibit further attack. Chloride ions can initiate the corrosion process by breaking down protective magnetite films (Fe_3O_4) that passivate the interior surfaces of carbon steel steam piping. Localized corrosive attack is also enhanced by the migration of chloride ions beneath scale deposits and within crevices, where iron chlorides can hydrolyze, generating HCl ($FeCl_2 + 2H_2O \rightarrow Fe(OH)_2 + 2HCl$). Pitting corrosion is predominant under stagnant or low turbulence flow regimes, such as within the dead-legs of tees, or just inside welded valve ports. At The Geysers, damage can be just as severe in high velocity, turbulent, piping configurations due to the combined effects of corrosion/erosion when entrained particulates, such as exfoliated corrosion products, are present.

Dewpoint Corrosion Phenomenon

Volatile chloride corrosion of geothermal production piping and equipment is analogous in many ways to dewpoint corrosion in fossil fuel power plant flue gas systems. Dewpoint corrosion occurs when a gas is cooled below the saturation temperature relevant to the concentration of a condensable corrosive species contained in the gas. Power plants burning coal containing on average 0.3 wt. % Cl and 1.5 wt. % S will emit flue gas with an HCl concentration of about 200 ppm_v and total sulfur oxide concentration of about 1200 ppm_v[22]. The presence of acid gases in the flue gas stream causes acidic condensate to form at temperatures much higher than the saturation temperatures for pure water vapor. Several "dewpoint temperatures" are associated with these flue gas systems, beginning with the lowest vapor pressure component, H_2SO_4, which typically condenses in the 120 to 150°C range, then HCl condensing at 50 to 60°C and water vapor below 40°C. Upon initial condensation, liquid films contain up to 80% by wt. sulfuric acid, and as temperatures decline, the condensate will contain thousands of ppm_w hydrochloric acid. Corrosion rates of mild steel studied in simple flue gas systems correlate well with the rates of acid deposition, as shown in Diagram 2. Above the acid dewpoint temperature, the corrosion rate is nil, but increases rapidly just below the dewpoint as acid deposits and follows a decrease in the acid deposition rate about 40°C below the dewpoint temperature. This decrease is considered to be due to a lower diffusion rate of acid through the boundary layer as the acid is transformed from a supersaturated vapor to a condensed mist. Corrosion rates increase rapidly again near the water dewpoint temperature as the bulk of the acid dissolves in the condensate. When possible, the primary method of dewpoint corrosion mitigation is to maintain the flue gas temperature above the acid dewpoint temperature. Under these conditions, the corrosion rate of mild steel is negligible.

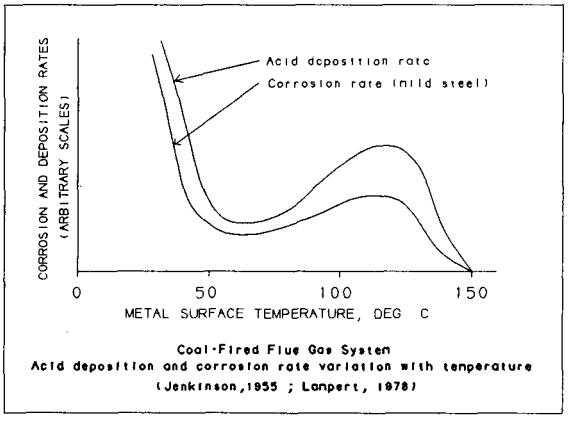

Diagram 2

Most flue gas streams require wet scrubbers for desulfurization, making it impossible to maintain temperatures above the acid-dewpoint. The prime area of corrosion within wet scrubbers is in the hot gas quench zone. At the wet/dry interface, rapid cooling occurs that can induce condensation immediately upstream of the alkaline scrubbing liquor. Solid deposits form downstream of the interface in the wet zone which can also promote localized attack. As the wet/dry interface line shifts with changing load conditions, deposits can trap concentrated acids and shield them from the high-pH scrubbing solution. Under these conditions, the most effective means to combat corrosion is to line the exposed walls with sheets of high alloy material, such as Hastelloy C-276.

Within geothermal well casings and gathering systems, the concept of acid-dewpoint temperature is important whenever volatile chloride is produced in dry steam. Corrosion rates vary dramatically with differences in volatile chloride concentrations and levels of steam superheat, and correlate qualitatively with expected acid deposition rates. Wells producing acid-chloride at The Geysers can be grouped into three general categories on the basis of dewpoint corrosion phenomenon.

1. ***Wells producing steam with high levels of superheat, 30-120°F above the pure water saturation temperature.*** These wells have low general corrosion rates in the well casing, wellhead and surface piping regions, but can cause substantial corrosion in the downstream gathering system as pipeline heat-loss or contact with saturated steam results in acid-dewpoint conditions. These wells are also highly subject to localized corrosion in the near wellhead region at points of conductive heat loss induced by exposed wellhead wing valves, piping tees, pipeline supports, and instrument taps. The highest volatile-chloride producing wells at The Geysers are in this category.

2. ***Wells producing low-superheat (10-20°F) or saturated steam.*** At the same acid-chloride concentration, these wells typically have much higher general corrosion rates than Group 1 wells, since they are normally at or below the acid dewpoint temperature. Temperature profile measurements across a pipe diameter for these wells often indicates a superheated core with near-saturation conditions at the pipe walls. Most corrosion damage is associated with the wellhead and near-wellhead piping, with some downhole problems. These can be the most difficult wells to maintain in production.

3. ***Wells producing significant quantities of water (condensate), with steam qualities of 95 to 99%.*** Corrosion damage for these wells is limited mostly to the well casing, with essentially all the acid-chloride in solution and often completely reacted with iron when it reaches the wellhead. Stoichiometric ratios of iron to chloride frequently approach the 2 to 1 limit, rendering the liquid relatively noncorrosive to surface piping as long as oxygen is excluded. Downhole corrosion is usually severe, resulting in casing perforation and failures. These wells have a limited lifetime if the casing is left unprotected.

It is important to note that individual wells can progress through all three groupings, depending upon production modes (wellhead pressure), changing reservoir conditions and production history (new wells). A Group 1 well can be transformed to a Group 3 well by a downhole problem such as a bridge, causing a reduction in steam flowrate and wellbore condensation. New production wells in high chloride areas can progress steadily from Group 3 to Group 1 conditions as local reservoir liquid is depleted.

In addition to steam superheat conditions, the acid-dewpoint is controlled by the concentrations of volatile electrolytes in the steam. The presence of ammonia can induce the formation of saturated ammonium chloride solutions at temperatures well above the dewpoint of pure steam or steam containing only HCl. Ammonium chloride has a much lower vapor pressure than hydrogen chloride in aqueous solutions, causing this dewpoint elevation. Diagram 3 shows the calculated dewpoint temperature of steam containing 10 ppm_w and 100 ppm_w HCl and a range of ammonia concentrations typical for The Geysers. At 130 psia, a dewpoint temperature of 376°F is possible, 28°F above the 348°F pure water saturation temperature, with original steam phase concentrations of 100 ppm_w HCl and 800 ppm_w NH_3. Just below this dewpoint, the ammonium chloride concentration in liquid films and droplets would be about 7 molal (25% by wt. Cl^-) and have a pH of 3.3 units. At 10 ppm_w HCl and 200 ppm_w NH_3, the dewpoint would be elevated by 10°F and initial liquid pH values would be about 3.5 units (7% by wt. Cl^-). Actual dewpoints could vary depending upon nucleation factors, such as the presence of particulate matter, or localized external heat sinks. Metal ions generated in corrosion processes could cause hysteresis effects, resulting in liquids stable at temperatures above the initial dewpoint due to the formation of highly concentrated non-volatile $FeCl_2$ solutions.

Dewpoint corrosion can be minimized at the wellheads and adjacent surface piping of Group 1 and Group 2 wells by adequate thermal insulation techniques. Wellhead cellars must be free of standing water and the surface casing should be insulated to 10 or 20 feet below grade. Wellhead wing valves must be entirely insulated or eliminated completely from the wellhead configuration. At least 4" thick insulation should be provided on the wellhead tee, and all piping, vessels and blind flanges downstream. Pipeline supports should be insulated from and never welded to the pipeline. Instrument taps should be minimized and thoroughly insulated.

Production modes are also critical in minimizing dewpoint corrosion. Wells should be produced at the lowest wellhead pressure possible to maximize superheat. High chloride wells should only be produced in an on/off mode, either full flow or shut-in, but never under throttled production that might generate dewpoint conditions.

Volatile chloride corrosion at The Geysers is also similar to conventional flue gas dewpoint corrosion with respect to problems within the quench zone of scrubbing equipment. Superheated steam is rapidly brought to saturation near the water/caustic injection point as part of the corrosion mitigation process. Pipe wall temperature gradients can reach 100°F over very short intervals, inducing acid-dewpoint conditions adjacent to the alkaline wet zone. The alkaline wet region may not completely coat the pipe until several feet downstream of injection, and its coverage will vary depending upon superheat, steam velocity, water injection rate and piping/nozzle geometry. Scale deposits can trap acid-chloride beneath as the wet/dry

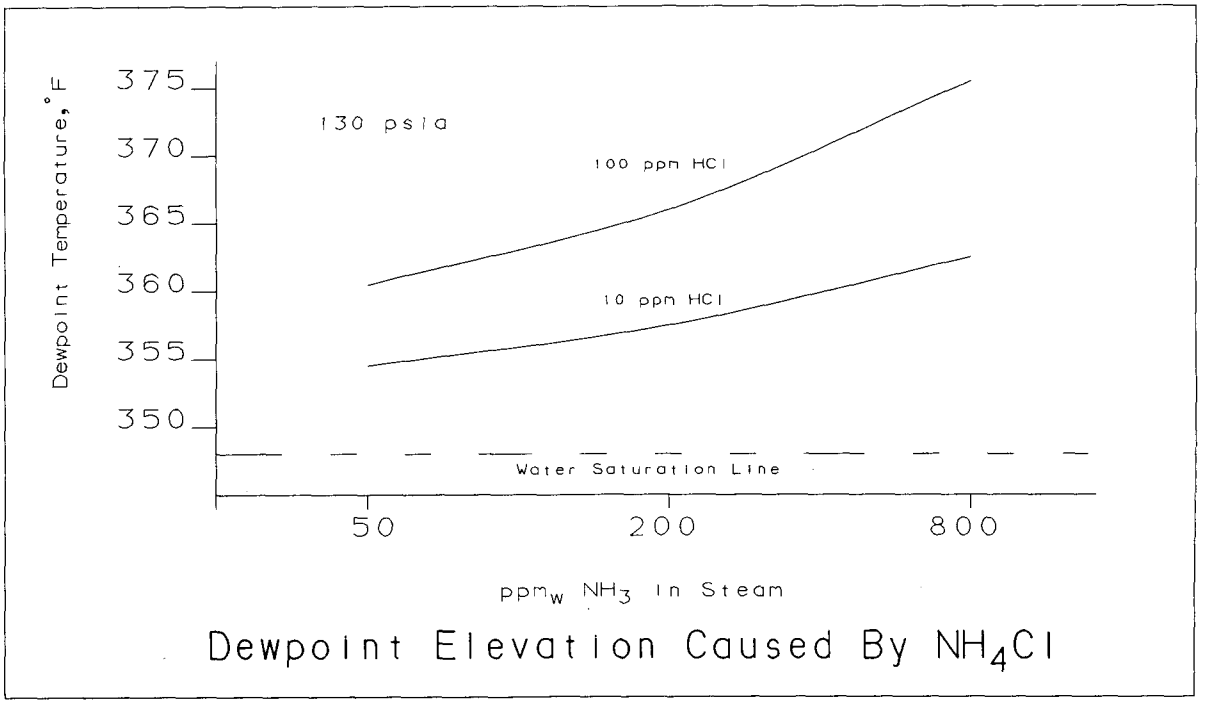

Diagram 3

interface shifts with changing production conditions. Corrosion in this zone is highly localized and can only be effectively eliminated through the use of high-alloy or lined mixing spools.

PROCESS CHEMISTRY

Concentrated solutions of ammonium chloride can deposit on the pipe walls of volatile chloride producing wells at the Geysers resulting in pH values of 3.0 to 3.8 units at 175 to 200°C. The excess of ammonia in Geysers steam is not effective in neutralizing HCl, since ammonia becomes a very weak base at high temperatures, and actually increases the acid dewpoint temperature and acid deposition rate. The basis of the current acid chloride corrosion mitigation process at The Geysers is steam scrubbing and neutralization through the injection of hotwell condensate and sodium hydroxide near the wellhead and subsequent water removal using steam/liquid separators.

Preliminary assessments indicated that the addition of only water to scrub and dilute the acid chloride from Geysers wells would result in unacceptably low pH values for carbon steel piping (pH 4 to 5.5 units at 175°C)[23]. It was obvious that neutralizing amines, commonly used in steam systems to control pH where trace carbonic acid is present, would be costly and ineffective due to the high acidity and relatively large quantities of chloride to neutralize. Chemical modeling has shown that sodium carbonate would be effective in neutralizing the acid chloride, but this chemical would be expensive and difficult to handle due to its availability only as a relatively dilute solution (15% by weight).

Sodium hydroxide was chosen due to its low cost, availability as a concentrated solution (25 - 50% by weight), and the fact that it reacts rapidly with CO_2 under steam line conditions, effectively forming a sodium carbonate solution[23,24], thus minimizing the possibility of free hydroxide entering the turbine and causing caustic embrittlement or cracking.

The hydration of CO_2 proceeds rapidly at Geysers steam-line pressures and temperatures in the presence of free hydroxide, according to the reactions:

$$CO_2 + OH^- \rightarrow HCO_3^-$$
(fast)

$$HCO_3^- + OH^- \rightarrow CO_3^= + H_2O$$
(instantaneous)

Diagram 4 depicts the rate of reaction under typical conditions, indicating that excess hydroxide is rapidly converted to carbonate, while the equilibrium pH stabilizes in the alkaline region. The interaction of CO_2 in the corrosion mitigation process is critical in eliminating potential problems due to caustic corrosion and embrittlement, while CO_2 partial pressures are low enough to maintain alkaline scrubbing conditions.

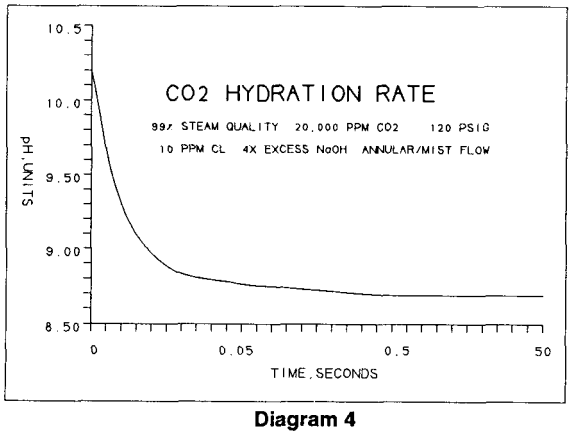

Diagram 4

Boric acid is another natural component of Geysers steam that is a significant pH buffer in the corrosion mitigation process, although unlike CO_2, boric acid does not benefit the process chemistry. The presence of boric acid requires excess caustic injection to maintain the scrub-water pH above 7.8 units due to the boric acid pka of about 9.0 at the process temperature. This effect is most obvious in lower chloride wells (<10 ppm_w) where boron to chloride ratios can be very high, requiring over 8 moles of NaOH per mole HCl to maintain the pH above 8.0 units.

The ideal pH range of the process water has been determined to be 8.0 to 8.5 units (at process temperature), based on extensive corrosion rate tests utilizing corrosimeter probes during system operation at varying caustic injection rates. As shown in Diagram 5, boric acid is the primary pH controlling species in this pH range under typical Geysers conditions. A NaOH/HCl mole ratio of over 8 to 1 would be required for steam containing 100 ppm boron to achieve a pH of 8.25 units under the conditions shown, and a NaOH/HCl ratio under 2 to 1 would be required if no boron was present. Hydrogen sulfide only affects the pH above 8.25 units and therefore is not a factor when maintaining the process at this pH value. Ammonia has no effect above 8.0 units, but is important in the low pH range. Under the conditions shown in Diagram 5, steam containing 50 ppm boron yields a process water pH of 6.5 units at a NaOH/HCl ratio of 1, however, this pH would drop to 4.8 units if ammonia was absent. Carbon dioxide is a major pH buffering component of Geysers steam, although in a typical concentration range of 2,000 to 20,000 ppm_w, the pH values shown in Diagram 5 differ by no more than 0.2 units at NaOH/HCl ratios above 2.

In order to validate the pH and electrolyte equilibria computer modeling used to study the corrosion mitigation process chemistry, direct comparisons are routinely made between model predicted chemistry and analytically measured values. The model incorporates the effects of HCl, NH_3, NaOH, H_3BO_3, H_2S and H_2CO_3 electrolyte equilibria in addition to vapor/liquid partitioning and CO_2 hydration kinetics.

Analytically determined values for the vapor and liquid phase species in the separators, including total water mass and enthalpy, are input to the model which computes high-temperature pH, electrolyte dissociations and vapor/liquid distributions. Comparison of the calculated concentrations for dissolved electrolytes such as H_2S and NH_3 to measured concentrations indicates that the model adequately describes the chemistry, since the distributions of these species are very sensitive to pH conditions. Table 1 summarizes the model validation data over a wide range of steam qualities and NaOH to chloride ratios from previously published data for the Aidlin project.

As expected, the high temperature pH values are consistently lower than the measured values at 20°C due to the increasing acidity of water and other weak electrolytes with temperature. This effect is most pronounced at pH values above 8 units, as hydrogen ions become very scarce.

The fact that the computed versus measured concentrations of volatile electrolytes in the separator water (Table 1) are in substantial agreement also demonstrates that the vapor/liquid chemistry was essentially in equilibrium for these tests. Although CO_2 absorption and hydration is the slowest of the vapor/liquid reactions, this species was also determined to be in equilibrium by varying the modeled reaction time from 2 seconds (actual) to 60 seconds. Complete CO_2 hydration occurs within about 0.5 seconds under the conditions studied. Evaluation of the vapor/liquid equilibrium for these gases provides an important tool in accessing the overall mass transfer efficiency of a corrosion mitigation scrubbing system. Scale deposition within corrosion mitigation systems can be a problem if the residual water fraction after injection is too low. Sodium borate is the least soluble product

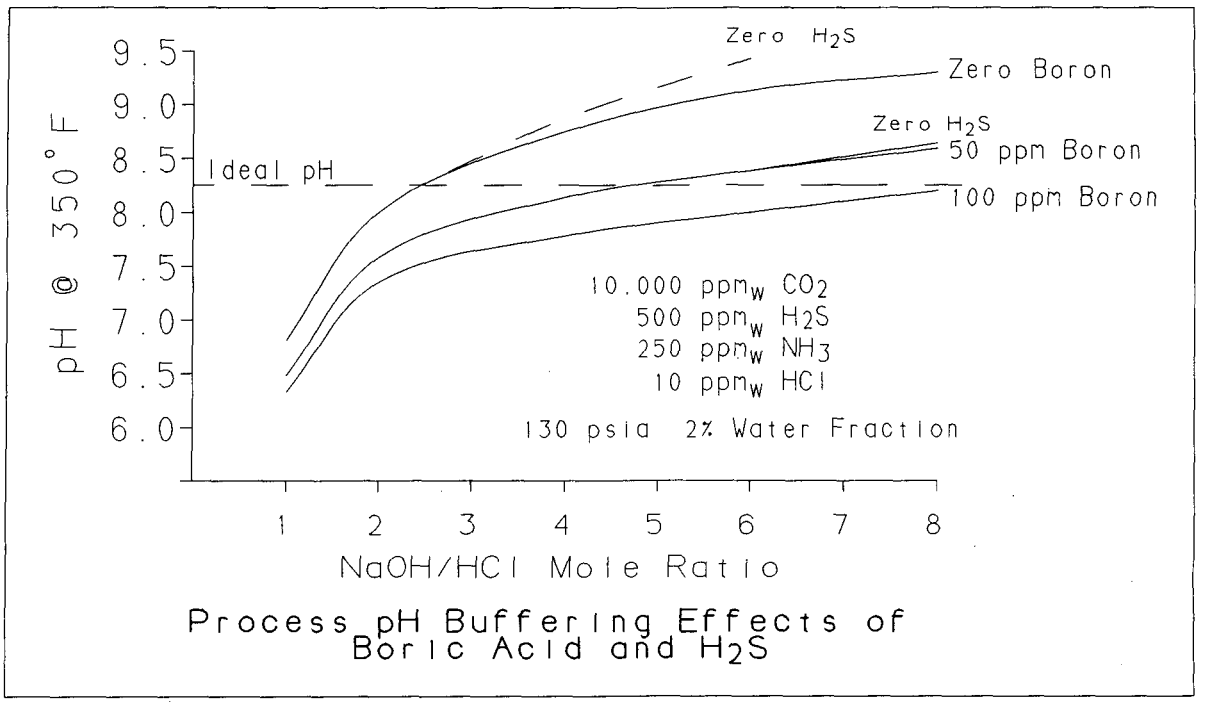

Diagram 5

of the process, and has been known to deposit in separators and plug water drain lines when residual water fractions drop below 0.5%. Under most conditions at The Geysers, the solubility limit of sodium borate is not exceeded if water fractions are maintained in the 1-2% range. Iron sulfide is a common scale deposit for Group 3 wells that produce substantial quantities of dissolved iron which can plug rock-trap strainers and separator baffles as dissolved iron contacts the alkaline scrubbing solution. The use of untreated surface or ground water for injection results in calcium carbonate scaling of injection nozzles and mixing spools due to the calcium content of these waters, the high process temperature and high carbonate concentrations. Hotwell condensate is currently used exclusively as the source of injection water due to the low concentrations of dissolved minerals and oxygen.

MECHANICAL CONSIDERATIONS

The selection of water/caustic injection points for a Geysers well depends on the type of well (i.e., Group 1, 2, or 3) and the existing wellhead/piping configuration. For a Group 1 well that can be maintained sufficiently above the acid-dewpoint temperature at the wellhead, injection can be performed immediately downstream of the rock catcher, as shown in Diagram 6 (point A). Unless the injection spool is protected through the use of high alloy materials, corrosion induced by desuperheating near the alkaline wet region is highly possible for Group 1 wells. For this reason, injection should not occur further upstream where repairs and well isolation may be more difficult.

Group 2 wells produced under near-saturated conditions are best protected by injection through a 3-inch wing valve (Point B) or at the wellhead tee (Point C). Increased corrosion induced upstream of injection is not a significant problem for these wells since dewpoint conditions already exist, making it important to protect as much of the wellhead as possible. Injection at these points will flood the rock catcher leg, which should be blown-down periodically to prevent build-up of excessive salt concentrations, but not automatically or continuously which would prematurely remove the scrubbing water.

Wells in the Group 3 category can be treated as Group 2 wells if the casing is protected with coated, high alloy or "sacrificial" liners. If downhole protection does not exist, these wells should be treated using downhole injection techniques. Tubing of adequate diameter for the water injection requirements can be lowered downhole through a 45° to 60° angle 3-inch wing valve and lubricator assembly, similar to downhole calcite scale inhibitor injection applications (point D)[25]. The injection depth will depend upon the amount of casing considered critical to protect and the mechanical integrity of the injection tubing string. A restrictor at the end of

Table 1. Computer Model Validation Data

Well	Steam Quality	NaOH/Cl Mole Ratio	Computed, ppm_w			Measured, ppm_w				
			pH[1]	H_2S	NH_3	pH[2]	H_2S	NH_3	Cl	B
AD40	98.2	1.2	7.29	57	105	7.30	60	116	2080	2150
AD40	98.1	1.9	8.02	205	99.3	8.10	187	103	2520	2620
AD10	98.1	5.8	8.09	92.2	41.0	8.20	103	41.0	201	1520
AD20	94.8	120	8.46	150	45.3	8.80	159	47.5	7.7	301

1. pH units at process temperature (175-200°C).
2. pH units at 20°C.

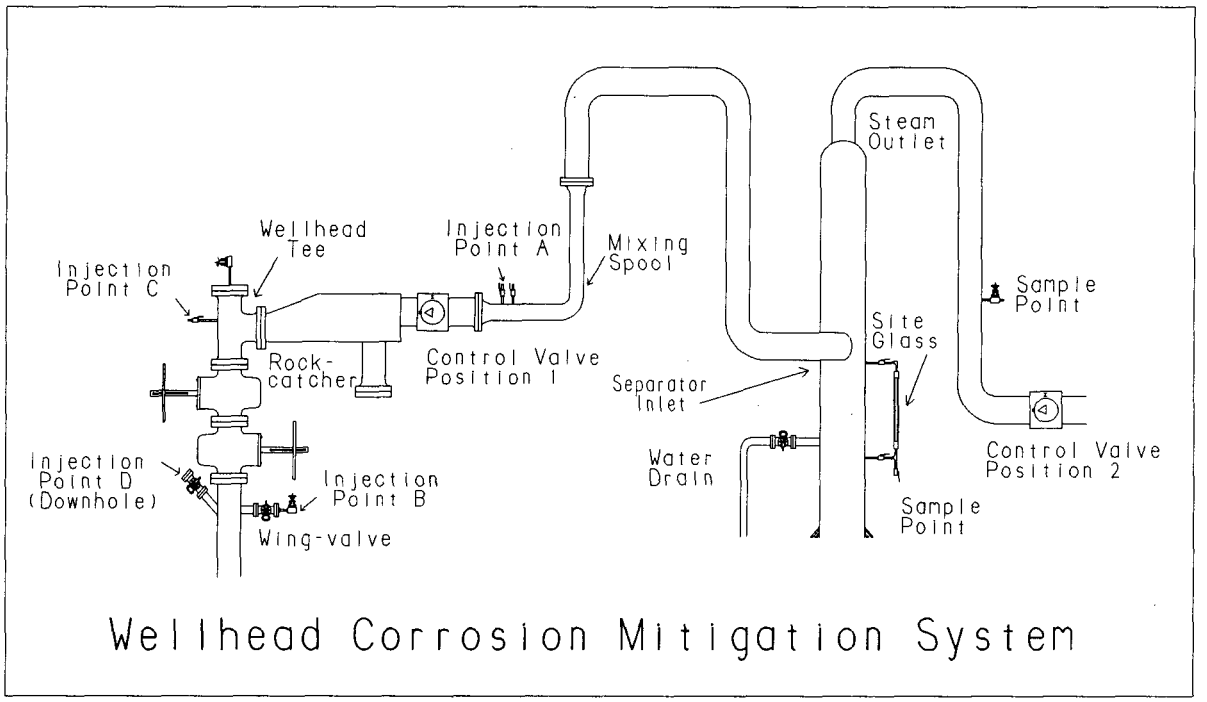

Diagram 6

the tubing must be sized to maintain adequate backpressure and prevent boiling of the injection fluid given the injection water rate, wellhead pressure, and injection depth. Alloy tubing is recommended for this service due to the injection mixture composition and temperature.

At surface injection points, retractable injection probes should be utilized in conjunction with spray nozzles. This enables servicing of the nozzles during production and adjustment of the nozzle tip position in the flow stream. Nozzles should be sized for maximum pressure drop to increase the spray penetration into the steam flow. Multiple probes placed around the circumference of an injection spool and spaced 1 to 2 feet apart on the axis may also improve contacting. However, inspection of injection spools after service indicates that the spray patterns from nozzles degrade rapidly in the steam flow, leaving fan-shaped water marks expanding axially downstream from the nozzle tips.

Mixing spools located immediately downstream from the injection point provide most of the vapor/liquid contacting. These spools are simply smaller diameter piping sections without internal components. This section of pipe can be incorporated with the injection spool (point A) and/or extend up the vertical riser section of an expansion loop. Optimal mass transfer occurs under high velocity annular/mist flow regimes where the pipe behaves as a wetted-wall absorber. Extensive studies of H_2S mass transfer from steam into caustic solutions under similar conditions at The Geysers has shown that the highest efficiencies are obtained at steam velocities of 300-500 ft/sec[24]. The high velocity mixing sections can vary in length from 10 to 20 feet.

As shown in Diagram 6, steam/water separators are best located after an expansion loop to maximize vapor/liquid contacting time. The highest separation efficiencies are achieved with the vertical recycling separators common to The Geysers. Horizontal style separators are typically less efficient, but are much less costly to install into existing wellpad piping systems. Horizontal separators are more easily fouled by particulates and scale deposits which can degrade their performance dramatically. This can be a problem with Group 3 wells producing dissolved iron and particulate corrosion products which form deposits upon contact with the alkaline scrubbing solution.

The flow control valve for a well can be placed immediately after the rock catcher or downstream from the separator, as shown in Diagram 6 (Positions 1 and 2). If located in the latter position, steam scrubbing and separation pressures would be equivalent to wellhead pressure rather than line pressure. Under these conditions, less injection water is required to achieve the same steam moisture content for scrubbing. Given a 70 psig pressure drop across the control valve, about 20% less water would be required for a typical well. This factor can be important in certain areas of The Geysers where limited hotwell condensate is available for injection. Water separation upstream of the control valve also results in superheated steam entering the gathering system which can minimize condensation and corrosion rates.

The gathering system can also play an important role in steam purification. Entrained water from separators and condensate enriched in impurities can be effectively removed through multiple stages of drop-pots spaced throughout the gathering system. These drop-pots must have properly operating automatic drain valves to be of any use, however. In addition, manual dumping of the drop-pot contents periodically helps prevent the build-up of excessive salt concentrations and solids.

The final stage of steam purification before entry to the turbine occurs at the "desuperheating" system upstream of the plant inlet. Hotwell condensate is injected through multiple sets of spray nozzles into the main steam line upstream of a steam/water separator. The steam is desuperheated and brought to approximately 0.5 to 2% moisture content. Injection nozzles are often placed in the vertical riser to a separator which provides minimal contact time but reasonable chloride removal. Mass transfer efficiencies can be improved by injecting further upstream of the separator or through the use of a steam venturi mixing device[26]. A two-stage scrubbing process with two vertical separators in series was employed at the Aidlin project to maximize turbine steam purity. Vertical

recycling separators are normally used at the plant inlets for high moisture removal efficiencies. Under optimum conditions, desuperheating systems at The Geysers can remove over 95% of the residual chloride from the main steam.

MONITORING TECHNIQUES

Chloride Survey Techniques

The identification of acid-chloride producing wells requires specialized sampling and analysis techniques. Steam field surveys to locate these wells are critical in that corrective action must be taken before costly well casing, pipeline and power plant damage or field accidents occur. Accurate wellhead temperature and pressure measurements during sampling and information regarding water production are required to initially classify a well in the Group 1, 2 or 3 category.

Most of the acid-chloride produced by Group 3 wells is in the liquid phase and significant amounts produced by Group 2 wells can be associated with concentrated liquid films and droplets, making representative sampling extremely difficult. A Group 3 well typically produces measurable quantities of liquid which can be collected from an in-line separator, if present. Measurements of chloride concentrations in the separator water and separator outlet steam in conjunction with the respective flowrates can be used to calculate total flow chloride concentrations for such wells.

Group 2 wells producing less than 100% steam quality should be sampled using isokinetic probe techniques as close to the wellhead as possible. The 3-inch wing valves below the wellhead master valves (Diagram 6) provide an ideal isokinetic probe sampling location. Through the use of an isokinetic sample nozzle that extracts steam at the same velocity as the bulk flow at several points across the pipe diameter, representative samples of vapor and liquid droplets can be collected, as depicted in Diagram 7. Major flow disturbances such as bends in piping should be limited to 8 pipe diameters upstream and 2 pipe diameters downstream of the sample point. Sample nozzles are sized for the steam velocity expected and isokinetic sample rates are based on the formula:

R = (An/Ap) (7.57) Qs
R = Sample rate, g/min steam condensate
An = Cross sectional area of nozzle face
Ap = Cross-sectional area of pipe
Qs = Steam flowrate, lbs/hr

Adjustments can be made for reduced velocities near pipe walls due to friction factors in turbulent flow conditions[27].

Group 1 and Group 2 wells above the acid dewpoint at the wellhead can be accurately sampled with a non-isokinetic probe technique since all the acid chloride is in the vapor phase. Sampling should be performed upstream of the rock catcher which may contain liquid, either at the wellhead tee or 3-inch wing valve, as shown in Diagram 6. Probe tip geometry and sample rate are not important when sampling gaseous species, although a probe is critical in eliminating condensation loss which occurs when sampling directly from large side-wall mounted valves. Sampling directly from the 3-inch wellhead wing valve of a superheated well can result in chloride measurements less than 50% of actual total flow concentrations. However, if a 1-inch bleed flow is maintained through the wing valve for an hour or more, chloride concentrations typically approach the total flow value for Group 1 wells.

Steam samples collected by the various methods are condensed directly in a stainless steel tubing condenser immersed in an ice bath or circulating cooling fluid. Condensate samples are often analyzed for sodium and other alkali and alkaline earth metals to verify the chloride measured is volatile chloride and not associated with water entries to the wellbore. Measurements of condensate pH are of little value at The Geysers in interpreting the chloride chemistry since the excess ammonia neutralizes HCl at ambient temperature and the pH is controlled primarily by CO_2 and H_2S partial pressures. This is demonstrated by the fact that a typical wellhead steam pH at The Geysers is 5.5 units after condensation at atmospheric pressure, and over 9.0 units when condensed under vacuum in a power plant, regardless of chloride content.

Qualitative chloride surveys can be conducted by sampling liquid accumulated in production well separators or drop-pots

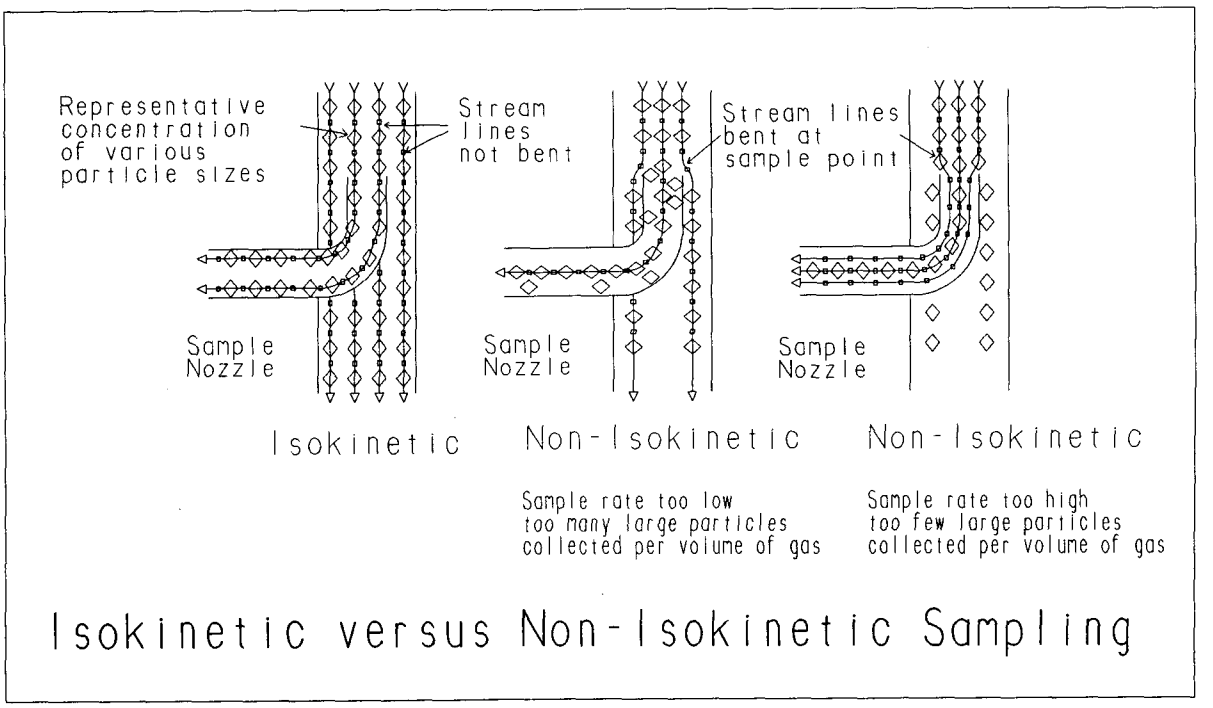

Diagram 7

that have been blown dry 6-24 hours before testing. Chloride concentrations over 10 ppm usually indicate a significant acid chloride producing well if sodium, potassium and calcium are absent. The analysis of these liquids for dissolved iron and manganese provides insight into active corrosion processes. Dissolved manganese to iron ratios are often in the same range as reported for carbon steel casing and pipe (0.5 - 1.5%). Samples for these metals must be passed through an in-line filter upstream of the condenser and collected in nitric acid to eliminate solids and prevent precipitation before analysis. Measurements of pH must be performed in the field since the oxidation of dissolved iron in samples exposed to air can drastically lower the pH. Ammonia measurements are useful in estimating the high temperature pH of these liquids due to the inverse relationship of water phase ammonia concentration and pH in vapor/liquid systems. Boron concentrations can be used to ascertain the extent of vapor/liquid equilibrium based on known boric acid distribution coefficients. The above assays are also important in characterizing Group 3 wells where corrosion processes are dominated by the water phase chemistry.

Corrosion Mitigation System Monitoring

The initial start-up of a corrosion mitigation station requires sampling and analysis of the injection water/caustic mixture, separator water and separator outlet steam in order to adjust and optimize the process chemistry. Regular, less extensive monitoring is required to maintain the chemical parameters in the proper range and to verify efficient equipment operation. Process flowrates, temperature and pressure data must be obtained concurrently during sampling to perform a complete mass and heat balance evaluation. Many of these measurements must be performed directly in the field or based on chemical mass balances due to the unreliability of distributed control system (DCS) instrumentation at The Geysers.

Injection fluid samples are collected downstream of the caustic pump, before the injection nozzles, by slowly filling a 1 liter plastic bottle using a needle valve for flow regulation. The sample should be integrated over a 5 minute interval in order to average concentration surges caused by pulse-type metering pumps. This injection mixture is analyzed for sodium to verify the water injection rate based on caustic dilution and for chloride which should be accounted for as a contaminant of the sodium hydroxide solution. The injection mixture temperature must be measured for heat balance calculations. Before or after sampling the injection fluid, precise caustic injection rates are measured using a calibrated volumetric draw-down tube on the suction of the caustic pump. The caustic feed solution is also sampled to verify the exact concentration by density or sodium measurement if not previously determined.

Separator water samples are collected from the separator drain piping or liquid-level sight glass connection. Samples for iron and manganese analysis are usually collected unfiltered and treated with nitric acid for preservation. Dissolved iron and manganese produced by a well through corrosion processes precipitates as sulfides upon contact with the alkaline scrubbing solution injected into the well, making it necessary to perform a total metals analysis to account for these species. Untreated samples are collected for Cl, Na, B and pH analysis which provides the primary chemical data needed for process evaluation and adjustment.

Samples for total inorganic carbon (CO_2) and NH_3 are collected in gas-tight glass vials and H_2S samples are collected in a cadmium chloride preservative solution. These species are important when modeling the high temperature pH and extent of gas/liquid equilibrium.

The volumetric flowrate of water into the separator is measured by timing the rate of water level rise observed at the sight glass after the separator discharge has been isolated. The separation pressure can be assumed to be equivalent to the outlet steam line pressure and used to estimate the separator temperature.

Separator outlet steam samples must be collected using an isokinetic probe, usually at the vertical down-leg of the steam piping (Diagram 6). Steam condensate samples are collected at four to five points across the pipe diameter to obtain an accurate moisture profile. In cases of substantial liquid entrainment (>0.5% outlet moisture), up to 10 points may be required. Samples are collected for sodium and chloride analysis to determine the outlet steam quality, liquid entrained chloride concentrations and residual volatile chloride concentrations for separator efficiency and mass transfer evaluations. Steam samples may also be collected for boron, silica and iron analyses to determine levels of these impurities and for gas analyses to perform pH and vapor/liquid equilibrium modeling. Temperature measurement profiles can be performed using a probe at the same sample port to evaluate thermal equilibrium conditions.

Samples for direct total flow chloride determinations can be collected at the wellhead in cases where the water/caustic is injected downstream of the rock catcher, provided the temperature is above the acid dewpoint. Wellhead superheat measurements can also be determined under these conditions as a verification of heat/mass balance calculated enthalpies. These methods would be the same as described previously for chloride survey techniques.

Gathering system drop-pots downstream from a corrosion mitigation system separator are often monitored to qualitatively evaluate liquid entrained and vaporous carry-over. Ratios of sodium to chloride provide an indication of residual vapor phase chloride if these ratios decline at increasing distances from a well separator. In some cases, the total salt concentration in drop-pots increase further from the well separator when pipeline superheat levels are high and drop-pots are not draining properly. Other sampling and interpretive techniques for drop-pot fluids would be the same as described for chloride survey testing.

Analytical Methodologies

Trace level chloride analysis of geothermal steam condensate is plagued by interferences from dissolved gases such as hydrogen sulfide, ammonia and carbon dioxide. Complete removal of H_2S is required before direct potentiometric ion-specific electrode measurements can be performed due to the positive response of sulfide ions. These measurements are usually only valid to about 1 ppm Cl^- unless the sample is preconcentrated. Precipitation titrations using silver or lead also require elimination of sulfide and most of the ammonia which complexes the metal ions and obscures the end-point. These titrations are accurate to about 10 ppm Cl^- if the samples are pretreated properly. Conventional water-analysis ion-chromatography methods are overwhelmed by high concentrations of sulfide, ammonium and bicarbonate ions. These species overload separation columns and conductivity detectors and make it impossible to concentrate samples by ion-exchange methods. The current method used to achieve high accuracy, low-level detection of chloride in this matrix is by high resolution gradient ion chromatography in conjunction with conventional chemical suppression and detection by digital conductivity measurement (Dionex 4500i system). This method provides detection limits to 0.010 ppm_w with minimal interference problems.

Trace level sodium analyses in steam condensate are performed by flame atomic absorption spectroscopy with detection limits down to 0.002 ppm_w. The main difficulty in this procedure is preventing sodium contamination. Iron concentrations in steam condensate are determined by graphite furnace atomic absorption to detection limits of 0.005 ppm_w. Boron analyses are performed by inductively coupled emission spectroscopy (ICP) or azomethine colorimetry. Ammonia is

routinely determined by a flow injection analysis procedure involving gas diffusion across a Teflon membrane with conductivity detection, allowing direct analysis without pretreatment to remove sulfide. Determinations of pH are performed in the field using a Ross pH electrode to minimize sulfide interferences and a temperature compensation probe.

Mass and Heat Balance Calculations

Values for wellhead enthalpy, steam and water fractions in the scrubbing process, caustic and chloride mass flow rates and residual separator steam impurities are necessary for the optimization and routine operation of the corrosion mitigation process. Many of these parameters cannot be measured directly, and due to problems in instrumentation and variations in system designs, few are consistently available. Table 2 summarizes the process parameters that are measured or calculated and the relevant mass and heat balance equations used by a computer program configured for this application. Since many parameters can be obtained through more than one type of measurement or calculation, this computer mathematical modeling program is used with iterative and back-solving capabilities to achieve complete mass and heat balances with various types of input data. Table 2 includes typical input data and calculated results for a corrosion mitigation system mass and heat balance.

Water injection rates are often calculated or at least verified based on the caustic pump rate and sodium concentration in the injection water. The water mass flowrate after injection (residual water) is normally based on the change in sodium concentration due to the flashing of injection water or condensation of steam. Wellhead enthalpy can then be calculated through heat and mass balance equations using the injection water temperature, mass flowrate of water before and after injection, the separator pressure and steam outlet flowrate. This information is necessary to determine the separator inlet moisture fraction and to calculate the required injection water rate when adjusting this moisture fraction.

The residual water flowrate is also used to calculate the total mass flow of chloride in conjunction with the separator water chloride concentration. The separator fill rate is measured when possible and compared with the residual water flowrate based on the sodium balance calculations. The difference between these two rates can be used to estimate liquid entrainment in the separator outlet steam in cases of excessive separator water carryover. Total flow chloride mass flowrates based on the residual water flowrate and chloride concentration are unaffected by separator efficiency, but are normally adjusted for mass transfer efficiency.

Isokinetic sampling of the separator outlet steam is performed to obtain concentrations of sodium and chloride used to determine entrained liquid and residual volatile chloride levels, which are the basis of separator efficiency and mass transfer efficiency calculations. Sodium measured in the separator steam is assumed to be present entirely in entrained droplets of separator water, which has a directly measurable sodium concentration. Based on the simple mass balance calculation (Table 2), the moisture content of the separator steam can be determined. The ratio of sodium to chloride concentration in these droplets is assumed to be equivalent to the sodium/chloride ratio in the separator water. Liquid entrained chloride concentrations in the separator steam are then based on the steam phase sodium concentration and sodium to chloride ratio. The difference between the total measured chloride concentration in the separator steam and the calculated liquid-entrained chloride concentration is the result of residual volatile chloride not absorbed in the scrubbing process. A typical separator outlet steam sodium and chloride concentration profile is shown in Diagram 8. Moisture concentrations are normally higher near the pipe walls as indicated by the sodium levels, and decline toward the pipe center where much of the chloride may still be in the volatile form.

A primary use of the completed heat and mass balance for a corrosion mitigation system is to simultaneously optimize the separator efficiency and mass transfer efficiency. The steam quality, in terms of moisture content, at a separator outlet improves non-linearly as inlet water fractions are reduced. However, reducing the inlet water fraction raises the dissolved sodium and chloride concentrations in direct proportion which can result in greater mass flowrates of liquid entrained impurities even though outlet moisture levels are lower. Mass

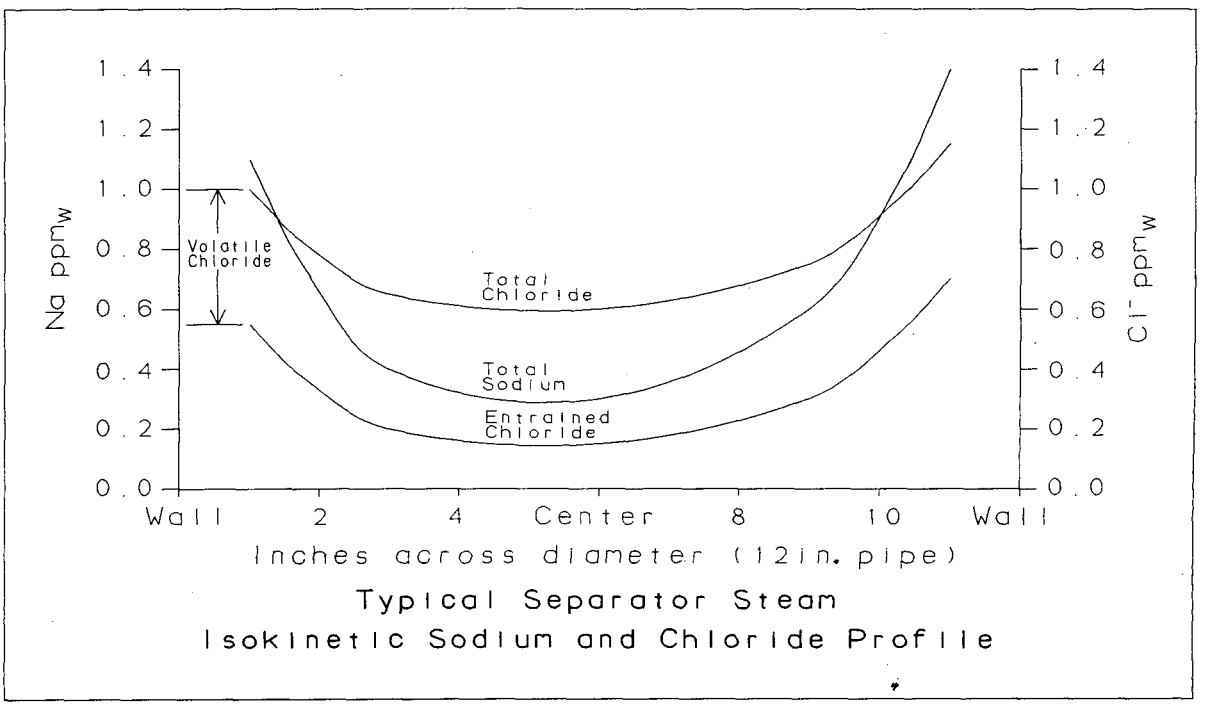

Diagram 8

Table 2

Variables

Input	Name	Output	Unit	Comments
146	P		psig	Separation pressure
	T	363.34859	F	Separation temperature
	HF	335.89539	BTU/lb	Water enthalpy
	HG	1195.95	BTU/lb	Sat. steam enthalpy
85	TW		F	Injection water temperature
	FW	3419.0599	lb/hr	Injection water mass rate
	FGI	71406.182	lb/hr	Steam mass rate initial
	HGI	1227.4841	BTU/lb	Steam enthalpy initial
72900	FGF		lb/hr	Steam mass rate final
	FFF	1925.2414	lb/hr	Water mass rate final
13.5	BARO		psia	Barometric pressure
	GFRAC	97.427016		Steam fraction
	FFRAC	2.5729839		Water fraction
2.91	DR		in/min	NaOH drawdown rate
	NGPH	1.5008587	gph	NaOH injection volumetric rate
	NMR	4.9888543	lb/hr	NaOH mass rate
	NACONC	1489.9904	ppmw	Na conc. separator water
839	NAW		ppmw	Na conc. injection water
	CLR	1.2379302	lb/hr	Chloride mass rate
643	CLCONC		ppmw	Cl conc. separator water
	NACL	3.5262468		Na/Cl mole ratio
	CLTOT	17.336458	ppmw	Cl conc. in total flow
.35	NASS		ppmw	NA conc. in separator steam
.29	CLSS		ppmw	Cl conc. in separator steam
	ENTCL	.01101091	lb/hr	Entrained Cl in separator steam
	VOLCL	.01013009	lb/hr	Volatile Cl in separator steam
	SQUAL	99.97651	%	Separator steam quality
	MTE	99.181691	%	Mass transfer efficiency
	TRE	98.29223	%	Total Cl removal efficiency

Equations

Equation	Comments
PA=TVP(T)	Steam saturation pressure function
T=PVT(PA)	Steam saturation temperature function
HF=PVH_F(PA)	Water enthalpy function
HG=PVH_FG(PA)	Steam enthalpy function
HFG=PVH_G(PA)	Latent heat function
VF=PVV_F(PA)	Steam volume function
PA+P+BARO	Absolute pressure
PW=TVP(TW)	Injection water saturation pressure
TW=PVT(PW)	Injection water saturation temperature
VFW=PVV_F(PW)	Injection water volume function
HFW=PVH_F(PW)	Injection water enthalpy function
FGF=((HGI*FHI)+(HFW*FW)-(FGI+FW)*HF)/(HG-HF)	Enthalpy/mass balance
FFF=(FGI+FW)-FGF	Mass balance
GFRAC=FGF/(FGF+FFF)*100	Steam fraction
FFRAC=(100-GFRAC)	Water fraction
GPMSEP=FFF*VF*7.48/60	Separator water volumetric flow
NAOHR=DR*32.54	NaOH volumetric rate
NGPH=NAOHR*.01585	NaOH volumetric rate
NMR=NGPH*3.324	NaOH mass rate
NACONC=(NMR/FFF)*10^6*23/40	Na mass balance separator water
NAW=(NMR/FW)*10^6*23/40	Na mass balance injection water
CLR=(CLCONC*FFF)/10^6	Total mass flow Cl
NACL+(NMR/CLR)*35/40	Na/Cl mole ratio
CLTOT=(CLR/FGI)*10^6	Total flow Cl concentration
ENTCL=(NASS/NACL)*35/23*FGF/10^6	Entrained Cl separator steam
VOLCL=(CLSS*FGF/10^6)-ENTCL	Volatile Cl separator steam
SQUAL=(1-NASS/NACONC)*100	Separator steam quality
MTE=(1-VOLCL/CLR)*100	Mass transfer efficiency
TRE=(1-(ENTCL+VOLCL)/CLR)*100	Total removal efficiency

transfer of volatile chloride to the liquid phase also degrades with decreasing inlet water fractions, generating higher concentrations of vapor phase chloride in the separator steam. By properly evaluating this process and adjusting the water injection rate, both liquid and vapor-phase impurities exiting the separator can be minimized. Diagram 9 displays these process relationships as a function of separator inlet water fraction for a typical corrosion mitigation system. As shown, both entrained sodium chloride and residual volatile chloride can usually be minimized at separator inlet moisture levels of about 2%. These curves will shift depending upon the specific separator configuration used and inlet flowrates, making it necessary to test each system for precise optimization.

Corrosion Rate Measurements

The process chemistry of the corrosion mitigation system has been largely optimized through the use of electrical resistance corrosion probes. These instruments provide a measurement of corrosion rate as the cross-sectional area of an exposed steel surface is reduced by corrosion, resulting in an electrical resistivity change across the element relative to a shielded reference element at the same temperature. Incremental changes in electrical resistivity are directly proportional to the rate of metal loss, allowing corrosion rate measurements over fairly short intervals (hours to days). Continuous data collection via transmission directly to computers can be used to provide nearly real-time trends in corrosion rates. Corrosion probes placed in the two-phase region of a corrosion mitigation system have enabled the optimization of process water pH and salt content by monitoring relative changes in corrosion rates as water and caustic injection rates are adjusted. Corrosion probes are also placed downstream of separators to monitor the effects of residual volatile and entrained chloride on the gathering system and upstream of injection when possible to evaluate acid dewpoint corrosion.

Both cylindrical "finger" probes and flat flush mount probes have been used successfully at The Geysers. The cylindrical probes are extremely durable due to their welded construction, but flush-mount probes probably generate more realistic corrosion data for pipewalls under dewpoint and two-phase flow conditions. High temperature probes must be specified, and in the case of the flush mount probes, special high temperature epoxy is required in construction. The primary limitation in these devices is that general and pitting corrosion cannot be differentiated, rendering the results generated in terms of mils/year metal loss only qualitative under most conditions at The Geysers.

Ultrasonic thickness testing is routinely performed as a direct measurement of corrosion damage to piping systems. Ultrasonic thickness instruments measure the elapsed time required for sound waves to pass through and reflect back from a pipe wall. Calibration is performed using specimens of the material to be tested in a range of known thicknesses. Corrections for changes in sound velocity through the material as a function of temperature are made. Also, high-temperature probes must be used for steam piping measurements. This testing is critical to determine if piping can be safely kept in service and to locate spots of localized corrosion damage requiring repair. Measurements are made over a grid pattern across areas suspected to be damaged or known to be prone to localized corrosion. Regular monitoring of the same locations can provide a direct indication of corrosion rates. The limitation in this method is also the fact that most corrosion due to acid chloride is highly localized, making it difficult to pinpoint damage over large areas of pipe.

CONCLUSIONS

Volatile chloride produced in superheated steam from certain areas at The Geysers can deposit in piping at temperatures well above the steam saturation temperature through the formation of concentrated ammonium chloride solutions, a process known as acid dewpoint corrosion. Wells producing acid-chloride at The Geysers can be classified into three general groups based on acid dewpoint phenomenon: *high superheat, low superheat or saturated and low steam quality wells.* These categories represent distinctly different corrosion processes and require specialized treatment to effectively control corrosion. The pH of acid-chloride liquids in steam lines can be as low as 3.0 units, even with excess ammonia present, which causes rapid localized corrosion of carbon steel through the destabilization of protective magnetite films and

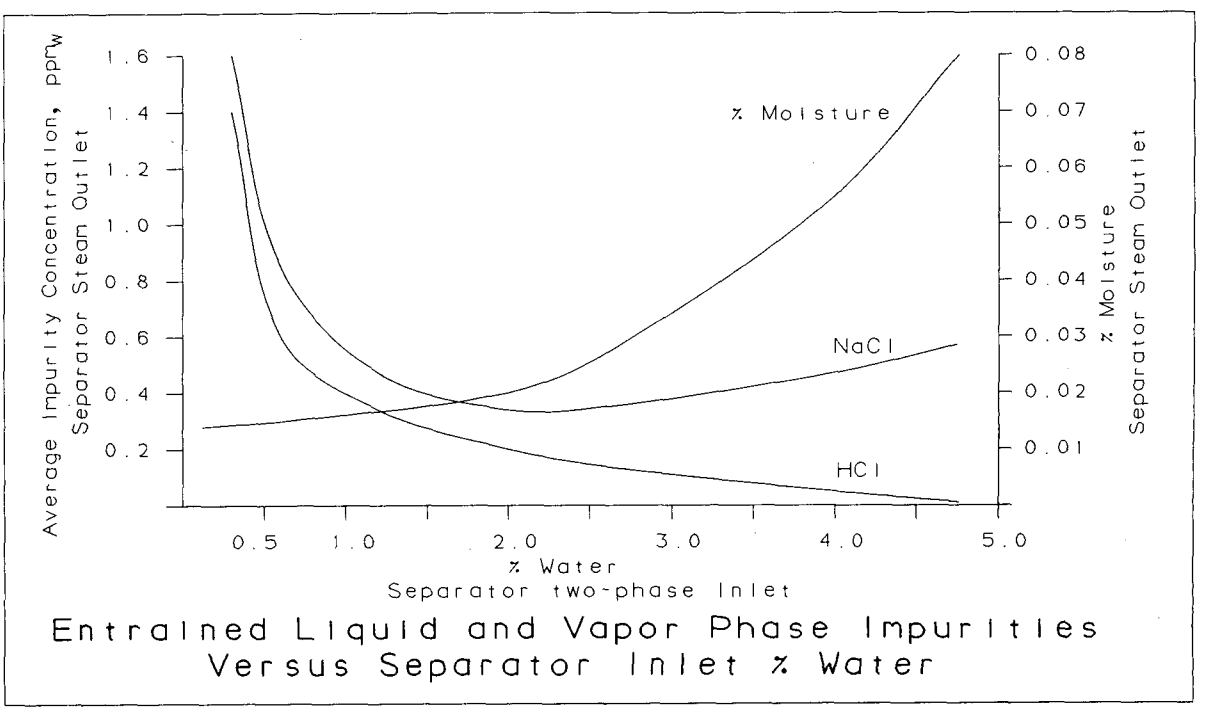

Diagram 9

hydrogen ion reduction. This corrosion process has caused extensive damage to well casing, pipelines and possibly steam turbines at The Geysers. However, corrosion can be mitigated by the injection of water and caustic near the wellhead of acid-chloride-producing wells, or downhole, with subsequent liquid removal using steam/water separators.

Process parameters have been defined to minimize corrosion rates and residual steam-phase impurities, resulting in corrosion rates of less than 10 mil/yr and turbine steam purities well below 50 ppb chloride. Carbon dioxide in Geysers steam benefits the process by neutralizing excess hydroxide and buffering the pH in an optimum range, while boric acid hinders the process by increasing caustic requirements and forming sodium borate deposits. Precise scrubbing process water fractions, properly designed injection hardware and state-of-the-art vapor/liquid separation equipment are critical to the overall efficiency. The development of steam sampling and analysis methodologies for trace impurities, refinement of corrosimeter and ultrasonic corrosion testing, and use of chemical modeling programs has enabled the optimization of the corrosion mitigation process. At least 1.5 million lbs/hr of produced steam at The Geysers is currently treated by this process with minimal operational costs.

REFERENCES

1. Hirtz, P, Miller, J., and Prabhu, E., 1990, Operational Results of a Dry-Steam Resource Chloride Corrosion Mitigation System, Geothermal Resources Council Transactions, Volume 14, Part II, August, 1990

2. Allegrini, G., and Benvenuti, G., 1970, Corrosion Characteristics and Geothermal Power Plant Protection, U.N. Symposium on the Development and Utilization of Geothermal Resources, Geothermics, Vol. 2, Part 1

3. Ellis, P.F., II, and Anliker, D.M., 1982, Geothermal Power Plant Corrosion Experience - A Global Survey

4. Rivera, R.J., D'Amore, F., Guisti, D., Rossi, R., and Tomaselli, F., 1990, Geothermal Project at St. Lucia (W.I.) - A Preliminary Assessment of the Resource, Stanford Res. Eng. Workshop, Jan. 1990

5. White, D.E., and Waring, G.A., 1963, Volcanic Emanations, Data of Geochemistry, M. Fleischer, ed., U.S.G.S. Prof. Paper 440-K, pp. 29

6. D'Amore, F., and Truesdell, A. H., 1979, Models for Steam Chemistry at Larderello and The Geysers, Proceedings, Fifth Workshop, Geothermal Reservoir Engineering, Stanford University, Stanford, CA, Dec. 12-14, 1979, p. 283-297

7. Truesdell, A.H., Haizlip, J.R., Armannsson, H., and D'Amore, F., 1988, Origin and Transport of Chloride in Superheated Geothermal Steam, Proceedings, International Workshop of the Deposition of Solids in Geothermal Systems, Reykjavik, Iceland

8. Allmon, W.E., 1983, Deposition of Corrosive Salts from Steam, The Babcock & Wilcox Co. NP-3002 Research Project 1068-1

9. Allmon, W.E., Berthold, J.W., and Mravich, N.J., 1984, Role of Chemical Additives in Transporting and Depositing Corrosive Impurities in Steam, The Babcock & Wilcox Company EPRI NP-3487 Research Project 1068-1

10. Haizlip, J.R., and Truesdell, A.H., 1989, Hydrogen Chloride in Superheated Steam and Chloride in Deep Brine at The Geysers Geothermal Field, California, Proceedings, 13th Workshop on Geothermal Reservoir Eng., Stanford, CA., Jan. 1989, p. 93-100

11. Andersen, G., 1989, A Thermodynamic Model for Predicting HCl Partial Pressure Above a High Temperature Hypersaline Geothermal Fluid, Geothermal Resources Council, Transactions, Vol. 13, Oct. 1989, p. 221-225

12. Tatarinov, B.P., Lukashov, Y.M., and Sholichev, A.T., 1966, Solubility of Chlorides in Saturated Steam, Therm., Eng. 13 (11), 77

13. Stryrikovich, M.A., Martynova, O.I., and Belova, Z.S., 1965, Some Features of the Carry-Over of Sodium Chloride from Boiling Water into Steam, Therm. Eng. 12 (9), 115

14. Fursenko, J.F., and Kuznetsov, N.V., 1970, Investigation of the Electrolytic Properties of Steam Solutions of Sodium Chloride at High Temperatures, Therm. Eng. 17 (2), 112

15. Tskhvirashvili, D.G., Chikhladze, N.M., and Berishvili, Z.D., 1975, The Distributions of Salt - Electrolytes between Boiling Water and Dry Saturated Steam, Therm. Eng. 22 (2), 72

16. Fournier, R.O., 1983, Active Hydrothermal Systems as Analogs of Fossil Systems, in the Role of Heat in the Development of Energy and Mineral Resources in the Basin and Range Province, Geothermal Resources Council Special Report 13, p. 263-284

17. D'Amore, F., Truesdell, A.H., and Haizlip, J.R., 1990, Production of HCl by Mineral Reactions in High-Temperature Geothermal Systems, Stanford Res. Eng. Workshop, Jan. 1990

18. Bussert, B.W., Curran, R.M., and Gould, G.C., 1983, The Effect of Water Chemistry on the Reliability of Modern Large Steam Turbines, EPRI NP-3002

19. Mercado, S., 1979, The Cerro Prieto GTE Plant Turbine Running Five Years Without Corrosion Problems, Corrosion 79, The International Corrosion Forum Devoted Exclusively to the Protection and Performance of Materials, Mar. 1979, Atlanta, Georgia

20. Conover, M., Ellis, P., and Curzon, A., 1980, Material Selection Guidelines for Geothermal Power Systems - An Overview, ASTM Pub. 717

21. Fontana, M.G., 1986, Corrosion Engineering, Third Edition, McGraw-Hill

22. Holmes, D.R., 1985, Dewpoint Corrosion, Ellis Horwood Limited

23. Hirtz, P., 1989, Thermochem, Inc., report to Mission Power Engineering on corrosion mitigation system design parameters

24. Hirtz, P., Mac Phee, T, 1989, Development of a Safer and More Efficient Method for Abatement of H_2S during Geothermal Well Drilling, Geothermal Resources Council, Transactions, Vol. 13, Oct 1989, p. 403-407

25. Lovekin, J., 1990, Control of Calcium Carbonate Scale Using Concentric Tubing, Geothermal Resource Council Transactions, Vol. 14, August 1990

26. Hibara, Y., Hara, N., and Sakanashi, H., 1989, Steam Purities of Geothermal Power Plants, Geothermal Resources Council Annual Meeting, October 1989

27. Peña, J.M., and Campbell, H.E., 1987, Steam Wetness Measurement Using a Transversable Retractable Probe, Geothermal Resources Council, Transactions, Vol. 11, October 1987

PROCEEDINGS, Sixteenth Workshop on Geothermal Reservoir Engineering
Stanford University, Stanford, California, January 23-25, 1991
SGP-TR-134

ANALYSIS OF REINJECTION STRATEGIES FOR THE GEYSERS

Mike Shook and D.D. Faulder

Idaho National Engineering Lab Idaho Falls, ID 83415-2107

ABSTRACT

The Geysers has undergone severe pressure decline in recent years, and reinjection of condensate is thought to be one key to sustaining current steam production. Other methods of pressure maintenance include load cycling, or reduction of steam production during off-peak hours. It is likely that a combination of these two will prove to be optimum in providing pressure and fluid maintenance.

This paper presents preliminary results of a study of various injection schemes for The Geysers. A number of injection scenarios are investigated, and an optimum scheme (based on specific parameters) is identified for two different quantities of reinjection.

INTRODUCTION

The Geysers is a mature geothermal field that has undergone severe pressure decline in recent years. Reinjection is thought to be one key to sustaining reservoir pressure and deliverability, but care must be taken in designing an injection scheme that avoids local quenching of the reservoir and/or premature breakthrough of the injectate. Given the current drought conditions in Northern California, water availability is another issue, and injectate must be used in as efficient a manner as possible. These concerns dictate the need for careful study of various injection strategies to identify the more efficient uses of injectate. Given the lack of regular well spacing and the number of wells present, it may not be possible to identify the optimum strategy; however, the less efficient schemes can certainly be identified.

The purpose of this paper is to compare reservoir response at The Geysers to a variety of injection schemes in order to identify the more efficient uses of available injectate. We have selected reservoir properties from the literature that are representative of The Geysers, and used actual surface well locations from an older section of the field. From a base case depletion scenario without reinjection, we then study the effect of reinjecting 30% of the produced mass (approximately the fraction currently reinjected). Different injection scenarios include using a single injector, and then using increasing numbers of injectors in order to find an optimum number. We then examine the effect of increased reinjection using our optimum case as a starting point.

Two points are worth noting at this stage. First, we are using 12 wells in this study, and to find a true optimum would require 12! simulations. We have elected instead to use engineering judgement to determine which wells to convert to injectors; therefore we hope to find what might be termed a "local" optimum. Also, this study addresses an optimum with respect to the technical side only; a later paper is planned that will discuss the relationship between the technical and economic optima.

The simulator used in this study is TETRAD, a fully implicit, multi-phase, multi-component, finite difference geothermal simulator. It has been

Work supported by the U.S. Department of Energy under
DOE Contract No. DE-AC07-76IDO1570.

validated against a number of geothermal problem sets, and yields results comparable to those published elsewhere (e.g., Stanford Special Panel on Geothermal Model Inter-comparison Study, 1980).

MODEL DESCRIPTION

Petrophysical Data

The area used in this study encompasses a portion of The Geysers near Power Plants 3 and 4. This is an area of the field that has undergone some of the more severe pressure declines. The area used here is approximately 3000 feet by 1800 feet, and is 7000 feet thick. Of the more than 20 wells in this general area, 12 were included in our study. While we recognize the limitations associated with assuming a no-flow boundary in these simulations, additional wells exist just outside our study area. For the base case of no reinjection these "imaging" wells would tend to create a no-flow boundary, thus minimizing our error. The simulated field is shown in Figure 1.

The fractured nature of the field has been modelled using the Warren and Root dual porosity model (Warren and Root, 1963) with a shape factor as defined by Gillman and Kazemi (1983). Matrix block length (and thus fracture spacing) used is 150 ft., similar to that reported by Dykstra (1981). Williamson (1990) presented an algorithm for assigning porosities as a function of depth which was used in these simulations as well. Permeabilities used in this study compare favorably with those published elsewhere (Williamson, 1990; Bodvarsson, *et al.* , 1989).

In setting up this problem, we have neglected several physical phenomena; in particular, capillary imbibition, non-condensible gases, and geochemistry effects have been omitted. These can play an important role in reservoir studies, and should be examined in a future study.

Initial Conditions

The initial saturations used are consistent with a stable heat pipe in fractured porous media. Gas saturations in the fractures are in excess of 0.99, and the matrix gas saturation was 0.75. The matrix saturations are among the poorest-known data required for a simulation study, and can exert significant influence on reservoir response. A wide range of initial matrix gas saturations have been used in various studies, ranging from about 0.1 (Pruess, 1985) to 0.75 (Bodvarsson *et al.*, 1989). How this parameter affects our results will be addressed in a future analysis.

The initial pressure and temperature used in this study are 514.7 psia, and 470° F, corresponding to typical initial conditions at The Geysers. The datum was the top of the reservoir, with P and T increasing with depth according to vapor-static conditions. These initial conditions were used in a pre-exploitation simulation to ensure stability. Results indicated that these parameters constituted a stable initial condition.

Petrophysical properties and initial conditions are summarized in Table 1.

EXPLOITATION AND PRESSURE MAINTANANCE

Base Case

The base case of this study involves fluid depletion without any reinjection. Wells were produced on a bottom hole pressure constraint of 150 psig. After a short transient of rapid production decline, all 12 wells stabilized for several years, and then began an exponential decline of about 20%/yr. This decline rate is somewhat higher than other published estimations (Williamson, 1990; Barker *et al.* , 1989), perhaps due to differences in initial water saturations. Field-wide cumulative production histories are given in Figure 2. This figure shows that in the absence of fluid replacement, the reservoir is depleted in less than 15 years. In fact, at t = 4350 days (~ 12 years), over 95% of the mass initially present has been produced, and only about 4% of the energy recovered. This case shows the

inefficiency of heat extraction through fluid depletion.

30% Reinjection

From the results of our base case, it is obvious that reinjection must be used in order to improve heat extraction. The following sections investigate the effect of a variety of reinjection schemes, where 30% of the produced fluid is reinjected. The injected fluid is assumed to be water at 150° F, and all injection and production is assumed to take place in the uppermost layer. Since we are faced with irregular well spacing, engineering judgement must be used in determining which wells should be converted to injection. The two primary rules of thumb used in selecting injectors were: 1) to separate injectors, and 2) to inject (where possible) nearer the middle of the field. In two cases, sensitivity runs were also made, changing which wells were converted to injection. In both cases, while individual well responses changed, changes in overall field response were minimal. Therefore, while we acknowledge sensitivity to different cases, we feel that these results are indicative of the effect of the different injection strategies.

The first case of reinjection involves 30% of field-wide production being reinjected into Well 11 (see Figure 1). Cumulative production histories for this case are given in Figures 3 and 4. For comparison purposes the base case results are also given in these figures. Because of the relatively small volume of fluid being reinjected this reinjection scenario does not accelerate production very much, but rather results in incremental recovery of both mass and energy. By reinjecting 30% of mass produced into one central well, energy recovery has increased by 35%, to a total of 5.4% of the energy in place.

It is interesting to note that by reinjecting only 30% of the produced mass, we are still operating in a depletion mode. In a gas field (and as the reservoir pressure is reduced through production this reservoir boils) virtually all mass in place can be recovered due to the high mobility of the fluid. Thus, every case studied here should result in the same amount of fluid recovered. Different injection schemes will increase or decrease the rate of recovery. Therefore, any differences in mass recovered in the following sections can be attributed to an extremely low (but nonzero) production rate when the simulation was terminated. In every case, however, over 95% of the theoretically-recoverable mass was recovered prior to termination of the run.

The second injection study distributes the injectate over 3 wells. We have selected Well 8, 23, and 16 as injectors, though several different configurations were examined. Wells nearest each injector were linked to provide the injectate. Cumulative recovery histories comparing the 1-injector and 3-injector cases are given in Figures 5 and 6. Although ultimate recovery for each case is virtually the same, increasing the number of injectors results in an acceleration in recovery of about 8 years. It is obvious that we are moving toward an optimum case.

Increasing the number of injectors to five (Wells 8, 14, 17, 19, and 20) yields an additional acceleration in energy recovery. Comparisons between the 3-injector vs. the 5-injector case can be made from Figures 7 and 8. The reduction of injectate on a "per-well" basis results in less local quenching of the reservoir. This in turn leads to improved areal pressure support, resulting in speedier recovery of energy. The increase in the number of injectors is this case results in another 5 year acceleration in recovery.

The final variation in this section is to convert 7 of the wells to injection. Wells 8, 9, 10, 11, 16, 17, 19, and 23 were converted for this run. Production histories for this case are given in Figures 9 and 10. Rate of recovery for this case is appreciably worse than in the five injector run. In fact, the rate of energy recovery in this run is very similar to that of the 3-injector case. The results of this run indicate that, while less injection per well can lead

to less local quenching, spreading injectate over too large an area can result in insufficient pressure maintenance. On the basis of these results, it appears that injection through five wells effectively balances the negative effects of local quenching with improved areal pressure support.

This result should be qualified: *For the reservoir description used in this study, given the well spacing relative to the field boundaries and the amount of fluid reinjected, the optimum number of injection wells was found to be five.* These qualifications are important, since these studies were performed under a fixed and ideal set of conditions. Different reservoir descriptions or well spacings could easily lead to a different optimum. The more important result from this analysis is that a simulation study can be used in devising an optimum injection strategy.

Having arrived at an optimum injection strategy for the initial scenario of 30% reinjection, a question arises concerning what effect increased injection has on this optimum case. Analysis of the runs made in the previous section reveals that a small amount of quenching occurred around each injector. Obviously, increasing the amount of fluid reinjected can lead to increased quenching, an undesirable occurrence. Increased injectate also leads to improved heat extraction; we therefore need to study the effect increased injection has on a given injection strategy. While we recognize the difficulty in obtaining additional fluid for injection, this study evaluates the additional benefit of increased fluid availability. Two possible sources of additional injectate are through additional surface water acquisition and improved power plant design and operation.

60 % Reinjection

The first run in this study involves the same well configuration discussed above for the 5-injector case, the one difference being that 60% of the produced mass is reinjected. Steam and total mass production histories for this run are given in Figure 11. The difference between these curves is liquid production. As can be seen from this figure, the liquid phase cut during much of this run is in excess of 15%. This liquid production is due to excessive quenching, and represents a poor efficiency in injectate use.

In the previous study, we saw that increased number of injectors resulted in less local quenching, and so we increased the number of injectors to 7. The cumulative gas and total mass produced for this case is given in Figure 12. As in our 5-injector case, injecting 60% of the produced mass results in premature breakthrough of injectate, again resulting in a water cut of over 15%.

A third simulation was made in which three injectors were selected on the basis of their distance from other wells. In this way we hoped to reduce production of a liquid phase. Production histories for this case are given in Figure 13. In comparing the results from Figs. 11-13, one can readily see that, indeed, by injecting at a distance from production wells, one minimizes the production of liquid. This also results in a slight reduction in steam recovery; however, the reduction in water production probably offsets this. As we are still operating in a depletion mode, this results in a delay in production, not a loss. The delay in recovery is a direct result of the reduction in mobility of the fluid, as noted by Bodvarsson *et al.* (1985).

The energy recovery history for the most successful case above (3 injectors) is given in Figure 14. Also presented in this figure is the energy recovery from the optimum 30% reinjection case. Differences between these curves suggest several conclusions concerning our 60% reinjection case. First, it appears that reinjecting 60% of the produced mass results in appreciable quenching, independent of the pattern used. It does, however, appear that an increased distance between injection and production reduces the amount of liquid produced. Finally, reinjection on this scale results in a significant delay in heat

extraction. It also results in a large increase in total heat extracted. When these simulations were terminated at 40 years, approximately 40% of the recoverable mass in still in the reservoir. This amount is on the order of mass initially in place; thus, energy extraction can be nearly doubled, albeit over an increased time period. Prudent reservoir management would dictate shutting in wells at large water cut, thereby increasing both the efficiency of the injectate and the length of the recovery period. However, the version of TETRAD used in this study does not support the option of shutting in geothermal wells as a function of liquid production fractions.

CONCLUSIONS

Based on the results of studies presented here, and limited to the same assumptions made here, we make the following conclusions:

1) An optimum number of injection wells can be determined for a given well pattern through simulation studies.

2) Given the irregular well spacing found in The Geysers, this optimum cannot be determined without careful examination of a variety of schemes.

3) The optimum configuration changes as the injection scenario changes, and therefore must be determined for each set of injection conditions.

4) Increasing the fraction of reinjected mass results in local quenching of the reservoir. Above some threshold fraction of reinjection, the fluid should be reinjected as far from production wells as possible. While this decreases the rate of steam recovery, it also reduces the amount of liquid produced.

5) While increasing the fraction of mass reinjected results in a delay in energy recovery, it also results in an increase of total energy recovered. The delay in steam recovery can probably be reduced through careful management of wells that show excessive water production.

ACNOWLEDGMENTS

We gratefully acknowledge useful discussions with Larry Murray of UNOCAL and Steve Enedy of NCPA, and thank the management of EG&G for permission to publish this work.

REFERENCES

Barker, B.J., M.S. Gulati, M.A. Bryan, and K.L. Riedel, "Geysers Reservoir Performance", *Trans.*, Geothermal Resources Council , **13**, October, 1989

Bodvarsson, G.S., K. Pruess, and M. O'Sullivan, "Injection and Energy Recovery in Fractured Geothermal Reservoirs", *Society of Petroleum Engin. J.*, August, 1985.

Bodvarsson, G.S., S. Gaulke, and M. Ripperda, "Some Consideration on Resource Evaluation of The Geysers", *Trans.*, Geothermal Resources Council , **13**, October, 1989

Dykstra, H., IV. Reservoir Assessment, in: *A Reservoir Assessment of The Geysers Geothermal Field*, Publication TR27, California Division of Oil and Gas, Sacramento, California, 1981.

Gilman, J.R., and H. Kazemi, "Improvements in Simulation of Naturally Fractured Reservoirs", *Society of Petroleum Engin. J.*, August, 1983.

Pruess, K., "A Quantitative Model of Vapor Dominated Geothermal Reservoirs as Heat Pipes in Fractured Porous Rock", *Trans.*, Geothermal Resources Council, **13**, August, 1985

Stanford Special Panel on Geothermal Model Intercomparison Study, *Proceedings*, 6th Workshop on Geothermal Reservoir Engineering, Stanford, Ca., Dec. 1980.

Warren, J.E., and P.J. Root, "The Behavior of Naturally Fractured Reservoirs", *Society of Petroleum Engin. J.*, Sept., 1963.

Williamson, K.H., Reservoir Simulation of The Geysers Geothermal Field", *Proceedings*, 15th Workshop on Geothermal Reservoir Engineering, Stanford, Ca., Jan. 1990.

Table 1: Petrophysical Properties and Initial Conditions

Petrophysical Properties	Matrix	Fractures
Porosity	$0.047 \geq \varphi \geq 0.03$ decreasing with depth	$0.02 \geq \varphi \geq 0.013$
Permeability (md)	0.01	20.
Relative Permeabilities		
Liquid	$k_{rl} = 1.33(S_l - 0.25)$	$k_{rl} = S_l$
Steam	$k_{rg} = S_g$	$k_{rg} = S_g$

Rock Heat Capacity = 0.238 BTU/lb_m

Rock Density = 165 lb_m/ft^3

Rock Thermal Conductivity = 40 BTU/lb_m·°F·D

Matrix Block Size = 150. ft.

Heat Flux = 0.158 BTU/hr.· ft^2 (500 mW/m^2)

Initial Conditions

Pressure = 500 psig

Temperature = 470° F

Datum: Top of reservoir

Mass Initially in Place = 2.01×10^{10} lb_m

Energy Initially in Place = 6.04×10^{14} BTU

Grid Data

Nx = 15 Δx = 198 ft.

Ny = 9 Δy = 194 ft.

Dx = 8 2250 ft $\geq \Delta x \geq$ 50 ft.

Figure 1: Schematic of Study Area Showing Well Locations
Wells located in center of blocks

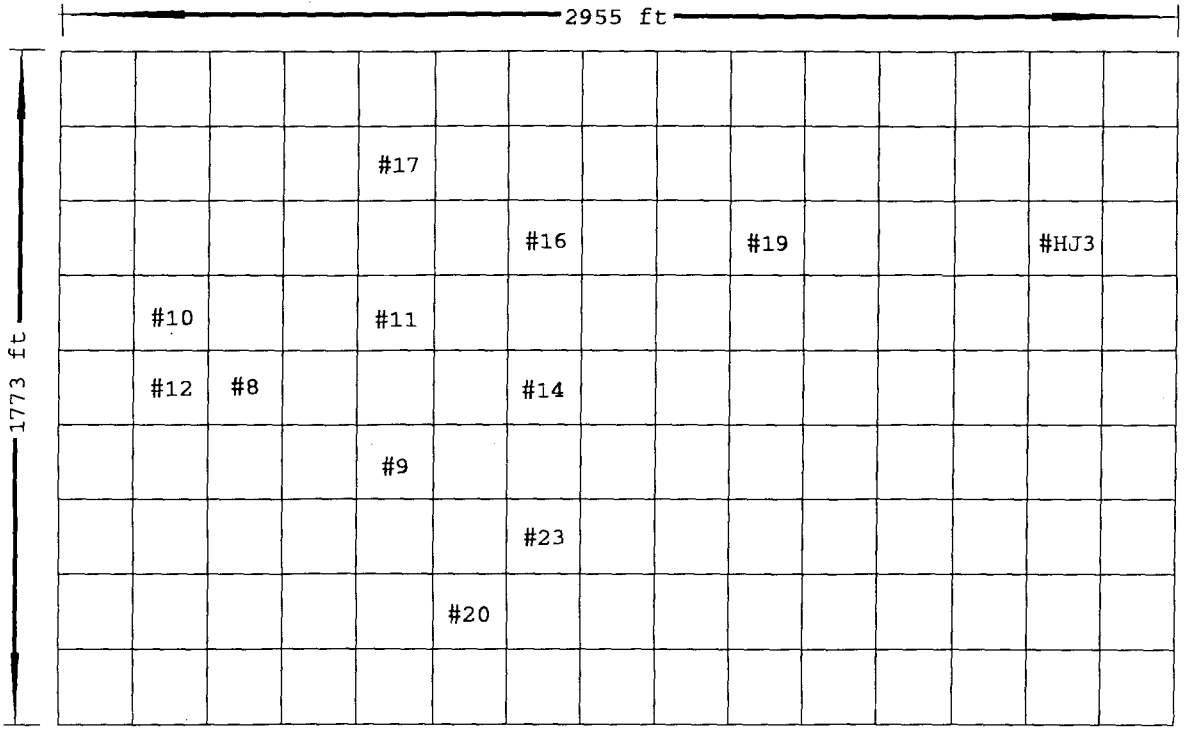

Figure 2: Cummulative Steam or Steam Energy Histories for Base Case – no Reinjection

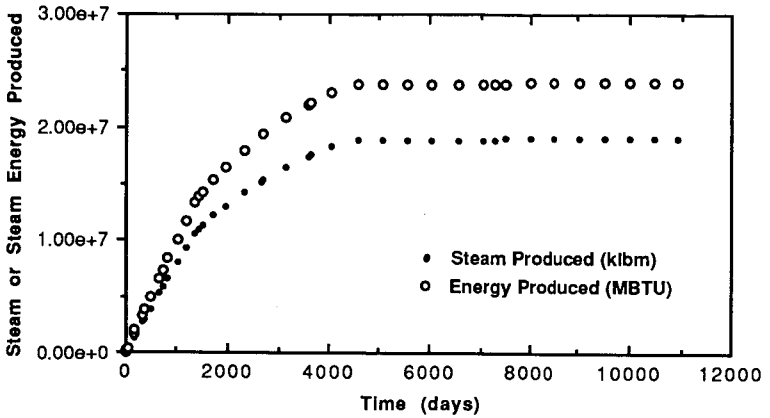

Figure 3: Comparison in Steam Production – No Reinjection vs. 1-Injector Case

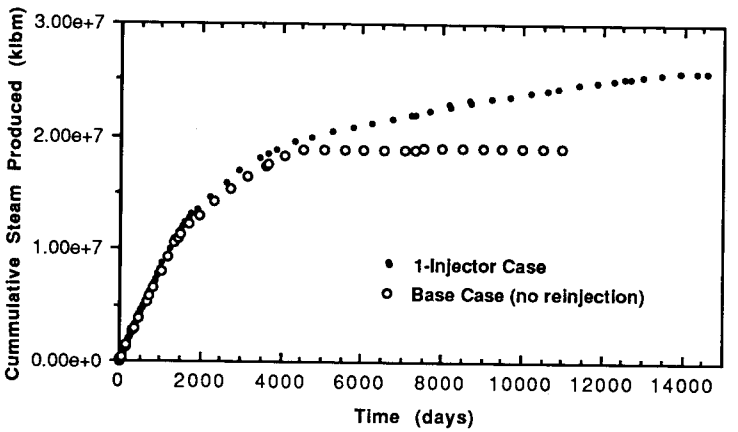

Figure 4: Comparison in Energy Recovery Histories – No Reinjection vs. 1-Injector Case

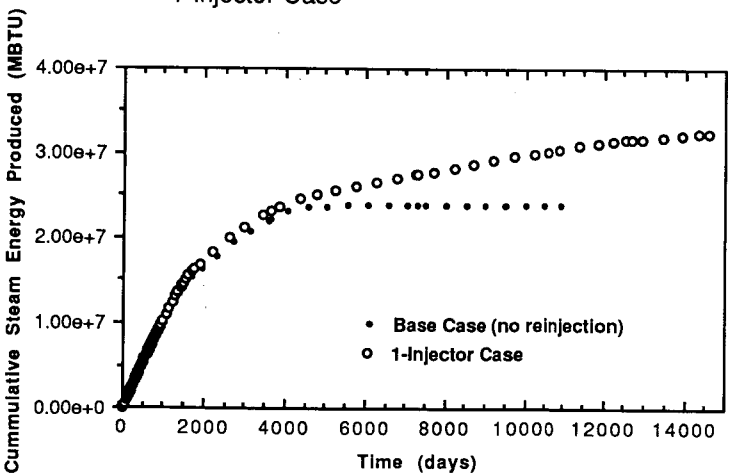

Figure 5: Comparison in Steam Production – 1-Injector vs. 3-Injectors

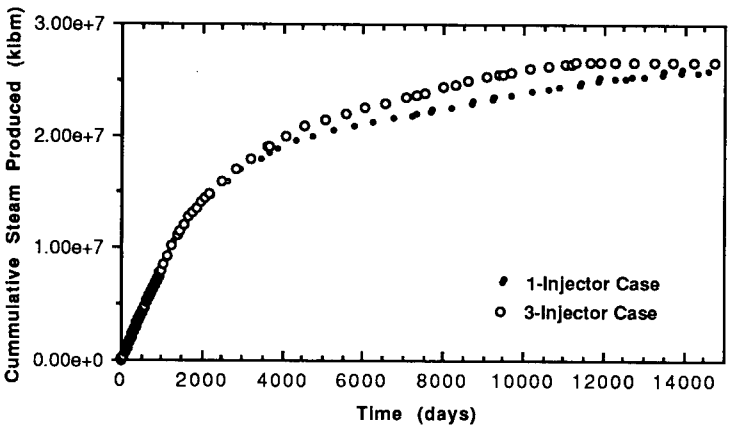

Figure 6: Comparison in Energy Recovery – 1-Injector vs. 3-Injectors

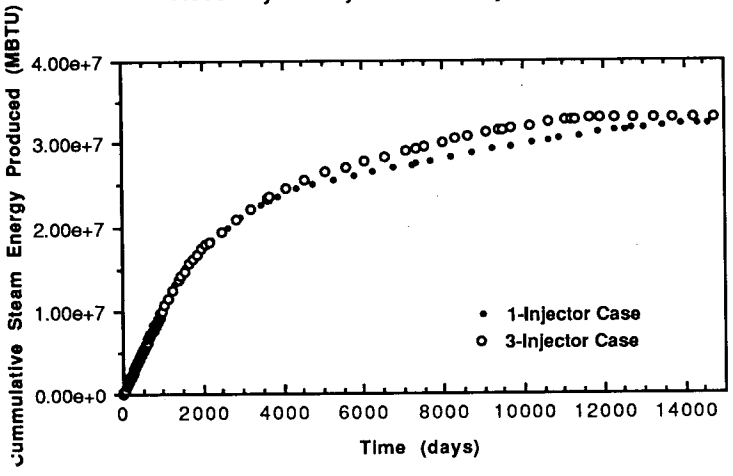

Figure 7: Comparison in Steam Production – 3-Injectors vs. 5-Injectors

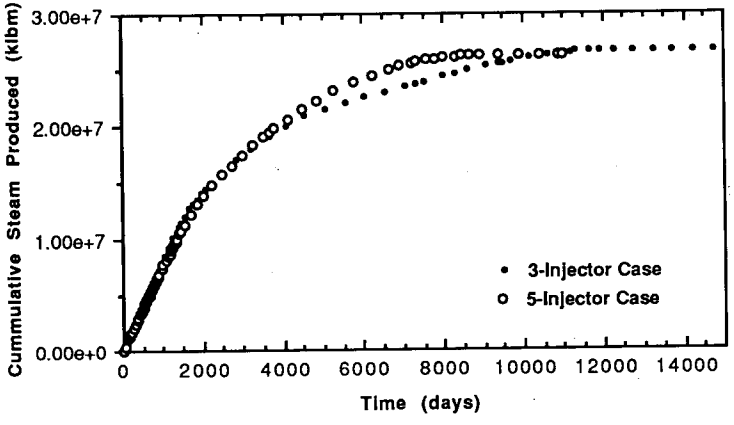

Figure 8: Comparison in Energy Recovery – 3-Injectors vs. 5-Injectors

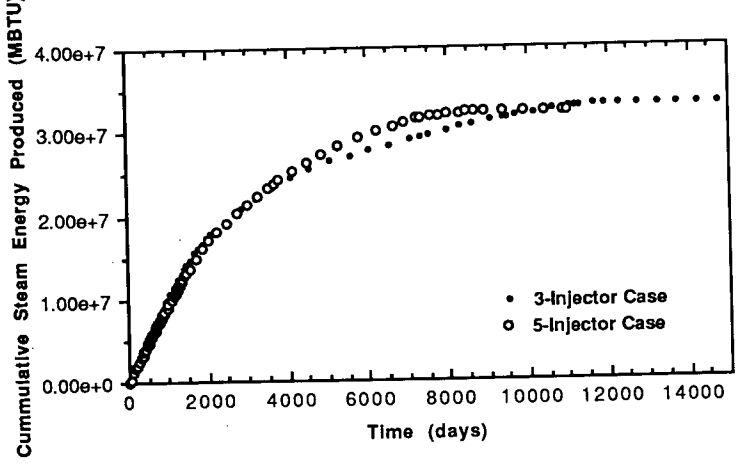

Figure 9: Comparison in Steam Production – 5-Injectors vs. 7-Injectors

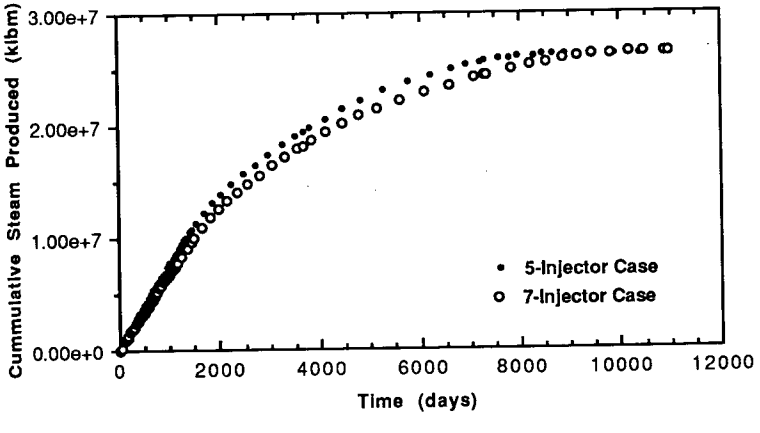

Figure 10: Comparison in Energy Recovery – 5-Injectors vs. 7-Injectors

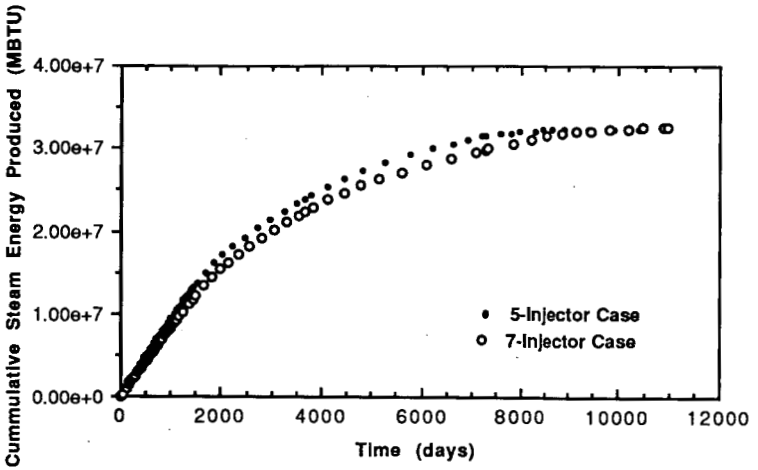

Figure 11: Cummulative Steam or Total Mass Production; 60% Reinjection, 5 Injectors

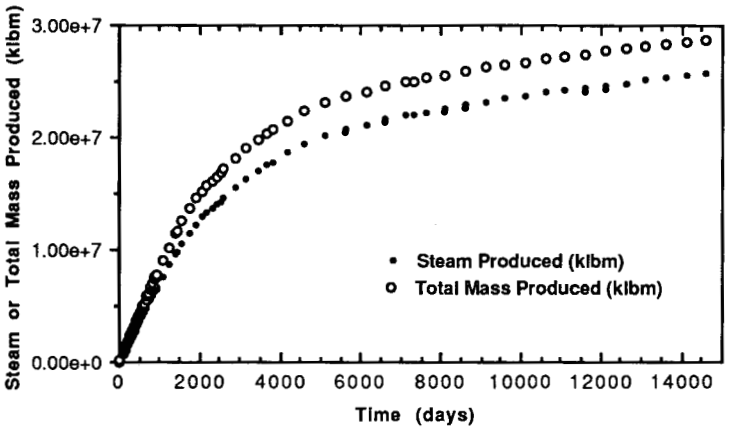

Figure 12: Cummulative Steam or Total Mass Production; 60% Reinjection, 7 Injectors

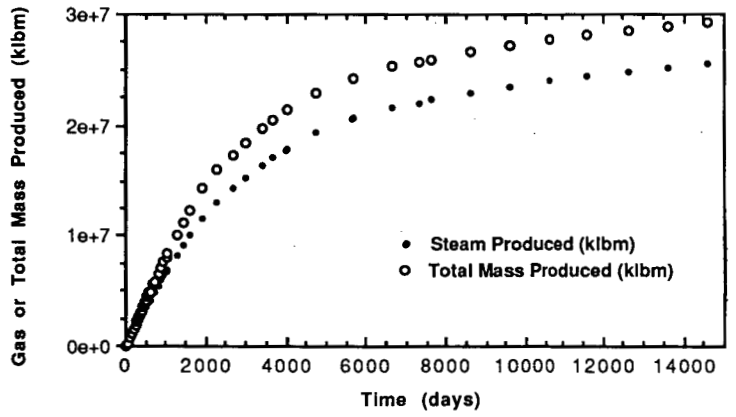

Figure 13: Cummulative Steam or Total Mass Production; 60% Reinjection, 3 Injectors

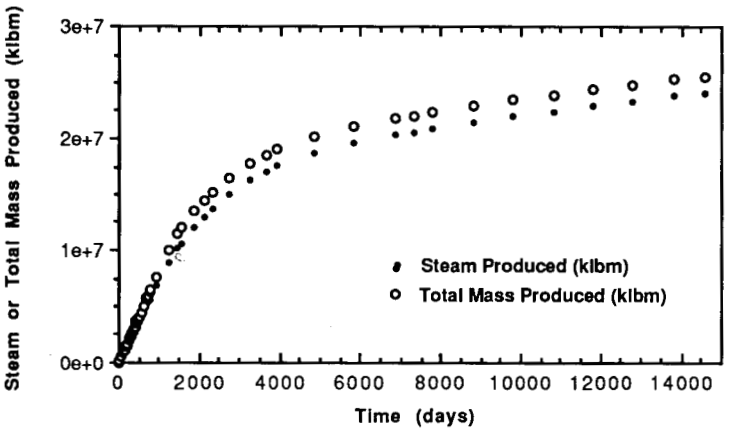

Figure 14: Comparison in Energy Recovery – 60% Reinjection, 3 Wells vs. 30% Reinjection, 5 Wells

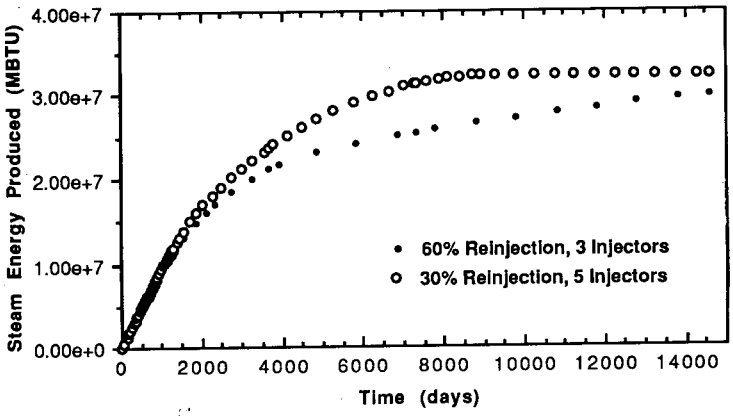

PROCEEDINGS, Sixteenth Workshop on Geothermal Reservoir Engineering
Stanford University, Stanford, California, January 23-25, 1991
SGP-TR-134

Fracture Patterns in Graywacke Outcrops at The Geysers Geothermal Field

Charles G. Sammis and Lin Ji An, Department of Geological Sciences
I. Ershaghi, Petroleum Engineering Program

University of Southern California

Introduction

The Geysers geothermal field covers an area of more than 35,000 acres and represents one of the most significant steam fields in the world. The heterogeneous nature of the reservoir, its fracture network and non-sedimentary rock distinguish it from ordinary sandstone reservoirs in terms of reservoir definition and evaluation (Stockton et al. 1984).

Analysis of cuttings, record of steam entries, temperature and pressure surveys and spinner logs have contributed to an understanding of the subsurface geology and rock characteristics of the Geysers. Few conventional electrical log data are available for the main body of the reservoir. It is generally believed that while the fractures are the main conducts for fluid transport through the reservoirs, tight rocks between the major fractures contain the bulk of the fluid reserves. No independent measurement of liquid and vapor saturation can be made from the existing downhole tools.

Pressure depletion in The Geysers geothermal field has become a major concern to the operators and utility companies in recent years. Plans for further development activities and future field management are contingent upon accurate computer modeling and definition of the field. The primary issues in reliable characterization of The Geysers field are the role of the rock matrix in holding liquid reserves and providing pressure support, the nature of fracture network, extent of liquid saturation in the reservoirs and injection pattern strategies to maximize heat recovery.

Current modeling of The Geysers field is done through the use of general purpose geothermal reservoir simulators. Approaches employed include treating the reservoir as a single porosity equivalent or a dual porosity system. These simulators include formulation to represent transport of heat, steam and water. Heterogeneities are represented by spatial variations in formation or fracture permeability–thickness product, porosity or fluid saturations. Conceptual models based on dual porosity representations have been shown to duplicate the history. Prediction of future performance is, however, not reliable because of uncertainties in assumptions of the initial state of the reservoir. Specifically, several different initial state conditions have led to a fairly good match of the historical data. Selection of the exact initial conditions is a major dilemma. In dual porosity models, the complex nature of fracture network is formulated by a systematic, well-organized set of orthogonal fractures. Also, the exact nature of matrix-fracture interaction, and the role of adsorption and capillarity in pressure support are not well-defined.

In The Geysers geothermal field, steam production is mainly from a system of fractures in the otherwise tight graywacke reservoir rock. Structure of other rocks such as felsite making limited steam flow contribution to the production will not be included in the study. These highly fractured reservoir rocks are sealed by cap rocks consisting primarily of serpentinite, greenstone, and melange (McLaughlin 1977). The producing steam field lies within a wide shear zone bounded by the right lateral Maacama and Collayomi Fault zones (Fig. 1).

The accommodation of simple shear by brittle fracture has produced the network of cracks from which steam is currently produced; older Franciscan imbricate thrust faults are assumed to be inactive and hydrothermally sealed (Hebein, 1985, 1986). The largest fractures in the reservoir can be detected during drilling as they produce a sudden and measurable increase in steam pressure. The average spacing between these major steam producing fractures is on the order of 100-500 feet.

The complexity of multiphase flow in fractured systems requires careful measurements to obtain representative fracture models that can be used for local as well as regional studies. One approach is based on the equivalent porous medium concept, where the fractured medium is treated as a heterogeneous, anisotropic continuum with no distinction between fractures and the rock matrix. Next is the approach based on discretization where each fracture is explicitly defined. Under this procedure, a numerical code is used with individual elements defining the matrix and fractures of the network model (Shapiro and Anderson 1985). Other approaches include statistical methods (Long et al. 1987) and multiporosity models (Barenblatt et al. 1960, Warren and Root 1963, Huyakorn et al. 1983, Abdassah and Ershaghi 1986 and Arbogast 1986). However, as far as modeling of the simultaneous flow of steam and water is concerned, no rigorous attempt has been made to use modern ideas involving fractal statistical models.

Conventional reservoir simulations of the Geysers field (Pruess and Narasimhan 1985) typically use a double porosity model (Warren and Root 1963). This model considers production from a regular network of fractures (in this case the largest fractures) which are embedded in a porous matrix (assumed here to represent the porosity and permeability of all the smaller fractures in the networks. The matrix is usually assumed not to be interconnected so that flow to and from wells occurs only through the fracture network which is assumed to be perfectly connected. Although various improvements and modifications of the original model have been proposed, they all pertain to

the well-ordered but rather restricted structure described above.

Although such a model may be appropriate for production from a uniform set of fractures which drain porous reservoir rock, the fracture network produced by shear in the otherwise impermeable Geysers reservoir rock differs from these idealized models in one very important way. Beal and Box (1989) from the steam entry data observed that there are variations in geometry, density and permeability of the fractures in The Geysers.

It has been widely observed that the fracture pattern in crustal shear zones is developed over a wide range of scales (Tchalenko 1970). Thus, a single matrix block size may not be adequate. It has also been observed that fracture patterns in shear zones are "self-similar" in the sense that the fracture pattern observed at the largest scales is reproduced over and over again at ever decreasing scales (Sammis et al. 1987, Barton and Hsieh 1989). Such hierarchical systems are best described using the language of fractal geometry. Transport processes in fractal systems are totally different from those in non-fractal media and cannot be adequately described by the classical differential equations of transport. Lumping the transport properties of all but the largest fractures of a fractal network into a "matrix porosity and permeability" is a gross and unphysical approximation. Recent success in simulating fractured petroleum reservoirs using a fractal network of fractures (Matthews et al. 1989) suggests that the same approach may be useful in simulating and predicting the production of The Geysers reservoir.

Reservoir Fracture Characterization at The Geysers

The ultimate value of a numerical simulator for The Geysers depends on an accurate characterization of the fracture pattern. Hebein (1986) has mapped the fracture pattern at the Geysers at scales on the order of 10-100 meters under the assumption that local drainage patterns are fault controlled. The drainage patterns are consistent with the hierarchical pattern of shears expected in such a shear zone. He concludes: "Considerably more work is required to adequately map fracture trends and enhancements in the Geysers steam field." We propose to extend Hebein's work to smaller scales by accurately mapping fracture patterns at the outcrop scale from centimeters to tens of meters.

A similar analysis has been carried out by the U.S. Geological Survey as part of the effort to characterize the geologic and hydrologic framework at Yucca Mountain, Nevada (Barton and Larsen 1985; Barton et al. 1986; summarized in Barton and Hsieh 1989). The site is currently being evaluated by the U.S. Department of Energy as a potential underground repository for high-level radioactive waste. The primary objective of the mapping studies is to use the methods developed by Barton and co-workers to characterize the fracture patterns observed in the outcrops and cores from The Geysers and, thereby, to place realistic constraints on the proposed numerical reservoir simulations.

For our two-dimensional study at The Geysers, we chose a graywacke outcrop in which a fresh vertical wall (about 30 m high by 100 m wide) had been cut to form a pad for one of the steam wells. Fracture traces were highly visible on the face of the wall because most had been filled with hydrothermal mineral deposits of contrasting color to the graywacke. Fracture maps were prepared from photomosaic images; three examples are shown in Figures 2,3, and 4.

These patterns were tested for self-similarity using a box counting algorithm illustrated schematically in Figure 5. In this method, the minimum number of boxes, N, required to cover all the fractures, is determined as a function of the size of the box r(r = the length of one edge). Self-similar distributions are characterized by a power-law relation between N and r

$$N \quad \alpha \quad r^{D_f}$$

where D_f is the fractal dimension.

As an example of how this method works; consider first a line. The number of boxes required to cover a line is directly proportional to their dimension r. Hence the dimension of a line is 1. Now consider a regular homogeneous pattern of lines. The number of boxes required to cover such a pattern increases as r^2, and the fractal dimension is 2 - such patterns uniformly fill a plane. Finally, consider the fractal pattern shown in Figure 6. Because of the spatial clustering in this pattern, the number of boxes required to cover only increases by a factor of 3 each time the box size is reduced by a factor of 1/2. The fractal dimension in this case is $D_f = 1.58$.

Application of the box counting algorithm to the fracture patterns at the Geysers gives the log N vs log r plots shown in Figures 7, 8 and 9. These patterns are seen to be self-similar over a range of scales which vary by about a factor of ten. The dimensions are in the range $1.7 < D_f < 1.9$, similar to the results obtained by Barton and Hsieh (1989) for fracture patterns at Yucca Mountain.

The known steam entry depths in many wells of the field can be used to help characterize the geometry of the fracture depth pattern and test for fractal structure. Assuming that steam depths represent locations where the borehole intersects the fractures, the distribution intervals between such fractures gives a measure of the self-similarity of the network. If the pattern is fractal, then the intervals between fractures should follow a power law distribution where the power is a measure of the fractal dimension of the reservoir (it should be 1 less than the fractal dimension of a 2-D planar section mapped at the surface).

Discussion

Having established the self-similarity of fracture patterns at the outcrop scale, we now wish to see if this self-similarity extends to the regional scale. That is, we wish to see if the larger steam-producing fractures are part of this same hierarchal pattern which may then be exploited to model the heat extraction process. This will be accomplished by extending the fracture mapping to a more regional scale, by examing the core from the reservoir and by analyzing the pattern of steam entries in the large number of wells where they have been recorded.

Acknowledgments

This study was supported by the Geothermal Division of the U.S. Dept. of Energy through Lawrence Berkely Laboratory and in part by California State Lands Commission. The authors thank these agencies for their support and for permission to publish the paper. Cooperation of the staff at Unocal Geothermal in providing access to the outcrops is much appreciated. We are particularly thankful to

Marcelo Lippman and Karsten Pruess from LBL for their critical review of the manuscript.

References

1. Abdassah, D. and Ershaghi, I. SPE Formation Evaluation Journal 1, 113 (1986).
2. Arbogast T., in Numerical Simulation in Oil Recovery, M.F. Wheeler (ed), **23**, Springer Verlag, New York (1986).
3. Barenblatt G.I., Zheltov I.P. and Kochina N., Prikl. Mat. Mekh **24**, 852 (1960).
4. Barton C.C., Larsen E., and Baechle P.E., (abst.) EOS, Trans. Am. Geophys. U. **66**, 1098 (1985).
5. Barton C.C., Gott C.B., and Montgomery J.R., (abst.) EOS, Trans. Am. Geophys. U. **67**, 870 (1986).
6. Barton C.C. and Hsieh P.A., A Field Guide for the 1989 International Geologic Congress A.G.U. (1989).
7. Beall, J.J. and Box, W.T., The Nature of Steam Bearing Fractures in the South Geysers Reservoir, GRC Transaction, **13**, 441 (1989).
8. Brown S.R. and Scholz C.H., J. Geophys. Res. **90**, 5531 (1985).
9. Hebein, J.J., Geothermal Resources Council Bulletin **14**, #6, 13-16, (1985).
10. Hebein, J.J., Proceedings, Eleventh Workshop on Geothermal Reservoir Engineering, pp. 43-49 Stanford University, Stanford, California (1986).
11. Huyakorn P.S., Lester B.H. and Fast C. R., Water Resource Res. **19**, 1019 (1983).
12. Long J.C.S. and Billaux D., Water Res. Res. **23**, 1201 (1987).
13. Mathews, J.L., Emanuel, A.S., and Edwards, K.A., J. Pet. Tech **41**, 1136 (1989).
14. McLaughlin, R.J., USGS Open File Report, No. 78-389 (1977).
15. Pruess, K. and Narasimhan, T.N., SPEJ, 14-26 (1985).
16. Sammis C.G., King G.C.P., and Beigel R., PAGEOPH **125**, 777 (1987).
17. Shapiro A.M. and Anderson J., Adv. Water Resources **86**, 106 (1985).
18. Stockton, A.D., Thomas, R.P., Chapman, R.H., and Dykstra, H., J. Pet. Tech., 2137-2159 (1984).
19. Tchalenko, J.S., Geol. Soc. Am. Bull., **81**, 1625-1640, (1970).
20. Warren J.E. and Root P.J., Soc. Pet. Eng. J., 245 (1963).

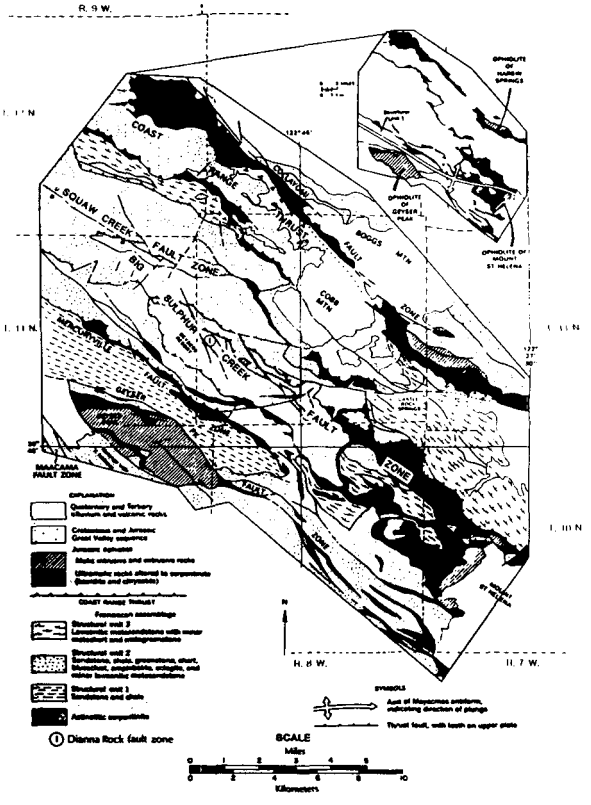

Fig. 1. Geologic map of The Geysers Geothermal Field. (After McLoughfin 1977)

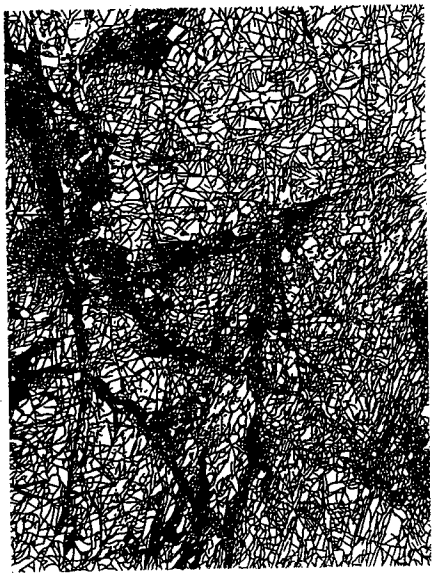

Fig. 2. Fracture map for a graywacke outcrops at The Geysers geothermal field. The area shown is about 2 meters by 1 meter.

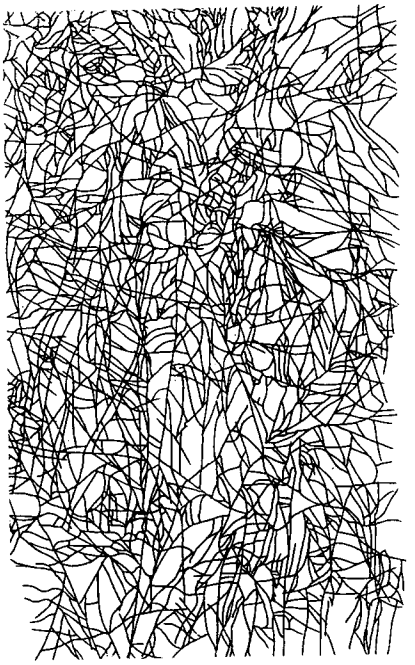

Fig. 3. A fracture map from a graywacke outcrop at The Geysers geothermal field. The area shown is about 0.5 meters by 1 meter.

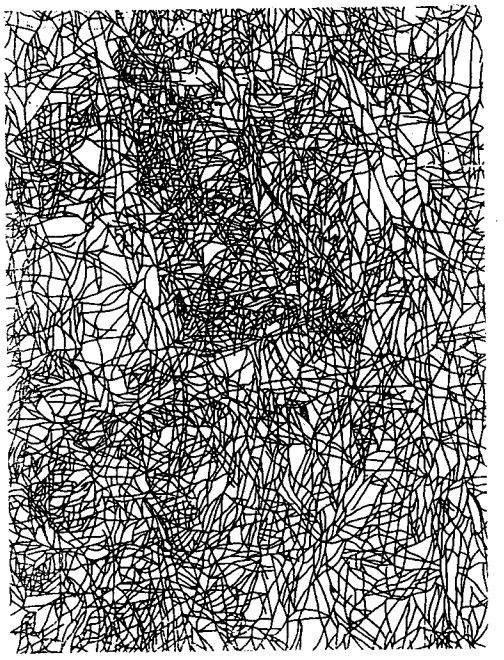

Fig. 4. A fracture map from a graywacke outcrop at The Geysers geothermal field. The area shown is about 0.5 meters by 1 meter.

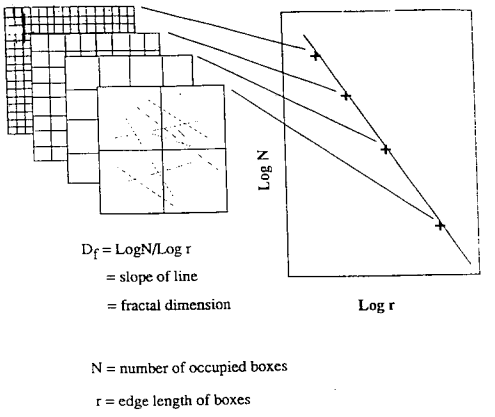

Fig. 5. A schematic diagram showing how the box counting algorithm is used to measure the fractal dimension of a fracture pattern. The grid is moved until the number of occupied boxes is a minimum.

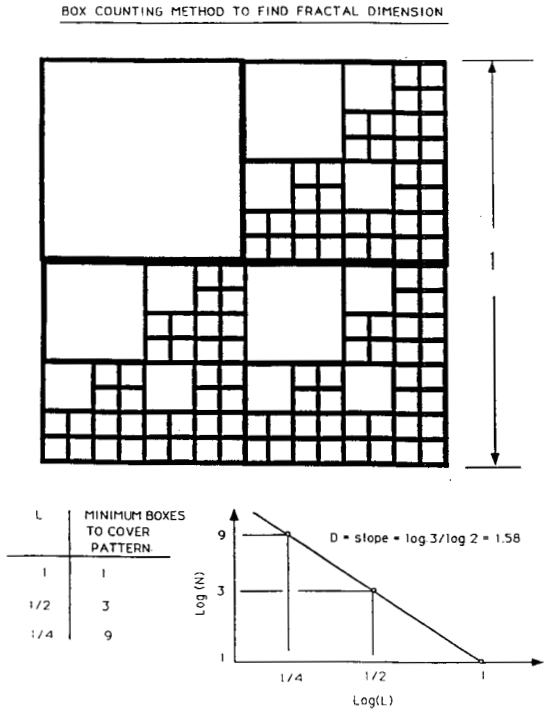

Fig. 6. An example of how the box counting algorithm is used to measure the fractal dimension of a specific fractal pattern. Note that the clustering at all scales produces a fractal dimension between a line (1) and a plane (2). The dimension of this pattern is $D_f = 1.58$.

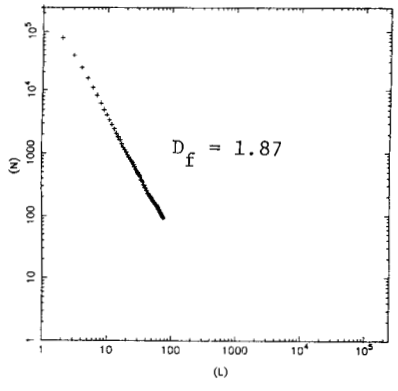

Fig. 7. Results of the box counting fractal analysis of the pattern in Fig. 2.

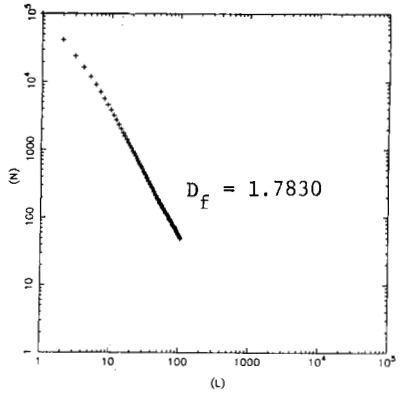

Fig. 8. Results of the box counting fractal analysis of the pattern in Fig. 3.

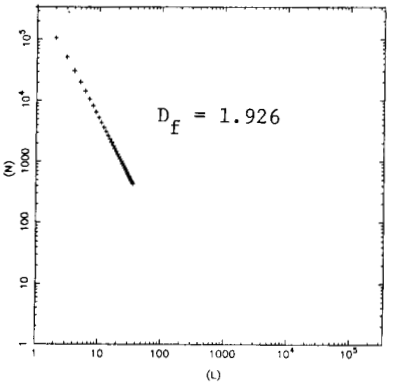

Fig. 9. Results of the box counting fractal analysis of the pattern in Fig. 4.

PROCEEDINGS, Sixteenth Workshop on Geothermal Reservoir Engineering
Stanford University, Stanford, California, January 23-25, 1991
SGP-TR-134

One-Dimensional Steam Flow in Porous Media under Desorption

Cuong Phu Nghiem and Henry J. Ramey Jr.

Stanford University

ABSTRACT

Performance forecasting for an hypothetical field with Geysers greywacke rock is performed to demonstrate the importance of desorption effect, the actual adsorption isotherm was found to be well approximated by the Langmuir equation. Results obtained suggest that adsorption is the dominant mechanism for steam in geothermal reservoirs.

OBJECTIVE

Adsorption was investigated in connection with the vapor-pressure lowering phenomena in geothermal reservoir (Hsieh and Ramey, 1980). Results obtained show that adsorption is a plausible mechanism for steam storage in reservoir and does provide an explanation for the vapor-pressure lowering phenomena. Recent studies of adsorption in geothermal reservoirs focus on estimates of resource size and reservoir longevity (Economides and Miller, 1985 and Ramey, 1990).

The purpose of this work is to incorporate the desorption model in the equation for steam flow in geothermal reservoirs for reservoir performance forecasting. We simulate the vertical flow in reservoir in one- dimension, assuming the steam to be superheated and desorption as the mechanism for steam generation in reservoir for the case of production.

MATHEMATICAL MODEL

The steam flow model used is similar to the one presented by Herkelrath et al. (1982,1983). The porous medium is assumed to be homogeneous and isotropic and the adsorbed water is assumed to be immobile. A mass balance for the flow of steam is:

$$\frac{\partial \phi \rho_v (1 - S_w)}{\partial t} + \phi \rho_w \frac{\partial S_w}{\partial t} - \frac{\partial}{\partial x}[\frac{k}{\mu}\rho_v(\frac{dp}{dx} - \rho_v g)] + q = 0 \quad (1)$$

The second term in Eq.1 describes the mass tranfer between the adsorbed water and steam. It is a sink term during adsorption and a source term when desorption occurs. The fourth term represents the production of steam through wells.

We neglect an energy balance, assuming that the changes in temperature in the reservoir (primary due to vaporization of adsorbed liquid, Herkelrath et al. (1983)) are small.

Adsorption is described phenomenologically in terms of an empirical adsorption function, X= f(p,T) where X is the amount adsorbed, customarily expressed as gram water/gram rock. one usually measures the adsorption isotherm, $X = f_T(p)$. In this work, the adsorption isotherm is assumed to be invariant with temperature (Hseih and Ramey, 1980/Herkelrath et al. 1983). We assume also that there is no hysteresis between adsorption and desorption. Bumb and Mc Kee (1988) observed that the Langmuir (1909) isotherm represents methane adsorption on coal very well. Although the Langmuir expression has largely been replaced by the BET equation, Hsieh and Ramey (1983), the Langmuir equation was tested against water vapor adsorption data for Topopah Spring welded tuff, Herkelrath and O'Neal II (1985); and unpublished Geysers greywacke water vapor adsorption data, Herkelrath (1990). Surprisingly, the equation was found to match measured adsorption data over the entire relative pressure range to $p/p_0 = 1$. The Langmuir equation has the form

$$X = \frac{p/p_0}{a + b(p/p_0)} \quad (2)$$

with p_0 as saturation pressure.

This equation was found to match the unpublished greywacke water vapor adsorption data and other water vapor data. Fig.1 presents a comparison of Eq.2 and experimental measurements. The agreement is reasonable, and surprising. The BET equation did not match the data over the entire pressure range.

PROCEDURE

Steam is treated as a real gas and the pseudo-pressure substitution is applied to Eq.1. Eq.1 is rewritten in terms of X, and then in terms of a pseudo-pressure m(p), see Al-Hussainy, et al., 1966:

$$m(p) = \int_{p_m}^{p} \frac{p}{\mu(p) z(P)} dp \quad (3)$$

where p_m is an arbitrary pressure, perhaps at the lowest pressure of interest in the problem.

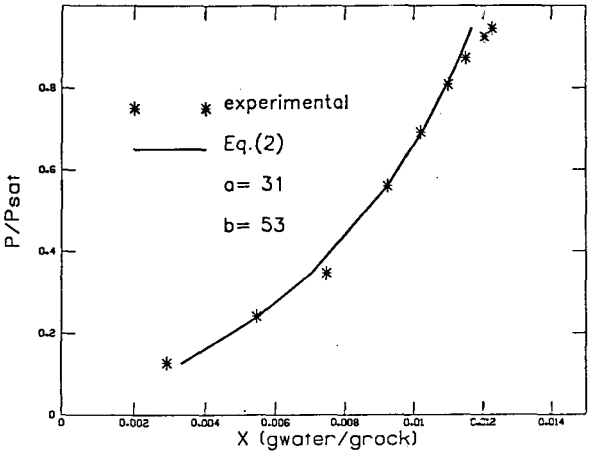

Fig. 1. Adsorption isotherm

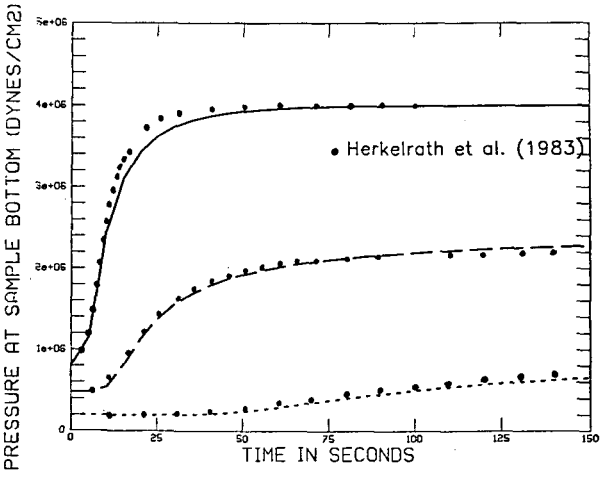

Fig. 2. Pressure response at the closed end of a core subjected to an abrupt increase increase in pressure at the other end

The resulting equation has a form similar to the diffusivity equation:

$$A\frac{\partial m}{\partial t} + B\frac{\partial^2 m}{\partial x^2} + C\frac{\partial m}{\partial x} + qRT = 0 \qquad (4)$$

where:

$$A = \phi M \mu C_g (1 - \frac{\rho_r}{\rho_w}\frac{1-\phi}{\phi}X) + (\frac{zRT}{p_v} - \frac{M}{\rho_w})\rho_r(1-\phi)\mu\frac{\partial X}{\partial p_v}$$

$$B = -MK$$

$$C = \frac{M^2}{RT}\frac{2KgP_vC_g}{z}$$

where C_g is the isothermal compressibility of steam, ρ_r the rock density, and z is the gas law deviation factor.

Eq.5 is solved by finite-difference methods. The solution in terms of m(p) may be transformed to pressure p using a chart of m(p) vs. p.

RESULTS

The computer program developed was first checked for the flow of air in porous media (no adsorption) by comparing results with those of Aronofsky and Jenkins (1951). Results are not shown. However, very good agreement was obtained.

The program was then checked for the case of steam adsorption in natural soil considered by Herkelrath, et al., (1983). Acceptable agreement was obtained, Fig.2.

The model investigated considers steam extraction under either constant pressure or under constant discharge rate. Regarding the last case, we may switch the constant rate discharge mode to constant pressure mode when the pressure in the producing block becomes lower than a specified pressure. Steam is assumed to be initially saturated. It is superheated and coexists in equilibrium with adsorbed water in the reservoir during the desorption process. Although the transient steam injection program was initially prepared to model transient bench-scale experiments like those described by Herkelrath, et al., (1983), the program may be used to study behavior of full-scale geothermal systems like a Geysers field unit. The example considered is a 50 MW unit which requires a steam rate of 1 MMlb/hr steam. The reservoir is a column of Greywacke rock 5000 feet high, having an area of 400 acres, 0.1 porosity and a vertical permeability of 300 md. Initial conditions were saturated steam at 500^oF. The desorption process, associated with the decrease of p/p_o, is assumed to be described by Eq.2.

We are interested in a reservoir engineering study of vapor-dominated systems, a graph of p/z vs cumulative production and production rate vs time are used for analysis. Although plots of p/z vs cumulative production do not give straight lines to estimate initial steam in place, Ramey (1990), some useful information still can be collected.

To investigate the adsorption effect and the compression effect in the geothermal reservoir, we solve Eq.1, for cases without the adsorption term (gas theory) and without the compression term (steam can only be stored as adsorbed water). Figs.3, 4 and 5 present results obtained for the case of production under constant pressure and for the case with specified rate and then constant pressure. The specified maximum rate is taken to be 10^6 lbs/hour, and the lowest pressure in the producing bloc to be 114.7 psia.

Fig.3 shows the pressure behavior in the reservoir under production at a specified pressure. The strong similarity between the p/z behavior for the case of

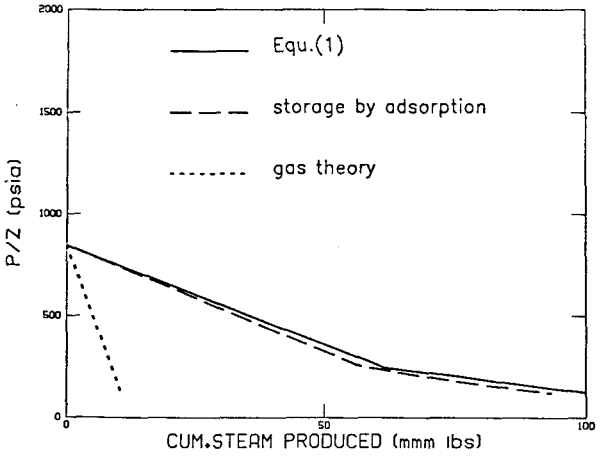

Fig. 3. Production under constant pressure

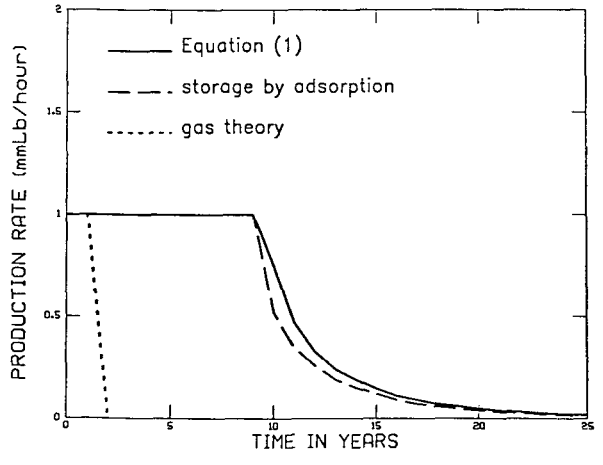

Fig. 4. Production history according to different theories

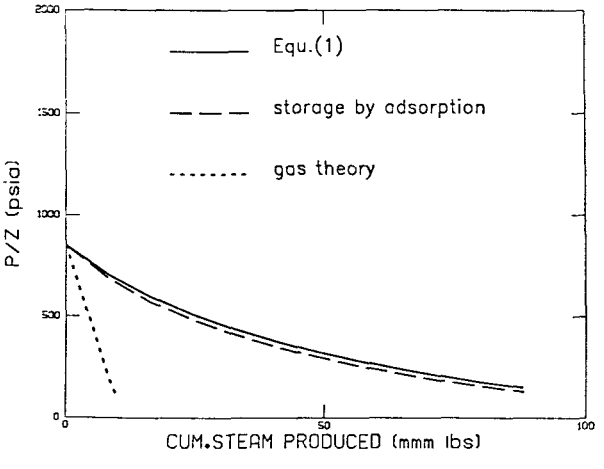

Fig. 5. P/Z behavior according to different theories

compression and adsorption and for the case of adsorption alone suggests that the steam stored in pore space is negligible. Furthermore, the shapes of those p/z vs cumulative production curves show some resemblance to the shape of the desorption isotherm in Fig.1. This may be attributed to the equilibrium state of the reservoir under production, most of the steam vaporized when desorption are produced. For comparison, the straight line shape, according to gas theory, assuming steam released by free expansion is shown in the same figure.

Fig.4 presents production history for the case of specified rate. It confirms that steam is solely stored by adsorption and demonstrates the the effect of adsorption on production forecasting.

Finally, the p/z behavior obtained for the last case does show a shape similar to the one found observed for the Big Geyser Area Shallow Zone and for the italian reservoirs (Ramey, 1980) is presented in Fig.5. It looks significantly different from those in Fig.3. This may be attributed to the fact that the desorption process has been monitored when a flow rate is specified.

REFERENCES

Al-Hussainy, R., Ramey Jr., H.J. and Crawford, P.B.: *The Flow of Real Gases Through Porous Media*, JPT (May 1966), 624-636.

Aronofsky, J.S., and Jenkins, R.: *Unsteady Flow Of Gas Through Porous Media, One-Dimensional Case*, Proc. First U.S Ntl Cong. Appl. Mech., Am. Soc. Mech. Engrs. (June, 1951).

Bumb, A.C. and McKee, C.R.: *Gas-Well Testing in the Presence of Desorption for Coalbed Methane and Devonian Shale.* SPEFE (March 1988), 179-185.

Economides, M.J, and Miller, F.G.: *The Effects of Adsorption Phenomena in the Evaluation of Vapour-dominated Geothermal Reservoirs.* Geothermics (1985), 14, No.1, 3-27.

Herkelrath, W.N., and Moench, A.F.: *Laboratory Investigations of the Physics of Steam Flow in a Porous Medium.* USGS Open-File Report 82-95, 1982.

Herkelrath, W.N., Moench, A.F., and C.F.O'Neal II: *Laboratory Investigations of Steam Flow in Porous Medium. Water Resources Research* (August 1983), 19, No.4, 931-937.

Herkelrath, W.N., and O'Neal II, C.F.: *Water Vapor Adsorption in Low Permeability Rocks.* Proc. 17th Int. Cong. Int. Assn. of Hydrogeologists (January 1985).

Herkelrath, W.N.: personal communication with H.J. Ramey Jr. (1990).

Hsieh, C.H.: *Vapor Pressure Lowering in Porous Media.* PhD Diss., Stanford University (1980).

Hsieh, C.H., and Ramey Jr., H.J.: *Vapor-Pressure Lowering in Geothermal Systems.* SPEJ (February 1983) 157-167.

Ramey Jr., H.J.: *Adsorption in Vapor-dominated Systems.* Proceedings of the Geothermal Program Review VIII The National Strategy-The Role of Geothermal Technology Development" (April 1990).

PROCEEDINGS, Sixteenth Workshop on Geothermal Reservoir Engineering
Stanford University, Stanford, California, January 23-25, 1991
SGP-TR-134

A PRELIMINARY ASSESSMENT OF A MEDIUM-ENTHALPY GEOTHERMAL RESOURCE IN NAGQU (TIBET) PEOPLE'S REPUBLIC OF CHINA

Battistelli, A.*, Rivera, R.J.*, D'Amore, F.**, Wu, F.***, Rossi, R.*, and Luzi, C*

* Aquater S.p.A., San Lorenzo in Campo, PS, Italy.
** Istituto Internazionale per le Ricerche Geotermiche, Pisa, Italy.
*** Geothermal Development Corporation of Tibet Autonomous Region, Beijing, PRC.

ABSTRACT

The Nagqu geothermal field is a single-phase, liquid-dominated system at reservoir conditions, having a high gas content. This field is located at an elevation of about 4,500 m (asl), in the vicinity of the City of Nagqu, which is one of the most important cities of Tibet. The reservoir rock is made of a highly fractured, low-permeability sedimentary sequence. During the implementation of the study described in this paper, fluid production was mainly obtained from two out of four possible productive wells. The main fault systems are located in a NE-SW and E-W directions, which seem to control fluid movement at depth. The geothermal field is restricted to a small area where hydrothermal manifestations are located. Reservoir temperature is 114 °C, gas content is in the range of 0.5 to 0.6 percent by mass, being mainly CO_2. Reservoir transmissivity in the area of the wells is very high. Reservoir response to changes in flow rate in any of the producing wells could be detected almost immediately in the observation wells, which were distant between 300 to 900 m, depending on the production-observation well arrangement.
Calcium carbonate scaling was present in all producing wells. This deposition was controlled by the CO_2 partial pressure. Description of well testing results is provided, as well as the thermodynamics and geochemistry of reservoir fluids.

INTRODUCTION

The Himalayan Mountain Range is about 250 to 300 km wide and nearly 2,000 km long. There are over 400 areas of active hydrothermal manifestations in the whole zone, including hydrothermal eruptions such as craters, geysers, fumaroles, boiling springs, hot and warm springs, etc.. Surge of geothermal manifestations is strictly controlled by active tectonics.
Nagqu geothermal field is located in Northern Tibet, two kilometers southward of Nagqu Town (see Fig. 1), at an altitude ranging between 4,500 to 4,700 m (asl). The area is characterized by plateau-type morphology with relatively broad flat topography and limited differences in height (100 to 200 m). Hydrography is well developed in the surroundings of the geothermal field and is represented by the Nagqu River and its tributaries, which originate from the northern mountain area and flow southward into the Nujang water system. The rivers flow rates vary greatly with the seasons. The Qiqu river flow rate at Nagqu Town is 69.6 m^3/s during the rainy period and can be totally absent during the dry season. According to meteorological records from 1981 to 1986 (El. Des. Inst. of SW China, 1989), the annual average temperature is about -2°C, rainfall is about 400 mm and the relative humidity is 50%.

GEOLOGY

Stratigraphy

The basement of the geothermal field is mainly represented by Middle-Jurassic mudstones and sandstones, (Geothermal Geological Team, 1989). In reference to the stratigraphy disclosed by wells, mudstones are prevailing in SW and NE sectors of the geothermal field, mudstone-sandstone interlayerings are prevailing eastward and silicified, fractured sandstone are present in the NW part. Upper Cretaceous magmatic rocks are scattered over the area; they are mainly represented by medium-acidic volcanics, which underwent dynamometamorphism showing laminated and blastic textures; radiometric data revealed ages ranging from 80 to 101 Ma. Neogenic sediments formed by conglomerate in the lower part with sandstone-conglomerate interbeddings in the upper layers outcrop in the area of thermal manifestations. Quarternary deposits are widespread and are represented by the following sequence:

- Lower Pleistocene lake and swamp deposits
- Middle Pleistocene glaciofluvial deposits
- Upper Pleistocene glaciofluvial and alluvium
- Holocene alluvium and diluvium with swampy deposits.

Structure

The most important structural feature in the geothermal field area is represented by an anticline, whose axis trends NE 70°, with dip angle of strata varying from 40 to 60°. After the folding stage, tectonic events of Himalayan stages produced two main faults systems trending NE-SW and E-W: the latter event is older than the NE trend and shows evident compressive characteristics. The NE-SW trending faults are more widespread being produced by tensile stresses. These two tectonic trends have been the most significative alignments in more recent stages of Himalayan tectonics, and even at the present time they represent the active fault belts along which the hydrothermal activity is developed.
Moreover, in the area of the geothermal field a NW trend is present which is strictly connected with the geothermal manifestations (Fig.2), consisting of warm and hot springs, thermal swamps, steaming grounds and deposition of hydrotermal minerals such as kaolinite, silica, pyrite, sulphates and carbonates.

GENERAL BACKGROUND OF FIELD CONDITIONS

A total of 15 exploratory wells have been drilled in the Nagqu Geothermal Field (Fig. 1). Well depth is ranging between 80 and about 400 m, with the exception of wells ZK1005 and ZK1203, drilled down to 503 and 708 m, respectively. Wells ZK1005, 1007, 1105 and 1203 have a 9 5/8" or a 13 3/8" production casing set at depth ranging between 37 and 94 m. Wells ZK1104 and 1303 are completed with both a surface casing and a 9 5/8" production casing, whereas in all remaining wells only a conductor pipe has been installed.
Six wells have been drilled in the productive area, which has a surface of about 600.000 m^2. Among them well ZK001, the shallowest one, did not reach any productive zone but showed high temperature
(about 110 °C at 80 m); the other wells, ZK1005, 1104, 1105, 1203 and 1303 are completed with a casing head flange and a master valve as static well head pressure ranging from 3.9 to 5.2 bara is present. Well ZK1105 can not be used for production purposes as it is damaged by a fish with top located at about 104 m. The four productive wells were tested by Chinese experts after drilling completion and for about one week, during a production test of the whole field. During the field survey conducted on this study, only two wells were tested, ZK1203 and 1104. Wells ZK1005 and 1303 were used as observation wells during all field activities.

RESERVOIR FLUID MAIN CHARACTERISTICS

Tables 1 and 2 show the water and gas compositions, respectively.

Table 1. pH value and chemical composition (mg/kg) of reservoir water.

pH	5.8	CO_2	5240
Na^+	1004 (±23)	HCO_3^-	2000
K^+	66 (± 4)	SO_4^{2-}	200
Ca^{2+}	22.5	Cl^-	248
Mg^{2+}	6.0(± 0.7)	F^-	8 (± 1)
Al^{3+}	0.035	B	9 (± 0.5)
Fe^{2+}	0.05	NH_3	6
Li^+	2.7	SiO_2	75

Table 2. Average dry gas composition (Vol %) and gas/water ratio (molar).

CO_2	99.5	
H_2	0.0018	± 0.0006
CH_4	0.25	± 0.06
CO	0.000005	± 0.000001
H_2S^*	0.024	± 0.012
N_2	0.21	± 0.08
Ar	0.0035	± 0.0020
He	0.0013	± 0.0005
gas/(total H_2O) = 0.0022		

* A concentraction of 0.04% was measured in samples analized in the field and is considered as most reliable

As it can be seen from this table, CO_2 is the main component of dissolved gases. Thermometamorphism can be considered the main process for the occurrence of CO_2 in this thermal area.
Measured ^{13}C content of - 1.6 ± 0.6 ‰ confirmed this hypothesis, since a CO_2 concentration of this order can normally be considered as linked to a crustal origin from sediments with no organic or volcanic (mantle) components. This conclusion is supported by the fact that plotting the measured N_2 - Ar - He concentrations on a triangular diagram (Giggenbach et al., 1983) the position of this point is located along the line connecting the meteoric component to the He corner, suggesting a crustal component in the order of 75%.

The carbon monoxide content can be used to estimate the CO_2 partial pressure using the so called water-gas shift reaction (Chiodini

and Cioni, 1989), by maing the following chemical equilibrium:

$$CO_2 + H_2 = CO + H_2O$$

arranging the expression of the equilibrium constant by introducing $P(H_2O)$, the following relation is obtained for a pure liquid phase:

$$\log P(CO_2) = 0.491 + 192.4/T + 0.979 \log T + \log (CO/H_2) + \log B(CO) - \log B(H_2)$$

where B(i) is the distribution coefficient for each gas species. From gas composition a value of $P_{CO_2} = 11.6$ bar is obtained.

For productive wells, where the gas/(total H_2O) and the reservoir temperature are known, the maximum value of $P(CO_2)$ in the aquifer can be computed, assuming a pure liquid phase, by the following equation:

$$\log P(CO_2) = \log (CO_2/H_2) + \log B(CO_2) + \log P(H_2O)$$

In our case for well ZK1203 a value of 12.8 bar is obtained. Gas composition can be used to compute equilibrium temperature. Two indipendent chemical equations can be used:

$$CH_4 + 3CO_2 = 4CO + 2H_2O$$

$$CH_4 + 2H_2O = 4H_2 + CO_2$$

the derived geothermometric equations for a pure liquid phase are:

$$4\log (CO/CO_2) - \log (CH_4/CO_2) = 4.73 - 12913.84/T + 0.719 \log T - 4\log B(CO) + 3\log B(CO_2) + \log B(CH_4)$$

$$4\log (H_2/H_2O) - \log (CH_4/CO_2) + 4\log P(CO_2) = -15.35 - 3952.8/T + 4.635 \log T + 4\log A(H_2) + \log A(CO_2) - \log A(CH_4)$$

where A(i) is a term related to the vapor fraction with respect to total water in the reservoir and the molal distribution coefficient B(i), (D'Amore and Truesdell, 1985). The computed temperature are respectively 110°C and 112°C for a $P(CO_2) = 11.6$ bar.
Reservoir fluid temperatures were also computed based upon both the thermal equilibrium of mineral assemblages and the application of some empirical geothermometers.
Computer program WATCH2 (Arnorsson et al., 1982) was used to perform calculations of dissolved species in thermal equilibrium with alteration minerals. Calculated reservoir equilibrium temperature by this method was 118 ± 6°C, with the following mineral assemblage: kaolinite, calcite, quartz, K-feldspar, Ca-Mg-Na-K montmorillonites, Mg-K-illite, K-mica, Mg-chlorite, fluorite, magnetite and goethite. Most of the minerals used in the mineral assemblage calculations perfomed have been found in the study of the local aquifer (Geothermal Geological Team, 1989).
The low enthalpy of fluids from the Nagqu geothermal system was confirmed by the application of some selected empirical geothermometers (average temperature 125 ± 9°C). Using gas composition (CO_2, H_2S, H_2 and CH_4) and the geothermometer of D'Amore and Panichi (1980) a temperature of 123°C was obtained. A summary of results obtained from the application of several empirical geothermometers follows:

Table 4. Computed temperatures with different geothermometers.

Geothermometer	Source	T,°C
Na-K-Ca-Mg	Fournier (1981)	114
Quartz(no steam loss)	Fournier and Potter (1982)	122
K-Mg	Giggenbach et al. (1983)	123
Na-Li	Kharaka et al. (1982)	137
Mg-Li	Kharaka and Mariner (1989)	132

Stable isotopes water composition

For both wells the following average Deuterium and $\delta^{18}O$ contents have been measured for the brine sampled at separation temperature of 96±1 °C:

$$\delta D = 149.8 \pm 0.5 \text{ (‰ VS. SMOW)}$$

$$\delta^{18}O = 18.0 \pm 0.05 \text{ (‰ VS. SMOW)}$$

Fig. 3 reports measured values as points A. Line B-C represents the local meteoric line drawn using data from Nyingzhong and Yangyixiang thermal areas for cold waters (Aquater, 1989). Point NZ11 corresponds to a lake located at an altitude of 5,050 m (asl). Point YX8 is the isotopic composition of a river whose recharge area is located at an average altitude of about 5,500 m (asl). On the other hand, line A-D has been drawn considering the theoretical isotopical composition produced by evaporation at 115°C. No major effects of water-rock interaction have been accounted for considering the low enthalpy of the system. According to this assumption, point D would represent the isotopical composition of meteoric water recharging the geothermal system. Since $\delta^{18}O$ values change of about 0.3 units every 100 m and considering the elevation of YX8 and NZ11, the recharge area indicated by point D has an average elevation of about 5,600 m (asl).

The absence of tritium in the water suggests a long residence time of the meteoric water in the reservoir, with an age exceeding 30 years. Then, we may exclude any mixing with local shallow waters. This can explain the good agreement between measured and computed temperatures using water composition.

Fluid Scaling Tendency

Produced fluids at Nagqu exhibited a high scaling tendency. Scale was made of $CaCO_3$ mainly. Scaling tendency was evaluated by means of the saturation index, I_S (Corsi, 1986):

$$I_S = \log \frac{[Ca^{++}]Alk^2}{P_T \cdot y_{CO_2}} + 10.22 + 2.739E\text{-}2\ T - 1.38E\text{-}5\ T^2 - 1.079E\text{-}8\ P_T - 2.52\ I^{1/2} + 0.919\ I$$

where I, $[Ca^{++}]$ and Alk are expressed in mol/l of water, P_T in Pa and T in °C. $I_S>0$ indicates a supersaturated scaling solution and $I_S<0$ an undersaturated solution.
The mole fraction of CO_2, y_{CO_2} was calculated from Dalton law:

$$P_{CO_2} = y_{CO_2} \ P_T$$

Calculated I_S value at reservoir conditions was 0.28; meanwhile at atmospheric conditions was 3.45. From these results, it is evident that produced fluid at reservoir conditions is slightly supersaturated, while at the end of the isoenthalpic flashing process shows a high scaling tendency. In fact, during the production tests carried out substantial diameter reductions were observed both in the surface lines and downhole.

PRODUCTION TESTING

Carbonate scale deposition, characteristic of productive wells in the Nagqu Field, affects both the production technology and the measurement procedures. As routinelly performed in productive wells of the Yangbajing field, located about 220 km south of Nagqu, carbonate scale deposits are mechanically removed using a heavy pipe lowered downhole by means of an electric winch. According to the experience gained in operating Yangbajing power plant, the method is effective for shallow wells when the scale build-up rate is not severe. In Nagqu wells, because of higher CO_2 partial pressure, the scale deposition is quite fast and the mechanical cleaning seems to be necessary each 2 to 4 days.

Production tests were performed during this study using the well known "lip method" established by James (1966). The output curves were determined with 3 production steps that lasted about 2 days each. Before each step, well ZK1203 was cleaned using the mechanical device, whereas well ZK1104, that produced previously only for testing purposes, was not cleaned. Different lip pipe diameters were used for the 3 steps (4", 5" and 6") on each well. A fourth production step on both wells was carried out mainly for interference test purposes.
During the processing of flow rate data, both the gas content of discharged fluid and the scale build-up at the lip pipe were accounted for, the former being the most important. The gas content in the pre-flashed fluid was estimated to be about 5,300 to 5,700 ppm in wells ZK1203 and 1104, respectively. Published methods to correct the lip pressure readings were applied since the effect of CO_2 partial pressure at lip conditions was proved to be quite high. In fact, although the gas content is not so high if compared with other geothermal fields, its effect becomes important because of low fluid enthalpy. Liquid enthalpy was calculated at flash conditions to be about 470 kJ/kg; thus the vapour phase mass fraction at lip conditions (pressure ranging between 1.10 and 1.79 bara) was very low, between 0.029 to 0.012 . The gas mass fraction in the vapour phase was relatively high, ranging from about 0.18 to 0.41, with gas partial pressure between 0.09 to 0.40 bar.
These figures were computed by simulating the isoenthalpic fluid flow from conditions at the producing zones, to atmospheric pressure (0.6 bara).
A thermodynamical package based upon the method proposed by Sutton (1976) and updated later by O'Sullivan et al. (1985) has been used with minor modifications as an equation of state for the H_2O-CO_2 system. To correct the lip pressure readings several methods were tested: James (1970), Karamarakar and Cheng (1980), Grant et al. (1982a) and Grant et al. (1982b). The first three proved to be quite consistent in the range of measured lip pressures, whereas the last one gave a higher correction. It was decided to use the method suggested by Karamarakar and Cheng, as it is based on a theoretical assessment of James' method made using two-phase flow models at the lip pipe. According to this method, correction to measured lip pressures are as follows:

$$Plip_c = Plip\ (1 - Y/m)$$

where:
Y = ratio between the mass of gas and steam in the vapour phase at lip conditions;

$$m = 2.4 - 9.6E\text{-}4\ (Plip - Patm) + Y$$

Corrected lip pressures were about 92 % and 77 % of original readings at lip pressures of 1.10 and 1.79 bara, respectively.

Another factor influencing flow rate measurements was the scale build-up inside the

lip pipe. Average scale thickness measured after two days of production was ranging between 2 and 7 mm; the thickness was higher in the smaller diameters. As a first approximation, a linear increase in scale thickness during production steps was considered to evaluate the actual lip pipe inside diameter to be used in James' equation.

PRODUCTION TESTS RESULTS

Production output curves determined on wells ZK1203 and 1104 are shown in Fig. 4 (Aquater, 1990).

The effect of non-condensible gases is evident in Fig. 5 where pressure profiles recorded in well ZK1203 under static conditions and during production steps of the output curve are plotted. Two-phase flow is clearly present above 100 m during the highest tested flow rate.
Temperature profile T3 recorded at the same time of P3 is also shown. The profile shows the quite uniform temperature distribution down to 700 m, with temperature ranging between 111.5 to 113 °C.
The effect of CO_2 content on boiling pressure can easily be seen in Fig. 6. It illustrates P-T data collected during dynamic surveys at well ZK1203, compared with the pure water saturation line if no dissolved gases were present. Taking into account the accuracy of P-T measurements, the departure from a nearly isothermal flow can be detected at a total pressure of about 14.5 ± 1.0 bara. Good agreement is obtained with the data measured in well ZK1104, which indicated a boiling pressure of about 16.0 ± 1.0 bara as well as with the values obtained through the processing of chemical data. The CO_2 partial pressure at boiling conditions is between 8 and 9 times the steam pressure, which is not a very common feature.

WELL TESTING

Pressure buildup tests

For the characterization of the reservoir, buildup tests were conducted at the two producing wells. Downhole pressure changes were measured by means of mechanical, Amerada-type pressure sensing-recording devices. An extremely fast pressure recovery was observed in all tests performed, which coupled with the limited accuracy of the mechanical type of sensors used, did not allow the recording of enough quality data to perform either adequate type-curve or semilog analyses.
Heavy leaks of fluids at the wellhead prevented a complete shut-in of the wells, and increased the difficulty of the analysis of the well tests.

Preliminary diagnosis analyses by means of log-log plots of both pressure-difference vs. time and pressure derivative function vs. time were performed. Matching of pressure-difference vs. time data to type-curve was not feasible due to the extremely short stabilization period and also the small range of pressure differences involved. On the other hand, matching of the pressure derivative function vs. time was not either possible due to the large scatter of data points even after performing several attempts of pressure derivative calculation using different smoothing parameters. Fig. 7 shows data from one of these tests. Type curves published by Bourdet et al. (1984) were used.

Interference Tests

To carry out interference tests, the two extreme wells ZK1005 and ZK1303 were chosen as observation wells, while internal wells ZK1104 and ZK1203 were active wells (see Fig. 1). Wellhead pressures and smoothed production data during the test are shown in Fig. 8. To ensure that wellhead measurements would provide reliable data, recordings of such measurements on well ZK1303 for one week previous to the start of the interference test were carried out, excluding in this way the possible effect of any gaseous column inside the well.
Interpretation of interference tests was carried out by means of type-curve matching procedures, using both a homogenous system and a naturally-fractured reservoir system models, applied to pressure response produced by a single production step, without accounting for the effect of previous steps.

A) Type-curve matching using a model for a homogenous system.

For this purpose, the type-curve for a homogeneous system published by Ramey (1980) was used. Interpretation equations for this model are as follows (nomenclature at the end of paper):

$$kh = 141.2\, q\mu B \left(P_D / \Delta P\right)_M$$

$$\phi c_t h = \frac{0.000264\, k\, h}{\mu r^2} \left(\frac{\Delta t}{t_D / r_D{}^2}\right)_M$$

Units in these eqs.are: k(md), h(ft), q(STB/day), P(Psi), B(STB/bbl), μ(cp), r(ft), t(hr), φ(fraction).

Fig. 9 shows the match of field data with the published type curve obtained for test period IT2 shown in Fig. 8. Table 4 below shows results obtained from matches during flow periods IT1 through IT3 of Fig. 8.

B) Type - curve matching using a double - porosity, naturally fractured system model.

Taking into account that from geological

Table 4. Results of field data matching with a homogenous reservoir model.

FLOW PERIOD	kh (d m)	$\phi\ c_t h$ (m bar^{-1})
IT1	402.1	269 E-5
IT2	455.7	343 E-5
IT3	338.5	53 E-5

evidence, reservoir rock consists of fractured-sedimentary rock, the use of a naturally fractured, double-porosity model seems justified. The model published by Deruyck et al. (1982) was used for the interpretation. It was found that the model that assumes transient interporosity flow between the system of fractures and the matrix blocks, better fitted measured field data and so it was the one selected.

Interpretation equations are as follows:

a) For the log-log analysis:

$$k_f h = 141.2\ q\ B\ \mu (P_D/\Delta P)_M$$

$$(\phi V c_t)_f\ h = \frac{0.000264\ k_f h}{\mu r^2} \left(\frac{\Delta t}{t_D/r_D^2}\right)_M$$

$$(\phi\ V\ c_t)_{f+M}\ h = \frac{(\phi\ V\ c_t)_f\ h}{\omega}$$

b) For the semilog analysis

$$k_f h = \frac{162.6\ q\ B\mu}{m}$$

$$(\phi\ V c_t)_{f+M}\ h = \frac{k_f h}{\mu r^2}\ 10^{-a}$$

$$a = \frac{P_{1h}}{m} + 3.23$$

Fig. 10 illustrates the match obtained for data from period IT2. A summary of results of fitting field data with the published type-curve is given in Table 5, below.

Fig. 11 shows a semilog plot of data from period IT2. From the slope of the straight line in this figure the following values for reservoir parameters are obtained:

$k_f h$ = 288 (d m)

Table 5. Results of field data matching with a double - porosity, naturally fractured system model.

Flow Period	$k_f h$ (d m)	ω	$(\phi\ V\ c_t)_{f+M} h$ (m bar^{-1})
IT1	287	1.0 E-2	100 E-4
IT2	314	1.5 E-2	174 E-4
IT3	299	*	*

* The test was too short and no response from the matrix was yet evident.

$(\phi\ V\ c_t)_{f+M}\ h$= 68.2 E-4 (m bar^{-1})

As it can be seen by comparison with results of the type-curve matches given in Table 5, the $k_f h$ value calculated with the semilog method agrees well with those calculated by the type-curve procedure; meanwhile, the storativity value is somehow lower.
Therefore, it can be concluded that the high transmissivities obtained from the type-curve analysis, confirm the presence of a highly fractured system, with transmissivity ranging between 338 to 456 d m if a homogenous system model is assumed or from 287 to 314 d m if a naturally fractured system model is considered. Based upon geological evidences, the later seems to be more realistic. In this model the fracture system acts as the main fluid conduits, while the matrix represents the main source of fluid storage.

FITTING OF INTERFERENCE DATA USING SIMPLE LUMPED PARAMETER MODEL

As can be seen in Fig. 8, the response of two observation wells seems to be very similar. The two sets of data showed a linear relationship with a unit slope and a standard deviation of 0.0099 bar. This result suggests that the effect of fluid extraction was to produce a quite uniform decline of pressure throughout the reservoir. In this case the use of lumped parameter models to interprete the interference data was considered suitable.

As a first approach the assumption of a steady state recharge to the reservoir from a supporting aquifer was evaluated according to the Schiltuis equation (Olsen, 1984). In this approach a mass balance takes into account three main contributions: the fluid produced from the system, the recharge to the system, and the liquid expansion in the reservoir due to the lowering of average reservoir pressure.
According to the Schiltuis assumption the water recharge is directly proportional to the pressure drawdown in the reservoir. The

aquifer will supply any rate extracted by the wells after an initial drawdown during which there is a pressure decline depending on the rate of production and reservoir storage coefficient. According to the conceptual reservoir model, the vertical recharge through faults and highly fractured zones was modeled considering a linear aquifer recharging the reservoir. Examining the results, it was concluded that this model was not able to provide a good fit of field data.

Next approach was to consider fluid recharge to the reservoir under transient conditions. Under these conditions reservoir behaviour is described by a material balance equation and a simplified solution to the diffusivity equation. The solution used was that presented by Hurst (Olsen, 1984 - Brock, 1986) for an infinite linear aquifer recharging the reservoir.
The characteristic parameter defined by Hurst for a linear system is a ratio of aquifer and reservoir parameters and a geometric factor. It is defined as follows:

$$\lambda = \frac{c_a \mu_a}{1\ c_r \mu_r}$$

The general solution to be used is as follows:

$$Po - P(tn) = B \sum_{j=0}^{n} \Delta W_j \quad M(\lambda^2 (t_D - t_{Dj}))$$

where:

$$M(\lambda^2 t_D) = \frac{1}{\lambda^2} (e^{\lambda^2 t_D} \quad erfc(\lambda \sqrt{t_D}) - 1 + \frac{2 \lambda \sqrt{t_D}}{\pi^{0.5}}$$

$$t_D = \frac{k_a}{\phi_a \mu_a c_a} t$$

for a linear infinite reservoir;

$$B = \frac{\mu_a c_a}{k_a V \varrho_R c_R}$$

For a given value of λ parameter, it is possible to determine the B parameter through a linear regression analysis using the least square criterion. The standard deviation of calculated pressure drops respect to the measured ones is determined at the same time. The solution is represented by the couple B-λ that gives the minimum standard deviation. Considering the data recorded at Nagqu field, the plot of standard deviation vs. λ does not show any minimum but it stabilizes around 0.023 bar for λ greater than about 0.1 m-1, slowly decreasig for λ --> ∞.

As pointed out by Brock (1986), under these conditions it is not possible to determine reservoir parameters, but by using a high value of λ in the flattened part of the curve, a history match and a prediction can still be performed. Under these conditions, the size of the reservoir can be considered as small compared with the size of the system (reservoir+aquifer), so that the reservoir has practically no influence in determining the system behaviour. Although this fact seems to be in good agreement with geological data suggesting a limited reservoir extension, it must be recognized that production period was short and that perhaps data collected under longer production history could show some features not evident during the period tested.
The history match is shown in Fig. 12, where calculated and measured pressures are plotted. Even if the history match can be considered satisfactory from the point of view of matching accuracy (standard deviation was 0.023 bar), the interpretation still has to be considered as a preliminary one. In fact, the interference test covers a short period of about 580 hours and a small amount of fluid extracted, about 48.6 Mkg, with a maximum pressure drawdown of only 0.43 bar.

PRELIMINARY ASSESSMENT OF RESULTS

Eventhough the reservoir is liquid dominated, the high partial pressure of non-condensible gases can be very important in determining both the natural reservoir state and future reservoir behaviour under exploitation. From analysis of data collected, it is evident that in the central part of the field, where vertical upflow of fluid at nearly constant temperature is present, boiling conditions should be reached at depths ranging from 100 to 120 m. This means that a two-phase zone could evolve in the upper part of the reservoir. If this two-phase shallow zone should be present, the reservoir compressibility would be higher than that coming from a liquid phase only, because of liquid vaporization as pressure decreases. This mechanism could furnish a support to pressure stabilization in addition to that supplied by the recharging aquifer.
The above mentioned mechanism could be important in altering reservoir behaviour respect to that of a pure liquid phase in case of long term industrial production. A mass rate extraction of about 80 kg/s has been estimated necessary to produce about 0.9 MWe with an air cooled binary cycle plant. The continous extraction at this level could produce an important reservoir depletion, extending downwards the two-phase zone.
To properly assess the feasibility of the preliminary results obtained in this study, longer production tests at rates close to 80 kg/s should supply additional data very helpful in assessing long term reservoir behaviour under industrial exploitation level

rates.

CONCLUSIONS

Based upon the analysis of the data collected from the tests performed at wells from the Nagqu Geothermal Field and the analyses performed at the fluid samples collected, the following conclusions can be withdrawn:

1. The area of geothermal field and its surroundings do not present any evidences of volcanic activity able to produce an anomalous thermal gradient. According to the values achieved with drilling, it can be noted that the thermal gradient decreases sharply outside the area of producing wells; furthermore the values of the thermal gradient are controlled by structural trends. In fact wells ZK1403 and ZK903 located 0.8 to 1.2 km respectively away from producing wells show gradients varying from 4.2 to 7.6 °C/100 m, while ZK807 located 2 km away from productive wells, but closer to an active tectonic trend shows a gradient of 14.5 °C/100 m (Geothermal Geological Team, 1989). The producing wells tested pratically exhibit no gradient, with temperature almost constant from about 200 m down to total depth and values between 113 to 115°C. This fact demonstrates the uprise of geothermal fluids along fault planes and lack of anomaly far from those planes. Crustal origin of dissolved gases is a further demonstration of the absence of any magmatic-type heat source.

2. According to the data provided by the Geothermal Geological Team (1989), cap rock and reservoir formations can not be distinguished. In fact the Quaternary deposits does not present any cover characteristics; below these depeposits, drilling of geothermal wells crossed mainly Jurassic formations represented by mudstone, siltstone and sandstone with very low to null primary permeability. Tectonic activity can produce fractured sandstone layers, which can act as storing levels for geothermal fluids; but limited lateral extension of such layers away from the faults, confines the interest of these reservoirs to the surroundings of the active faults. Such a conclusion is proved to be valid by the thermal gradient distribution obtained in the drilled wells.

3. The reservoir tapped by means of the wells drilled at the Nagqu field corresponds to a liquid dominated reservoir containing compressed water at a measured temperature between 113 and 115 °C. Estimated reservoir fluid temperatures from water rock equilibria and empirical geothermometers are in good agreement with measured temperature.

4. Produced fluids at the surface are two-phase with a steam content in the order of 5% at atmospheric conditions, and high gas content of about 5,500 ppm in total fluid. The pH in the reservoir has been computed as 5.8. Water is bicarbonate-alkaline and shows a strong scaling nature with deposition of $CaCO_3$.

5. From the behaviour shown by the reservoir during the interference test performed, a reservoir volume of limited extension could be inferred.

6. Matching of measured data by means of lumped-parameter models have shown that pressure drawdown in the reservoir under exploitation will be dependent on aquifer recharge. Recharge in the reservoir seems to be controlled by the uplift of hot fluids through vertical fractures.

7. Results obtained from the interpretation of the well testing program carried out in the field have shown that the reservoir behaves as a high-permeability, double porosity, naturally fractured system.

8. Preliminary forecast of future reservoir behaviour based upon the small amount of production data available and the high gas content, indicates that pressure drawdown at the reservoir induced by exploitation, could favour the evolution of a two-phase zone in the upper portion of the reservoir, as exploitation time proceeds.

9. For the two producing wells tested, the flashing zone under the flow rates ranges covered in determination of the characteristic production curves, was located between 100 and 130 m (from ground level).

10. The estimated boiling pressure ranges between 14.5 to 16.0 ± 1.0 bara.

11. A crustal origin has been identified for gas produced from both, the ^{13}C content in CO_2 and the relative position of the produced gas composition in a H_2-N_2-He diagram.

12. An underground circulation time greater than 30 years for the produced fluid was confirmed from the absence of tritium in fluids sampled. Departure of δD vs. $\delta^{18}O$ data from the meteoric straight line can be explained by a steam loss from the reservoir prior to well production. Presence of numerous small thermal manifestations all over the field seem to confirm this conclusion.

AKNOWLEDGEMENTS

The authors wish to acknowledge the U.N.D.P. (D.T.C.D.) and the Geothermal Development Corporation of Tibet Autonomous Region (PRC) for permission to publish this paper, and the Nagqu Prefecture Administration for its help in solving all logistic problems during field activities implementation.

NOMENCLATURE

Alk	alkalinity, mol/l
B	formation volume factor, m^3/m^3 (STB/bbl)
B(i)	distribution coefficient of gas i, dimensionless
c	compressibility, Pa^{-1} (psi^{-1})
h	producing formation thickness, m (ft)
I	ionic strenght, mol l^{-1}
Is	saturation index, dimensionless
k	permeability, m^2 (d m)
l	reservoir thickness, m (ft)
m	correction factor in Karamarakar equation, dimensionless slope from the semilog straight line, bar/cycle (psi/cycle)
P	pressure, bar (psi)
Patm	atmospheric pressure, bara
Plip	lip pressure, bara
P_T	total pressure, Pa
q_T	volumetric flow rate, m^3/h (STB/d)
Y	gas/steam ratio at lip conditions, dimensionless
Y_{CO2}	molar fraction of CO_2 in the vapor phase
Y_s	steam/total water ratio, fraction
r	radius, m (ft)
t	time, s (hr)
V	volume, m^3
X	mole fraction
ϕ	porosity, fraction
λ	Hurst parameter, m-1
μ	water dynamic viscosity, Pa s (cp)
ϱ	density, kg/m^3
ω	storativity ratio, dimensionless

Main subscripts:

a	aquifer
c	corrected
D	dimensionless
f	fracture
M	matrix
r	reservoir
t	total

REFERENCES

Aquater, 1989, "Preliminary Technical Report", U.N.D.T.C.D. Contract N. TCD-CON 9/89, Project N. CPR/88/007, unpublished report.

Aquater, 1990, "Engineering Services in the Nagqu Geothermal Field of Tibet (PRC)", U.N.D.T.C.D. Contract N. TCD-CON 9/89, Project N. CPR/88/007, unpublished report.

Arnorsson, S., Sigurdsson, S. and Svavarsson, H., 1982, "The chemistry of geothermal waters in Iceland. I. Calculation of aqueous speciation from 0° to 370°C", Geochim. Cosmochim. Acta, 46, pp. 1513-1532.

Barnes, I., Irwin, W.P. and White, D.E., 1978, "Global distribution of carbon dioxide discharges, and major zones of seismicity", U.S.G.S. Report, Water Resources Investigation, pp. 78-79.

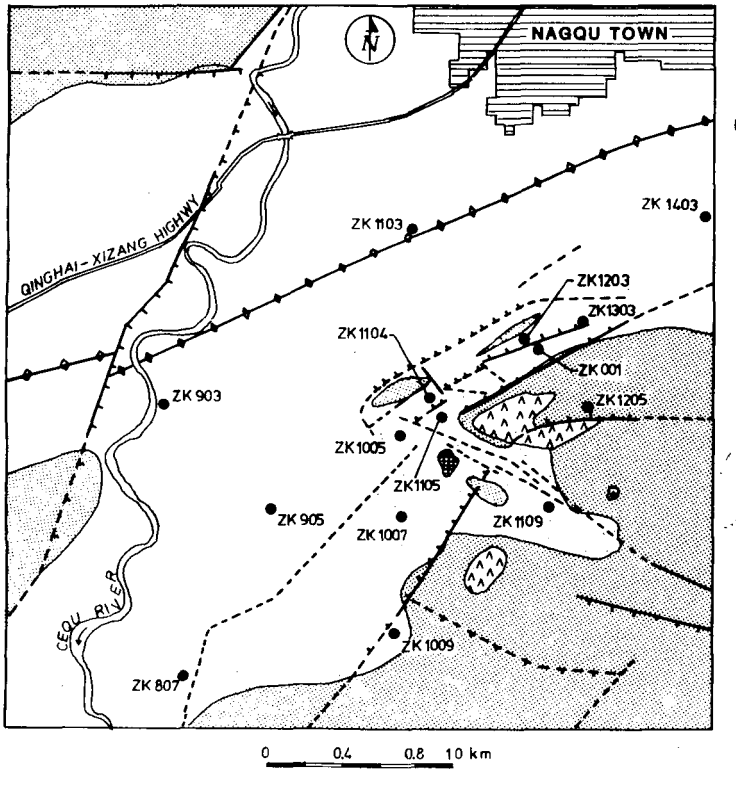

FIG.1

GEOLOGICAL SKETCH MAP OF NAGQU GEOTHERMAL FIELD

From: Geothermal Geological Team, B. G. M. R. of Tibet (1989) modified

LEGEND

- Sandstone and conglomerate (Neogene)
- Tuff (Upper Cretaceous)
- Sandstone (Jurassic)
- Mudstone (Jurassic)
- Fault, hachures on downthrown side
- Anticline axis
- ZK 1105 well location

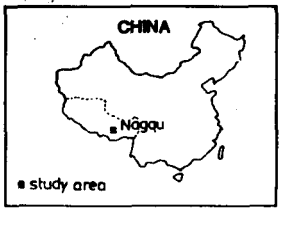

Bourdet, D.P., Ayoub, J.A. and Pirard, Y.M., 1984, "Use of Pressure Derivative in Well Test Interpretation", Paper SPE 12777, presented at the 1984 Cal. Reg. Meet., Long Beach, CA, April 11-13, 1984.

Brock, D. C., 1986, "Compressibility Effects in Modeling Two-Phase Liquid Dominated Geothermal Reservoirs", SGP-TR-102, Stanford University, Stanford, CA.

Chiodini, G. and Cioni, R., 1989, "Gas geobarometry for hydrothermal systems and its application to various Italian geothermal areas", Appl. Geochem., 4, pp. 455-464.

Corsi, R., 1986, "Scaling and corrosion in geothermal equipment: problems and preventive measures", Geothermics, Vol. 14, N. 5/6, pp. 839-856.

D'Amore, F. and Panichi, C. 1980, "Evaluation of deep temperatures of hydrothermal systems by a new gas-geothermometer", Geoch. Cosm. Acta, 44, pp. 549-556.

D'Amore, F. and Truesdell, A.M., 1985, "Calculation of geothermal reservoir temperatures and steam fractions from gas compositions", Geoth. Res. Counc. Trans., 9, Part. 1, pp. 305-310.

D'Amore, F., Fancelli, R., Saracco, L. and Truesdell, A.H., 1987, "Gas geothermometry based on CO content. Application in Italian Geothermal Fields", 12th Workshop on Geoth. Res. Eng., Stanford University, Stanford, CA, pp. 247-252.

D'Amore, F. and Truesdell, A.H., 1988, "A review of solubilities and equilibrium constants for gaseous species of geothermal interest"., Sci. Géol. Bull. Strasbourg, 41, 3-4, pp. 309-332.

Deruyck, B.G., Bourdet, D.P., Da Prat, G. and Ramey, H.J. Jr., 1982, "Interpretation of Interference Tests in Reservoirs with Double Porosity Behaviour-Theory and Field Examples", Paper SPE 11025 presented at the 57th Annual Fall Tech. Conf. and Ex. of the SPE of AIME, New Orleans, LA, Sept. 26-29, 1982.

Electricity Designing Institute of Southwestern China, 1989, "Report on Feasibility of Constructing Nagqu Geopower Station, Xizang (Tibetan) Autonomous Region, P. R. China", Index No. F075K, Ministry of Energy, Chengdu, Sichuan Province, unpublished report.

Fouillac, C., and Michard, G., 1981, "Sodium/lithium ratio in water applied to the geothermometry of geothermal waters", Geothermics, v.10, pp. 55-70.

Fournier, R.O., 1981, "Application of water geochemistry to geothermal exploration and reservoir engineering", Chapt. 4 in Geothermal Systems: Principles and Case Histories, L. Ryback and L.J. P. Muffler eds. Wiley New York, pp. 109-143.

Fournier, R.O., and Potter, R.W., 1982, "A revised and expanded silica (quartz) geothermometer", Geoth. Res. Couns. Bull., v. 11, pp. 3-9.

Fig. 2 Prospecting view of Nagqu field

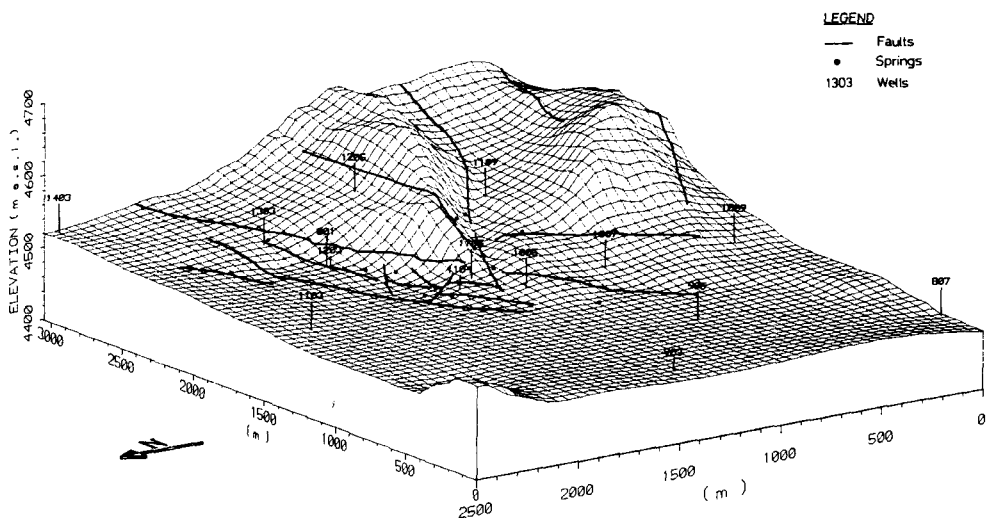

Geothermal Geological Team, 1989, "The report on the Feasibility Study of Nagqu Geothermal Field, Tibet, P. R. China", Bureau of Geology and Mineral Resources of Tibet, unpublished report.

Giggenbach, W.F., Gonfiantini, R., Jangi, B.L. and Truesdell, A.H., (1983), "Isotopic and chemical composition of Pazabati valley geothermal discharges, north-west Himalaya, India", Geothermics 12, pp. 199-222.

Giggenbach, W.F. and Goguel, R.L., 1989, "Collection and analysis of geothermal and volcanic water and gas discharges", New Zealand D.S.I.R. Report n. cd 2401, pp. 1-81.

Grant, M. A., Donaldson, I. G. and Bixley, P. F., 1982a, "Geothermal Reservoir Engineering", Academic Press.

Grant, M. A., James, R. and Bixley, P. F., 1982b, "A Modified Gas Correction for The Lip Pressure Method", Proc. 8th Workshop Geoth. Res. Eng., Stanford University, Stanford, CA.

Helgeson, H.C., Delany, J.M., Nesbitt, H.W. and Bird, D.K., 1978, "Summary and critique of the thermodynamic properties of rock-forming minerals", Am. J. of Sci., 278-A, pp. 1-229.

James, R., 1966, "Measurements of Steam-Water Mixtures Discharging at the Speed of Sound to the Atmosphere", New Zealand Eng., Vol. 2, Part 2, pp. 1676.

James, R., 1970, "Factors Controlling Borehole Performance", U.N. Symp. on the Dev. and Ut. of Geoth. Res., Pisa, Geothermics, Vol. 2, Part 2.

Karamarakar, M. and Cheng, P., 1980, "A Theoretical Assessment of James' Method for the Determination of Geothermal Wellbore Discharge Characteristics", Geoth. Res. Eng. Manag. Progr., LBL-11498, GREMP-12, UC-66a.

Kharaka, Y.K., Lico, M.S. and Law, C.M., 1982, "Chemical geothermometers applied to formation waters, Gulf of Mexico and California Basins (ABS.)", Am. Assoc. Petrol. Geol. Bull., 66, 588.

Kharaka, Y.K. and Mariner, R.H., 1989, "Chemical geothermometers and their application to formation waters from sedimentary basins", in Naeser N.D. and Mc Collon T.M. (EDS.), Thermal history of sedimentary basins, Springer-Verlag, New York, pp. 99-117.

Olsen, G., 1984, "Depletion Modeling of Liquid Dominated Geothermal Reservoirs", Master's Report, Stanford University, Stanford, CA..

O'Sullivan, M. J., Bodvarsson, G. S., Pruess, K. and Blakeley, M. R., 1985, "Fluid and Heat Flow In Gas-Rich Geothermal Reservoirs", Soc. of Pet. Eng. J., Apr. 1985, 215-226.

Ramey, H.J. Jr., 1980, "A Drawdown and Buildup Type - Curve for Interference Testing", 3rd Int. Well Test Symp., LBL, UC.

Sutton, F. M., 1976, "Pressure-temperature curves for a two-phase mixture of water and carbon dioxide", New Zealand J. of Sci., Vol.19, 297-301.

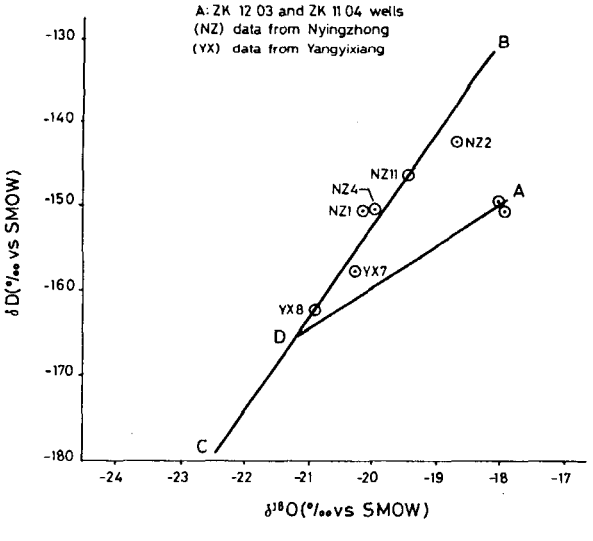

Fig. 3 Stable isotopes water composition

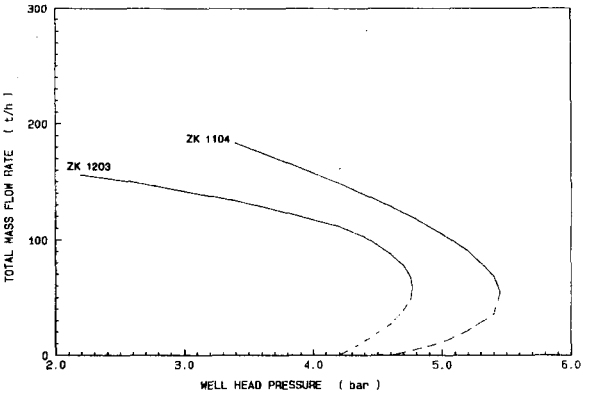

Fig. 4 Output curves of wells ZK 1104 and ZK 1203

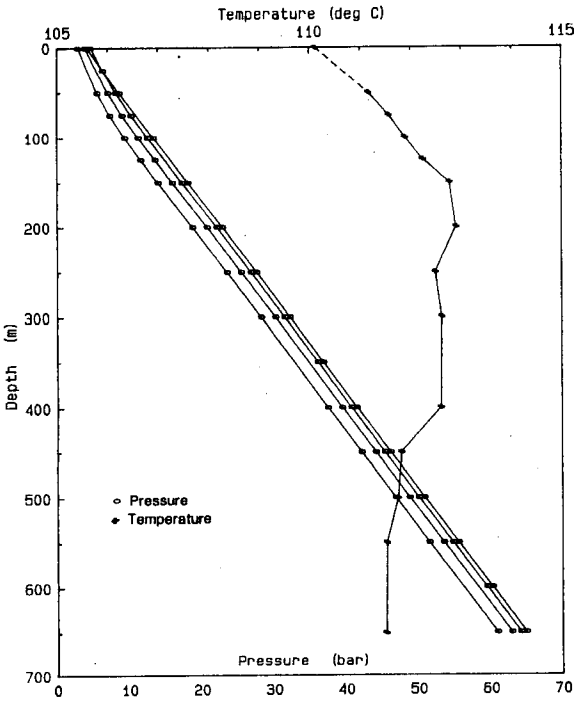

Fig. 5 Measured pressure and temperature profiles of well ZK 1203

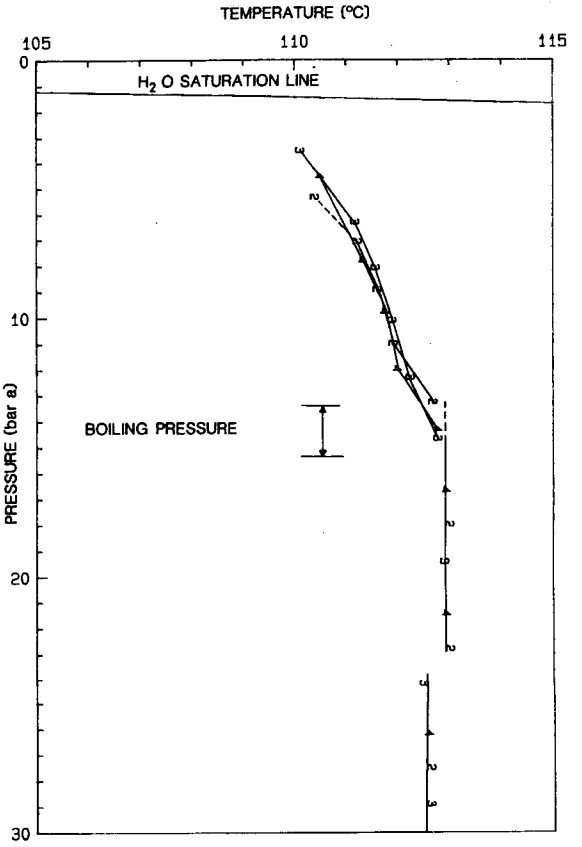

Fig. 6 Pressure-temperature data measured at well ZK 1203 compared with the H_2O saturation line

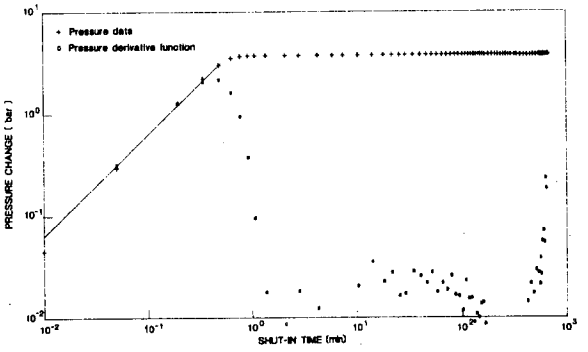

Fig. 7 Composite plot of pressure change and pressure derivative function vs. time for a build-up test performed at well ZK 1203 after IT1 production step

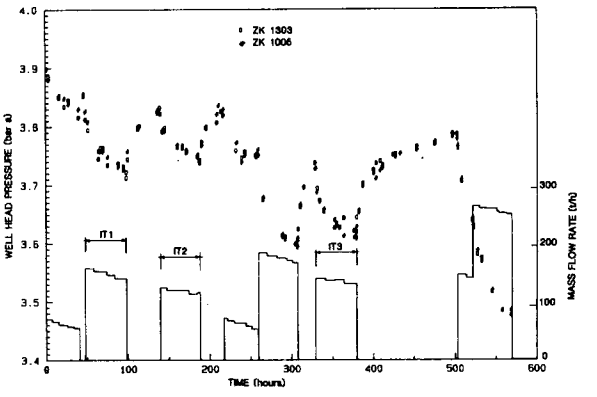

Fig. 8 Well head pressure and smoothed production history vs. time

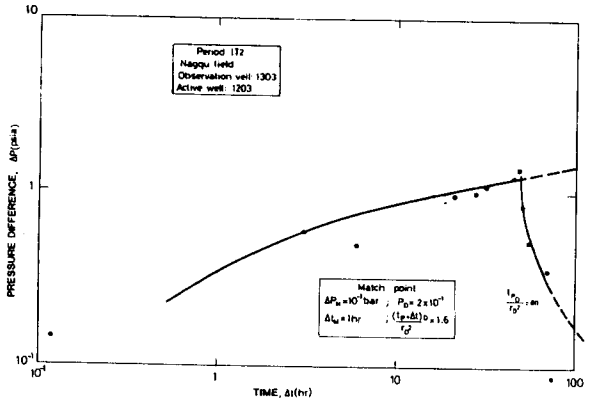

Fig. 9 Type curve match of data from period IT2 by means of a homogeneous model

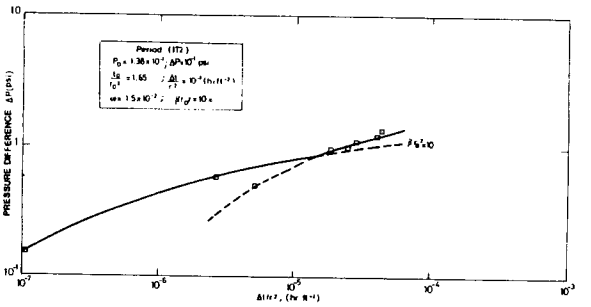

Fig. 10 Type curve match of data from period IT2 by means of a naturally- fractured, double porosity model

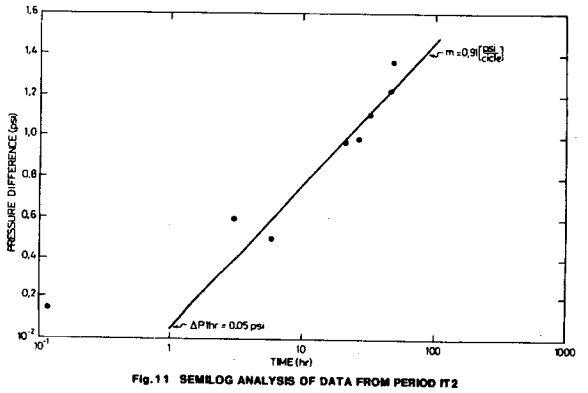

Fig. 11 Semilog analysis of data from period IT2

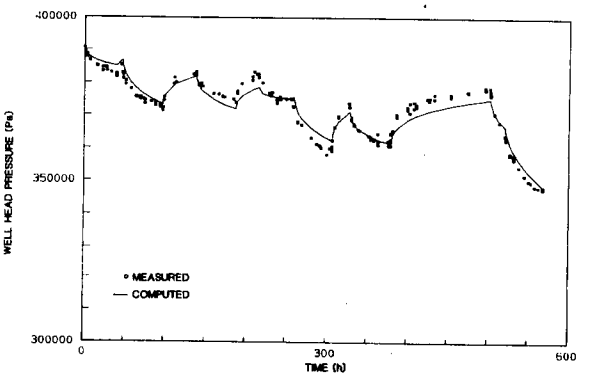

Fig. 12 Well head pressure data match using the lumped parameter model with water recharge according to Hurst simplified model

PROCEEDINGS, Sixteenth Workshop on Geothermal Reservoir Engineering
Stanford University, Stanford, California, January 23-25, 1991
SGP-TR-134

CONCEPTUAL GEOLOGIC MODEL AND NATIVE STATE MODEL OF THE ROOSEVELT HOT SPRINGS HYDROTHERMAL SYSTEM

D. D. Faulder

Idaho National Engineering Laboratory
P. O. Box 1625, Idaho Falls, ID 83415-2107

ABSTRACT

A conceptual geologic model of the Roosevelt Hot Springs hydrothermal system was developed by a review of the available literature. The hydrothermal system consists of a meteoric recharge area in the Mineral Mountains, fluid circulation paths to depth, a heat source, and an outflow plume. A conceptual model based on the available data can be simulated in the native state using parameters that fall within observed ranges. The model temperatures, recharge rates, and fluid travel times are sensitive to the permeability in the Mineral Mountains. The simulation results suggests the presence of a magma chamber at depth as the likely heat source. A two-dimensional study of the hydrothermal system can be used to establish boundary conditions for further study of the geothermal reservoir.

INTRODUCTION

The Roosevelt Hot Springs (RHS) hydrothermal system was the site of an active exploration program starting in 1974. A 500°F liquid-dominated reservoir was discovered through exploration drilling in 1975. The Roosevelt Hot Springs Unit (RHSU) was formed in April 1976 and was the first geothermal unit approved by the United States Department of Interior. A 25 MW_e geothermal power plant started operations in 1984. The location of the study area is shown in Figure 1.

The Roosevelt Hot Springs area has been used as a natural laboratory for the development and testing of geothermal exploration and evaluation methods, involving geologic, geophysical, geochemical, and reservoir testing. A literature review for the RHS system reveals over 180 geoscience titles. These many sources were used to develop a conceptual geologic model of the hydrothermal system.

This work was prepared for the U.S. Department of Energy under Contract No. DE-AC07-79ID01570.

A two-dimensional reservoir model of the hydrothermal system is used to investigate the conceptual model and the physical constraints of the system. The native state simulation study tests the conceptual geologic model and establishes reservoir boundary conditions. As the simulation study progresses, the conceptual geologic model provides a reference for adjusting reservoir parameters.

GEOLOGY

The RHS geothermal system is located on the eastern edge of the Basin and Range physiographic province and at the transition between the Colorado Plateau and the Basin and Range. The geothermal system lies to the west of the batholith of the Mineral Mountains, the first range west of the Wasatch Front. The Mineral Mountains are a north-south trending horst bounded by Basin and Range normal faults. A geologic map of the area is given in Figure 2.

Eruptive History

The Mineral Mountains intrusive complex has a history of magmatic activity since the Oligocene time (Neilson et al., 1986). The oldest phase began about 25 Ma with intrusives into Precambrian rocks. This pluton was then intruded by the main intrusive complex about 22 Ma. About 9.0 to 9.6 Ma an igneous sequence was emplaced. The earliest volcanic activity occurred 7.9 Ma along the west side of the range. The final volcanic episode started in the Twin Peaks volcanic complex about 2.7 Ma with the eruption of rhyolite domes and widespread basalt flows. The last rhyolitic volcanism occurred between .8 and .5 Ma and resulted in twelve domes in the central Mineral Mountains and the Bailey Ridge rhyolite flow just east of the reservoir. Chemical similarity of all the domes suggests they were derived form the same magma source (Ward et al., 1978).

Structure

The structural geology of the RHS has been studied by many workers. A brief description of the features that follows draws upon the work of Nielson et al. (1978), Ward et al. (1978), Bruhn et al. (1982), Ross et al. (1982), Nielson et al. (1986), and Nielson

(1989). The commercial geothermal reservoir is closely associated with the Negro Mag and Opal Dome Faults. Structural features are important in controlling the reservoir characteristics and boundaries.

The Negro Mag Fault is an east-striking, high angle, oblique slip with significant right lateral shear fault. This range cutting fault is the major driving fault defining local active structures and is active into the deep basement. The Negro Mag Fault is located along the axis of a complex graben structure 4 miles across. This graben forms a low in the crest of the Mineral Mountains, separating a Pleistocene rhyolite dome complex to the south from lower and more dissected ground containing no rhyolite domes to the north. The Bailey Ridge rhyolite appears to have erupted from faults associated with this graben, suggesting the structure has been present since at least the early Pleistocene.

The highly conspicuous Opal Mound Fault is a north-south normal fault marked by alluvial scarps, surface alterations, and opaline deposits which attest to geologically recent activity and extensive leakage of the reservoir along this feature. The Opal Dome Fault separates a graben to the east from a narrow horst to the west.

Low- to moderate-angle denudation faults occurs throughout the Mineral Mountains, but are most common in the geothermal area. The faults dip between 5° and 35° to the west with an estimated maximum depth of formation of 16,000 feet (Bruhn et al., 1982). These low-angle faults developed after the emplacement and consolidation of the Tertiary pluton complex and pre-date rhyolite domes and flows dated at 0.5 Ma.

The older, low-angle faults consist of up to 650 feet zone of cataclasis separating rocks of the Mineral Mountains intrusive complex from overlying sedimentary rocks. The Cave Canyon Fault represents this style of faulting.

A second series of listric normal faults occurs cutting principally rocks of the Mineral Mountains intrusive complex. The Wildhorse Canyon and Salt Cove Faults are representative of this style of faulting. The Wildhorse Canyon Fault is a continuous feature on the west side of the Mineral Mountains. This feature contains a number of NW, high angle cataclasite zones up to 12 feet thick in hills south of Big Cedar Cove. The Salt Cove Fault is a similar, parallel structure, east of the Wildhorse Canyon Fault.

The joint system through the central Mineral Mountains is relatively homogenous and consists of three major joint sets. Two sets of steeply dipping, sub-orthogonal extension joints trend northward and eastward, occurring roughly parallel and perpendicular to the strike of the contacts between igneous and country rocks. The joint spacing varies from 3 to 95 feet to less than two inches in areas of intense faulting. A third joint set consists of gently to moderately westward dipping joints generally having smooth planar surfaces with a joint spacing varying from greater than 3 feet to 4 inches in highly faulted areas. The joint system in the Precambrian rocks is similar to the pluton.

Geophysics

The surface heat flow map of the area clearly shows the location of the shallow geothermal reservoir, (Figure 3). Surface heat flow above the known reservoir is greater than 1000 mW/m^{-2}, with a large plume extending to the northwest, (Wilson and Chapman, 1980). Continuation with depth of the heat flow data shows an eastward extension along the Negro Mag fault. The large plume northwest of the intersection of the Negro Mag and Opal Dome Faults is associated with outflow from the geothermal reservoir. The regional heat flow is 92 mW/m^{-2}, while heat flow measured at depth from the Acord 1-26 well was 146 mW/m^{-2} (East, 1981).

The total aeromagnetic intensity residual map of the RHS area shows the dominance of east-west features that cut the Mineral Mountains and extend east into the Beaver Valley, reflecting the structure at depth.

Gravity modeling and filtering by Becker (1985) indicates an anomalous gravity low centered 13,000 - 20,000 feet below the reservoir with a density contrast of approximately -.15 g/cc. This result closely corresponds to work by Robinson and Iyer's (1981) investigation of P-wave structure of the crust and uppermost mantle. Their work showed a clear pattern of relatively low velocity (5 to 7 per cent less than the surrounding rock) material extending up from the upper mantle to a depth of about 16,000 feet under the west side of the Mineral Mountains. This plume is centered near the geothermal area, but extends to the north and south at depth. The degree of velocity change modeled would indicate a temperature increase of about 1080° to 1,530°F, indicating for typical crustal rocks some degree of melting.

Pre-production microseismic monitoring detected several episodic east-west swarms south of the Negro Mag Fault, (G. Zandt and D. Nielson, written communication). Focal depths were clustered at two distinct depths of 10,000 feet and 26,000 feet. The interval in-between was aseismic. The microseismicity demonstrates the Negro Mag graben system is still active, see Figure 2.

Geochemistry

The thermal waters were by characterized Capuano and Cole (1982) as a dilute sodium chloride brine, with approximately 7000 mg/l total dissolved solids. The Na-K-Ca and SiO_2 geothermometers indicate deep geothermal temperatures of 466° and 550°F for the Roosevelt seep and deep well fluid samples, respectively. Analysis of fluid samples from wells and springs in the RHS area suggests that they are derived from a common reservoir source, with variations due largely to mixing with shallow groundwater. The least mixing of thermal fluids with the shallow groundwater occurs for wells in close proximity with the Negro Mag Fault (Vuataz and Goff, 1987).

The stable isotopic composition of the thermal fluids indicates they are of meteoric origin with the water derived primarily from the Mineral Mountains with perhaps some contribution from the Tushar Mountains to the east, (Bowman and Rohrs, 1981). The thermal fluids have a δD value of -116 and a $\delta^{18}O$ value of -13.7. Stable isotopic studies of the age of Great Basin thermal waters by Flynn (1990) suggest the RHS waters may be 10,000 to 15,000 years old, (Flynn, personal communication). Tritium content of the thermal fluids are very low, $\leq$ 1 TU, (Vuataz and Goff, 1987).

Several attempts have been made to date the age of the hydrothermal system. Paleo-magnetic dating of opal from the Opal Dome suggest a minimum age of 12,000 years and a length of activity from 35,000 to 70,000 years. There were correlative problems and the maximum age could be as old as 350,000 years, (Brown, 1977). Hydration dating of obsidian in the alluvium yielded ages of 220,000, 257,000, and 330,000 years, (Bryant et al., 1977). These dates are maximum times for obsidian hydration in alluvium based on a hydration rate at 40°F, (Parry et al., 1978). The range of all these dates are poorly constrained.

Hydrology

The shallow alluvial aquifer west of the RHS area has a potentiometric surface dipping northwest toward the Milford Valley (Mower and Cordova, 1974,). Flow in the aquifer is stratigraphically controlled by flow in horizontal, permeable Quaternary alluvial deposits of sands and gravels. Concentrations of boron and chloride in the aquifer clearly show a large outflow plume from the high temperature thermal system trending northwest down the hydrologic gradient (Vuataz and Goff, 1987). The outflow plume is leaking over the Opal Dome horst, with the plume centered at the intersection of the Opal Dome and Negro Mag faults. The Opal Dome horst acts as a hydrologic barrier to the geothermal reservoir.

A aquifer test was made in well 26-9-18. The test results indicate a permeability of 1560 mD, assuming an aquifer thickness of 320 feet (Vuataz and Goff, 1987). The thickness of the principal aquifer west of Negro Mag Wash varies from greater than 500 feet west of the reservoir to 100 to 300 feet in the center of Milford Valley (Mower and Cordova, 1974).

The central Mineral Mountains receive an average annual precipitation of 16 to 25 inches, at elevations of 6400 to 8600 feet (Mower and Cordova, 1974). Vautaz and Goff concluded the shallow aquifer was recharged by precipitation in the Mineral Mountains with a minimum residence time of 70 years. The total recharge in the Mineral Mountains was estimated by Smith (1980) at 7650 acre-ft/year. An estimated 650 acre-ft of this total is available for the RHS area. The elevation difference of more than 980 feet between Beaver Valley and Milford Valley may allow some component of inter-basin flow.

RESERVOIR ENGINEERING

The primary reservoir has a reported fluid volume of 19 billion barrels from two long-term flow tests (three months and nine months) of a single well, RHSU 54-3 (Kerna and Allen, 1984). Assuming a primary reservoir dimension of 10,000 by 23,000 feet (from heat flow data) and 10,000 feet deep (2500 feet below the deepest well), an average total porosity of 4.7% is calculated. Well test information indicates the wells are able to flow from 300 Klbm/hr to over 1,000 Klbm/hr (Butz and Plooster, 1979) or receive injectate at rates of up to 1,850 Klbm/hr (Rosser et al., 1984), indicative of a highly fractured reservoir .

Applying the concept of a permeability window (Forster and Smith, 1989) and assuming a bulk permeability of ~.01 mD representative of granite, maximum temperatures will from a fracture permeability of ~1000 mD. This estimate is in agreement with the qualitative assessments of reservoir permeability above.

The pre-exploitation reservoir pressure in RHSU 14-2 is 1365 psia at 2950 ft below the surface, (Butz and Plooster, 1979). This pressure is assumed to be representative of the geothermal reservoir.

Temperature data was compiled from several sources, (Wilson and Chapman, 1980, Shannon et al., 1983). A comparison of several wells in the RHS area show three types of profiles, two conductive and one convective, (Figure 4). The Acord 1-26 well measured a bottomhole temperature of 446°F at 12,645 feet, and a gradient at depth of 2.95°F/100 feet. The Acord 1-26 profile was extrapolated from these measurements. This profile closely matches the RHSU 24-36 profile to about 3000 feet, with RHSU 24-36 showing hotter temperatures and a slightly higher gradient below this depth,

suggesting a closer proximity to a heat source. RHSU 24-36 is located north-east of the known geothermal reservoir and at a higher elevation. The RHSU 9-1 and RHSU 52-21 profiles are intermediate in temperatures, with a similar gradient as the Acord, but hotter. These two wells are located in close proximity to the geothermal reservoir but are non-productive. The RHSU 14-2 and RHSU 72-16 profiles show a convective system at 500°F. Extrapolation of the RHSU 24-36 and RHSU 14-2 profiles indicates an intersection at approximately 12,000 feet. This depth is similar to the shallow depth of micro-seismicity.

CONCEPTUAL MODEL

A conceptual model of a hydrothermal system needs to address four components of a dynamic flow system: fluid recharge, fluid circulation paths, a heat source, and an outflow plume. The geothermal reservoir at Roosevelt Hot Springs can be modeled as a dynamic flow system into and out of a intensively fractured graben.

Meteoric recharge is primarily from precipitation on the crest and west flank of the central Mineral Mountains. A small contribution from inter-basin transfer from Beaver Valley to the east to Milford Valley through the Negro Mag graben structure is possible.

Downward circulation of recharge waters occur in the Mineral Mountains east of the geothermal reservoir. The extensive joint and fracture system coupled with the complex east-west graben associated with the Negro Mag fault allows meteoric waters to circulate to depths controlled by the presence of open fractures. Microseismicity suggests open fractures may exist at depths of 10,000 and 26,000 feet. The waters heat up at depth and flow hydrologically down gradient until they encounter deep-seated normal faults such as the Opal Dome and/or Negro Mag Faults. Upwelling occurs along these high permeability features, with lateral flow into the Opal Dome graben. The intersection of the Opal Dome and Negro Mag grabens and the low angle faults provides an intensively fractured geothermal reservoir for the thermal fluids. Circulation in the reservoir takes place in the complex, well- developed, three-dimensional permeability structure.

Two sources of heat for the hydrothermal system need to be considered: deep circulation in an area with high regional heat flow, or a shallow magma chamber. Both possibilities can be investigated through simulation studies. The preferred heat source at RHS is the plume of partial melt material under the western, central Mineral Mountains. As modeled by Robinson and Iyer (1981), and Becker (1986), this plume extends from a depth of about 16,000 feet to at least as far as the upper mantle. The 16,000 feet depth has been inferred by Nielsen et al. (1986) to be at approximately the brittle-ductile boundary. Thus, open fractures could be supported to this depth and provide permeable pathways for convecting water. Cooling of the magma chamber with time could result in the development of deeper fractures.

The outflow of thermal water occurs over the Opal Dome horst and is centered at the intersection of the Opal Dome and Negro Mag faults. A plume of hot water then mixes and dilutes with cooler water in the shallow aquifer as it flows down the hydrologic gradient to Milford Valley.

A schematic of the conceptual model is presented in Figure 5. The location of select wells is projected on the figure. Key features of the conceptual model are identified.

The deep structure of the Roosevelt hydrothermal system is a matter of conjecture, with the possibility that a hotter, deeper system may exist below the known reservoir. The microseismic gap between 10,000 and 26,400 feet suggests the presence of an intermediate impermeable seal, allowing a second, deeper, hotter system to develop with leakage between the two systems occurring through the deep-seated normal faults. A hotter system is also suggested by extrapolation of the temperature profile data with an intersection at about 12,000 feet. A continuation of the RHSU 24-36 profile suggests a deeper system could exist with some leakage into the shallow system, with insufficient residence time be detected by geochemistry. The presence of deeper, hotter systems below geothermal reservoirs has been documented for The Geysers (Walters, 1988) and suggested for Valles Caldera (Hulen et al., 1989) and Dixie Valley (Doughty et al., 1990).

NATIVE STATE SIMULATION OF THE HYDROTHERMAL SYSTEM

A two-dimensional, east-west vertical cross-section was used to simulate the conceptual geologic model. The model length is 41,250 feet covering the crest of the Mineral Mountains to the center of Milford Valley, a distance with a surface relief of 3,200 feet. A numerical grid of 20 by 8 blocks was used in these simulations. The ground surface defines the top of the model with a depth of 19,800 feet below the ground surface. The simulation studies were performed using TETRAD, a fully implicit, finite difference geothermal simulator, (Vinsome, 1990). The simulator has been validated against a number of geothermal problems and yields results comparable to those published elsewhere (Stanford Special Panel on Geothermal Model Intercomparison Study, 1980).

A basal heat flux of 150 mW/m^2 was assumed. The initial temperature distribution was based on the Acord 1-26 temperature profile. The Mineral Mountains side was modeled as a no-flow boundary at depth. A constant pressure

boundary on the Milford Valley side, with a pressure gradient assigned according to the temperature profile of the Acord 1-26 well was used. The high water table configuration of Smith (1980) was used. This configuration closely matched the elevations of springs in the Mineral Mountains noted by Vuataz and Goff (1987). Meteoric recharge at a temperature of 40°F was approximated using steady state aquifers at the water table to the east of the geothermal reservoir. The actual recharge rate is unknown, but a range of 1% to 5% of the annual precipitation in the Mineral Mountains is considered to be realistic.

The permeability of the Mineral Mountains massif was estimated from the joint system distribution of the Central Mineral Mountains. The fracture width is unknown so a width of 100 μm was used. A fracture width of 100 μm and a joint spacing 3 to 100 feet, results in fracture permeability range from Reiss (1980) of 167 mD to 5.6 mD, respectively. A matrix permeability of 0.01 mD was assumed and calculating the system average permeability by the method of Aguilera (1980) results in an average permeability of 0.027 mD to 0.010 mD. Values of 0.5 mD and 0.05 mD were used for the mountain massif. These values are higher than calculated above, but were used to establish an upper limit. The massif is located east of the reservoir and extends to a depth of about 15,000 feet. The average permeability in the Mineral Mountains influences the fluid travel time from meteoric recharge to the geothermal reservoir. A porosity of 1% was used.

The structural complexity of the geothermal reservoir was reduced by assuming the Opal Dome Fault is a high permeability zone extending to about 17,000 feet. This simplification ignored the role of the Negro Mag Fault as the major driving fault defining local active structures. This deep seated high permeability zone is a synthesis of the Opal Dome and Negro Mag faults features. A permeability of 500 mD, reducing with depth to 10 mD, was used for this feature. The Opal Dome horst was assigned a permeability of 0.001 mD.

The shallow aquifers west of the geothermal reservoir was given a permeability of 1000 mD and 500 mD, decreasing with depth to 0.01 mD. The horizontal and vertical permeability structure used in the study is presented in Figures 6 and 7.

A straight line relative permeability relationship was used with a residual water saturation of 25% and a residual gas saturation of 1%.

Results

Simulation runs were made to adjust the model, calibrate the location of the water table, and investigate model sensitivity to the permeability structure. The model is extremely sensitive to the permeability in the mountain massif. A uniform basal temperature of 639° F, based on the Acord 1-26 profile was used. A tracer component with the same properties of water was used to track recharge flow paths and travel times.

A model run using a permeability of 0.5 mD in the mountain massif clearly shows the cooling of the mountain massif, the upwelling in the high permeability fault zone, and the shallow outflow plume. Thus the essential features of a hydrothermal system were present. The model temperatures and pressures reached steady-state conditions after about 30,000 years. The temperatures in the shallow geothermal reservoir range from 169° to 254°F (Figure 8) and had a fluid travel time of about 800 years. The steady state recharge rate was 35 Klbm/hr. This implies an annual meteoric recharge of 1.11 inches (113 acre-ft) for a model width of 3,000 feet.

A second simulation used a reduced permeability in the mountain massif of 0.05 mD. The model temperatures reached steady-state conditions after 50,000 years. The temperatures in the shallow reservoir range from 204° to 353°F (Figure 9) and had a fluid travel time of about 8,000 years. The steady state recharge rate was 12 Klbm/hr, implying an annual meteoric recharge rate of .38 inches.

The 0.05 mD case generally results in simulated temperatures within 30°F measured in outlying wells Acord 1-26, RHSU 24-36, and RHSU 9-1. However, the temperature in the geothermal reservoir is several hundred degrees cooler than measured. It appears that the high temperatures observed in the geothermal reservoir are unlikely to be due solely to a high regional heat flow and suggests the presence of a magma chamber.

The simulated recharge rate implies a recharge of about 2% of the annual precipitation in the central Mineral Mountains. This is a reasonable value for the arid climate in the study area.

CONCLUSIONS

A conceptual model based on available data can be simulated using values of parameters that fall within observed ranges.

Model temperatures, recharge rates and fluid travel times are sensitive to the permeability in the Mineral Mountains.

The boundary conditions for further simulation of the geothermal reservoir can be established by two-dimensional native state simulation.

ACKNOWLEDGEMENTS

Special thanks to Mr. Jim Moore, California Energy Company, Inc. for permission to present temperature profile data from well RHSU 24-36.

REFERENCES

Aguilera, R., Naturally fractured reservoirs, PennWell Publishing Company, Tulsa, p. 258, 1980.

Becker, D. J., Modelling of the hydrothermal system, Mineral Mountains vicinity, Utah, Masters Thesis, Southern Methodist University, 136 p., 1985.

Bowman, J. R. and D. T. Rohrs, Light stable isotope studies of spring and thermal waters from the Roosevelt Hot Springs and Cove Fort/Sulphurdale areas and of clay minerals from the Roosevelt Hot Springs area, Dept. of Geology and Geophysics, Univ. of Utah, DOE/ID 12079-44, 36 p., 1981.

Brown, F. H., Attempt at paleomagnetic dating of opal, Roosevelt Hot Springs KGRA, Univ. of Utah, IDO-1601-T5, 15 p., 1977.

Bryant, N.L., W. T. Parry, Hydrothermal alteration at Roosevelt Hot Springs KGRA - DDH 1976-1, Dept. of Geology and Geophysics, Univ. of Utah, DOE/ID/01601-T9, 96 p., 1977.

Bruhn, R. L., M. R. Yusas, and F. Huertas, Mechanic of low-angle faulting: an example from Roosevelt Hot Springs geothermal area, Utah, *Tectonphysics*, 86, p. 343-361, 1982.

Butz, J. and M. Plooster, Subsurface investigation at the Roosevelt KGRA, Utah, Denver Research Inst., CO, DOE/ET/28389-1, 81 p., 1979.

Capuano, R. M. and D. R. Cole, Fluid-mineral equilibria in a hydrothermal system, Roosevelt Hot Springs, Utah, *Geochimica et Cosmochimica Acta*, 46, 1353-1364, 1982.

Doughty, C., G. S. Bodvarsson, and W. R. Benoit, Reservoir model studies of the Dixie Valley geothermal field, Lawrence Berkeley Laboratory, LBL-29126, 14 p., 1990.

East, J., Hot dry rock geothermal potential of Roosevelt Hot Springs area: review of data and recommendations, Los Alamos National Lab, LA-8751-HDR, 46 p., 1981.

Forster, C. and L. Smith, The influence of groundwater flow on thermal regimes in mountainous terrain: a model study, *Journal Geophysical Research*, 94(B7), p. 9439-9451, 1989.

Flynn, T. and P. K. Buchanan, Geothermal fluid genesis in the Great Basin, Division of Earth Sciences, Univ. of Nevada, Las Vegas, DOE/ID/12784-1, 165 p., 1990.

Geothermex, Geothermal reservoir assessment of Roosevelt Hot Springs, Geothermal Power Company, Novato, CA, DOE/ET/28406-1, 81 p., 1982.

Goff, F., F. D. Vuataz, and C. O. Grigsby, The hydrothermal outflow plume of Valles Caldera, New Mexico and a comparison with other outflow plumes, *Journal of Geophysical Research*, 93(B6), p. 6041-6058, 1988.

Hulen, J. B., Gardner, J,. N., F. Goff, D. L. Nielson, J. N. Moore, J. A. Musgrave, M. M. Lemieux, K. Meeker, and M. G. Snow, The Sulphur Springs hydrothermal system, past and present: initial results from continental scientific drilling program corehole VC-2B, Valles Caldera, New Mexico, Geothermal Resources Council, *Transactions*, Vol. 13, p. 149-156, 1989.

Kerna, M. J. and T. S. Allen, Roosevelt Hot Springs development, a case history, Geothermal Resources Council, *Transactions*, Vol. 8, p. 75-77, 1984.

Mower, R. W. and R. M. Cordova, Water resources of the Milford area, Utah with emphasis on ground water, State of Utah Department of Natural Resource Technical Publication No. 43, 106 p., 1974.

Mower, R. W., Hydrology of the Beaver Valley area, Beaver County, Utah with emphasis on ground water, State of Utah Department of Natural Resource Technical Publication No. 63, 90 p., 1978.

Nielson, D.L., Stress in geothermal systems, Geothermal Resources Council,*Transactions*, Vol. 13, p. 271-276, 1989.

Nielson, D. L., S. H. Evans, and B. S. Sibbett, Magmatic, structural, and hydrothermal evolution of the Mineral Mountains intrusive complex, Utah, *Geological Society of America Bulletin*, 97, p. 765-777, 1986.

Nielson, D. L., B. S. Sibbett, D. B. McKinney, J. B. Hulen, J. N. Moore, S. M. Samburg, Geology of Roosevelt Hot Springs KGRA, Beaver County, Utah, Univ. of Utah Research Institute, IDO/78-1701.b.1.1.3, 120 p., 1978.

Parry, W. T., N. L. Bryant, R. E. Dedolph, J. M. Ballantyne, G. H. Ballantyne, D. T. Rohrs, and J. L. Mason, Hydrothermal alteration at the Roosevelt Hot Springs thermal area, Utah, Dept. of Geology and Geophysics, Univ. of Utah, DOE/ET/28392-17, 38 p., 1978.

Reiss, L. H., The reservoir engineering aspects of fractured formations, Gulf Publishing Company, Houston, p. 71-77, 1980.

Robinson, R. and H. M. Iyer, Declination of a low-velocity body under the Roosevelt Hot Springs geothermal area, Utah, using teleseismic P-wave data, *Geophysics*, 46(10), p. 1456-1466, 1981.

Ross, H. P., D. L. Nielson, and J. N. Moore, Roosevelt Hot Springs geothermal system, Utah-case study, *American Association of Petroleum Geologist Bulletin*, 66(7), p. 879-902, 1982.

Rosser, J. R., M. A. Payne, and T. S. Allen, An update on the role of step-rate injectivity testing in liquid dominated, highly fractured geothermal reservoirs, Geothermal Resources Council, *Transactions*, Vol. 8, p. 343-348, 1984.

Shannon, S. S., Jr., R. Pettitt, J. Rowley, F. Goff, M. Mathews, and J. J. Jacobson, Acord 1-26 Hot, dry well, Roosevelt Hot Springs hot dry rock prospect, Utah, Los Alamos National Laboratory, LA-9857-HDR, 15 p., 1983.

Smith, L., Model study of the regional hydrogeological regime, Roosevelt Hot Springs, Utah, University of Utah, DOE/ET/29392-44, 39 p., 1980.

Vinsome, P. K. W., TETRAD user manual, DYAD Engineering, Calgary, Alberta, 190 p. 1990.

Vuataz, F. D, and F. Goff, Water geochemistry and hydrogeology of the shallow aquifer at Roosevelt Hot Springs, Southern Utah, Los Alamos National Laboratory, LA-11160-HDR, 63 p., 1987.

Walters, M. A., J. N. Sternfield, J. R. Haizlip, A. F. Drenick, and J. Combs, A vapor-dominated reservoir exceeding 600°F at The Geysers, Sonoma County, California, Proceedings Thirteenth Workshop on Geothermal Reservoir Engineering, Stanford Univ., Stanford, CA, SGP-113, p. 73-81, 1988.

Ward, S. H., W. T. Parry, W. P. Nash, W. R. Sill, K. L. Cook, R. B. Smith, D. S. Chapman, F. H. Brown, J. A. Whelan, and J. R. Bowman, A summary of the geology, geochemistry, and geophysics of the Roosevelt Hot Springs thermal area, Utah, *Geophysics*, 43(7), p. 1515-1542, 1978.

Wilson, W. R. and D. S. Chapman, Three topical reports: I. Thermal studies at Roosevelt Hot Springs, Utah, II. Heat flow above an arbitrarily dipping plane of heat sources, III. A datum correction for heat flow measurements made above on an arbitrary surface, Dept. of Geology and Geophysics, Univ. of Utah, DOE/ID/12079-19, 144 p., 1980.

Figure 1 Location of Roosevelt Hot Springs hydrothermal system.

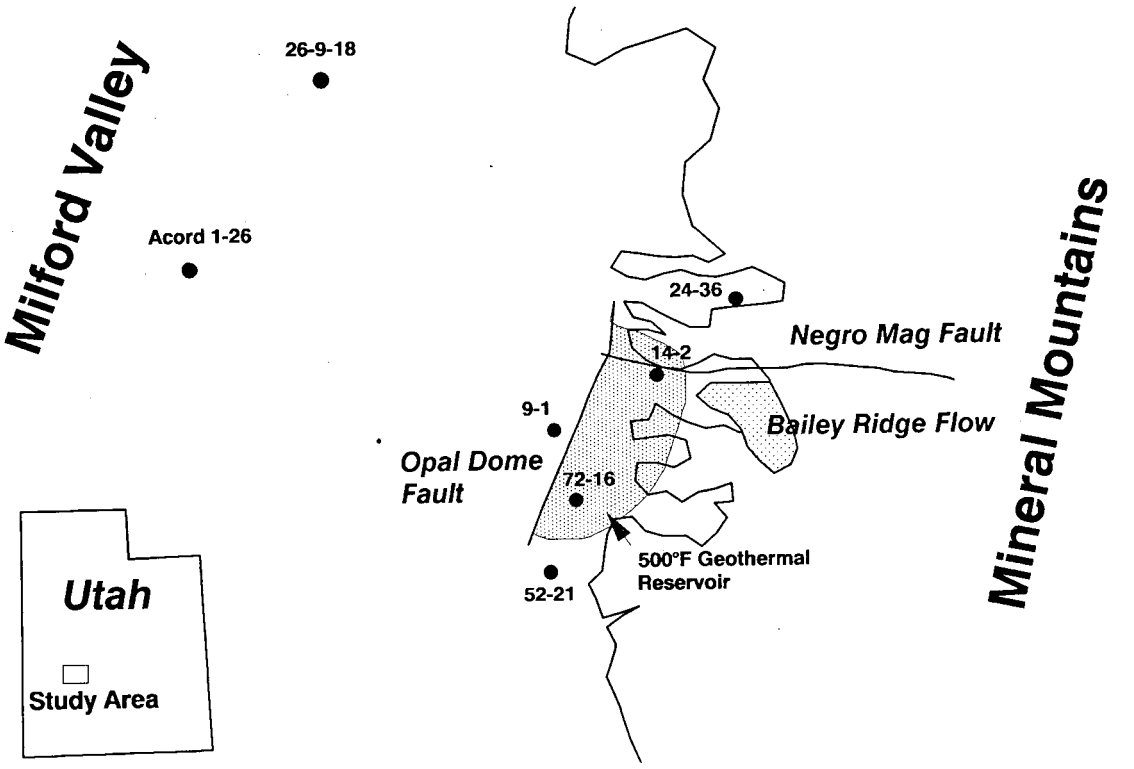

Figure 2 Geologic map of Roosevelt Hot Springs showing mapped faults and pre-production seismicity from Nielson (1989).

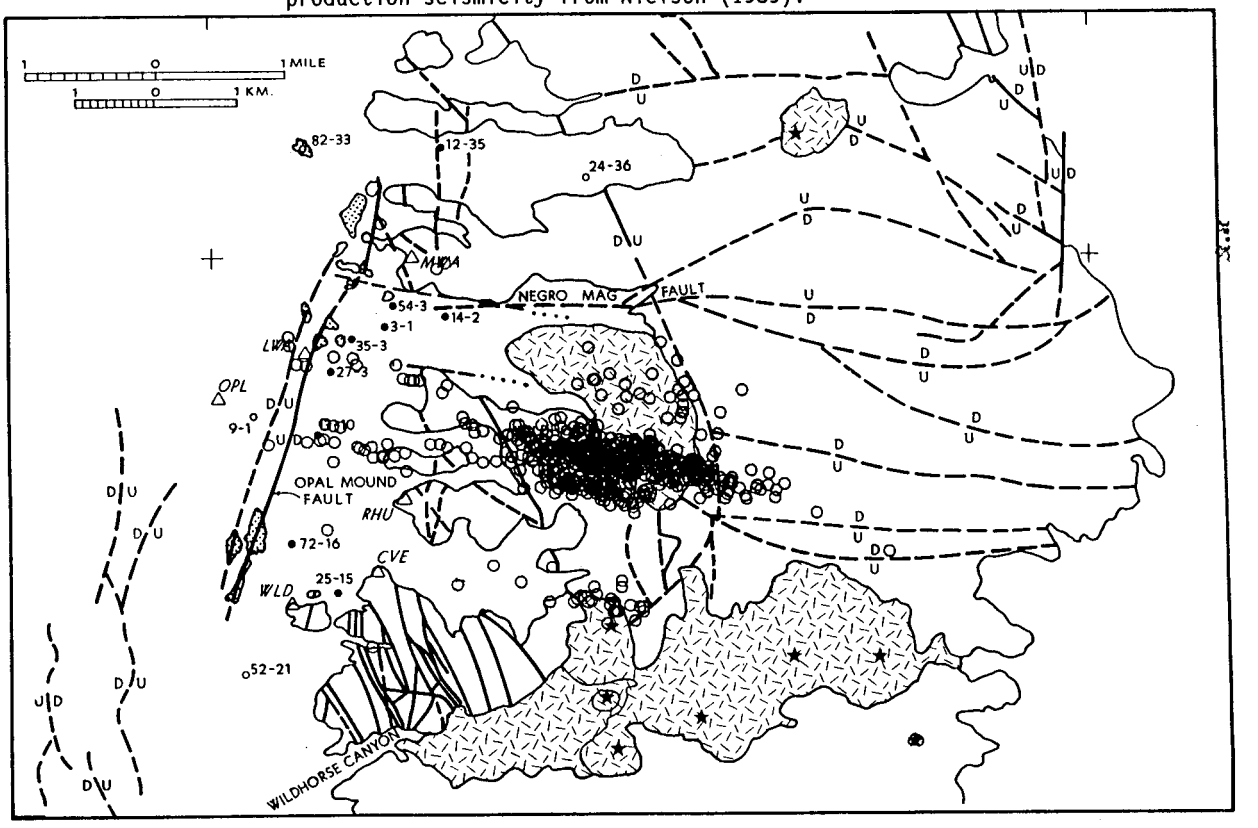

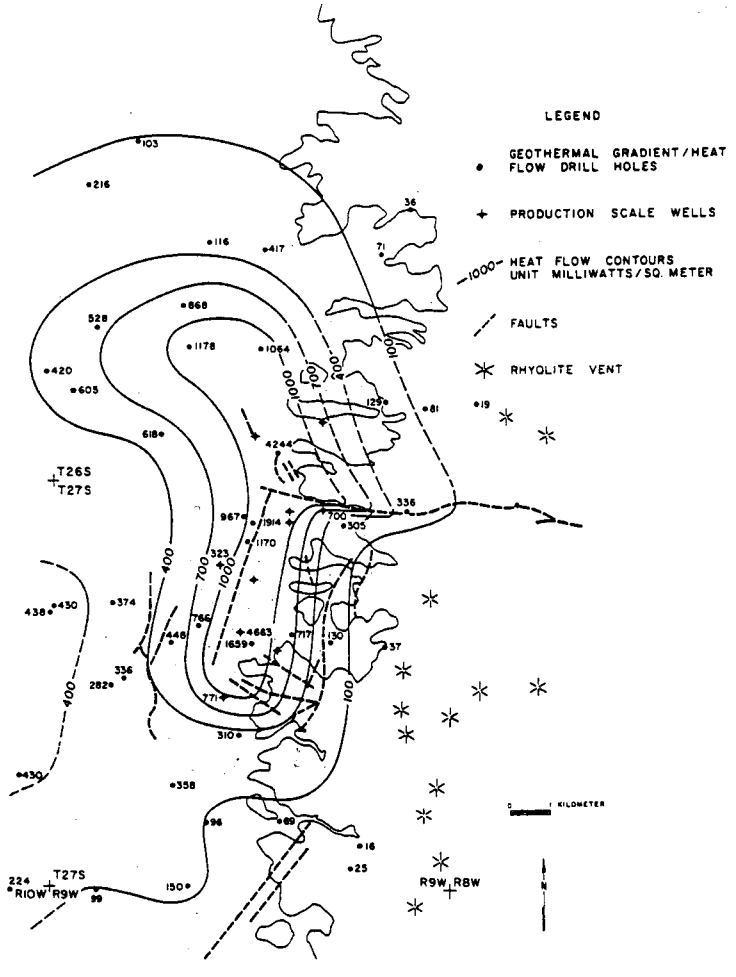

Figure 3

Surface conductive heat flow for Roosevelt Hot Springs from Wilson and Chapman (1980).

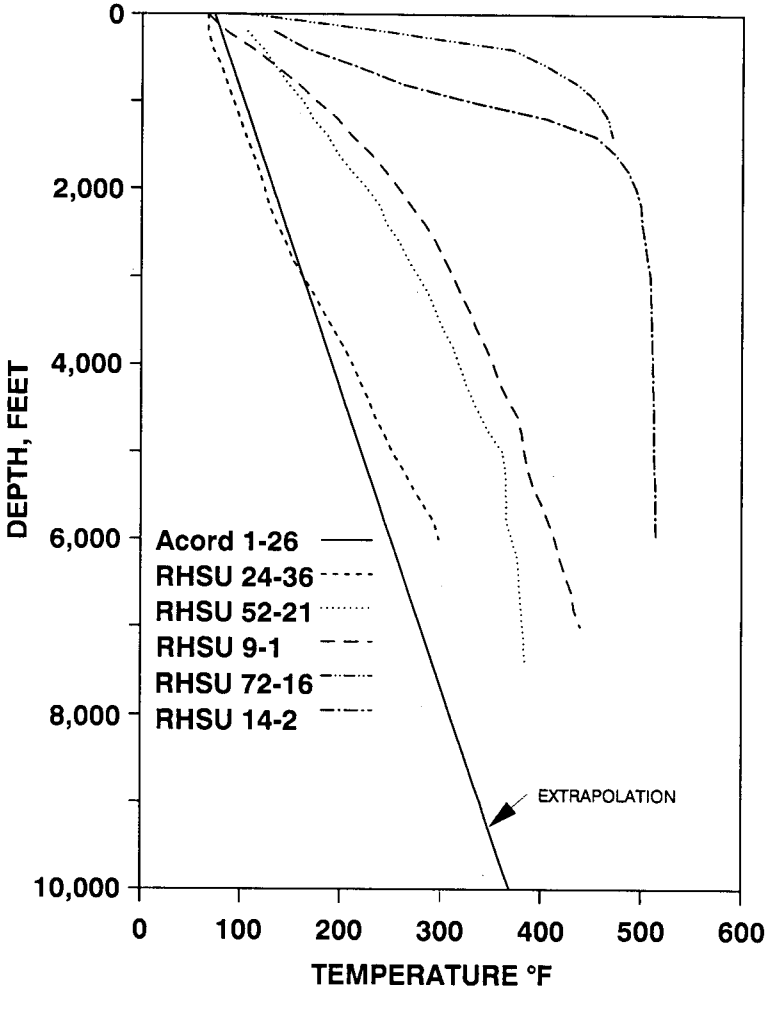

Figure 4 Temperature profiles of select wells.

Figure 5 Conceptual geologic model of the Roosevelt Hot Spring hydrothermal system.

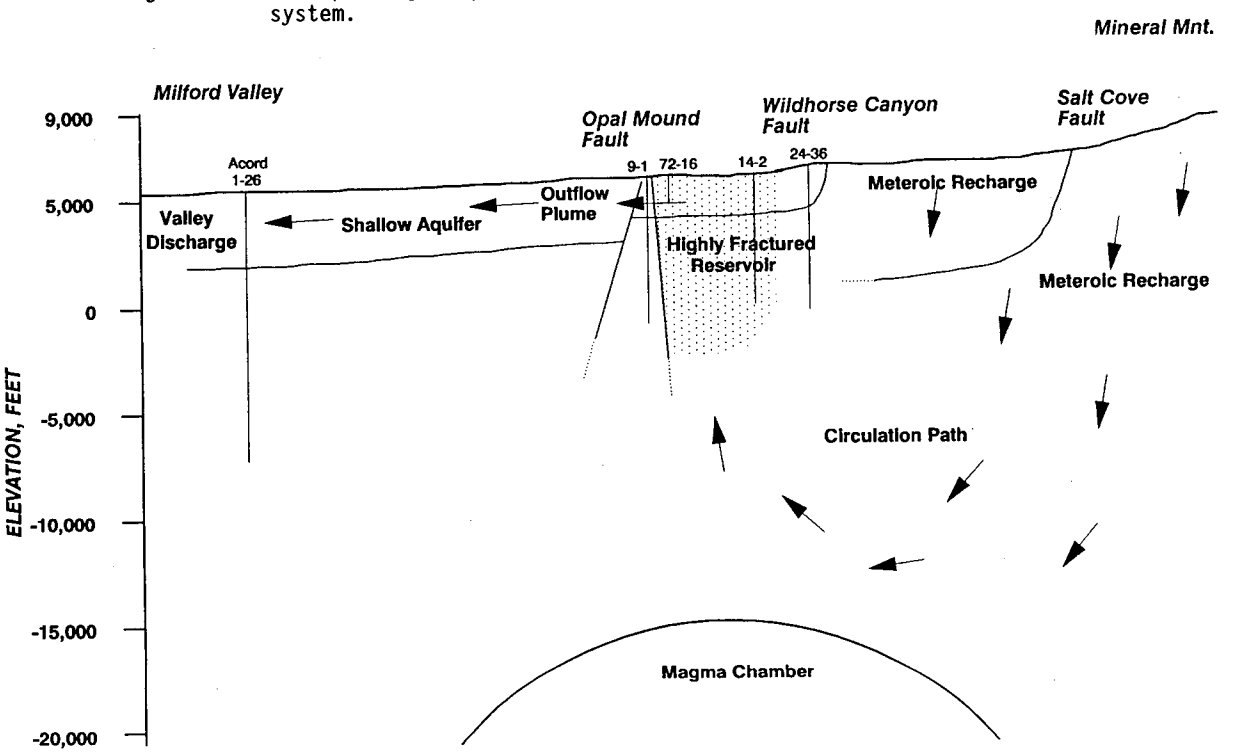

Figure 6 Horizontal permeability (mD) used in the simulation, note 0.5 mD in mountains massif.

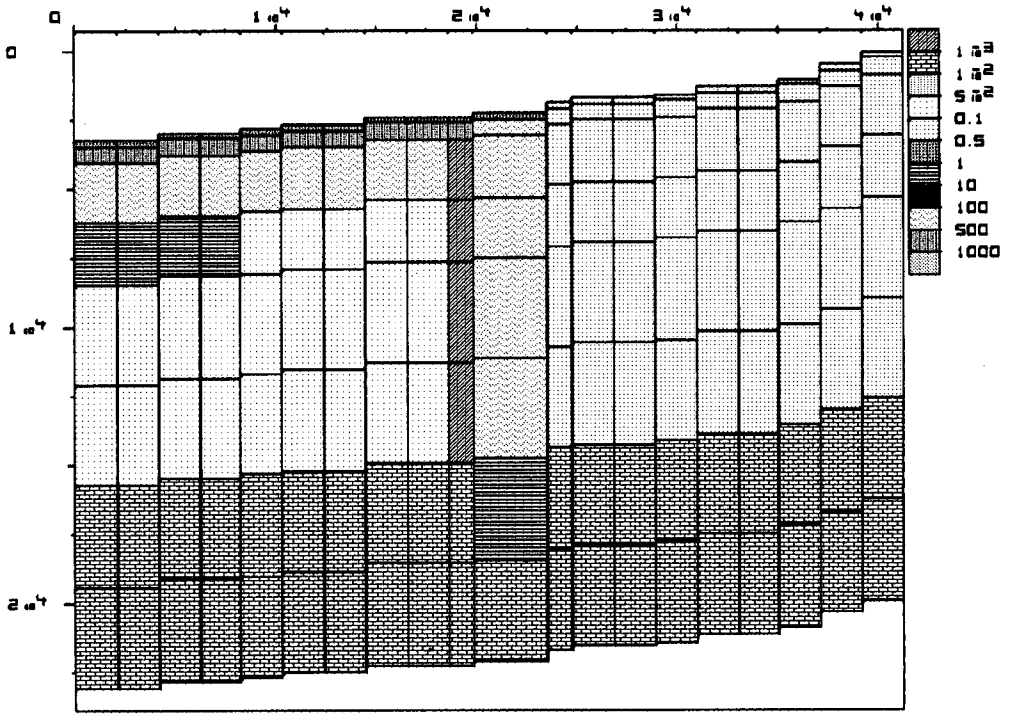

Figure 7 Vertical permeability (mD) used in the simulation study, note 0.5 mD in mountain massif.

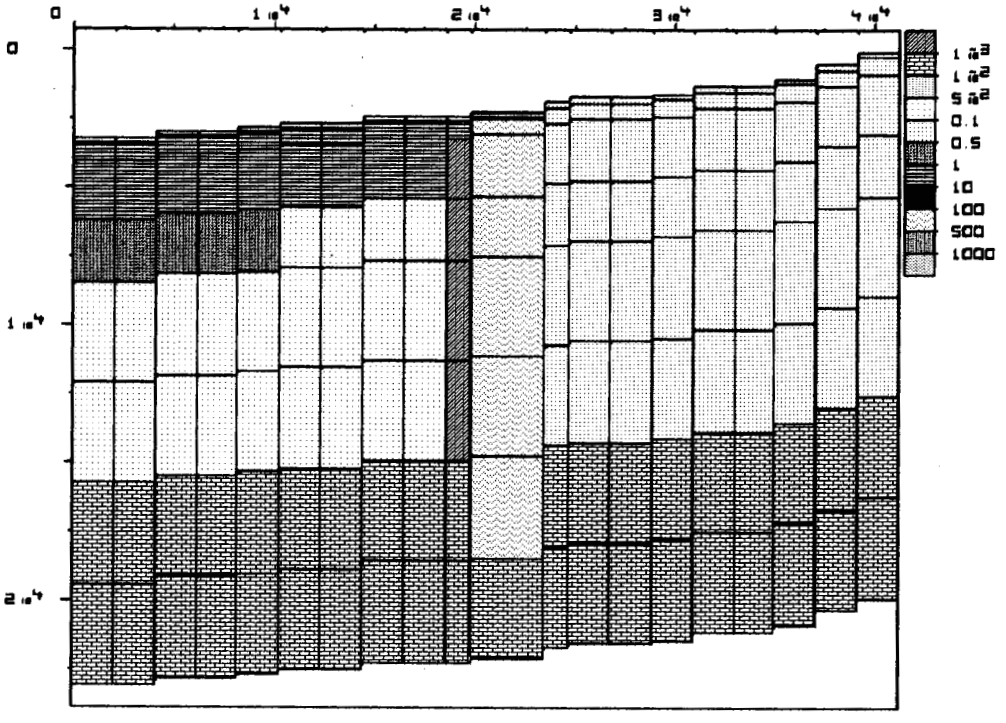

Figure 8 Model temperatures (°F) after 30,000 years for 0.5 mD in mountain massif.

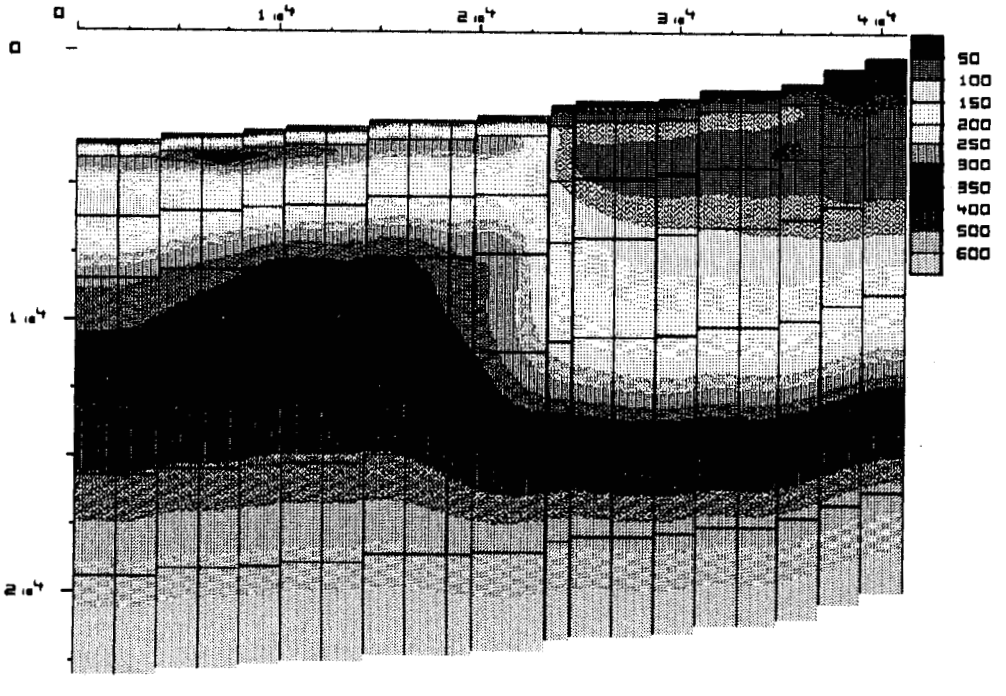

Figure 9 Model temperatures (°F) after 50,000 years for 0.05 mD in mountain massif.

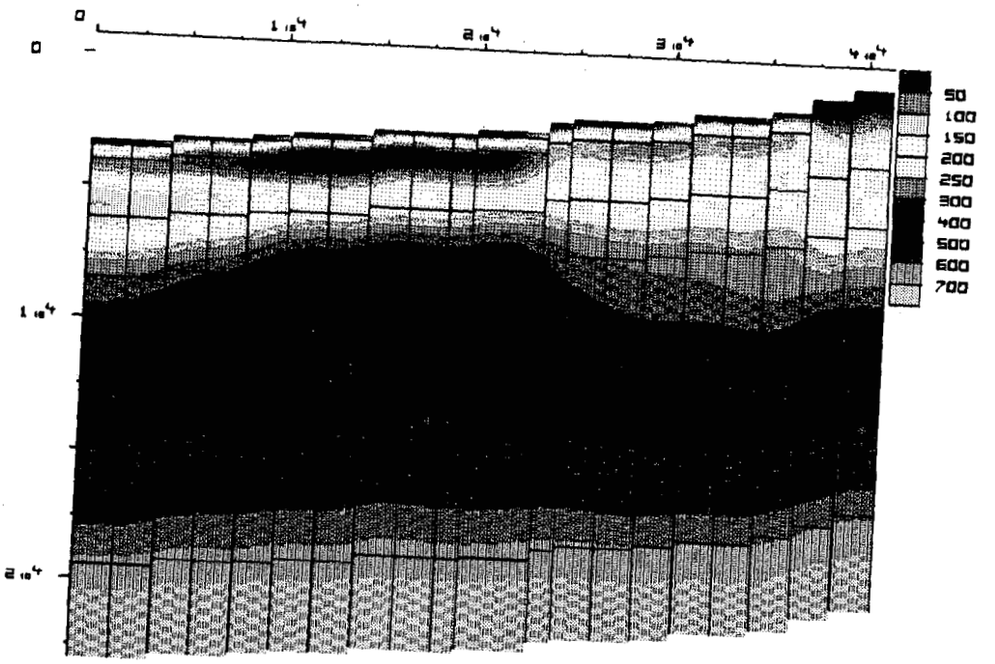

PROCEEDINGS, Sixteenth Workshop on Geothermal Reservoir Engineering
Stanford University, Stanford, California, January 23-25, 1991
SGP-TR-134

RESERVOIR ENGINEERING STUDIES OF SMALL LOW-TEMPERATURE HYDROTHERMAL SYSTEMS IN ICELAND

Gudni Axelsson

National Energy Authority, Grensásvegur 9, 108 Reykjavík, ICELAND

ABSTRACT

Geothermal energy provides more than one third of the energy consumed in Iceland. Its primary use is for space heating and most of the 28 public *hitaveitur* (district heating services) in Iceland utilize small low-temperature geothermal fields that have a natural heat output of only a few 100 kW_t to a few MW_t. All of these small reservoirs respond to production by declining pressure and some by declining temperature. During the 1980's the emphasis in geothermal research in Iceland shifted from exploration to reservoir engineering. The reservoir engineering work carried out concurrent with the exploitation of these small fields includes: testing of individual wells, field wide tests, monitoring the response of reservoirs to long-term production and simple modeling.

INTRODUCTION

Geothermal energy plays a major role in the energy economy of Iceland. At present it provides more than one third of the energy consumed by the 250.000 inhabitants, or about 8500 GWh. The primary use of geothermal energy is for space heating and about 85% of all residential buildings in Iceland are heated by geothermal energy, in addition to most commercial and industrial buildings.

Most towns and communities in Iceland use geothermal water directly for space heating. The water is provided by various district heating sevices, which are named *hitaveitur* (plural) in Icelandic (hitaveita in the singular). At the present there are 28 public *hitaveitur* operating in Iceland (Figure 1) and excluding the few largest ones, such as the one serving the capital city of Reykjavík, they serve communities with only a few hundred to a few thousand inhabitants each.

The smaller *hitaveitur* use energy from some of the numerous low-temperature geothermal areas which are found in Iceland (Figure 1). The low-temperature areas, which have a reservoir temperature less than 150 °C, are all located outside the volcanic zone passing through the island. The largest low-temperature areas are located in SW-Iceland on the flanks of the volcanic zone, but smaller areas are found throughout the contry. The surface manifestations of the low-temperature activity are hot or boiling springs. Spring flow rates range from almost 0 l/s to a maximum of 180 l/s from a single spring.

The heat-source for the low-temperature activity is belived to be the abnormally hot crust in Iceland. Bodvarsson (1982, 1983) proposed a model for the heat-source mechanism of the activity, that appears to be consistent with the data now available (Björnsson et al., 1990). According to his model, which is presented in Figure 2, the recharge to a low-temperature system is shallow ground water flow from the highlands to the lowlands. Inside a geothermal area the water sinks through an open fracture, or along a dike, to a depth of a few km where it takes up heat from the hot adjacent rock and ascends subsequently because of reduced density. This convection transfers heat from the deeper parts of the system to the shallow parts. The fracture is closed at depth, but according to Bodvarsson's model the fracture opens up and continuously migrates downward during the heat mining process by cooling and contraction of the adjacent rock. Thus the low-temperature activity is a transient process. A steady state process can not explain the natural heat output of the largest low-temperature systems in Iceland, which may be of the order of 200 MW_t.

Recent data on the low-temperature systems indicate that dikes may not be the primary fluid conductors, but rather younger fractures or faults. In addition many of the low-temperature systems seem to be located at the intersections of such fractures or faults and older dikes (Björnsson et al., 1990).

Theoretical calculations based on Bodvarsson's model (Axelsson, 1985) indicate that the existence and heat output of the low-temperature systems is controlled by the temperature conditions in the crust and in particular the local stress field, which controls whether open fractures are available for the heat mining process and how fast these fractures can migrate downward. Given the abnormal thermal conditions in the crust of Iceland it appears therefore that the regional tectonics and the resulting local stress field control the low-temperature activity.

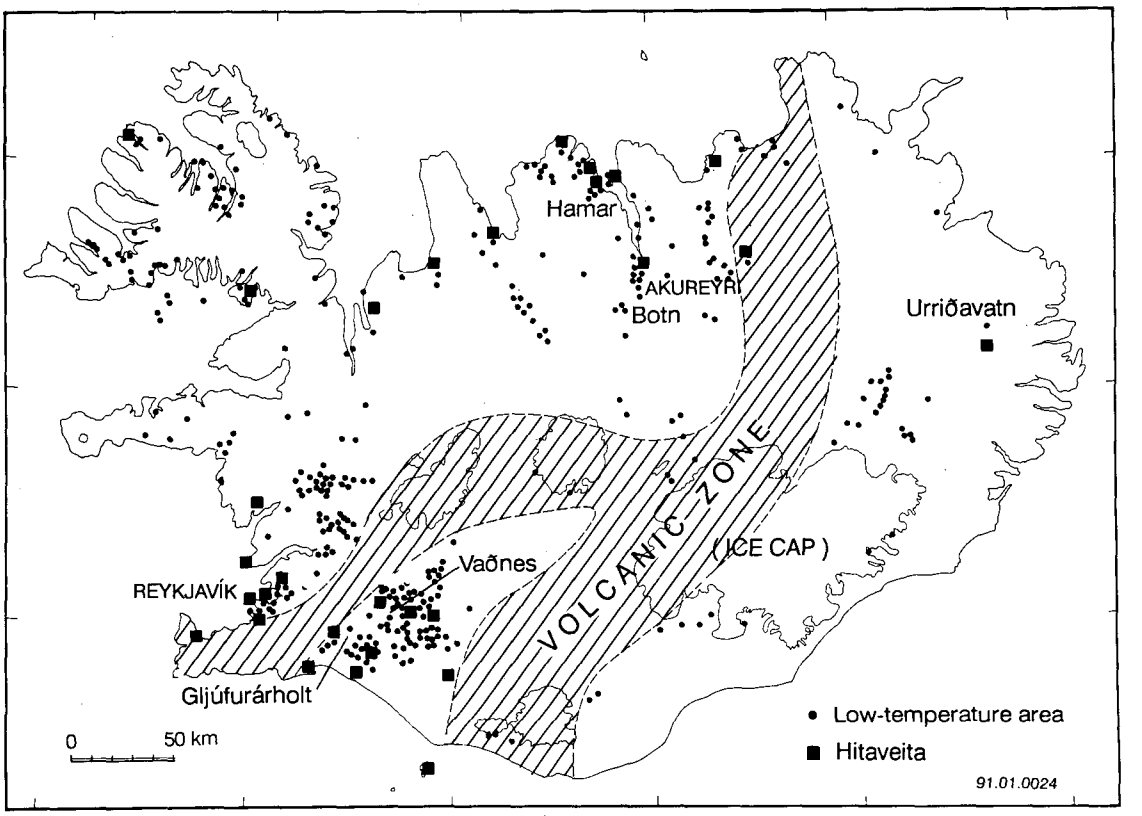

Figure 1. *Low-temperature hydrothermal areas and public* hitaveitur (*district heating services*) *in Iceland*

Most hitaveitur utilize the smaller low-temperature fields. The natural heat output of these fields is only of the order of a few 100 kW_t to a few MW_t, but the average power need of the smaller hitaveitur is between 5 and 20 MW_t. All of the reservoirs therefore respond to production by declining pressure and some also by declining temperature. Most of the low-temperature reservoirs currently under exploitation have been utilized for a decade or more. Considerable amounts of data on the response of these reservoirs are therefore available.

In this paper the reservoir engineering work carried out in connection with the exploitation of these small low-temperature fields will be discussed. The testing of individual wells, field wide tests, monitoring during long-term production and methods of modeling the reservoirs will be discussed and a few examples presented. The purpose of the reservoir engineering work has been to obtain information on the nature of the reservoirs, assess their production potential and predict their response to future utilization, in order to define long term operational strategies for the geothermal fields. The facts that data on the details of the subsurface conditions are in most cases scarce, and that funds for reservoir engineering work are often limited, constrain the methods that have been used to study and model the fields.

RESERVOIR ENGINEERING STUDIES

Regular reservoir engineering studies of geothermal fields in Iceland started in the mid 1960's (Thorsteinsson and Elíasson, 1970). For the next two decades the main emphasis in geothermal research in Iceland was, however, on geophysical and geological exploration of potential production fields for *hitaveitur*

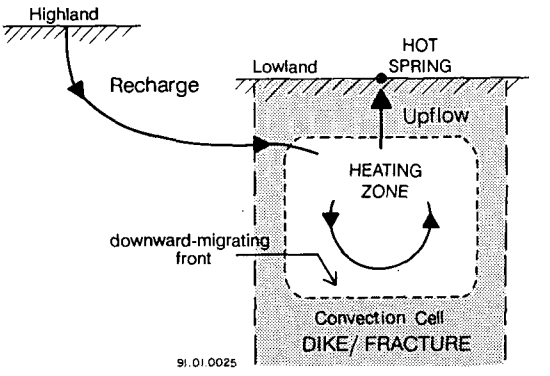

Figure 2. *Model of a low-temperature system in Iceland. Based on Bodvarsson (1983).*

that were in the planning stage, or already operating. Most of the wells currently in use by *hitaveitur* were drilled during this period.

The emphasis in geothermal research in Iceland changed during the 1980's. By that time more than 80% of the population enjoyed heating by geothermal energy, and the latest public *hitaveita* started operation in 1981. Therefore the need for geothermal exploration decreased considerably. However, the *hitaveitur* started encountering various problems associated with the production from the geothermal fields and the response of the reservoirs to long-term production (Sigurðsson et al.,1985). In many cases the potential of a reservoir turned out to be less than previously belived and interests in long term operational strategies for the geothermal fields increased. Thus the emphasis shifted to geothermal reservoir engineering.

The reservoir engineering work carried out concurrent with the utilization of the small low-temperature fields includes:

A. Short-term pump, injection and free-flow tests of individual production wells, of only a few hours duration.

B. Long-term tests such as build-up and interference tests, with a duration of days or weeks, that often involve several wells.

C. Tracer tests of several weeks duration.

D. Monitoring the response of a reservoir to long-term production.

E. Simple modeling based on data aquired under A to D above.

The short-term tests (A) provide information on the characteristics of production wells, such as pressure drop due to turbulence, but very limited information on the properties of a geothermal reservoir. Longer-term build-up and interference tests (B) provide more information on the properties of a reservoir, such as permeability and storage, and on the nature and boundaries of a reservoir. This information is, however, usually not sufficient to make accurate predictions on the long-term response of reservoirs to hot water production. Tracer tests (C) will not be discussed in this paper.

The most important information on the nature, properties and size of a geothermal reservoir are obtained by careful monitoring (D) of its production and response history. Monitoring is an important part of field management as well as the basis for reservoir engineering work, such as modeling. Increased emphasis has therefore been placed on monitoring in recent years in Iceland, and most *hitaveitur* follow a monitoring program as outlined below. It should be mentioned that in most of the small low-temperature fields now utilized production is by pumping from deep (>500m) wells. The following items are monitored:

1. Flow-rate history of each production well and a field as a whole.
2. Temperature of the water produced.
3. Water level in production well(s).
4. Water level in observation well(s) inside a geothermal reservoir.
5. Water level in observation wells(s) outside a geothermal reservoir.
6. Chemical content of the water produced.
7. Temperature logs in observation wells.

Not all items in the above list are monitored in the small low-temperature fields utilized by *hitaveitur* in Iceland. In a few fields the monitoring is still incomplete. But in most fields at least items 1, 2, 3 and 4 are monitored once a day to once a week and the chemical content (6) at least once a year. In a few cases the monitoring is computerized.

Simple modeling (E) has been used extensively for the small geothermal reservoirs, in particular to model their long-term response to production. Most of the reservoirs respond to production by decreasing pressure, which is monitored as water level changes in observation wells. Lumped models have been used successfully to simulate the pressure response data from several low-temperature reservoirs in Iceland. Axelsson (1989) has described the most commonly used method, which tackles the simulation as an inverse problem. It uses an automatic non-linear least-squares iterative technique which requires very little time compared to more detailed distributed parameter numerical modeling techniques. Detailed numerical modeling has only been attempted for a very limited number of the small low-temperature reservoirs. The reasons for this are that data on the subsurface conditions in these reservoir are often very limited and in addition that funds for detailed modeling have not been available to the smaller *hitaveitur*.

EXAMPLES

A few examples of reservoir engineering studies of small low-temperature fields in Iceland will now be presented. The examples are from the following areas: Vaðnes and Gljúfurárholt in SW-Iceland which are utilized by the surrounding farms and vacation homes. Urriðavatn in E-Iceland utilized by the Egilsstaðir *hitaveita* which serves a population of 1600. Botn in N-Iceland which is one of four small low-temperature fields utilized by the Akureyri *hitaveita* which serves a population of 13,000. Hamar in N-Iceland utilized by the Dalvík *hitaveita* which serves a population of 1400. The locations of the fields are shown in Figure 1.

Well tests

Figure 3 shows the results of short-term step-rate pumping tests of two wells of approximately the same depth (300 - 400 m) and diameter (0.2 m), but with

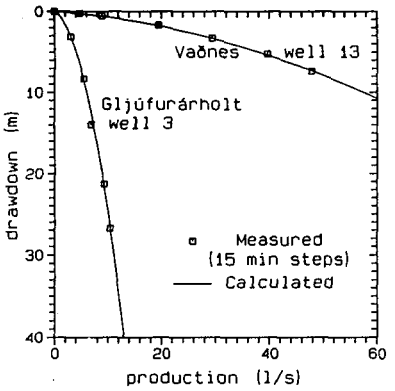

Figure 3. *Results of short-term step-rate pumping tests in the Vaðnes and Gljúfurárholt fields.*

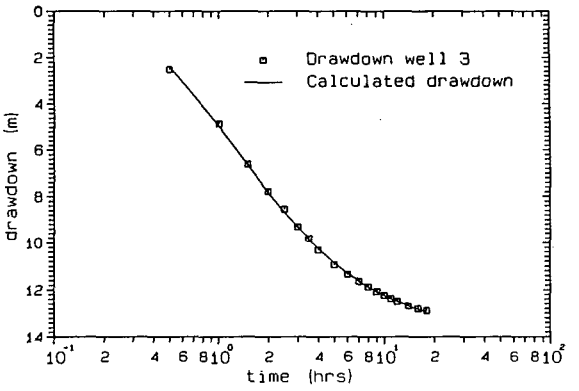

Figure 4. *Results of an interference test in the Urriðavatn field in 1987.*

otherwise very different characteristics. One is in the Vaðnes field and the other in the Gljúfurárholt field. They are both small low-temperature fields, Vaðnes with a reservoir temperature of about 80 °C and Gljúfurárholt about 100 °C. The turbulence pressure loss in the wells can be approximated by:

$$(1) \qquad \Delta h = C q^2$$

where Δh is the loss in terms of water level, C is a constant and q the pumping rate. Well 13 in the Vaðnes field is highly productive with very little drawdown due to turbulence, or C = 0.0022 m/(l/s)^2. Well 3 in the Gljúfurárholt field is a poor producer with great drawdown due to tubulence, or C = 0.207 m/(l/s)^2. In addition the permeability is much lower in the Gljúfurárholt reservoir than in the Vaðnes reservoir.

Long-term tests

Figure 4 shows the results of a 24 hour interference test performed in the Urriðavatn low-temperature field. The Urriðavatn field is located at the bottom of a small lake and production from the field started in late 1979 (Axelsson et al.,1988). A total of 8 wells have been drilled into the reservoir but only wells 4, 5 and 8 turned out to be productive. Wells 4 and 5 only intersected shallow (200 - 300 m) aquifers and the temperature of the water produced from these wells decreased drastically the 3 - 4 years they were in use. Well 8 intersected a good aquifer at around 800 m depth. Production from that well started in late 1983 and the response of the reservoir after that time will be discussed later in this paper.

During the interference test 15 l/s were pumped from well 5 and the resulting drawdown observed in well 3 130 m away. The data were simulated by a simple analytical model of a homogeneous and isotropic *vertical slab* of width b with two-dimensional flow and constant pressure at the surface. A vertical slab is consistent with the conceptual model of the field and the constant pressure is maintained by the lake above the reservoir. Based on this model the apparent permeability width of the upper part of the Urriðavatn reservoir is bk = 1.0×10^{-11} m^2 and the apparent compressibility width bc_t = 6.5×10^{-9} m/Pa, where c_t is the compressibility of the liquid saturated formation. Assuming that the width is about 100 m this corresponds to a permeability of 10^{-13} m^2 and a porosity of 9.0%.

Figures 6 and 7 show the data obtained during an 11 week long build-up and interference test performed in the Botn field (Flóvenz et al., 1989) during the summer of 1990. Pumping from well H-10, the main production well in the field, was stopped for about a month and then restarted in early July (Figure 6). The resulting water level changes were monitored in several wells inside as well as outside the field (Figure 5). The water level changes in wells B-2, B-4 and H-12 are presented in Figure 7. The data obtained are currently being analyzed but the first results indicate a small reservoir with a limited permeability that, however, appears to be connected to a much larger geothermal system.

The water level changes in well H-12 are very strange. On one hand the water level does not start to rise in that well until 5 days after the pressure build-up starts in the reservoir. On the other hand the water level starts to drop at the same moment the water level

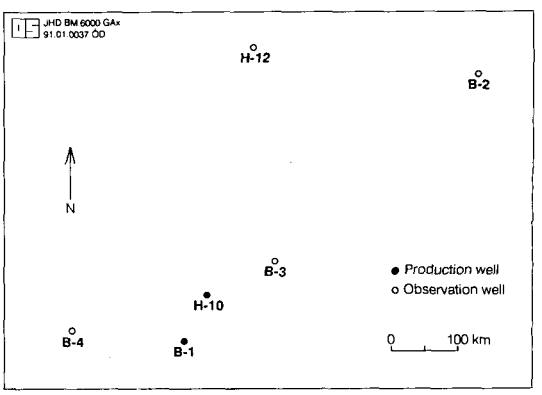

Figure 5. *Production and observation wells in the Botn field.*

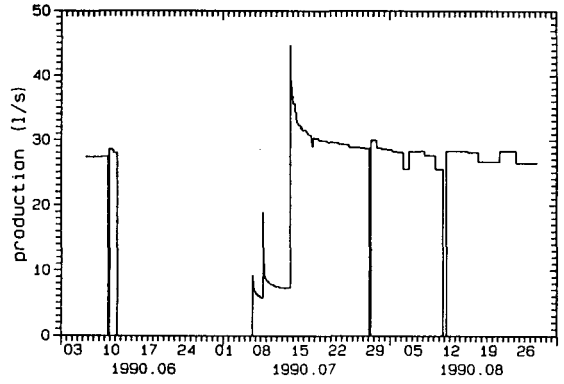

Figure 6. *Production from well H-10 in the Botn field during the summer of 1990.*

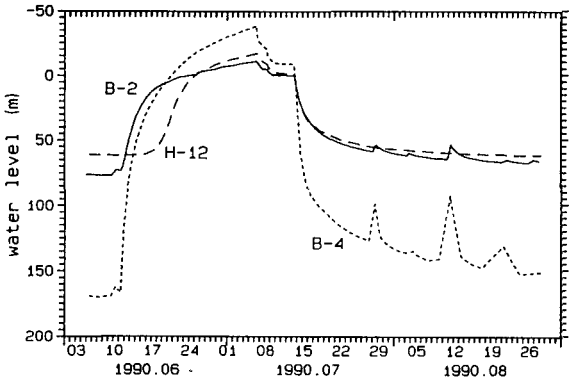

Figure 7. *Water level changes in wells B-2, B-4 and H-12 in the Botn field during the summer of 1990.*

starts to drop in the other wells. A possible explanation is that fractures along dikes that connect the production well (H-10) and well H-12 were closed before the build-up period because of the great pressure drawdown in the reservoir. As the pressure increased in the reservoir the fractures may have opened slowly until after about 5 days they had opened all the way to well H-12. When the drawdown started again the fractures were open, resulting in a simulataneous drawdown in H-12 and the other wells. This kind of behavior has not been observed previously in Iceland.

Monitoring and simple modeling

The first of two examples of simple modeling, based on long-term monitoring, presented here is from the Hamar field. Production from this small field started in 1969. Two production wells, with feed zones between depths of 500 and 800 m, are currently in use and the reservoir temperature is 64 °C. Figure 8 shows a 7 year record of the production from the field and the resulting water level changes. The figure also shows the water level changes simulated by the lumped model approach discussed earlier (Axelsson, 1988). The lumped model used is shown in Figure 9. According to the model the innermost part of the reservoir has a

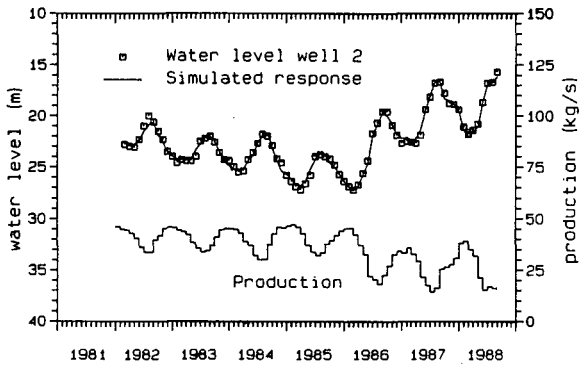

Figure 8. *Production from the Hamar field along with observed and simulated water level changes.*

storage coefficient Vc_t = 0.071 m^3/Pa, where V is the volume of that part of the reservoir and c_t its compressibility. Assuming that the porosity of the innermost part is between 5 and 10 % then its volume is between 1.1 and 1.6 km^3. The recharge part of the reservoir appears to be unconfined (free-surface) and cover an area of 8 to 12 km^2 (assuming porosities between 10 and 15 %). Thus the recharge part of the lumped model may represent the groundwater system in the area.

The average permeability of the Hamar reservoir was estimated as follows: First the *unit step response* of the reservoir was calculated by the lumped model. The *unit step response* is the response to a constant production of a unit volume (or mass) per unit time. Then the *unit step response* was simulated by a simple analytical model of an unconfined (free-surface) homogeneous and isotropic half-space (Axelsson and Bodvarsson, 1987). The results are presented in Figure 10. An unconfined model was chosen in view of the results of the lumped modeling. Based on this model the apparent permeability of the Hamar reservoir is 9.6×10^{-15} m^2.

The main objective of reservoir engineering work is to assess the production potential of a geothermal reservoir and predict its response to future utilization. In the case of the Hamar field the lumped model was used to predict the water level drawdown in the reservoir for different future production rates. The results are presented in Figure 11. It should be

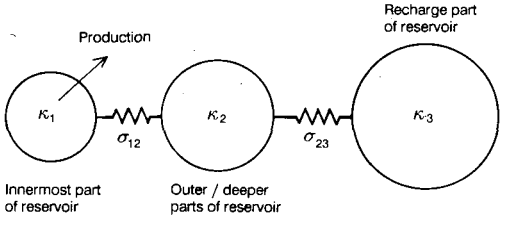

Figure 9. *Three capacitor lumped parameter model of the Hamar reservoir.*

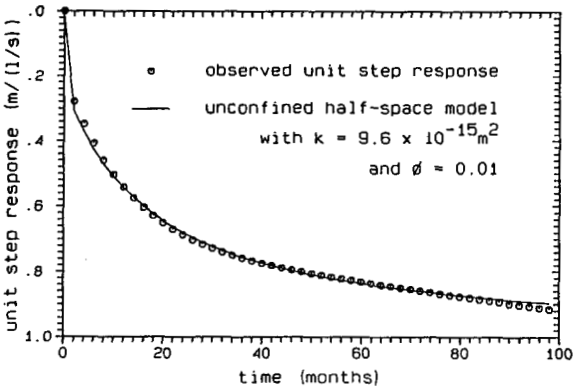

Figure 10. *Observed and calculated unit step response of the Hamar reservoir.*

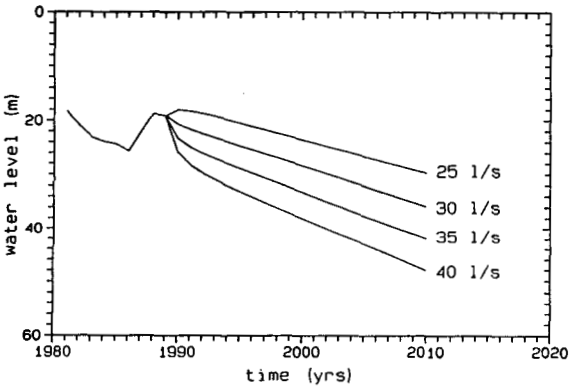

Figure 11. *Predicted water level changes in the Hamar reservoir.*

emphasized here that since the recharge into the Hamar system may be cold groundwater the temperature of the water produced may eventually decrease in addition to the predicted water level changes. No cooling has, however, been observed to date in the Hamar field.

The last example presented here is the long-term response of the Urriðavatn low-temperature reservoir. Figures 12 and 13 show the production from the field since late 1983 along with the resulting changes in temperature and chloride content (Axelsson et al., 1989). It is believed that down-flow of cold water from the lake above the field into the geothermal reservoir is causing these changes. The chloride content of the freshwater in the lake is about 10 mg/kg. The chloride content of the water produced therefore indicates mixing by freshwater of up to 20 %. It is evident that the cooling of the water produced will continue in the future. The future rate of decline is of a great importance for the management of the Egilsstaðir *hitaveita*. An attempt has been made to predict the changes in temperature for different cases of future production by using a simple curve-fitting approach. The results are presented in Figure 14.

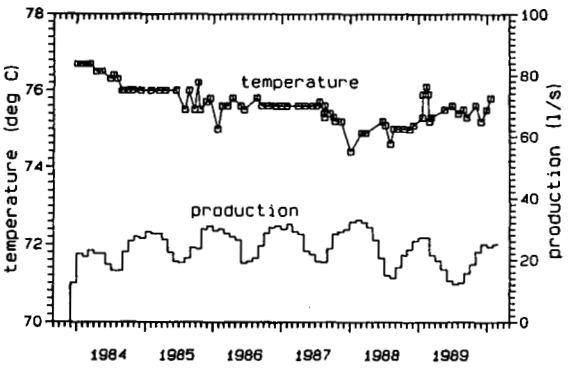

Figure 12. *Production from well 8 in the Urriðavatn field and resulting changes in temperature.*

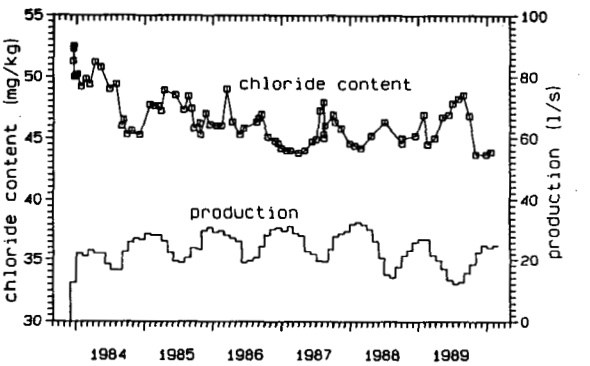

Figure 13. *Production from well 8 in the Urriðavatn field and resulting changes in chloride content.*

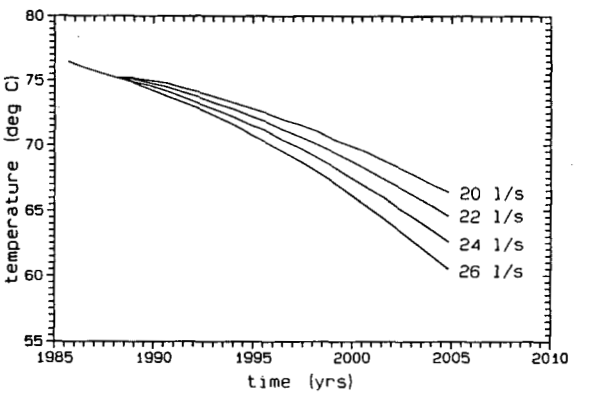

Figure 14. *Predicted changes in temperature of water produced from well 8 in the Urriðavatn field.*

CONCLUDING REMARKS

Geothermal energy is of a great economical importance in Iceland and many small low-temperature geothermal fields are utilized for space heating. The emphasis on geothermal reservoir engineering has increased steadily since the early 1980's. In this paper the reservoir engineering work carried out concurrent with the utilization of small low-temperature geothermal areas in Iceland has been discussed. A few examples were also presented; two involving short-term well tests, two involving longer-term interference and buildup tests and finally two examples involving monitoring and simple modeling.

Most of the small low-temperature reservoirs utilized in Iceland respond to production by water level changes and simple lumped models have been used successfully to simulate their response. A method described by Axelsson (1989) has to date been used to simulate response data from 10 small low-temperature fields in Iceland. However, a few low-temperature fields have also responded by declining temperature. Changes in temperature can be expected in the future in most, if not all, of the small fields utilized in addition to the long-term water level changes.

The emphasis on geothermal reservoir engineering is likely to continue in the future. For the small low-temperature reservoirs the emphasis may be expected to be in the following areas:

- Continued research into *the nature of the low-temperature activity.* Great amounts of data are available on the low-temperature activity in Iceland but several questions on the nature of the activity remain unanswered.
- Continued *monitoring* of production and response histories. In a few of the small fields in Iceland monitoring is still incomplete.
- *Detailed numerical modeling* where simple modeling is insufficient. This involves natural-state modeling, well-by-well modeling and combined modeling of pressure, temperature and chemical changes.
- *Re-injection tests* including comprehensive monitoring programs. Injection may help maintain pressures and extract more energy from some of the small geothermal reservoirs in the future. But before long-term injection can be started in any of the fields careful re-injection tests need to be performed.

ACKNOWLEDGEMENTS

I would like to thank the Egilsstaðir, Akureyri and Dalvík *hitaveitur* for allowing puplication of the data from the Urriðavatn, Botn and Hamar geothermal fields. I also thank my colleagues at the National Energy Authority for their contributions and Benedikt Steingrímsson and Valgarður Stefánsson for reviewing the paper.

REFERENCES

Axelsson, G., 1989, Simulation of pressure response data from geothermal reservoirs by lumped parameter models, **Fourteenth Workshop on Geothermal Reservoir Engineering, Jan. 1989,** Stanford University, 7 pp.

Axelsson, G., 1988, The Hamar geothermal field in Svarfaðardalur. The production capacity of production wells of the Dalvík hitaveita. (in Icelandic), report OS-88053/JHD-11, National Energy Authority, Reykjavík, 68 pp.

Axelsson, G., 1985, Hydrology and thermomechanics of liquid-dominated hydrothermal systems in Iceland, Ph.D. Thesis, Oregon State University, Corvallis, Oregon, 291 pp.

Axelsson, G., H. Ármannsson, G. Sverrisdóttir and M. Ólafsson, 1989, The Egilsstaðir hitaveita. Monitoring of the Urriðavatn geothermal field in 1988. (in Icelandic), report OS-89024/JHD-09 B, National Energy Authority, Reykjavík, 33 pp.

Axelsson, G. and G. Bodvarsson, 1987, Analysis of production data from fractured liquid-dominated geothermal reservoirs in Iceland, **Geoth. Resources Council Trans., 11,** 573-580.

Bodvarsson, G., 1983, Temperature/flow statistics and thermomechanics of low-temperature geothermal systems in Iceland, **J. Volcanol. Geothermal Res., 19,** 255-280.

Bodvarsson, G., 1982, Glaciation and geothermal processes in Iceland, **Jökull, 32,** 21-28.

Björnsson, A., G. Axelsson and Ó.G. Flóvenz, 1990, The nature of hot spring systems in Iceland (in Icelandic), **Náttúrufræðingurinn, 60,** 15-38.

Flóvenz, Ó.G., Á. Guðmundsson, Þ. Thorsteinsson and G.P. Hersir, 1989, The Botn geothermal area. Results of geothermal research 1981-1989. (in Icelandic), report OS-89018/JHD-03, National Energy Authority, Reykjavík, 92 pp.

Sigurðsson, Ó, S.P. Kjaran, Þ. Thorsteinsson, V. Stefánsson and G. Pálmason, 1985, Experience of exploiting Icelandic geothermal reservoirs, **Geoth. Resources Council Trans., Int. Volume,** 177-182.

Thorsteinsson, Þ. and J. Elíasson, 1970, Geohydrology of the Laugarnes hydrothermal system in Reykjavik, Iceland, **Geothermics, Spec. Iss. 2, 2,** 1191-1204.

PROCEEDINGS, Sixteenth Workshop on Geothermal Reservoir Engineering
Stanford University, Stanford, California, January 23-25, 1991
SGP-TR-134

NUMERICAL SIMULATION OF THE SUMIKAWA GEOTHERMAL FIELD IN THE NATURAL STATE

J.W. Pritchett*, S.K. Garg*, K. Ariki+, and Y. Kawano•

***S-CUBED, +Mitsubishi Materials Corporation, •New Energy and Industrial Technology Development Organization**

Introduction

This paper presents some results from a numerical simulation study of the natural state of the liquid-dominated high-temperature Sumikawa geothermal prospect (Pritchett *et. al.*, 1989). Sumikawa is located in the Hachimantai volcanic zone of the Sengan thermal area in northern Honshu, Japan. Exploratory studies have been in progress at Sumikawa since 1981 by Mitsubishi Materials Corporation (MMC) and Mitsubishi Gas Chemical Corporation (MGC); this comprehensive program incorporates a variety of geochemical and geophysical surveys and an extensive preliminary drilling investigation (now exceeding sixteen wells). The drilling program has revealed a complex geological structure and has made possible a very thorough pressure-transient testing program involving both single-well and long-term interference tests. These exploratory studies have been carried out jointly by MMC and NEDO (the New Energy and Industrial Technology Development Organization, an agency of the Japanese government).

Geological Setting

Sumikawa is located in mountainous terrain; Mt. Yake (just to the southwest of the Sumikawa area) and Mt Hachimantai (just to the southeast) are both active volcanoes. Figure 1 shows the location of the field in relation to regional structure; also shown are the locations of the operating geothermal fields at Kakkonda, Matsukawa and Ohnuma. The Sumikawa prospect lies approximately 2 km to the west of the Ohnuma geothermal power station (also operated by MMC). Ohnuma produces about 10 MW of electricity from a small (~ 0.6 km diameter) borefield immediately surrounding the power station.

A pronounced north-south trending gravity low has been identified to the north of the Sumikawa field, indicative of a graben structure (see Figure 1); the two active volcanoes (Mt. Yake and Mt. Hachimantai) and the Senosawa uplift zone obscure this feature farther south. Major regional tectonic features (faults, uplifts and depressions) strike north-south. Figure 1 also shows east-west lineaments along which the Quaternary volcanoes in the region (including Mt. Yake and Mt. Hachimantai) are aligned; these lineaments are believed to represent regional fracture zones. The geothermal activity in the Sumikawa/Ohnuma area is believed to originate from such an east-west fracture zone connecting Mt. Yake and Mt. Hachimantai, just to the south of the drilled area.

Figure 2 shows the local area, including both the Sumikawa and Ohnuma fields as well as the sub-region chosen for our numerical simulation study of Sumikawa. Within the study area, the ground surface averages ~ 1000 meters above sea level (ASL), but slopes sharply down from south (> 1300 m ASL near Mt. Yake) to north (< 700 m ASL near the Akagawa hot spring area). As shown, exploratory drilling is concentrated near the center of the study area; drilling to the north is sparse and shallow, and drilling to the south of well SA-2 is precluded by the Towada-Hachimantai National Park boundary. The high well density in the central part of the study area provides good resolution of the underlying geological structure. Figures 3 and 4 illustrate vertical geological sections (based on drilling logs) corresponding to sections A–A′ (east-west) and B-B′ (north-south) shown in Figure 2, respectively. Figure 3 indicates that the Sumikawa prospect lies on the western boundary of the regional north-south graben structure, with substantial downward displacements (> 1 km) in deep layers from west to east. The major geological formations in the area are as follows, in order of increasing depth:

"ST" Formation: Surficial andesitic tuffs, lavas and pyroclastics of Recent origin.

"LS" Formation: Lake sediments; Pleistocene tuffs, sandstones, siltstones and mudstones.

"DA" Formation: Pliocene dacites, dacitic tuffs and breccias.

"DI"Formation: Dacitic dike located in the extreme northwest of the study area.

"MV" Formation: "Marine/Volcanic Complex"; interbedded Miocene dacitic volcanic rocks and "black-shale" marine sediments.

"AA" Formation: Altered andesitic rocks which are apparently extensively fractured.

"GR" Formation: Crystalline intrusive rocks, mainly granodiorite and diorite.

Hydrological Characteristics

Measured underground temperatures at Sumikawa exhibit substantial dependences upon both depth and north-south position. As shown in Figure 5, temperatures at sea level elevation (~ 1 km depth) decline sharply to the north. This temperature distribution supports the hypothesis that the source of the geothermal fluids at depth is the inferred east-west deep fracture zone which connects the Mt. Yake and Mt. Hachimantai volcanoes. The highest temperature measured so far at Sumikawa is near bottomhole in well

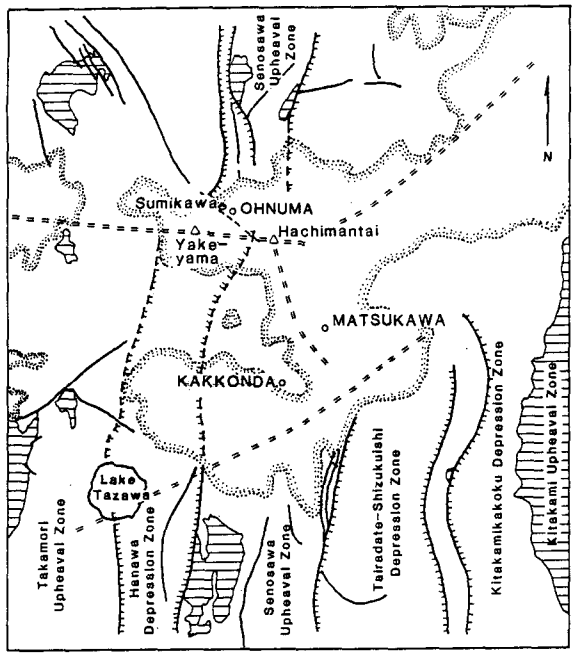

Figure 1. Area considered in mathematical simulation studies, showing computational grid spacing and well locations.

SA-2 (320°C), which is also the southernmost well at Sumikawa. Shut-in temperature surveys in the deepest wells show evidence of temperature inversions (maximum temperatures above bottomhole) which is suggestive of substantial convective heat transfer at depth.

Determinations of stable shut-in feedpoint pressures in the Sumikawa wells indicate that at relatively shallow depths (above ~ 300 m ASL), underground pressures vary horizontally and that a large shallow region of sub-hydrostatic vertical pressure gradient is present in the southern part of the area (near Mt. Yake), which is indicative of the presence of a shallow two-phase flow region in the southern part of the field. At greater depths, however, stable pressures are remarkably uniform: pressure depends only on elevation with respect to sea level, with an average gradient around 80 bars per kilometer of depth (hydrostatic for ~ 240°C).

Substantial natural outflows of hot fluids at the surface are observed at Sumikawa, mainly from a series of hot spring areas which is oriented approximately north-south and which lies midway between the Sumikawa and Ohnuma fields. Within the present study area, the major natural discharge points are the Sumikawa and Akagawa hot springs in the northeastern part of the study area. Additional hot spring areas are present farther north, which appear to be part of the same hydrological system. The total heat output from these surface discharges is of order 30 MW.

Reservoir fluids at Sumikawa may be regarded as pure H_2O for the purposes of reservoir engineering studies. Salinities are generally low (< 5000 ppm) and the incondensable gas content is typically less than one part per thousand by volume of the steam.

Many of the exploratory wells in the Sumikawa area have been discharged for periods of time ranging from a few hours to several months. Several fluid-injection tests have also been conducted. Discharge enthalpies from some of these wells are significantly in excess of saturated liquid values: in a few cases (wells S-1, SA-2 and SA-4), discharge enthalpies corresponding to pure saturated steam have been observed. This implies that these wells are producing from an underground two-phase zone within the reservoir. The most productive well at Sumikawa is also the deepest (well SN-7D, 2486 m): SN-7D is capable of discharging fluid at rates around 150 kg/s with wellhead enthalpy near 1200 J/g from feedzones located within the deepest ("GR") formation. Most other productive wells at Sumikawa withdraw fluid from the shallower "AA" formation.

A substantial body of pressure-transient data has been collected using downhole capillary-tube gauges from a number of wells in the field during these flow tests (Maki, Pritchett and Garg, 1988; Garg *et. al.*, 1991). Measurements have been performed both in flowing wells and in shut-in observation holes. Briefly, the results of the pressure transient experiments may be summarized as follows. On the whole, permeabilities at Sumikawa are both heterogeneous and highly anisotropic. Interference tests have shown that north-south communication is often quite good, whereas east-west communication is poorer and vertical communication is very low, on the average.

Apparently, the lake sediment ("LS") formation acts as a caprock for the geothermal reservoir—the absence of this formation and the relatively low ground surface elevations in the northeastern part of the study area are responsible for the substantial fluid discharges observed at the Akagawa and Sumikawa hot spring areas. Permeabilities in the "DA" formation are moderate (of the order of 10 millidarcies, depending somewhat on depth). The "marine/volcanic complex" (MV formation) is highly anisotropic, with moderate horizontal permeability but very low average vertical permeability. The "altered andesite" AA formation is quite permeable, particularly in the north-south direction—pressure test interpretations yield values in excess of 100 millidarcies. Finally, pressure-transient evidence from well SN-7D has revealed the presence of a very deep permeable horizon within the "GR" layer as well. Thus, three of the formations at Sumikawa ("DA", "AA" and "GR" appear to be fairly permeable; the "LS" layer is an impermeable aquitard, and the "MV" formation, while permeable to horizontal fluid motion, acts as a barrier to vertical flow. All rock permeability at Sumikawa is presumably due to the presence of fractures, since laboratory tests of cores indicate essentially no matrix permeability in any of these formations.

Numerical Representation

The objective of our study was to develop a mathematical representation of the Sumikawa area in the natural state. The approach was to use a numerical reservoir simulator and, starting from essentially arbitrary but physically plausible initial conditions, to compute a time-dependent evolution of the system toward an essentially steady condition. Then, computed results and observed facts were compared, and appropriate adjustments in available free parameters were made to try to improve the match between computations and observations. The entire time-dependent calculation was then repeated using these revised parameter values, and results were again compared

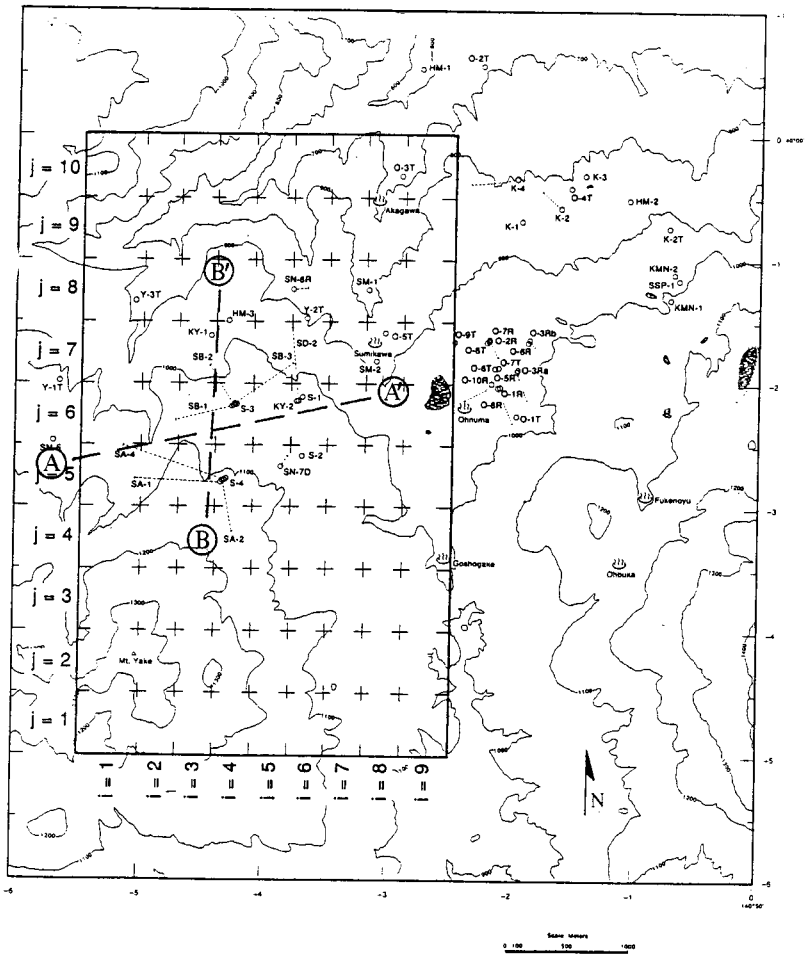

Figure 2. Tectonic map of the Sumikawa area.

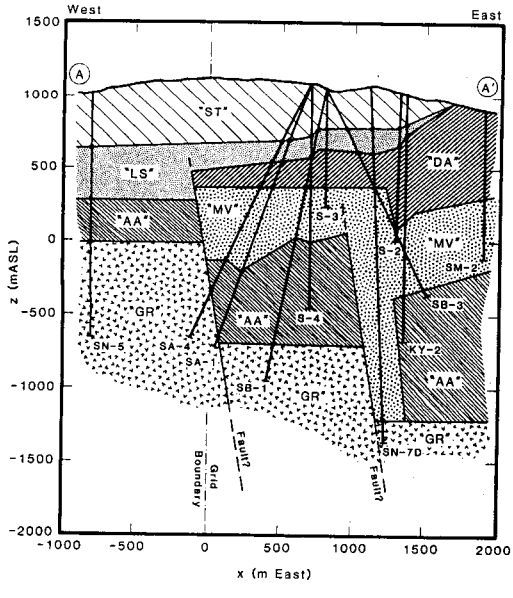

Figure 3. East-west A–A′ geological cross-section through the Sumikawa area.

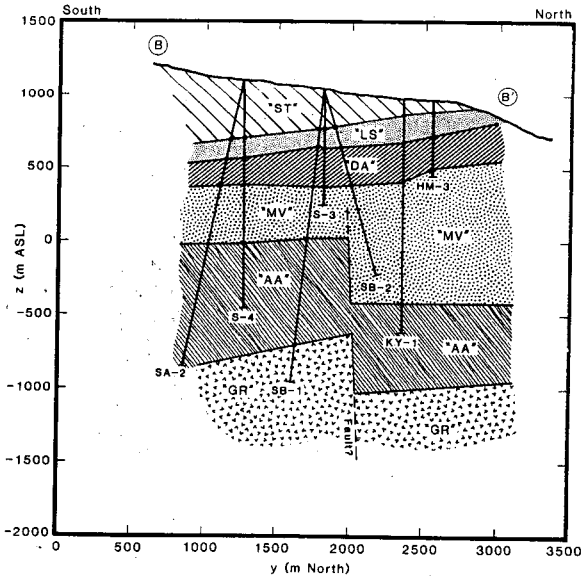

Figure 4. North-south geological cross-section B–B′ through the Sumikawa area.

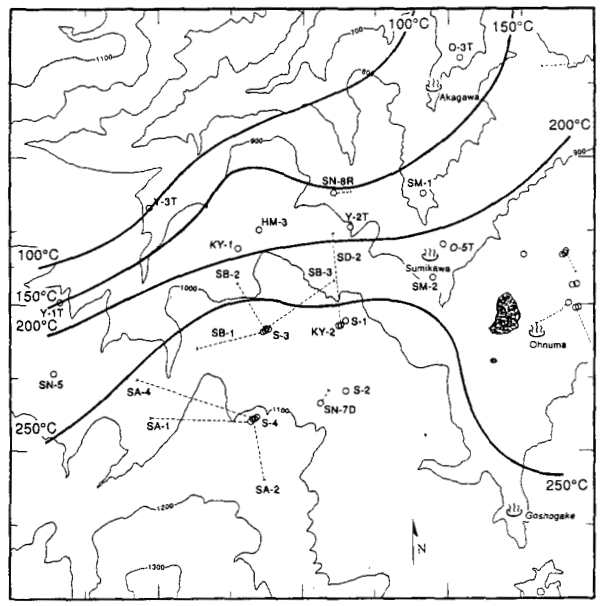

Figure 5. Temperatures at sea-level elevation in the Sumikawa/Ohnuma area.

with observations. This iterative process was repeated until a satisfactory match between computed properties (pressures, temperatures, surface discharge rates, etc.) and field observations was achieved. For this purpose, 42 such long-term calculations were required.

For this study, the STAR geothermal reservoir simulator was employed (Pritchett, 1989). All rock formations were treated as porous media, and the fluid was treated as pure H_2O. As discussed by Pritchett and Garg (1990), despite the fact that Sumikawa is a fracture-dominated reservoir, a porous-medium representation may be employed to describe the system in the natural state. A three-dimensional grid system was used, with 10 grid blocks (each 500 meters in size) in the north-south direction, 9 grid blocks (300 to 500 meters in size) in the east-west direction (see Figure 2), and a total of 16 vertical layers, ranging from 100 to 300 meters in vertical thickness. The horizontal grid area is $3 \times 5 = 15$ square kilometers, and the grid extends vertically from –1600 m ASL to +1200 m ASL; the total number of grid blocks is 1440, but some of the uppermost grid blocks are "void" owing to the irregular topography at Sumikawa.

A maximum time-step size of 8 years was employed, and most of the calculations were carried out to 30,000 years, requiring nearly 4000 time-steps per case. As initial conditions, it was simply assumed that temperature varied linearly between air temperature (10°C) at the ground surface and 250°C at –1600 m ASL (the bottom of the grid) at $t = 0$. This is substantially colder than the present temperature distribution, so that the system heated up during the time-dependent calculations. These initial conditions correspond to all-liquid conditions everywhere (no steam is present underground at $t = 0$).

Formation Properties and Boundary Conditions

Numerous free parameters were available for optimizing agreement between calculations and measurements; these were varied, as appropriate, from one calculation to the next. Basically, the free parameters included (1) certain parameters establishing the boundary conditions on the perimeter of the computing volume, (2) those rock formation permeabilities which were not constrained by pressure transient test results, and (3) the detailed geological structure where it was not well-established by drilling evidence (particularly in the southern part of the study area). In the remainder of this paper, we will present the results of the final calculation (Case 42), which appears to adequately represent the natural-state prevailing in the Sumikawa field.

Many of the required rock properties (porosity, density, heat capacity, thermal conductivity, compressibility) were treated as invariant during the study: these properties were obtained by averaging the results of laboratory tests performed upon core samples from the field. These values are listed in Table I. Furthermore, for all calculations, it was assumed that capillary effects could be neglected, and that the relative permeability functions could be treated as straight lines with residual steam saturation = 0.05 and residual liquid saturation = 0.3.

Table 1. Rock physical properties assumed for numerical simulations.

Formation	Porosity	Grain Density (kg/m^3)	Elastic Modulus (kbar)	Grain Heat Capacity (J/kg/deg)	Grain Conductivity (W/m/deg)
"ST"	0.11	2640	200	1000	1.9
"LS"	0.34	2690	200	980	2.9
"DA"	0.15	2640	300	940	3.0
"DI"	0.15	2640	300	940	3.0
"MV"	0.10	2660	500	910	3.3
"AA"	0.04	2730	600	830	2.5
"GR"	0.02	2710	600	750	3.0

Not surprisingly, the most important rock properties are the absolute permeabilities in the various coordinate directions. Some of these values were established (or at least constrained) by the results of pressure-transient tests, as discussed above; the remainder were treated as free parameters in the matching process. The final values are listed in Table II. Note that the "ST", "LS" and "DA" formations were treated as homogeneous and isotropic, with permeabilities of 1, 0.01 and 10 millidarcies respectively. The "MV" ("marine/volcanic complex") formation was treated as anisotropic, with 1 millidarcy vertical permeability and depth-dependent horizontal permeability. The extremely permeable "AA" formation was treated as very anistropic and was also subdivided into a "northern" and "southern" part, based mainly on pressure-transient evidence. Also note that all vertical permeabilities in the two deepest layers along the southern boundary of the grid were set to 10 millidarcies, irrespective of the type of rock present—this was done to represent the presumed "fracture zone" which connects Mt. Yake and Mt. Hachimantai and which provides the conduit for the hot fluids which charge the Sumikawa aquifers.

Table 2. Rock permeabilities used in final Sumikawa natural-state simulation.

Formation	Absolute Formation Permeability			Location*
	x-direction (east-west)	y-direction (north-south)	z-direction (vertical)	
"ST"	1.00 md	1.00 md	1.00 md	everywhere
"LS"	0.01 md	0.01 md	0.01 md	everywhere
"DA"	10.00 md	10.00 md	10.00 md	everywhere
"DI"	0.50 md	0.50 md	0.50 md	everywhere
"MV"	10.00 md	10.00 md	1.00 md	above 50 m ASL; $k > 6$
	2.00 md	2.00 md	1.00 md	below 50 m ASL
"AA"	20.00 md	200.00 md	2.00 md	north of -3000 m N; $j > 4$
	20.00 md	20.00 md	10.00 md	south of -3000 m N
"GR"	60.00 md	60.00 md	0.10 md	within "deep permeable zone"**
	0.10 md	0.10 md	0.10 md	elsewhere

*Note: all grid blocks with $j = 1$, $k = 1$ or 2 are assigned vertical permeability = 10.00 md to represent upflow region fracture zone along southern grid boundary at depth.

**Deep permeable zone restricted to deepest layer ($k = 1$) below −1300 m ASL; includes blocks [1,1,1], [1,2,1], [1,3,1], [2-9,1-10,1].

Each of the 1440 grid blocks was assigned one or another of the above rock formations (or was flagged "void") for purposes of each calculation. As noted above, this assignment of rock formations to individual grid blocks was constrained by drilling data in the central part of the study area, but a certain degree of latitude was permitted outside the drilled area. As an illustration, Figure 6 shows the assignments finally made to the grid blocks in the north-south section "$i = 3$". Note the resemblance between the central part of Figure 6 and Figure 4.

The fundamental character of the boundary conditions imposed on the various grid boundary surfaces did not change from case to case, but the values of many of the pertinent parameters involved were permitted to change. Provision was made for both mass and heat flow through the upper surface of the computational grid (that is, through the horizontal upper faces of the uppermost non-void grid blocks in each of the $[i,j]$ vertical columns of blocks). For pressure, the boundary condition was imposed by requiring that the mass flow through this upper surface be sufficient to maintain the pressure in each such uppermost block at its initial value, which was taken to depend only upon the distance of the center of the uppermost grid block below the local ground surface, as established by topographic maps. Optimum results were obtained by assuming that the one-bar surface (water table) lies 158 meters below the local ground surface, on the average. The temperature within each such uppermost grid block was likewise fixed at the initial value, given by assuming an air temperature of 10°C and a shallow temperature gradient of 0.1°C per meter of depth.

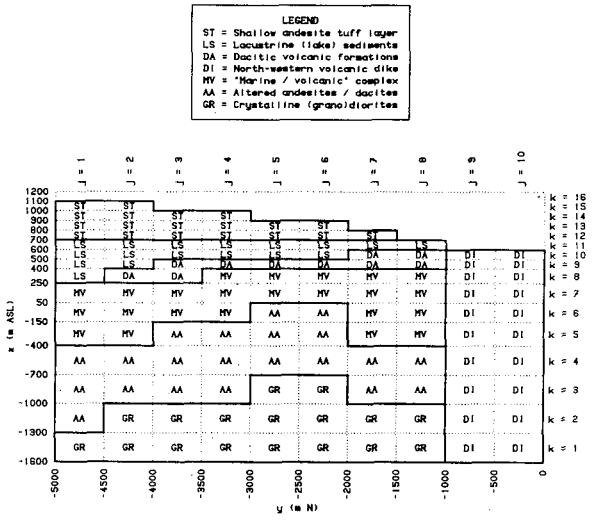

Figure 6. North-south vertical section through grid blocks with east-west index i = 3 (–4700 m E to –4400 m E). Solid lines separate grid blocks containing different rock formations; broken lines separate grid blocks within the same formation. Empty blocks above the surface are not delineated.

The bottom surface of the computational grid was treated as impermeable, but a uniform upward conductive heat flux was imposed—the final value was 0.4 watts per square meter (equivalent to 6 MW over the entire lower surface). The east and west vertical faces of the grid were treated as impermeable and insulated. Impermeable and insulated conditions were likewise imposed along most of the southern vertical surface, but in the deepest layer a mass-source of hot fluid was imposed along this boundary, representing the inflow of deep hot water from the deep Mt. Yake-Mt. Hachimantai fracture zone. As shown in Figure 7, although the mass inflow rate was uniformly distributed (and totaled 10 kg/s in the final calculation), the specific internal energy of the inflowing fluid was highest to the west (near the Mt. Yake volcano). The thermal input power represented by this deep inflow zone amounts to ~ 25 MW, significantly in excess of the 6 MW conductive heating; the total is 31 MW, in good agreement with available estimates of surface heat flow from the area. These parameter values were all adjusted several times during the course of the series of calculations. Finally, along the northern vertical face of

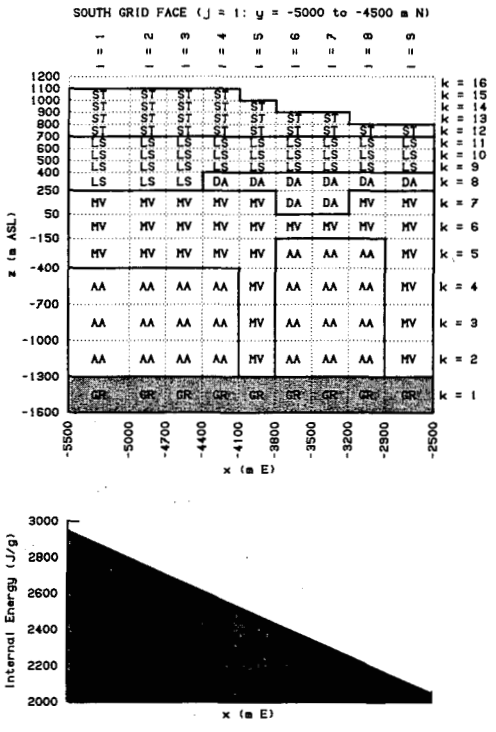

Figure 7. Upper: Southernmost vertical east-west plane of grid blocks. Shaded grid blocks contain fluid sources representing hot upflow from depth. Upflow rate is uniform, total is 10 kg/s. Lower: Internal energy of inflowing fluid varies linearly from 2950 J/g at x = –5500 m E to 2050 J/g at x = –2500 m E.

the grid, most of the surface was treated as impermeable and insulated, but a mass-sink was imposed in a single subsurface grid block located at the top of the permeable "AA" aquifer in the northeast corner of the grid (see Figure 8) to represent fluid flowing northward out of the study area which presumably supplies the hot spring areas to the north of the study area boundary. The mass withdrawal rate along the northern boundary was varied from case to case—the final value selected was 10 kg/s, which (coincidentally) is the same as the deep inflow rate from the southern boundary. Therefore, in the final model, no net inflow or outflow of fluid occurs at depth—the 10 kg/s inflow from the south is balanced by the 10 kg/s outflow to the north.

The Computed Natural State

The Case 42 calculation was carried out to t = 30,000 years, by which time essentially steady conditions prevail. Figure 9 shows how the total thermal energy within the computing volume changed with time—also shown is the derivative with time of this quantity (the net input power). Note that, at early times, an oscillation (of period ~ 1000 years) can be observed in the net input power. This oscillation is not of numerical origin, since the computational time-step is much shorter (8 years). The oscillation dies out after significant quantities of steam have formed underground. These oscillations are associated with a periodic convective pattern which develops at early times. Although these oscillations may be of interest from an academic point of view, they do not persist long so the matter was not pursued in detail.

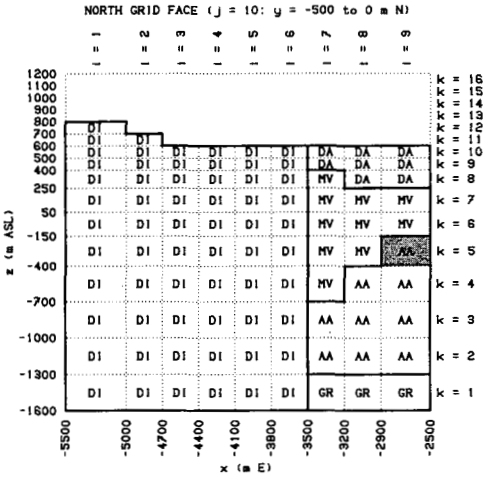

Figure 8. Northernmost vertical east-west plane of grid blocks. Shaded grid block contains fluid sink (10 kg/s) representing northern outflow from grid toward Zenikawa, Toroko and Shibari.

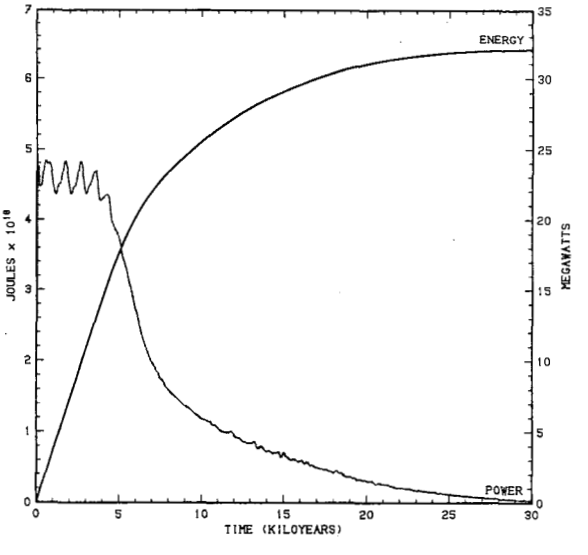

Figure 9. Change in total grid thermal energy versus time and net input power versus time for natural state calculation.

Figures 10 and 11 show north-south cross-sections for i = 3 and i = 8 (respectively). The section depicted in Figure 10 is the same as shown in Figure 6, and passes through the most extensively drilled portion of the Sumikawa field. The section in Figure 11 is farther east, and passes through the natural surface discharge areas (the Akagawa and Sumikawa hot springs). These cross-sections show (as contours) the distributions of stable subsurface temperature. Also shown (as small arrows) is the

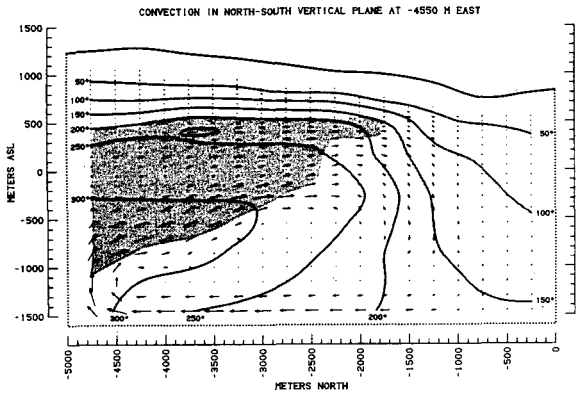

Figure 10. Computed nature-state fluid mass flux distribution in north-south vertical plane at x = –4550 m E (i = 3). Contours represent natural-state temperature. Shaded area indicates location of two-phase region.

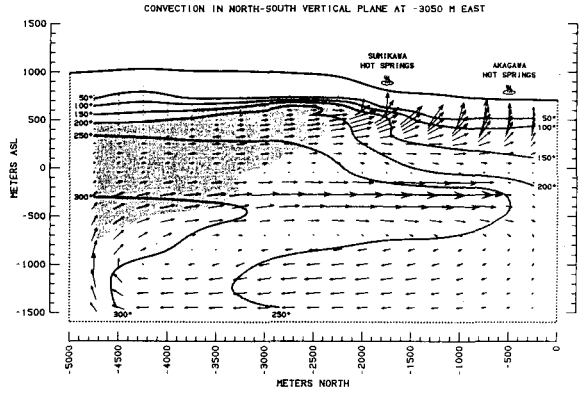

Figure 11. Computed natural-state fluid mass flux distribution in north-south vertical plane at x = –3050 m E (i = 8). Contours represent natural-state temperature. Shaded area indicates location of two-phase region.

Table 3. Comparison between computed and measured temperatures.

Well	Elevation (m ASL)	Temperature (Celsius) Computed	Measured	Difference
O-5T	+80	210.4	210	+0.4
Y-2T	+290	172.0	170	+2.0
Y-3T	+405	59.9	60	−0.1
KY-1	−570	200.9	200	+0.9
KY-2	−675	260.1	260	+0.1
S-4	−410	289.1	290	−0.9
SA-1	−690	272.6	280	−7.4
SA-2	−340	297.4	300	−2.6
SA-4	−130	269.6	270	−0.4
S-3	+350	232.2	230	+2.2
SB-1	−550	256.5	260	−3.5
SB-2	−220	238.2	240	−1.8
SB-3	+170	242.1	240	+2.1
SN-7D	−1220	241.4	240	+1.4

Table 4. Comparison between computed and measured pressures.

Well	Elevation (m ASL)	Pressure (bars) Computed	Measured	Difference
O-5T	+ 80	52.4	55	−2.6
KY-1	− 570	103.8	104	−0.2
S-2	+ 130	50.4	52	−1.6
S-4	− 410	92.1	93	−0.9
SA-1	− 690	112.3	114	−1.7
S-3	+ 350	32.5	33	−0.5
SB-1	− 550	102.3	103	−0.7
SB-2	− 220	77.3	78	−0.7
SB-3	+ 170	46.4	46	+0.4
SN-7D	−1220	151.0	149	+2.0

underground fluid mass flux distribution and (as a shaded area) the spatial extent of the two-phase (water/steam) flow zone. The unshaded area contains no underground *in-situ* steam. The relationship between the underground fluid flow pattern and the temperature distribution is reasonably clear. It is noteworthy that two distinct convection systems are apparently present—the deeper in the "AA" and "GR" deep permeable formations, and the shallower above the "MV" aquitard.

Comparisons between stable temperatures measured at the feedpoints of shut-in wells and corresponding computed temperatures (obtained by linear interpolation among principal grid point values) are indicated in Table III. Clearly, the computed temperature distribution represents the measured values about as well as could reasonably be expected: most of the computed values are within 3°C of measured temperatures. Also, the surface manifestation of the computed underground flow pattern (the calculated distribution of surface discharge) corresponds well with observations. The total computed upflow (total upflow from those surface blocks in which the flow direction is upward) for the entire surface is 37 kg/s. Four-fifths of this discharge emanates from just four grid blocks (i = 8; i = 7–10) in the northeastern part of the grid, where the hot springs at Sumikawa and Akagawa are located.

Finally, Figure 12 shows how the computed natural-state pressure distribution compares with measured stable feedpoint pressure values in wells. Agreement is seen to be quite good. Quantitative comparisons between measured and computed downhole pressures are provided in Table IV.

Accordingly, it is believed that the mathematical representation outlined above represents the Sumikawa geothermal system about as well as it can be represented

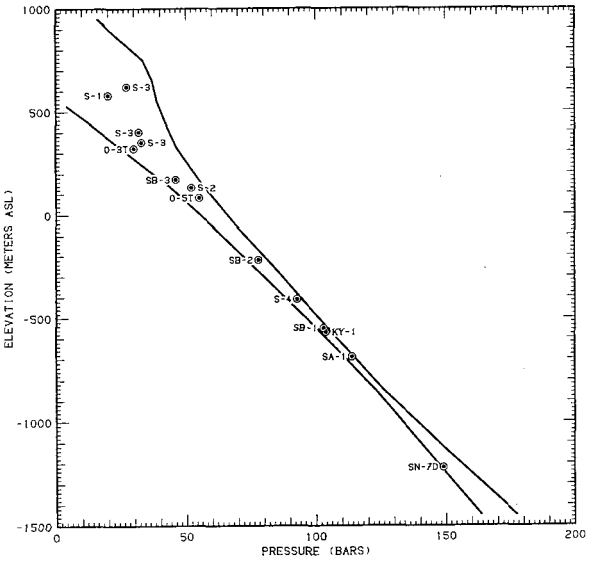

Figure 12. Comparison between measured downhole feedpoint pressures in wells and computed pressures. Solid lines indicate range of computed pressures (over grid horizontal area) for fixed elevations.

given the existing state of knowledge about the field. Parametric calculations (using the above natural-state mathematical model as a starting point) to predict system response under exploitation for electrical power have also been carried out, and indicate that the field should be capable of delivering sufficient steam for a power station of 50 MWe capacity or more for at least fifty years. Accordingly, we believe that the Sumikawa field is an excellent candidate for future development for electrical power.

References

Garg, S. K., J. W. Pritchett, K. Ariki and Y. Kawano (1991), "Pressure Interference Testing of the Sumikawa Geothermal Field", Proc. Sixteenth Workshop on Geothermal Reservoir Engineering, Stanford University.

Maki, H., J. W. Pritchett and S. K. Garg (1988), "Interpretation of a Pressure Interference Test of the Sumikawa Geothermal Field" Proc. International Symposium on Geothermal Energy 1988: Exploration and Development of Geothermal Resources, Kumamoto/Beppu, Japan.

Pritchett, J. W., S. K. Garg, H. Maki and Y. Kubota (1989), "Hydrology of the Sumikawa Geothermal Prospect, Japan" Proc. Fourteenth Workshop on Geothermal Reservoir Engineering, Stanford University.

Pritchett, J. W. (1989), "STAR User's Manual" S-CUBED Report SSS-TR-89-10242.

Pritchett, J. W. and S. K. Garg (1990), "On Similitude, Heat Conduction, and Two-Phase Flow in Fractured Porous Media", Proc. Fifteenth Workshop on Geothermal Reservoir Engineering, Stanford University.

PROCEEDINGS, Sixteenth Workshop on Geothermal Reservoir Engineering
Stanford University, Stanford, California, January 23-25, 1991
SGP-TR-134

COMPARISON OF THERMAL COOLDOWN ESTIMATES IN THE RUSSKIE KOMAROVTSY PETROGEOTHERMAL RESERVOIR

Paul Kruger
Stanford Geothermal Program
Stanford University

Yuri Dyadkin, Semon Gendler, Elena Artemieva, Nina Smirnova
Heat Physics Department
Leningrad Mining Institute

ABSTRACT

A comparison of several models to estimate the rate of thermal cooldown in artificial circulation geothermal reservoirs was made for the Russkie Komarovtsy fracture-stimulated reservoir, which will be located near the town of Uzhgorod in the Zakarpate region of the Ukraine SSR. The economic viability of this moderate-temperature resource depends on sustained flow above the minimum abandonment temperature for a period sufficient to recover investment and operating costs. The rate of heat extraction for the required flowrate depends on the fracture distribution in the reservoir. Results of the SGP 1-D Heat Sweep model are compared to approximate analytical and numerical models developed at the Leningrad Mining Institute, based on a common set of initial conditions for the Russkie Komarovtsy reservoir. The comparison shows that all of the models yielded reasonably similar thermal decline estimates with a satisfactory lifetime of about 25 years to abandonment temperature.

INTRODUCTION

Commercial development of the extensive, widely distributed petrogeothermal resources in the world depends on attaining economic efficiency in heat extraction from natural and artificially-fractured geothermal reservoirs by circulation of water as a heat-carrier fluid. Methods to predict the rate and lifetime of heat extraction from these moderate-temperature resources are very important for early decisions affecting their long-term development in the USA, USSR, and other countries seeking alternate sources of indigenous energy. The ability to develop commercial technology for heat-extraction at a sufficient rate over a satisfactory amortization period requires understanding of the complex heat and mass transfer processes involved. Heat transfer in fractured petrogeothermal reservoirs is a very complicated process (Dyadkin, 1989) dependent on a combination of geometric parameters of reservoir structure, hydrologic flow regimes, production and reinjection practices, and thermal properties of the fractured-rock formation. Pre-production data for many of these parameters are generally sparse, and heat extraction predictions for specific potential projects must be made from best estimates and suitable models of the geothermal system.

The economic feasibility of energy extraction from fracture-stimulated reservoirs with artificial circulation systems has been estimated (e.g., Boguslavsky, 1981; Murphy, et al, 1985; Dyadkin, 1985) with many assumptions concerning the processes of unsteady, non-isothermal flow of circulating fluid through a reservoir of fracture and matrix permeability distributions and of heat transfer rates for planar and irregular shaped rock blocks. Models have been developed for estimating heat extraction from such reservoirs (e.g., Gringarten, et al, 1978; Hunsbedt, et al, 1979; Pruess, 1983; Dyadkin and Gendler, 1985). In view of the need to improve the ability of heat extraction models to predict the behavior of yet undeveloped resources based on available data, a comparison was made between models developed at the Leningrad Mining Institute with the model developed at the Stanford Geothermal Program. The LMI heat-physics models, described by Smirnova (1978); Artemieva (1979a,1979b); Gendler and Pavlov (1980); Mukhin and Smirnova (1981); Artemieva and Piskacheva (1983); Dyadkin and Gendler (1985); and Artemieva and Stroganova (1986), were developed for several thermal aspects of mining operations. The SGP 1-D Heat Sweep model, described by Hunsbedt, et al (1977,1978,1979); Kuo, et al (1977); Kruger (1982); Hunsbedt, Lam, and Kruger (1983); and Lam and Kruger (1988), was developed for early analysis of prospective geothermal reservoirs based on pre-production data for estimating thermal recovery from reinjected fluid as a function of production strategy and reservoir characteristics.

To estimate the extent of uncertainty in modeling thermal extraction in an artificial circulation system, the 1-D Heat Sweep model has been compared with other heat extraction models, such as the LBL Reservoir Simulator (Lam, et al, 1988) and the Fenton Hill Hot Dry Rock reservoir model (Robinson and Kruger, 1988). As a basis for comparison of the LMI physical and numerical models with the SGP 1-D model, a test case was made of the Russkie Komarovtsy geothermal prospect, which is planned to be the first experimental demonstration of a moderate-temperature petrothermal resource created by hydrofracturing stimulation as an artificial circulation system. This case was chosen to examine the reliability of estimating lifetimes of moderate-temperature petrogeothermal resources, where the production time to reach abandonment temperature at the required flowrate is critical for providing a reliable and economic heat source.

RUSSKIE KOMAROVTSY GEOTHERMAL FIELD

The prime candidate for the first demonstration project of economic heat extraction from moderate-temperature petrogeothermal resources prevalent in the USSR is the Russkie Komarovtsy field in the Zakarpate region of the Ukraine SSR. This site was selected from an initial list of 16 candidate sites compiled from a national survey of USSR regions for a GeoTES (geothermal heat energy station) to provide a hot-water supply for municipal and agricultural heating. The demonstration project is designed to produce thermal water through a connected network of three large parallel hydrofractures at a constant flowrate, augmented by fossil-fuel heating, if necessary, over a useful lifetime in excess of 10 years.

Figure 1 shows a schematic section of the reservoir after five phases of reservoir creation by hydraulic fracturing. The resource consists of a massive granodiorite intrusive of 740 m thickness at a mean temperature of 124 °C, situated almost horizontally at a depth of 1900 to 2640 m. A description of the geologic setting was given by Vainblat and Drozdetskaya (1987). The hydrofracturing scheme was designed by Dyadkin (1987) and co-workers and the economics of heat extraction were estimated by Boguslavsky (1987). Early estimates of the fracture geometry were described in Dyadkin and Kruger (1989). Dyadkin, in 1990, provided updated estimates of the anticipated hydrofracturing results and comparative analyses of the heat extraction are based on the revised dimensions of the reservoir and planned flowrates to achieve economic return.

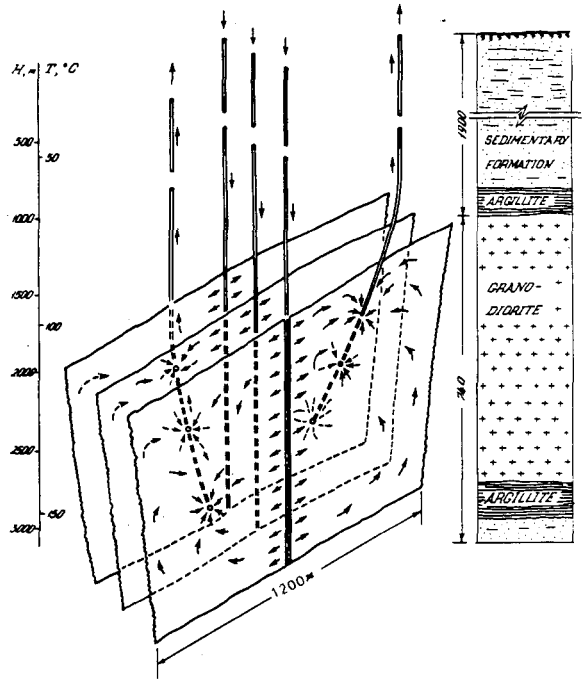

Fig. 1. Schematic of the Russkie Komarovtsy two-wing, three-parallel hydrofractured reservoir. (from Dyadkin and Kruger, 1989).

The three parallel-fracture reservoir will have an extractable heat content of HC = 9.88×10^{15} J for thermal drawdown from the mean initial temperature of 124 °C to the abandonment temperature of 110 °C. For a 10-year production lifetime at the anticipated flowrate of 11 kg/s per fracture, the mean heat extraction rate would be about 3130 kJ/s. The set of input data common to the comparison runs by the LMI and SGP models is listed in Table 1. Data specific for rock mechanical properties in the heat physics models are given in the respective publications.

THE LMI HEAT EXTRACTION MODELS

Analytical and numerical heatphysics models have been developed at LMI (Dyadkin and Gendler, 1985) for thermal mining processes over a number of years. An approximate analytical solution for bottom-hole fluid temperature after heat transfer in a vertically fractured rock to circulating fluid was examined by Smirnova (1978). The approach to the problem was adopted from Lauwerier (1955) for heat transport in an oil layer with injection of hot water. The method of Lauwerier is discussed by Prats (1986). The solution of the governing equations was derived with double application of the Laplace transform, first with respect to distance into the layer, and second with respect to time. The back transforms (from Carslaw and Jaeger, 1948) was of the form of the complimentary error function for the dimensionless fluid temperature:

$$\theta_f = \frac{T_r - T_f}{T_r - T_i} = erfc\frac{1}{\sqrt{J}} \qquad (1)$$

$$J = \left[\frac{Q_f C_w \rho_w}{W_f L_f}\right]^2 \frac{t - \frac{W_f L_f \delta}{Q_f}}{\lambda C \rho} \qquad (2)$$

where

T_r = mean initial formation temperature, °C
T_f = production well bottom-hole fluid temperature, °C
T_i = injection well bottom-hole fluid temperature, °C
ρ, ρ_w = density of rock, water, kg/m³
Q_f = water flow rate in fracture, m³/s
W_f, L_f = width, length of fracture, m
δ = mean fracture aperture, m
C, C_w = specific heat capacity of rock, water, J/kg°C
λ = thermal conductivity of rock, W/m°C
t = time, sec

If $t \gg (W_f L_f \delta)/Q_f$, then the dimensionless temperature in Equ. (1) can be approximated by the Austin formula in Gringarten, et al (1978) as

$$\theta = erfc\left(\frac{L_r W_r}{Q_f \rho_w C_w}\sqrt{\frac{\lambda \rho C}{t}}\right) \qquad (3)$$

Dyadkin and Gendler (1985) note that the approximation is correct for the relationship of modified Grashof number to Reynolds number over the range

Table 1
Russkie Komarovtsy Modeling Data Set

Parameter	Value	Parameter	Value
Reservoir Characteristics		Thermal Properties	
Rock Type: Granodiorite		Rock Density	2650 kg/m³
Dimensions		Rock Specific Heat	1000 J/kg°C
Length	1200 m	Thermal Conductivity	2.1 W/m°C
Width	300 m	Water Density (mean)	945 kg/m³
Height	740 m	Water Specific Heat	4200 J/kg°C
Mean Frac. Spacing	variable		
Porosity	0.00066		
Production Characteristics			
Initial Temperature	124 °C		
Injection Temperature	30 °C		
Abandonment Temp	110 °C		
Circulation Flowrate	36.9 kg/s		

$0 < (Gr^*/12\ Re) < 12$, where the two numbers are defined as:

$$Gr^* = \frac{g\alpha_f \Delta T_f \Delta L_f \delta^2}{\mu^2} \qquad (4)$$

$$Re = \frac{W_f}{\delta}\mu$$

where

g = gravitational constant, 9.81 m/s²
α_f = thermal expansion coefficient for water, °C⁻¹
ΔT_f = temperature change across fracture length, °C
ΔL_f = fracture length between well pair, m
δ = fracture aperture, m
μ = fluid viscosity, Pa.s

The LMI numerical model was developed by Artemieva (1979a,b) from consideration of the stability of a non-uniformly heated fluid flowing in a horizontal fracture. The approach was based on the use of Rayleigh and Peclet numbers in appropriate ranges, determined numerically. The modified Rayleigh number is derived from injection parameters and the Peclet number accounts for non-uniform permeability and temperature dependence of fluid viscosity. Dyadkin and Gendler (1985) note that the investigation of the heat exchange process in fractured rock was given in Artemieva and Piskacheva (1983). Numerical solution of the hydrodynamic equations was carried out for vertical rectangular fractures of constant aperture. Results of the numerical calculations confirmed the basic conclusions reported by McFarland (1975) for the Fenton Hill hydrofractures as estimated at that time. It was also noted that the numerical solution was satisfied for the range of modified Grashof and Reynolds number criteria adapted for the analytical model.

THE SGP 1-D HEAT SWEEP MODEL

The 1-D linear heat sweep model was initially developed for analysis of experimental measurements of heat extraction from an assembly of arbitrary-shaped rock blocks in a laboratory model of a fractured-rock reservoir (Hunsbedt, et al, 1977). The model has been improved to provide for radial and doublet flow (Lam, 1989) and for non-uniform initial temperature distribution (Lam and Kruger, 1988). The differential equations which describe heat transfer from an assembly of rock blocks with a single mean equivalent-sphere radius to the surrounding fluid in linear heat sweep circulation are given in Kruger (1982). The nondimensional fluid temperature at location x and time t, can be expressed in terms of three parameters: N_{tu}, γ, and q,

$$T_f^*(x^*, t^*) = \frac{T_f(X, t) - T_e}{T_i - T_e} = f(N_{tu}, \gamma, q) \qquad (5)$$

where

x^* = x/L, nondimensional linear distance from injection well to production well
t^* = t/t_{res}, nondimensional flow time
N_{tu} = τ/t_{res}, number of heat transfer units, given by the ratio of the thermal time constant of the rock blocks to the mean residence time of the fluid
γ = thermal storage ratio, thermal energy stored in the surrounding fluid relative to that in the rock blocks
q = external heat transfer parameter per unit flow path length.

The "number of heat transfer units" parameter indicates the relative thermal aspects of the flowing reservoir, based on anticipated flowrate through the fracture flow path. For small values ($N_{tu} < 10$), the reservoir is heat transfer limited. The rate of heat conduction to the rock block surfaces is insufficient for effective heating of the circulating fluid, resulting in rapid decline in produced water temperature.

Fig. 2 shows the equivalent flow geometry for the Russkie Komarovtsy three parallel hydrofractured reservoir as a one-dimensional linear heat sweep problem. The model considers the question as two independent flows through 600 m of fracture path length with various values of mean fracture spacing. With the LMI assumption of fully competent rock without

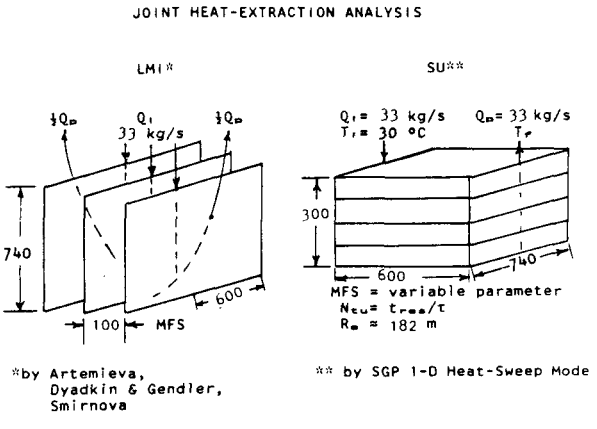

Fig. 2. Equivalent flow geometry for one wing of the Russkie Komarovtsy reservoir for 1-D linear heat sweep modeling.

natural fractures following hydrofracturing, the volume of each rock block would be V_b = 600x100x740 = 4.44×10^7 m³ and the equivalent heat transfer spherical radius would be $R_e = \psi_K (3V_b/4\pi)^{1/3}$ = 182 m. The thermal time constant of the rock block is

$$\tau = R_e^2/3\alpha \ (0.2\text{-}1/Bi) \qquad (6)$$

where

ψ_K = Kuo sphericity (Kuo, et al, 1977) = 0.83
α = thermal diffusivity of the rock
Bi = Biot number of the rock

For an equivalent radius of 182 m, the time constant is 88.7 years. Based on the LMI estimated minimum required flowrate of 11 kg/s per fracture to achieve economic thermal energy extraction, the mean residence time would be 0.08 years (29 days). The "number of heat transfer units", thus for any such flowrate would be of the order of 0.001, much too small for effective heat extraction rate. Therefore, in estimating the Russkie Komarovtsy reservoir production, it was assumed that natural fractures would exist as flow paths, and calculations were made for a range of mean fracture spacings from 50 m (R_e = 25 m, with a correspondingly smaller thermal time constant).

RESULTS

Fig. 3 shows the cooldown results calculated by the LMI analytical model (solid lines) and the LMI numerical model (dashed lines) as a function of flowrate through the main hydrofractures. The values from 5.5 to 50 kg/s per fracture represent the range of needed flowrates for economic return. For a flowrate of 11 kg/s per fracture, the analytical model predicts a lifetime of 25 years to the abandonment temperature of 110 °C.

Fig. 4 shows the corresponding cooldown estimates calculated by the SGP 1-D heat sweep model for competent rock blocks with MFS of 354 m for an

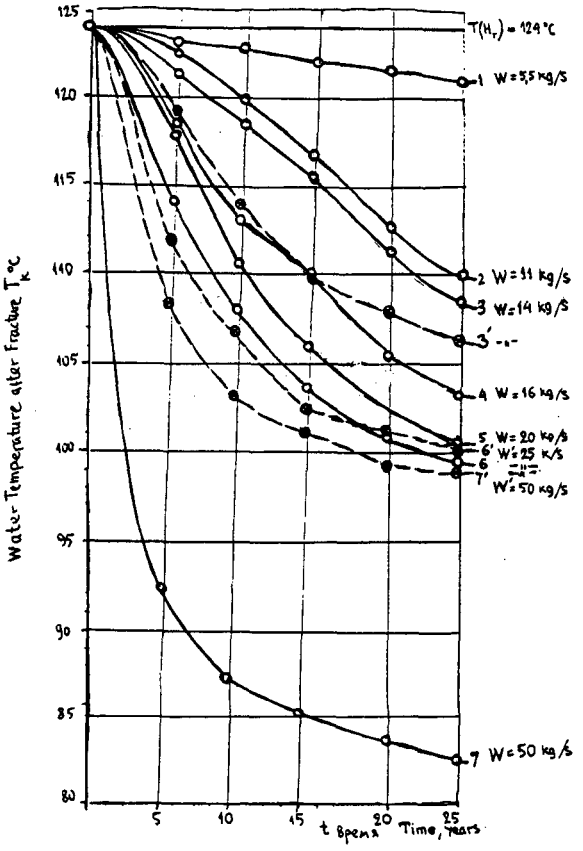

Fig. 3. Results of LMI cooldown estimates as a function of flowrate through the principal hydrofractures by the numerical model (solid lines) and the analytical model (broken lines). (hand carried from LMI by Y. Dyadkin, September, 1990)

equivalent radius of 182 m. The values for flowrate of 5.5 and 11 kg/s per fracture show cooldown to abandonment temperature in less than two years. Larger flowrates would result in even faster cooldown to 110 °C. Fig. 5 shows the calculated cooldown for a flowrate of 11 kg/s per fracture as a function of mean fracture spacing. For MFS values around 50-100 m, cooldown to 110 °C would be longer than 25 years, and above 200 m, the cooldown time would be less than 10 years, the minimum amortization period. A match with the LMI analytical method for the anticipated flowrate of 11 kg/s per hydrofracture occurs for a MFS of about 160 m.

Table 2 gives a summary of the cooldown results for the range of flowrates considered. The values for the LMI analytical model agree well with the LMI numerical model for flowrates of 14 and 25 kg/s, but differ somewhat for 50 kg/s. The SGP model shows the very rapid temperature decline for the assumption of MFS = 354 m (τ = 88.7 y) for competent rock blocks after hydrofracturing. The small value of 50 m (τ = 1.77 y) shows adequate heat transfer with essentially no cooldown for 10 years at flowrates up to about 25 kg/s per fracture and possibly sustained production at

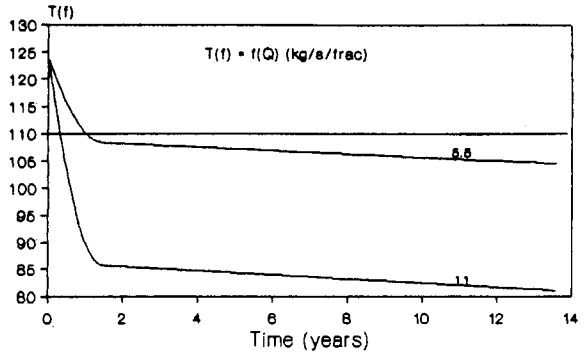

Fig. 4. Results of SGP cooldown estimates as a function of flowrate around the hydrofractured rock blocks with equivalent radius of 182 m.

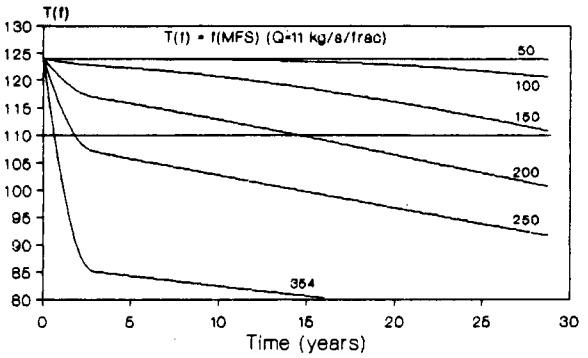

Fig. 5. Results of SGP cooldown estimates as a function of mean fracture spacing for the LMI anticipated flowrate of 11 kg/s per hydrofracture.

Table 2
Comparison of LMI-SGP Calculated Results

	Bottom-hole Fluid Temperature (°C) after 10 years of Production				
	LMI Model		SGP MFS (m)		
Flowrate (kg/s/fracture)	Numerical	Analytical	354	160	50
5.5	123	--	106	124	124
11.0	120	--	83	120	124
14.0	118	114	--	115	124
16.0	113	--	--	110	124
20.0	111	--	--	104	124
25.0	108	107	--	97	123
50.0	87	103	--	72	108

50 kg/s for almost 10 years. At the match MFS of 160 m (τ = 18.1 y), the calculated values follow those of the LMI models at flowrates to about 20 kg/s and decline faster thereafter.

DISCUSSION

The comparison of the two LMI models and the SGP model has pointed out some key aspects with respect to the resulting hydrodynamic regime for heat extraction by a circulating fluid. Foremost of these is the actual results of the massive hydraulic fracturing which creates the artificial reservoir. The possibilities of creating competent parallel hydrofractured blocks without associated interconnections through opened natural fractures is discussed by Dyadkin, et al (1990). It is apparent that independent means (such as seismic response or tracers) to ascertain the actual volume and heat content of the fractured rock constituting the reservoir is needed. A second key aspect is the actual flow paths taken by the injected fluid. The three models assume the flow is uniformly distributed, and in the LMI models, primarily in the hydrofractures. The rate of heat transfer with distance between wells and time is thus strongly influenced by the flow and initial temperature distributions. A third aspect is the induced changes in the reservoir with production time. Fracture patterns and rock thermal properties are likely to change with temperature and pressure changes over the lifetime of the reservoir. Since each of these aspects is unknown during the planning and initial production phases at a newly created petrogeothermal resource, the ability to estimate possible ranges of productivity becomes very important. When estimates made by models of diverse assumptions provide a reasonable range of potential results, the confidence level of making investment decisions rises markedly. Although many differences exist between the LMI analytical and numerical models and between the LMI and SGP models, the agreement in range of expectations is sufficiently good to consider that given the large uncertainties in the above mentioned aspects of heat extraction, the estimated lifetime of the Russkie Komarovtsy petrogeothermal resource should provide the minimum return of hot water supply at the required flowrate for a minimum of 10 years and likely for 25 years without the need for fossil-fuel augmentation.

REFERENCES

Artemieva, E.L., Numerical Simulation of Mixed Convection in Water-Saturated Geothermal Seams, pp. 102-106, "Physical Processes in Mining Operations", No. 6 (LMI Press, Leningrad, 1979a).

Artemieva, E.L., Influence of Liquid Viscosity on Filtration Process in Porous Seams, pp. 84-91, "Physical Processes in Mining Operations", No. 7 (LMI Press, Leningrad, 1979b).

Artemieva, E.L. and T.Yu. Piskacheva, Mixed Convection in a Vertical Hydraulic Fracture, pp. 82-89, "Heatphysical Processes in Mining Technology" (LMI Press, Leningrad, 1983).

Artemieva, E.L. and E.V. Stroganova, Stability of a Non-uniform Heated Liquid in a Porous Horizontal Seam, pp.3-7, "Mechanics of Liquids and Gases", No.6, (Acamemy of Sciences, USSR, Moscow, 1986).

Boguslavsky, E.I., Economic-Mathematical Simulation of Geothermal Circulation Systems, p.104, "Heatphysical Processes in Mining Technology" (LMI Press, Leningrad, 1981).

Boguslavsky, E.I., Economic-Mathematical Modeling and Experimental Parameters of a GCS with Hydrofracturing of the Zakarpate GeoTES, pp. 107-110, "Engineering-Physical Conditions of Fracturing Hard Rock" (LMI Press, Leningrad, 1987).

Carslaw, H.J. and J.C. Yaeger, "Conduction of Heat in Solids" (Oxford Press, Oxford, 1948).

Dyadkin, Yu.D. and S.G. Gendler, "Heat-Mass Transfer Processes in Geothermal Energy Extraction" (LMI Press, Leningrad, 1985).

Dyadkin, Yu.D., Method of Calculating Hydrofracturing Parameters for Hard Rock at Great Depth, pp. 71-84, "Engineering-Physical Conditions of Fracturing Hard Rock" (LMI Press, Leningrad, 1987).

Dyadkin, Yu.D., "Mining of Geothermal Deposits" (Nedra, Moscow, 1989).

Dyadkin, Yu.D. and P. Kruger, Heat Extraction from Low-Temperature Fractured Petrothermal Resources, pp. 190-200, "Hot Dry Rock Geothermal Energy", Proceedings, CSM International Conference, Cornwall, UK, June, 1989 (Robinson Sci. Pub., London, 1990).

Dyadkin, Yu.D., S.G. Gendler, and N.N. Smirnova, "Geothermal Thermophysics" (Nauka, Leningrad, 1990), in press.

Gendler, S.G. and I.A. Pavlov, A Method for Heat Transfer in Heterogeneous Media Task Solution, Engr.Phys.J. 39, No.1, 29-32,(1980).

Gringarten, A, P. Witherspoon, and Y. Ohnishi, Theory of Heat Extraction from Fractured Hot Dry Rock, J.Geophys.Res. 8, 241-253 (1978).

Hunsbedt, A., P. Kruger, and A.L. London, Laboratory Studies of Non-Isothermal Field Production from Fractured Geothermal Reservoirs, Paper 77-HT-53, Proceedings, ASME/AIChE 18th National Heat Transfer Conference, Salt Lake City, UT, August, 1977.

Hunsbedt, A., P. Kruger, and A.L. London, Energy Extraction from a Laboratory Model Fractured Geothermal Reservoir, J.Petro.Tech. 30, No.5, 712-718 (1978).

Hunsbedt, A., R. Iregui, P. Kruger, and A.L. London, Energy Recovery from Fracture-Stimulated Geothermal Reservoirs, Paper 79-HT-92, Proceedings, ASME/AIChE 19th National Heat Transfer Conference, San Diego, CA, August, 1979.

Hunsbedt, A., S. Lam, and P. Kruger, User's Manual for the 1-D Linear Heat Sweep Model, SGP Technical Report SGP-TR-75, 1983.

Kruger, P., Experimental Studies on Heat Extraction from Fractured Geothermal Reservoirs, pp. 373-397 in S. Nemat-Nasser, H. Abe, and S. Hirakawa, Eds., "First Japan-U.S. Seminar on Hydraulic Fracturing and Geothermal Energy" (M. Nijhoff, Tokyo, 1982).

Kuo, M.C.T., P. Kruger, and W.E. Brigham, Shape-Factor Correlations for Transient Heat Conduction from Irregular-Shaped Rock Fragments to Surrounding Fluid, Paper 77-HT-54, Proceedings, ASME/AIChE 18th National Heat Transfer Conference, Salt Lake City, UT, August, 1977.

Lam, S., Ph.D. Dissertaion, Mechanical Engineering Department, Stanford University, 1989.

Lam, S. and P. Kruger, 1-D Doublet Heat Sweep Model, Proceedings, 10th New Zealand Geothermal Workshop, (Univ. of Auckland, NZ, November, 1988).

Lam, S., A. Hunsbedt, P. Kruger, and K. Pruess, Analysis of the Stanford Geothermal Reservoir Model Experiments Using the LBL Reservoir Simulator, Geothermics 17, 595-605 (1988).

Lauwerier, H.A., The Transport of Heat in Oil Layer Caused by Injection of Hot Fluid, Appl.Sci.Res. 5, No.2-3, 145-150, (1955).

McFarland, R.D., Geothermal Reservoir Model - Crack Plane Model, LANL Int. Report, 1975.

Mukhin, V.A. and N.N. Smirnova, Experimental Investigation of Transient Heat Extraction in Porous Media with Fluid Filtration, J. Appld. Mech. and Tech. Phys. Vol. 4, pp. 110-115, (Nauka, Novosibirsk, 1981).

Murphy, H.D., R. Drake, J. Tester, and G. Zyvoloski, Economics of a Conceptual 75 MW Hot Dry Rock Electric Power Station, Geothermics 14, 459-574 (1985).

Prats, M., "Thermal Recovery", 2nd edi. Monograph No.7, (SPE, New York, 1986).

Pruess, K., Development of the General Purpose Simulator MULKOM, Technical Report LBL-15500 (Lawrence Berkeley Lab., Earth Science Division, 1983).

Robinson, B.A. and P. Kruger, A Comparison of Two Heat Transfer Models for Estimating Thermal Drawdown in Hot Dry Rock Reservoirs, pp. 113-120, Proceedings, 13th SGP Workshop on Geothermal Reservoir Engineering (Stanford Univ., January, 1988).

Smirnova, N.N., Solution of Equations of Heat Transfer with Filtration by Method of Reducing System to Equivalent Equations of Heat Conduction, pp. 61-68, Proceedings, Physical Hydrodynamics and Heat Transfer, (Inst. Themophysics, Ac.Sci.USSR, Novosibirsk, 1978).

Vainblat, A.B. and S.L. Drozdetskaya, Calculation of Fracturing the Hard Rock Region for Construction of the Zakarpate GeoTES, pp. 102-106, "Engineering-Physical Conditions of Fracturing Hard Rock" (LMI Press, Leningrad, 1987).

PROCEEDINGS, Sixteenth Workshop on Geothermal Reservoir Engineering
Stanford University, Stanford, California, January 23-25, 1991
SGP-TR-134

PREDICTION AND PREVENTION OF SILICA SCALING AT LOW LEVELS OF OVERSATURATION: CASE STUDIES, AND CALCULATIONS FOR UENOTAI GEOTHERMAL FIELD, AKITA PREFECTURE, JAPAN

Christopher W. Klein[1], Shun Iwata[2], Rituo Takeuchi[2], Tohsaku Naka[2]

1. GeothermEx, Inc., Richmond, California, USA
2. Akita Geothermal Energy Co., Ltd., Tokyo, Japan

ABSTRACT

Production system design studies often include site-specific silica scaling field experiments, conducted because the onset and rate of scaling are believed difficult to predict, particularly at relatively low levels of oversaturation such as may exist in separators, flowlines, and injection wells. However, observed scaling occurrences (Cerro Prieto, Dixie Valley, Svartsengi, Otake, Hatchobaru, Milos, experimental work) actually conform fairly well to existing theory and rate equations. It should be possible to predict low level scaling with sufficient confidence for production and injection system design and, in cases where oversaturation is allowed, to design systems with foresight to suppress or manage the scale which develops. A promising suppression technology is fluid pH reduction by mixing with non-condensible gases and/or condensate. Calculations for injection lines at Uenotai geothermal field indicate molecular deposition at rates of 0.1 to 1 mm/yr, and some potential for particle deposition at points of turbulence, which can be suppressed by an order of magnitude with about 500 ppm CO_2. Further improvements of predictive technique will benefit from more uniformity in designing experiments, reporting results, and reporting measurements of scaling in actual production systems.

INTRODUCTION

In spite of the phenomenal industry success in learning to manage the severe silica scaling from hypersaline geothermal brine at the Salton Sea in California, scale development from low levels of oversaturation in more typical, lower salinity waters remains a nuisance. The pressure/temperature at which a boiling wellflow saturates with amorphous silica often is used to constrain the design of production conditions. When oversaturation is allowed, typical scale management includes periodic clean-out or replacement of separators and pressurized disposal lines, and allowing the fluid to flash to atmospheric pressure so that silica can be driven out of solution and removed by chemical/-mechanical means (e.g., flocculation and settling) before the residual brine is injected back into the reservoir. Where the oversaturation of pressurized brine is not too severe, direct injection may be practiced. However, silica scale is often the inferred cause of mild to severe permeability losses in injection wells.

Because silica scaling mechanisms are fairly complex and poorly quantified, it has been common to design scale management on the basis of local field experiments. From our experience with published and unpublished studies, comparison of results has been hindered by a lack of uniformity in experimental design, methodology and reporting.

In this context, a study was undertaken to assist production - injection system design at Akita Geothermal Energy Company's Uenotai Field (Menzies and others, 1990; Robertson-Tait and others,1990). The purpose of this work was to review existing theory and case studies, produce a model of expected fluid behavior and scaling, and make design recommendations.

It was assumed that steam separation would occur at 8.1 or 9.3 bar (170 or 175°C), and that maximum injection pipeline residence times would be 20 to 45 minutes during 30 years of production. The residence times were calculated from production simulations and preliminary pipeline designs. Averaged fluid samples from two similar wells were considered. Table 1 provides an example. A correction was made for the slightly different average pressures of the water and gas samples. Note that the Uenotai water is quite dilute, in spite of high reservoir temperature (c.280°C at well T-51).

SCALING MECHANISMS

When reservoir water boils and loses steam through a pressure drop silica saturation can be simply calculated using a graphical solution (figure 1). The figure shows the solubilities of quartz (Fournier and Potter, 1982), chalcedony (determinations by Fournier, 1981 and Arnorsson and others, 1983), and amorphous silica (Fournier, 1981; Chen and Marshall, 1982; Fournier and Marshall, 1983), all plotted at steam saturation enthalpy. A straight line passes through two known

Table 1 : Averaged Sample Data, Well T-51

Total flow enthalpy 447.98 cal/gm

Water fraction:
Separation pressure 5.0 bar
(9 to 17 samples each parameter)

Parameter	mg/l	Parameter	mg/l
Ca	0.39	Tot.Alk(as HCO_3)	56.08
Mg	0.04	SO_4	31.24
Na	180.50	Cl	247.56
K	37.14	SiO_2	892.27
Li	0.55	F	2.34
Cs	0.03	B	1.24
NH_4	0.42	H_2S	11.76
Al	1.38		
As	0.24	pH (lab.)	8.89/22°C

TDS(meas.)	1,374.06	Ion balance	
TDS(sum)	1,418.69	(difference/sum)	+1.29
TDS_m/TDS_s	0.969		

Gas fraction:
Separation pressure 4.5 bar
(9 to 11 samples each parameter)

Dry gas CO_2	83.98	vol.%
H_2S	6.48	
N_2	4.06	
CH_4	5.66	
H_2	4.94	
Gas/steam	2,727.	mm/1,000m

points (steam at separation pressure and the reservoir) and leads to the silica concentration in the residual liquid. The case shown is the wellhead at Uenotai well T-51 during a 3 month flow test in 1988, when there was 340 mg/kg oversaturation with amorphous silica, and a thick deposit of soft white scale formed on the control valve (wellhead conditions 4 bar/142°C).

A complete review of silica chemistry with respect to oversaturation response is beyond the scope of this paper, but a summary of the most essential and satisfactory theory is needed. Major bibliographies are provided by Marsh and others (1975), Iler (1979) and Chan (1989).

The dissolved silica usually reported as SiO_2 behaves in solution as a molecule named silicic acid, written as $Si(OH)_4^\circ$ or $H_4SiO_4^\circ$. This can be described as a combination of SiO_2 with two water molecules. More essential is the concept that it contains four separate -OH groups bonded to a central Si atom. In turn, these "silinol" groups have two essential behaviors.

One behavior is acidity. A silinol group can loose its proton (H^+), although silicic acid is weak and therefore insignificantly ionized at low pH. The loss of one proton produces silicate ion:

$$H_4SiO_4^\circ = H_3SiO_4^- + H^+.$$

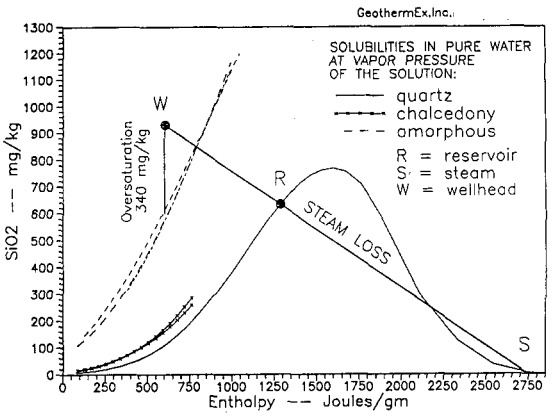

Figure 1. Silica versus enthalpy during boiling.

The proportion of silicate ion to unionized silica ($H_3SiO_4^-/H_4SiO_4^\circ$) is about 1/100 at pH 7.8 (25°C), rising to 1/1 at pH 9.8 (25°C). From 25°C to about 175°-200°C the acidity increases by about an order of magnitude (1/1 ratio at about pH 8.8); then it decreases again as temperature rises further. $H_2SiO_4^=$, which forms when a second proton is lost, remains nearly insignificant except at very high pH. Some $H_3SiO_4^-$ is conventionally considered to combine with Na^+ to form dissolved sodium silicate, $NaH_3SiO_4^\circ$.

The second behavior is reactions between silinol groups to form the Si-O-Si bonds in silica minerals. These reactions determine the maximum undissociated $H_4SiO_4^\circ$ in a solution at a given temperature. Solution composition also has an effect, whereas pressure has little effect unless extremely high.

Reservoir water at thermodynamic equilibrium typically contains $H_4SiO_4^\circ$ in a concentration determined by the least-soluble solid phase, pure SiO_2 as quartz. Below about 180°C, quartz tends to develop in a particular form called chalcedony, which has somewhat higher solubility (figure 1). When a quartz-saturated solution oversaturates by boiling, it rarely forms quartz scale unless temperature remains above about 220°C, because the rate of crystal growth is extremely slow relative to wellbore processes.

In such cases, a boiling/cooling solution can eventually oversaturate to the point where $H_4SiO_4^\circ$ becomes limited by Si-O-Si bonding into polymers. The initial step in this process is a "condensation reaction", between two silicic acid molecules:

$$H_4SiO_4^\circ + H_3SiO_4^- = H_6Si_2O_7^\circ + OH^-.$$

Deposition onto a solid surface begins by an analogous process, where dissolved silicic acid reacts with an -OH group on a corroded iron.

Compared to quartz crystals, the growing polymers are messy, with irregular surfaces, numerous remaining silinol groups, and infinitely branching structures.

However, they equilibrate with a predictable concentration of low molecular weight silicic acids; this concentration defines the solubility of amorphous silica (figure 1). It is common to refer to this solubility as the concentration of monomeric silica (also termed m-SiO_2) or $H_4SiO_4°$; this terminology is used herein. In actuality, the soluble silica is a mixture of low molecular weight silicic acids (monomer, dimer, trimer; Marsh and others, 1975).

In all cases of solubility (quartz, chalcedony, amorphous silica), any ionized silica present exists in addition to $H_4SiO_4°$. As a consequence, the apparent solubility given by total SiO_2 in solution (T-SiO_2 = unionized SiO_2 + ionized SiO_2) increases as pH increases. Figures 2 and 3 show the difference between total SiO_2 and SiO_2 in $H_4SiO_4°$ calculated for the Uenotai fluid, plotted versus pressure and then temperature instead of enthalpy. The relevant calculations are described in Appendix A.

pH also exerts significant control on polymerization rate. The causes of this are not completely understood, but implied by the condensation reaction as written above. Polymers grow by collision of an unionized -OH unit on one molecule with an ionized $-O^-$ on another, releasing OH^- into solution (Marsh and others, 1975). This indicates that polymerization rates should be at a maximum when the concentrations of available -OH and $-O^-$ on growth surfaces are equal. In a slightly oversaturated solution, this is the pH at which $H_4SiO_4°$ = $H_3SiO_4^-$ (pH 9.8 at 25°C; 8.8 at 175°-200°C, see above). Large polymers have higher acidity, so a strongly oversaturated solution can exhibit its maximum growth rate at somewhat lower pH.

The pH effect generally is observed, and as an approximate rule lowering pH slows kinetics by a factor of about 10 for every pH unit (e.g. Rothbaum and others, 1979; Hirowatari and Yamaguchi, 1990).

In an oversaturated solution, the relationship between polymer growth and actual scale deposition is a function of combined chemical and physical processes which follow two dominant and essentially competing pathways: molecular deposition and particle deposition.

Molecular deposition occurs when the growing polymer surface is a solid, to which silicic acid and silicate ions migrate by circulation and diffusion. The rate of deposition is a function of temperature, supersaturation, and the density of silinol groups ionized to -Si-O^- on the solid growth surface. The effective surface density increases with salinity and, of course, pH (Weres and others, 1982). This rate is discussed further below.

Particle deposition follows nucleation and growth of suspended polymers. The starting process is termed homogeneous nucleation because the polymers develop spontaneously in solution and not by deposition onto foreign particles or ions of other solutes. This is a chemically reversible process. It starts with an "induction period" which rolls smoothly, on a logarithmic time scale, into a period of rapid polymer growth, then slowing growth as the oversaturation of the solution is depleted. At low levels of oversaturation (and/or low pH) the induction period can last minutes to hours. When initial supersaturation exceeds about 2 to 2.5, the induction period often is instantaneous, and polymer growth very rapid.

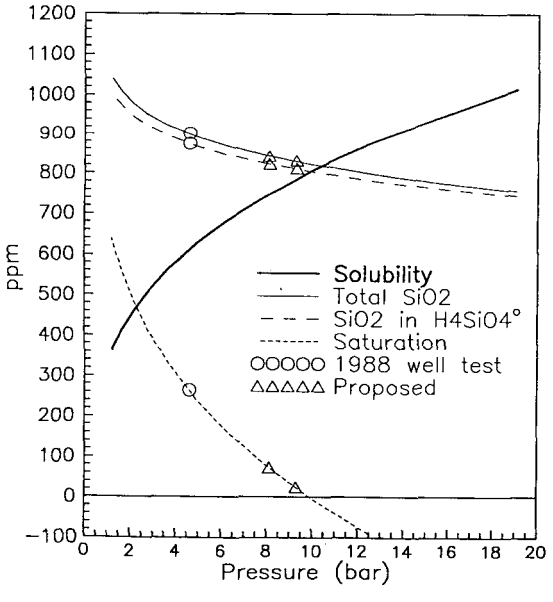

Figure 2. Silica versus pressure, Uenotai well T-51.

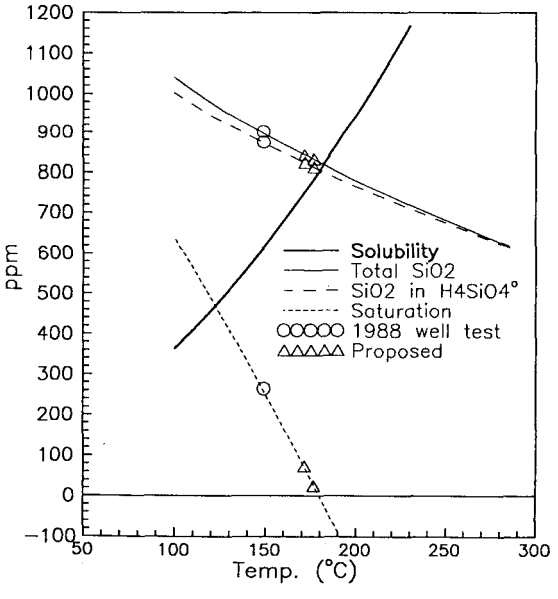

Figure 3. Silica versus temperature, Uenotai well T-51.

Many studies of induction period and polymerization rate have been published (e.g., see Kindle and others, 1974; Hurtado and Mercado, 1990; and Thordarson and Tomasson, 1989). However, it must be considered that such studies typically are context specific, depending strongly on SiO_2 concentration, temperature, salinity and pH. Induction will be shorter at higher SiO_2; for a given SiO_2 level induction will be shorter at lower temperature, higher salinity, and higher pH, except when counteracted at very high pH by increased solubility. Marsh and others (1975) also note that many studies of polymerization rate have been flawed by inadequate experimental technique and misinterpretation of results. Weres and others (1982) have discussed a computer program for calculation of nucleation rates (see below).

The properties of the growing polymers, such as individual size and acidity, change continuously as they grow, and different solutions mature differently. For example, the relatively low nucleation rates at high temperatures cause formation of fewer particles which tend eventually to become larger. At low temperature there typically is a higher supersaturation ratio, and nucleation produces larger numbers of smaller particles. High pH causes rapid growth of many particles which aggregate quickly into larger units, whereas low pH promotes the continued separate growth of smaller particles.

There is a loosely defined size (usually termed "critical size") above which the growing polymers are considered to be colloidal particles. At this point they are spherical in shape, and once greater than about 10 nm in diameter, they apparently grow by molecular deposition at the same rate as surface scale. There is competition between surface scale and suspended particles for the supply of excess $Si(OH)_4$ in solution. Therefore, when the particles are abundant and growing, the rate of molecular deposition onto solid surfaces (e.g., pipe walls) may decrease, because the particles are taking $Si(OH)_4$ out of solution.

The colloidal particles can deposit as scale when they reach solid surfaces, driven by diffusion, flow turbulence, and sometimes gravity. If these transfer processes are rapid, scale can grow on the surface much more rapidly than it could by molecular deposition alone. Mass transfer tends to be most rapid at low temperature, when particle sizes are small, and at high turbulence. Adhesion of particles onto solid surfaces appears to be both a chemical and a physical process; once adhered, the particles can become cemented by further molecular deposition. In static or slowly flowing regimes, the scaling process can be affected further by coagulation or flocculation of colloidal particles to give either a precipitate or a suspended semi-solid material, or a gel; some solutions form stable colloids which do not precipitate.

Molecular deposition is primarily responsible for producing hard, vitreous, often dark colored scale, with density about 2.1 to 2.3 g/cc. In contrast, particle deposition produces white, fluffy, scale with dry density about 0.95 g/cc. Exceptions to these rules have been described, including hard scale believed to have deposited by particle deposition, and soft white scale which formed at low oversaturation within the expected induction period (Jamieson, 1984). Changes in flow rates or supersaturation may be marked by alternating laminae of vitreous and fluffy scale. In pipelines, the scale often forms radial ridges transverse to the flowpath, which can cause considerable roughness to fluid flow (e.g., Stock, 1990).

SCALING EXPERIENCE

Several recent reports of scaling experience were considered in light of the processes above. Available descriptions are typically incomplete (see recommendations below), but most allow an illustration of scaling rate or effects in relation to temperature or pressure and SiO_2 concentration.

Cerro Prieto, Mexico: Scaling in a pilot facility and in disposal lines (figure 4) has been described by Hurtado and Mercado (1990). The pilot plant data represent fluid from one well processed at a rate of 9.1 t/hr through two or three stages of steam separation. Scaling in the plant was highly concentrated at points of turbulence, and figure 4 shows what appear to have been the maximum scaling rates. The scale was not described, but probably formed by particle deposition.

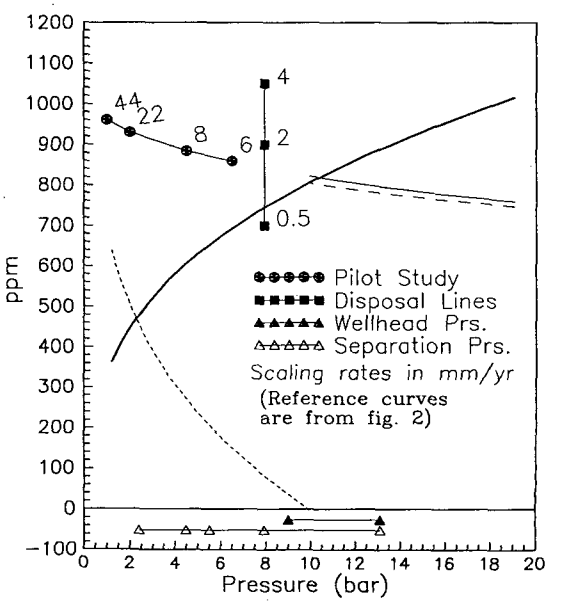

Figure 4. Silica versus pressure, showing scaling rates, Cerro Prieto.

The disposal line data represent maximum rates at 7 wells flowing for 6 years at 170°C. The rates of 0.5 and 4 mm/yr were measured in single flow lines, and SiO_2 for the point at 0.5 mm/yr probably has been underreported. The point at 2 mm/yr is the rough average of 1 mm/yr to 3 mm/yr at 5 wells with SiO_2 between 800 and 1000 ppm. Scale morphologies were not described.

Figure 4 also shows the range of wellhead pressures and steam separation pressures currently in use at Cerro Prieto. Most wellhead pressures are above the point of silica saturation, but steam separation pressures are low enough to allow scaling to occur.

Dixie Valley, Nevada (chemical data courtesy of Oxbow Geothermal Corp., W.R. Benoit, private communication): The reservoir water at Dixie Valley is almost as dilute as at Uenotai, although temperature is lower and alkalinity is higher, so that pH at a given temperature is higher by about 0.5. Cl in injection lines is 395 mg/l. Figure 5 shows total SiO_2 in high pressure separators and at injection wellheads, and unionized SiO_2 at injection wellheads. We calculate that pH at the injection temperature of 106°C is 8.3, so there is a large difference between total SiO_2 and unionized SiO_2. Data from Stock (1990) indicate that injection line residence times vary from 27 to 58 minutes, with most injection wells 30 minutes downstream from a production separator.

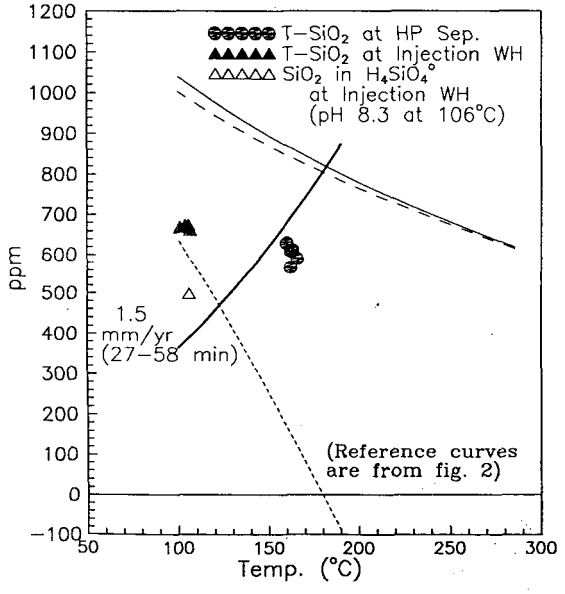

Figure 5. Silica versus temperature at Dixie Valley, with injection line scaling rate.

In straight runs of the injection line, thin silica scale was deposited in 2 to 3 mm high radial sawtooth ridges which faced upstream (Stock, 1990). The duration of flow was not reported but probably was 1 to 2 years; hence the average 1.5 mm/yr on figure 5. In one elbow, the scale was as thick as 6.5 to 13 mm, and consisted of thin flakes oriented almost perpendicular to the pipe walls in an extreme form of the sawtooth ridge pattern. Generally the surface of the scale could be easily scraped to a smooth base, and no hard glass scale was seen. Particle deposition is indicated, and explained by rapid nucleation at very high pH.

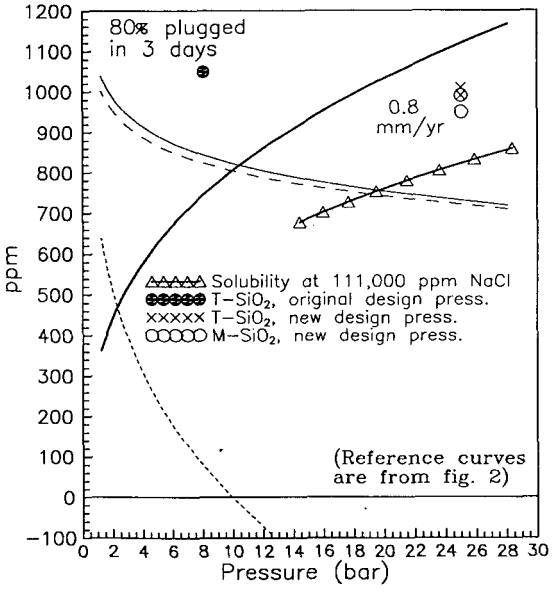

Figure 6. Silica versus pressure at Milos, Greece, with injection line scaling rate.

Milos, Greece: The water contains about 65,000 ppm Cl, so the high salinity requires recalculation of amorphous silica solubility (figure 6). When this water was produced at the original design pressure 8 bar abs., there was extreme scale deposition (Hibara and others, 1989; Karabelas and others, 1989). To manage this, the production system was re-designed to separate steam and water at 25 bar abs. The brine was then pumped under pressure about 1 km to an injection well. In this new system, metal sulfides deposited in the 2 phase line and separator, iron-enriched amorphous silica scale deposited along much of the length of the injection line, and about 0.8 mm/yr of nearly pure silica scale deposited on the pipeline walls and on coupons near the injection wellhead. The injection well showed no damage after six months. There were several system outages during the 3 months of coupon test flow; Hibara and others (1989) believe that cooling during these periods may have caused some of the measured 0.8 mm/yr scale formation.

Hibara and others (1989) described the coupon scale only as "layers with voids between", whereas Karabelas and others (1989) used "a clearly opaline substance" to describe another scale sample from about the same point. A micrograph showed that this substance

consisted mainly of flaky grains with diameter about 1-10 μm, also with a few large grains of sulfides in a siliceous matrix. The sulfide was likely carried in from upstream. The morphology suggests particle deposition cemented by considerable molecular deposition. Hibara and others (1989) measured the SiO_2 in the 25 bar brine and reported that there was less than 50 ppm oversaturation. Our own calculation of solubility indicates closer to 100 ppm oversaturation.

Otake and Hatchobaru, Japan: At Otake (figure 7) a cooled mix of production waters from atmospheric flash was injected for two years into two wells at 80°C, 60°C and 50°C (Itoi and others, 1989). Total SiO_2 was measured in the mix after cooling to 95°C, and total and monomeric SiO_2 were measured in samples collected from downhole in the two injection wells. Figure 7 shows only the 95°C mix and concentrations in the 80°C water. There was a considerable loss of injectivity, especially at 60°C and 50°C, and caliper logs and televiewer logs showed scale in the injection well casings and liner slots.

At Hatchobaru (Hirowatari and Yamaguchi, 1990) a continuous flow of brine cooled to various temperatures was mixed in a pilot apparatus with gas extracted from the power station (70% CO_2). Scale deposition was measured after 24 to 72 hours of flow. The unaltered brine had pH about 7.5 and average SiO_2 850 mg/l, and apparently it formed scale at 0.4 to 1.6 mm/yr, although the data are sketchy and the morphology of the scale was not described. In contrast, gas-treated brine at 59°C with pH 5.3 formed scale at only 0.01 mm/yr (converted from mg/day assuming density 2.2).

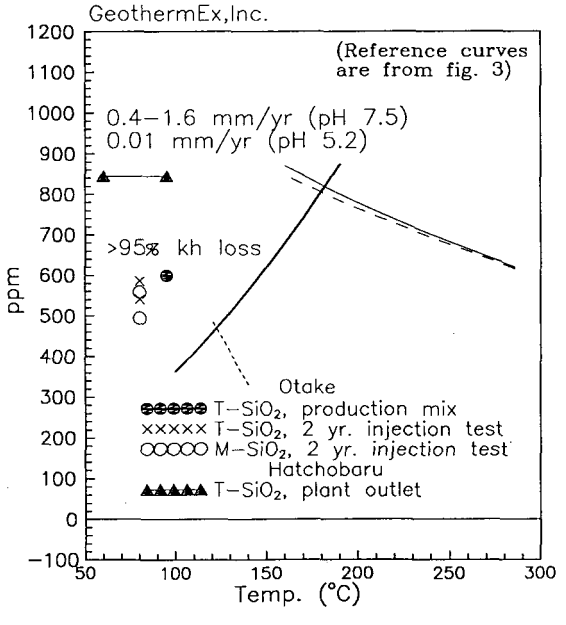

Figure 7. Silica versus temperature at Otake and Hatchobaru, with scaling data.

Svartsengi, Iceland: The brine here is two-thirds seawater. Thordarsson and Tomasson (1989) report that after vacuum separation at 0.3 bar/70°C, the brine pH is 7.9 and there is strong scaling; therefore, surface disposal is used. Brine with 550 ppm total SiO_2 has been used for studies of pH and temperature effect on polymerization. In 1984, this brine was mixed with condensate and gases to lower the pH, in order to inhibit scaling and allow a long-term injection test (Hauksson and Gudmundsson, 1986). The mixture pH was 6.4 to 6.8, and it was oversaturated by about 200 mg/l. Scaling rates from the mixture after 13 to 22 days of flow were 2.8 to 3.0 mm/yr downstream of injection line pumps, 4.6 to 6.6 mm/yr on the front of an orifice at the injection wellhead, and 0.04 mm/yr on the back of the same orifice. Residence time was c.15 minutes. Particle deposition is indicated.

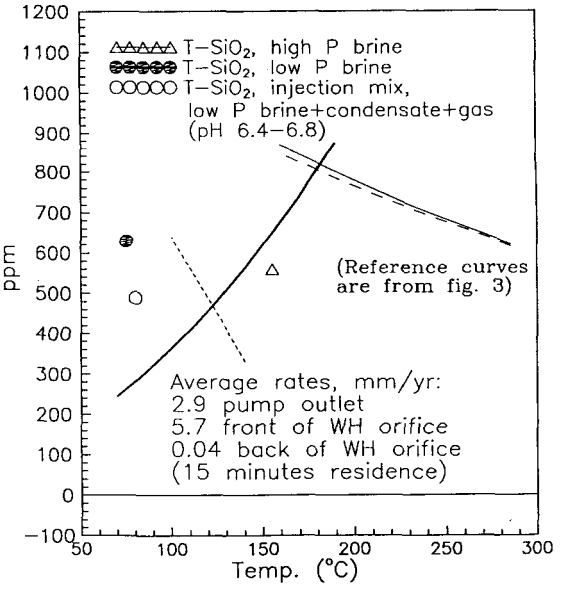

Figure 8. Silica versus temperature at Svartsengi, with injection line scaling rate.

Mroczek and McDowell (1990): This well-controlled and documented experimental work was conducted by passing separated brine from a well through a pipeline for 29 to 35 days. Then the pipeline was cut into even sections and the amount of scale in each section determined. Eight experiments were run, two each with separator pressure set for 180°C, 160°C, 140°C and 120°C. At each pressure there was one experiment with a brine flowrate of 3 l/sec, and another with a rate of 30 l/sec; this produced total residence times of 7 minutes and 0.7 minutes. Total SiO_2 and monomeric SiO_2 were measured in water samples collected at the inlet and outlet. Salinity and pH were not reported, but saturation ratios and T-SiO_2 values suggest that there was essentially no ionized silica.

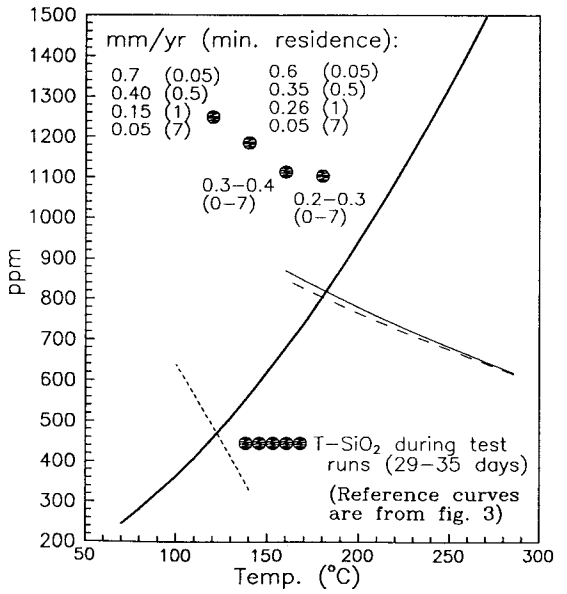

Figure 9. Silica versus temperature, scaling experiments of Mroczek and McDowell (1990).

Results are summarized on figure 9. At 180°C and 160°C, the induction time for polymerization was not reached, even at 7 minutes. Scaling rates were 0.2 to 0.3 mm/yr at 180°C (assuming density 2.2), increasing to 0.3 to 0.4 mm/yr at 160°C. At 140°C and 120°C, there was measurable polymer formation, even at the pipe inlet, and the polymer concentration increased through the pipeline; the increase at 120°C was twice that at 140°C. Therefore, scaling in the pipeline decreased dramatically along the length of the pipe, as monomeric SiO_2 was removed from solution into the suspended polymer. In all cases, the scale which formed was hard and glassy, with density about 2 gm/cc.

Mroczek and McDowell (1990) also performed some tests of silica deposition using gravel beds substituted for the open pipeline. Results were imprecise because the mass of silica deposited proved hard to measure. However, at 180°C and 160°C, there was a hard silica scale which deposited uniformly along the length of the beds. At 140°C and 120°C, there were soft, loosely adhering deposits at the bed inlet, with hard deposits downstream at 140°C, but no deposits elsewhere at 120°C. The bed inlet was a point of high flow rate and turbulence.

Summary: The scaling reports above are dominated by particle deposition. Observed rates are compiled on figure 10, showing only the rates from unaltered brine at the approximate concentration of unionized, monomeric SiO_2 in solution. The particle deposition rates are highly variable, but the pilot plant experience at Cerro Prieto may be the result of excessive turbulence. Therefore, it appears that oversaturation below about 150 ppm is unlikely to produce scale at a rate exceeding 2 or 3 mm/yr, as long as excessive turbulence is avoided. Against this the molecular deposition data of Mroczek and McDowell (1990) provide a lower limit.

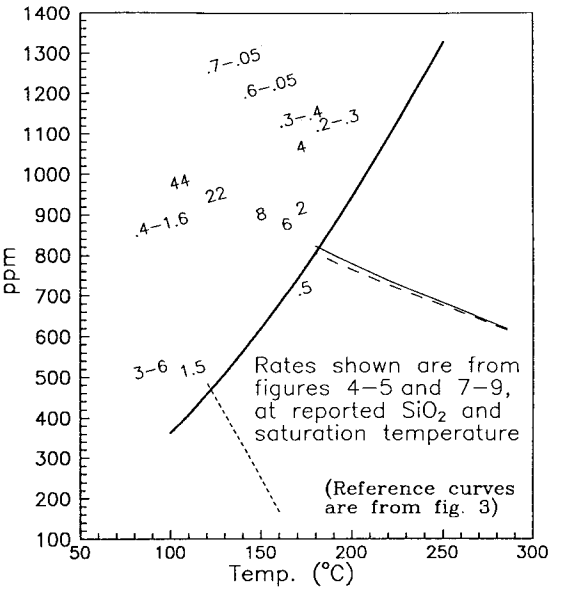

Figure 10. Silica versus temperature, showing summary of reported scaling rates.

KINETIC STUDIES

Weres and others (1982) studied polymerization and particle growth in aqueous solutions up to 100°C and containing up to 1 M NaCl (35,000 ppm Cl), to obtain rate equations for homogeneous nucleation and molecular deposition. This work produced graphs and equations for calculating molecular deposition rate and suspended particle growth rate. Jamieson (1984) has published some general mathematical relationships which describe the rate of mass transfer of particles from suspension in flowing solutions to surrounding solid surfaces. However, these have not yet been integrated with expressions for particle nucleation and growth, and calculations of particle scaling rates are not yet routinely possible.

Figure 11 (after Weres and others, 1982) shows rates of molecular deposition versus temperature and the concentration of unionized SiO_2 at a pH of 7 and NaCl salinity equivalent to about 2,400 ppm Cl. Corrections for different pH or salinity can be calculated. The quadrilateral outline on figure 11 corresponds to experimental data; rate lines outside this area were calculated. The dotted line connects points of maximum rate at given SiO_2.

Weres and others (1982) have cautioned that figure 11 and their rate equations should not be overused for scaling predictions. Their experimental data were collected at relatively low temperature, by adding known amounts of colloidal silica of known surface area to oversaturated solutions, and monitoring the loss of monomeric SiO_2. This process presented to their silica solutions a widely dispersed area of curved surfaces; thus, their experimental conditions were different from scale deposition on the wall of a pipe.

The work of Mroczek and McDowell (1990) suggests, however, that under the right conditions a prediction can be quite accurate. The predicted points for Mroczek and McDowell on figure 11 are plotted simply at total SiO_2 and temperature; measured points are plotted at temperature and observed rate. There is excellent agreement at 120°C, good agreement at 140°C, and progressively poorer agreement at 160°C and 180°C, with the predicted rates exceeding those actually observed.

Molecular deposition rates predicted for Dixie Valley and for Uenotai during 1988 (figure 11) are one to two orders of magnitude lower than the particle deposition rates actually observed and described above.

PREDICTION FOR UENOTAI

The proposed production conditions at Uenotai are illustrated by table 2 and figures 2 and 3. The figures show a particular case, while table 2 lists an average of several cases.

Table 2 : Uenotai production conditions

- 10.8 bar/182°C:
  saturation with amorphous SiO_2
- 9.3 bar/175°C:
  total SiO_2 = 850 ppm
  pH 7.2
  Cl = 225 ppm
  70 ppm oversaturation
  saturation ratio 1.1
- 8.1 bar/170°C:
  110 ppm oversaturation
  saturation ratio 1.2.
- pipeline residence maximum 20 to 45 minutes

These conditions indicate molecular deposition at about 0.1 to 0.15 mm/yr (figure 11), although this figure is approximate. Furthermore, it is expected that molecular deposition will be more significant as a scaling mechanism that particle deposition, because pH and salinity will not be particularly high, residence time will be relatively short, and supersaturation ratio low. The indicated oversaturation is below the range applicable to the homogeneous nucleation rate equations of Weres and others (1982), which prompts their guideline that molecular deposition should be dominant. Furthermore, a comparison with nucleation rate curves for higher oversaturation (Weres and others (1982)) furthermore indicates that the induction period will not be reached.

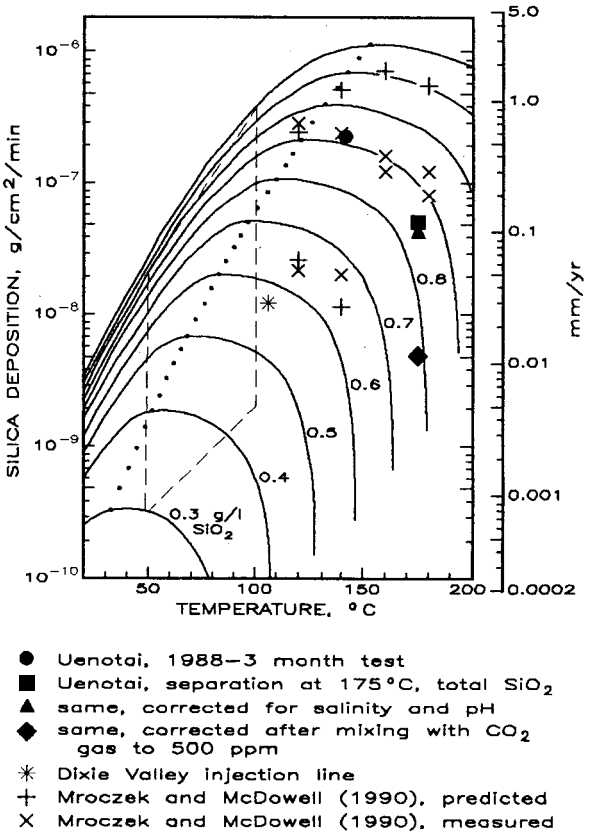

Figure 11. Rates of molecular deposition versus temperature and silica concentration (after Weres and others, 1982).

The experimental evidence of Mroczek and McDowell (1990) suggests that scaling rates will be nearly uniform along the length of the injection pipelines, with some extra build-up possible at points of turbulence. The scale is more likely to be hard than soft. Soft scale which does develop is likely to be fairly rough, forming radial ridges transverse to pipeline flow, which cause impedance. A conservative interpretation of the general experience with injection lines elsewhere indicates that some scale should be considered probable, but not likely at rates exceeding 1 mm/yr to 2 mm/yr. Therefore, a strategy to suppress or manage the expected scale has been recommended.

SUPPRESSION BY GAS OR CONDENSATE MIXING

Gas mixing to lower solution pH and suppress scale development has been discussed above. Figure 12 is a model of dissolving various amounts of CO_2 into the injection line brine, after separating the brine from steam at 175°C. The particular case modeled starts at 50 ppm oversaturation. Between 25 ppm and 500 ppm total C in solution as CO_2, there is a dramatic drop of pH from 7.2 to 5.8, while unionized SiO_2 climbs from 822 ppm to 850 ppm and oversaturation increases from 50 ppm to 75 ppm. The increase of oversaturation is completely counterbalanced by the lowered pH, and molecular deposition rate drops from 0.15 to 0.01 mm/yr (figure 11). This should also effectively eliminate any tendency for particle formation and deposition. pH and scaling potential can be lowered further with additional CO_2, but this hardly seems necessary.

It should be noted that P_{CO2} for 500 ppm is only 1.5 bar. The 500 ppm level is achieved by mixing about 0.025 t/hr non-condensible gases (13 m^3 at 1 atm.) per 50 t/hr of water flow. At Uenotai there are a number of excess enthalpy wells, and it was calculated that the gas needed for mixing into the total injection brine flow would be supplied by only 8% of the total steam flow.

For comparison with the gas mixing, we note the following: 1) mixing 50 t/hr water flow with 17.5 t/hr condensate at 60°C also lowers the molecular deposition rate to 0.01 mm/yr, and; 2) all oversaturation in 175°C water would be removed by mixing with an equal amount of 60°C condensate, and; 3) mixing with a combination of gas and condensate may have a beneficial effect by reducing winter-time freezing of vapor in the gas line.

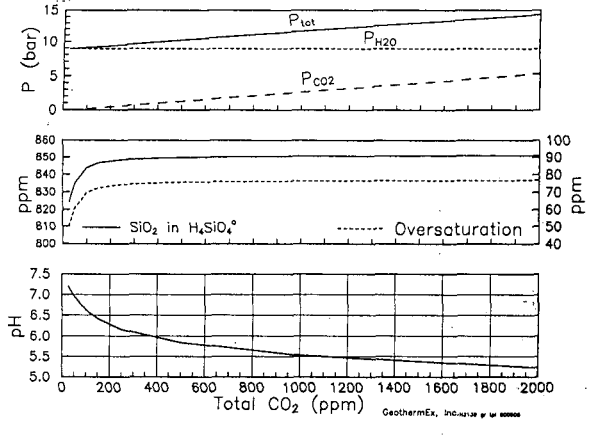

Figure 12. Effect of mixing CO_2 into the water fraction at 175°C, Uenotai well T-51.

MANAGEMENT STRATEGIES

In addition to scale suppression strategies, the following is recommended for scale management at low levels of oversaturation:

1) Design the injection system to minimize residence time and avoid turbulence.

2) Install pressure ports on injection lines to allow monitoring for scale-related impedance.

3) Install inspection ports and scaling coupon ports on the injection lines.

4) Install ports at both ends of injection lines to allow inserting a clean-out pig.

RECOMMENDATIONS FOR DATA GATHERING

It was clear from the literature review that further improvements of predictive technique will benefit from more uniformity in designing experiments, reporting results, and reporting descriptions of scale. We strongly recommend that the following be included in all reports of silica scale in production systems, pilot plants, or experimental systems:

1) Complete chemical analysis of the major elements and pH in the scale-forming water, collected at an upstream sample point.

2) Temperature, total SiO_2, monomeric SiO_2 (by colorimetry), and pH (with sample temperature) at upstream and downstream sample points. The technique of sampling and colorimetric measurement must be researched and applied carefully to give reliable results.

3) Complete analyses of the major elements and gas species in a separated water and steam sample suite, including pH, total flow enthalpy and separation P/T. The purpose of this is to allow modeling the fluid at different pressures and temperatures.

4) A short but considered description of scale morphology *vis-a-vis* the probable dominance of molecular deposition or particle deposition.

5) A description of scale thickness and location *vis-a-vis* uniformity and *vis-a-vis* flow turbulence.

6) A description of scaling rate, or total period of fluid flow in relation to scale mass or thickness. Rates should be reported both in mg/area/time and mm/yr with scale density.

7) A description of system volume and flow rate, or fluid residence time.

ACKNOWLEDGEMENTS

Appreciation is given Akita Geothermal Energy Company and to Oxbow Geothermal Corp., for permission to report chemical data.

REFERENCES

Arnorsson, S. and S. Sigurdsson (1982), "The Chemistry of Geothermal Waters in Iceland. I. Calculation of Aqueous Speciation from 0° to 370°C," Geochimica et Cosmochimica Acta, Vol.46, pp.1513-1532.

Arnorsson, S., E. Gunnlaugsson, and H. Svavarsson (1983), "The Chemistry of Geothermal Waters in Iceland. III. Chemical Geothermometry in Geothermal Investigations," Geochimica et Cosmochimica Acta, Vol.47, pp.567-577.

Chan, S.H. (1989), "A Review on Solubility and Polymerization of Silica," Geothermics, Vol.18, No.1/2, pp.49-56.

Chen, C.T.A. and W.L. Marshall (1982), "Amorphous Silica Solubilities - IV. Behavior in Pure Water and Aqueous Sodium Chloride, and Magnesium Sulfate Solutions up to 350°C," Geochimica et Cosmochimica Acta, Vol.46, pp.279-287.

DiPippo, R. (1985), "A Simplified Method for Estimating the Silica Scaling Potential in Geothermal Power Plants," Geothermal Resources Council BULLETIN, Vol.14, No.5, May 1985, pp.3-9.

Fournier, R.O. (1981), "Application of Water Chemistry to Geothermal Exploration and Reservoir Engineering," Chapt.4 in "Geothermal Systems: Principles and Case Histories," L. Ryback and L.J.P. Muffler, eds.. Wiley, New York, pp.109-143.

Fournier, R.O. (1985), "The Behavior of Silica in Hydrothermal Solutions," in "Geology and Geochemistry of Epithermal Systems. Reviews in Economic Geology," Vol.2. B.R. Berger and P.M. Bethke, Eds., Society of Economic Geologists, p.61

Fournier, R.O., and W.L. Marshall,W.L. (1983), "Calculation of Amorphous Silica Solubilities at 25° to 300°C and Apparent Cation Hydration Numbers in Aqueous Salt Solutions Using the Concept of Effective Density of Water," Geochimica et Cosmochimica Acta, Vol.47, pp.587-596.

Fournier, R.O., and R.W. Potter,II (1982), "A Revised and Expanded Silica (Quartz) Geothermometer," Geothermal Resources Council BULLETIN, Vol.11, No.11, November 1982, pp.3-12.

Fournier, R.O., and J.J. Rowe (1977), "The Solubility of Amorphous Silica in Water at High Temperatures and High Pressures," American Mineralogist, Vol.62, pp.1052-1056.

Hauksson, T., and J.S. Gudmundsson (1986), "Silica Deposition During Injection in Svartsengi Field," Geothermal Resources Council TRANSACTIONS, Vol.10, pp.377-384.

Henley, R.W., A.H. Truesdell, P.B. Barton Jr., and J.A. Whitney (1984), "Fluid-Mineral Equilibria in Hydrothermal Systems," Society of Economic Geologists, Reviews in Economic Geology, Vol.1.

Hibara, Y., M. Tahara, and S. Hidenori (1989), "Operating Results and Reinjection of Milos Field in Greece," Geothermics, Vol.18, No.1/2, pp.129-135.

Hirowatari, K. and M. Yamaguchi (1990), "Experimental Study on a Scale Prevention Method Using Exhausted Gases from Geothermal Power Stations," Geothermal Resources Council TRANSACTIONS, Vol.14, Part II, August 1990, pp.1599-1602.

Hurtado, R., and S. Mercado (1990), "Scale Control Studies at the Cerro Prieto Geothermal Field," Geothermal Resources Council TRANSACTIONS, Vol.14, Part II, August 1990, pp.1603-1610.

Iler, R.K. (1979), "The Chemistry of Silica - Solubility, Polymerization, Colloid and Surface Properties, and Biochemistry," John Wiley & Sons, Inc., N.Y..

Itoi, R., M. Fukada, K. Jinno, K. Hirowatari, N. Shinohara and T. Tomita (1989) "Long-term Experiments of Waster Water Injection in the Otake Geothermal Field, Japan," Geothermics, Vol.18, No.1/2, pp.153-60.

Jamieson, R.E. (1984), "Simulation of the Silica Scaling Process," Proceedings of the 6th New Zealand Geothermal Workshop, University of Auckland Geothermal Institute, pp.135-140.

Karabelas, A.J., N. Andritos, A. Mouza, M. Mitrakas, F. Vrouzi, and K. Christanis (1989), "Characteristics of Scales from the Milos Geothermal Plant," Geothermics, Vol.18, No.1/2, pp.169-174.

Kindle, C.H., B.W. Mercer, R.P. Elmore, S.C. Blair and D.A. Myers (1984), "Geothermal Injection Treatment: Process Chemistry, Field Experiences and Design Options," Batelle Pacific Northwest Laboratory, PNL-4767 UC-66d.

Marsh, A.R.III, G. Klein, and T. Vermeulen (1975), "Polymerization Kinetics and Equilibria of Silicic Acid in Aqueous Solution," University of California Lawrence Berkeley Laboratory Report LBL-4415, October 1975.

Menzies, A.J., E.U. Antunez, S.K. Sanyal, T. Naka, R. Takeuchi, S. Iwata, Y. Saeki and T. Inoue (1990), "A Case History of a Multi-Well Interference Test Program at the Uenotai Geothermal Field, Akita Prefecture, Japan," Geothermal Resources Council TRANSACTIONS, Vol.14, Part II, August 1990, pp.1241-1248.

Mroczek, E.K., and G. McDowell (1990), "Silica Scaling Field Experiments," Geothermal Resources Council TRANSACTIONS, Vol.14, Part II, August 1990, pp.1619-1625.

Robertson-Tait, A., C.W. Klein, J.R. McNitt, T. Naka, R. Takeuchi, S. Iwata, Y. Saeki, and T. Inoue (1990), "Heat Source and Fluid Migration Concepts at the

Uenotai Geothermal Field, Akita Prefecture, Japan," Geothermal Resources Council TRANSACTIONS, Vol.14, Part II, August 1990, pp.1325-1331.

Rothbaum, H.P., B.H. Anderson, R.F. Harrison, A.G. Rohde and A. Slatter (1979), "Effect of Silica Polymerization and pH on Geothermal Scaling," Geothermics, Vol.8, pp.1-20.

Stock, D.D. (1990), "The Use of Pressure Drop Measurements to Monitor Scale Build-up in Pipelines and Wells," Geothermal Resources Council TRANSACTIONS, Vol.14, Part II, August 1990, pp.1645-1651.

Thordarsson, H. and Th. Tomasson (1989), "Brine Clarification at Svartsengi, Iceland: Effect of pH and Temperature on the Precipitation of Silica and its Properties," Geothermics, Vol.18, No.1/2, pp.287-294.

Weres, O., A. Yee and L. Tsao (1982), "Equations and Type Curves for Predicting the Polymerization of Amorphous Silica in Geothermal Brine," Society of Petroleum Engineers Journal, Vol.22, No.1, pp.9-16.

APPENDIX A: FLUID MODELING CALCULATIONS - THE SILICA PROBLEM

Fluid modeling calculations for this report were done using a modified version of a thermodynamic speciation-solubility computer code described by Arnorsson and Sigurdsson (1982). Equilibrium constant data for silica species were taken from: Fournier and Potter, 1982 (quartz); Fournier and Rowe, 1977 (amorphous silica); Fournier, 1985 and personal comm. for correction to expression "r" (log K_{H4SiO4}), and; Arnorsson and Sigurdsson, 1982 (log $K_{H3SiO4-}$, log $K_{NaH3SiO4}$).

Thermodynamic codes of this type all depend on a measurement of pH at some known temperature, along with the sample composition, as a basis for calculating pH at some new temperature, with or without addition back to the sample of volatilized gases, H_2O, precipitated/dissolved minerals, etc.. In essence, the codes relate measured pH to some pH-dependent parameter which can be calculated, such as a sum of weak acid ions or "total ionizable H". Then they calculate what the new value of this parameter should be at the new temperature, and iterate to find the pH which produces that value (see review in Henley and others, 1984, chapter 7).

The correctness of pH calculations can be affected by a problem inherent in standard methods of sample analysis and input of data to the computer codes. It is not clear from a survey of the literature how widely this problem has been considered, but it has been very relevant to calculations using fluids from Uenotai.

The problem is a mismatch between measured total SiO_2 and the measured pH. The reported total SiO_2 has been measured by some technique (AA, colorimetry on a diluted sample) designed to determine all of the SiO_2 present in the water at the time of sample collection. pH is measured in a cooled sample, often several days after the sample was collected. The measured value is the result of a balance of numerous simultaneous chemical equilibria which naturally occur to keep the sample in a natural state of charge balance. In a geothermal water sample, this process is dominated by carbonate species, silica species, sulfide species, boron species, ammonia species, and others, with the silica species being particularly significant at pH above about 8. The computer code simulates this process, using the total SiO_2 measurement to calculate the contribution of the silica species equilibria. Unfortunately, if the sample is oversaturated with respect to amorphous silica, the real concentration of SiO_2 which contributes to determining pH is <u>less</u> than the measured total, because some fraction of the total is trapped in suspended colloidal polymers. In the real solution, the effect of this is buffered to some degree by the fact that the acidity of the polymers is higher than the acidity of monomeric SiO_2 (Marsh and others, 1975). As far as we know, this is not quantified in any of the existing computer codes.

The result is that the codes may overestimate the contribution of silica species to the parameter which they use later to determine pH at some different temperature. The size and impact of the miscalculation increases with increasing oversaturation, and increasing ratio (silica species/carbonate species). The existence of the miscalculation becomes most apparent when the water is very dilute but has very high silica, as seen by comparing measured ion balance with speciated ion balance. For example, in the sample of table 1, the ion balance of species determined by analysis is +1.29%, but the speciated ion balance is greater than -12.5% (if all of the measured alkalinity is due to silica, and more negative if some alkalinity is due to carbonic acid species), because of the large amount of $H_3SiO_4^-$ calculated to be present.

For the sample of table 1, the overestimation results in calculating a reservoir pH (at 285°C) which is too high

by as much as 0.4. This is seen by first calculating reservoir speciation using the measured pH and SiO_2. The result is pH 7.40/285°C. Next, take the same sample, charge balance the analytical species with Cl^-, then adjust pH to get a speciated balance. The result (pH 8.11/22°C) is ideally the pH the sample would have had were all SiO_2 present in monomeric form. Using it as input, reservoir speciation gives pH 7.0/285°C.

This adjustment procedure is risky because of sensitivity to analytical errors, but for the Uenotai samples it appeared likely to give more valid estimates of pH in the reservoir and at various steam separation conditions, than using the measured pH value.

PROCEEDINGS, Sixteenth Workshop on Geothermal Reservoir Engineering
Stanford University, Stanford, California, January 23-25, 1991
SGP-TR-134

HEAT DELIVERABILITY OF HOMOGENEOUS GEOTHERMAL RESERVOIRS

Eduardo R. Iglesias and Sara L. Moya

Instituto de Investigaciones Electricas

Apartado Postal 475, Cuernavaca 96000, Mexico

ABSTRACT

For the last two decades, the petroleum industry has been successfully using simple inflow performance relationships (IPR's) to predict oil deliverability. In contrast, the geothermal industry lacked a simple and reliable method to estimate geothermal wells' heat deliverability. To addres this gap in the standard geothermal-reservoir-assessment arsenal, we developed generalized dimensionless geothermal inflow performance relationships (GIPR's). These "reference curves" may be regarded as an approximate general solution of the equations describing the practically important case of radial 2-phase inflow. Based on this approximate solution, we outline a straightforward approach to estimate the reservoir contribution to geothermal wells' heat and mass deliverability for 2-phase reservoirs. This approach is far less costly and in most cases as reliable as numerically modelling the reservoir, which is the alternative for 2-phase inflow.

INTRODUCTION

For the last few decades, the petroleum industry has been successfully using inflow performance relationships (IPR's) to predict well productivities. These IPR's relate the volumetric oil flow rate q_o of a well to the corresponding sandface flowing pressure p. For liquid inflow the relationship between these variables is a straight line. In this case one can define a unique productivity index $J = q_o/(p - p_R)$, where p_R is the average reservoir pressure.

For 2-phase inflow the relationship between q_o and p is non-linear, as first pointed out by Evinger and Muskat (1942). Thus, a unique productivity index cannot be defined for this case. Gilbert (1954) was the first to propose methods of well analysis to use the information of the nonlinear relationships, and named these curves IPR's. Vogel (1968) numerically synthesized the IPR's corresponding to a broad set of different oil properties, formation properties, initial conditions and cumulative recovery, for solution-gas-drive reservoirs. In this work Vogel demonstrated that, normalizing q_o to the maximum flow rate $q_{o(max)}$ and p to the average reservoir pressure, the resulting dimensionless IPR's are remarkably similar to each other. Taking advantage of this approximate self-similarity, he proposed his now famous "reference curve"

$$q_o/q_{o(max)} = 1 - 0.2(p/p_R) - 0.8(p/p_R)^2, \quad (1)$$

widely used in the oil industry since then. Vogel's seminal work has been extended, refined and variously applied by numerous authors (e.g., Standing, 1970; Al-Saadoon, 1980; Weiss et al., 1981; Dias-Couto and Golan, 1982; Mishra and Caudle, 1984; Kelkar and Cox, 1985; Camacho and Raghavan, 1989).

In contrast, the geothermal industry has made scant use of inflow performance relationships. Examples in the literature of IPR's applied to geothermal problems are few. They include assessment of productivity index and of reservoir parameters for wells fed by single-phase water and steam (Iglesias et al. 1983a, 1983b), and optimization of development strategy for liquid-dominated reservoirs (Marcou, 1985).

The scarce application of IPR's to geothermal problems reveals an important gap in the standard reservoir-assessment arsenal.

This work contributes generalized dimensionless IPR's appropriate for geothermal use. These geothermal IPR's (GIPR's) address geothermal heat deliverability, while reflecting that geothermal heat mining is inextricably linked to fluid production. Thus, the new GIPR's relate fluid production, heat production and reservoir pressure. In this contribution we examine the practically important case of 2-phase inflow.

GEOTHERMAL DELIVERABILITY

The main geothermal commodity is heat. However, heat is extracted via fluid production. Thus, to describe geothermal productivity it is necessary to relate fluid and heat production. Moreover, geothermal heat production is determined by reservoir and wellbore characteristics. There are good conceptual and practical reasons to differentiate these contributions. In this paper we concentrate on the reservoir contribution.

For 2-phase inflow, heat production is determined by reservoir temperature, pressure and shape, permeability (k), relative permeability (k_{rel}), fluid thermophysical properties and skin factor. The same variables control mass production. A distinct trait of 2-phase inflow is that the specific enthalpy of the fluid discharge increases with mass flow rate. This trait reflects heat transfer from the formation to the fluid, associated with boiling.

Heat deliverability also depends on reservoir history, mainly because the average reservoir pressure generally decreases with cumulative mass production (M_C). Additionally, the rate of decrease of p_R depends on whether the reservoir is closed or recharged (either naturally or by reinjection). Recharge also impacts on heat deliverability via the temperature of the recharged fluids. For simplicity, this work is restricted to characterizing heat deliverability in closed reservoirs with no reinjection.

METHOD

To characterize geothermal heat and fluid deliverabilities for 2-phase inflow, we assessed their dependence on unperturbed reservoir initial conditions, on cumulative mass production and on fluid and formation properties. We accomplished this by numerically modeling a number of relevant cases, which are summarized in Table 1.

The model is a closed, cylindrical, homogeneous reservoir with a fully penetrating well at its center. No skin effects were accounted for. We neglected vertical components of fluid flow. The reservoir is bounded above and below by impermeable formations. Conductive heat flow from the overlying and underlying formations was also neglected.

The computational work was done with a reliable numerical reservoir simulator (Pruess and Schroeder, 1980). The model neglects effects associated with dissolved gases or solids: the thermophysical properties of pure water substance are assumed for the fluid. All the cases of Table 1 were simulated using a 28 zone radial grid. The positions of the nodes are given by $r_n = 0.1(2)^{(n-1)/2}$, which locates the last node at 1158.52 m from the origin. Reservoir thickness is 100 m. Table 2 summarizes the assumed formation properties.

The cases of Table 1 include Corey-type and linear (also termed X-type) relative permeabilities. These are the most widely used in the geothermal literature. For both types, the residual saturations were assumed equal to 0.3 for liquid and to 0.05 for steam.

The initial temperature of the unperturbed reservoir (T_{init}) is also shown in Table 1, along with the assumed permeability and the computed cumulative mass produced (percent of initial fluid mass in-place), for each case.

In every case, the unperturbed initial conditions were pure liquid at the saturation pressure corresponding to T_{init}. Therefore, 2-phase inflow sets in as soon as production begins, and average reservoir pressure and temperature decrease with cumulative mass production.

RESULTS AND DISCUSSION

We computed geothermal inflow performance curves for each value of M_C, for all cases in Table 1. These curves relate sandface flowing pressure, discharge thermal power P (= Wh, where h is the specific enthalpy of the total discharge) and mass flow rate. Figures 1-3 illustrate these results for T_{init} = 250°C, k_{rel} = Corey, k = 10 mD, M_C = 5-35%.

Then, we normalized these curves to the corresponding maximum values of mass flow rate W_{max}, thermal power P_{max} and reservoir pressure p_R. The resulting dimensionless GIPR's corresponding to the cases shown in Figs. 1-3 are presented in Figs. 4-6. It is readily apparent that the pseudo-data[1] points tend to collapse into relatively narrow strips, in the dimensionless form. Since

[1]We refer to our computed results as pseudo-data to distinguish them from true data, as recommended by the American Geophysical Union.

T_{init}, k and k_{rel} are fixed for Figs. 4-5, the spread of the pseudo-data points reflects the effect of reservoir depletion on heat and mass deliverability, for this particular reservoir. Note also the tight non-linear correlation between heat and mass deliverability (Fig. 6). Though not shown here, similar effects are present for all reservoirs listed in Table 1.

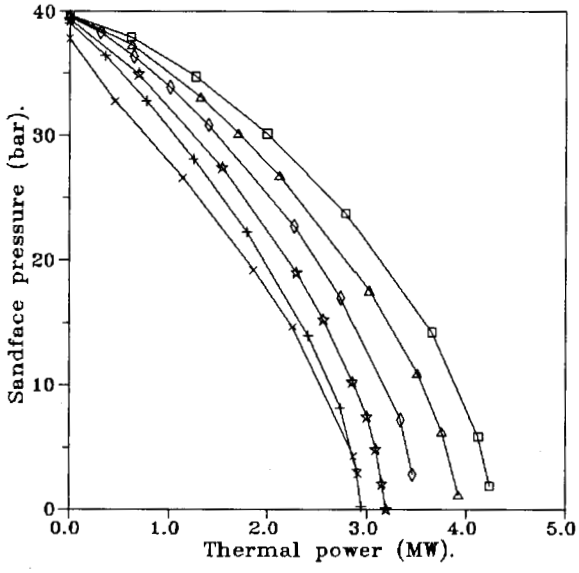

Fig. 1. Pressure - power relationships for T_{init} = 250°C, k_{rel} = Corey, k = 10 mD, M_C = 5, 10, 15, 20, 25, 35%. M_C increases towards lower curves.

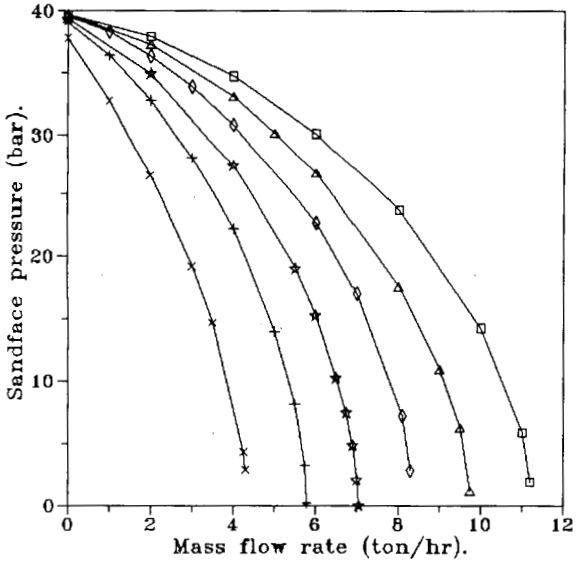

Fig. 2. Pressure - flow rate relationships for T_{init} = 250°C, k_{rel} = Corey, k = 10 mD, M_C = 5, 10, 15, 20, 25, 35%. M_C increases towards lower curves.

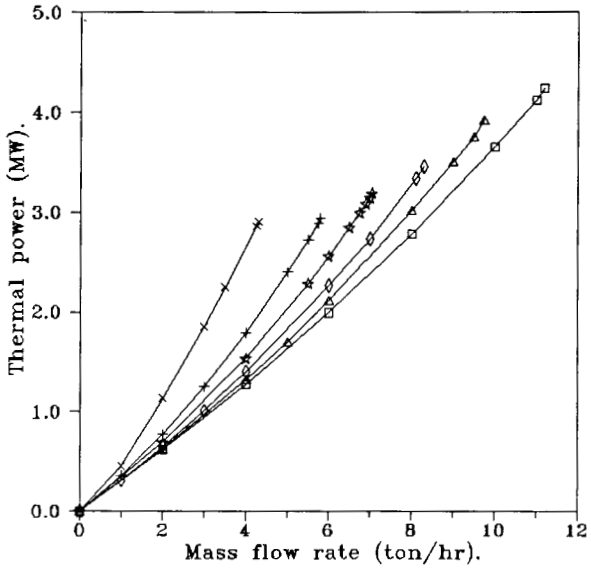

Fig. 3. Power - flow rate relationships for T_{init} = 250°C, k_{rel} = Corey, k = 10 mD, M_C = 5, 10, 15, 20, 25, 35%. M_C increases towards upper curves.

Table 1. Cases studied

k_{rel}	T_{init} (°C)	k (md)	Cumulative mass produced (%)
Corey	250	10	5
			10
			15
			20
			25
			35
Corey	250	100	5
			35
Corey	250	1000	4
			20
			29
			33
Corey	350	10	5
			35
Corey	350	100	5
			35
Linear	250	10	5
			35
Linear	250	100	5
			35
Linear	250	1000	4
			20
			33
Linear	350	10	5
			35
Linear	350	100	5
			35

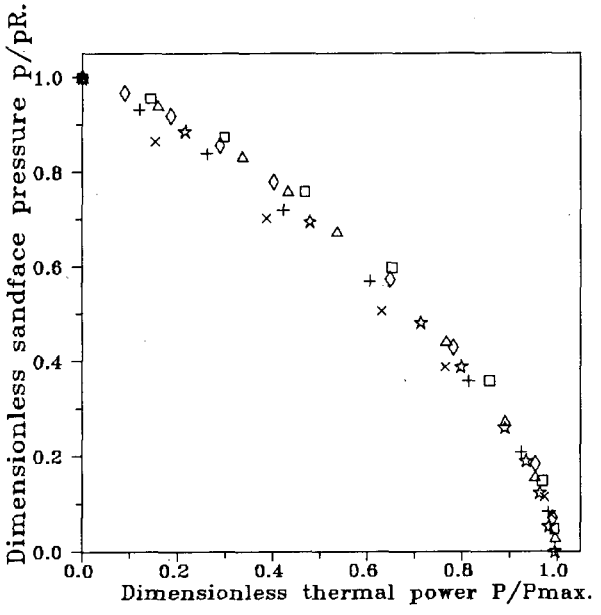

Fig. 4. Dimensionless relationships corresponding to Fig. 1 (same simbols).

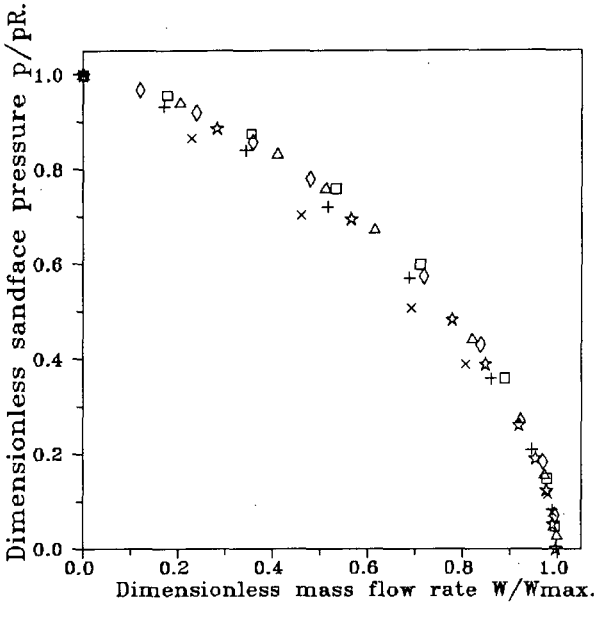

Fig. 5. Dimensionless relationships corresponding to Fig. 2 (same simbols).

The combined effects of reservoir initial conditions, permeability, relative permeability and reservoir depletion on dimensionless heat and mass deliverability are shown in Figs. 7-9. These figures summarize the results corresponding to all cases of Table 1. Note that despite the wide range of reservoir parameters, fluid properties and cumulative production covered, the relatively tight grouping of the

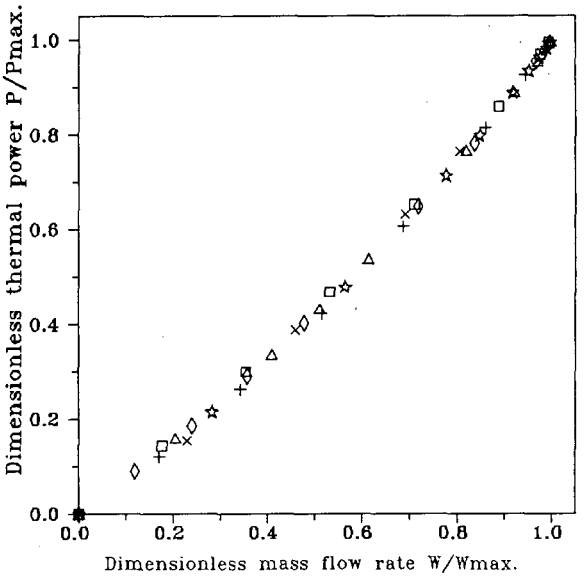

Fig. 6. Dimensionless relationships corresponding to Fig. 3 (same simbols).

computed results persists. As demonstrated by Vogel's dimensionless IPR's succes, this approximate self-similarity can be exploited for practical engineering purpouses.

We fitted the "reference curves" shown as continuous lines in Figs. 7 and 8 to the dimensionless heat deliverability results and thermal power - mass flowrate correlation, respectively. Thus, we exploited the close correlation between dimensionless thermal power and mass flowrate demonstrated in Fig. 8, while directly addresing geothermal heat deliverability. These reference curves may be regarded as an approximate general solution of the equations describing radial 2-phase geothermal inflow.

Table 2. Formation properties.

Porosity	0.10
Bulk density	2,700 kg/m^3
Thermal conductivity	2.0 $W^{m-1}{}^{\circ}C^{-1}$
Specific heat	1,000 $Jkg^{-1}{}^{\circ}C^{-1}$

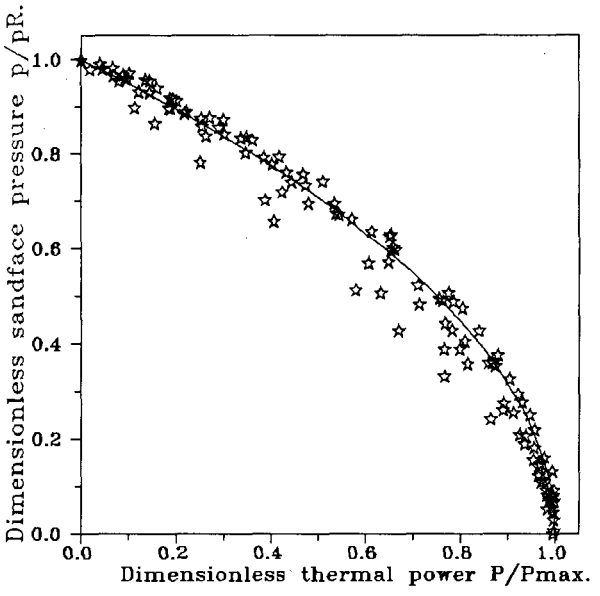

Fig. 7. Dimensionless pressure - power relationships including all cases in Table 1. The continuous line is the reference curve of eq. (2).

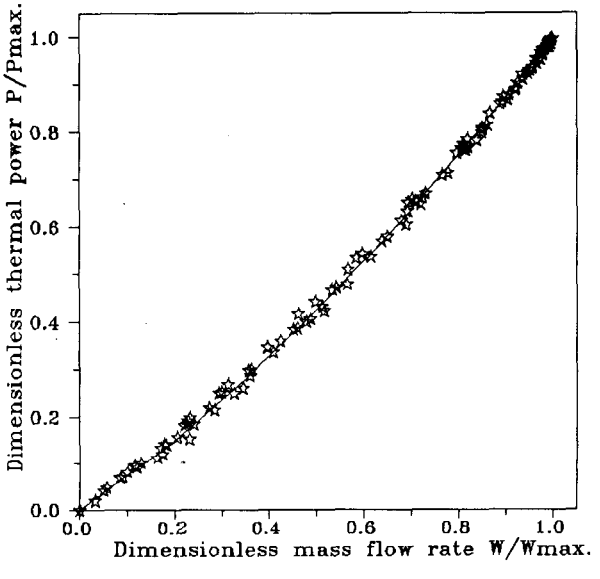

Fig. 8. Dimensionless power - flowrate relationships including all cases in Table 1. The continuous line is the reference curve of eq. (3).

For expediency we chose simple empirical expressions to fit to our results. Thus, the dimensionless heat deliverability results were fitted with

$$P_D = 1 - p_D^2, \qquad (2)$$

where $P_D = P/P_{max}$ and $p_D = p/p_R$, and the dimensionless power - flow rate relationship by

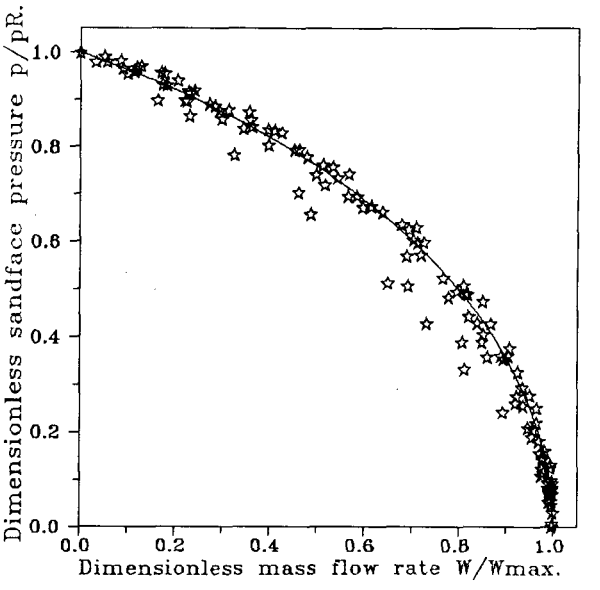

Fig. 9. Dimensionless pressure - flow rate relationships including all cases in Table 1. The continuous line is the reference curve of eqs. (3) or (4).

$$P_D = 0.7W_D + 0.3W_D^2, \qquad (3)$$

where $W_D = W/W_{max}$.

From (2) and (3) follows

$$p_D = (1 - 0.7W_D - 0.3W_D^2)^{0.5}, \qquad (4)$$

or

$$W_D = [-0.7 + (1.69 - 1.2p_D^2)^{0.5}]/0.6 \qquad (5)$$

which is plotted in Fig. 9 as a solid line. This "derived" fit looks reasonably satisfying to us.

Expressions (2)-(5), together with the definitions of the dimensionless variables may be used to estimate the reservoir contribution to geothermal wells' heat and mass deliverability. This straightforward approach is far less costly and probably as reliable as numerically modelling the reservoir. A further advantage of this approach stems from the simplicity and low cost associated with the input data necessary to estimate heat and mass deliverability with it. The necessary data may be gathered by simple wellhead measurements of mass flowrate and total discharge enthalpy, plus one downhole pressure measurement. This compares favorably with the expense and complication involved in gathering reliable information about reservoir parameters (e.g., permeability, relative permeabilities, thermal conductivity, average pressure) necessary for numerically modelling the reservoir.

SUMMARY AND CONCLUSIONS

Until present, the geothermal industry lacked a simple and reliable method to estimate the reservoir contribution to geothermal wells' heat deliverability.

To addres this gap in the standard geothermal-reservoir-assessment arsenal we developed generalized dimensionless geothermal inflow performance relationships (GIPR's). These "reference curves" may be regarded as an approximate general solution of the equations describing radial 2-phase geothermal inflow. They relate dimensionless thermal power, sandface pressure and mass flow rate, for the practically important case of 2-phase inflow in closed reservoirs. Our results include the effects of unperturbed reservoir initial conditions, fluid and formation properties and history of reservoir production. Effects associated with skin, reservoir shape, reinjection and dissolved gases and solids, were neglected.

The "reference curves" presented here provide a straightforward approach to estimate the reservoir contribution to geothermal wells' heat and mass deliverability for 2-phase reservoirs. This approach is far less costly and in most cases as reliable as numerically modelling the reservoir, which is the alternative for 2-phase inflow.

REFERENCES

Al-Saadoon, F.T., 1980. Predicting present and future well productivities for solution-gas-drive reservoirs, J. Pet. Tech., May 1980, pp. 868-870.

Camacho, R.G. and Raghavan R., 1989. Inflow performance relationships for solution-gas-drive reservoirs, J. Pet. Tech., vol. 41, no. 5, pp. 541-550.

Dias-Couto, L.E. and Golan M., 1982. General inflow performance relationship for solution-gas reservoir wells, J. Pet. Tech., Feb. 1982, pp. 285-288.

Evinger, H.H. and Muskat, M., 1942. Calculations of theoretical productivity factor, Trans. AIME **146** , 126-139.

Gilbert, W.E., 1954. Flowing and gas-lift well performance, Drill. and Prod. Prac., API, pp. 126-.

Iglesias, E.R., Arellano, V., Garfias, A., Miranda C., Hernandez, J. and Gonzalez J., 1983a. A method to recover useful geothermal reservoir parameters from production characteristic curves - (1) Steam reservoirs, Proc. 9th Workshop Geothermal Reservoir Engineering, 285-290, Report SGP-TR-74 Stanford University.

Iglesias, E.R., Arellano, V., and Molinar R., 1983b. A method to recover useful geothermal reservoir parameters from production characteristic curves - (2) Hot water reservoirs, Proc. 9th Workshop Geothermal Reservoir Engineering, 291-297, Report SGP-TR-74 Stanford University.

Kelkar, B.G. and Cox, R., 1985. Unified relationship to predict future IPR curves for solution gas-drive reservoirs, Paper SPE-14239, 60th Annual Technical Conference and Exhibition of the Soc. Pet. Eng., 8 pp.

Marcou, J.A., 1985. Optimizing development strategy for liquid dominated geothermal reservoirs, Stanford Geothermal Program, Report SGP-TR-90, Stanford University.

Mishra, S. and Caudle, B.H., 1984. A simplified procedure for gas deliverability calculations using dimensionless IPR curves, Paper SPE-13231, 59th Annual Technical Conference and Exhibition of Soc. Pet. Eng., 9 pp.

Pruess, K. and Schroeder R.C., 1980. SHAFT79 user's manual, Report LBL-10861, Lawrence Berkeley Laboratory, Berkeley, California.

Standing, M.B., 1970. Inflow performance relationships for damaged wells producing by solution-gas drive, J. Pet. Tech., Nov. 1970, pp. 1399-1400.

Vogel, J.V., 1968. Inflow performance relationships for solution-gas drive wells, J. Pet. Tech., Jan. 1968, pp.83-92.

Weiss, E.M., Taylor J.G. and Toronyi R.M., 1981. Productivity testing using production logging techniques, Paper SPE-9610, Middle East Oil Technical Conference of the Soc. Pet. Eng., 12 pp.

PROCEEDINGS, Sixteenth Workshop on Geothermal Reservoir Engineering
Stanford University, Stanford, California, January 23-25, 1991
SGP-TR-134

SIMULATING A CHALLENGING WATER DOMINATED GEOTHERMAL SYSTEM: THE CERRO PRIETO FIELD, BAJA CALIFORNIA, MEXICO

E. U. Antunez, A. J. Menzies and S. K. Sanyal

GeothermEx, Inc.
5221 Central Ave. Suite 201
Richmond, CA 94804

ABSTRACT

A three dimensional, multiphase, numerical simulation model of the Cerro Prieto field was developed and used to verify that the present installed capacity (620 MW) can be sustained for 30 years and to evaluate the impact of an 80 MW addition to the installed capacity in the NE-E of the field on the present production areas.

Cerro Prieto is the largest known water-dominated geothermal reservoir in the world, with more than 175 wells drilled to date and 17 years of production history. Wells here produce fluids of varying enthalpy, from moderate-temperature water to dry steam. The varying enthalpy and a complex interaction between the reservoir and the surrounding aquifer posed a real simulation challenge. The simulation approach used to reproduce the major features of the initial-state and the production history of the field is discussed in this paper.

From this study it was concluded that the field is capable of sustaining its present 620 MW total installed capacity for 30 years and the addition of the proposed 80 MW should have a negligible effect on the present production area.

INTRODUCTION

Cerro Prieto, located 20 miles SE of Mexicali in Baja California, was the first geothermal reservoir in Mexico developed by Comisión Federal de Electricidad (CFE) for commercial use. Commercial production began in April 1973 at the Cerro Prieto One (CP-I) plant, figure 1. In 1980, CFE began field development planning and drilling for the Cerro Prieto Two (CP-II) and Cerro Prieto Three (CP-III) power plants. To date the field has a total installed capacity of 620 MW. In mid-1989, the field was being run at approximately 500 to 550 MW (80 to 90% of installed capacity) but it is the stated intention of CFE to increase capacity to 620 MW by early 1991. It is also intended to further expand the field capacity to 700 MW by 1992 by installing four 20 MW modular turbine-generators to the east of the present development area. This proposed development area is known as CP-IV. The present study was carried out to verify that the present installed capacity can be sustained for 30 years and to evaluate the possible impact of the CP-IV development on the existing CP-I, II and III production areas.

THE RESERVOIR

The Cerro Prieto reservoir (known as Unit B) consists of hydrothermally altered Tertiary sandstones confined at the top by a caprock formed of one or more shale units overlain by unconsolidated clastic sediments (Unit A) and underlain by crystalline basement rocks, figure 3. A new hydrogeologic model of the field has been developed based on GeothermEx interpretation of subsurface geology and on the three dimensional distribution of temperature. This model consists of several northeast- and northwest-trending faults with small offsets intersecting the reservoir, locally acting as barriers to flow and confining the reservoir within well-defined structural blocks at particular levels, figures 2 and 3. Despite the local impedance to flow by faults, the entire reservoir appears to be connected. Major northeast- and northwest-trending faults, including the Cerro Prieto fault, bound the geothermal field at its margins. These faults act as hydrologic boundaries.

The reservoir has been subdivided in a shallow reservoir located at a depth of 1,000 to 1,500 m (3,300 to 5,000 ft), present only under the CP-I production area (figure 3b), and a deep reservoir present in all production areas at a depth below 1,600 m (5,250 ft) in the western side of the field and deepening to the northeast of the field (figure 3a and 3b). Both zones of the reservoir (shallow and deep) communicate through the system of fractures.

In its 17 years of production the reservoir has evolved from a totally water dominated system, perhaps with a small initial steam zone (Mercado, 1990), to a system that has zones of liquid, two phases, dry steam, and a zone with a cooling trend due to the influx of cold water from the groundwater aquifer.

THE SIMULATION PROCESS

The numerical simulation of a geothermal reservoir is generally conducted in three stages: 1) initial-state modeling; 2) history matching; and 3) exploitation simulation.

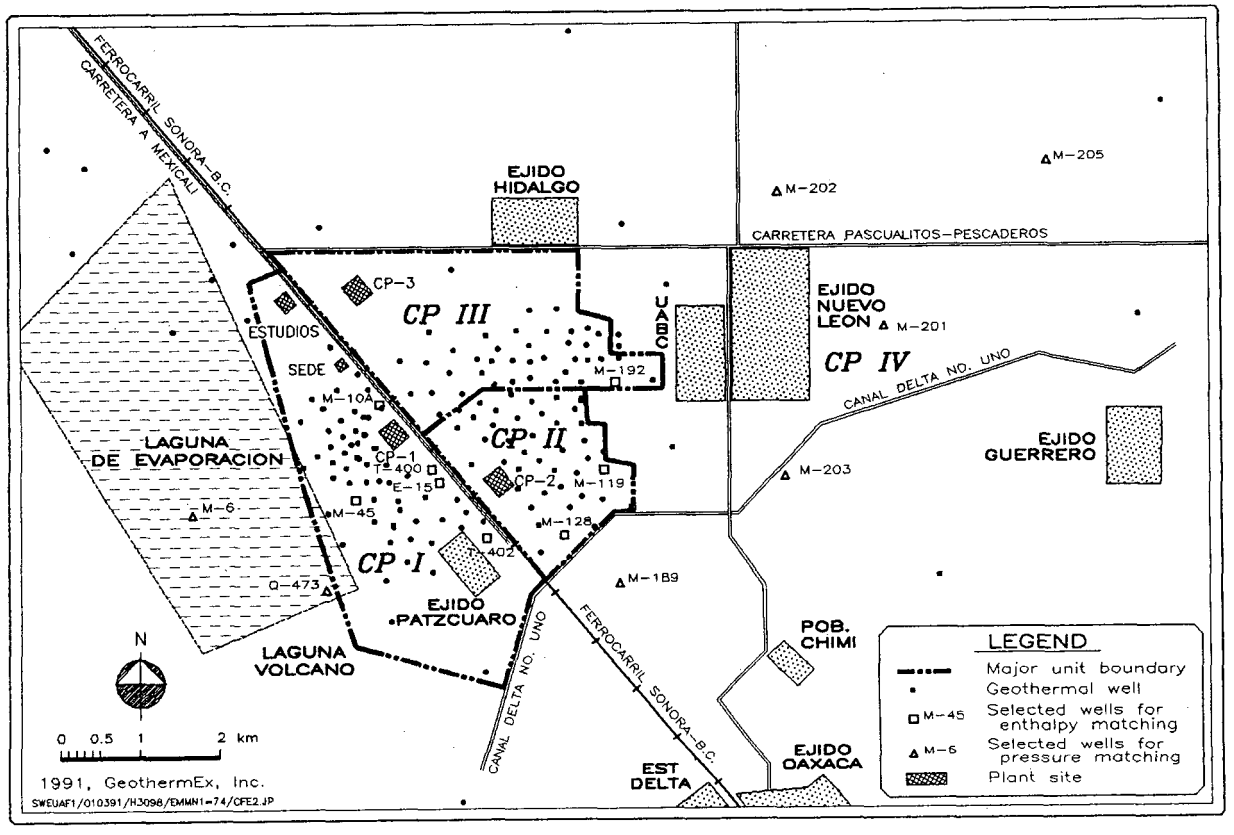

Figure 1. Cerro Prieto wellfield.

In the initial-state modeling, the main goal is to verify the temperature distribution and heat/mass discharge aspects of the model. The major rock properties of importance are permeability and thermal conductivity. Unlike exploitation modeling, storage related parameters such as porosity, density and specific heat of the rock are not sensitive initial-state modeling parameters. Therefore in initial-state modeling it suffices to use average values of porosity, density and specific heat of the rock.

Measured temperatures provide the most reliable calibration criteria for the initial-state modeling. Permeabilities in the x, y and z directions are the main variables used to match the measured temperatures; once a match is obtained, it is assumed that the model represents the permeability distribution reasonably well. However, the initial-state match is not very sensitive to storage terms such as porosity. Therefore, matching of the production history provides a way of checking that the storage terms in the model are reasonable. History matching consists of entering the total mass production/injection rates for all active wells and matching the calculated enthalpy and pressure drawdown behavior of the wells with the observed behavior by trial and error. However, the production history may reflect only a small area of the reservoir and the resulting changes in porosity or permeability may not necessarily apply to the total simulation model. Therefore, in matching the production history it may only be necessary to make changes to hydraulic parameters in blocks located close to the active or observation wells.

If the history matching requires changes to the permeability distribution over a significant area of the model, it may be necessary to re-run the initial-state model to confirm that the calculated initial temperature

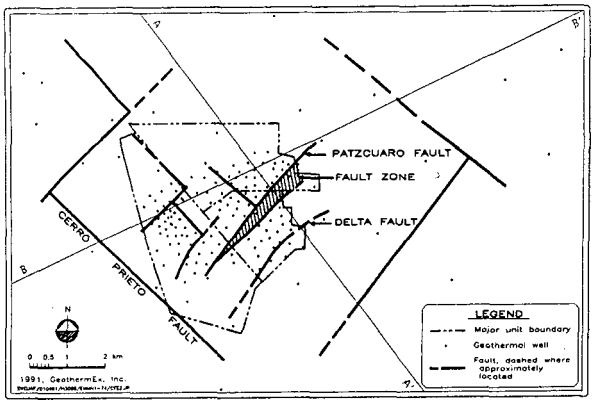

Figure 2. Map of inferred faults and orientation of the cross sections.

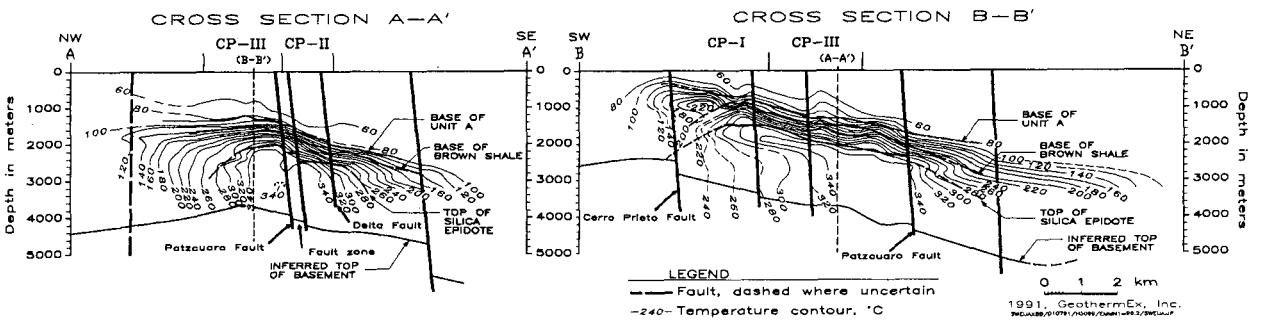

Figure 3. Cross sections of the field (faults, lithology and inferred temperature contours).

and pressure distributions are still in reasonable agreement with the measured data. If the calculated initial pressure and temperature distributions no longer agree with the measured data, then the modeling process is continued until a more consistent model is obtained that fits both the initial temperature and pressure distributions and the production history. Once this last step is accomplished, the model is fully calibrated and can be used with confidence to make predictions of the behavior of a reservoir under any given exploitation scenario.

For numerical modeling, we have used a simulation code originally developed by the Lawrence Berkeley Laboratory under a grant of the U.S. Department of Energy and subsequently improved by GeothermEx. The simulator uses an integrated finite-difference formulation. The chief advantage of the IFD method is geometric flexibility.

DESCRIPTION OF THE CERRO PRIETO INITIAL-STATE MODEL

The simulation model for the Cerro Prieto field is oriented in a NE - SW direction and includes the present exploitation areas of Cerro Prieto I, II and III and the area proposed for CP-IV. The model covers a total area of 135 km^2 (10 km in the NW - SE direction and 13.5 km in the SW - NE direction), much larger than CFE's leasehold area. The large area was required, however, to ensure a reasonable representation of the overall geological framework and to reduce the effects of the boundary conditions on the simulation model. Figure 1 shows the wellfield and the location of the present production areas.

In the vertical dimension, the model extends from the topographic surface, which has an average elevation of +10 m msl (mean sea level) to -4,490 m msl (0 to 4500 m depth). The total thickness is subdivided into 9 layers; the first five layers have thickness of 1000, 400, 100, 300, 700 m, respectively, while layers 6 to 9 all have a thickness of 500 m. A 3-dimensional view of the simulation grid, including the 9 vertical layers and the location of the CP-I, CP-II and CP-III production areas, is shown in Figure 4.

An additional layer (layer 10) is in contact with the bottom of the model and is used as a boundary layer providing both heat and mass to the model from below. The volume assigned to this bottom boundary layer is large enough to avoid variation of its initial conditions in the geological time required by initial-state simulation.

The simulation model is composed of 347 elements, with 28 elements being used as boundary blocks; 9 in the bottom layer, one to model the boundary created by the atmosphere at the top of the model and 18 in contact with the southeastern edge of layers 1 to 7 to simulate the aquifer contained in Unit A (unconsolidated clastic sediments located on top of the reservoir). The boundary conditions in the atmospheric block at the top of the model are essentially those of a heat sink at atmospheric pressure and temperature.

Four generalized rock types are defined within the model to represent the major geological formations encountered in the Cerro Prieto geothermal area: (a) UNA - Unit A, Quaternary deltaic sediments and alluvial fan sediments (unconsolidated and partially consolidated clastic sediments); (b) UNB - Unit B, Tertiary sedimentary rocks (sandstone and shale) (c) UNC - Unit C, crystalline basement rocks; and (d) BSH - brown shale. It was necessary to further subdivide the basic rock types to account for variations in rock

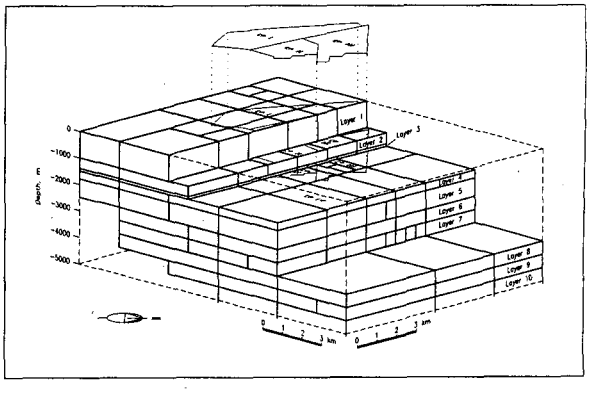

Figure 4. Three-dimensional view of the simulation model for Cerro Prieto.

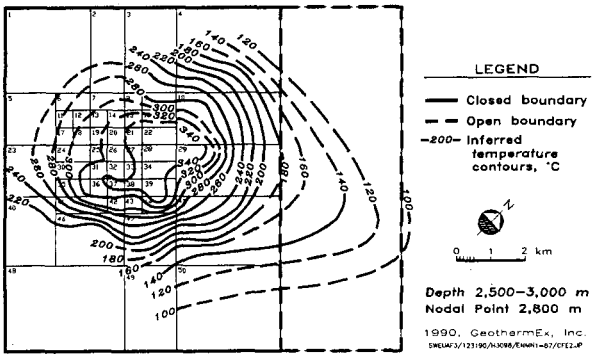

Figure 5. Layer 6 of the Cerro Prieto simulation model, inferred temperature contours and boundary conditions.

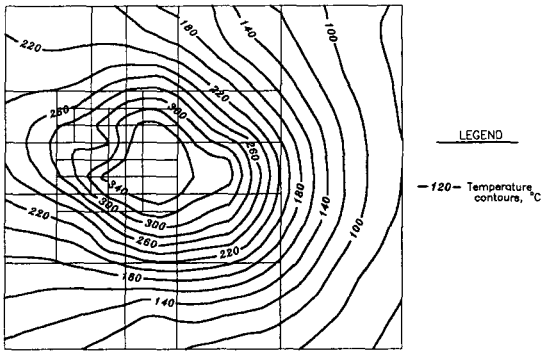

Figure 6. Layer 6 of the Cerro Prieto simulation model, calculated temperature contours.

hydrologic properties, especially permeability. The values of density, porosity, thermal conductivity and specific heat for each rock type were set according to values provided by CFE. As mentioned before, the initial-state model results are not sensitive to these parameters; the model results at this stage are mainly controlled by the permeability distribution.

Pressure and temperature were fixed in some blocks west of the CP-I area in layers 1 to 4 to provide low temperature water to the system in response to pressure changes. The temperature and pressure assigned to each of these constant pressure, constant temperature blocks were set according to the available measured data. The location of these blocks correspond to points where water influx through the south-west boundary of the simulated area was suspected.

Figures 5 shows a contour map of the inferred initial temperatures for layer 6. For comparison a contour map of the calculated temperature distribution in layer 6 is shown in figure 6; these results were obtained after numerous simulation runs where the permeabilities of the basic rock types were varied until reasonable matches were obtained between the measured and calculated temperature distributions at various levels. The calculated initial pressures within the geothermal system were also matched to the measured initial pressure data. Comparing the calculated temperature contours in figure 6 with the inferred contours in figure 5 shows that the model has been able to reproduce the shape of the temperature anomaly in reasonable detail considering the relative coarseness of the grid block layout.

According to the results of initial-state simulation, the upflow occurs mainly from the northeast moving up and southward below 1,800 m; above this depth the geothermal fluids flow towards the northwest, discharging to the atmosphere northwest of CP-I (in layer 1 of the simulation model).

Below the 1,800 m depth it is clear from the initial-state simulation that the Pátzcuaro fault plays an important role in the recharge to the CP-I, CP-II and CP-III production areas. Above the 1,800 m depth the fluid moves to the surface through identified faults. The connection between the shallow and deep reservoirs occurs through a very limited area underlying the CP-I production area at a depth of approximately 1,500 to 1,800 m.

The recharge to the reservoir comes from below -4,500 m msl, northeast of the present CP-II and CP-III production areas. Fluid entering the geothermal system has a temperature close to the critical point, spreading to the sides and cooling down as it moves through the Pátzcuaro fault. A heat source, which by trial-and-error was located beneath the CP-II and CP-III production areas, with more influence on the CP-III side, provides additional heat to the incoming fluid and sustains the high temperatures noted in all three production areas. The above-mentioned heat source is probably associated with the Vulcano fault system.

The permeability data that gave the "best" match to the initial-state indicate that the Cerro Prieto geothermal field has moderately high permeability compared to other high temperature geothermal systems.

HISTORY MATCHING

The enthalpy and piezometric data collected from production and observation wells since 1973 provided both qualitative and quantitative information on reservoir parameters in the Cerro Prieto geothermal field. The data were also used in the numerical simulation modeling as a way of further verifying or calibrating the initial-state model.

For the Cerro Prieto geothermal field the selection of the blocks used for history matching was based on the known completion intervals or production zones in production and observation wells. More than 175 wells had been drilled during the 17 years of production history of the field (1973 to 1990); it was beyond the scope of this project to consider each well individually. Therefore, in the blocks with more than one well, the

wells were grouped together to create a pseudo-well. Each pseudo-well represented a group of wells with similar production characteristics. The pseudo-well produced the total mass of all the wells that it was representing, at an average enthalpy and wellhead pressure. The node of the block where a grouped well was physically located within the simulation grid was chosen as the location of the pseudo-well. Note that the grouping of the wells was kept in mind during the initial gridding of the simulation model. During that process, zones with specific flow conditions (single phase, two phase and areas in which cooling is occurring) were taken into account.

As an example of history matching, figure 7 presents the production enthalpy matching for well M-45. In addition, figures 8 and 9 present examples of the match to the variations in piezometric levels (converted to pressure change) for observation wells Q-473, located SW of the CP-I plant and well M-203 located east of the CP-II production area. Well M-203 is located in the area to be developed for CP-IV, see figure 1 for the location of wells.

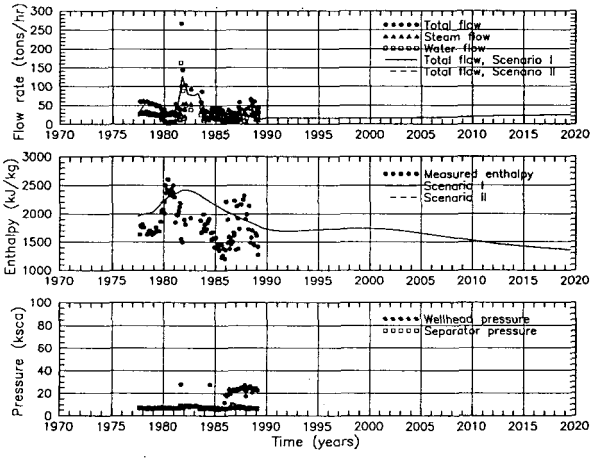

Figure 7. Production flow rates, enthalpy match and forecast by simulation, and pressures (plant CP-I), well M-45.

Figure 7 shows the match to the measured enthalpy for well M-45 (plant CP-I). The match is considered reasonable as it includes the most important characteristics of the measured enthalpy data, namely, the increase in enthalpy in late 1979 due to the additional production to supply steam to units 3 and 4 of CP-I and the later cooling trend. The additional production is believed to have caused the inflow of colder water which has resulted in the cooling noted in some areas of CP-I. To simulate the influx of colder water at this depth, it was necessary to allow the water to enter the production area both laterally from the east and west and also from the upper layers (layer 1).

Reasonable enthalpy matches were also obtained for other wells selected (shown in figure 1) to further refine the calibration of the model.

As mentioned above, the changes in piezometric level also provided data that were matched for calibration of the model. For all the wells that were considered (shown in figure 1), reasonable matches were obtained to the pressure data, suggesting that the volume of the reservoir and the boundaries of the system are well represented by the model.

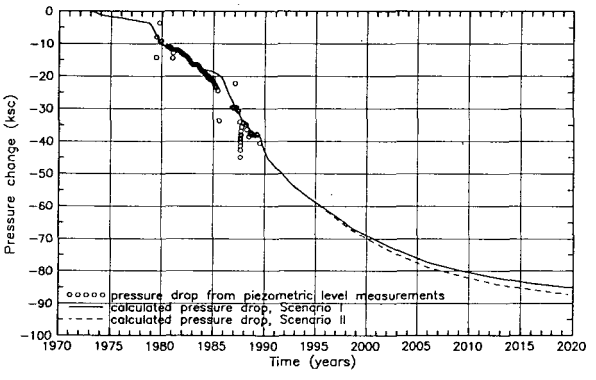

Figure 8. Pressure change match and forecast by simulation, observation well Q-473.

The match to the pressure changes in well Q-473 is presented in figure 8. According to the simulation results this well is located in a zone of good permeability and is in good communication with both the shallow and deep reservoirs. The best match to the pressure response measured in this well was obtained with no recharge to the production zone from the southwest. The production from the current production areas cuts off the recharge to this well from the northeast, which explains its relatively high pressure drop.

Wells M-201, M-202, M-203 and M-205 are located in the proposed CP-IV production area (see figure 1), the measured piezometric level from these four wells provided the only useful information for history matching in the CP-IV area. Several runs were required to obtain good matches to the available pressure data (piezometric levels).

The matches to wells M-201, M-203 (figure 9) were obtained by considering that these wells are confined to a layer which, according to the simulation results, has a horizontal permeability of approximately 20 md. This layer is bounded on top and bottom and to the northeast by impermeable layers. This implies that the wells do not communicate vertically with the recharge zone and that they are in horizontal communication with the reservoir only to the west-southwest.

The measured and calculated pressure changes for well M-202 were matched by considering that this well is completed in a low permeability zone (k_x = 0.5, k_y = 0.5 and k_z = 0.1 md) . The measured piezometric levels in this well suggests an attenuated response to present

production due to some recharge from the bottom. The well is also considered to be near an impermeable boundary to the northeast.

The match to the measured pressure changes (piezometric levels) for well M-205 was achieved by considering that the well produces from a layer bounded by impermeable formations to the top, bottom, southeast and northeast but with excellent horizontal communication with the recharge zone to the northwest and southwest. Since this well is close to what is believed to be the main recharge zone, its response to the current production for CP-I, II and III is very mild. If problems associated with initially discharging these wells due to the great depth of the producing zone (greater than 3,500 m) can be overcome, this area should have a good potential for future production.

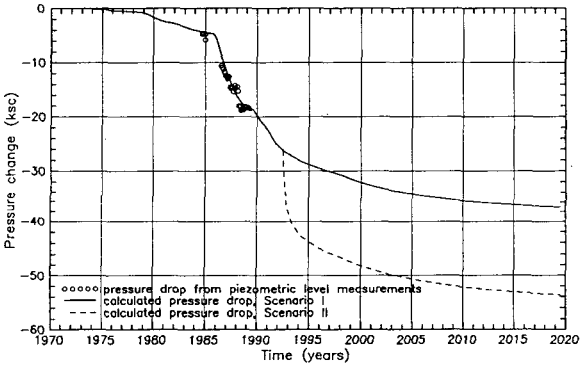

Figure 9. Pressure change match and forecast by simulation, observation well M-203.

EXPLOITATION SIMULATION

The successful calibration of the model against the initial-state as well as the production history of the field validated the use of the model for predicting the likely field response to future production.

In the present analysis, two exploitation scenarios were considered; the first based on maintaining the present total development of 620 MW in the CP-I, CP-II and CP-III areas and the second including an additional development of 80 MW in the CP-IV area, for a total development of 700 MW. It is assumed that the total steam requirement for the first scenario will be approximately 5,300 T/hr and an additional steam flow of 600 T/hr will be needed for the CP-IV development (Scenario II). Injection is not included in either of the scenarios.

In running the scenarios, the required steam rate from each block at an assumed average separator pressure of 8 ksca was input to the model. The simulator then uses the block discharge enthalpy and the separator pressure to calculate the steam fraction produced from each block. Note that due to the relative permeability functions used, the produced steam fraction will be different from the block steam fraction. The produced steam fraction is then used by the simulator to calculate the total mass flow rate required from each block to provide the required steam rate. Hence, the model can maintain a constant steam flow rate even though changes in enthalpy may be occurring due to cooling or boiling in the reservoir.

In both scenarios it is assumed that the present level of production (550 MW) will be maintained until the beginning of 1991 when sufficient additional wells will have been drilled to increase overall output to 620 MW. This is in line with CFE's current plans to increase field output to match the installed capacity. This additional production of approximately 600 T/hr steam is to be provided from deep wells located in layer 7 (3,000 to 3,500 m) in the CP-II and III areas. For Scenario I, the 620 MW capacity is then maintained until 2019.5, giving a total forecasting time of 30 years. For Scenario II, it is assumed that the CP-IV development of 80 MW will be in operation in mid-1992 and that a total output of 700 MW will then be maintained until 2019.5. The production blocks for Scenario I are based on the present production area while the locations of the CP-IV production blocks in layers 8 and 9 are based on the location and completion data of wells M-201, 202, 203 and 205.

The main reasons for running these two scenarios are to: (a) show that the field can produce the required steam for the developments considered, and; (b) evaluate the impact of the CP-IV development on the present production area. However, it should be noted that the simulated effect of CP-IV production on the current production area is based on the matching of a limited piezometric level database from wells M-201, 202, 203 and 205.

Figures 7 and 10 present examples of the calculated flow rate and enthalpy changes for the example production wells. The results for both scenarios are presented on the plots. Figure 7 shows the flow rate and enthalpy changes for well M-45 which is located in layer 2. The well is a typical production well for CP-I. The results show that the enthalpy remains reasonably constant at its present value of approximately 1,700 kJ/kg for 12 years and then declines to 1,350 kJ/kg by the end of the 30 years. The enthalpy decline is consistent with the calculated temperatures and steam saturations for layer 2, which show both a reduction in temperature of approximately 30°C from 1989.5 to 2019.5 and a reduction in the size of the two-phase zone. These changes are explained by the influx of cold water in response to continued pressure drawdown.

Some blocks in layer 4, showed that continued production causes an increase in discharge enthalpy due to the increase in steam saturation. This finally results in production of dry steam. This is typical of the wells located in the central area of layer 4 (CP-III). However,

in running the exploitation scenarios it was necessary to reduce production from layer 4 due to excessive pressure drawdown. Make-up production was provided from blocks in layers 5 and 6.

Wells located in layer 5 and layer 6, in the Cerro Prieto II area maintained relatively constant single-phase water enthalpies, indicating that steam is not forming in the vicinity of these wells. This is particularly encouraging as it will lessen the potential problems of scaling which have been associated with the two-phase production wells to the north in the CP-III area.

Figure 8 presents the calculated pressure changes in observation well Q-473 located in layer 5 (block 27). This plot indicates that for Scenario I, the pressure drops will approximately double during the next 30 years; this was also noticed in the other matched observation wells. For Scenario II, the results show only a slight increase in pressure drawdown for well Q-473 (figure 8). Hence, this suggests that the additional production for CP-IV will not have a significant impact on the CP-I, II and III production areas.

Wells located in the CP-IV area, M-201, 202, 203 (in layer 8) and M-205 (in layer 9), showed calculated pressure drops at the end of the 30 years of forecast behavior for Scenario I of approximately the same order of magnitude as the measured pressure drop in 1989.5. For Scenario II, production of 150 T/hr of steam is assumed to occur from the above four "wells" and this causes different pressure drops in all of them.

In well M-201, the production causes a maximum additional pressure change of approximately 26 ksc during the 30 years of prediction history compared to Scenario I. This gives an overall pressure drop of 63 ksc for Scenario II over the 30 years. In well M-202, the production of 150 T/h of steam causes a maximum additional pressure change of approximately 33 ksc during the 30 years to give an overall pressure drawdown of 45 ksc. The results for M-203 (figure 9) are similar to wells M-201 and 202, with 16 ksc of additional pressure drop and an overall pressure drop of 54 ksc in the year 2019.5 while M-205 has a significantly smaller overall pressure drop of only 12 ksc. The much smaller pressure change in well M-205, when compared to the other CP-IV wells, is due to it's proximity to the recharge zone in the model. The predicted pressure changes for the CP-IV wells are not excessive when the pressure changes that have occurred to date in the present production area (up to 40 ksc) are considered.

Figure 10 shows as an example, the flow rates, enthalpies and block pressures calculated for the CP-IV well M-203. This figure indicates that the discharge enthalpies remain reasonably constant at single phase water values (1,500 to 1,650 kJ/kg). This observation is also valid for the other three wells in the CP-IV area (M-201, M-202 and M-205) indicating that the pressure drops in layers 8 and 9 are not sufficient to cause steam formation in the reservoir.

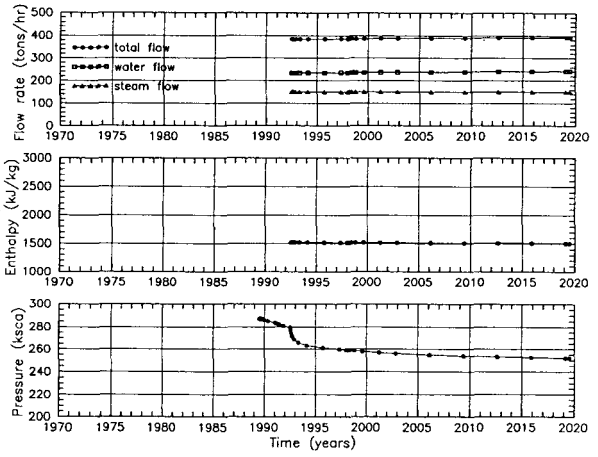

Figure 10. Production forecast for well M-203 for scenario II.

Figure 11 presents the total flow rate and average enthalpy calculated from the simulation model and compares them with the measured data. The flow rate data are input to the simulation model; hence the match with the measured data indicates that the overall production from the field has been accurately reproduced in the model. The calculated average enthalpy is in reasonable agreement with the measured data although there are differences from 1976 to 1979 when the measured data are lower and from 1987 to the present when the measured data are higher. The earlier difference suggests that the model is not fully accounting for the cooling in the shallower layers while the latter difference suggests that the model is not producing sufficient steam. The plot also indicates that the overall mass flow rate required for Scenario I is approximately 13,500 T/hr and 15,000 T/hr for Scenario II. The

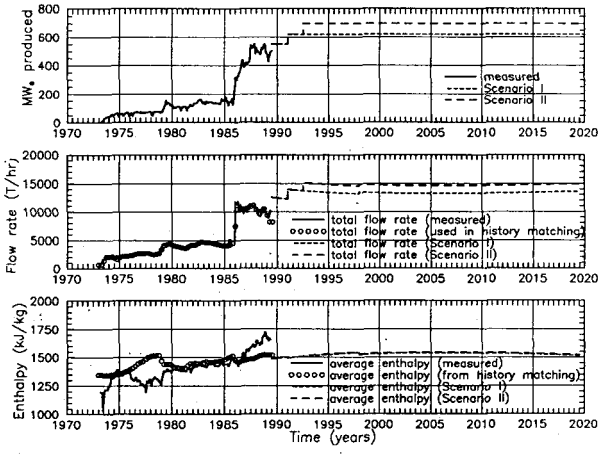

Figure 11. History and forecast of power generation, flow rate and enthalpy for scenarios I and II.

average enthalpy for both scenarios remains reasonably constant at 1,500 to 1,550 kJ/kg for the full 30 years; suggesting that the production is mainly derived from single-phase water at greater than 320°C. This is consistent with the fact that 68% of the present production is coming from layer 5 or below; this increases to approximately 80% for both scenarios by 1998.

Overall, the results from the two scenarios suggest that the Cerro Prieto field can support a development of 700 MW for the next 30 years provided that sufficient deliverability can be found in the deeper layers (greater than 2,500 m) of the system. The deep deliverability is required as it appears from the simulation results that the shallower layers, particularly layers 4 and 5, will incur problems due to excessive drawdown. Hence it will be necessary to move production from the 1,500 to 2,500 m depth interval to the deeper intervals in which the calculated drawdown is not excessive.

The simulation results also suggest that the production for CP-IV will have a negligible impact on the present production area.

CONCLUSIONS

A three dimensional numerical simulation model of the field was developed and used for prediction of reservoir behavior under various development scenarios. The objectives were a) to predict the behavior of the current production areas of CP-I, CP-II and CP-III; and b) evaluate the impact of the development of CP-IV on the current production areas. Based on the calibration of the model and the simulation results, the following conclusions regarding the Cerro Prieto field were drawn:

1. The Pátzcuaro fault proved to be the single most important fault in the system, with most of the recharge to the production areas occurring through this fault.

2. The recharge to the reservoir comes from below -4,500 m msl, northeast of the present CP-II and CP-III production areas. Fluid entering the geothermal system has a temperature close to the critical point; however, it spreads out to the sides and cools down as it moves through the Pátzcuaro fault.

3. Better temperature matches were obtained by incorporating an additional heat source beneath the CP-II and CP-III production areas. This heat source provides additional heat to the incoming fluid and sustains the high temperatures noted in the three present production areas.

4. The matches to the measured enthalpies from the chosen individual production wells and the overall discharge enthalpy for the field are considered to be satisfactory. The calculated enthalpies show that in general terms, the influx of colder water to the shallow reservoir and flashing in the deep reservoir were reproduced by the simulator.

5. The pressure response at the observation wells could be matched reasonably well suggesting that the volume of the reservoir and the boundaries of the system are well represented by the simulator.

6. The overall pressure change calculated by the simulation model in the deeper layers is consistent with the available measured data. At shallower levels, the simulation model appears to be conservative; the calculated pressure changes are higher than the available measured data would suggest. This may indicate that the permeabilities used in some areas of the upper layers of the model should be increased or that the model is underestimating the pressure support from the influx of cold water.

7. The overall pressure drop caused by continued production from Cerro Prieto will approximately double from its present average level of 40 ksc over the next 30 years. However, the average field enthalpy will remain reasonably constant due to the increase in relative production from the deeper, single-phase areas of the reservoir.

8. A total installed capacity of 700 MW, including 80 MW in CP-IV, appears to be sustainable at the Cerro Prieto geothermal field provided that sufficient deep deliverability (greater than 2,500 m) can be found in the present production area (CP-I, II and III). Additional testing of the CP-IV area is also required to ensure that the wells can be discharged successfully.

9. According to the results of the simulation, the additional production required to generate 80 MW from CP-IV has a negligible impact on the current production areas of CP-I, II and III; it therefore appears that the development of CP-IV will not adversely affect the performance of the current production areas. However, until more wells are drilled and tested in the CP-IV area, this conclusion should be considered tentative.

10. The pressure changes predicted by simulation for the CP-IV wells are within reasonable limits, considering the pressure changes observed in the current production areas of CP-II and III.

11. The simulation results suggest that the production wells producing from 1,500 to 2,500 m may be adversely affected by excessive pressure drawdown and need to be replaced by production from deeper than 2,500 m over the next 10 years. At the present time only a few wells are drilled below the 2,500 m depth in the CP-III area, thus further drilling, well testing and reservoir modeling will be required to resolve this issue.

ACKNOWLEDGEMENTS

We gratefully acknowledge the continuous cooperation and understanding we have received from the management and staff of CFE. We would like to especially thank Ing. Miguel Ramírez Gutiérrez (General Manager of Geothermal Electrical Projects) and Dr. Gerardo Hiriart LeBert (Deputy Manager of Studies) for their kind support during this study. We are indebted to the CFE staff for providing us with and explaining to us the vast data base on the Cerro Prieto reservoir.

REFERENCES

Mercado, S., Bermejo, F.J., and Heard, C. (1990), "Detection of a Possible Steam Zone Below the Present Zone of Exploitation in Cerro Prieto", Geothermal Resources Council TRANSACTIONS, Vol. 14, Part II, August 1990, pp. 927 - 932

GeothermEx, Inc., 1989, "Phase I Evaluation of the Cerro Prieto Geothermal Field, Baja California Norte, Mexico, Report presented to Comisión Federal de Electricidad, December 1989.

GeothermEx, Inc., 1990, "Phase II Evaluation of the Cerro Prieto Geothermal Field, Baja California Norte, Mexico, Report presented to Comisión Federal de Electricidad, August 1990.

PROCEEDINGS, Sixteenth Workshop on Geothermal Reservoir Engineering
Stanford University, Stanford, California, January 23-25, 1991
SGP-TR-134

NUMERICAL MODELING OF THE INITIAL STATE AND MATCHING OF WELL TEST DATA FROM THE ZUNIL GEOTHERMAL FIELD, GUATEMALA

A. J. Menzies[1], E. E. Granados[1], S. K. Sanyal[1],
L. Mérida-I.[2], and A. Caicedo-A.[3]

[1]GeothermEx Inc., Richmond, CA
[2]Cordón y Mérida Ings., Guatemala City, Guatemala
[3]Instituto Nacional de Electrificación, Guatemala City, Guatemala

ABSTRACT

A significant amount of geoscientific and reservoir engineering data have been collected from the Zunil geothermal field since 1973. The data have been used to define a conceptual model for the field which has formed the basis for the construction of a three dimensional numerical simulation model. The numerical model has successfully matched both the initial state of the reservoir, as indicated by subsurface temperature and pressure distributions within the presently drilled area, and available well test data. The well test data include short and long term discharge tests and a comprehensive pressure interference test. Calibration of the model will continue during 1991 when the results from drilling and testing of three additional deep wells are available. The model will then be used to study various long term production scenarios for the proposed 15 MW power development.

INTRODUCTION

The Zunil geothermal field is located near the city of Quetzaltenango, Guatemala; approximately 200 km west of Guatemala City (Figure 1). Exploration and development of the field has been ongoing since 1973 when the Instituto Nacional de Electrificación (INDE) began a surface exploration program to define the regional geothermal system in the Zunil area. The Japan International Cooperation Agency (JICA) provided assistance during this phase of the project. In 1976 an exploration drilling program commenced which involved the drilling of 11 slim thermal gradient holes to verify and expand the data base generated from surface exploration. The exploration program successfully delineated an area of approximately 4 km^2 on the east slope of the Cerro Quemado complex which appeared to be favorable for geothermal development.

With the success of the slim hole drilling program, six large diameter wells (ZCQ-1 to 6) were drilled by INDE during 1980-81 with the assistance of Electroconsult (ELC). The wells were completed at depths ranging from 812 to 1,310 m and encountered temperatures of up to 288°C. Testing and evaluation of the six large diameter wells continued from 1981 through 1989 and included short and long term discharge tests and a comprehensive pressure interference test. The locations of the six large diameter wells and a number of the slim holes are shown in Figure 2.

Figure 1. Location of Zunil geothermal field

In 1987, INDE signed a contract with Cordón y Mérida Ings., MK Ferguson Co. and MK Engineers, Inc. (CyM-MKE) to develop and engineer a 15 MW power plant at the Zunil geothermal field. As part of the contract, further well testing and geoscientific studies were undertaken. These studies included an integrated well testing program conducted during 1989 (Menzies *et al.*, 1990) which included flowing the four available production wells (ZCQ-3, 4, 5 and 6) and monitoring of pressure interference data. The geoscientific studies are summarized in Foley *et al.* (1990) and Adams *et al.* (1990).

The data collected from the Zunil geothermal field have been used to define a conceptual model of the

system which has formed the basis for the construction of a three dimensional numerical model. The measured subsurface temperature and pressure distributions, well test data and pressure interference data have been used to calibrate the numerical model.

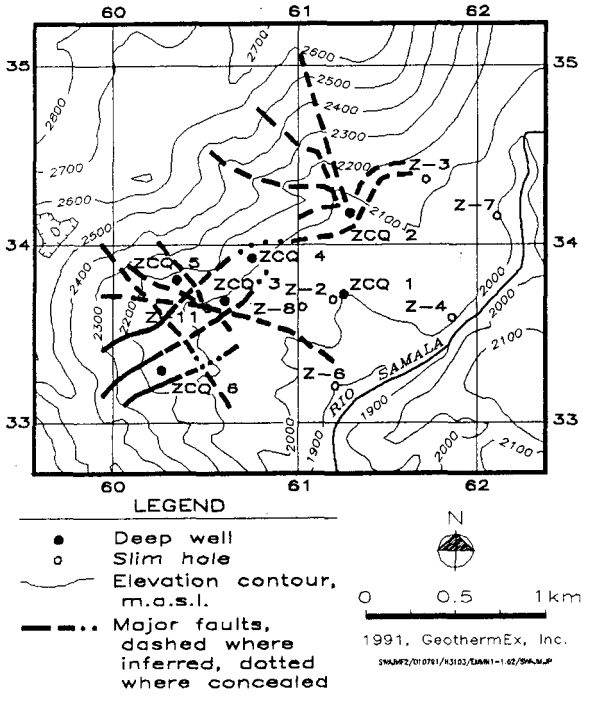

Figure 2. Well locations and major structural features

In this paper, the basic characteristics of the geothermal system are described along with the construction of the numerical model. Results from the model, including matches to the downhole temperature and pressure data and well test data are also discussed.

THE ZUNIL GEOTHERMAL FIELD

The wells drilled to date within the Zunil geothermal field have encountered features typical of many high temperature geothermal fields, for example Tongonan, Philippines (Whittome and Smith, 1979):

- A "cap" consisting of relatively low permeability rocks in which steam from the geothermal system mixes with groundwater. The rocks within the cap are mainly altered lava flows and breccias that range from dacite to andesite in composition and dacite ash-flow tuffs. Secondary mineralization is characterized by clay minerals.

- A high temperature reservoir located beneath the cap, in the vicinity of the granodioritic basement (Figure 3). The secondary mineralization within the reservoir is characterized by high temperature minerals such as epidote, quartz, chlorite and pyrite.

- A thick outflow plume which extends from the ZCQ wells, SE to the Rio Samala (Figure 2).

To help visualize the major features of the geothermal system, subsurface temperature contour maps are presented at 1,200 m msl (Figure 4) and 1,800 m msl (Figure 5). The highest temperatures encountered to date are to the W, in the vicinity of ZCQ-5 and 6. Both wells encounter temperatures of approximately 290°C below 1,200 m msl. This area is the major upflow area for the geothermal system.

The temperature contour map at 1,200 m msl (Figure 4) indicates the major direction of subsurface flow is ENE, through ZCQ-2. This is consistent with the major structural trends (Figure 2) which show that ZCQ-2 is located within the NE-SW fault trend. The relatively low thermal gradient between ZCQ-3 and 2 suggests that additional upflow is occurring within the fault zone in this area.

Temperature profiles in wells ZCQ-3, 5 and 6 are close to the "boiling-point-for-depth" curve, indicating that the maximum subsurface temperatures are controlled by local reservoir pressure. The measured pressure at 1,200 m msl (Figure 6) in ZCQ-6 (75 ksc.g) is significantly higher than in ZCQ-3 or 5 (64 to 67 ksc.g), suggesting that the lower temperatures in ZCQ-3 and 5 may be associated with lower pressures rather than being a function of distance from the upflow zone.

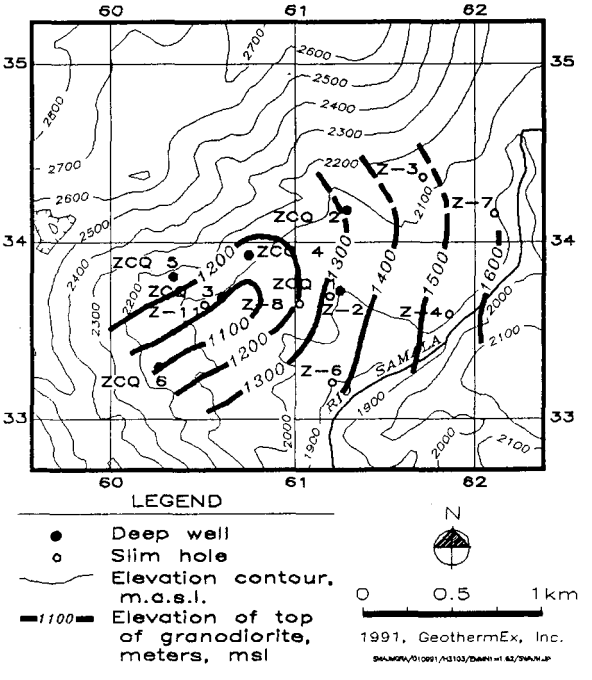

Figure 3. Contour map showing top of granodiorite

The high pressure gradient between ZCQ-6 and the rest of the deep wells is unusual in geothermal systems and indicates the presence of a low permeability area to the E of ZCQ-6. This is consistent with the results

from the interference testing conducted in 1989 (Menzies *et al.*, 1990) which showed little or no pressure response in ZCQ-6 when ZCQ-3 or 4 were flowing. The low reservoir permeability may be associated with the fault intersections (Figure 2) that occur to the E of ZCQ-6.

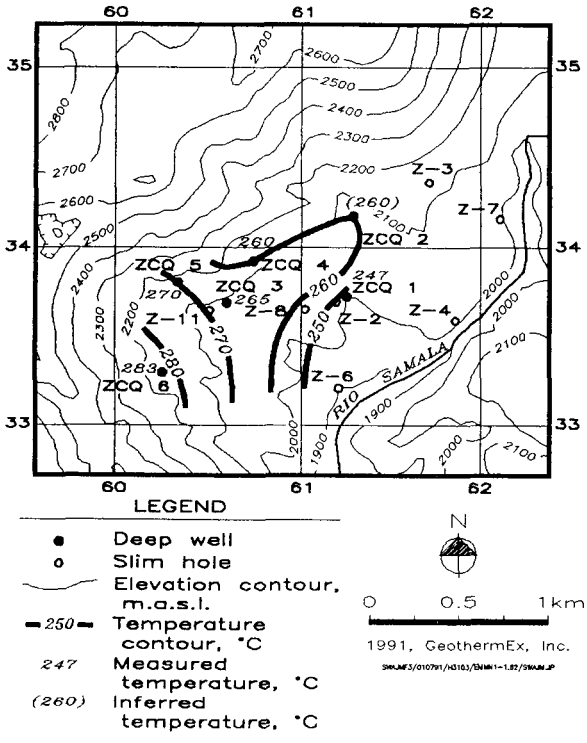

Figure 4. Temperature contour map at 1,200 m msl

At 1,800 m msl (Figure 5), the major direction of outflow shifts to the SE, through ZCQ-1 and Z-4. This outflow is controlled by the top of the granodiorite basement (Figure 3), which rises towards the SE and outcrops approximately 2.5 km to the E (Bethancourt and Dominco, 1982). Surface thermal manifestations occur within the Rio Samala valley (Figure 2); the majority being bicarbonate or acid-sulfate springs associated with steam heated ground waters. However, spring z-20, located near slim hole Z-4 (Figure 2), discharges Na-Cl water which can be related to the deep geothermal fluid.

WELL TEST DATA

Since the ZCQ wells were completed in 1980-81, a number of short and long term discharge tests have been conducted to determine well production characteristics. An interference test was also conducted during 1989 as part of an integrated well test program which involved discharging wells ZCQ-3, 4, 5 and 6 and injection to ZCQ-2. Analysis of the data from the 1989 test are presented in Menzies *et al.* (1990). Table 1 summarizes the well discharge

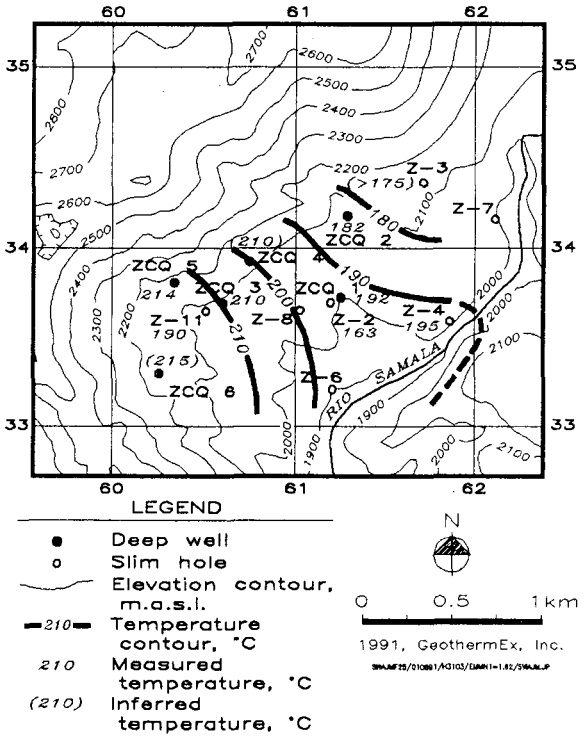

Figure 5. Temperature contour map at 1,800 m msl

characteristics based on the results from the 1989 flow tests.

The ZCQ wells were all drilled to the granodiorite basement. Well ZCQ-1 was completed deep within the basement; however it encountered no permeability and went through a temperature inversion after drilling into the basement. The other five wells encountered permeability at or near the basement contact while ZCQ-4 and 5 also encountered permeability within the overlying volcanics. The estimated thickness of the permeable zone at the basement contact is approximately 50 m (Bethancourt and Dominco, 1982).

Downhole survey and geochemical data suggest that wells ZCQ-3 and 6 produce predominantly from the contact zone and the discharge fluid is closest in chemical composition to the postulated parent fluid (Adams *et al.*, 1990). Their discharge enthalpies of 310 to 360 kcal/kg (Table 1) are higher than for single phase water at measured downhole temperatures. Either the discharge fluid is flashing in the reservoir or there is a small contribution from a two-phase or steam zone within the volcanics. Downhole surveys show that two-phase fluid is entering the wells under flowing conditions.

Well ZCQ-5 produces dry or superheated steam from the contact zone, even though the reservoir fluid is single phase water. Production of steam under these conditions indicates that the contact zone in the vicinity

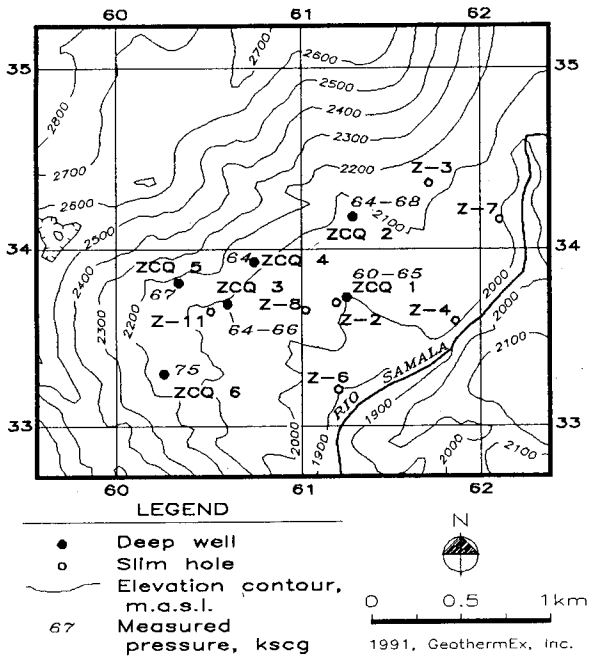

Figure 6. Pressure measurements at 1,200 m msl

of ZCQ-5 has very low permeability. The discharge from ZCQ-5 is also affected by cycling, suggesting the influence of additional permeable zone(s). Geochemical data (Michels, 1990) suggest these secondary zone(s) allow shallow, cooler fluid to enter the wellbore near the casing shoe.

Table 1: Power Capacities of Zunil Wells

Well	Wellhead pressure (ksca)	Mass flow rate (tons/hr)	Discharge enthalpy (cals/gm)	Power capacity (MW)
ZCQ-3*	9.0	105	340	4.8
ZCQ-3**	9.0	120	310	4.6
ZCQ-3***	7.0	80	360	4.1
ZCQ-4	7.0	50	600	5.7
ZCQ-5	10.0	33	580	3.5
ZCQ-6	8.0	50	360	2.5

* data from short term test (February 1989)
** data from start of long term test (March 1989)
*** data from end of long term test (July 1989)

Well ZCQ-4 produces high enthalpy fluid (550 to 600 kcal/kg) from the volcanics. It also has some permeability near the contact which causes significant cycling to occur in the well discharge. The discharge from the deeper permeable zones is apparent from downhole pressure data (Menzies *et al.*, 1990) and from spinner surveys (Dennis and VanEeckhout, 1990).

Well ZCQ-2 also encountered permeability at the contact zone but was found to be non-commercial when discharged. The well is presently designated as an injection well and was used successfully for this purpose during the 1989 well test program (Menzies *et al.*, 1990). Based on the 1989 test results, it is estimated that the well can accept at least 100 tons/hr of injection water.

The interference test conducted during 1989 showed that wells ZCQ-1, 3 and 4 are in good hydraulic communication but respond only weakly to injection in ZCQ-2. Wells ZCQ-5 and 6 did not respond significantly to the discharges of ZCQ-3 or 4 but the response in ZCQ-5 may have been affected by pressure changes associated with its own short term discharge. The lack of response in ZCQ-6 is consistent with the measured pressure data which suggest that a low permeability area exists between ZCQ-6 and the rest of the field.

The calculated reservoir transmissivities from analytical modeling of the interference responses and from pressure buildup data vary from 1,600 md.m to 8,500 md.m which are typical values for high temperature geothermal systems. The calculated storativities range from 0.01 to 0.024 m/ksc, suggesting the presence of two-phase conditions in the reservoir.

NUMERICAL MODEL DEVELOPMENT

A numerical model of the Zunil geothermal field was developed based on the conceptual model described above. The model is orientated in a SW-NE direction (Figure 7) and covers a total area of 8.06 km^2; 3.1 km in the SW-NE direction and 2.6 km in the SE-NW direction. The model consists of four layers and extends from the topographical surface (1,900 to 2,700 m msl) down to sea level.

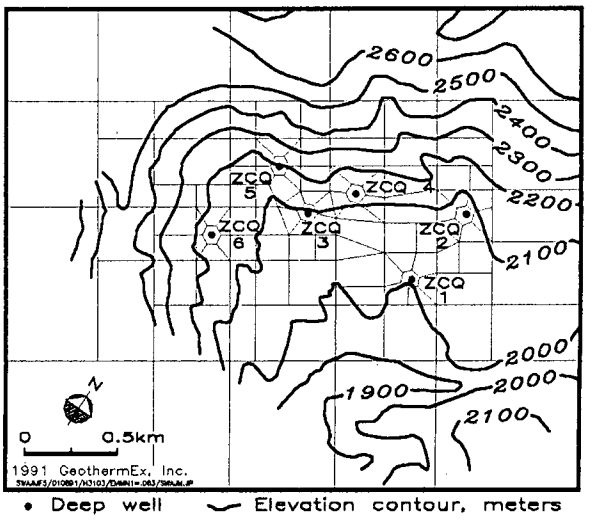

Figure 7. Grid block layout with well locations

Layer 1 extends from the topographical surface to 1,500 m msl and has a constant node level at 1,600 m msl. This layer is located within the volcanics and

includes the major production zone for ZCQ-4 and the outflow plume to the SE through ZCQ-1.

Layer 2 extends from 1,500 m msl to 1,000 m msl with the node level set at 1,200 m msl. This layer includes the contact zone between the granodiorite basement and the overlying volcanics which is the major source of present production as well as providing the injection zone in ZCQ-2. Subsurface outflow through ZCQ-2 occurs in this layer.

Layers 3 (1,000 m msl to 500 m msl) and 4 (500 m msl to sea level) are located within the granodiorite with node levels of 750 m msl and 250 m msl, respectively. At the present time, the only information available from these layers is temperature data from ZCQ-1 which was drilled to 695 m msl. However, the present ZD drilling program is designed to investigate deeper production (down to 200 m msl) and layers 3 and 4 have been included in the model for the purpose of modeling the ZD well results.

Boundary layers are used in the model to provide heat and mass inflow from depth and to model the heat sink provided by the atmosphere (1 ksc.a and 20°C). For both boundaries, very large volume blocks are used to ensure that the boundary conditions remain constant during the simulation process.

Each of the four main layers contain 114 grid blocks (Figure 7) and the total number of grid blocks used, including boundary blocks, is 459. The grid blocks are of irregular shape to improve reservoir definition in the vicinity of the production wells and to allow reasonable conformity to the fault trends and the shape of the granodiorite surface.

The computer program used for the modeling employs the "integral-finite-difference" (IFD) method to calculate the fully coupled flows of water and heat within the model. The IFD formulation also allows the use of irregular grid blocks which increases the flexibility of the model. The code was originally developed at Lawrence Berkeley Laboratory under U.S. Department of Energy funding and has been improved by GeothermEx for commercial use.

INITIAL STATE MODELING

In the initial state modeling, the main upflow zone is located to the NW of ZCQ-6. The fluid rises and then flows horizontally above the granodiorite in layers 1 and 2 to the ENE and SE. The hot upflow is initiated by setting the outflow rates in layers 1 and 2 and the model run until steady state conditions are obtained. The calculated temperature and pressure distributions are then compared with the measured data. If they do not agree, changes in outflow rate, source temperature, source pressure and permeability distribution are made and the simulation run is repeated. This process continues until a reasonable match is obtained.

To obtain a reasonable match to the initial state, a secondary upflow zone was required in the vicinity of ZCQ-4 and 2 in order to maintain the relatively low temperature gradient in this region (Figure 4). The locations of the upflow zones are shown in Figure 8.

After many iterations, steady state conditions were reached where the calculated temperature and pressure distributions were in good agreement with the measured data on the three layers for which measured data are available. The final model required outflow to the ENE in layer 2 of 7 tons/hr and outflow to the SE in layer 1 of 47 tons/hr. The outflow fluid is mainly provided by the upflow zone in the vicinity of ZCQ-6 (Figure 8), with a source temperature of 300°C at sea level.

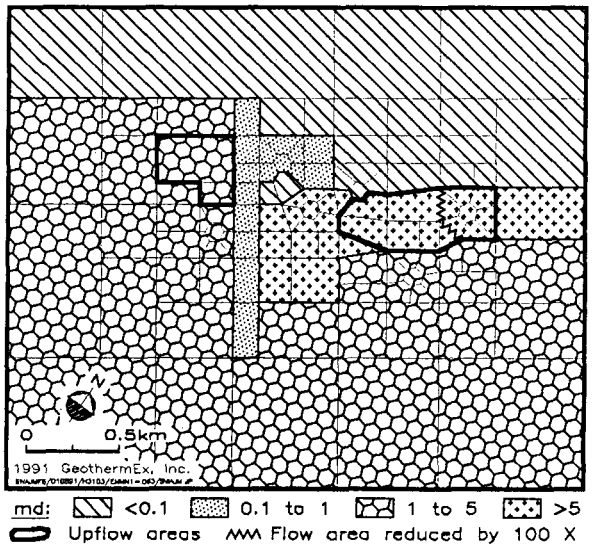

Figure 8. Permeability distribution in layer 2

The results for layer 2, including the permeability distribution, calculated temperature contours and calculated pressure contours are shown in Figures 8 to 10. The permeabilities used in layer 2 (Figure 8) range from 0.01 md up to 5.5 md. For the layer thickness of 500 m, these permeabilities correspond to transmissivities of 5 md.m to 2,750 md.m. The higher value is the same order of magnitude as the results from the analysis of the interference test data.

The very low permeabilities in layer 2 are mainly used to the NW where no data is presently available. The highest permeabilities define the flow conduit from ZCQ-3 through to ZCQ-2. Lower permeabilities are required to the SE to improve the match to measured temperatures in ZCQ-1 (Figure 9) and also between ZCQ-6 and 3 to match the high measured pressure gradient (Figure 10).

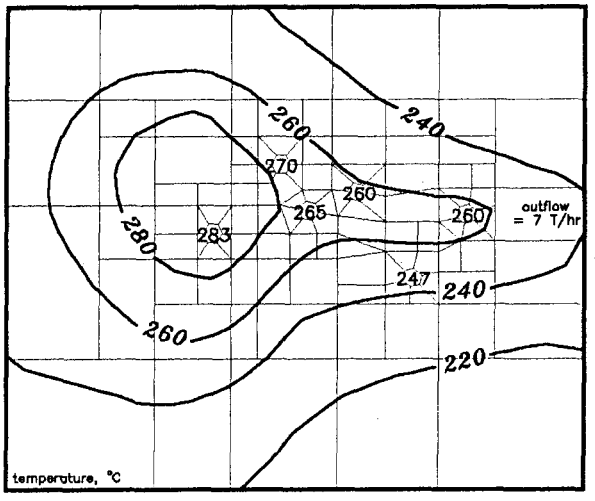

Figure 9. Comparison of calculated and measured temperature data, layer 2

In layer 1, a good match was obtained to the measured temperature data at 1,600 m msl (Figure 11), with a similar range of permeabilities to those used in layer 2. However, it was necessary to use a significantly higher outflow rate (47 tons/hr) to sustain the required temperatures. Two-phase conditions are also widespread in layer 1 (Figure 11), indicating that the calculated temperatures are functions of pressure; hence, if the temperature match is reasonable then the pressure distribution must also be reasonably correct. The presence of two-phase conditions is consistent with well data and the indications of steam in surface thermal manifestations.

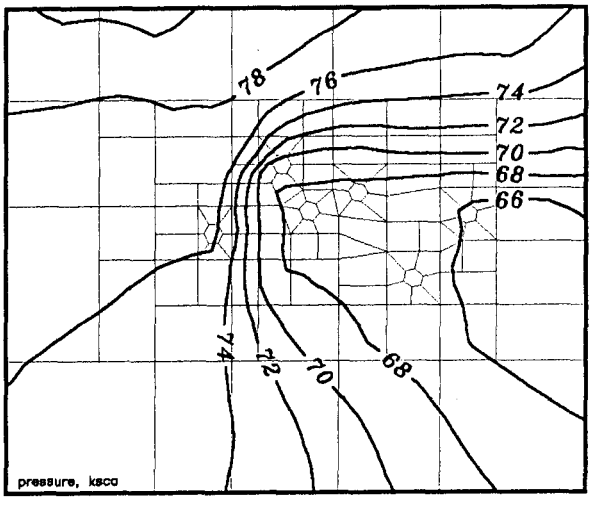

Figure 10. Calculated pressure contours, layer 2

In layers 3 and 4 the permeability has been set to 0.01 md away from the two upflow areas. This is an assumption at the present time due to the lack of data. However, a good match has been obtained to the measured temperature in layer 3 from ZCQ-1. The permeability distribution will probably be modified by the results from the drilling and testing of the ZD wells. Within the upflow zones, the permeabilities are higher; to the N of ZCQ-6, the permeability is 4 md and between ZCQ-4 and 2, the permeability is 0.5 md.

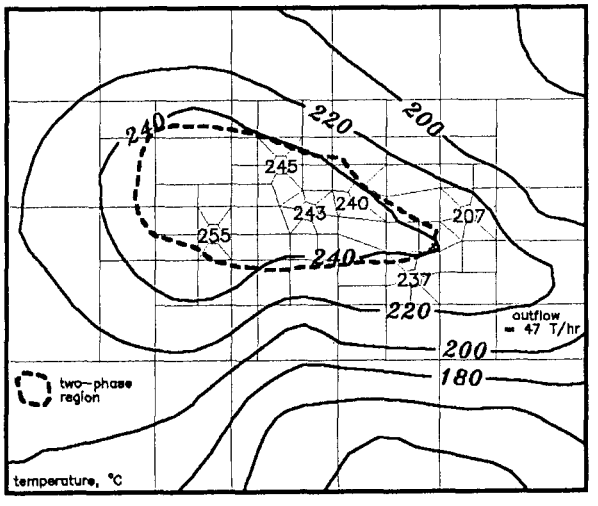

Figure 11. Comparison of calculated and measured temperature data, layer 1

MATCHING WELL TEST DATA

After successful completion of the initial state matching, the model was used to analyze the available well test data collected during the 1989 integrated well test and from long term flow test data collected during various periods from 1981 to 1986.

With the existence of two-phase conditions within the model, it is necessary to define "relative" permeability functions which control the relative flow of steam and water between grid blocks. Various functions were tried during the matching process but the Grant relative permeability functions gave the best results. These functions are based, in part, on analysis of field data from Wairakei, New Zealand (Grant, 1977) and the Corey relative permeability functions used in petroleum reservoir simulation. Residual water saturation of 0.3 and zero residual steam saturation were used in the modeling.

After a large number of runs, reasonable matches were obtained to both the 1989 test data and the earlier long term flow test data. During this process, it was necessary to modify the permeability and porosity distributions used in the initial state model. The model was rerun to steady state conditions to check that the match to the initial state had not been changed significantly. A model was finally obtained that provided a reasonable match to both the well test data and to the initial state.

Interference Test Data

Figure 12 presents the matches to the pressure interference data from wells ZCQ-1, 4 and 6. The data were collected during the discharges of ZCQ-3 and 4 and injection to ZCQ-2. Figure 12 shows that it was possible to obtain reasonable matches to the overall pressure changes, including the weak response to injection to ZCQ-2.

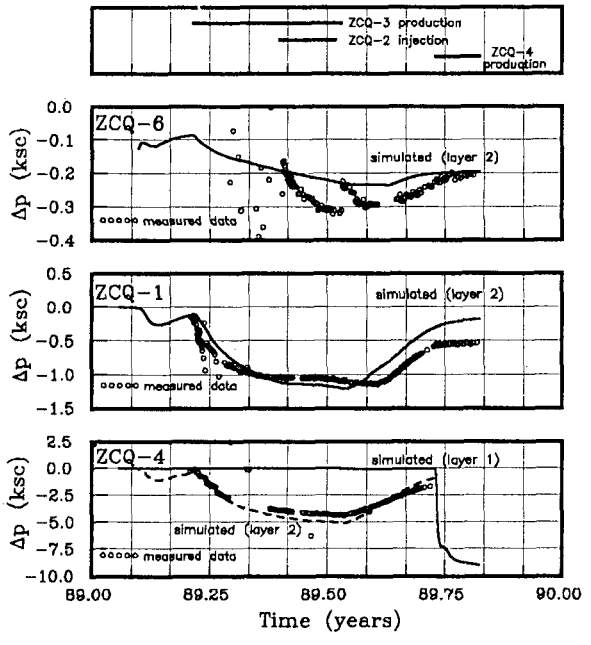

Figure 12. Comparison of calculated and measured observation well pressure responses

The data from ZCQ-1 proved difficult to match due to the significant delay in the recovery response. The reason for the delay is not well understood and is not consistent with the very fast response to the discharge of ZCQ-3. It was also not possible to obtain a satisfactory match to the flattening in the pressure response that occurred when ZCQ-4 was discharged. Well ZCQ-4 produces mainly from layer 1 in the model which is cased off in ZCQ-1. Further layers would probably be required in the model to improve the calculated response.

The final match to the ZCQ-1 data is based on the well being located in a low permeability region surrounded by higher permeability; possibly suggesting that the well was damaged during drilling. If other geometries were considered, such as more extensive zones of higher or lower permeability, the calculated pressure response was either too large or was delayed. The magnitude of the pressure response was also very sensitive to porosities in layer 1; higher porosity improved the match but affected the long term production enthalpy of ZCQ-4 while lower porosities caused excessive pressure drop in ZCQ-1.

To match the pressure response in ZCQ-4, it was necessary to locate the well in a low permeability region of layer 2 (Figure 8). This is consistent with the low productivity of the contact zone in ZCQ-4 and allowed a very good match to be obtained.

For matching the weak pressure responses in both ZCQ-1 and 4 to injection in ZCQ-2, it was necessary to reduce the effective flow area in the vicinity of ZCQ-2 by 100 times (Figure 8). This worked very well and did not change the initial state model significantly.

The successful match to the measured pressure response in ZCQ-6 (Figure 12) required the inclusion of a low permeability area (Figure 8) between ZCQ-6 and 3, with a permeability of 0.15 md.

Discharge Test Data

In using the model to match the discharge characteristics of individual wells, the "deliverability" option was used. With this option, the well flow rates are not specified but are calculated based on the productivity index (PI) of the well, fluid mobility in the vicinity of the well and the pressure difference at the feedzone:

$$q = \sum_{\beta\text{-liquid,vapor}} \frac{k_{r\beta}}{\mu_\beta} \rho_\beta PI(p_b - p_{wb})$$

The wellbore pressure (p_{wf}) is specified based on measured data from downhole pressure surveys. The PI is adjusted, along with permeability and porosity, until the model results match both the measured flow rate and enthalpy transients. Circular grid blocks are used in the vicinity of the active wells to improve the radial flow approximation within the model.

Successful matches were obtained to the discharge data from the four ZCQ wells using the above option; examples from ZCQ-3 and 4 are presented here. Figures 13 and 14 present matches to discharge data collected in 1989 and 1983-84 from well ZCQ-3 while Figures 15 and 16 present similar results for ZCQ-4 from 1989 and 1982.

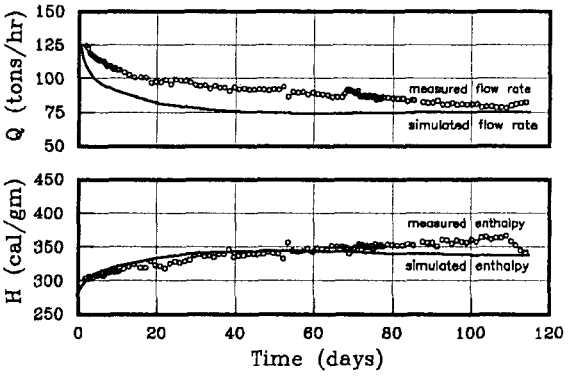

Figure 13. Matching of flow rate and enthalpy data from 1989 flow test, Well ZCQ-3

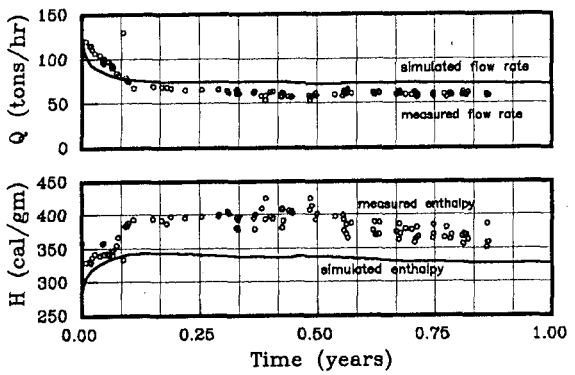

Figure 14. Matching of flow rate and enthalpy data from 1983-84 flow test, Well ZCQ-3

To obtain the matches to the measured data in ZCQ-3, it was necessary to use a very low effective porosity (0.3%) in the high permeability region of layer 2 (Figure 8). This corresponds to a porosity-thickness of 1.5 m, which is very low and indicates the reservoir has limited storage capacity; consistent with the approximate thickness of the contact zone, which is estimated to be 50 m. With this porosity, the model gives a good match to the initial enthalpy rise but calculates a higher initial flow rate decline. Overall, the matches are considered to be reasonable although the calculated enthalpy does not rise as high as the measured data over the long term.

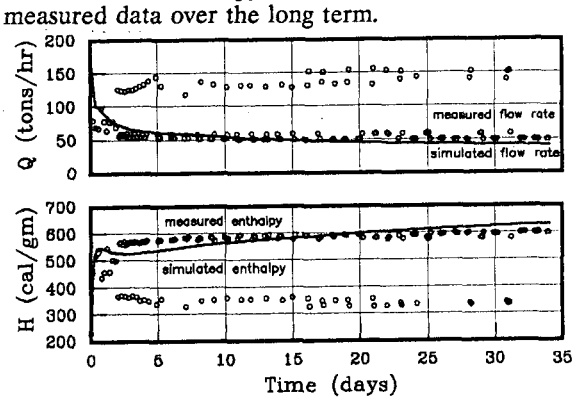

Figure 15. Matching of flow rate and enthalpy data from 1989 flow test, Well ZCQ-4

For ZCQ-4, production was assumed to occur from both layers 1 and 2 although the contribution from layer 2 is small due to the low permeability. A very good match was obtained to the 1989 data by using a porosity of 2% in layer 1. However, to match the long term data collected in 1982, it was necessary to reduce porosity in the outer blocks to 0.2% to maintain the high enthalpy. The results suggest that a lower porosity and/or permeability is probably required as the simulated flow rate remains higher than the measured data after approximately 0.25 years. However, as mentioned above, the lower porosity causes problems in matching the 1989 pressure interference response in ZCQ-1.

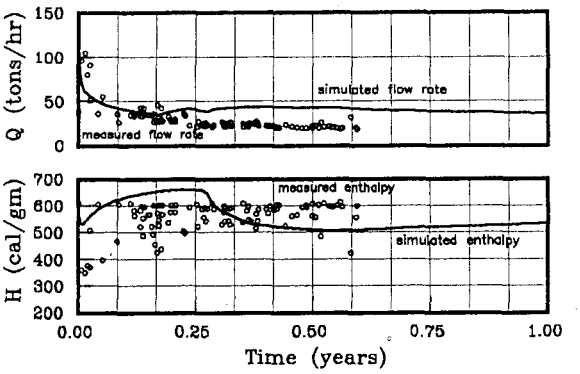

Figure 16. Matching of flow rate and enthalpy data from 1982 flow test, Well ZCQ-4

CONCLUSIONS

A three dimensional numerical model of the Zunil geothermal field has been successfully developed and calibrated against subsurface temperature and pressure data and well test data.

Matching of the initial state indicates that hot fluid rises in the vicinity of ZCQ-6 and flows both to the ENE and SE. A secondary upflow zone exists between ZCQ-3 and 2 which maintains the very low thermal gradient noted from well data. Reservoir permeabilities ranging from 0.01 md to 10 md and a natural flow through the system on the order of 50 tons/hr are required to match the subsurface temperature and pressure distributions.

Successful matches have been obtained to the available well test data, including flow test data and pressure interference data. The results indicate very low effective porosities (0.2 to 0.3%), indicating that the reservoir has a very low storage capacity.

Further calibration of the model will be undertaken when the ZD wells, which are presently being drilled, are completed and tested. These wells will provide much needed data on the deeper levels of the geothermal system. The model will then be used to predict field performance under a number of production scenarios associated with the proposed 15 MW development.

ACKNOWLEDGEMENTS

The studies of the Zunil geothermal field presented in this paper would not have been possible without the full support and co-operation of the Instituto Nacional de Electrificación (INDE), Morrison-Knudsen Environmental Services (MKE) and Cordón y Mérida Ings. (CyM). We would also like to thank the field staff who collected the geoscientific and well testing data; without them this study would not have been possible.

REFERENCES

Adams, M.C., L.L. Mink, J.N. Moore, L.D. White and A. Caicedo-A., 1990. Geochemistry and Hydrology of the Zunil Geothermal System, Guatemala. Geothermal Resources Council, Transactions, Vol. 14, Part II, pp. 837-844.

Bethancourt, H.R. and E. Dominco, 1982. Characteristics of the Zunil Geothermal Field (Western Guatemala). Geothermal Resources Council, Transactions, Vol. 6, pp. 241-244.

Dennis, B. and E. VanEeckhout, 1990. Well Logging Results from Three Geothermal Fields in Central America. Geothermal Resources Council, Transactions, Vol. 14, Part I, pp. 373-378.

Foley, D., J. N. Moore, S. J. Lutz, J.C. Palma-A., H.P. Ross, E. Tobias-G. and A.C. Tripp, 1990. Geology and Geophysics of the Zunil Geothermal System, Guatemala. Geothermal Resources Council, Transactions, Vol. 14, Part II, pp. 1405-1412.

Grant, M.A., 1977. Permeability Reduction Factors at Wairakei. AIChE-AIME Heat Transfer Conf., Paper No. 77-HT-52.

Menzies, A.J., E.E. Granados, S.K. Sanyal, L.L. Mink, L. Mérida-I. and A. Caicedo-A., 1990. An Integrated Test Program for the Definition of a High Temperature Geothermal Reservoir: A Case Study from the Zunil Geothermal Field, Guatemala. Geothermal Resources Council, Transactions, Vol. 14, Part II, pp. 1233-1239.

Michels, D.E., 1990. Zunil I, Quetzaltenango, Short Period Tests - 1989. Chemistry of Wellbore Discharges and Correlation with Reservoir Behavior. Internal report submitted to CyM and MKE.

Mink, L.L., L. Mérida-I. and A. Caicedo-A., 1988. Zunil, Guatemala Geothermal Project (Overview and Update). Geothermal Resources Council, Transactions, Vol. 12, pp. 185-191.

Whittome, A.J. and E.W. Smith, 1979. A Model of the Tongonan Geothermal Field. New Zealand Geothermal Workshop, Proceedings, Vol. 1, Part 1, pp 141-147.

PROCEEDINGS, Sixteenth Workshop on Geothermal Reservoir Engineering
Stanford University, Stanford, California, January 23-25, 1991
SGP-TR-134

Two-Phase Flow Visualization and Relative Permeability Measurement in Transparent Replicas of Rough-Walled Rock Fractures

P. Persoff, K. Pruess, and L. Myer

Earth Sciences Division, Lawrence Berkeley Laboratory,
University of California, Berkeley, CA 94720

ABSTRACT

Understanding and quantifying multi-phase flow in fractures is important for mathematical and numerical simulation of geothermal reservoirs, nuclear waste repositories, and petroleum reservoirs. While the cubic law for single-phase flow has been well established for parallel-plate fractures theoretically and experimentally, no reliable measurements of multi-phase flow in fractures have been reported. This work reports the design and fabrication of an apparatus for visualization of two-phase flow and for measurement of gas-liquid relative permeability in realistic rough-walled rock fractures. A transparent replica of a natural rock fracture from a core specimen is fabricated by molding and casting in clear epoxy. Simultaneous flow of gas and liquid with control of capillary pressure at inlet and outlet is achieved with the Hassler "sandwich" design: liquid is injected to the fracture through a porous block, while gas is injected directly to the edge of the fracture through channels in the porous block. A similar arrangement maintains capillary separation of the two phases at the outlet. Pressure drops in each phase across the fracture, and capillary pressures at the inlet and outlet, are controlled by means of pumps and needle valves, and are measured by differential and absolute pressure transducers. The clear epoxy cast of the natural fracture preserves the geometry of the fracture and permits visual observation of phase distributions. The fracture aperture distribution can be estimated by filling the fracture with a dyed liquid, and making pointwise measurements of the intensity of transmitted light. A set of two-phase flow experiments has been performed which has proven the viability of the basic experimental design, while also suggesting further improvements in the apparatus. Preliminary measurements are presented for single-phase permeability to liquid, and for relative permeabilities in simultaneous flow of liquid and gas.

INTRODUCTION

Understanding and quantifying multi-phase flow in fractures is important for mathematical and numerical simulation of geothermal reservoirs, nuclear waste repositories, and petroleum reservoirs. When two (or more) phases occupy the pore space in a permeable material, pores occupied by one phase are unavailable for flow by the other; each phase interferes with the flow of the other. In porous media, this interference is quantified by relative permeability functions, defined by

$$k_i = k k_{rel,i} \qquad (1)$$

where k_i is the effective permeability to phase i, k is the intrinsic permeability of the medium, and $k_{rel,i}$ is the relative permeability to phase i. When the medium is completely saturated with phase i, $k_{rel,i} = 1$. The $k_{rel,i}$ are strong functions of phase saturation, and are therefore critical to the mathematical modeling of multiphase flow. Such functions should be equally important for modeling multiphase flow in fractures. While the cubic law for single-phase flow in parallel-plate fractures has been well established theoretically and experimentally (Witherspoon et al. 1980), no reliable measurements of multi-phase flow in fractures have been reported. Pruess and Tsang (1989, 1990) reviewed limited theoretical and experimental work, and presented a method by which relative permeability functions could be derived from fracture geometry. The laboratory investigation of Romm (1966) and analysis of field data for fractured geothermal reservoirs by Pruess et al. (1983, 1984) and by Bodvarsson et al. (1987) both suggested that

$$k_{rel,w} + k_{rel,nw} = 1 \qquad (2)$$

for all values of saturation, where w and nw denote the wetting and non-wetting phases, respectively. Constancy of the sum indicates negligible phase interference. However, results of numerical simulation using stochastically generated single-fracture geometries by Pruess and Tsang (1989, 1990) showed strong phase interference, with the sum much less than 1 at intermediate saturations. Romm (1966) used parallel-plate fractures (i.e., unrealistic fracture geometry); and in systems with phase changes, such as geothermal reservoirs, the phase interference is much less than in flow systems without phase changes; so $\sum_i k_{rel,i} = 1$ may not apply to fractures in general.

One of the goals of the present work is to resolve the apparent discrepancy between these results. This paper

reports the design and fabrication of an apparatus for visualizing two-phase flow and measuring gas-liquid relative permeability in realistic rough-walled rock fractures. We also present preliminary relative permeability data for gas-liquid flow in a transparent replica which reproduces the geometry of a natural fracture.

APPARATUS

The apparatus was designed to measure the inlet and outlet pressures of two immiscible fluids as they flow through a transparent epoxy resin cast of both sides of a natural rough-walled rock fracture (see Figure 1). Special endcaps were fabricated to inject and receive two immiscible fluids (gas, water, or oil) at controlled rates and pressures. The method of Hassler (1944) with porous endcaps was used to avoid capillary end effects and maintain uniform capillary pressure $p_{cap} \equiv p_{gas} - p_{liq}$ across the entire fracture plane. The multiphase fluids can be observed visually, and recorded with video equipment or still photography.

Transparent Fracture Replica

The centerpiece of the apparatus is a clear 7.6 cm × 7.6 cm epoxy resin cast of both sides of a natural rough-walled rock fracture. The fracture was approximately perpendicular to the axis of an 11.5-cm diameter granite core from the Stripa mine, Sweden. Rhodorsil RTV 1556 silicone rubber (Rhone-Poulenc, Inc., Monmouth Junction, NJ) was used to make molds of each side of the fracture (yielding a "negative" of the fracture-wall topography). Then Eccobond 27 clear epoxy (Emerson and Cuming, Dewey and Almy Chemical Division, W. R. Grace Co., Canton, MA) was used in the mold to make replicas (positive) of the surface of each side of the fracture. Both the silicone rubber and the epoxy are viscous two-part liquid formulations, and many air bubbles were entrained during mixing. Bubbles were eliminated by placing the container in a vacuum chamber and expanding the bubbles until they rose and burst. The liquid was then poured into the mold (or onto the original fracture surface) and evacuation was repeated. The silicone rubber was cured at room temperature, and the epoxy was cured at 100°C for 4 hr. The epoxy replicas were mated and machined to a 3-inch square section of the fracture; the outer surfaces were also machined and polished flat and parallel. Holes were drilled through a separate block of the cured epoxy for capillary rise measurements; these measurements showed that water wets the cured epoxy with zero contact angle.

Endcaps

Special endcaps were fabricated to inject and receive two immiscible fluids at controlled rates and pressures. For these experiments, distilled water and nitrogen gas were used as the wetting and non-wetting phases, respectively. The purpose of the endcaps is to maintain a difference between the pressures in the wetting and non-wetting phases at the upstream and downstream edges of the fracture. The design of Hassler (1944) for measuring relative permeability in porous cores was modified for fractures. Essentially, the wetting phase is delivered to the fracture edge through a wettable porous block, while the non-wetting phase is delivered through grooves in the porous block (Fig. 1). The grooves alternate with the flats between the grooves to cover the entire fracture edge in sections 0.05-inch long. The block was machined from porous ceramic with pore size controlled to have a 1-bar air-entry pressure (Soilmoisture Equipment Co., Santa Barbara, CA). Therefore, as long as the capillary pressure at inlet or outlet was less than one bar, the phases would remain separated, and no gas could back up into the water injection line. The porous block was cemented into a brass casing using quick-setting epoxy (Double Bubble, Hardman Co., Belleville, NJ). Liquid was delivered through four stainless steel tubes cemented into holes in the block, and gas was delivered through a single tube into a plenum which connected all the grooves.

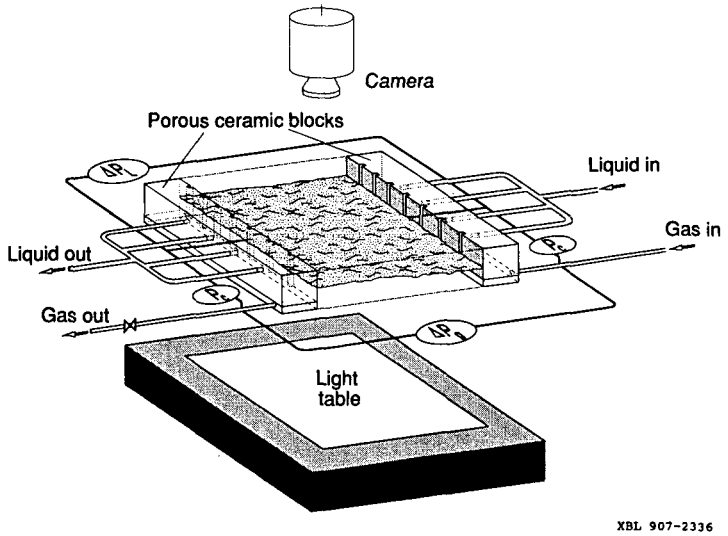

Figure 1. Apparatus for flow visualization and relative permeability measurement in transparent replica of a natural rock fracture. Ovals represent differential pressure transducers; absolute pressure transducers have been omitted for clarity. Note that gas is injected to a plenum which distributes it to vertical grooves in the porous block at the inlet end. Only seven grooves are shown in the figure; actually they are closely spaced with a total of 40 grooves. Rubber-lined steel bars which seal edges are not shown.

Control and Measurement of Flow Rates and Pressures

Four pressure taps sensed inlet and outlet gas pressure, and inlet and outlet liquid pressure. The gas pressure taps were located in the gas injection lines just outside the endcaps. In order to measure liquid pressure right at the fracture edges, a 0.25-inch hole was drilled completely through each porous block, and a liquid-pressure tap was cemented into this hole. The end of each liquid-pressure tap was filled with a plug of the same porous ceramic to prevent gas from invading the liquid-pressure tap (this is essentially the same as in Hassler's design). Absolute pressure transducers were used to measure the downstream absolute gas and liquid pressures, and differential pressure transducers were used to measure the inlet and outlet capillary pressures, and the pressure drops across the fracture in the gas and liquid phases (AP-10 and DP-15, Validyne Engineering Corp., Northridge, CA). This scheme permitted some redundancy and checking of measured pressures. Additionally, Bourdon-tube pressure-vacuum gauges were placed at all pressure taps and on the liquid lines bracketing the porous blocks. Micrometer needle valves (SS-2, Nupro Co., Willoughby, OH) were placed on both the gas and liquid outlet lines, to permit adjustment of each of the phase pressures at the outlet. During an experiment, inlet capillary pressure is set by flow rates; outlet capillary pressure is adjusted with the needle valves to equal it. Pressures and gas flow rates were automatically recorded.

The liquid flow was delivered by an LC-5000 syringe pump (ISCO, Lincoln, NE). Because the pump capacity is limited to 500 mL, it was occasionally necessary to refill the pump during the experiment, which takes about 5 minutes. To continue uninterrupted liquid flow during this time, a liquid reservoir was connected to the liquid injection line, and pressurized with nitrogen to the pressure indicated by the appropriate gauge. This allowed liquid delivery to continue at the same pressure that had existed during constant-rate delivery.

Gas was delivered through either of a pair of Brooks 5850E mass-flow controllers (Emerson Electric, Hatfield, PA), with capacities of 10 and 1000 mL/min at standard temperature and pressure.

Before assembling the endcaps to the inlet and outlet edges of the transparent fracture replica, a piece of glass-fiber filter (Reeve Angel 934 AH, Whatman, Inc., Clifton, NJ) was placed over the grooved face of the porous block to ensure liquid-phase capillary continuity. The filter was wetted and a scalpel was used to make slits in it over the grooves. Thus both gas and liquid had access to the fracture edges. The endcaps were placed over the fracture edges, and pressed against the fracture edges by means of threaded tension rods.

To confine all fluid flow to the fracture, the no-flow edges and the circumferences of the end caps were sealed. This was accomplished by six steel bars lined with 1/16" thick silicone rubber, which were pressed against the fracture replica by threaded rods. The fracture itself was loaded in compression between a pair of machined lucite blocks, using four Belleville spring washers (Associated Spring Gardena, CA) to apply a total load of 240 lb. over the 9 square inch area, corresponding to 26.7 psi. The entire assembly was leak tested under water at 20 psi gas pressure.

EXPERIMENTAL PROCEDURE

The apparatus was evacuated to a pressure above the vapor pressure of water, and water was injected to saturate the fracture and the porous blocks. Liquid permeability measurements were made at a range of flow rates. During this phase of the experiment, the portions of the apparatus that were designed to be gas-filled in two-phase flow conditions were liquid-filled (the liquid was later displaced when gas was admitted to the apparatus). This allowed two measurements each of the liquid inlet and outlet pressure, using the pressure taps normally dedicated to gas and liquid. These pairs of measurements did not agree at the outlet, the pressure measured by the liquid pressure tap was approximately 0.2 psi higher than that measured by the gas pressure tap, while at the inlet the pressure measured by the gas pressure tap was approximately 0.1 psi higher than that measured by the liquid pressure tap. These discrepancies result from the heterogeneity of the fracture. The gas pressure tap is connected to many distributed grooves, and thus averages over the entire edge (inlet or outlet) of the fracture, while the liquid pressure tap senses liquid only at one point along the edge. For non-uniform apertures, the pressure will generally not be uniform along the edge, especially at the outlet edge.

Several hours were needed for the liquid pressure transducers to attain steady readings in response to changes in the flow rate. This slow response resulted from the relatively low permeability of the porous endcaps (approximately 8 millidarcy) and from the presence of air bubbles which could not be eliminated from pressure taps and transducers. For a change in water pressure in the fracture to be felt by the transducer, enough water must flow through the porous plugs in the liquid pressure taps to compress the bubbles. To test for liquid leaks, the apparatus was pressurized and shut in. The pressures recorded during 24 hours showed that there was no leakage of liquid, but pressure variation during the day suggested that pressures changed with diurnal (day/night) variation in ambient temperatures.

After measuring the liquid permeability, two-phase flow was initiated by starting gas injection to the fracture. Gas displaced liquid from the endcap grooves and plenums, and made a flow path from inlet to exit. Visual observations were made, and pressure measurements were continued to steady state, and then the gas flow rate was increased and the liquid flow rate decreased stepwise to reach a new steady state. For each steady state after the first, the needle valve on the gas outlet line was

adjusted to get the outlet and inlet capillary pressure approximately equal, and each steady state was maintained for 24 hr or longer before proceeding to the next. Measurements were made at a series of eight flow conditions with gas-to-liquid flow rate ratios varying over three orders of magnitude.

Permeability Calculation

The permeability of a porous medium to gas is calculated by (Scheidegger, 1974)

$$k_g = \frac{2q_o\mu L p_o}{(p_i^2 - p_o^2)} \tag{3}$$

where k is permeability, q is the darcy flow velocity or volumetric flux [L/t], μ is the viscosity, L is the length from inlet to outlet, subscripts i and o represent inlet and outlet conditions, respectively, and subscript g refers to gas. If flow is not through a porous medium but through a series of parallel fractures with spacing h, then both sides of equation (3) can be multiplied by h to give

$$hk_g = \frac{2hq_o\mu L p_o}{(p_i^2 - p_o^2)} \tag{4}$$

Without knowledge of the fracture aperture, the value of q_o is not known, but the value of hq_o is known from continuity:

$$hq_o = \frac{Q_o}{w} \tag{5}$$

where Q is the volumetric flow rate [L^3/t] and w is the length of the fracture edge at inlet and outlet. Similarly, k_{liq} can not be measured, but hk_{liq} can be:

$$hk_{liq} = \frac{hq\mu L}{p_i - p_o} \tag{6}$$

where $hq = Q/w$; for incompressible fluids Q and q do not vary from inlet to outlet.

Relative permeabilities were calculated by normalizing the measured effective gas and liquid permeabilities to the liquid permeability of the fracture. To calculate ratios of gas and liquid flow rates, the gas flow rate was evaluated at the arithmetic average of the inlet and outlet gas pressures.

RESULTS

Competition between Gas and Liquid For Pore Occupancy

We view a rough-walled fracture as a two-dimensional heterogeneous porous medium, with pore sizes (apertures) varying across the fracture plane (Pruess and Tsang, 1989, 1990). Capillary theory then suggests that in gas-liquid flow in a fracture, the larger pore spaces will be occupied by gas, and the smaller ones by liquid. As long as the pressures and flow rates do not change, the pore occupancy should be static. Our visual observations of the fracture during two-phase flow conditions, however, indicated that there may not be a true steady state on the pore scale. We frequently observed events in which pores switched between gas and liquid occupancy, especially in liquid-dominated conditions. In a typical liquid-dominated flow condition, part of the gas flow path was always occupied by gas, but several stretches of the gas flow path were intermittently occupied by liquid. Trains of bubbles could be seen, separated by liquid, migrating through these stretches. Typically, no action (that is, no changes of pore occupancy) would be seen for a few minutes, then a train of bubbles would be seen to move through part of the gas flow path. A few seconds later, a train of bubbles would be seen marching through a second stretch of the gas flow path, and so on. These were portions of the flow path which were sometimes occupied by liquid. Two-phase flow shows structure on a small scale; many gas flow paths appear tube-like with width of order 1 mm or less in the fracture plane. To reconcile this picture of flow with the local-parallel-plate model of Pruess and Tsang (1989, 1990) might require an impracticably fine space discretization.

Additionally, in liquid-dominated flow regimes, steady pressures could not be reached; rather the system was disturbed by regular "hiccups" as shown in Figures 2a and 2b. Visual observations during these events showed that they were caused by periodic invasion and blockage of the gas flow path by liquid. A temporary blockage of the gas flow path caused the upstream gas pressure to increase, and the downstream gas pressure to decrease, as shown in Figure 2b. Visual observation while this happened showed that all gas flowed through a critical path (choke point) near one side edge of the fracture. A dead-end gas-filled pore upstream of the choke point became larger, acting as a surge chamber, until the pressure drop across the blocked throat became great enough for gas to displace water from the throat, and flow was restored, with several bubble trains flowing toward the exit as described earlier. The repeated reinvasion of gas filled pores by liquid is similar to the "snap-off" events described by Ransohoff and Radke (1988), except that the liquid films between buboles in our experiment collapsed instantly because they were not stabilized by surfactant. At dryer conditions, less water was available to invade gas flow paths and the throat-clearing events become less frequent and eventually cease altogether. Typical inlet and outlet pressures measured during a dryer steady state are shown in Figure 3, while typical inlet and outlet capillary pressures are shown in Figure 4.

Relative Permeability Data

Table 1 summarizes the steady-state data measured during single-phase flow of liquid and eight two-phase flow conditions, measured in order of increasing dryness. Note that equality of inlet and outlet capillary pressures was only achieved approximately. The values shown represent average values during a 24-hour or longer period.

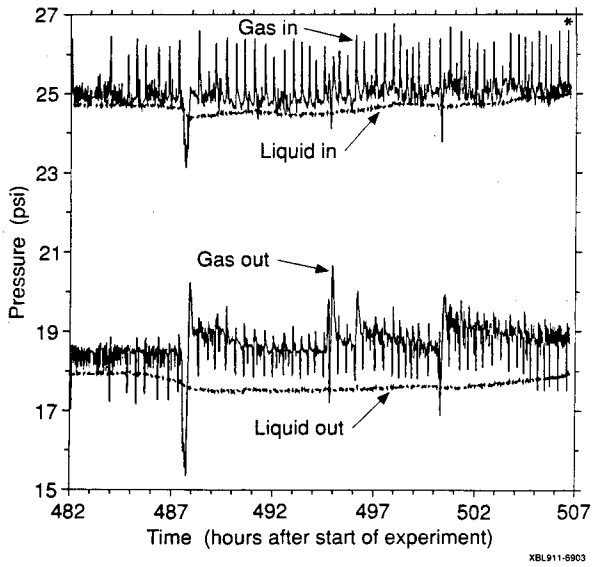

Figure 2a. Inlet and outlet fluid pressures measured during "steady" state with q_{gas}/q_{liq} = 9.5. The inlet and outlet capillary pressures were not equalized at this steady state. Note regular "hiccups" which result from blocking and clearing of gas flow path.

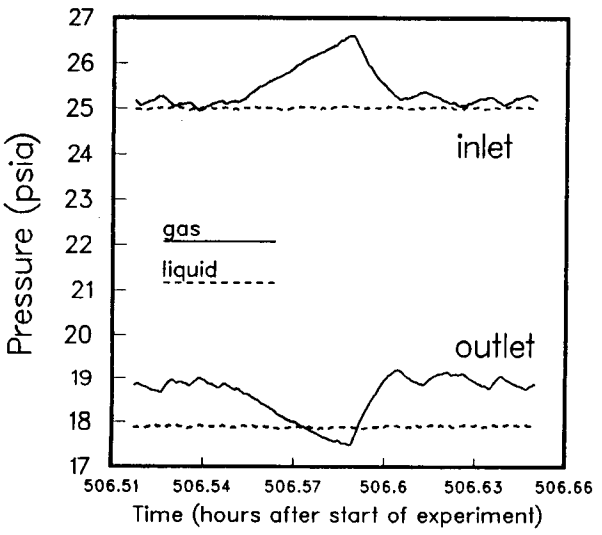

Figure 2b. Event marked by * in Figure 2a.

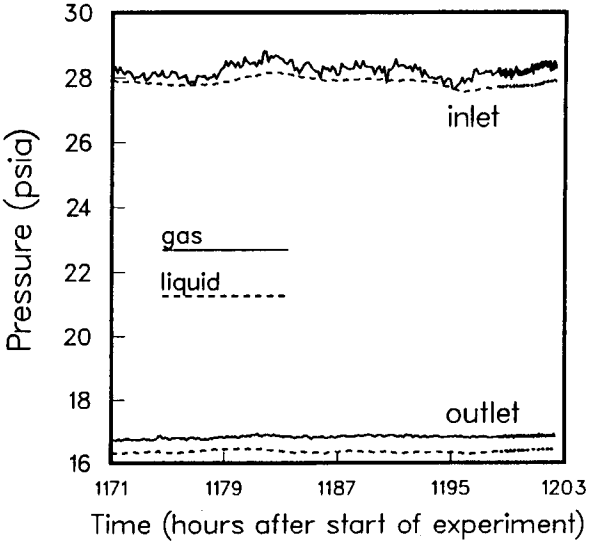

Figure 3. Inlet and outlet fluid pressures measured during steady state with q_{gas}/q_{liq} = 900. This is a dryer condition than shown in Figure 2, and "hiccups" did not occur.

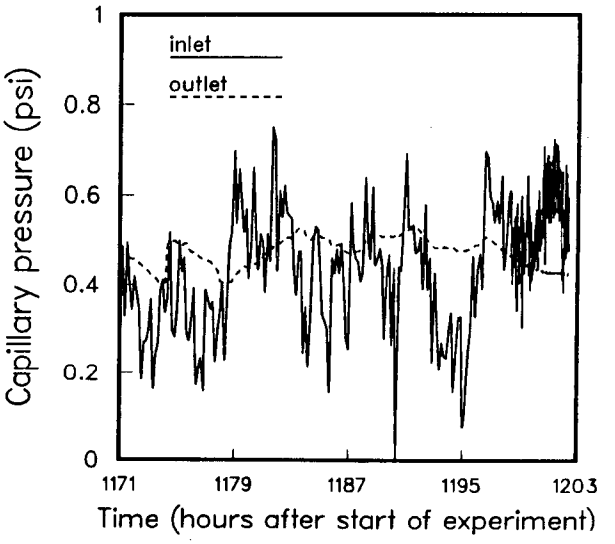

Figure 4. Inlet and outlet capillary pressures measured during steady state with q_{gas}/q_{liq} = 900.

The results for relative permeabilities are plotted in Figures 5 and 6. In Figure 5 the data were plotted against the gas:liquid flow rate ratio rather than against volumetric saturation, because volumetric phase saturations were not measured. In Figure 6, the gas and liquid relative permeabilities are plotted against each other to indicate the degree of phase interference. In both Figures 5 and 6, typical relative permeability curves for porous media are plotted for comparison. These curves were calculated using the formulas given by Corey (1954):

$$k_{rel,liq} = (S^*)^4 \quad (7)$$

$$k_{rel,gas} = (1-(S^*)^2)(1-S^*)^2 \quad (8)$$

where S is saturation, $S^* = (S_{liq}-S_{liq,r})/(1-S_{liq,r}-S_{gas,r})$, and subscript r refers to residual saturation. The Corey curves were calculated with the commonly used values of $S_{gas,r} = 0.05$ and $S_{liq,r} = 0.30$.

Table 1. Flow rates, pressures, and permeabilities

Flow rates		Pressures			Capillary pressures		Permeabilities			
$hq_{o,g}$ (m^2/s)	hq_{liq} (m^2/s)	$p_{g,i}$ (kPa)	$p_{g,o}$ (kPa)	Δp_{liq} (kPa)	inlet (kPa)	outlet (kPa)	hk_g (m^3)	hk_{liq} (m^3)	$k_{rel,g}$	$k_{rel,liq}$
liquid flow								5.09E-17		1.00
7.65E-8	8.02E-9	173.7	130.3	47.4	2.34	8.96	2.01E-18	1.29E-17	0.0395	0.2530
1.61E-7	8.02E-9	179.3	126.9	52.9	2.55	2.55	3.39E-18	1.16E-17	0.0666	0.2271
3.15E-7	8.02E-9	180.6	127.6	56.7	2.97	1.86	6.58E-18	1.08E-17	0.1292	0.2118
5.60E-7	8.02E-9	187.5	127.9	59.3	2.76	2.62	1.01E-17	1.03E-17	0.1994	0.2026
1.04E-6	8.02E-9	199.9	128.2	70.7	3.03	1.03	1.52E-17	8.65E-18	0.2970	0.1699
3.30E-6	2.73E-9	194.8	115.5	79.4	3.03	3.24	4.13E-17	2.62E-18	0.8132	0.0515
4.37E-6	1.37E-9	188.9	112.0	80.0	3.59	3.59	5.65E-17	1.31E-18	1.1092	0.0256
5.75E-6	5.47E-10	180.6	107.2	73.2	3.65	3.38	7.77E-17	5.69E-19	1.5273	0.0112

DISCUSSION

Fracture Aperture

The effective average aperture of the fracture can be estimated from the data using the cubic law: the permeability of a parallel plate aperture of thickness b is $b^2/12$. If a series of such apertures are separated by distance h, then the average permeability of the fractured medium is $(b^2/12)(b/h)$. Then

$$b = \sqrt[3]{12kh} \tag{9}$$

Using the experimentally determined value for hk_{liq} (Eq. 6), this gives an "average" aperture for the fracture of 8.5 μm. But because permeability is controlled by the smallest apertures, it is likely that the volume of the fracture divided by its area is much larger.

The aperture at critical pore throats can also be estimated. The visual observations of "throat-clearing" events such as shown in Figure 2b suggest that gas flow is blocked at a single pore throat. Assuming that the pressure drop across that throat increases until essentially all the pressure drop across the fracture occurs at that throat, the Young-Laplace law can be used to estimate the radius of the critical throat from the interfacial tension and observed pressure drop:

$$r = \frac{2\sigma}{\Delta p} \tag{10}$$

Reading the pressures from Figure 2b as 26.6 and 17.5 psi, (Δp = 9.1 psi = 62.7 kPa) and taking the surface tension σ as 0.07 N/m, then the radius is 2.2 μm, which agrees qualitatively with the estimate of "average" aperture.

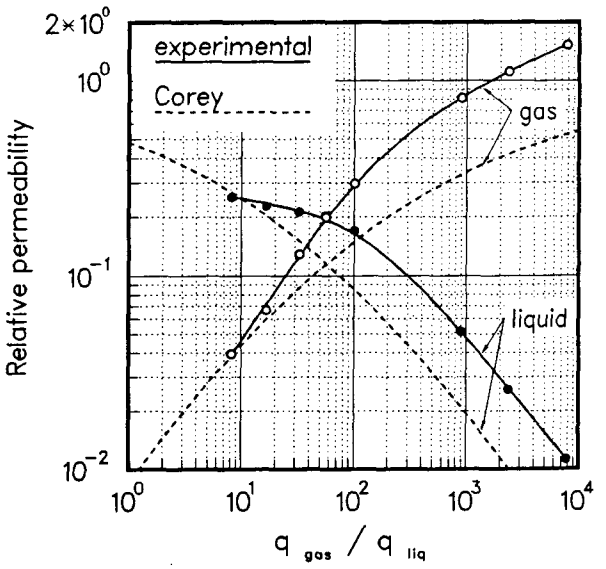

Figure 5. Relative permeabilities during steady states, plotted against ratio of flow rates. For comparison, a curve typical of porous media (Corey, 1954) is also plotted.

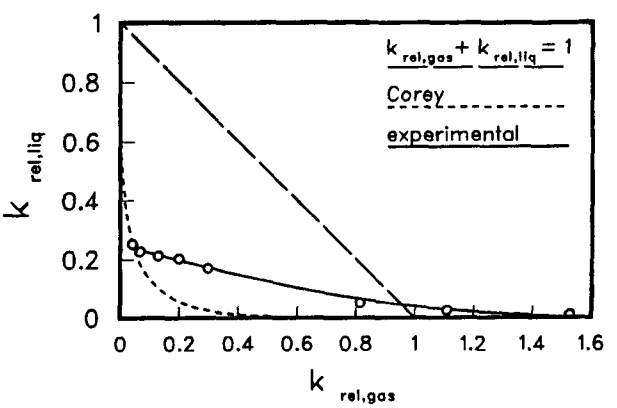

Figure 6. Gas and liquid relative permeabilities plotted against each other. For comparison, $k_{rel,gas} + k_{rel,liq} = 1$ and a curve typical of porous media (Corey 1954) are also plotted.

Control of Capillary Pressures

One of the intended goals of this work is that the outlet capillary pressure be controlled to equal the inlet capillary pressure. Because of the noisiness in the measured capillary pressures shown in Figure 4, this goal has only been achieved approximately. However, the inlet capillary pressures shown in Table 1 display reasonable behavior with changes in liquid saturation and flow rate ratio.

Figures 2a and 3, as well as the data collected at other steady states, show that the outlet pressures are relatively steady but the inlet pressures are more noisy. Because the outlet pressures are directly measured, but the inlet pressures are calculated as the sum of two measurements, the extra noise in the inlet pressure may be an artifact, resulting from accumulated experimental error. But such noise may also reflect many changes of phase occupancy, too small to cause the events shown in Figures 2a and 2b. In single-phase liquid flow, the calculated inlet pressures were no noisier than the outlet pressures. This suggests that the additional noise in the inlet pressures in two-phase flow is real. Additional absolute pressure taps will be added at the inlet end to confirm this.

The noise in capillary pressure measurements may also be an artifact, caused by differences in response time between the gas and liquid pressure taps. The gas pressure taps respond much more rapidly than the liquid pressure taps. It is therefore possible that the actual capillary pressure is steady while gas and liquid pressure vary together, but the measured capillary pressure reflects the lag in the liquid pressure taps.

During two-phase flow, the ratio of volumetric flow rates was varied from all liquid with no gas flowing, to a ratio of gas/liquid = 8000. Visual observations showed increasing gas saturation during the steady states, with the edges of the fracture desaturating first, and the center last. This means that the center of the fracture is the region of contact, with widest apertures and preferential flow paths for non-wetting fluid around the outside. Fracture apertures have not been measured but are expected to confirm this. This configuration suggests that some slight warpage of either the epoxy casts or silicone rubber molds may have occurred during curing. As such, it represents a deviation from the realistic fracture geometry which was intended. However, the roughness of the surfaces still appears to be accurately represented, and the localized contact area with regions of greater aperture is still typical of natural fractures.

Table 1 shows that gas relative permeability increases beyond 1, which may be due to experimental error or to non-Darcy flow effects. The cause of this discrepancy will be elucidated in further experiments.

IMPROVEMENTS TO THE APPARATUS

The preliminary results presented here confirm the feasibility of using the Hassler "sandwich" design for measuring relative permeability in fractures, and of observing phase saturation distribution in transparent fractures. However, they also indicate the need for several improvements which will be made for further experiments:

The molding technique will be improved so that the two sides of the fracture replica mate as well as the original rock. The tendency of the fracture replica to have a contact region only in the center can also be compensated for in the design of the compressing lucite blocks.

The number of liquid pressure taps in each end will be increased, so that liquid pressure will represent an average over the edge rather than a point value. The thickness of the porous blocks in the liquid pressure taps will be reduced, and gas bubbles in the liquid pressure taps eliminated, to reduce the response time of the liquid pressure measurements. Additional absolute pressure transducers will also be placed at the inlet.

The temperature will be controlled to eliminate day/night changes in pressure gradients that have been observed.

The fracture will be filled with a dyed liquid so that the fracture aperture can be estimated at every point using the measured intensity of transmitted light (see Cox et al., 1990).

A video camera with digital image processing capabilities will be added to allow analysis of saturation data.

Experiments will be done with actual rock fractures. This will lose the visualization capability, but gain realism in the fracture geometry and the wettability of surfaces.

SUMMARY AND PRELIMINARY CONCLUSIONS

Flow visualization has provided evidence that even for very slow flows, there may be no true steady states. Instead there is a continual succession of transient changes in phase occupancy at critical pore throats. At large values of liquid saturation, sufficient liquid is available to intermittently block some of the gas flow paths (or, in extreme cases, the only gas flow path). This results in continual episodes of throat blocking and clearing, as shown in Figure 2b. Such behavior is not generally observed in porous media, perhaps due to the much larger number of flow paths in typical sample sizes.

The limited experiments carried out so far have confirmed the viability of the Hassler design for achieving two-phase flow conditions in a small fracture under

well-defined capillary conditions, without end effects. A series of quasi-steady two-phase flow conditions has been achieved. Quantitative analysis is hampered by diurnal pressure fluctuations caused by temperature fluctuations in the laboratory. However, some preliminary conclusions can be drawn. The relative permeability data plotted in Figures 5 and 6 show that strong phase interference occurs between the gas and liquid phases, with the sum of gas and liquid relative permeabilities much less than 1 at intermediate saturations. The shapes of the curves suggest that phase interference occurs in fractures in much the same manner as in porous media.

ACKNOWLEDGMENTS

The authors are indebted to Marcelo Lippmann for a critical review of the manuscript. This work was supported by the Assistant Secretary for Conservation and Renewable Energy, Office of Renewable Energy Technologies, Geothermal Technology Division of the U.S. Department of Energy, under Contract no. DE-AC03-76SF00098. The use of brand names in this paper is for identification purposes only and does not imply endorsement by LBL or DOE.

REFERENCES

Bodvarsson, G. S., Pruess, K., Stefansson, V., and Ojiambo, S. B. (1987). East Olkaria geothermal field, Kenya, 1, History match with production and pressure decline data. *J. Geophys. Res. 92,* (B1), 521-539.

Corey, A. T. (1954). The interrelationship between gas and oil relative permeabilities, *Prod. Mon. 19,* 38-41.

Cox, B. L., Persoff, P., and Pruess, K. (1990). A casting and imaging technique for determining void geometry and relative permeability behavior of a single fracture specimen. paper presented at the Fifteenth Workshop on Geothermal Reservoir Engineering, Stanford Univ., Stanford, CA.

Hassler, G. L. (1944). Method and Apparatus for Permeability Measurements, U.S. Patent 2,345,935. April 4.

Pruess, K.. Bodvarsson, G. S., and Stefansson, V. (1983). Analysis of production data from the Krafla geothermal field, Iceland, Proc. Ninth Workshop on Geothermal Reservoir Engineering, Stanford Univ., Stanford, CA, pp. 345-350.

Pruess, K., Bodvarsson, G. S., Stefansson, V., and Eliasson, E. T. (1984). The Krafla geothermal field, Iceland, 4, History match and prediction of individual well performance, *Water Resources Research, 20* (11), 1561-1584.

Pruess, K. and Tsang, Y. W. (1989). On relative permeability of rough-walled fractures, Proc. Fourteenth Workshop on Geothermal Reservoir Engineering, Stanford Univ., Stanford, CA. pp. 123-130.

Pruess, K. and Tsang, Y. W. (1990). On two-phase relative permeability and capillary pressure in rough-walled rock fractures, *Water Resources Research, 26* (9), 1915-1926.

Romm, E. S. (1966). *Fluid Flow in Fractured Rocks* (in Russian), Nedra Publishing House, Moscow. (English translation, W. R. Blake, Bartlesville, OK, 1972.)

Ransohoff, T. C. and Radke, C. J. (1988). Mechanisms of foam generation in glass-bead packs, *SPE Reservoir Engineering,* May, 573-585.

Scheidegger, A. E. (1974). *The Physics of Flow Through Porous Media,* 3rd ed., University of Toronto Press, Toronto, p. 102.

Witherspoon, P. A., Wang, J. S. W., Iwai, K., and Gale, J. E. (1980). Validity of Cubic Law for Fluid Flow in a Deformable Rock Fracture, *Water Resources Research, 16,* (6) 1016-1024.

PROCEEDINGS, Sixteenth Workshop on Geothermal Reservoir Engineering
Stanford University, Stanford, California, January 23-25, 1991
SGP-TR-134

Grid Orientation Effects in the Simulation of Cold Water Injection into Depleted Vapor Zones

Karsten Pruess

Earth Sciences Division, Lawrence Berkeley Laboratory
University of California, Berkeley, CA 94720

Introduction

Vapor-dominated geothermal reservoirs such as Larderello, Italy, and The Geysers, California, are fundamentally water-short systems. This is apparent from the relatively low pressures in the natural state, typically about 35 bars at 1000 m depth, which is much below hydrostatic pressures. It is also apparent from the high heat content of the produced fluids, typically superheated steam.

Large-scale production from these systems has caused reservoir pressures and well flow rates to decline, leading to an underutilization of installed electrical generating capacity. Clearly, these reservoirs are beginning to run out of fluid, while heat reserves in place are still enormous. (At Larderello, there is a long-term trend of increasing formation temperatures in the upper productive zones of the reservoir; Sestini, 1970). Reinjection of colder waste waters, or injection of waters from a source other than the geothermal reservoir, is the primary means by which dwindling fluid reserves can be replenished.

A considerable body of field experience with injection has been accumulated at Larderello and The Geysers; the results have been mixed. There are well documented cases where injection has increased flow rates of nearby wells. Return of injected fluid as steam from production wells has been observed directly through chemical and isotopic changes of produced fluids (Giovannoni et al., 1981; Nuti et al., 1981). In other cases injection has caused thermal interference and has degraded the temperature and pressure of production wells.

Water injection into depleted vapor zones gives rise to complex two-phase fluid flow and heat transfer processes with phase change. These are further complicated by the fractured-porous nature of the reservoir rocks. An optimization of injection design and operating practice is desirable; this requires realistic and robust mathematical modeling capabilities.

Numerical Simulation of Water Injection

Water injection into a medium containing superheated vapor can be classified as a process of immiscible displacement, which is made considerably more complicated by the fact that some of the displacing water may vaporize, while some of the vapor undergoing displacement may condense. These phase change processes are accompanied by strong latent heat effects. The large contrast in thermophysical properties between water and vapor (see Table 1) gives rise to highly non-linear flow behavior.

A number of papers have presented numerical simulations of cold water injection into superheated vapor zones (O'Sullivan and Pruess, 1980; Schroeder et al., 1982; Calore et al., 1986; Pruess et al., 1987). These studies have demonstrated numerical simulation techniques that are capable of dealing with the highly non-linear processes, and have clarified some of the basic effects and phenomena. Flow around an injection well has been analyzed under the simplifying assumptions of horizontal flow only, and radial symmetry. Around the injection well, a single-phase liquid plume forms with a temperature equal to the injection temperature $T = T_{inj}$ (see Figure 1). Beyond this plume there is a region of single-phase liquid conditions, with temperature $T = T_f$ intermediate between injection temperature and original reservoir temperature T_o, $T_{inj} < T_f < T_o$. In a porous medium, and neglecting the (small) effects of heat conduction, the temperature and phase fronts are sharp. Heat conduction broadens the fronts slightly, while in fractured-porous media the delayed fluid flow and heat transfer between fractures and rock matrix can lead to very broad temperature fronts and extended two-phase zones containing a boiling mixture of water and vapor (Calore et al., 1986).

Injection effects are much more complicated when the possibility of vertical flow is taken into consideration (Calore et al., 1986). Vertical permeability permits injected water to flow downward in addition to outward. Because of the much larger density of liquid water as compared to vapor, downward flow of liquid does not require a pressure gradient, but can be driven by gravity force, even opposing a (sub-hydrostatic) gradient. The effect of gravity may dominate the pressure and temperature regime around an injection well. Much of the injected water may flow downward rather than outward from the injection well, partially vaporizing in the pro-

cess. Two-phase conditions may extend all the way to the injection well. The one-to-one correspondence between pressure and temperature in two-phase conditions can give rise to interesting heat pipe effects (water-vapor counterflow; Calore et al., 1986). Over time, temperatures near the injection well will decline. As long as two-phase conditions prevail, this will be accompanied by pressure decline, so that within the boiling injection plume vapor will flow towards the injection well rather than away from it. Vapor approaching the injection point will partially condense, and the associated latent heat effects will counter the cooling effects from continued injection. The entire injection plume may remain in boiling and nearly isothermal conditions, maintained by water-vapor counterflow (heat pipe). When the injection rate is increased, pressures near the injection well will also increase, and a single-phase liquid zone of limited extent may form. Temperatures in the liquid zone will decline towards the injection temperature. The flow processes are further complicated by preferential flow in fractures, and by the unstable nature of a displacement process in which a heavier phase (water) is invading a region with lighter fluid (vapor) from above.

Numerical simulation studies have shown that predictions of water injection into vapor zones are sensitive to space and time discretization effects. Space discretization effects are well known from immiscible displacement processes, where they cause a broadening of phase fronts (Aziz and Settari, 1977). These effects are aggravated in two-phase flow with phase change, because they affect the coupling between fluid flow and heat transfer, and alter the phase composition of the flowing two-phase mixture. Coarse gridding near the injection point will cause an over-prediction of vaporization rates. The one-to-one correspondence between temperatures and pressures in two-phase conditions can produce spurious flow effects (Schroeder et al., 1982; Pruess et al., 1987): when colder water enters a grid block that is in two-phase conditions, temperature and pressure of the two-phase mixture decline, causing spurious flow towards the injection point. In simulations of cold water injection into superheated vapor zones in two-dimensional R-Z geometry, the shape of the injection plume was found to depend sensitively on the computational grid used (unpublished work by the author with R. Celati and C. Calore).

Because of the sensitivity to space discretization effects, there is lingering concern about the realism and credibility of numerical simulation predictions for injection into superheated vapor zones. The present paper focusses on a particular kind of space discretization effects, associated not with the size of computational grid blocks but with the orientation of the grid lines. The basic mass and energy balance equations applicable for the process of water injection into isotropic media are rotationally invariant in the horizontal plane, while a computational grid introduces preferred directions. For example, a conventional finite-difference grid consisting of identical squares permits flow to or from a grid block only in discrete directions of 0°, 90°, 180°, and 270°. This discreteness in the rotational sense persists even as grid spacing is refined, causing grid orientation errors.

A potential for grid orientation errors exists also in the vertical plane, where the vector of gravitational acceleration defines a preferred direction. Simulation predictions may be sensitive to the orientation of grid lines with respect to the vertical.

Studies of two-phase immiscible displacement, and of steam flooding of hydrocarbon reservoirs, have shown that mere grid refinement is ineffective in reducing grid orientation errors. Such errors can be substantially eliminated only by increasing the number of flow directions considered in the finite difference grid. Conventional finite difference simulations employ a "five-point" differencing scheme, which considers flow between a grid cell and the four neighbors with which it shares interfaces (see Figure 2; P communicating with E, N, W, and S). Grid orientation effects can be substantially reduced by means of a "nine-point" approximation, which in addition considers the possibility of flow along the diagonal directions (P communicating with NE, NW, SW, and SE).

This paper examines grid orientation effects for simulation of water injection into depleted (low pressure) vapor zones. We study grid orientation effects not only in the horizontal plane, but also in the vertical direction. All simulations were carried out with LBL's general-purpose reservoir simulator TOUGH2 (Pruess, 1990), which implements the general MULKOM architecture for multiphase fluid and heat flows (Pruess, 1983, 1988).

2-D Areal Model

The nature and strength of grid orientation effects can be easily evaluated by comparing simulation results obtained from two different grids that have the same grid block size but different orientation. The customary approach is to consider a five-spot production-injection arrangement, and to compare simulations obtained with "parallel" and "diagonal" grids (see Figure 3; the terms "parallel" and "diagonal" denote the direction of grid lines relative to the lines connecting production and injection wells). We have performed simulations with the grids shown in Figure 3, using problem parameters applicable for depleted vapor zones at Larderello or The Geysers (see Table 2). Results for production rates and temperatures predicted from the two different grids are given in Table 3.

It is apparent that the predictions from both grids are very similar. Early on, there is slightly faster water migration towards the production well in the parallel grid, giving somewhat higher production rates and slightly faster cooling near the production well. In the middle period, 5 - 10 years, predictions from both grids are in excellent agreement, while subsequently there again is somewhat more cooling along the flowpath from

the injector to the producer in the parallel grid. Additional simulations were performed with a "two-waters" description of the process, where injected water can be distinguished from the vapor originally in place, so that the mixture of injected and in-place fluid extracted at the production well can be monitored. The parallel grid predicted a more rapid initial return of vaporized injected water than the diagonal grid. However, these differences persist for only a very brief period (a few weeks) after start of injection.

In summary, we conclude that grid orientation effects for simulation of water injection into low-pressure vapor zones are insignificant in 2-D areal models. This favorable result can be understood in terms of the "favorable mobility ratio" between injected and displaced fluid. When water displaces vapor, the displacing fluid has higher viscosity and poses greater resistance to flow. The parallel grid tends to facilitate migration from the injector to the producer; however, as more of the flow path towards the production well fills with liquid water, flow resistance increases, diminishing the preferential flow. An analogous process will take place in the diagonal grid. In this case, initial water flow will preferentially occur in the diagonal direction. As water saturation in this direction increases, the viscosity contrast will then diminish diagonal flow. In this fashion, a displacement with favorable mobility ratio will tend to reduce differences in numerical simulation predictions from grids with different orientations of grid lines.

Water injection into superheated vapor zones has characteristics opposite from those encountered in steam flooding of hydrocarbon reservoirs, an "unfavorable mobility ratio" displacement. In the latter process, the viscosity of the displacing fluids (steam and oil heated to high temperature) will be much less than the viscosity of the displaced fluids (water and oil at ambient temperature). Therefore, flow resistance along the path of displacing fluids will diminish, so that any preferential displacement in a particular direction will tend to get amplified, giving rise to very strong grid orientation effects (Coats and Ramesh, 1982).

2-D Vertical Section

The areal simulations discussed in the previous section may not give a realistic outlook on effects of water injection into low-pressure vapor zones. Liquid water is much heavier than steam and may flow preferentially downward from an injection point rather than outward. Injection of heavier fluid into lighter fluid from above is subject to gravitational instabilities (Schubert and Straus, 1980), which suggests a potential for strong grid orientation effects in the vertical direction.

To examine this possibility, we have performed simulations of water injection into vertical-section models, using parallel as well as diagonal grids. From a practical viewpoint, the main interest is in the effects of the injection plume on conditions in the surrounding reservoir. Volume, shape, and thermodynamic conditions of the plume must be modeled accurately so that the rate at which the boiling plume supplies vapor to the reservoir may be predicted. In the vicinity of an injection well, flow geometry is cylindrically symmetric, requiring a two-dimensional axisymmetric (R-Z) grid. However, in our studies we have employed two-dimensional linear vertical section (X-Z) grids, for the following reason. It is well established that grid orientation effects can often be alleviated by means of higher-order differencing methods, such as nine-point differencing. Our choice of an X-Z section was made because implementation of higher-order differencing is straightforward for grids of constant thickness. R-Z grids would pose added complications, because the volumes of grid blocks with constant vertical cross-sectional area increase with distance from the symmetry axis.

The model system chosen for simulation of water injection is shown in Figure 4. It has a vertical extent of 200 m, a thickness of 1 m, and a horizontal length of approximately 200 m (slightly different for the parallel and diagonal grids; see below). Injection is made at the top of the left vertical boundary, while at the right vertical boundary constant pressures corresponding to gravity equilibrium are maintained. The gravity equilibrium is obtained by first running initial conditions of T = 240°C and P = 10 bar to steady state. Problem parameters are given in Table 2.

Schematic diagrams of parallel and diagonal grids are shown in Figure 5. The parallel grid used in most simulations has a block size of $\Delta x = \Delta z = 10$ m. However, the left vertical boundary, where injection is made, is interpreted as a symmetry boundary, so that the first Δx is 5 m, and the first column of nodal points is located right on the boundary. For the diagonal grid we wish to employ grid blocks of approximately the same volume. The length of the diagonal in the parallel grid is $\sqrt{200}$ = 14.14 m. In order to cover the same vertical distance of 200 m in the diagonal grid, we take the length of the diagonal in the diagonal grid as 200/14 = 14.29 m, to which corresponds a side length of 10.10 m. Thus, the blocks in the diagonal grid have very nearly the same volume as those in the parallel grid. The parallel grid has 20 rows by 21 columns, and a total volume of 41,000 m^3, as compared to the diagonal grid which has 29 rows by 30 columns, with a volume of 42,142.8 m^3.

Results of simulations are presented as contour diagrams of injection plumes (region of two-phase or single-phase liquid conditions) after 717.01 days of simulated time (Figures 6 through 9), and as a table of fractions of injected water vaporized (Table 4). The plume diagrams provide a detailed picture of injection behavior, while the vaporization fractions give a broad aggregate measure.

Results for Five-Point Parallel and Diagonal Grids

Figure 6 compares the injection plumes after 717.01 days of simulated time with the parallel and diagonal grids, respectively. The discrepancies are very large indeed. In the parallel grid, all flow is vertically downward from the injection point. The vaporizing liquid flows towards the bottom of the flow system, and is then diverted laterally outward. There is no lateral component to liquid phase flow above the bottom row of grid blocks. The diagonal grid on the other hand predicts a plume of considerable lateral extent, approximately 50 m, with only a small amount of accumulation of two-phase fluid at the bottom. This comparison shows that grid orientation effects in the vertical can be extremely strong for water injection into low-pressure vapor zones. For comparison, another simulation was performed with the parallel grid, in which the regions of the plume were more finely discretized. The first (leftmost) column of grid blocks (Δx = 5 m) was further partitioned into three columns of Δx = 1 m, 2 m, 2 m, and the last (bottom-most) row with Δz = 10 m was partitioned into four rows of Δz = 5 m, 2 m, 2 m, and 1 m. The results were very similar to those of the coarser parallel mesh, indicating that the grid orientation errors are not overcome by finer discretization. We emphasize in passing the seriousness of grid size errors. Heat balance considerations show that complete vaporization of the injected water would cool a reservoir volume of 1 m^3 by 1.177 10^{-2} °C per second. If the entire "parallel grid" flow system of 41,000 m^3 volume would be represented with one grid block, total vaporization would effect a cooling by 17.78 °C over the 717.01 days injection period. In such a coarse grid the temperature would therefore remain above the saturation temperature at prevailing pressures of approximately 10 bars; all the injectate would be completely vaporized, and no injection plume would form.

Results for Nine-Point Differencing

After demonstration of extremely strong grid orientation effects in the vertical, the next set of simulations was carried out with the objective to determine whether these effects could be substantially eliminated by means of a differencing scheme with a higher order of rotational accuracy. Figure 7 compares predicted injection plumes after 717.01 days of simulated time for parallel and diagonal 9-point grids. The predictions for the shape of the injection plumes are similar, indicating that grid orientation effects have been much reduced. However, some significant differences persist. The diagonal 9-point simulation predicts significantly more water migration near the bottom of the reservoir. The plume predicted from the 9-point parallel grid detaches from the injection boundary about halfway down. Additional minor differences exist with respect to the phase distribution within the plume. Predictions for vaporization fractions, providing an integrated view of injection effects, agree well between the parallel and diagonal 9-point grids (Table 4).

It can be concluded that 9-point differencing cures much of the grid orientation problem, but significant grid orientation errors persist. This is not surprising in view of the fact that 9-point differencing is designed to preserve the rotational invariance of the Laplace operator to higher order (Forsythe and Wasow, 1960). This is the dominant term in pressure-driven displacement in the horizontal plane; however, the vertical flow in the present injection problem arises from the gravity term in Darcy's law, which contributes a first-order spatial derivative term in the governing equations. Improving on the finite-difference approximation of the Laplacian would not necessarily improve the discretized representation of the gravity flow term.

The problem considered so far - cold water injection into a porous medium containing superheated steam, subject to pressure and gravity forces, and heat exchange with phase transformation effects - is highly idealized. It simplifies the "real" problem by neglecting several physical effects, including capillary pressures, hydrodynamic dispersion, vapor pressure lowering, and formation heterogeneity (fractured-porous medium). While simplifying the physics, these idealizations actually make the problem more difficult and sensitive from the viewpoint of numerical simulation. The idealized problem considered so far is highly hyperbolic in nature, while incorporation of more realistic physical effects would make the problem more diffusive, or parabolic, and less subject to numerical discretization errors. For example, capillary pressure effects would tend to suck injected water into dryer regions, giving rise to horizontal flow of water away from the injection point.

Capillary Pressure Effects

Simulations incorporating capillary pressure effects were carried out to examine whether inclusion of such effects would significantly improve grid orientation performance. We have no data for capillary pressure functions applicable to the Larderello or Geysers systems, and have rather arbitrarily chosen the following functional form (Leverett, 1941; Udell and Fitch, 1985):

$$P_{cap} = -40 \cdot 10^6 \cdot \sigma \cdot f(S_l) \qquad (1)$$

where f = 1.417 $(1-S_l)$ - 2.120 $(1-S_l)^2$ + 1.263 $(1-S_l)^3$ is a function of liquid saturation S_l, and σ is the surface tension of water, a function of temperature.

Results of injection simulations with parallel and diagonal 9-point grids, incorporating capillary pressure effects, are shown in Figure 8. There is close agreement between the two predictions for the injection plume, indicating that grid orientation effects have been substantially eliminated. In addition to helping reduce grid orientation effects, inclusion of capillary forces has also eliminated the slumping of injected water to the reservoir bottom, and it has effected a certain lateral broadening of the plume. Predicted vaporization fractions from

parallel and diagonal grids show excellent agreement at all times (Table 4).

For completeness, we also present results of simulations with capillary pressure effects in 5-point parallel and diagonal grids (Figure 9). The discrepancies between the two grids are not very large, but considerably stronger than for 9-point differencing. Agreement between the predicted vaporization fractions is good (Table 4). For the diagonal grid, predictions from the 5- and 9-point schemes are very similar, while for the parallel grid the discrepancies are larger.

Discussion and Conclusions

The goal of numerically simulating injection is to provide a robust and realistic prediction of injection effects. Presently available numerical simulators can successfully model the basic physical processes associated with injection of cold water into superheated vapor zones, including highly non-linear phase transitions from vapor to two-phase to liquid conditions, and the associated strongly coupled fluid flow and heat transfer effects. However, this capability for simulating the basic processes does not necessarily guarantee realistic predictions for practical injection problems that involve multidimensional flow effects on a broad range of space and time scales.

Ideally, numerical simulation predictions should be independent of the orientation of the computational grid used. However, our studies showed a potential for very strong grid orientation errors, and determined remedies to alleviate them. Specific results for the parameters and conditions investigated in this study are as follows.

(1) Grid orientation effects in the horizontal plane are insignificant, as would be expected from the favorable mobility ratio between liquid and vapor phases (more viscous water displacing less viscous vapor).

(2) Grid orientation effects in the vertical direction can be exceedingly strong. The most commonly used rectangular grids with vertical grid lines may give totally erroneous results. These grid orientation errors are not diminished by finer space discretization.

The following observations pertain to grid orientation effects in the vertical plane.

(3) Diagonal grids (grid lines oriented at 45° to the vertical) perform rather well, yielding results free of obvious large errors.

(4) Higher-order differencing (9-point versus the conventional 5-point) significantly reduces grid orientation errors. Results for parallel and diagonal grids are in approximate agreement when 9-point differencing is used.

(5) The pathological features observed for 5-point differencing in parallel grids disappear when capillary pressure effects are taken into account. Inclusion of capillary pressures makes for a more realistic process description (obviously, appropriate capillary pressure data are required), and it simplifies the attainment of simulation results that are free of large errors.

Simulations including capillary pressure effects with parallel and diagonal grids are in approximate agreement and give generally acceptable results. The best results are obtained when 9-point differencing is used, but the improvements in numerical performance obtained by including capillary pressure effects are more significant than the improvements resulting from higher-order differencing. Capillary pressures combat the fingering associated with the gravitational instability of heavier fluid (water) over lighter fluid (vapor). Hydrodynamic dispersion, which has not been explicitly modeled in the present work, will have similar effects. The better performance of the diagonal grid, even when only 5-point differencing is used, may be interpreted as resulting from an artificial (numerical) dispersion perpendicular to the (vertical) direction of unstable gravitational fingering. Hydrodynamic dispersion effects are expected to be quite significant in fractured reservoirs, such as Larderello and The Geysers, and deserve further study. Future work should also address the special effects from the radially divergent (as opposed to linear) flow geometry around an injection well.

Acknowledgement

The author would like to thank Michael O'Sullivan for reviewing the manuscript and suggesting improvements. This work was supported by the Geothermal Technology Division, U. S. Department of Energy, under Contract No. DE-AC03-76SF00098. The numerical computations were performed at the National Energy Research Supercomputer Center, with support from the Office of Basic Energy Sciences, U. S. Department of Energy.

References

Calore, C., Pruess, K., and Celati, R., (1986). Modeling Studies of Cold Water Injection into Fluid-Depleted, Vapor-Dominated Geothermal Reservoirs, paper presented at the Eleventh Workshop Geothermal Reservoir Engineering, Stanford University, Stanford, Ca.

Coats, K. H., and Ramesh, A. B., (1982). Effects of Grid Type and Difference Scheme on Pattern Steamflood Simulation Results, paper SPE-11079, presented at the 57th Annual Fall Technical Conference and Exhibition of the Society of Petroleum Engineers, New Orleans, La.

Forsythe, G. E. and Wasow, W. R., (1960). *Finite-Difference Methods for Partial Differential Equations,* John Wiley and Sons, Inc., New York, London.

Giovannoni, A., Allegrini, G., Cappetti, G., and Celati, R. (1981). First Results of a Reinjection Experiment at

Larderello, Proceedings, Seventh Workshop Geothermal Reservoir Engineering, Stanford University, SGP-TR-55.

Leverett, M. C., (1941). Capillary Behavior in Porous Solids, *AIME Trans., 142,* 152.

Nuti, S., Calore, C. and Noto, P., (1981). Use of Environmental Isotopes as Natural Tracers in a Reinjection Experiment at Larderello, Proceedings, Seventh Workshop Geothermal Reservoir Engineering, Stanford University, SGP-TR-55.

O'Sullivan, M. J. and Pruess, K., (1980). Numerical Studies of the Energy Sweep in Five-Spot Geothermal Production/Injection Systems, Proceedings, Sixth Workshop Geothermal Reservoir Engineering, Stanford University, SGP-TR-50.

Schroeder, R. C., O'Sullivan, M. J., Pruess, K., Celati, R. and Ruffilli, C., (1982). Reinjection Studies of Vapor-Dominated Systems, *Geothermics, 11,* (2), 93-120.

Pruess K., (1983). Development of the General Purpose Simulator MULKOM, Annual Report 1982, Earth Sciences Division, Lawrence Berkeley Laboratory LBL-1550.

Pruess, K., (1988). SHAFT, MULKOM, TOUGH: A Set of Numerical Simulators for Multiphase Fluid and Heat Flow, *Geotermia, Rev. Mex. Geoenergia, 4,* (1) 185-202.

Pruess, K., (1990). TOUGH2 - A General-Purpose Numerical Simulator for Multiphase Fluid and Heat Flow, Lawrence Berkeley Laboratory Report LBL-29400.

Pruess, K. and Bodvarsson, G. S., (1983). A Seven-Point Finite Difference Method for Improved Grid Orientation Performance in Pattern Steam Floods, paper SPE-12252, presented at the Seventh Society of Petroleum Engineers Symposium on Reservoir Simulation, San Francisco.

Pruess, K., Calore, C., Celati, R. and Wu, Y. S., (1987). An Analytical Solution for Heat Transfer at a Boiling Front Moving through a Porous Medium, *Int. J. of Heat and Mass Transfer, 30,* (12) 2595-2602.

Schubert, G. and Straus, J. M., (1980). Gravitational Stability of Water over Steam in Vapor-Dominated Geothermal Systems, *J. Geophys. Res., 85,* 6505-6512.

Sestini, G., (1970). Superheating of Geothermal Steam, *Geothermics,* Special Issue 2, 622-648.

Udell, K. S. and Fitch, J. S., (1985). Heat and Mass Transfer in Capillary Porous Media Considering Evaporation, Condensation, and Non-condensible Gas Effects, paper presented at 23rd ASME/AIChE National Heat Transfer Conference, Denver, CO.

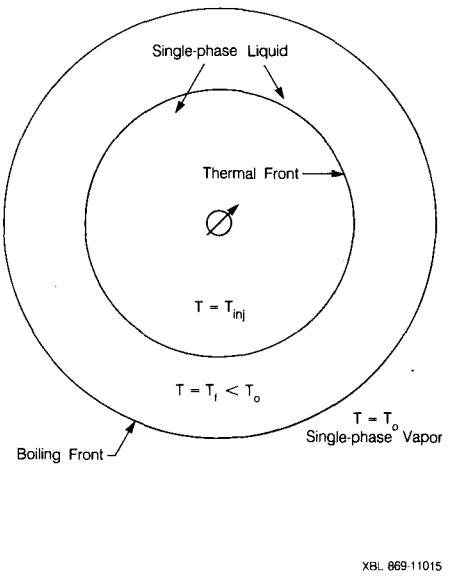

Figure 1. Schematic diagram of fronts for cold water injection into a super-heated vapor zone in 1-D radial flow approximation (from Pruess et al., 1987).

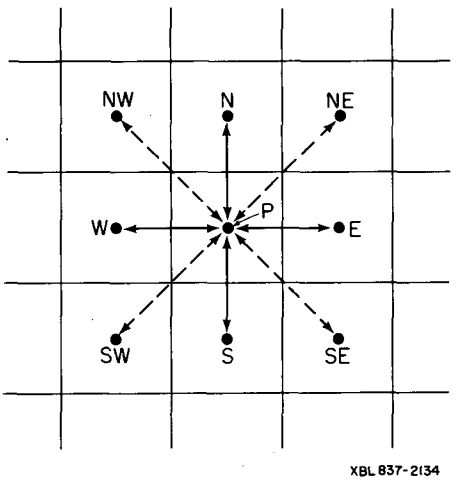

Figure 2. Five- and nine-point finite difference approximations (from Pruess and Bodvarsson, 1983).

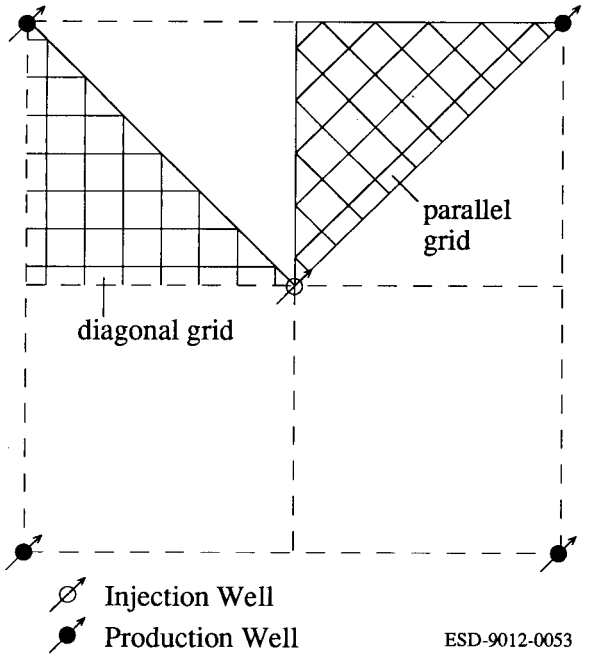

Figure 3. Five-spot well pattern with parallel and diagonal grids for modeling a 1/8 symmetry domain.

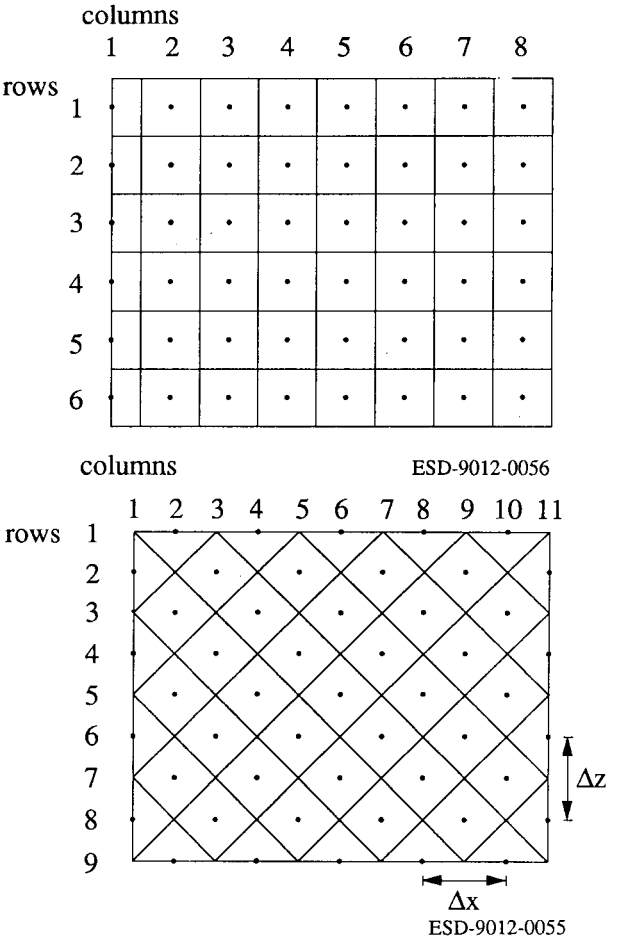

Figure 5. Schematic of parallel and diagonal grids used for modeling injection in 2-D vertical section.

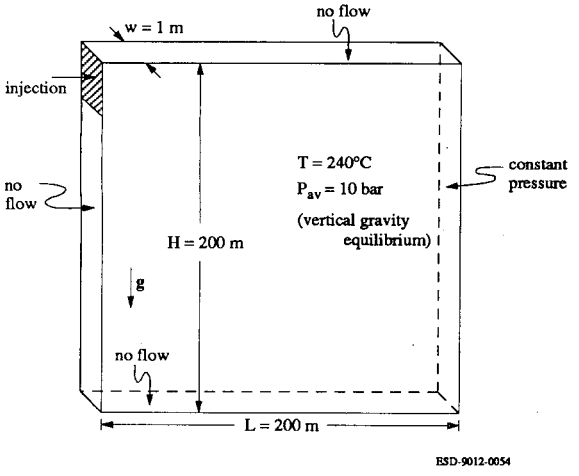

Figure 4. Schematic of 2-D vertical section.

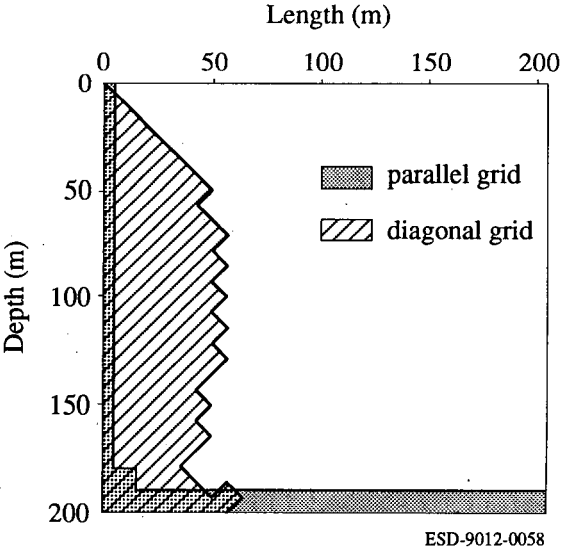

Figure 6. Simulated plumes after 717.01 days of injection in parallel and diagonal 5-point grids.

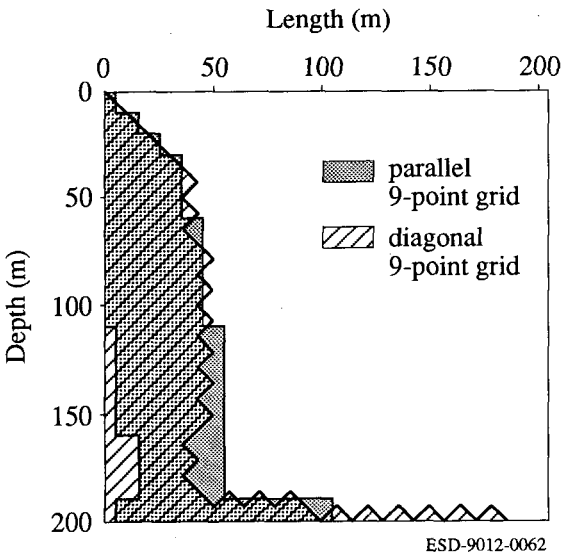

Figure 7. Simulated injection plumes after 717.01 days for 9-point differencing.

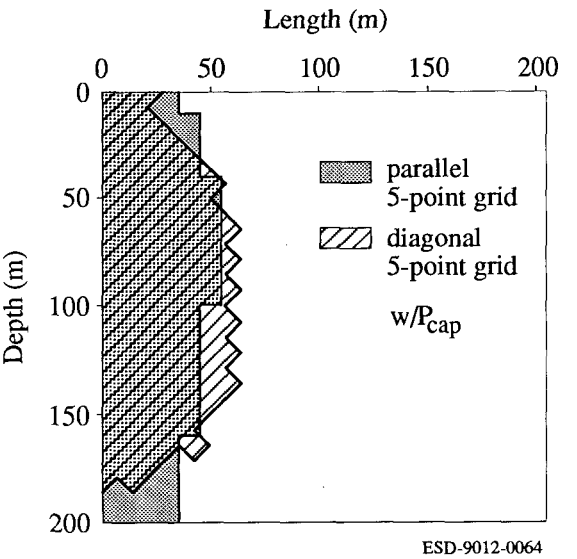

Figure 9. Simulated injection plumes after 717.01 days with capillary pressure effects included; 5-point differencing.

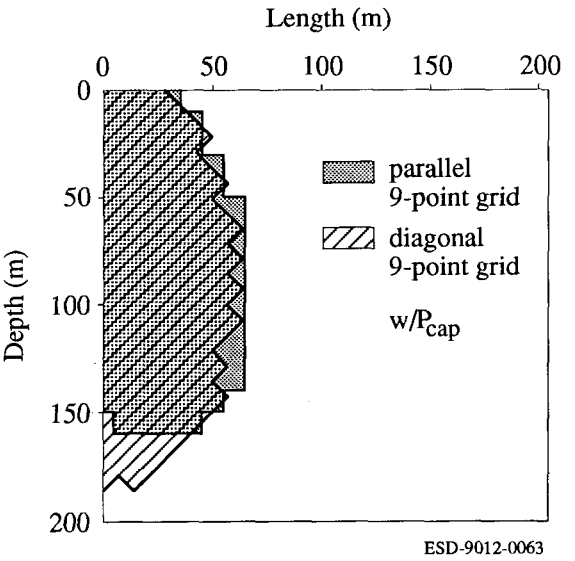

Figure 8. Simulated injection plumes after 717.01 days with capillary pressure effects included; 9-point differencing.

Table 1. Selected thermophysical properties of water and vapor at saturated conditions of 240°C.

	Density (kg/m^3)	Enthalpy (kJ/kg)	Viscosity (Pa·s)
Water	813.7	1037.3	$1.11 \cdot 10^{-4}$
Vapor	16.7	2803.8	$0.17 \cdot 10^{-4}$

Table 2. Parameters used in simulations.

Formation Parameters	
rock density	2600 kg/m^3
porosity	0.05
thermal conductivity	2.51 W/m°C
specific heat	920 J/kg°C
permeability	(a) $1 \cdot 10^{-13}$ m^2 (b) $1 \cdot 10^{-12}$ m^2
relative permeability	Corey curves with Slr = 0.30 Sgr = 0.05
capillary pressure	0, or Leverett J-function (see text)
Initial Conditions	
temperature	240°C
pressure	(a) 10 bar (b) gravity equilibrium with P_{av} = 10 bar
Injection Specifications	
enthalpy	126 kJ/kg (approximately 30°C)
injection rate	(a) 2.5 kg/s (b) 0.01 kg/s
Production Specifications	
(a) wellbore pressure	8 bar
(a) productivity index	$8.335 \cdot 10^{-12}$ m^3
(b) Variable rate at constant pressure boundary	

(a) 1/8 of five-spot with 208.5 m well spacing (20 acre), 200 m thick
(b) vertical X-Z section with depth = 200 m, thickness = 1 m

Table 3. Simulated production rates and temperatures for five-spot areal production-injection system, using parallel and diagonal grids.

Time (years)	Production Rate (kg/s)		Production Temperature (°C)	
	parallel	diagonal	parallel	diagonal
2	1.60	1.28	226.5	233.5
5	2.18	2.40	192.3	190.6
10	2.41	2.44	185.5	186.5
20	2.48	2.48	157.6	163.0

Table 4. Fraction of injected water vaporized for 2-D vertical section.

Time (days)	Grid	5-point		9-point	
		no P_{cap}	w/P_{cap}	no P_{cap}	w/P_{cap}
37.0	parallel	0.707	0.774	0.700	0.761
	diagonal	0.696	0.750	0.717	0.765
105.3	parallel	0.747	0.725	0.729	0.736
	diagonal	0.720	0.714	0.721	0.743
214.1	parallel	0.703	0.702	0.729	0.730
	diagonal	0.714	0.711	0.720	0.712
329.9	parallel	0.677	0.722	0.715	0.712
	diagonal	0.705	0.713	0.706	0.715
501.1	parallel	0.756 (*)	0.709	0.715	0.707
	diagonal	0.710	0.715	0.708	0.715
614.6	parallel	0.800 (*)	0.719	0.701	0.713
	diagonal	0.716	0.715	0.695	0.713
717.0	parallel	0.828 (*)	0.715	0.686	0.708
	diagonal	0.689	0.716	0.677	0.715

(*) Injection plume has penetrated constant-pressure boundary.

PROCEEDINGS, Sixteenth Workshop on Geothermal Reservoir Engineering
Stanford University, Stanford, California, January 23-25, 1991
SGP-TR-134

PRESSURE-INTERFERENCE TESTING OF THE SUMIKAWA GEOTHERMAL FIELD

S.K. Garg*, J.W. Pritchett*, K. Ariki+, and Y. Kawano•

***S-CUBED, +Mitsubishi Materials Corporation (MMC), •New Energy and Industrial Technology Development Organization (NEDO)**

Abstract

Pressure interference tests have been used to determine the permeability structure of the Sumikawa reservoir. Interference tests between wells S-4 and KY-1 have indicated the presence of a very high permeability (140 md) north-south channel in the altered andesite layer. Pressure buildup data from well SN-7D have provided indications of a high transmissivity (kh ~ 18 darcy-meters) reservoir located in the granodiorite layer; lack of pressure response in nearby shutin Sumikawa wells implies that the reservoir penetrated by SN-7D is isolated from the shallower reservoir in the altered andesites. The "altered andesite" and the "granodiorite" formations constitute the principal geothermal aquifers at Sumikawa. Pressure interference tests (wells KY-1 and SB-2, and wells KY-2 and SB-3) have also confirmed the presence of moderately high transmissivity (~ 2 darcy-meters) dacitic layers in the "marine-volcanic complex" formation. Because of its low vertical permeability, the "marine volcanic complex" formation constitutes an attractive target for the reinjection of waste geothermal fluids.

Introduction

The Sumikawa geothermal field is located in the Hachimantai volcanic area in northern Honshu, Japan. Figure 1 shows the region of particular interest. The area depicted is about 42 square kilometers; the Sumikawa geothermal field lies in the western part of the area. To the east, the Ohnuma geothermal power station has been producing about 10 MW of electrical power for several years using a small borefield immediately surrounding the power station. The terrain is extremely irregular; Mt. Yake lies in the southwest part of the illustrated area and Mt. Hachimantai is just to the southeast. To the north of these volcanic peaks, the terrain drops away rapidly. Between the Sumikawa prospect (which may be regarded as centered in the neighborhood of the S-series wells: S-1, S-2, S-3, and S-4) and the Ohnuma borefield is a north-south region of relatively low ground surface elevation where natural hot-springs and fumaroles are found.

The Sumikawa/Ohnuma area lies within a north-south oriented regional graben structure which extends many kilometers both north and south of the area shown in Figure 1. Indeed, the Sumikawa field itself appears to be located along the western edge of the graben. Figure 2 shows an east-west cross-section corresponding to line A–A′ in Figure 1. Figure 3 shows a similar north-south section (B–B′). These structural interpretations are based almost exclusively upon drilling experience. The major formations in order of increasing depth are:

"ST" Formation: Surficial andesitic tuffs, lavas and pyroclastics of recent origin (from Mt. Yake).

"LS" Formation: Lake sediments; Pleistocene tuffs, sandstones, siltstones and mudstones.

"DA" Formation: Pliocene dacites, dacitic tuffs and breccias.

"DI" Formation: Dacitic dike located generally north of the Kumazawa river.

"MV" Formation: "Marine/Volcanic Complex"; interbedded Miocene dacitic volcanic rocks and "black shale" oxygen-poor marine shales and sediments.

"AA" Formation: Altered andesitic rocks which are apparently extensively fractured.

"GR" Formation: Crystalline intrusive rocks (mainly granodiorite and diorite).

The lake sediments act as a caprock for the geothermal reservoir (see Pritchett *et al.*, 1989). The "GR" formation is the deepest so far encountered by drilling, but the pre-Tertiary basement which presumably underlies the above sequence has not yet been reached. The "DI" formation (known only from outcrops) is located north of the Kumazawa river (i.e. outside the main Sumikawa geothermal field) and is believed to extend to great depth.

In this paper, we discuss the pressure-interference testing of the Sumikawa geothermal field. The various pressure transient tests performed to-date have helped in clarifying the permeability structure of the Sumikawa reservoir. Interference tests have indicated the presence of (1) a very high permeability north-south channel in the altered andesite layer, and (2) moderately high transmissivity dacitic layers in the "marine/volcanic complex" formation. In addition, it appears that the deep "granodiorite" reservoir penetrated by well SN-7D is isolated from the overlying altered andesite reservoir.

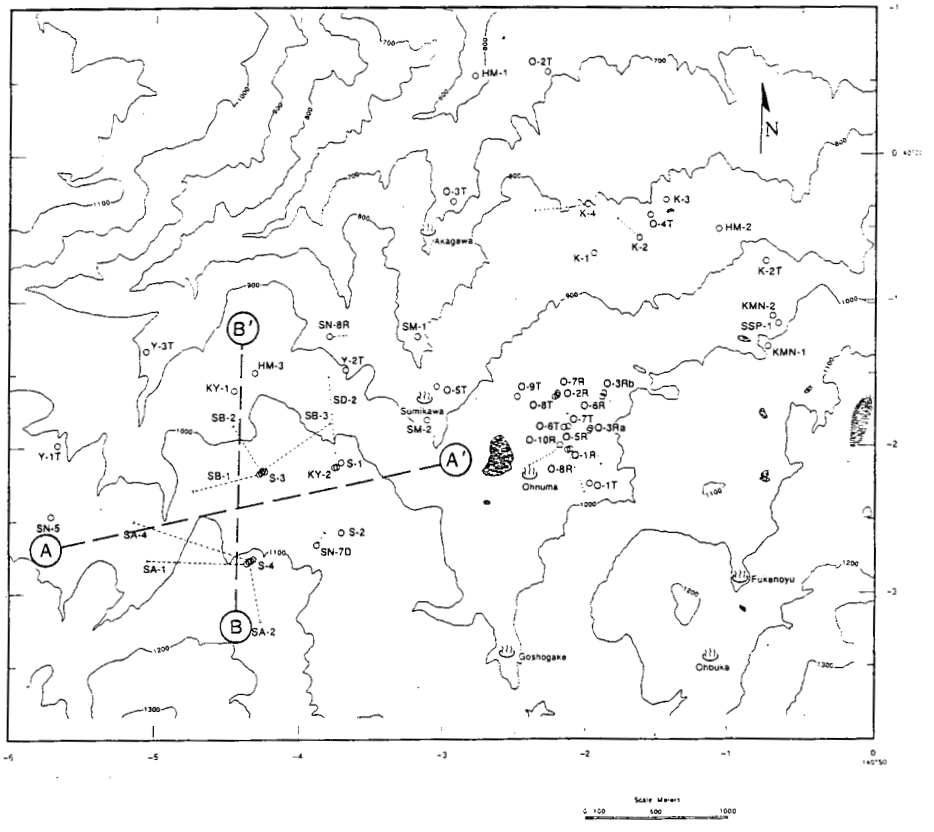

Figure 1. The Sumikawa/Ohnuma area, showing locations of wells and cross-sections A–A′ and B–B′

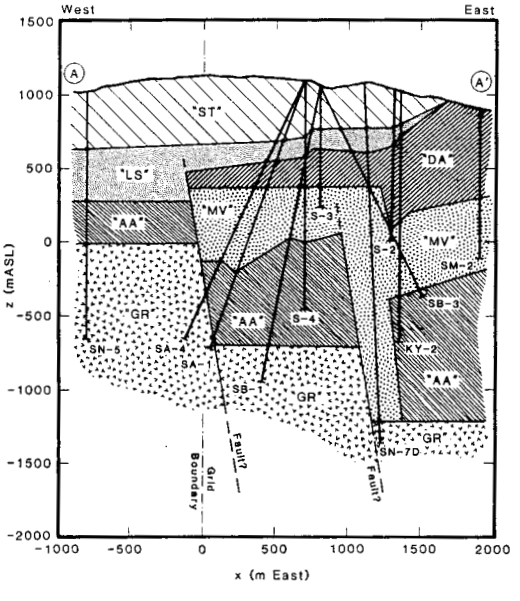

Figure 2. East-west A–A′ geological cross-section through the Sumikawa area.

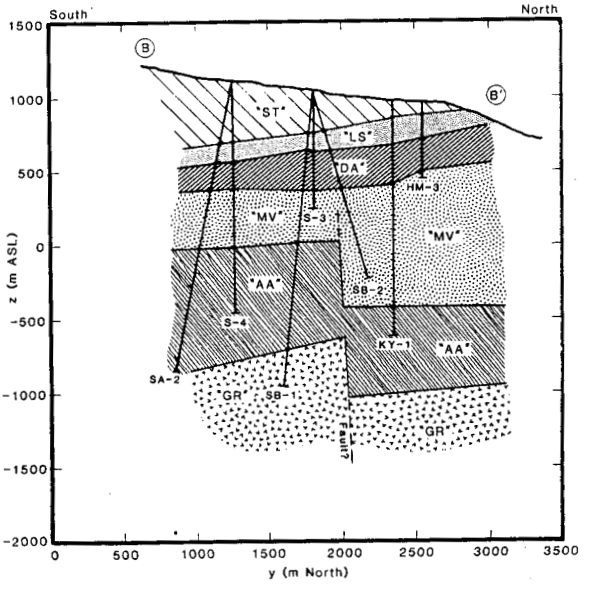

Figure 3. North-south geological cross-section B–B′ through the Sumikawa area.

Pressure Disturbances in Observation Well KY-1

In 1986, a large-scale pressure-interference experiment was carried out at Sumikawa. Deep well S-4 was discharged starting on September 2 and was subsequently shut in on November 3; the liquid fraction of the discharge was simultaneously reinjected into nearby shallow well S-2. Four shut-in observation wells (O-5T, S-3, KY-1 and KY-2) were equipped with downhole pressure gauges of the capillary-tube type. No signals attributable to the S-4 discharge were recorded in O-5T, KY-2 or S-3, but a clear and immediate response was observed in deep well KY-1, located 1.1 km north of S-4. Only two mud loss zones were encountered in the uncemented part of well KY-1: at –166 m ASL and at –568 m ASL. The deeper of these mud loss zones lies in the "altered andesite" layer and corresponds to the major feedpoint for well KY-1. The major feedpoint for well S-4 is located at –413 m ASL in the "altered andesite" layer.

All four "A" pad wells (SA-1, SA-2, SA-4, S-4) were discharged, essentially simultaneously, between October 22 and November 27, 1988. Except for a brief period in November, all of the liquid separated from SA-1 and S-4 (SA-2 and SA-4 discharged only dry steam) was reinjected into well SB-2. From November 17 to November 22, 1988, part of the separated liquid was also reinjected into wells SB-1 and SB-3. During the 1988 discharge test, well KY-1 was equipped with a downhole capillary tube pressure gauge. Based on the flow histories of various wells, it is concluded that the pressure signal recorded in KY-1 reflects the effects of production/reinjection into wells S-4, SB-1 and SB-2. The major feedpoint for well SB-1 is located at –551 m ASL in the altered andesite layer. The fluid injected into well SB-2 enters the reservoir at its major entry (–221 m ASL) located in a dacite layer within the "marine/volcanic complex". Thus S-4 and SB-1 apparently communicate with well KY-1 through the altered andesite layer; well SB-2 is connected to well KY-1 through the dacites (see Figure 4). Analysis of 1988 test data is severely handicapped by extremely sparse data concerning flow rates in various wells, and the reservoir parameter values inferred are not considered to be very reliable.

In April and May 1989, MMC injected cold water into several wells (SA-1, SA-2, SA-4, S-4, SB-1, SB-2 and SB-3). During the injection period, several shutin wells (KY-1, KY-2, S-3, S-4 and SN-7D) were equipped with downhole capillary-tube pressure gauges. No definite evidence of pressure interference was found in the records obtained from wells S-3, S-4 or SN-7D. Well KY-2 exhibited a pressure response to injection into well SB-3; these interference data are discussed in a later section. Figure 5 shows the pressure signal recorded in well KY-1 during April and May 1989. The pressure record (Figure 5) shows significant oscillations even prior to the start of injection at ~ 1098 hours (April 16, 1989). Besides the fictitious oscillations, the pressure record contains a number of gaps and apparently discontinuous shifts in pressure. Despite these difficulties with the KY-1 pressure record, it is possible to identify pressure changes attributable to injection into wells S-4, SB-1 and SB-2. These pressure changes are considered in detail in the following subsections.

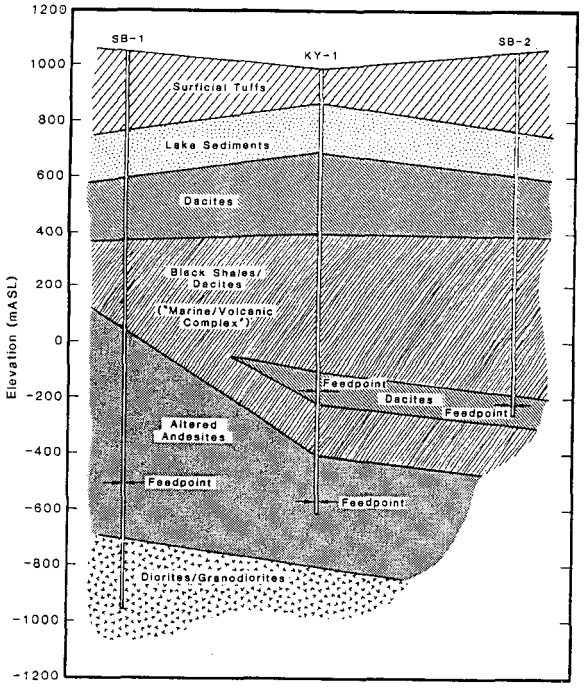

Figure 4. Correlations between stratigraphic logs in wells SB-1, SB-2 and KY-1.

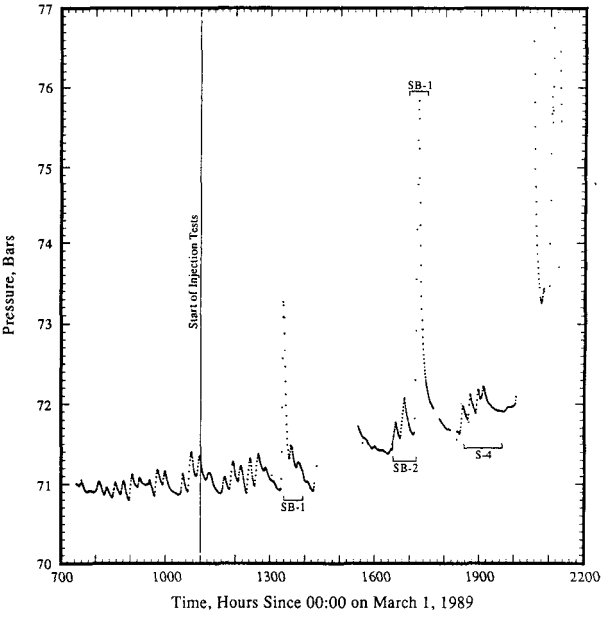

Figure 5. Measured pressure response in KY-1 during April and May 1989. Also indicated are the pressure responses believed to be associated with injection into wells S-4, SB-1 and SB-2.

As noted above, well KY-1 appears to be connected to two aquifers (a dacite layer in the "marine/volcanic complex" formation, and the altered andesites). The net pressure disturbance measured within well KY-1 at any time is the weighted average of the pressure distribution within the two aquifers outside the well; the weighting factors are the injectivities of the two feedzones involved. Assuming that the characteristic relaxation time for the well is small compared to the time scale associated with aquifer pressure disturbances, the time rate of change in well pressure $\dot{p}_w$ is given by:

$$\dot{p}_w = W_u \dot{p}_u + (1 - W_u)\dot{p}_l$$

where

W_u = fractional injectivity of the upper feedzone

$\dot{p}_u(\dot{p}_l)$ = time rate of change in pressure within the upper (lower) aquifer.

ϕ (porosity) = 0.15

The pressure disturbance within the upper aquifer is presumably that due to injection into well SB-2, and the disturbance in the lower aquifer is a linear combination of the disturbances caused by injection into (or production from) wells SB-1 and S-4. An estimate for W_u ($\approx$ 0.2) is presented in the next subsection.

Wells SB-2 and KY-1

The recorded KY-1 pressure signal shows influence of cold water injection into well SB-2 on May 8 and May 9, 1989 (see Figure 6). We treat the dacite aquifer intercepted by wells KY-1 and SB-2 as characterized by the following uniform properties:

$$\phi \text{ (porosity)} = 0.15$$

$$\mu \text{ (fluid viscosity)} = 1.2 \times 10^{-4} \text{ Pa - s}$$

$$C_T \text{ (total compressibility)} = 1.2 \times 10^{-9}/\text{Pa}$$

The spatial separation between the SB-2 feedpoint and the upper KY-1 feedpoint is 243 meters.

The classical line-source solution was utilized; well SB-2 was treated as a fully penetrating well for purposes of the analysis of interference at KY-1. Provision was made for a constant pressure linear aquifer boundary. A single interference signal cannot uniquely establish the orientation of the "constant pressure" boundary; only the following parametric relationship may be obtained;

$$(R\sin\theta)X + (R\cos\theta - A)Y = 2B^2$$

where

$$R^2 = A^2 + 4B^2$$

θ = any angle from 0 to 2π

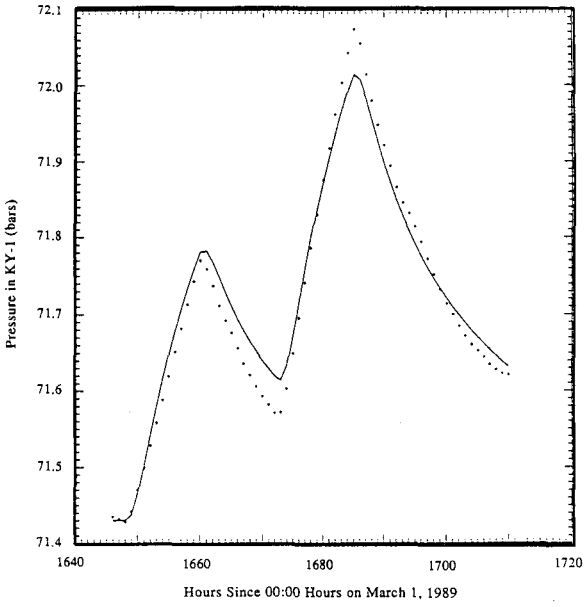

Figure 6. Comparison of pressure measurements in well KY-1 with computed response due to cold water injection into well SB-2 on May 8 and May 9, 1989 (t = 1647.7 to 1664.3 hours and t = 1672.1 to 1688.2 hours). —computed, • measurements

and where the "y" axis coincides with a line connecting the two feedpoints, the "x" axis is perpendicular to y, "A" represents the spatial separation between the two feedpoints (243 meters), the KY-1 feedpoint is located at $x = y = 0$, the SB-2 feedpoint is located at $x = 0$, $y = A =$ 243 meters, and the boundary is represented by the locus of points with $x = X$, $y = Y$. The unknown parameters in the model (p_i, initial reservoir pressure, k, dacite aquifer permeability; h, the aquifer thickness; B, the boundary distance) were varied in order to minimize deviations between calculations and observations. The values finally obtained were:

p_i (initial reservoir pressure) = 71.430 bars

k (permeability) = 25.2×10^{-15} m^2 = 25.2 millidarcies

h (thickness) = 647 W_u meters

B (boundary distance) = 567.6 meters

φ (rock porosity) = 0.05

The proper value for the aquifer thickness (h) depends upon the value selected for the relative injectivity of the upper feedzone in well KY-1 (W_u) This permits W_u to be estimated, at least approximately. Well logs indicate that the thickness of the dacite aquifer involved is in the neighborhood of 150 meters. Therefore, if we impose h =150 m, we obtain W_u= 0.232. Of course, h is not precisely known; accordingly, we have simply adopted the rounded value: W_u = 0.2. The permeability-thickness product of the dacite layer connecting the upper feedzone of well KY-1 with the feedpoint of well SB-2 is ~ 3.3 darcy-meters.

Wells KY-1 and S-4

Starting at 19:00 hours on May 16, 1989 ($t \sim 1843$ hours), cold water was intermittently injected into well S-4 until 14:00 hours on May 19, 1989; well KY-1 responded (see e.g. Figure 7) quickly to each change in the injection rate. For the sake of simplicity, we ignore the slight difference in elevation between the feedpoints of well S-4 (–413 m ASL) and well KY-1 (–566 m ASL), and treat well KY-1 as if it were located directly north of well S-4. Assuming that the coordinates of the S-4 feedpoint coincide with the origin ($x = y = z = 0$), the coordinates of the feedpoint of well KY-1 are ($x = 0$, $y = 1120$ meters, $z = 0$). A variety of geometrical flow models were considered in an attempt to interpret the measured pressure response in well KY-1. The best fit was obtained by assuming that well S-4 fully penetrates an areally infinite anisotropic reservoir with the following properties:

φ (rock porosity) = 0.05

μ (fluid viscosity) = 10^{-4} Pa - s

C_T (formation compressibility) = 1.7×10^{-9} Pa^{-1}

ρ (*in situ* fluid density) = 800 kg/m^3

k_y (north - south permeability): 141 md

k_x (east - west permeability): 3.36 md

h (formation thickness): 500 $(1 - W_u)$ meters

p_i (initial pressure): 71.599 bars

As noted above, a pressure response was also recorded in well KY-1 during a 1986 discharge test of well S-4. Although no downhole pressure measurements in well S-4 were made during the 1986 discharge test, it is certain that two-phase (water/steam) boiling flow was induced locally in the reservoir adjacent to the S-4 feedpoint by the pressure reduction associated with discharge. Well test pressure transient analysis is traditionally based on assumptions of single phase isothermal flow. As discussed by Garg and Pritchett (1988), these linear single-phase analysis techniques may be applied for interference test interpretation so long as the discharge rate history used in the analysis is suitable modified to reflect the influence of the two-phase zone in the vicinity of the production well. According to Pritchett *et al.* (1989), the effective discharge rate history for well S-4 may be represented as follows:

Time Interval	Effective Discharge Rate
prior to 09/02/86 11:20	0 kg/s
09/02/86 11:20 to 09/03/86 12:00	50 kg/s
09//03/86 12:00 to 09/07/86 00:00	42 kg/s
09/07/86 00:00 to 11/03/86 16:30	34 kg/s
11/03/86 16:30 to 11/29/86 09:00	4 kg/s

We next attempted to match the 1986 pressure interference response in KY-1 with an "anisotropic line-source model". Figure 8 compares the computed pressure response with the measurements. The following parameters were utilized in computing the pressure disturbance shown in Figure 8.

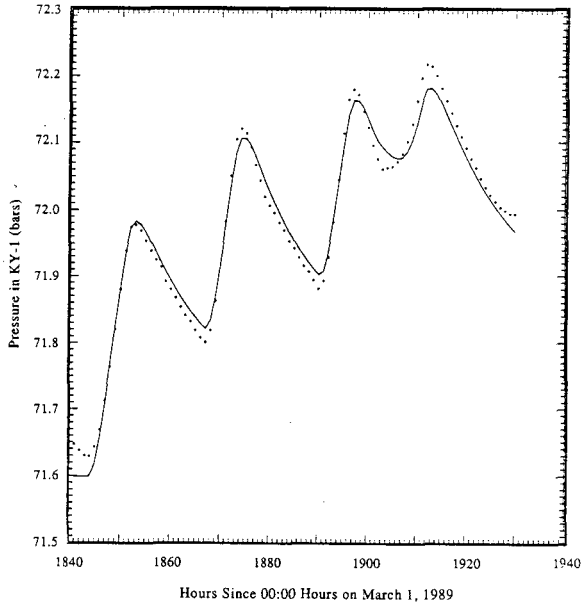

Figure 7. Comparison of computed (anisotropic line-source model) pressure response of KY-1 with measurements due to cold water injection into well S-4 (—computed, •measurements).

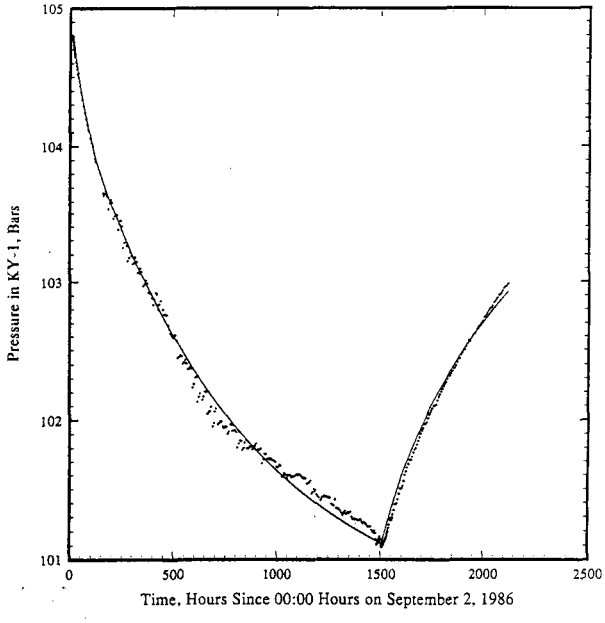

Figure 8. Comparison of computed (anisotropic line-source with boundaries) 1986 pressure disturbance in well KY-1 to measurements (—computed, •measurements).

k_y (north-south permeability): 139 md

k_x (east-west permeability): 28.2 md

h (formation thickness) = 498 m

distance to eastern (western) impermeable boundary, $\Delta x_e(\Delta x_w) = 630 \times (1-W_u)$ meters $\equiv$ 504 meters

distance to northern impermeable boundary Δy_n = 2030 meters

distance to southern constant pressure boundary, Δy_s = 8710 meters

The reservoir cross-section (0.498 × 1.008 ~ 0.50 km^2) and the distance to the northern and southern boundaries given by the above model is not too different from that presented earlier by Prichett *et al.* (1989). Within certain limits, the computed pressure response is not very sensitive to the exact value for the east-west permeability. Considering the uncertainty associated with the 1986 flow data, it is not possible to claim any great precision for the east-west permeability (28.2 md) needed to obtain the computed pressure response in Figure 8.

Figure 9 compares the measured pressures in KY-1 (April and May 1989) with the pressure response computed using the above described anisotropic line-source model with boundaries. All the parameter values, with the exception of k_x and initial pressure p_i, were held constant. The following values for k_x and p_i were utilized in computing the pressure response:

$$k_x = 5.82 \text{ md}, \qquad p_i = 71.614 \text{ bars}$$

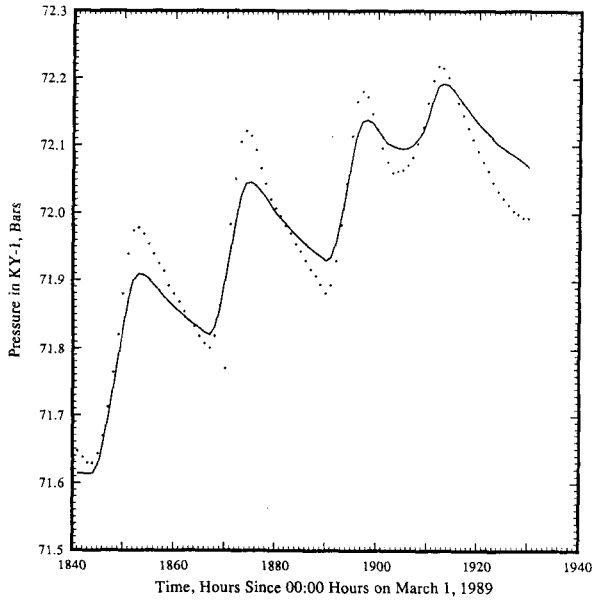

Figure 9. Comparison of pressure measurements in well KY-1 with computed (anisotropic line-source model with boundaries) response due to cold water injection into well S-4 (—computed, •measurements).

The agreement between the measured and computed response, while not as good as that shown in Figure 7, is certainly adequate. Furthermore, the east-west permeability value (5.82 md) is within a factor of three to five of that required to match the 1986 pressure response.

In conclusion, our interpretation of the pressure interference data shows that wells KY-1 and S-4 penetrate a north-south channel of high permeability; the permeability in the transverse (i.e. east-west) direction is, however, low (5 to 30 md). The cross-section of the north-south channel is ~ 0.5 km^2. The permeable channel is bounded to the north by an impermeable boundary. The inferred southern constant pressure boundary most likely corresponds to the two-phase water-steam zone in the reservoir.

Wells KY-1 and SB-1

Because of gaps in the recorded pressure response for well KY-1, it was possible to clearly identify pressure interference from only two episodes (April 25, 1989 and May 11, 1989) of cold water injection into well SB-1. In each case, the signal strength at well KY-1 was extremely high (several bars) despite the relatively small quantity of fluid injected into well SB-1 and despite the large separation between the well feedpoints.

The best fit to the pressure interference observations (see e.g. Figure 10) between wells SB-1 and KY-1 was obtained by using the conventional line-source model with a constant pressure boundary. Well SB-1 is apparently connected to well KY-1 by a single fracture. The permeability-thickness product of this fracture is only about ~ 0.11 darcy-meter and the porosity-thickness is only about 14 centimeters. This suggests that the aquifer volume involved is very small. As established by the interpretation of the pressure interference tests between wells KY-1 and S-4, the "altered andesite" formation is very permeable, and the cross-section area of the channel is substantial. This permeability is presumably due to the presence of a system of fractures (probably oriented approximately north-south); although well S-4 intersected only one of these fractures at its primary feedpoint, the frequent intersections of the individual fractures within the channel served to distribute the pressure signal from S-4 throughout the entire fracture network in the formation such that the apparent cross-section area and aquifer volume were substantial. In the case of well SB-1, however, the very high ratio of pressure disturbance to injection flowrate suggest that only a limited part of the fracture network was accessed by the pressure disturbance before it was felt at well KY-1. For example, it is possible that well SB-1 injects fluid into a single fracture which either intersects well KY-1 or passes very near the dominant KY-1 feedpoint; this fracture presumably eventually intersects the remainder of the fracture network, but only at considerable distance. The constant pressure boundary indicated by our analysis most likely implies that the fracture connecting wells KY-1 and SB-1 joins the rest of the fracture network at some indeterminate distance from well SB-1.

Pressure Disturbances in Well KY-2

Well KY-2 has several feedpoints between ~ 200 m ASL and ~ –500 m ASL. The top two feedzones (216 to 86 m ASL, and –24 to –44 m ASL) are located in dacite layers within the "marine/volcanic complex". The major

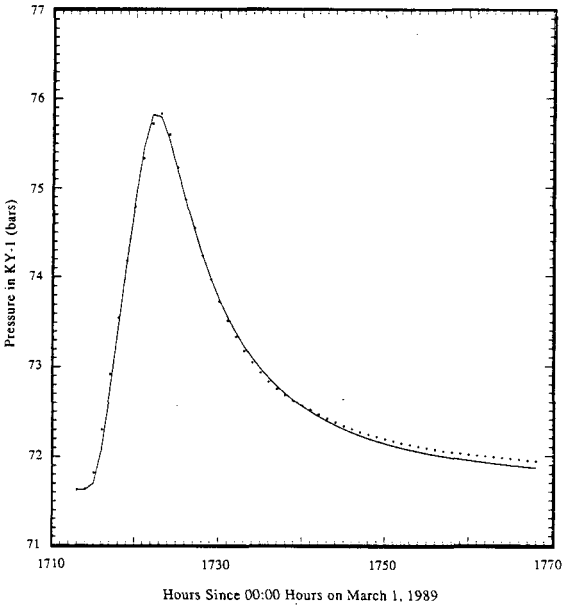

Figure 10. Comparison of pressure measurements in well KY-1 with computed response due to cold water injection into well SB-1 during the time interval from 9:16 hours (t = 1713.267 hours) on May 11, 1989 to 15:50 hours (t = 1719.833 hours) on May 11, 1989 (—computed, •measurements).

feedzone for well SB-3 occurs in the depth interval 249 to 89 m ASL; this depth interval contains the "marine/volcanic complex". During April and May 1989, cold water was intermittently injected into well SB-3, and a pressure interference response was observed in well KY-2 (see Figure 11). It is likely that wells SB-3 and KY-2 communicate through the upper feedpoint of well KY-2.

To analyze the pressure interference response of well KY-2, we assume that well SB-3 can be treated as a classical line-source in an aquifer with the following properties:

formation porosity, $\varphi = 0.15$

fluid viscosity, $\mu = 1.2 \times 10^{-4}$ Pa-s

total formation compressibility, $C_T = 1.2 \times 10^{-9}$ Pa^{-1}

Ignoring the slight difference in feedpoint elevations, the distance between KY-2 and SB-3 is ~ 414.3 meters. The unknown parameters are (1) initial formation pressure, p_i (2) formation permeability, k and (3) formation thickness, h. Minimization of error gives the following values for the model parameters:

initial formation pressure, $p_i = 44.0$ bars

formation permeability, $k = 12.8 \times 10^{-15}$ m^2 = 12.8 md

formation thickness, $h = 203$ meters

The computed pressure response is compared with the measurements in Figure 11. The permeability-thickness value of 2.6 darcy-meters for the dacite layer intercepted by wells KY-2 and SB-3 is comparable to that (3.3 darcy-meters) inferred for the dacite layer connecting wells KY-1 and SB-2.

Well SN-7D

Well SN-7D is the deepest well (total depth ~ 2486 m; true vertical depth ~ 2472 m) at Sumikawa. The major feedpoint for well SN-7D is located in the crystalline granodiorite/granite/diorite rocks at about –1230 m ASL; several minor feedzones are to be found in the overlying "marine/volcanic complex" formation. Well SN-7D is by far the best producer at Sumikawa; total (water plus steam) flow rates up to 500 tons/hour were recorded during a 1989 discharge test.

Downhole pressures were monitored using a gauge of the capillary tube type in at least three separate (two in 1988 and one in 1989) discharge tests. The pressure buildup data from these tests have been interpreted to indicate a very high transmissivity (permeability × thickness ~ 18 darcy-meters). It also appears that the volume of the deep zone tapped by well SN-7D is at least a few cubic kilometers. During the SN-7D discharge tests, five other wells (S-3, S-4, KY-1, KY-2, SN-8R) were, at one time or another, equipped with downhole pressure gauges. No signal attributable to the discharge of SN-7D was observed in any of these wells; this implies that the deep reservoir penetrated by well SN-7D is probably isolated from the shallower reservoir in the "altered andesites".

Structural Interpretation of "Channel Model"

The feedpoints of both wells S-4 and KY-1 are located within a deep altered andesite layer. Above this layer lies a thick formation consisting of alternating marine sediments (black shales) and dacite volcanic flows; because of the presence of the shales it is likely that the average vertical permeability is rather low. Below the andesite layer, a crystalline granitic layer (granodiorite formation) is to be found. The thickness of the permeable (andesite) layer, sandwiched between the marine/volcanic complex and the crystalline granitic basement, is about 0.5 to 0.6 kilometers. Since the cross-section area of the channel is ~ 0.5 km^2, it follows that the width (east-west) of the channel is about 1 km. It is noteworthy that, about 2 km farther to the east, a similar north-south permeable channel of ~ 1 km width (permeable zone III in Figure 12) was identified associated with the Ohnuma Geothermal Field based on stable shutin pressure evidence.

The granodorite formation appears to rise abruptly ~ 0.7 km west of well S-4 ; this geological discontinuity is an obvious candidate for the western boundary of the deep flow channel (permeable zone I in Figure 12). If this geometric interpretation is valid, the implication is that another north-south vertical barrier is present ~ 0.2 to 0.3 km east of well S-4. Such a flow barrier would lie between wells S-4, S-3, N60-KY-1 and 50-HM-3 (to the west) and wells S-2, S-1, N61-KY-2 and Y-2T (to the east). This eastern boundary most likely consists of "MV" black shale, as evidenced by drilling logs from well SN-7D.

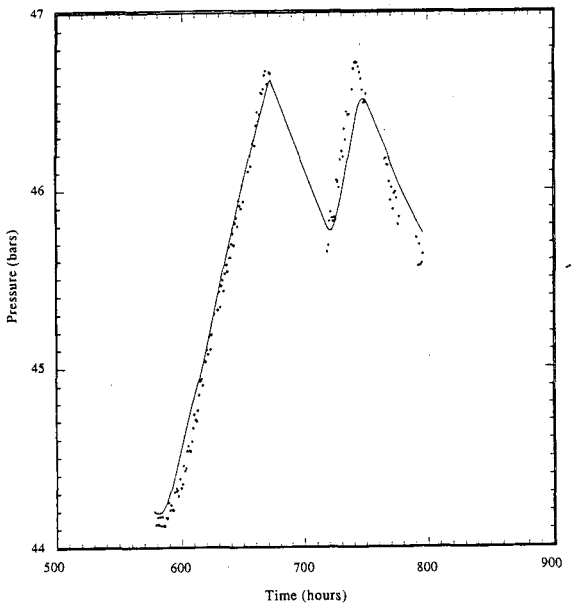

Figure 11. Pressure response of well KY-2 to cold water injection into well SB-3 from April 25, 1989 to May 25, 1989 (—computed, •measurements).

An east-west reservoir boundary located north of wells 0-3T and 0-4T was identified based on static pressure evidence (Pritchett *et al.*, 1989). The presence of this northern boundary is confirmed by the above interpretation of the signal observed in well KY-1 from the S-4 discharge test. This boundary is probably associated with the dacitic dike along the Kumazawa river.

The channel flow model also suggests the presence of a constant-pressure boundary located some 8.7 km south of well S-4. It seems implausible that the flow channel could extend so far south. The explanation for this peculiar result is intrinsic in the linear character of the flow model. In particular, it was assumed that the flow channel contains single-phase liquid. It is likely that two-phase conditions prevail under undisturbed conditions in the flow channel a short distance (less than 1 km) south of well S-4. This suggests that the actual position of the southern boundary is probably much closer to well S-4 than the 8.7 km indicated by the single-phase treatment.

Conclusions

Pressure transient tests have been invaluable in delineating the permeability-strucutre of the Sumikawa reservoir. Interference tests between wells S-4 and KY-1 have indicated the presence of a very high permeability (140 md) north-south channel in the altered andesite layer. Pressure buildup data from well SN-7D have provided

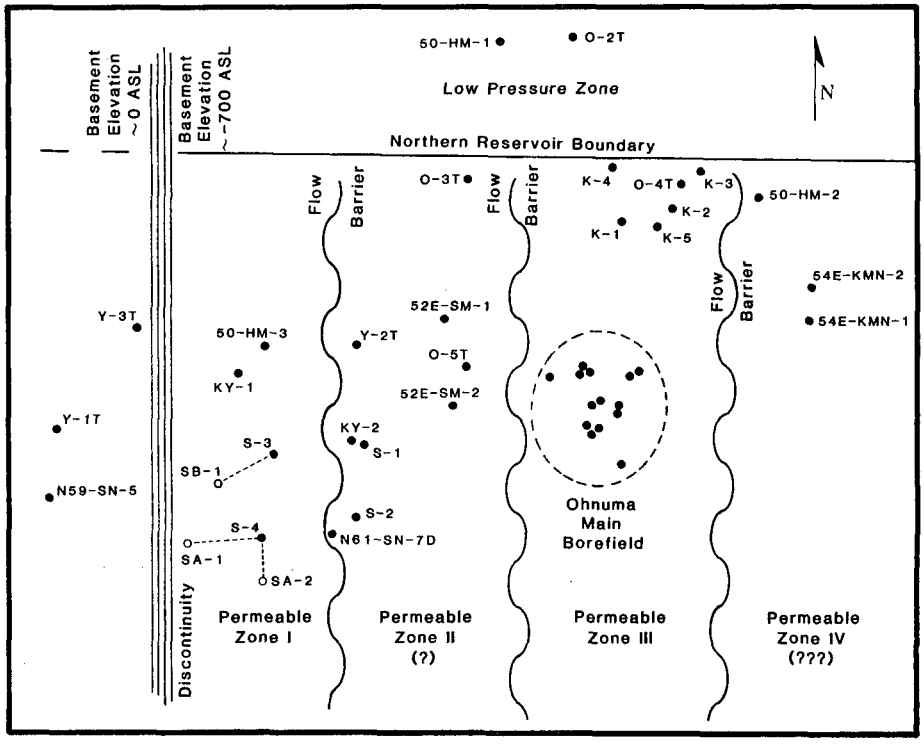

Figure 12. Estimated locations of deep permeable channels in Sumikawa/Ohnuma area.

indications of a high transmissivity (permeability × thickness ~ 18 darcy-meters) reservoir located in the crystalline rocks underlying the altered andesite layer. Lack of pressure response in shutin wells, however, indicates that the deep reservoir encountered by SN-7D is hydraulically isolated from the overlying "altered andesite" formation. At present, the "altered andesite" and the "granodiorite" formations are believed to constitute the principal geothermal aquifers at Sumikawa.

Pressure interference tests (wells KY-1 and SB-2, and wells KY-2 and SB-3) have also confirmed the presence of moderately high transmissivity (~ 2 darcy-meters) dacitic layers in the "marine/volcanic complex" formation. Because of its low vertical permeability, the "marine/volcanic complex" formation constitutes an attractive target for reinjection of waste geothermal fluids.

Acknowledgement

This work was sponsored by the New Energy and Industrial Technology Development Organization, Tokyo, Japan.

References

Garg, S. K. and J. W. Pritchett (1988), "Pressure Interference Data Analysis for Two-Phase (Water/Steam) Geothermal Reservoirs," *Water Resources Research, Vol. 24*, pp. 843–852.

Pritchett, J. W., S. K. Garg, H. Maki and Y. Kabota (1989), "Hydrology of the Sumikawa Geothermal Prospect, Japan," to appear in Proceedings 14th Workshop Geothermal Reservoir Engineering, Stanford University.

PROCEEDINGS, Sixteenth Workshop on Geothermal Reservoir Engineering
Stanford University, Stanford, California, January 23-25, 1991
SGP-TR-134

OPTIMIZING REINJECTION STRATEGY AT PALINPINON, PHILIPPINES BASED ON CHLORIDE DATA

Ma. Elena G. Urbino and Roland N. Horne

Stanford Geothermal Project
Department of Petroleum Engineering
School of Earth Sciences
Stanford University
Stanford, CA

ABSTRACT

One of the guidelines established for the safe and efficient management of the Palinpinon Geothermal Field is to adopt a production and well utilization strategy such that the rapid rate and magnitude of reinjection fluid returns leading to premature thermal breakthrough would be minimized. To help achieve this goal, sodium fluorescein and radioactive tracer tests have been conducted to determine the rate and extent of communication between the reinjection and producing sectors of the field. The first objective of this paper is to show how the results of these tests, together with information on field geometry and operating conditions were used in algorithms developed in Operations Research to allocate production and reinjection rates among the different Palinpinon wells.

Due to operational and economic constraints, such tracer tests were very limited in number and scope. This prevents obtaining information on the explicit interaction between each reinjection well and the producing wells. Hence, the chloride value of the producing well, was tested to determine if use of this parameter would enable identifying fast reinjection paths among different production/reinjection well pairs. The second aim, therefore, of this paper is to show the different methods of using the chloride data of the producing wells and the injection flow rates of the reinjection wells to provide a ranking of the pair of wells and, thereby, optimize the reinjection strategy of the field.

INTRODUCTION

The Palinpinon Geothermal Field (Figure 1) is one of two producing steamfields currently operated by the Philippine National Oil Company (PNOC). The steam requirement of the 112.5 MWe commercial plant, known as Palinpinon 1 has been met by 21 production wells and 10 reinjection wells which accept wastewater by gravity flow. Figure 2 shows the surface reticulation system, the production and reinjection multi-wells pads, as well as the well tracks. The need to reinject waste liquid effluent has been primarily dictated by environmental constraint, which in the Philippines prohibit full disposal into the rivers that are used for field irrigation. In addition to this, the other benefits of injection, such as maintaining reservoir pressures and increasing thermal recovery from rocks have been recognized.

Although injection wells have been drilled at the periphery of the field, preferably at the identified outflows, initial chemical monitoring of the produced fluids showed increases in well reservoir chloride values (Figure 3). This has been interpreted as evidence of the return of reinjected fluids to the production sector. To maximize productivity of the reservoir and prolong the economic life of the field, guidelines for the safe and efficient management of the Palinpinon reservoir have been established. These include the requirements of:

1) minimizing fluid residence times in the surface and downhole piping while operating reinjection wells to prevent or minimize silica deposition of injected fluid that is supersaturated with respect to amorphous silica.

2) minimizing steam wastage due to varying steam demand and supply by prioritizing high enthalpy production wells during peak steam requirements and choosing injection wells with additional capacity.

3) adopting a production and reinjection well utilization strategy such that the rapid rate and magnitude of reinjection fluids returns leading to premature thermal breakthrough would be minimized, if not avoided.

Towards this objective, a comprehensive testing and monitoring programme was instituted. This programme includes fluorescein and radioactive tracer testing to determine interaction between the injecting and producing blocks.

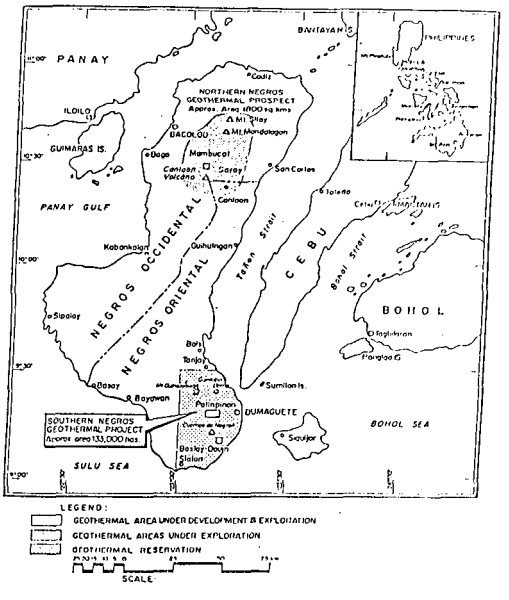

Figure 1 Location Map of Palinpinon Geothermal Field Southern Negros Geothermal Project

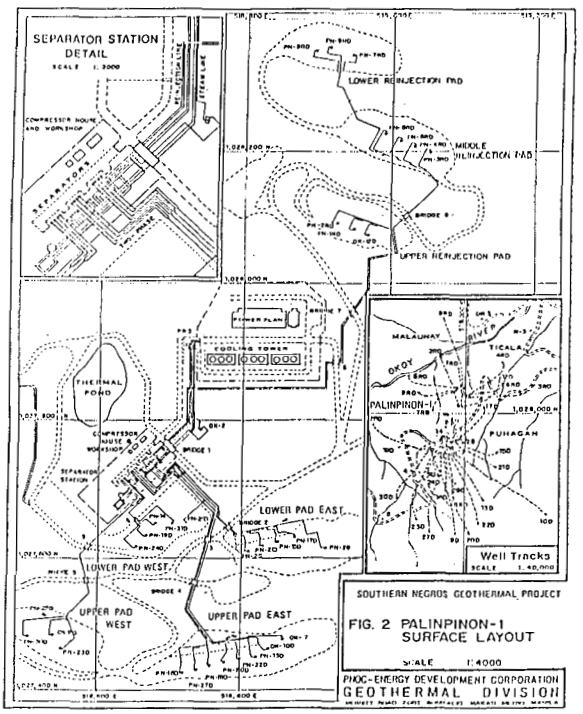

Figure 2 Palinpinon-1 Surface Layout

It is one aim of this paper to use the results of these tracer tests in algorithms of Operations Research to determine optimal production and reinjection rates among the different Palinpinon wells. However, since these tracer tests are limited, the other objective is to find another parameter that could be used in place of tracer return data in the optimization of production and reinjection strategy.

TRACER TESTS AT THE PALINPINON GEOTHERMAL FIELD

Table 1 shows the results of conducting fluorescein and radioactive tracer testing at Palinpinon 1. Sodium fluorescein dye was injected into OK-12RD, PN-1RD, and PN-9RD while radioactive Iodine-131 was injected into OK-12RD and PN-9RD. Amounts of the dye and radioactive tracer were increased with succeeding tests to expand the scope of the tests and overcome the limitations imposed by degradation of the tracers.

The results from Table 1 show that the eastern injection wells (OK-12RD, PN-1RD, and PN-6RD) communicate strongly with the eastern and central Puhagan wells such as PN-15D, PN-17D, PN-21D, PN-26, PN-28, and OK-7. The western injection well PN-9RD, likewise, interact with the western, southwestern, and central Puhagan wells such as PN-14, PN-19D, OK-9D, PN-23, PN-24D, PN-29D, PN-30D, PN-31D, OK-7, PN-26, PN-28, PN-16D, and PN-18D. Figure 4 shows the tracer breakthrough curve for OK-7 which had the earliest and strongest return during the PN-9RD tracer test. Coupled with interference testing and chemistry

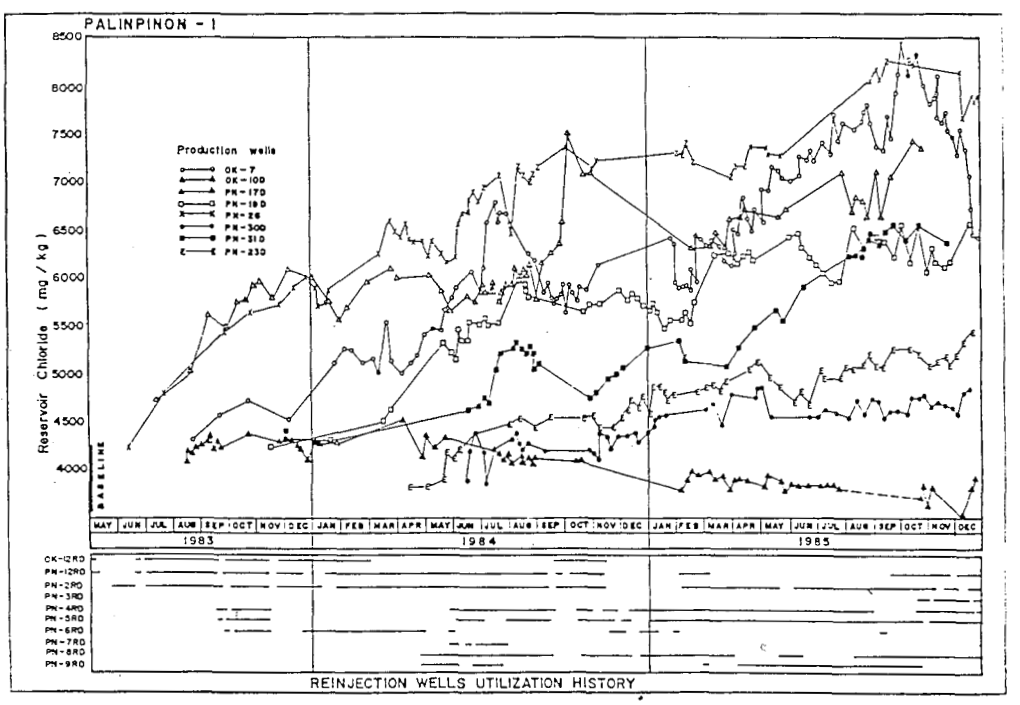

Figure 3 Reservoir Chloride vs Time

Table 1

Tracer Tests at the Palinpinon Geothermal Field

TRACER AMOUNT	RECIPIENT WELL (Inclusive Dates)	MONITORING WELLS, SPRINGS, RIVERS	R E S U L T S Positive Return	Transit Time	% Return
Iodine-131, 18.5 GBq (0.50 Ci)	OK-2 (15 Aug - 06 Sept 81)	OK-7, OK-12D, PN-13D PN-16D, OK-9D, OK-10D Ticala and Buhayan Springs	OK-7	16.0 days	0.23
			OK-12D	16.4 days	0.05
			PN-13D	16.2 days	0.10
Sodium Fluorescein 0.5 kg/test	OK-12RD (30 July - 02 Aug 83)	PN-6RD at different operating conditions	PN-6RD	.75-2.1 hours	8 - 55
Iodine-131, 20.2 GBq (0.545 Ci)	OK-12RD (03 Aug - 29 Aug 83)	OK-7, OK-10D, PN-15D, PN-17D, PN-21D, PN-26, PN-28, PN-29D, PN-3RD, PN-4RD, PN-6RD	OK-7	14.6 days	1.28
			OK-10D	13.8 days	1.35
			PN-15D	7.3 days	0.35
			PN-17D	3.9 days	8.22
				7.5 days	2.32
				10.5 days	2.52
			PN-28	6.0 days	0.58
			PN-21D	Traces on 4th and 9th day afte tracer injection	
			PN-26	Traces on 5th and 7th day afte tracer injection	
			PN-3RD	Very low traces	
			PN-4RD	Very low traces	
Sodium Fluorescein 2.0 kg	PN-1RD (28 Aug - 21 Sept 84)	OK-7, OK-9D, OK-10D, PN-15D, PN-16D, PN-17D, PN-18D, PN-19D, PN-23D, PN-24D, PN-29D, PN-30D, PN-31D, N-3, OK-2, RI 317/318, PN-3RD, PN-6RD, PN-9RD	PN-26	40.0 hours	
			PN-28	60.0 hours	
			OK-7	80.0 hours	
			OK-2	90.0 hours	
			PN-3RD	On downhole sample 27 hours after tracer injection	
			PN-6RD	On down hole sample 94 and 146 hours after injection	
			PN-9RD	On down hole sample 168 hours after injection	
Sodium fluorescein 10 kg Iodine-131, 67 GBq (1.81 Ci)	PN-9RD (26 Sept - 20 Oct 85)	OK-7, OK-9D, PN-16D, PN-17D, PN-18D, PN-19D, PN-23D, PN-26, PN-28, PN-29D, PN-30D, PN-31D RI 317/318	OK-7	5.7 days	29.20, 21.7*
			PN-29D	14.0 days	6.80, 4.6
			PN-26	11.0 days	3.90, 0.5
			PN-28	10.3 days	1.10, 0.3
			PN-18D	15.6 days	0.80, 1.6
			PN-30D	15.7 days	0.80, 1.6
			PN-23D	15.8 days	0.40, 1.6
			PN-31D	16.0 days	0.40, 1.6
			PN-16D	Tracer found in samples after 8-19 days	
			PN-19D	Tracer found in samples after 15-19 days	

*PNOC-EDC recalculated returns are in second column. Previous values for PN-26 and PN-28 believed to be erroneous due to innacurate flowrates used.

monitoring, results indicate fast interaction, too, of western injection wells PN-7RD and PN-8RD with the western and central Puhagan wells. Additional studies (PNOC-EDC, 1986) indicate that geological structures or faults are the preferred flowpaths of the reinjected fluids back to the producing wells.

From radioactive tracer testing, one can obtain the tracer breakthrough time, the peak tracer recovery time, the peak tracer concentration, and the fraction of tracer recovered. This presents an advantage over fluorescein testing where only breakthrough times and the quality (intensity) of the return were established during the test. This is why only the results of the radioactive tracer test were used for the algorithms in the optimization study as discussed later in this report.

Through this intensive chemical monitoring, tracer testing, as well as interference testing, injection and production wells with strong interactions have been identified; knowledge of which was employed to optimize the well utilization scheme. As an example, the northern and northeastern injection wells PN-2RD, PN-3RD, PN-4RD, and PN-5RD are considered "priority" in that they have exhibited minimal communications so far with the production wells. It is acknowledged that though almost all production wells produce reinjected fluid in varying proportions, the rate and magnitude of reinjection fluid returns are dependent on the combination of wells used for injection and production at any given time. It would be an advantage, therefore, to find a tool that would demonstrate or assess the interaction of a given injector/producer pair with time.

OPTIMIZATION STRATEGY

The results of the tracer tests, information on field geometry together with operating conditions were used to test algorithms in Operations Research to allocate reinjection and production rates in Palinpinon wells. These algorithms were modified by Lovekin (1987) to optimize injection scheduling in a geothermal field.

Essentially, under this strategy, the reservoir is idealized as a network of channels or arcs connecting each pair of wells in the field. The arc cost, c_{ij}, expresses the likelihood of thermal breakthrough resulting from the movement of a unit fluid from injection i to producer j. It consists of weighting factors which are taken from tracer return data, field geometry and field operating conditions as shown by Equation 1.

$$c_{ij} = \frac{1}{t_i}\,\frac{1}{t_p}\,C_p \cdot f \cdot \frac{1}{L^2}\,e^{sh} \cdot \frac{q_p}{q_{pt}}\,\frac{1}{q_{rt}} \qquad (1)$$

where

t_i = initial tracer response, days
t_p = peak tracer response, days
C_p = peak tracer concentration, t^{-1}
f = fractional tracer recovery
L = horizontal distance between wells, meters
h = elevation difference between production and injection zones, meters
s = scaling factor
q_p = producing rate under operating conditions
q_{rt} = injection rate during tracer testing

The results of the tracer tests demonstrate that the earlier the breakthrough or initial tracer response, the greater the tracer return, and the greater the likelihood for thermal breakthrough. Hence, the times of initial (t_i) and peak (t_p) tracer response are made to be inversely related to the arc cost c_{ij}. In contrast, the fraction of tracer recovered (f) and the peak tracer concentration (Cp) are made linear to the arc cost.

For a porous-media type of reservoir, the thermal recovery of injected fluid depends on the heat exchanged between the fluid and the rocks. Since this rock surface heat area is proportional to L^2, then the probability of thermal breakthrough is greater for smaller surface area. This means an inverse relationship between L^2 and the arc cost. The elevation difference (h) between the producing and injecting zone is made linear to the arc cost due to the fact that injected fluid, being cooler and denser would tend to sink down the reservoir. Hence, it is intuitive that a deep producing well would have a higher chance of communicating with an injection well, than a shallow producing well would. Since h could be positive (producing zone below the injection zone) or negative, it appears in the equation as an exponential term e^{sh}, with a scaling factor s to keep it from dominating the rest of the weighting factors.

In a similar manner, producing and injecting rates during the tracer tests (q_{pt} and q_{rt}), can also be made as weighting factors. A well which produces at a small rate and manifests positive tracer return would have a higher likelihood of being affected by injection returns than another well which is producing at a higher rate with similar returns. Therefore, q_{pt}, and with the same logic, q_{rt}, are inversely related to the arc cost.

It is to be emphasized that all the factors need not be used to get the arc costs. Some factors could be deleted, and others weighed or included depending on which ones the developer deem to be important on the basis of reservoir behavior and information.

The sum of the arc costs from a particular injection well to all the producing wells is its cost coefficient. The unknown or decision variable is the reinjection rate, q_{ri}, into injection well i. The product of the injection rate and the arc cost is the breakthrough index for the specific arc or injection/production pair of wells as expressed by Equation 2.

$$b_{ij} = c_{ij} q_{ri} \qquad (2)$$

The summation of breakthrough indices for all arcs is then the fieldwide breakthrough index B. Under the optimization strategy, it is this index which is the objective function that has to be minimized subject to well capacities and field operating constraints.

Two algorithms were used for optimization strategy:
1) linear programming which employs the simplex method, and
2) quadratic programming

Linear Programming

In the linear programming algorithm, the objective functions to be minimized are shown by Eqs. 3 and 4.

Minimize:

$$B_1 = \sum_{i=1}^{N_1} \sum_{j=1}^{N_2} c_{ij} q_{ri} \qquad (3)$$

subject to

$$q_{ri} \le q_{rimax}$$
$$\Sigma\, q_{ri} = Q_{rtot}$$
$$q_{ri} \ge 0 \qquad i = 1, N_1$$

Minimize:

$$B_2 = \sum_{i=1}^{N_1} \sum_{j=1}^{N_2} c_{ij} q_{pj} \qquad (4)$$

subject to

$$q_{pj} \le q_{pjmax}$$
$$\Sigma\, q_{pj} = Q_{ptot}$$
$$q_{pj} \ge 0 \qquad j = 1, N_2$$

where N_1 = number of injectors
N_2 = number of producers
q_{ri} = injection rate into well i
q_{pj} = producing rate from well j
q_{rimax} = maximum permissible rate into well i
q_{pjmax} = maximum permissible rate from well j
Q_{rtot} = total required injection rate
Q_{ptot} = total required producing rate

In this algorithm, the mutual dependence of injection and production rates is accounted for by alternately exchanging their roles as decision variables and weighting factors.

Quadratic Programming:

On the other hand, the formulation for the second algorithm is shown by Equation 5.

Minimize:

$$B = \sum_{i=1}^{N_1} \sum_{j=1}^{N_2} c_{ij} q_{ri} q_{pj} \qquad (5)$$

where the variables and constraints are the same and combined as in the first formulation. In this approach, the interdependence of injection and production rates is explicitly acknowledged by treating both as decision variables and including them in the objective function as a product. Hence, the objective function becomes a quadratic and the problem is solved by a quadratic programming (QP) solver.

Preliminary Results Using Tracer Return Data

The results of the two radioactive tracer tests shown in Table 1 were used in the above algorithms. Specifically, the mean transit recovery time, the fraction recovered, the aerial and vertical separation between the injection and production pair of wells, the flowrates during the tracer tests, as well as the maximum flowrates of all the wells were used as input in the algorithms. In this test, it was assumed that only OK-12RD and PN-9RD are the reinjection wells. The problem calls for allocating the

Table 2

Allocation of Production Rates Among Palinpinon Wells Using Linear (LPAL) and Quadratic Programming (QPAL)

Qrtotal = 260 kg/s; Qptotal varies

L P A L 3						Q P A L		
Qptotal kg/s	Injectors	Qrinjected kg/s	Curtailed Producers	Qpcurtailed kg/s	Cost Coefficients	Injectors	Curtailed Producers	Qpcurtailed kg/s
930	OK-12RD	165	OK-7	Total	0.099200	OK-12RD	OK-7	Total
	PN-9RD	95	PN-17D	Total	0.046800	PN-9RD	PN-17D	Total
			PN-26	Total	0.013900		PN-26	Total
			PN-28	Total	0.009600		PN-28	Total
			PN-29D	Total	0.003900		PN-29D	Total
			PN-18D	3	0.003200		PN-18D	3
900	OK-12RD	165	OK-7	Total	0.099200	OK-12RD	OK-7	Total
	PN-9RD	95	PN-17D	Total	0.046800	PN-9RD	PN-17D	Total
			PN-26	Total	0.013900		PN-26	Total
			PN-28	Total	0.009600		PN-28	Total
			PN-29D	Total	0.003900		PN-29D	Total
			PN-18D	33	0.003200		PN-18D	33
850	OK-12RD	165	OK-7	Total	0.099200	OK-12RD	OK-7	Total
	PN-9RD	95	PN-17D	Total	0.046800	PN-9RD	PN-17D	Total
			PN-26	Total	0.013900		PN-26	Total
			PN-28	Total	0.009600		PN-28	Total
			PN-29D	Total	0.003900		PN-29D	Total
			PN-18D	Total	0.003200		PN-18D	Total
			OK-10D	19	0.001000		OK-10D	19
800	OK-12RD	165	OK-7	Total	0.099200	OK-12RD	OK-7	Total
	PN-9RD	95	PN-17D	Total	0.046800	PN-9RD	PN-17D	Total
			PN-26	Total	0.013900		PN-26	Total
			PN-28	Total	0.009600		PN-28	Total
			PN-29D	Total	0.003900		PN-29D	Total
			PN-18D	Total	0.003200		PN-18D	Total
			OK-10D	Total	0.001000		OK-10D	Total
			PN-31D	17	0.000640		PN-31D	17
750	OK-12RD	165	OK-7	Total	0.099200	OK-12RD	OK-7	Total
	PN-9RD	95	PN-17D	Total	0.046800	PN-9RD	PN-17D	Total
			PN-26	Total	0.013900		PN-26	Total
			PN-28	Total	0.009600		PN-28	Total
			PN-29D	Total	0.003900		PN-29D	Total
			PN-18D	Total	0.003200		PN-18D	Total
			OK-10D	Total	0.001000		OK-10D	Total
			PN-31D	Total	0.000640		PN-31D	Total
			PN-15D	2	0.000300		PN-15D	2
700	OK-12RD	165	OK-7	Total	0.099200	OK-12RD	OK-7	Total
	PN-9RD	95	PN-17D	Total	0.046800	PN-9RD	PN-17D	Total
			PN-26	Total	0.013900		PN-26	Total
			PN-28	Total	0.009600		PN-28	Total
			PN-29D	Total	0.003900		PN-29D	Total
			PN-18D	Total	0.003200		PN-18D	Total
			OK-10D	Total	0.001000		OK-10D	Total
			PN-31D	Total	0.000640		PN-31D	Total
			PN-15D	52	0.000300		PN-15D	52
650	OK-12RD	165	OK-7	Total	0.099200	OK-12RD	OK-7	Total
	PN-9RD	95	PN-17D	Total	0.046800	PN-9RD	PN-17D	Total
			PN-26	Total	0.013900		PN-26	Total
			PN-28	Total	0.009600		PN-28	Total
			PN-29D	Total	0.003900		PN-29D	Total
			PN-18D	Total	0.003200		PN-18D	Total
			OK-10D	Total	0.001000		OK-10D	Total
			PN-31D	Total	0.000640		PN-31D	Total
			PN-15D	Total	0.000300		PN-15D	Total
			PN-30D	30	0.000095		PN-30D	30

production rates among the different wells as the required total production rate decreases from 930 kg/s.

The results as shown by Table 2 indicate that the two approaches or algorithms give similar results. As the required total field load decreased, the producing rates was reduced and production wells were shut in one-by-one depending on its potential damage to the field as manifested by the injector/producer cost coefficient. The higher the cost coefficient, the more serious is the potential for thermal breakthrough. However, these cost coefficients which enable the explicit ranking of the wells are present only in the linear programming algorithm. Nevertheless, as seen from Table 2, the actual allocations provided by quadratic programming duplicate those of linear programming.

It can be concluded, therefore, that by knowing the arc costs, the programs obtain the optimal rate allocation for both injection and production wells.

USE OF CHLORIDE DATA

Due to economic and operational constraints, radioactive tracer cannot be injected into every reinjection well. Similarly, not all the production wells can be monitored during a tracer test. To find another parameter which can be used to optimize reinjection strategy, attention was turned to the reservoir chloride measurement of the production wells as shown by Figure 3. It has been established by the PNOC geochemists that the chloride values of a producing well can be used as an indication

of the extent of reinjection returns to this well. The correlation or strength of the relationship between the chloride of a producing well and the flowrate of an injecting well was obtained in four different ways. Figure 4 shows in graphical form the different methods used to correlate the chloride values of a production well with the injection flowrates of an injection well. It should be remembered when comparing, that these numbers represent a relative assessment of the producer/injector pair potential for thermal breakthrough.

1. First, the correlation between the chloride value with time of a production well and the mass flowrate with time of an injection well was obtained (Figure 4a).

2. Second, the correlation between the chloride value with time of a production well and the total mass flowrate with time of an injection well was calculated (Figure 4b).

3. Third, the correlation between the deviation of the chloride value of a production well from the best fit line and the flowrate rate of an injection well was computed (Figure 4c).

4. Lastly, the chloride value with time of a production well was expressed as a linear combination of the mass flowrates of the injection wells.

The first method (Figure 4a) of chloride-flowrate correlation stems from the observation that the chloride values of a production well are affected when particular injection wells are disconnected from or hooked on line. If an injection well communicates strongly with a production well, then putting this injection well on line is usually followed by a substantial increase in the chloride measurements of the affected well. Once it is removed from service, there is an accompanying decrease in the chloride data of the producing well.

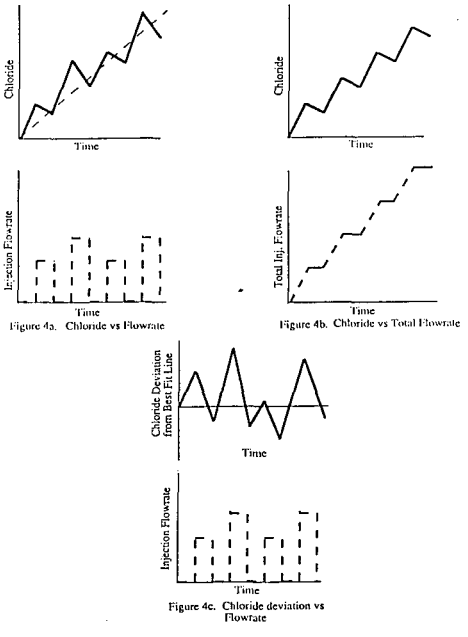

Figure 4a. Chloride vs Flowrate

Figure 4b. Chloride vs Total Flowrate

Figure 4c. Chloride deviation vs Flowrate

Figure 4 Chloride vs Flowrate Correlation Methods

In the second method (Figure 4b), what is examined is the relationship between chloride and the total flowrate. Since the chloride value of a production well at a particular time is the cumulative effect, it is reasonable to see the relationship between this chloride value and the total flowrate of the injection well. Given the hypothetical case of an injection well affecting strongly a production well, the plots of the two variables with time would be similar to Figure 4b.

On the other hand, it is also desirable to examine the relationship between the magnitude of the increases in chloride value of a production well with the flowrate of an injection well. Going back to the hypothetical case, it would be logical to expect that the effect of a high injection rate would be a greater step change in the chloride value of the production well. The magnitude of this change is measured by the deviation of the chloride value from the best fit line and this deviation is then correlated with the injection flowrate at that time (Figure 4c).

The effect of a particular injection well on a certain production well can be concluded unambiguously only when all other factors are held constant (such as injection flowrates of other injection wells and producing rates of all other wells are unchanged). This is complicated by the fact that a single injection well could interact with more than one production well. As a consequence, the net effect on a production well at a particular time interval would be due to the effects of the particular injection wells which were active in the same time interval. To take this into account, the last method seeks to express the chloride value of the production well as a linear combination of the injection flowrates of all the active reinjection wells at the concerned time. This is illustrated by Equation 6.

$$Cl_i = a_o + \sum_{j=1}^{n} a_j q_j \qquad (6)$$

where Cl_i = chloride value of well i at time t
a_o = initial chloride value at time t
a_j = correlation coefficient between production well i and injection well j
q_j = mass flowrate of injection well j
n = number of injection wells

The system of linear equations is put in matrix form and then solved simultaneously by a matrix solver like the Gauss-Jordan method of elimination.

Results of the Chloride Data Methods

The plots of the first three chloride methods are shown in Figures 5 to 12 using the wells OK-7, PN-9RD, PN-28 and PN-2RD. The first method is demonstrated by Figures 5 and 6, the second by Figures 7 and 8, and the third by Figures 9 and 10. Figures 11 and 12 have been included for comparison.

Figure 5a reflects the increase in monthly chloride values of well OK-7 and Figure 5b shows the monthly injection flowrates of PN-9RD. For an injector/producer pair with strong communication, it has been observed that the crests and troughs of the injection plot usually coincide with those of the producing well. This is reflected in high correlation coefficients during these times as

demonstrated by Figure 6a. In this case, this would infer and confirm that there is good communication between OK-7 and PN-9RD. Figure 6b exhibits the effect if the correlation is calculated with a shift in time of the chloride values of OK-7. This was done to accommodate the reasoning that the increase in chloride value is an effect, and that there could be a lag or delay in the response of the producing well. In spite of the shift, the general trend of the correlation plot remains the same.

Figure 7b shows the plot of the cumulative flowrate with time of PN-9RD. The correlation with time of the chloride data with total rate shown in Figure 8 remain remarkably high throughout. The same pattern has been demonstrated by the rest of the OK-7/injection well pairs. The other plots of producing/injecting pairs show that the general trend for a particular production well remains the same with almost all the injection wells. This would indicate that this method can not be used to assess and differentiate the relationship between a producer and an injector.

Figure 9a is the same plot of OK-7 monthly chloride but with the dashed line representing the linearly regressed line to this curve. The deviations from this best fit line are plotted in Figure 9b and the correlation between the deviation and injection rate is shown in Figure 10. It can be seen that this plot of Figure 10 (Cldev-flowrate) and that of Figure 6 (Cl-flowrate) are similar.

Figures 11a and 11b show the chloride values of PN-28 and the flowrates of PN-2RD. These are correlated and the results plotted in Figure 12. One would note that the correlation values remain negative implying a lesser degree of interaction or communication between PN-28 and PN-2RD. When Figure 12 is compared with that of Figure 6, both being chloride-flowrate correlation, the immediate disparity in the relationship between OK-7/PN-9RD and PN-28/PN-2RD can be concluded.

Table 3 gives a tentative summary of the coefficients obtained from the four chloride methods. The method of chloride-total rate correlation (the second method) has been disregarded and, therefore, not included in this tabulation. For the linear combination method, the table only shows the correlation taken for the whole data set. For the chloride-rate correlations, the numbers chosen were either the average or those taken at the time the injection well has stopped injecting. The table shows:

1) In slightly more than half of the tabulated results, the calculated chloride-flowrate correlation is similar and very close to that of the chloride deviation-flowrate correlation. When only the signs of the correlation are compared, this increases to about 70%.

2) In general, the relationship shown by the linear combination coefficients agree with the observed relationships. For example, there is a high coefficient of correlation of OK-7 and PN-26 with PN-9RD, PN-8RD, and PN-1RD.

The limitation imposed by the two chloride-rate correlation methods (first and third) as shown by the dashed line is due to the fact that during the time considered the reinjection well was not injecting. Similarly, the linear combination method fails when the matrix is singular and no solution to the system of linear equations can be found.

A detailed study is ongoing and there is a need to examine the criteria for choosing which numbers best represent the relationship of injector/producer pair.

SUMMARY AND CONCLUSIONS

The tracer return data, together with field geometry and operating conditions have been used to allocate production and injection rates among the Palinpinon wells using algorithms in Operations Research.

The theory behind the optimization strategy is that the reservoir can be visualized as a network of arcs connecting injector to producer. Each arc has a potential for thermal breakthrough caused by fluid flow from injector to producer and this potential is measured by the arc cost. The methods for optimization make use of linear programming and quadratic programming where the objective function to be minimized is the fieldwide breakthrough index defined to be the product of the arc cost and the flowrate.

The results of allocation are the same for both linear and quadratic programming. However, cost coefficients which provide a ranking of the injector/producer pair according to the potential for thermal breakthrough is provided only in linear programming.

Chloride was examined as another parameter for optimization since it has been observed to be an indicator of the extent of reinjection returns to a producing well. Four different methods of finding the correlation between the chloride value and the flowrate were examined. In general, there has been agreement between the chloride-rate correlation and the chloride deviation-rate correlation. The linear combination method also shows encouraging signs. However, there is a need to examine the factors behind the disparities in the results. Nevertheless, the initial results of the study have been encouraging and points out that the correlation between chloride and flowrate can be used as arc costs in optimizing production and reinjection strategy.

REFERENCES

1. Lovekin, J., and Horne, R.N.: "Optimization of Injection Scheduling in Geothermal Fields," G.R.C. Transactions, 11, 1987.

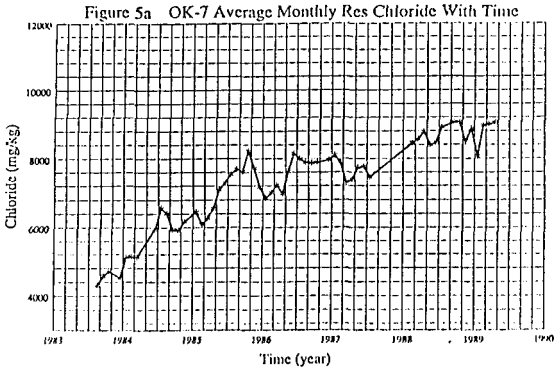

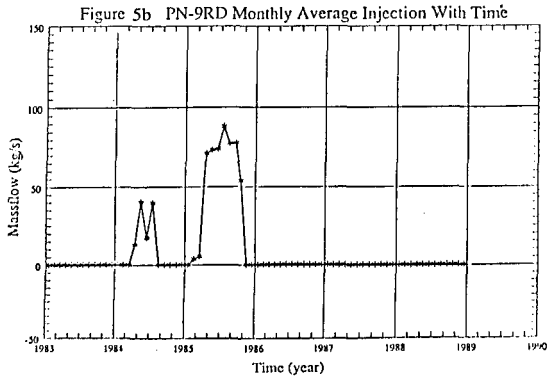

Figure 5 OK-7 Chloride and PN-9RD Flowrate

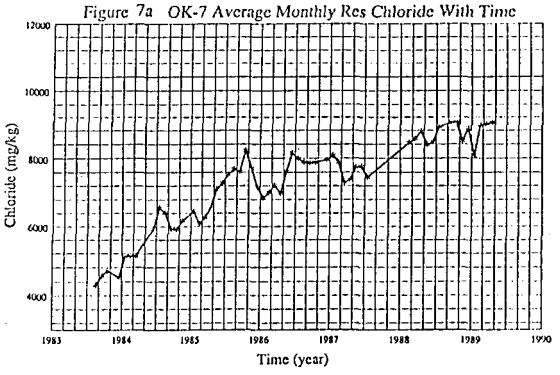

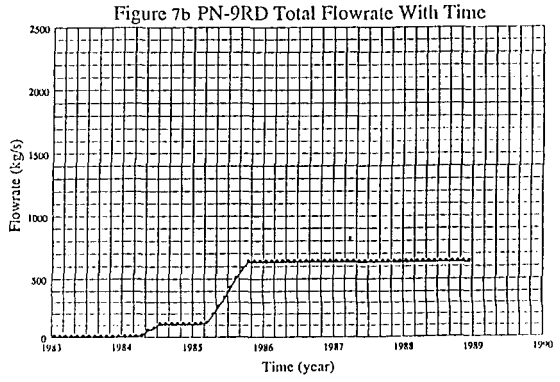

Figure 7 OK-7 Chloride and PN-9RD Total Flowrate

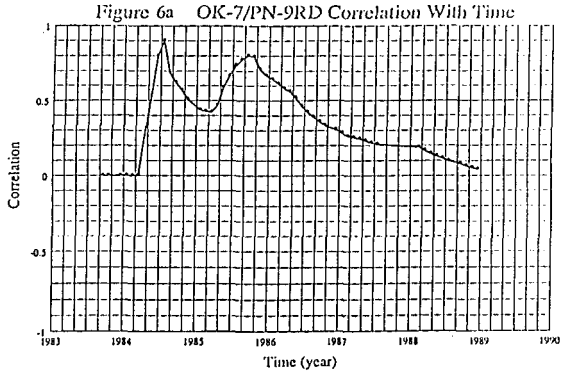

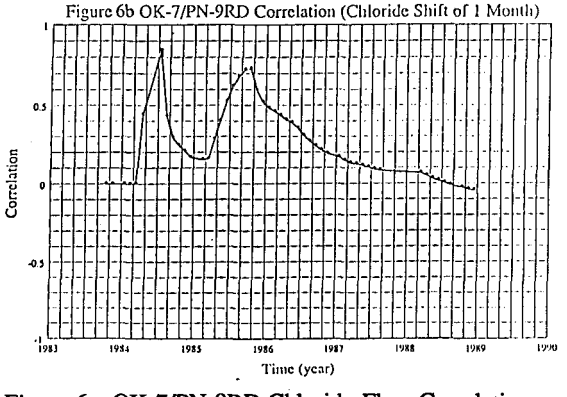

Figure 6 OK-7/PN-9RD Chloride-Flow Correlation

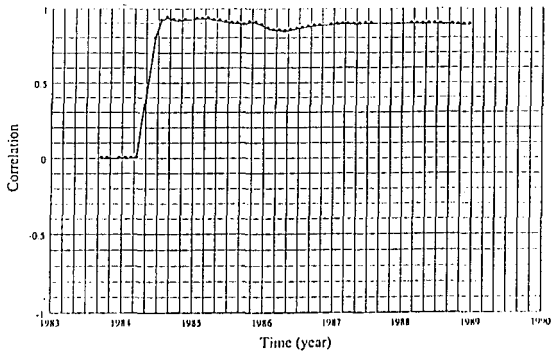

Figure 8 OK-7/PN-9RD Cl-Total Fow Correlation

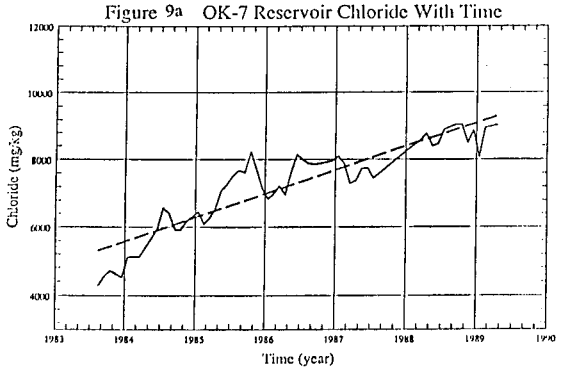

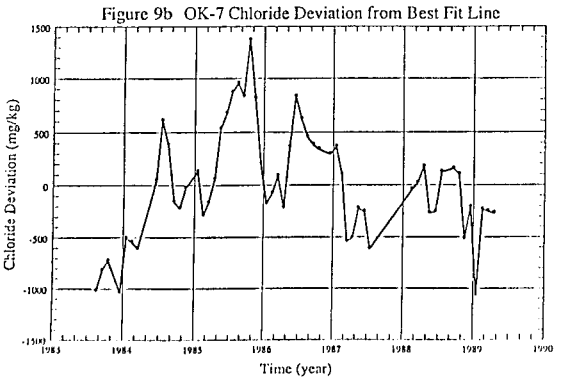

Figure 9 OK-7 Chloride and Deviation

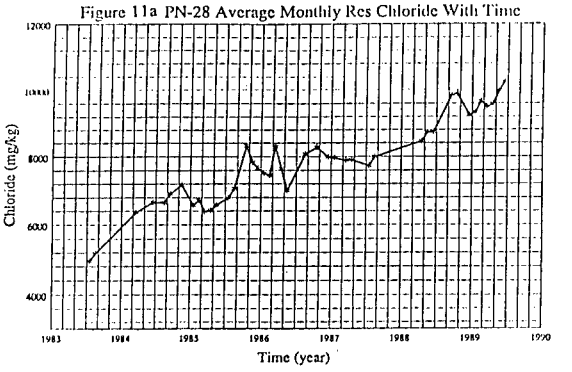

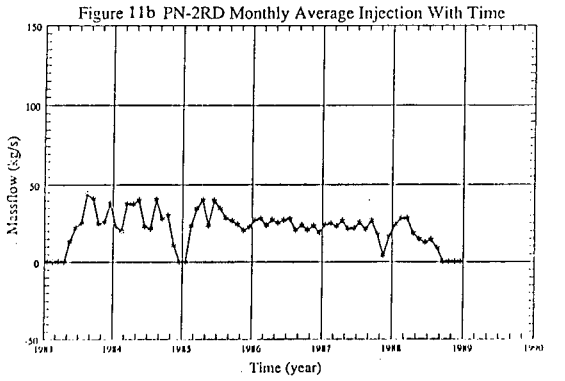

Figure 11 PN-28 Chloride and PN-2RD Flowrate

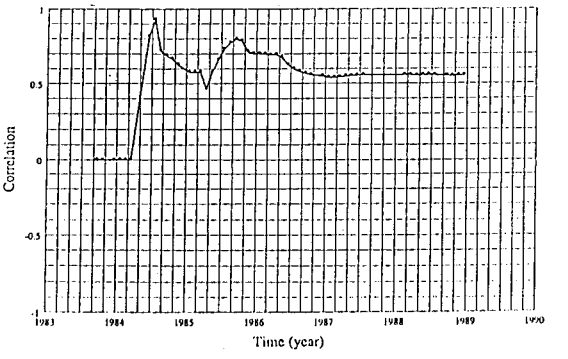

Figure 10 OK-7/PN-9RD Cldeviation-Flow Correlation

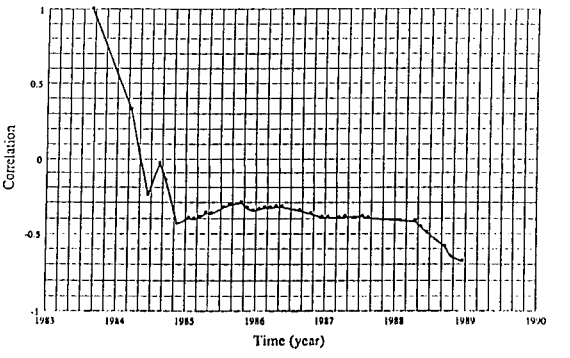

Figure 12 PN-28/PN-2RD Chloride-Flow Correlation

Table 3
Summary of Chloride - Flowrate Correlation

		REINJECTION WELLS								
PRODUCTION WELL	METHOD	PN-1RD	PN-2RD	PN-3RD	PN-4RD	PN-5RD	PN-6RD	PN-7RD	PN-8RD	PN-9RD
OK-10D	Cldev-Flow Corr	0.4320	-0.1310	-0.2740	-0.3800	-0.5690	0.3240	0.3590	-0.0330	-0.3910
	Cl-Flow Corr	0.3420	-0.2850	-0.0600	-0.3520	-0.4560	0.3320	0.4190	-0.0400	-0.3890
	Linear Comb Coeff	4.0440	-11.5100	1.7370	2.8710	-7.6590	4.1940	5.2960	2.6470	1.8320
OK-7	Cldev-Flow Corr	-0.1650	-0.1580	0.0270	0.4680	0.6140	-0.5050	0.9300	0.8160	0.9260
	Cl-Flow Corr	-0.4840	-0.4110	0.6370	0.4600	0.7790	-0.1310	0.9050	0.3730	0.9000
	Linear Comb Coeff	11.9300	-21.9200	28.5600	5.0000	11.2100	8.1530	-6.8300	20.9400	29.3800
PN-15D	Cldev-Flow Corr	0.2420	0.1510	-0.4720	-0.6670	-0.5340	0.3950	-0.4150	-0.5100	-0.7190
	Cl-Flow Corr	-0.2660	-0.5452	0.6250	0.5820	0.7840	0.3470	0.2620	0.5110	0.3040
	Linear Comb Coeff	12.9800	-19.0200	37.1400	-1.5330	-6.5890	5.3900	-0.2979	11.0600	0.2206
PN-26	Cldev-Flow Corr	0.0910	-0.1440	0.3050	0.3010	0.5460	-0.2830	0.7950	0.4000	0.5000
	Cl-Flow Corr	0.1150	-0.1260	0.7550	0.4520	0.5380	-0.3860	0.8010	0.1910	0.4730
	Linear Comb Coeff	9.4090	-14.7200	25.2200	5.4490	5.4950	7.6020	-6.2060	21.3000	17.0900
PN-28	Cldev-Flow Corr	0.4480	-0.1720	-0.0130	-0.0590	-0.0640	0.2230	0.5000	-0.2130	-
	Cl-Flow Corr	-0.0190	-0.4050	0.6790	0.5600	0.5320	0.2670	0.7470	-0.2010	-
	Linear Comb Coeff	9.7210	-8.9670	22.6100	-4.6030	15.1300	8.7520	-1.4170	-0.3865	-
PN-30D	Cldev-Flow Corr	-0.0840	-0.2100	-0.1630	0.0040	-0.1020	0.1720	-	-0.2130	-
	Cl-Flow Corr	-0.0900	-0.2470	-0.1620	-0.0640	-0.1020	0.1950	-	-0.2010	-
	Linear Comb Coeff	1.0040	-7.3590	4.7760	7.5970	-5.4280	1.7240	-	-0.3865	-

PROCEEDINGS, Sixteenth Workshop on Geothermal Reservoir Engineering
Stanford University, Stanford, California, January 23-25, 1991
SGP-TR-134

Modifications to TOUGH and Analysis of Build-up Data of PTS (Pressure/Temperature/Spinner) Logging in a Two-phase Condition

Okabe, T., Osato, K. and Takasugi, S.

Department of Technology, Geothermal Energy Research and Development Co., Ltd., 11-7, Kabuto-cho, Nihonbashi, Chuo-ku, Tokyo 103, Japan

Abstract

The original version of TOUGH(Pruess, 1987) requires a large amount of CPU time for large 2D or 3D problems. This has prevented us from using the original TOUGH on several actual field simulations. Therefore, we have modified the original TOUGH to make less CPU time and allow us to use new TOUGH on large problems. For reducing the CPU time, two new matrix inversion methods were implemented on the original TOUGH.

In this report, first we summarize new matrix inversion method implemented in new TOUGH and second we show inspection results of the accuracy and improvements of speed, and then we show the case study results. Before conducting this case study, the porous medium model for the case study is optimized. As the case study we tried to analyze build-up data acquired by PTS (Pressure/Temperature/Spinner) logging in a two-phase condition. We have been successful in obtaining a good match to PTS data.

1. Introduction

1-1. Modifications to TOUGH

Modifications to TOUGH were done in cooperation with the New Zealand Department of Scientific and Industrial Research(DSIR) (White, 1990). The aims of the modifications are

- to reduce CPU time needed to solve problems and
- increase the number of elements that could be included in TOUGH simulations.

These aims were motivated by the desire to perform the actual field simulation described later in this report. For achieving these aims, two new matrix inversion methods were made available in new TOUGH. One method is a direct one to solve Jacobian matrix for 1D problems such as a single layer and radial flow problem, and the other is a modified Successive Over Relaxation(SOR) method, intended for use on 2D and 3D problems with a large number of elements.

As assessment of new TOUGH, two aspects have been assessed, the accuracy and the speed improvement. To inspect the accuracy, Garg's model as specified in the TOUGH user's guide was used. And to inspect the speed improvement, 1D, 2D and 3D model were used.

1-2. Analysis of Build-up Data

Build-up data are obtained from either PTS logging or pressure monitoring, in most cases. For analysis of build-up data, in the single-phase case, we can use pressure transient test analysis software such as "Multi-Rate Multi-Well" simulator(Schroeder et al., 1984). The assumptions made in this kind of simulator are that the reservoir is unbounded (no closed or constant pressure boundaries laterally), isotropic (flow independent of direction) and confined above and below (no leakage). Since we use an "Early Time Analysis" option, the reliability of the results is excellent. If two-phase conditions occur in the reservoir, it is necessary to use a reservoir simulator like TOUGH. We also found that the wellbore simulator(for instance,Miller, 1984) is useful in both single-phase and two-phase cases.

Before analyzing build-up data, the model for new TOUGH was optimized. The model assumes 1D radial flow, and includes the well block. Optimization involved the construction of fine grids near the well, and consideration of the build-up response. And we tried to match with the actual PTS data obtained by PTS logging in Japan.

2. Modifications to TOUGH, and Assessment

2-1. Modifications to TOUGH

We ran the original TOUGH under a profiler to detect the areas of the code that would most benefit from modification. As a result, in case of problems with a few elements(ex. 1D model) almost 70 % of the CPU time is spent calculating thermodynamic properties of water and steam and in case of problems with large number of connections between elements(ex. 2D or 3D model) almost 80 % of the CPU time is spent on matrix inversion.
Here regarding numerical equation solved by TOUGH, the mass and energy balance equations(1) can be discretized in space using the integral finite difference method and time derivatives are approximated using a fully implicit first rder method. Then the mass and energy balance equations can be reduced to a set of nonlinear algebraic equations(2).

$$\frac{t}{dt}\int_{V_n} M^{(\kappa)} dv = \int_{\Gamma_n} F^{(\kappa)} \cdot n \, d\Gamma + \int_{V_n} q^{(\kappa)} dv \qquad (1)$$

where

V_n : an arbitrary flow domain

Γ_n : area of V_n

$M^{(\kappa)}$: a volume-normalized extensive amount of component κ per unit volume

$F^{(\kappa)}$: flux of component κ

$q^{(\kappa)}$: sink and source of component κ per unit volume

κ : water, air, heat

$$R_n^{(\kappa)k+1} \equiv M_n^{(\kappa)k+1} - M_n^{(\kappa)k} - \frac{\Delta t}{V_n}\{\Sigma A_{nm} F_{nm}^{(\kappa)k+1} + V_n q_n^{(\kappa)k+1}\} \qquad (2)$$

where

$R^{(\kappa)k+1}$: residual form

A_{nm} : interface areas

$F_{nm}^{(\kappa)k+1}$: flux of component κ

The subscripts(nm) mean that the respective quantities are to be evaluated at the interface between volume elements n and m.

k labels the time step and $\Delta t = t^{k+1} - t^k$.

Above-mentioned equations are presented in more detail in the TOUGH user's guide.

For a system that has N grid blocks that is a set of nonlinear equations in the 3N primary variables. Because for each volume element there are three primary variables(Single-phase: Pressure, Temperature, Air mass fraction ; Two-phase: Pressure, Gas saturation, Temperature). To solve nonlinear equations we perform Newton Raphson iteration.

Denoting the primary variables at time k+1 as $x_1 \cdots x_{3N}$ the Newton Raphson iteration is

$$x^{i+1} = x^i - J^{-1} R^{k+1}(x^i) \qquad (3)$$

J is the Jacobian matrix of the system $J = \partial R_i^{i+1} / \partial x_i$
This 3N*3N sparse Jacobian matrix dominates the CPU time for most problems. This matrix inversion is normally done using the Gaussian elimination. But by exploiting properties of the matrices, the CPU time to solve problems becomes faster than the Gaussian elimination. Then we have made available two new matrix inversions to it. One is a generalized Thomas algorithm for tri-diagonal matrices which is only applicable for 1D problems. The other is an iterative method to solve (3). Figure 1. shows the typical structure of Jacobian matrices for 1, 2 and 3D problems.

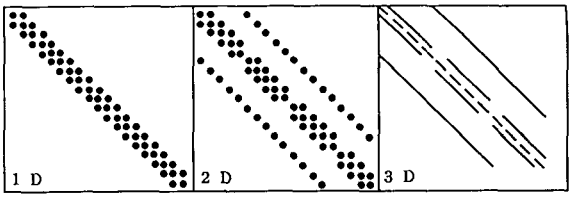

Figure 1. Some different structures

In order to use an iterative solution technique for (3), we used a modified Successive Over Relaxation(SOR) method. If J = D - U - L, the conventional SOR method to solve the problem Jx = R is defined as

$$(D - \omega L) x^{m+1} = ((1-\omega) D + \omega U) x^m + R) \qquad (4)$$

where

D : diagonal mtrix

U : strictly upper triangular matrix

L : strictly lower triangular matrix

As equation (4) is not suitable for Jacobian matrices generated by TOUGH, there is no guarantee that at all the diagonal elements are non zero. As a counter-measure, the equation (4) is modified to premultiply (4) by the inverse of the block diagonal matrix formed from the 3*3 matrices on the diagonal J.

$$(I-\omega L')\,x^{m+1} = ((1-\omega)I+\omega U')\,x^{m}+R' \qquad (5)$$

The matrix

$$\mathcal{L}_\omega = (I-\omega L')^{-1}((1-\omega)I+\omega U') \qquad (6)$$

is called the point Successive Over Relaxation matrix.

And optimum omega value is given below.

$$\omega = 2/(1+\sqrt{1-\mu^2}) \qquad (7)$$

μ is the largest eigenvalue of (L'+U') which is accompanied with property A matrix(which is referred by Young, 1954). A matrix with this property can be transformed by a permutation matrix and thus transformed Jacobian matrix is shown in Figure 2. for example. But if this Jacobian matrix does not have the property A, it may be fail to converge. And also it may be problem that the cases are consist of polygonal elements because one may not be able to transform in this way.

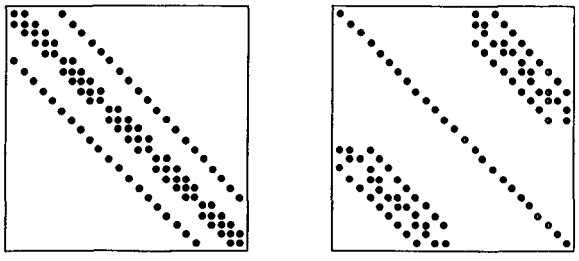

Figure 2. Permutations of the Jacobian Matrix for 2D Problem

As a further work, SUPST and COWAT in the code for thermodynamic routines were rewritten to remove all unnecessary array references and many of the large exponentiation. Consequently SUPST and COWAT was 40 - 70 % faster than the original.

2-2. Assessment of new TOUGH

(1) Accuracy

To verify accuracy, Garg's model as specified in the TOUGH user's guide was used. Figure 3.(a) shows the results of this calculation. New and original TOUGH are in good agreement with each other, and also match Garg's semi-analytical theory. The new TOUGH was 1.9 times faster than original TOUGH.

In the 1980 Stanford Geothermal Workshop, there was a DOE comparison of existing geothermal simulators and analytical solutions. We have compared new TOUGH with these reported results. Figure 3.(b) shows the results of this comparison in enthalpy, for two-phase radial flow in a porous medium.

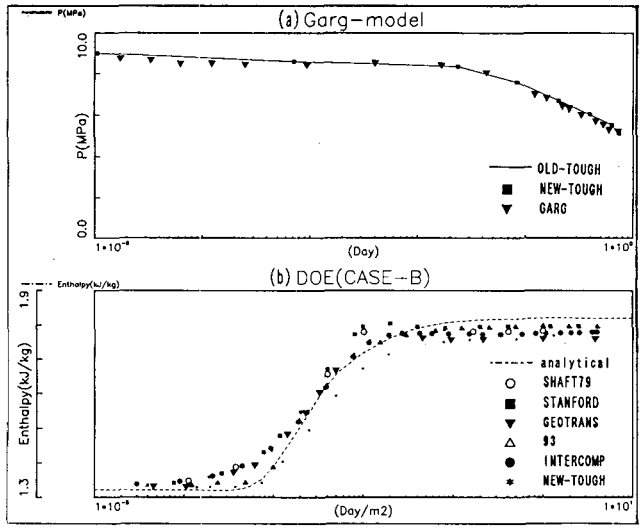

Figure 3. Comparison of NEW TOUGH with Garg's Model and DOE (Case-B)

(2) Speed

A comparison of CPU time is shown in Table-1. A speed improvement is observed, with simulations being 1.9 times faster for the 1D problem, 1.5 times faster for 2D problem and 23 times faster for 3D problem. The nature of the problems simulated is indicated in Table-1.

Table-1. Comparison of CPU Time

Dimension	Elements	Connections	CPU Time (sec)			Remarks
			Original	New	Ratio	
1 D	50	49	215.9	114.4	1.89	Garg's Model
2 D	164	289	348.4	224.3	1.55	2D Infiltration Problem
3 D	196	459	2076.6	89.9	23.10	Cubic Model

3. Analysis of Build-up Data of PTS Logging in a Two-phase condition

3-1. PTS Data and Analysis

PTS logging has been available for five years, and has been used in many geothermal regions in Japan. The quality of PTS data is excellent, and the analysis of such data is very useful for reservoir evaluation. Methods for analyzing PTS data are mentioned in Introduction.

3-2. Optimization of the Model

Before running the case study we optimized the grid used to model the area surrounding the well.

We assume radial flow in a uniform porous medium towards a well of radius 0.2 meters.

The initial grid consisted of a well block, 500 equal thickness(1 meter) cylindrical blocks followed by 100 elements of gradually increasing thickness.

This grid was optimized in the following way.

(1) Calculation of drawdown and confirmation of boiling front

Using the initial grid, pressure drawdown was calculated and the presence of a boiling front was confirmed. The grid was then refined out as the boiling front and the calculation repeated.

Figure-4a and -4b show pressure and temperature curves after 20 days production for various block thickness. As can be seen the boiling front lies between 1.75 and 2 meters from the well block.

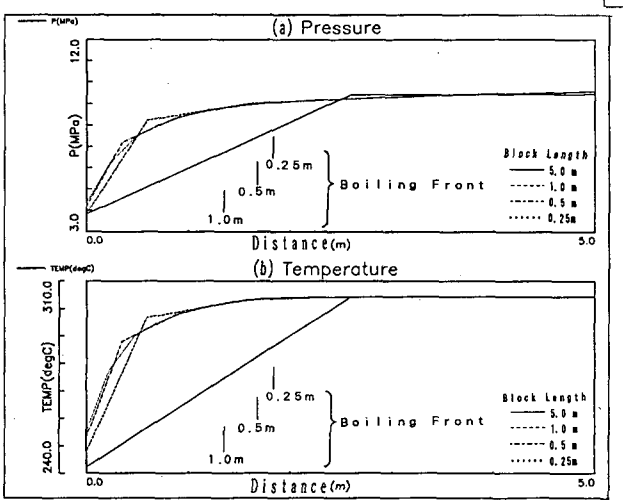

Figure 4. Draw-Down Curves for Various Block Length

Refining the grid around the well smooths the curves out to the boiling front but has little effect past the front.

The temperature and pressure calculated using the finest grid were used as initial conditions for the pressure build-up calculation.

(2) Calculation pressure and temperature build-up, and confirmation of convergence

Figure 5. shows pressure and temperature curves for various block sizes 8,000 seconds after well shutdown. As block size is reduced these curves converge to a limit. It is apparent from these curves that there is little benefit in reducing the block size below 0.5 meters.

Then 0.5 meters block size model is used as an optimized model for the case study.

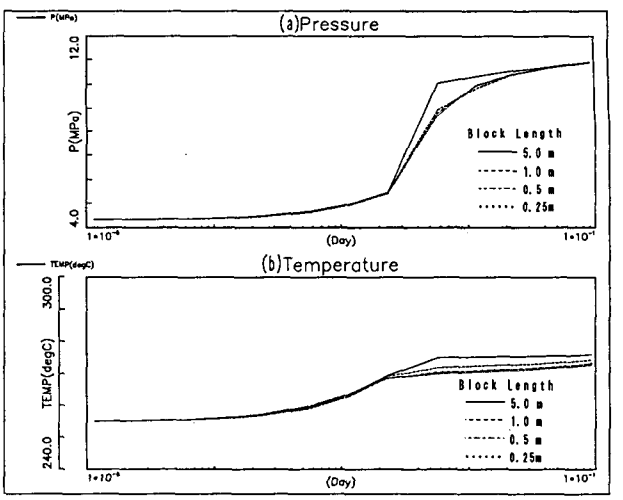

Figure 5. Build-up Curves for Various Block Length

3-3. Case Study

Data used in this case study was acquired by PTS logging in Japan. At that time the well was in a two-phase condition and flashing was in the formation. Before shutdown the pressure and temperature at the main feed point were 3.4 MPa and 237.4 deg. C respectively, and flow rate was 13.94 kg/s. After shutdown we recorded PTS data at the feed point in the well for about 2 hours.

In this time the pressure recovered to 6.2 MPa and temperature to 271.9 deg. C. Figure 6. shows the matching curves.

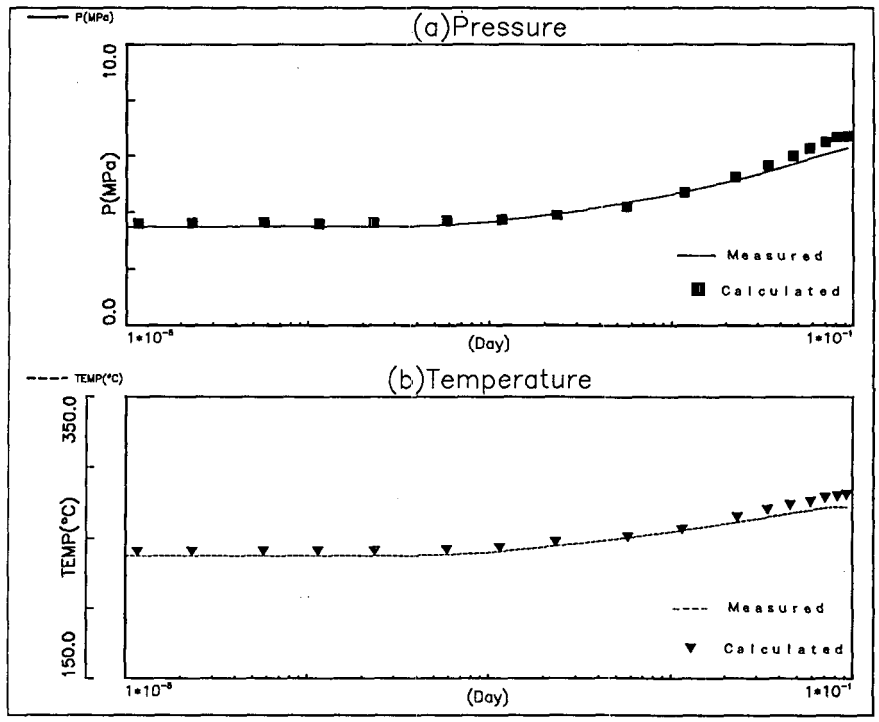

Figure 6. Matching Curves for Pressure and Temperature

4. Conclusions and Future Research

We drew following conclusions from the work described in this report.

(1) The modified SOR method for 2D and 3D problems, Thomas algorithm for 1D problems made the CPU time less required and made us possible to handle with larger problem.

We confirmed the speed-up and the accuracy of new TOUGH. The speed improvement was most excellent for 3D problems. For instance, new TOUGH was 23 times faster than original one.

(2) Grids for the case study were optimized using a uniform porous medium model. Then, we tried to match this PTS data and could have a good agreement.

As a future research, we will try to match this PTS data using double porosity model.

5. References

Young, D. (1954): Iterative Methods for Solving Partial Differential equations of elliptic type, Trans. Amer. Math. Soc.

Varga, R. S. (1962): Matrix Iterative Analysis, London, Prentce-Hall International. New Jersey, Prentice-Hall.

Wachspress, E. L. (1966): Iterative Solution of Elliptic System, London, Prentice-Hall, Inc.

Miller, C.W. (1979): Numerical Model of Transient Two-phase Flow in Wellbore, LBL-9056

Stanford Geothermal Program(SGP) (1981): Proceedings of the Special Panel on Geothermal Model Intercomparison Study, Rep. SGP-TR-42. Stanford University, Stanford, California.

Schroeder, R.C. and Miller, C.W. (1984): User Guide for MRMW- PC, BG Software, Oakland, California

Pruess, K. (1987): TOUGH USER'S GUIDE, LBL-20700.

White, S. (1990): Speeding Up TOUGH, TOUGH Workshop, LBL, California.

Okabe, T., Osato, K. and Takasugi, S. (1990): Case Study Using Faster TOUGH, TOUGH Workshop, LBL, California.

PROCEEDINGS, Sixteenth Workshop on Geothermal Reservoir Engineering
Stanford University, Stanford, California, January 23-25, 1991
SGP-TR-134

VARIATIONS IN DISSOLVED GAS COMPOSITIONS OF RESERVOIR FLUIDS FROM THE COSO GEOTHERMAL FIELD

Alan E. Williams[1] and John F. Copp[2]

[1]I.G.P.P. Univ. of Calif., Riverside, CA 92521
[2]California Energy Company Inc., Inyokern, CA 93527

ABSTRACT

Gas concentrations and ratios in 110 analyses of geothermal fluids from 47 wells in the Coso geothermal system illustrate the complexity of this two-phase reservoir in its natural state. Two geographically distinct regions of single-phase (liquid) reservoir are present and possess distinctive gas and liquid compositions. Relationships in soluble and insoluble gases preclude derivation of these waters from a common parent by boiling or condensation alone. These two regions may represent two limbs of fluid migration away from an area of two-phase upwelling. During migration, the upwelling fluids mix with chemically evolved waters of moderately dissimilar composition. CO_2 rich fluids found in the limb in the southeastern portion of the Coso field are chemically distinct from liquids in the northern limb of the field. Steam-rich portions of the reservoir also indicate distinctive gas compositions. Steam sampled from wells in the central and southwestern Coso reservoir is unusually enriched in both H_2S and H_2. Such a large enrichment in both a soluble and insoluble gas cannot be produced by boiling of any liquid yet observed in single-phase portions of the field. In accord with an upflow-lateral mixing model for the Coso field, at least three end-member thermal fluids having distinct gas and liquid compositions appear to have interacted (through mixing, boiling and steam migration) to produce the observed natural state of the reservoir.

INTRODUCTION

The recent development of production facilities in the Coso geothermal system has permitted unprecedented geochemical observations of a large portion of the reservoir in nearly its natural state. Unlike most active geothermal systems developed to date, the rapid expansion of facilities at Coso allowed 3-dimensional sampling of fluids from much of the reservoir prior to extensive modification of fluid compositions and distributions by long term production induced effects.

To facilitate the discussion of geochemical sub-regions, four geographical designations will be used in this paper: 1) Northwestern region, including all wells which lie to the north and west of the Devils Kitchen (Fig. 1), an old mercury mine and site of active fumaroles, 2) Steam Cap region, located immediately south of Devils Kitchen, 3) Southwestern region, which includes the hottest wells, and 4) Southeastern region, somewhat to the south and east of the southwestern wells. Figure 1 illustrates these sub-regions as well as the locations of Devils Kitchen and Coso Hot Springs, where upwelling steam and gases have created an assemblage of mudpots and fumaroles.

Although the Coso field has been known for some time because of surface expressions at both Coso Hot Springs and at the Devils Kitchen area, data concerning the deep reservoir chemistry has only recently been acquired. Preliminary studies of reservoir fluid chemistry from two early wells (CGEH #1 and COSO #1) were first reported in Fournier et al. (1980). In their limited sample set (two wells) Fournier et al. (1980) recognized the presence of a Cl^--rich (~2300 mg/kg) liquid-dominated geothermal system which appeared to be relatively homogeneous in chemical composition. Minor variations in the chemical compositions of the fluids sampled from these two wells appeared to be primarily due to temperature dependent cation exchange reactions in the regions tapped by these two wells. Reservoir temperatures of 240-250°C and 205°C were inferred for the COSO #1 and CGEH #1 regions respectively. Their results seemed to indicate that

the fumarole and acid-sulfate surface manifestations seen at Coso Hot Springs and the Devils Kitchen (Fig. 1) were only shallow phenomena disguising an alkali-chloride liquid dominated system at depth.

More recently, Moore et al. (1989, 1990) and Williams and McKibben (1990a,b) reported a more detailed picture of the deep reservoir chemistry at Coso as indicated by sampling of numerous production wells. Their results indicate a widespread and variable presence of reservoir steam (much of which may be induced by production) and substantial variations in the natural state chemistry across the field.

Consistent decreases in Cl^- and CO_2 concentrations in analyses from 28 wells and roughly linear Cl-enthalpy relations between deep steam-rich southwestern wells and both shallower wells in the north and liquid-only wells in the southeast (Fig. 1) were observed and interpreted by Moore et al. (1989, 1990) as indicating mixing of rising hot, saline, CO_2 rich geothermal fluids with cooler, dilute groundwaters. They thus interpreted the natural convective reservoir flow as upwelling in the southwest portion of the field then spreading as plumes of mixing fluids to the north and southeast.

Observations of regional variations in concentrations of additional dissolved components in fluids from 47 Coso wells (Williams and McKibben, 1990a,b) indicate that reservoir mixing is not simple. Variations in Cl/B, Cl/F (Fig. 2) and other element ratios indicate that several distinct liquids are present and that end member waters are most likely chemically evolved thermal fluids.

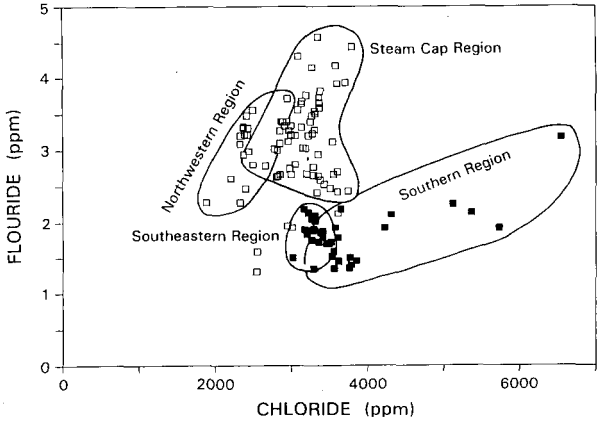

FIGURE 2. Fluoride vs. Chloride plot of Coso thermal fluids. Geographic regions of distinctive chemistry are indicated for northern well samples (open squares) and southern well samples (filled squares).

Because of compositional variations induced by mixing, boiling and water-rock interaction within the reservoir, Williams and McKibben (1990a,b) were able to discern as many as five distinct geochemical sub-regions within the Coso reservoir (some shown on Fig. 1 and Fig. 2). Such regional variations illustrate the effects of natural state flow, boiling and mixing and provide ideal natural tracers to monitor production induced changes in reservoir flow.

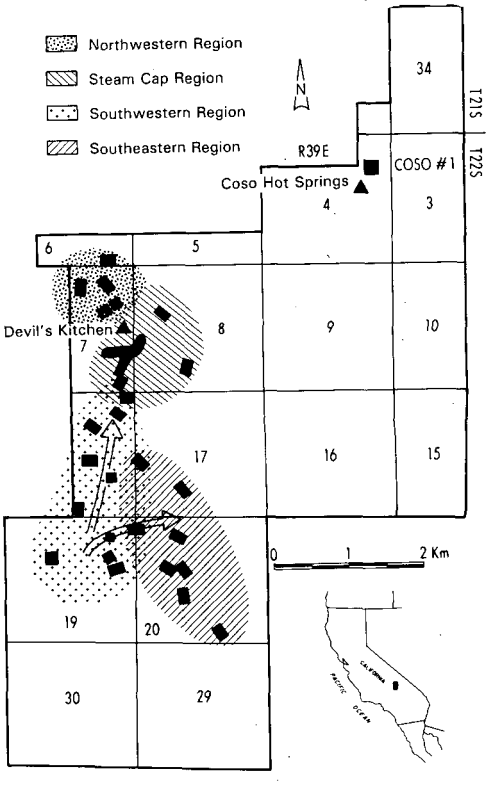

FIGURE 1. Map of the Coso geothermal field, showing well pads (black rectangles) from which multiple directional wells are drilled and surface thermal manifestations (triangles). Geochemically defined sub-regions have been indicated as well as hypothetical fluid flow-mixing directions (arrows).

PRODUCTION FLUID CHEMISTRY

At this time, 151 analyses provided by California Energy Co. Inc. (CECI). of fluids from 47 Coso geothermal wells are being utilized for our interpretations. The majority of the samples were gathered during initial production testing of wells, so accurate measured enthalpy data also exist. Many additional analyses exist for liquid samples from the midsection of the field. Due to interlaboratory inconsistencies however, this data has been excluded from our present interpretations. A sufficient number of accurate analyses from this region exist to roughly characterize its chemistry. For 110 samplings, complete gas analyses are available. These have been augmented by additional samplings by UCR for specific (CO_2, H_2S) gas concentration and isotope measurements.

Where possible, well-head liquid and steam samples collected using a miniseparator have been recomputed to provide reservoir concentrations. In two-phase reservoir regions, and zones of production induced excess enthalpy however, such recalculations can become quite inaccurate. For this reason some of our discussion will rely on raw well-head gas ratio and concentration data.
Analyses show significant and consistent regional variations in the chemistry of both the fluids and the gases analyzed. In this paper we will present data and provide interpretations of the variations observed in gas analyses of the steam phase of producing wells.

Gas Geothermometry and Estimates of Reservoir Steam

Complete gas analyses of well-head steam samples have been shown useful in estimating both reservoir temperature and steam fraction (D'Amore and Panichi, 1980; D'Amore and Celati, 1983; D'Amore and Truesdell, 1985). Since the Coso system includes two-phase reservoir regions, the approach of D'Amore and Truesdell (1985) was deemed most appropriate for this study. Using gas ratios involving CO_2, CH_4, H_2S, and H_2, reasonable reservoir temperatures and useful steam fraction relations are generated. Regional groupings similar to those developed from other fluid chemical studies (Williams and McKibben, 1990a,b) are also apparent in this gas ratio plot (Fig. 3).

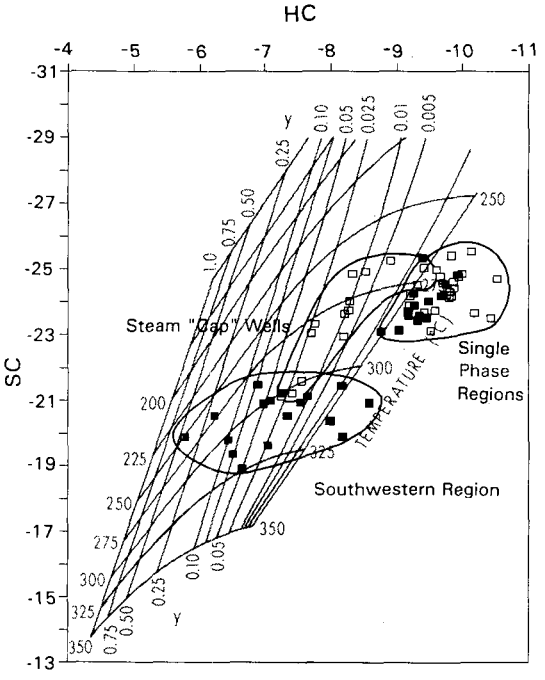

FIGURE 3. Gas ratio plot (after D'Amore and Truesdell, 1985). Symbols as in Fig. 2. Grid gives computed reservoir temperatures and steam fractions (y).

Using molar ratios for Fig. 3, (after D'Amore and Truesdell, 1985):

$$SC = 6 \text{ Log } H_2S/H_2O - 0.5 \text{ Log } CH_4/CO_2$$

$$HC = 2 \text{ Log } H_2/H_2O - 0.5 \text{ Log } CH_4/CO_2$$

Shallow wells producing from the naturally occurring steam "cap" in the northern region of Coso (Williams and McKibben, 1990a,b), show relatively low temperatures (~275° C) and significant reservoir steam fractions (Fig. 3). The deep, high enthalpy wells in the southwestern region, however, show far higher temperatures (300-325° C) and variable, but generally very high reservoir steam fractions, in accord with well-head enthalpy measurements (Moore et al., 1989, 1990; Williams and McKibben, 1990a,b).

It is interresting to note that despite extreme differences in gas concentrations (Moore et al., 1989, 1990), gas ratios imply single phase reservoirs and similar temperatures (~275° C) for wells in both the southeastern and northern regions.

If significant steam loss occurred in the evolution of either of these liquids, subsequent gas re-equilibration must also have taken place to give the observed relationships.

Single-Phase Reservoir Regions

Significant and systematic differences in reservoir gas concentrations are seen between the two liquid-only regions of the Coso field. For instance, CO_2 concentrations in northern portions of the Coso reservoir are nearly three times lower than those found in liquid phase wells in the southeastern region (Fig. 4). Methane concentrations behave in a similar manner, but other gases (H_2, Ar, H_2S and N_2), do not show as significant depletions (Fig. 4). These gases span a wide range of liquid-steam partitioning at geothermal temperatures and the observed relationships appear to preclude derivation of these single-phase fluids from a common parent by boiling or condensation alone. To illustrate this, we have included concentration trajectories (using gas partition relationships from Giggenbach (1980)) for hypothetical reservoir boiling (arrows on Fig. 4). Steam losses of 7 to 25 % at temperatures of 280-340° C respectively are necessary to traverse the plotted trajectories. It is apparent from this and other similar plots that northern and southern fluids cannot be related to a common parent by boiling alone.

A less obvious, but quite significant regional difference in gas ratios can be seen in a plot of well-head nitrogen vs. argon concentrations (Fig. 5). It is apparent that, for a wide array of wells sampled and analysed over several years, Ar/N_2 ratios (Fig. 5) are consistently lower in all southern wells (both single and two-phase) than in northern wells. Geothermal fluids are generally of meteoric origin (in equilibrium with air), and often show Ar/N_2 ratios similar to the .017 value of air (Hulston and McCabe, 1962; Ellis and Mahon, 1977). Such values are observed for all northern Coso geothermal fluids but far lower ratios (typically less than .010) are observed for fluids from southern regions. It is unreasonable to assume that such a consistent pattern would be produced from sampling or analytical errors. Thus, there appears to be either an argon deficiency or a nitrogen excess in the southern Coso reservoir. Although a small variation

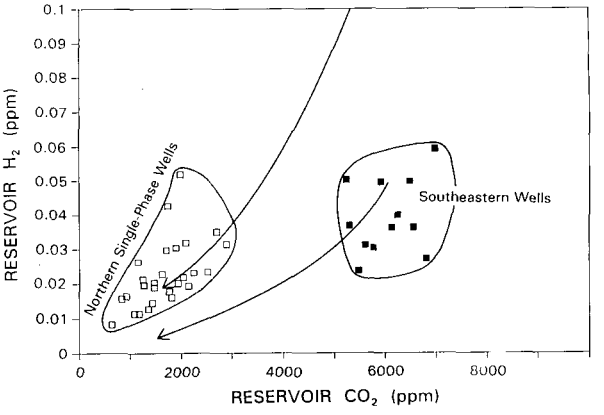

FIGURE 4. Plot of reservoir H_2 and CO_2 concentrations for liquid-only regions. Arrows indicate hypothetical gas loss trends for aprox. 300° C. closed system reservoir boiling.

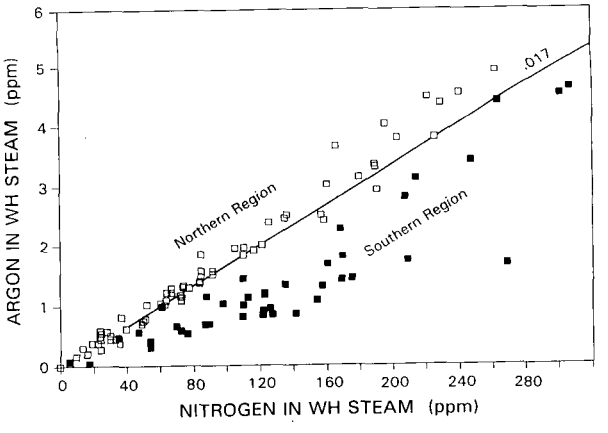

FIGURE 5. Argon and Nitrogen concentrations in wellhead steam samples from northern (open squares) and southern (filled squares) Coso wells. Line (.017) indicates Ar/N_2 ratio of air.

in this ratio could come from extensive boiling, this regional variation more likely indicates an intrinsic difference in the fluids from these two portions of the field. Little data is available concerning concentrations of these gases in other geologic environments, but possible sources of variability may be; 1) volcanic gas input to the deep geothermal fluid, or 2) organic-rich sediments.

Subsurface hydrothermal alteration and the present existence of a steam "cap" in the northern limb of the Coso field indicate some degree of boiling and substantial degassing of fluids in these sub-regions (Moore et al., 1989, 1990). However, both gas ratio analysis (Fig. 3) and gas concentration plots (Fig. 4), argue against gas loss as the sole mechanism for creating the regional reservoir gas concentration gradients. Instead, we feel it is likely that different thermal fluid end members provide much of the chemical signature (Fig. 2; Fig. 4) which distinguishes fluids in different regions. Significant differences in the Ar/N_2 ratio, particularly between northern and southeastern Coso reservoir regions (Fig. 5) also supports the presence of end member thermal fluids with distinctly different chemical signatures.

Two-Phase Reservoir Regions

Both the steam cap region and the southwestern region of Coso (Fig. 1) are generally known as two-phase portions of the reservoir (Moore et al., 1989, 1990; Williams and McKibben, 1990a,b) although not all wells show reservoir steam contributions. It is not obvious if the two-phase regions represent areas of natural state reservoir boiling or are results of pressure decreases associated with production. Physical evidence and production data support the existence of a natural steam cap in the north, which expanded with increased production. Physical evidence concerning the natural state of the southwestern region is less clear. Early pressure-temperature surveys indicated a single phase liquid reservoir but some aspects of hydrothermal alteration and geochemistry imply a two phase state.

Two-phase reservoir samples show extreme variations in gas composition. A plot of CO_2 vs. H_2S concentrations for all steam samples corrected to represent total produced fluid compositions (Fig. 6) indicates five distinct groupings having recognizable gas concentrations and H_2S/CO_2 ratios. Two of these groups represent the liquid-only regions in the northern and southeastern regions of Coso. They plot in the extreme lower, left-hand corner of this diagram. Steam-rich well data typically fall on a linear array having an H_2S/CO_2 ratio of approximately .015, but a small cluster of two-phase wells (all located in the south-central portion of the field near the common corner of sections 17,18,19 and 20; Fig. 1) indicate somewhat lower ratios. Steam-rich wells tapping the shallow steam "cap" in the northern region of Coso form another cluster at relatively low gas concentrations.

Data from wells in the northern steam "cap" appear compatible with reservoir boiling and steam separation (at temperatures less than 275° C) from liquids equivalent to those in nearby single phase wells.

Utilizing the gas partition equations of Giggenbach, (1980), it can be easily shown that gas concentrations and ratios of the southwestern two-phase wells cannot be produced by boiling any known Coso single-phase liquid at reasonable reservoir temperatures. A gas concentration trajectory (arrow) is illustrated as an example (Fig. 6).

In order to identify fluids produced from homogeneous sources we have cross plotted well-head gas and solute concentrations (Fig. 7). On such a diagram, progressive partitioning between coexisting steam and liquid phases traces an hyperbolic curve as boiling proceeds. Single phase reservoir production data provide examples of such curves. Asymptotes of such curves give starting reservoir solute and gas concentrations.

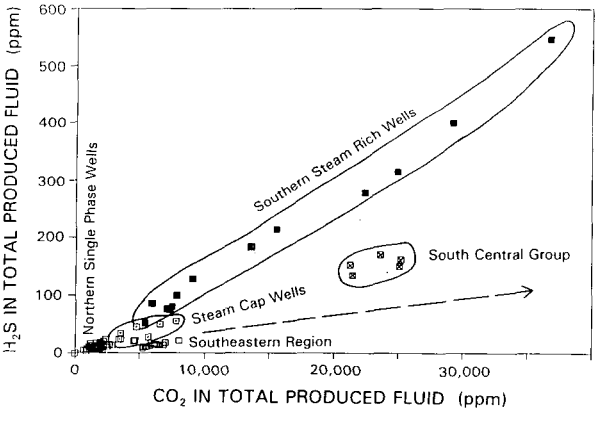

FIGURE 6. H_2S vs. CO_2 content of total production from Coso wells. Regional groupings have been indicated and an approximate 300° C. boiling trend (arrow) for known Coso reservoir liquids is shown.

Although data is sparse, there appears to be no simple correlation between CO_2 and Cl- concentrations in the samples from southwestern Coso wells. There is thus no single homogeneous reservoir fluid from which these wells produce. It is therefore most reasonable to view their gas concentrations (the linear array on Fig. 6) as a mixing line between known Coso geothermal fluids and a relatively homogeneous vapor having concentrations of CO_2 and H_2S of at least 40,000 and 600 ppm respectively. This steam component is most likely contributed directly to production from gas-rich steam in the reservoir. The small group of south-central wells shown on Fig. 6 appear to have a somewhat more complex origin. As shown on Fig. 7, these analyses follow a well defined hyperbolic curve implying as much as 30 % steam loss. Such compositions illustrate boiling of a liquid with Cl^- of approx. 3500 ppm and CO_2 of approx. 25,000 ppm. Unless this curve is fortuitous, it most likely represents boiling of an homogeneous mixture of southwestern and southeastern liquids.

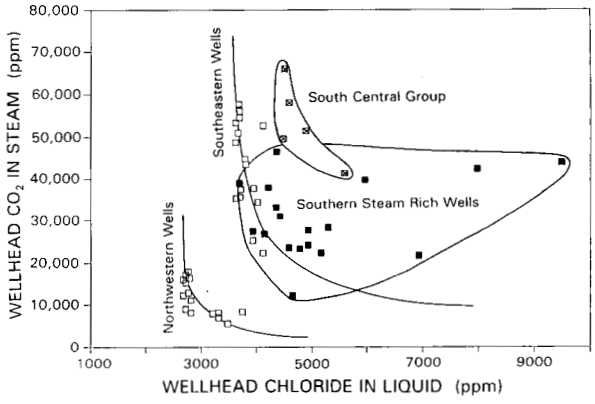

FIGURE 7. Wellhead concentrations of Cl in liquid and CO_2 in steam have been plotted. Hyperbolic curves produced by progressive boiling of homogeneous liquid regions are shown. Scattered data indicates variable boiling and mixing of different reservoir fluids.

SUMMARY

Interpretation of data from well-head sampling of geothermal fluids at Coso provides an excellent 3-dimensional picture of the natural state distribution of dissolved solids and gases across the field. Gas concentrations and ratios in particular, permit us to evaluate potential mechanisms for producing the diverse chemical signatures seen in Coso fluids.

Two distinct fluids occupy single-phase reservoir regions in the northern and southeastern portions of the field, and it appears unlikely that these fluids could have been produced directly from a common parent since their distinctive chemical signatures preclude evolution from a single hydrothermal liquid by boiling or dilution alone. At least two chemically distinct geothermal end members are required.

A third geothermal fluid is required to provide the observed deep reservoir steam which has extremely high H_2 and H_2S concentrations. Fluids sampled early in the production history of the Coso field represent natural state mixtures of these three end member liquids, steam produced by reservoir boiling, and residual boiled liquids.

The wide variations in reservoir chemistry document the effects of natural state flow, boiling and mixing in the Coso field and provide natural tracers with which to monitor production induced changes in the reservoir.

ACKNOWLEDGEMENTS

This is report 90-36 of the Center for Geothermal Resources Research, IGPP, Univ. of Calif., Riverside. We thank California Energy Company, Inc. and the U. S. Navy for access to samples, analyses and information. P. Hirtz also provided floppies of original chemical data files for interpretations done at UCR. This work was funded through a research grant from the National Science Foundation (grant No. EAR-8804864).

REFERENCES

D'Amore, F. and R. Celati (1983) Methodology for Calculating Steam Quality in Geothermal Reservoirs. Geothermics, 12, 2/3, 129-140.

D'Amore, F. and C. Panichi (1980) Evaluation of Deep Temperatures of Hydrothermal Systems by a new Gas Geothermometer. Geochim. et Cosmochim Acta, 44, 549-556.

D'Amore, F. and A.H. Truesdell (1985) Calculation of Geothermal Reservoir Temperatures and Steam Fractions from Gas Compositions. Geoth. Resources Council Trans., 9, 305-310.

Ellis, A.J. and W.A. Mahon (1977) Chemistry and Geothermal Systems. Academic Press, New York.

Fournier, R.O., J.M. Thompson and C.F. Austin (1980) Interpretation of Chemical Analysis of Waters Collected from Two Geothermal Wells at Coso, California. Jour. Geophys. Res., 85, 2405-2410.

Giggenbach, W.F. (1980) Geothermal Gas Equilibria. Geochim. et Cosmochim. Acta., 44, 2021-2032.

Hulston, J.R. and W.J. McCabe (1962) Mass Spectrometer measurements in the Thermal Areas of New Zealand. Geochim. et Cosmochim. Acta, 26, 383-397.

Moore, J.N., M.C. Adams, B.P. Bishop and P. Hirtz (1989) A fluid flow model of the Coso geothermal system; Data from production fluids and fluid inclusions; Univ. of Utah Earth Sci. Lab. Report ESL-89001-JP.

Moore, J.N., M.C. Adams, B. Bishop-Golan, J.F. Copp, and P. Hirtz (1990) Geochemical Structure of the Coso Geothermal System, California. in, J.L. Moore and M.E. Erskine, eds. Amer. Assoc. of Petroleum Geologists field trip guidebook, AAPG EMD #1. 25-39.

Williams, A.E. and M.A. McKibben (1990a) Isotopic and Chemical Characteristics of Reservoir Fluids from the Coso Geothermal Field; China Lake Naval Weapons Center, California. in. J.L. Moore and M.E. Erskine, eds. Amer. Assoc. of Petroleum Geologists field trip guidebook, AAPG EMD #1. 85-102.

Williams, A.E. and M.A. McKibben (1990b) Isotopic and Chemical Constraints on Reservoir Fluids from the Coso Geothermal Field, California. Geoth. Res. Council Trans. 14, 1545-1552.

PROCEEDINGS, Sixteenth Workshop on Geothermal Reservoir Engineering
Stanford University, Stanford, California, January 23-25, 1991
SGP-TR-134

GEYSERING DISCHARGE OF A GEOTHERMAL WELLBORE AT ZUNIL, GUATEMALA

DONALD E. MICHELS

Don Michels Associates
P.O. Box 8652
Missoula, Montana 59807
406/728-2576

ABSTRACT

Within two hours after discharge began, for a production test in 1989 of well ZCQ-4, pressure variations changed from approximately sinusoidal to a cycle of sudden and complex peak discharge pressures, to 9 bar, separated by irregular pressure declines to 5 bar. Initial cycle periods of 42 minutes evolved to 150 minutes by day 20 of continuous testing, when three of four surge peaks were well separated. Chemical signatures of fluids discharged with pressure surges were distinctive. When combined with downwell pressure measurements, assignments can be made for elevations of fluid entry points. The variety of chemical signatures indicates a scarcity of interzone connectivity. These constrained discharges are suspected to derive from altered rubble zones between layered volcanic rocks.

SETTING: Geothermal exploration of the Zunil area began in 1973 with a regional study by Instituto Nacional de Electrificación (INDE). Reconnaissaince geology, geophysics, and geochemistry, assisted by the Japan International Cooperation Agency (JICA) led to drilling eleven temperature gradient holes. These were followed by six deep geothermal wells, drilled in 1980-81 and subsequently tested with assistance of Electroconsult. Four of these deep wells produce neutral sodium chloride fluids with geothermometer temperatures in the general range of 240 to 280°C. In 1987, a contract to develop and engineer a 15 Mw power plant was awarded to MK Engineers, MK Ferguson Co., and Cordon y Merida Ings. Retesting of the wells was necessary and partial results for ZCQ-3, -4, -5, and -6 are reported by Menzies, et al (1990). A geologic summary is provided by Foley, et al (1990).

Lithologies at Zunil are a basement of granodiorite overlain unconformably by lava flows and ash-flow tuffs associated with a proposed caldera (Foley, et al, 1990). Volcanic rocks range in age from Tertiary to Pleistocene and involve four volcanic sequences, each with multiple flows and/or tuffs. The six deep wells all penetrate the volcanic series and intersect the granodiorite at elevations of 1090 to 1270 m ASL. Elevation differences are suspected due partly to faults. These faults are also suspected to channel upflow of hot fluids, although current production zones are variously within the volcanics and the rubble zone at the top of the granodiorite.

Surface elevation at ZCQ-4 is 2117 m ASL and granodiorite was encountered at 1140 m. The completion interval includes three of the four volcanic sequences. Prior to studies in 1989, ZCQ-4 was tested on five occasions between March 1981 and September 1985. The apparent power potential of ZCQ-4 is the largest among the Zunil wells, 5.7 Mw, including considerable excess enthalpy, (Menzies, et al, 1990), but marred by severe pressure surges. Surges were present as early as 1982, substantially in the form found by 1989 testing, but described only as a graph. A brief description of the 1989 surging is available (Menzies, et al, 1990).

The surging is important because its persistence and chemical variety indicate poor vertical connectivity among producing zones, surprising in view of suspected fluid production control through the field by northwest and northeast-trending faults. Geysering also complicates evaluation of the well's power potential and depletion forecasts. The relative independence of the geysering zones makes it impractical to interpret downwell pressure measurements in the usual way. Also, production zones experience different ratios of times for discharge/recharge. Furthermore, the chemical compositions of the production zones do not appear to stabilize, complicating forecasts of scaling tendencies, fluid enthalpy, etc. Severity of the surging makes the well an impractical supply to a power plant. Selection of a best remedial method requires good understanding of the sources and causes of the surging.

EVOLUTION OF PRESSURE CYCLING: Figure 1 shows the evolution of the pressure cycling during the first four days. The figure is a composite of parts of Barton chart records of flowline pressures. Trough-to-peak pressure excursions amounted to more than 50 percent of the scale range of the Barton chart, nominally 5 to 9 bars pressure in the flowline. Corresponding flowline temperatures are 160 to 182 C. Time interval between similar points on the cycles was initially about 42 minutes, but increased to 78 minutes per cycle by about the 70th hour. Peaks were labeled "A", "B"... in order of their appearance in the record. The relative intensities of the peaks shifted during the first few days, but the general features of the cycling were otherwise similar. By day 16, the pressure cycling had evolved to a period of 120 minutes and the peaks that had earlier been clustered into a group became well separated and individually narrow.

On day 17, a unique pressure drop with an associated pressure spike (peak D) was "inserted" during one cycle, at a chart location just preceding the highest pressure surge (Figure 2). It occurred with increasing regularity during the next two weeks and by day 34 it was a part of all cycles. Cycles without the D-peak were 120 minutes long, those with it were 150 minutes.

This cycling of identifiable surges was also observed in 1982, but with longer cycle periods; 185 versus 120 minutes without, and 208 versus 180 minutes with "D". The longer periods in 1982 may be related to the longer preceding time of discharge, more than three months, compared to one month for Figure 2. Absence of the "D" peak three months into the 1982 record suggests it may have been waning. Similarity of the cycling pattern of March 1982 and October 1989 indicates that the number and relative potency of feed zones to ZCQ-4 has not changed in any substantial way.

FIGURE 1: PRESSURE CYCLING IN ZCQ-4
INITIAL EVOLUTION IN 1989

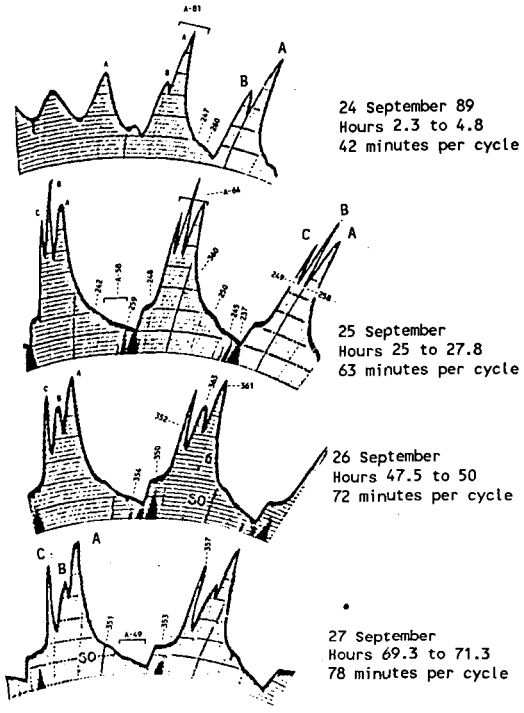

FIGURE 2: PRESSURE CYCLING IN ZCQ-4
CONTINUED EVOLUTION IN 1989

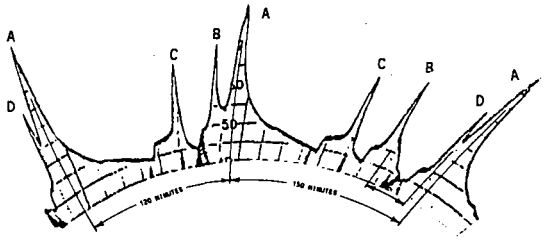

DAY 17: MIXED CYCLES

PEAK "D" IS ABSENT FROM THE LEFT SIDE CYCLE

GASES IN DISCHARGE FLUIDS

A syringe method of gas sampling (modified after Michels, 1978) was used to obtain a series of twenty-three gas measurements during a 90-minute time interval. The intent was to use natural CO_2 as a tracer for individual production zones. Figure 3 shows the gas-sampling events in relation to the pressure variations taken from the Barton record of the same time. Also shown in Figure 3 are pressures derived from the temperatures measured in the steam separator at the times of sample collection, showing that the separator fairly tracks the flowline. Resolving the narrow pressure peaks is not perfect due to the discontinuous measurements of time for the sampling events.

ZUNIL I QUETZALTENANGO

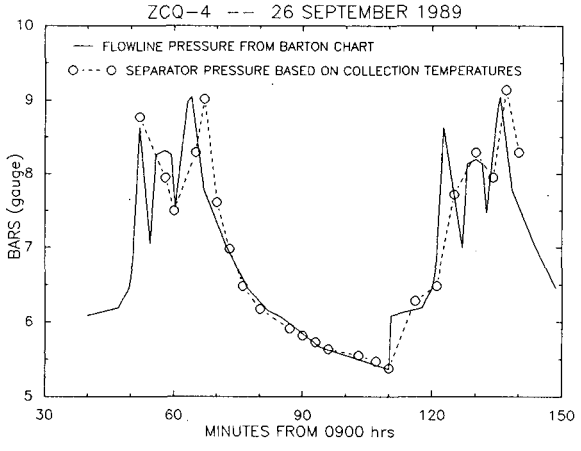

FIGURE 3: SAMPLING FOR CO2 DURING PRESSURE SURGES

The resulting CO_2 concentrations in steam are plotted versus time in Figure 4. This complicated behavior emphasizes composition contrasts among fluids which mix in proportions that vary through the pressure cycle. For example, if the discharge were a single fluid of stable composition, decreases in flowline pressure would signal an increased steam fraction diluting the CO_2 concentration. However, between 75 and 110 minutes in the figure, CO_2 content increases during pressure decline, following "A". This signals a reversal of dominance between two input fluids of different gas content.

ZUNIL I QUETZALTENANGO

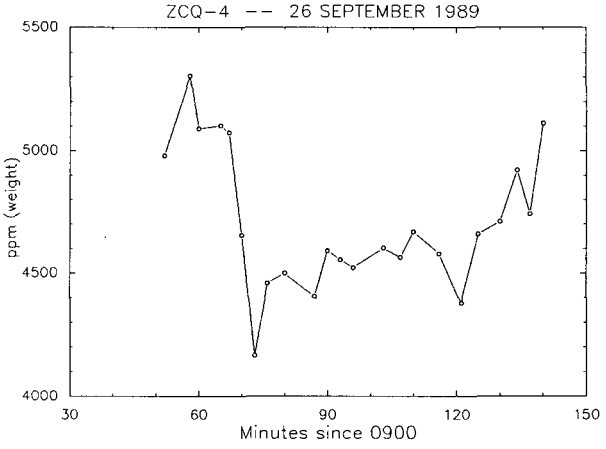

FIGURE 4: CO2 IN STEAM

Figure 5 shows CO_2 concentration (total discharge basis) plotted versus separator pressure. Lines connect data points in a time sequence which covers slightly more than one pressure cycle. The diagonal, elongated pattern of plotted points from pressure of 5.4 to 7 bars indicates a fluid mixture of two components. Similarly, the elongate pattern between 8 and 9.5 bars indicates another two-component mixture. Because these two indicators are displaced in pressure and relate to specific parts of the pressure cycling, they indicate at least four production zones contributing CO_2 to the ZCQ-4 discharge.

BRINE COMPOSITIONS Correlation of the pressure cycle with the brine sampling followed a different procedure. Samples were taken at the times of certain events in cycles of different days. In the early test days, pressure surges were not well separated, so sample contrasts reflect mutual contamination as well as day-to-day differences. Samples were taken also of the discharges during pressure minima.

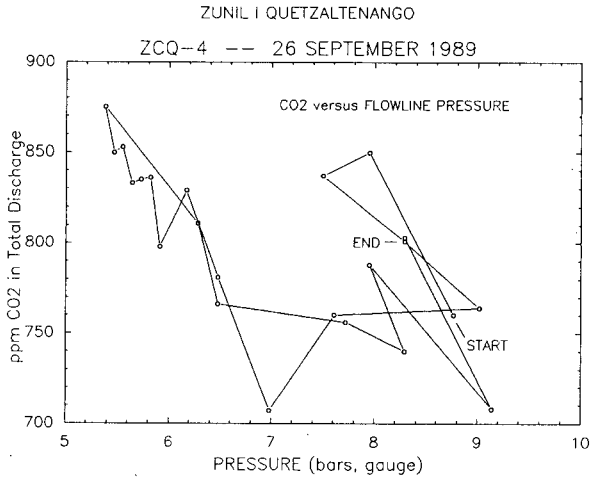

FIGURE 5: CO2 IN THE PRESSURE CYCLE

The extended cycle periods of the last test days permitted a better sampling of individual surges and of the pressure minima between them. These are compared in Table 1, which is arranged with higher quartz temperatures toward the left side and ranked concentrations of components based on the "A" surge composition.

TABLE 1: COMPOSITION OF SURGE BRINES

SURGE	A	D	C	B
----------SEPTEMBER 1989----------				
T-qtz	252		242	248
Chloride	1120		1167	1170
Sodium	675		701	691
Silica	480		439	464
Potassium	113		111	116
Bicarbonate	40.7		37.2	37.9
Sulfate	33.6		35.7	33.7
Boron	31.9		32.9	32.3
Calcium	19.0		22.0	19.6
Arsenic	8.55		7.53	9.33
Lithium	6.29		6.69	6.45
Ammonium	.51			.54
Antimony	.81			.66
Strontium	.18		.63	.19
----------OCTOBER 1989----------				
SURGE	A	D	C	B
T-qtz	258	248	245	241
Chloride	1011	1196	1249	1207
Sodium	604	706	724	689
Silica	509	465	451	431
Potassium	117	119	118	116
Bicarbonate	52.6	41.8	45.6	45
Sulfate	26.3	30.5	35.5	31.1
Boron	26.0	31.0	32.7	30.5
Calcium	14.7	20.5	23.5	20.2
Arsenic	6.66	6.89	7.80	6.87
Lithium	5.42	6.19	6.48	5.96
Bromide	4.51	6.36	5.56	5.81
Fluoride	1.25	1.38	1.34	1.31
Ammonium	.66		.76	.70
Antimony	.62		.64	1.28
Strontium	.13	.18	.22	.18

Brine compositions, obtained for a 244-day period of testing in 1983, are suspected to represent weir samples (CyM-MKF, 1989). Apparently, no attempt was made to sample according to pressure variations. Concentrations in 1983 are mostly higher than in 1989, by factors up to 3.4 beyond the effect of steam losses. Figure 6A shows persistently increasing concentrations that all begin at values greater than the 1989 counterparts.

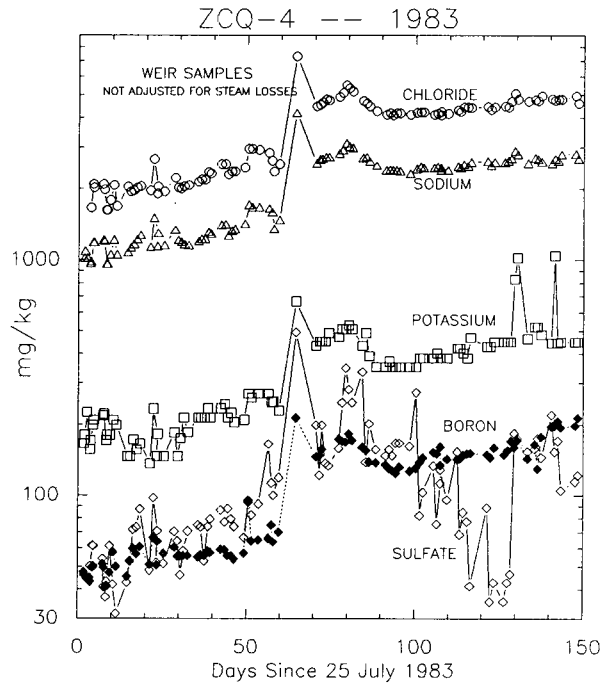

FIGURE 6A: MAJOR COMPONENTS versus TIME

These 1983 data show significant symptoms of being evapo-concentrated, for example, the Cl/Na ratio varies little, 1.733±.048. More general indications are shown in Figure 6B, a log-log plot of chloride versus other selected components. In a log-log plot evapo-concentration yields scatter fields with unit slope. A reference line is included in the figure. The observed data largely falls on parallel trends of nearly unit slope. Fine structures within scatter areas indicate other features of mixing with production zones, but will not be considered further, here.

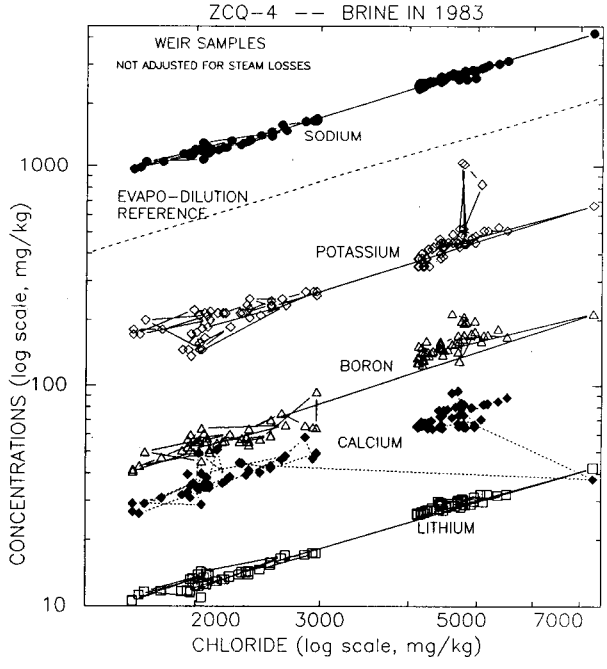

FIGURE 6B: TEST FOR EVAPO-CONCENTRATION

GEYSER ACTION IN ZCQ-4

The pressure surges of Figure 2 are mirrored in the shallower parts of the wellbore, but occur inverted at deeper levels. Temperature and pressure tools were suspended at 415 meters and recorded data through approximately one full cycle (four surges) (Pruett Industries, 1989). There, variations in pressure were essentially like the surface variations and temperature correspondences indicate that the instruments were in two-phase (brine-steam) conditions. Subsequently, the instruments were lowered to 800 meters for an additional period. There, the pressure-temperature values indicated that most of the time, conditions were one-phase liquid. Figure 7 shows results for both depths. *[The time axis for the 800-meter record has been displaced 150 minutes (one cycle) in Figure 7 in order to align events with the 415-meter record.]* This shows that low-pressure events at 800 meters are exactly one pressure cycle away from the high-pressure events measured at 415 meters, yielding two views of the same causal factors.

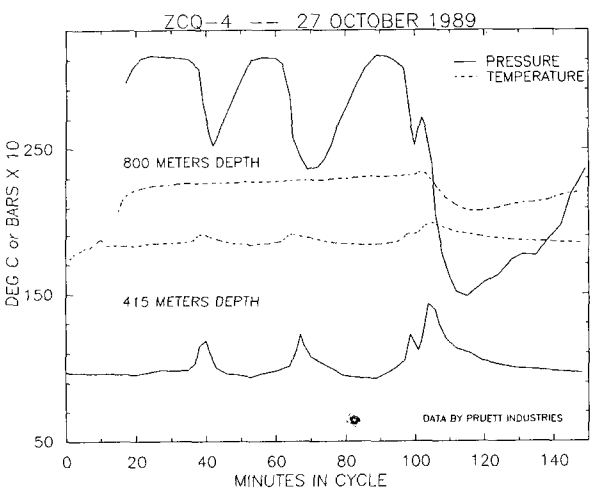

FIGURE 7: CYCLE CONDITIONS IN WELLBORE

Local pressure minima at 800 m represent discharges from a liquid column of different heights above the instruments and each minimum represents a geyser-like discharge that yields a pressure maximum in the two-phase zone of the upper wellbore and surface equipment. The most severe pressure minimum at 800 m corresponds to the largest pressure surge at the surface. This geyser action is driven from below 800 meters. Insight about this action can be deduced by recasting the data from 800 m as a plot of temperature versus pressure.

For a two-phase watery system, true pressure-temperature coordinates cannot exist above the vapor-liquid line, shown dashed in Figure 8. Data from known two-phase (vapor-liquid) systems which plot above that line are defective, but may be explained or adjusted. Considerable raw data for Figure 8 did plot (initially) in the forbidden region. Accordingly, all temperature data were arbitrarily reduced by 10 degrees, before plotting as shown. This adjustment places several data coordinates close to the vapor pressure line, corresponding to two-phase conditions at those times.

Five plotted points in the left side of the graph, slightly above the two-phase invariant line, are suspected to represent changing two-phase conditions at 800 meters which occur faster than the Kuster temperature gauge can follow (thermal inertia). This leg of the plot, at pressures less than 24 bars, represents a geyser-like discharge driven from below.

After the pressure reversal, the plot again follows a path approximately parallel to the vapor pressure curve. This segment represents increasing pressure on a two-phase system. Mismatch with the vapor pressure curve can be assigned jointly to thermal inertia of the temperature gauge and to a (plausible) component of CO_2 pressure. At pressures above 18 bars, the trend diverges from the two-phase invariant, indicating that the single-phase liquid level has risen enough to surround the instruments. The temperature at that point, about 204°C, is much less than the static temperature at that depth (253°C) measured earlier (Pruett Industries, 1989).

Pressure, indicated in Figure 8, continues to rise, in the single-phase condition, to the position marked END (of the measured record) at about 28 bars. The trend extends to the START (of the measured record) at about 31.5 bars, single phase), which completes the cycle. The nineteen plotted points (after START) show oscillations of pressure during a steady increase of temperature and include geyser events C, B, and D.

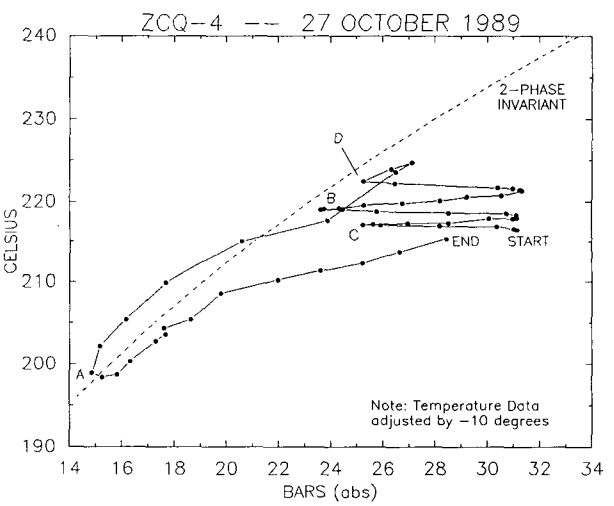

FIGURE 8: CYCLE CONDITIONS AT 800 METERS DEPTH

In Figure 8, pressure following the last peak, near 27 bars, decreases with decreasing temperature. This is interpreted as boiling, suspected to originate below 800 meters and triggered by the (measured) pressure minimum due to "D". Mismatch with the vapor pressure curve, about 3 degrees, or 1.7 bar, could be due to CO_2 pressure or to effects of liquid from the lower part of the wellbore beginning to move upwardly, past the instruments. Subsequently, the pressure falls below 24 bars, apparently in two-phase conditions, completing the cycle with a geyser-like discharge, driven from below 800 meters depth.

GEYSER DYNAMICS AND INTERPLAY: A time interval of about 30 minutes occurs between the maximum temperature and the graph point (near 20 bar, Fig. 8) where single-phase liquid reappears at 800 meters. Of the four pressure maxima per cycle (Figure 2) only peak "A" has an uninterrupted discharge that long. Geothermometers of surge "A" correspond to zones below 850 meters, hence, it seems clear that the geyser discharge from below 800 meters is due to surge "A". The three pressure maxima for 800 meters in Figure 7, are relatively flat-topped peaks of the same magnitude. Because Figure 8 indicates single-phase liquid present at those times the pressure magnitude at 800 meters can be considered in two components; the weight of overlying single-phase liquid plus the vapor pressure at the top of the one-phase column, where two-phase conditions begin.

The periodically lower pressures at 800 meters represent events that reduce the height of the liquid column. The local pressure minimum corresponding to surge "B" is at a higher pressure than for "C", indicating a higher elevation for the top of the liquid column during "B" events than for "C" events.

The "D" peak of the surface pressure record (Figure 2) is a short-lived pressure minimum in Figure 7 where it appears to trigger the "A" surge. It seems that "D" does not reach its potential minimum before being overpowered by "A". Thus, its depth is not precisely calculable. Since the quartz temperature for D is higher than all others, except "A", elevation of "D" input can be inferred to be between those of "C" and "A".

The top of the one-phase liquid surges up and down in the wellbore during cycling. Its highest elevation is indicated by the three local pressure maxima that have equal magnitude. This limiting level is interpreted as a persistent steam entry, overpowering waning surges from below.

Geyser actions end with collapse of flash-cooled liquid toward the well bottom, after geysering feeder channels become so depleted they no longer overpower the shallow, persistent steam entry. Stagnant liquid, fallen in the wellbore, rewarms from rock heat. A new geyser event begins when a temperature-driven increase in vapor pressure can lift the overlying part of the liquid column of the wellbore, overpowering other current inputs.

GEYSER ELEVATIONS: Elevations of geyser inputs above 800 m depth can be estimated from liquid pressure gradient for the column (0.0832 bar/meter for liquid of 204-224°C), and H_2O vapor pressure at (the temperature of) the top of the liquid column. The minimum temperature at 800 meters, 204°C, observed when fluid falls down after the "A" geyser event, suggests conditions at the persistent steam entry when it overpowers the waning surge. From steam tables, 204°C corresponds to 16.0 bar(g). Table 2 shows relevant data and results. This sequence of depths is in agreement with the sequence of quartz temperatures derived for the fluids of individual surges (Table 2).

The maximum feasible depth for flash initiation in the "A" source can be estimated, based on its quartz temperature, gas content, and maximum pressure at 800 meters. Geyser action can begin when the warming of liquid by rock heat increases vapor pressure of one-phase liquid to the local wellbore pressure.

TABLE 2: DEPTHS OF INITIATION FOR GEYSER EVENTS

Surge	A	D	C	B	M
P-800	2-phase	<24.5	22.9	24.5	30.5
P net	---	<8.5	6.9	8.5	14.5
Liquid height	---	<102	82	102	174
Depth	<1072	>698	718	698	626
T qtz	258	248	246	241	[205]

From the maximum pressure at 800 meters, 30.5 bg, hydraulic pressure increases down the liquid column. There is a depth, below which, fluid at A-like temperatures cannot boil. That limiting depth is given by vapor pressure of A-type fluid, which has two components, water vapor (steam table) and CO_2. Using 850 ppm as the CO_2 content and CO_2 solubility given by Ellis and Golding (1963), yields 1.78 bar as the CO_2 pressure component; total vapor pressure at 258°C is 44.4 bg. Other values and results are given in Table 3.

Since "A" was functioning prior to the appearance of "D" in the surface pressure record, "A" clearly is capable of self-triggering. Alternatively, surge "D" yielding a local pressure minimum in the liquid column could trigger an "A" surge before the liquid temperature/pressure of "A" reaches the requirement for self-triggering. Thus, two plausible depths for the "A" zone can be computed. One is based on the liquid column with top at the persistent steam entry (626 m), the other with top of the liquid column lower, but not deeper than the entry for surge "D". Maximum depths for these two mechanisms are 977 and 1072 m, for "A" self-trigger and "D" trigger, (Table 3). The shallower "maximum" depth seems more plausible. The actual depth of "A" could be less than indicated in Table 3. A shallower depth also allows geysering to begin at a fluid temperature lower than the original wellbore temperature at that depth. The cycle period depends partly on heat transfer between rock and residual, partly flashed water in the parts of the channels nearest the wellbore.

CONSIDERATIONS OF ENTHALPY: The increasing time period for cycles represents depletion of rock heat. In terms of heat conduction, the temperature gradient in the rock away from the fluid flow channels decreases with time (repetition of cycles). If the mass of liquid heated in the channels were the same in successive cycles, and if the starting temperatures were similar, then increasing increments of time are needed for conductive heat to raise temperatures to the requirements for geysering. The rate of change of cycle period versus fluid production could yield information about the porosity structure in the rock.

The maximum temperature reached during this cycle (224°C at 800 meters) is much below all the geothermometer temperatures for quartz (235-258°C) and Na/K (244-274°C), as well as below the static temperature for the depth (252°C). This low measured temperature indicates that liquid which fills the wellbore after the geyser discharge derives from partially boiled liquids that fell from above. This includes the last-delivered liquid from the deep zone, which failed to get high enough in the wellbore to be incorporated with discharge from the subsequent dominant production.

After the geyser action, wellbore fluid at 800 meters is essentially static. The increase from lowest single-phase temperature (204°C) to the temperature at the start of the geyser (224°C) must be due to heat flow into the wellbore from adjacent rocks. This extra heating can be expressed later, during boiling, and is equivalent to about 2.5 percent steam, in addition to what might be expected from a simple adiabatic release, starting at T_{quartz} of the previous cycle.

Heat absorbed by residual liquids, after they fall back during the last stages of geysering, appears modest to small in amount. However, pickup of heat by hotter fluids, arriving to recharge channels near the wellbore, would be negligible.

TABLE 3: MAXIMUM DEPTH OF THE "A" GEYSER

	Self-Trigger	"D"-Trigger
P-800	30.5	24.5
$(P_{H2O})_{258}$	44.4	44.4
$(P_{CO2})_{850}$	1.78	1.78
$Gradient_{224-258}$	.0796 b/m	.0796
Increment	197 m	272 m
Depth	997	1072

Thus, the main part of a geyser discharge probably incorporates negligible rock heat. Further interpretation in this regard might be useful when forecasting the extent that rock heat could be recovered by the cycling discharge of ZCQ-4. The extension of cycle time from the initial 42 minutes to 150 minutes (after 34 days of discharge) would seem to be mostly due to mining of rock heat near the wellbore. Detailed analysis of the changes in cycle periods and masses of discharged fluids could yield quantitative calculations about the dimensions of the rock mass involved.

The energy output from the well can be obtained by summing the outputs of the separate discharges (Table 4). Between the surge events, discharge is mainly steam. Boundaries between surge and interlude discharges can be defined in the surface pressure record. On the pressure traces for waning surges, distinct, flattened segments occur near the 48 percent Barton scale dimension (Figure 2). They

generally separate contrasting local slopes of pressure change. These are marked in Figure 2 and are referenced in Table 4 as time boundaries between elements of the discharge record.

TABLE 4: DISCHARGE ENERGY DETAIL -- ZCQ-4

Discharge	Minutes	deg C	j/g
D	0-8	248	1073
A	8-42	258	1124
M1	42-82	205	2793
C	82-105	246	1061
M2	105-115	205	2793
B	115-132	241	1042
M3	132-150	205	2793
Time average enthalpy:			1860

The model on which Table 4 is based considers a geysering discharge to dominate the wellbore pressure regime so that all other (potential) feed zones are blocked, until the surge subsides. Thus, single-phase liquid enthalpy values are appropriate during surges. Rock heat is negligible, as described earlier, and indepèndent steam zones are inoperative.

During interludes, the "steam" zone at 626 m depth discharges mainly steam, with some liquid derived partly, perhaps mostly, from the previous surge. This steam zone may be related to the zone which discharged highly evaporated water in 1983 (Figs. 6A, -B), implying connection to substantial open space where boiling can accomodate phase separation most of the time. Liquids in the 1989 surges do not show significant evapo-concentration.

The time average enthalpy given in Table 5 does not accurately represent the well's energy potential. The required mass average enthalpy cannot be calculated because rate measurements have not been resolved for the individual surges.

The model of Table 4 differs from that of Menzies, et al (1990) who do not recognize surge "D". They further simplified their enthalpy/energy model by considering only two modes; 1380 j/g for "A" and 2510 j/g for the remainder of the cycle. Both correspond to mixed-phase inputs to the wellbore. Using James Tube/weir data, they obtained discharge rates of 12 and 37 kg/sec for "A" and "other", respectively. Using the same data as were involved with Figures 2 and 7 of this report, they selected 24 minutes as the duration of "A", versus 34 minutes used in Table 4. The difference may be due to identifications of apparent boundaries. For this report, the choice was mainly influenced by "flattened" parts of the Barton pressure record (Fig. 2), described earlier, and suspected due to discharge of liquid from the steam zones, received as an injection from the surge fluids.

CONCLUSIONS: At least five inflow zones participate with well ZCQ-4. Three are prominent geysers and a minor fourth geyser appears to trigger the largest, although the largest functioned mainly by self-triggering during the first twenty days of testing.

Geysering requires a kind of switching mechanism to periodically initiate discharge after a depleted zone has been (partly) regenerated. In this case, the "switch" is related to enthalpy transfer from rock to stagnant water in the wellbore and nearby feeder fractures. The cycle period increased with time, suggesting that heat had been mined near the wellbore. The amount of heat mined per cycle may be small, associated mainly with the liquid in the wellbore that is relatively stagnant between surge events. Additional rock heat would be mined near the fluid flow pathways away from the well, also consistent with a lengthening cycle period.

Road cuts and gullies in the area show extensive hydrothermal alteration at interfaces between layered volcanic rocks. Since the surge liquids have distinctive geothermometer temperatures, it is reasonable to suspect that fluids feeding the well are similarly confined to interlayer spaces. Failure of surges to fuse over time indicates their ultimate sources are not well connected beyond the vicinity of the wellbore. Thus, fault connections, if any, must be relatively impermeable or remote.

Gas sampling at close intervals of time (23 in 90 minutes) was effective for making early identification of the complex discharge. Four end-menber compositions were indicated.

Brine sampling showed contrasts among the surge fluids, but all were dilute compared with earlier testing. For example, the highest chloride concentrations encountered in 1989 were near 1250 ppm (reservoir basis) versus >5500 ppm in 1983. Those high concentrations are due largely to evapo-concentration, indicating that the boiling space in some volcanic rocks provides for extensive separation of steam from liquid. Those spaces probably connect to the shallowest production zone in ZCQ-4, which yields mainly steam. The circumstances which enable discharge of residual liquids were not encountered in the 1989 testing. They may be technically unusual and significant to operations.

Downwell measurements of pressure for full cycles at multiple depths were essential for exposing details of the geyser mechanism. However, the chemical data most clearly shows the individuality of inflow zones. Neither kind of data is adequate, alone, for a useful study of this phenomena.

ACKNOWLEDGEMENTS

This report was made possible with the encouragement of INDE, MK Engineers, and Cordon y Merida Ings. Special thanks to Eduardo Granados for helpful discussions, especially on site.

REFERENCES

CYM-MKF, 1989, Prueba integrada informe de avance: in Planta Geotermoeléctrica de 15 MW Proyecto Zunil I Quetzaltenango, Rpt by Cordon y Merida ings. and MK-Ferguson Co., to Instito Nacional de Electrificación, August, Part II. Pruebas Químicas.

Ellis, A.J. and R.M. Golding, 1963, The solubility of carbon dioxide above 100 C in water and in sodium chloride solutions: Amer. J. Sci., v. 261, p. 47-61.

Foley, Duncan, et al, 1990, Geology and geophysics of the Zunil geothermal system, Guatemala: Geothermal Res. Coun. Trans., v.14, p. 1405-1412.

Menzies, A.J., et al, 1990, An integrated test program for the definition of a high temperature geothermal reservoir -- a case study from the Zunil geothermal field, Guatemala: Geothermal Res. Coun. Trans., v. 14, p. 1233-1239.

Michels, D.E., 1978, CO_2 in geothermal steam -- a rapid, precise, and accurate field assay technique: Geothermal Res. Coun. Trans., v.2, p. 445-448.

Pruett Industries, 1989, personal communication.

PROCEEDINGS, Sixteenth Workshop on Geothermal Reservoir Engineering
Stanford University, Stanford, California, January 23-25, 1991
SGP-TR-134

HYDROCHEMICAL FEATURES OF A GEOTHERMAL TEST WELL IN A VOLCANIC CALDERA, MT. PINATUBO, PHILIPPINES

D.E. Michels[1], V.C. Clemente[2], and M.N. Ramos[2]

[1]*Don Michels Associates*
P.O. Box 8652
Missoula, Montana, 59807
406/728-2576

[2]*Philippine National Oil Company*
Geothermal Division - EDC
Fort Bonifacio, Metro Manila
Republic of the Philippines

ABSTRACT

Mt. Pinatubo is one of several recent-age volcanoes along the west Luzon volcanic arc. A fumarole near the summit emits gases with magmatic characteristics. Several thermal springs on the east and west flanks yield various fluid types, including neutral chloride and bicarbonate. Three wellbores probed the Mt. Pinatubo caldera from elevations of +1230 through -1600 mRSL. Trajectories may be described as: central, crossing a boundary wall from the inside, and skirting a wall [probably] on the inside. Brine discharges indicate severe evapo-concentration effects accompanied by other phenomena. Severity of evapo-concentration indicates low fluid mobility near the wellbores. Large variations for ratios of component concentrations were observed, indicating negligible natural circulation (mixing). Implications about fluid movements and heat transfer processes are explored. Three components of steam can be quantified and all are significant; separate entry, adiabatic boiling, and boiling by rock heat.

SETTING: The West Luzon Volcanic Arc results from eastward subduction of the Manila Trench and includes a number of major stratovolcanoes of dominantly andesitic composition. Mt. Pinatubo is in western Luzon, north of Bataan peninsula, where the northwest Iba fracture (or graben) intersects the Arc. This region of Luzon has been built upon the Zambales Ophiolite Complex, part of the Eocene oceanic crust, along with overlying, unconformable marine, non-marine, and volcaniclastic sediments. These tilt eastward, forming the western margin of the Central Luzon Basin. Mt. Pinatubo (Figure 1) is locally the most prominent of several volcanic vents, mostly aligned along the north-trending volcanic axis. Initial volcanism began in late Pliocene and consists of andesitic to basaltic-andesitic lavas, tuffs, breccias, and lahars. Younger volcanics are dominantly dacitic ash-flow and ash-fall tuffs with minor andesitic-to-dacitic lavas and breccias.

GEOLOGIC CROSS-SECTION THROUGH MT. PINATUBO

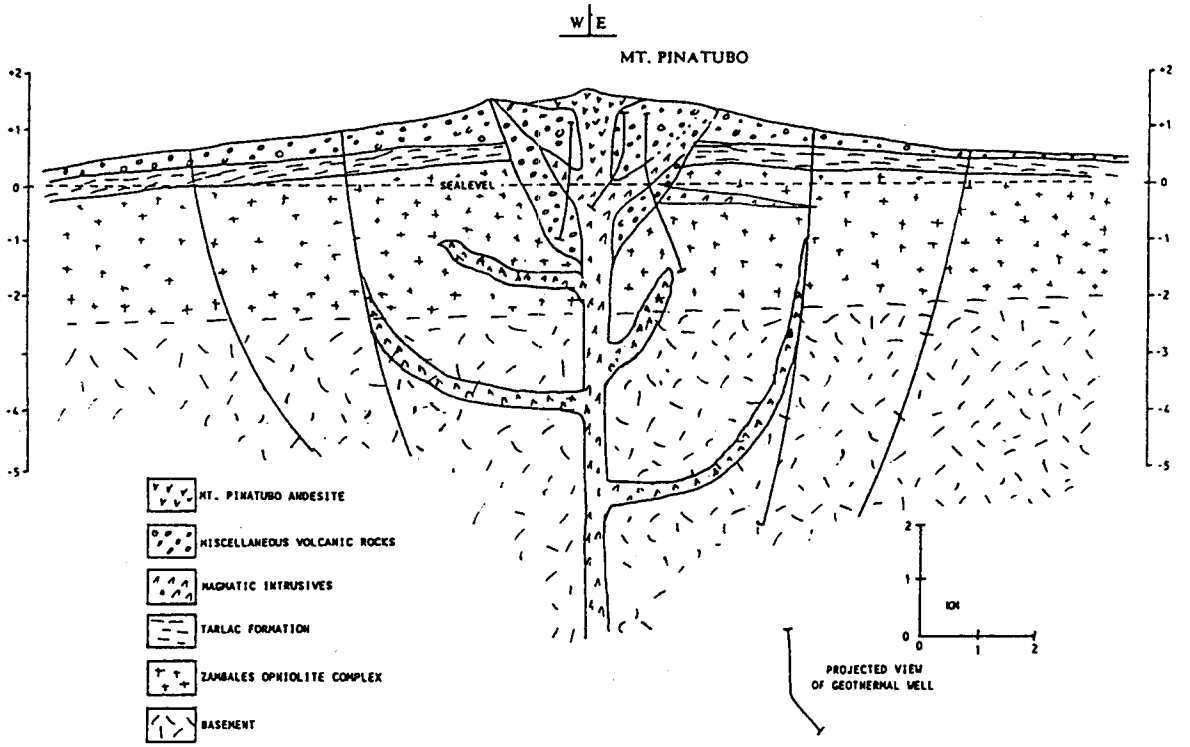

SUMMARY OF INVESTIGATIONS: The Mt. Pinatubo area is considered a prospect for geothermal energy development. Three deep wells were drilled and tested in 1988-90, following geological, geophysical, and geochemical investigations. Wellhead elevations were 1098 to 1230 mASL. Wellfluids were obtained from depths of +100 to -1600 mRSL, and most were acidic, a feature recognized as indicating magmatic origins of some components. All wells yield fluids with excess enthalpy, partly due to separate steam discharges, but considerable boiling by rock heat is apparent for wells PIN-1 and PIN-3D. Downwell samples were obtained from static wellbores (PIN-2D and -3D), after, or between periods of discharge. These downwell compositions show uneven correspondences with the compositions of discharged fluids. Collectively, the variations among wellfluid compositions, and trends during production, indicate that fluid circulations are constrained. Some H_2O in wellfluids is suspected to be meteoric, but there are significant indications for the presence of magmatic components. No isotope data are available.

The wells had low permeabilities which, with magmatic associations, denies their participation with a general upflow of liquid from some deeper source. PIN-2D and -3D were the hottest wells (338 C @ -400 mRSL, and 330 C @ -1092 mRSL). They were located closest to the axis of magma movement during massive eruption events of Mt. Pinatubo. These rocks are hot precisely because they are not significantly involved with circulations of meteoric water. The other deep well, PIN-1, was the coolest (260 C @ -1400 mRSL). It discharged a large variety of fluid compositions. The vicinity of PIN-1 could be considered as an area where meteoric waters collect, moving generally downward, not up, as they enter a hydrothermal circulation system.

Features shared by the three wells and wellfluids are acidity, that makes them unworkably corrosive as resources for a geothermal power plant, and low mass productivity, which makes them uneconomic in an energy sense. Details of their fluid compositions show large contrasts among nominal fluids from separate wells and relatively enormous contrasts among discharges from individual wells at different times.

Both poor productivity and acidic character of the fluids relate to the nature of rocks penetrated by the wellbores. These are relatively fresh magmatic rocks, relatively protected from water-rock chemical action involving meteoric water. The discharged fluids are highly interesting because they expose a magmatic rock at its last stages of cooling and early stages of interaction with fluids from meteoric sources. In this sense, the fluids may be considered "rock-dominated", as evidenced by their acidity which derives from the magmatic volatiles associated with cooling, now in its last stages.

AN INTERPRETIVE APPROACH: Fluid samples from the three Pinatubo wells were not only distinct from one another in a compositional sense, but they also reflect the actions of physical processes and events that accompany well testing. Accordingly, chemical data may be applied to non-chemical questions about the reservoir structure, how the fluids are distributed within it, and how fluids mix, or are constrained from mixing. For these applications, data are handled according to statistical concepts or in regard to some mathematical principles which describe processes, such as heat transfer and evaporation. Since these wells did not deliver fluids in the ways that other commercial wells deliver fluids, the chemical data may be used for defining and describing the uncommon processes actually involved. This report will focus on PIN-3D as an example of how fluids are altered by testing in these uncommon environments.

The data treatments used here are not a complete set. They are provided to show how results and implications, from one interpretive step, may be combined with some outside fact, leading to a subsequent interpretive step, which develops into a series. The series is emphatically not presented as a pattern for reviewing other sets of resource data. Specifically, the circumstances of available data and the results of each interpretive step will make the review process a unique sequence of steps for each resource.

PIN-3D: was completed through the interval -260 to -1092 mRSL, near the caldera boundary, where it passes through dacitic rocks and multiple dikes. The well is deep enough to intercept the O'Donnell formation and Zambales Ophiolite Complex, but they were not reported. Perhaps dikes have hidden their presence, or the well is actually inside the caldera. Clearly, the fluids have strong magmatic connections.

Water loss and heat-up surveys indicate one production interval, a suspected intersection with Marunot fault, near -400 mRSL. Maximum measured temperature was 330°C at TD (-1092 mRSL) after a very short heat-up period. Temperature at -400 was 225°C. Static water level was at the wellhead (1098 mASL).

PIN-3D was discharged initially on 2-3 December 1989, but fluids appeared diluted with drilling and injection waters. The definitive test began 18 December 1989 and continued through 26 January 1990. An initial discharge rate near 4 kg/s diminished within two days. Final conditions in January were near 2.5 kg/s at 0.18 Mpag.

FLUID COMPOSITIONS: Thirty-three complete analyses of liquids and gases are available. Fluid pH on 2-3 December was near 7, but only 4.32 upon start-up 18 December, with most subsequent values in the range 3.2 to 3.7. Concentrations of brine components increased persistently during the testing and concentrations of several components, such as iron, magnesium, manganese, and calcium were relatively high compared to geothermal waters in other sites. Sulfate concentrations were relatively less than in the other PIN-wells.

Discharge fluids contained excess enthalpy that increased during the testing. This was interpreted as boiling due to additions of rock heat. Steam addition was also indicated by a chloride-enthalpy plot which incorporated an unusually concentrated sample, 158,000 ppm Cl. Two chloride concentrations among thirty-three samples exceeded 100,000 ppm, all others were less than 60,000 ppm.

A preliminary estimate of reservoir chloride concentration was obtained by establishing a linear regression between chloride concentration and measured (wellhead) enthalpy. Then, by assigning a reservoir enthalpy, a corresponding chloride concentration could be identified. The selected enthalpy corresponded to an early measurement of enthalpy, 1401 j/g, and indicated Cl_{res} = 10,320 ppm. That enthalpy value corresponds to a single-phase liquid at 310°C. This early enthalpy value may correspond to a "heat-contaminated" fluid. To the extent that 310°C overestimates the average initial temperature of the fluid mixture, the corresponding reservoir chloride concentration will be underestimated.

Discharged fluids showed a variety of concentrations and ranges of concentration ratios. Most of the concentration ranges are associated with increased boiling due to rock heat that increased during later stages of testing. The ranges of ratio values were less variable than for PIN-1, but perhaps that is due to the shorter period of testing and the much smaller amounts of fluids produced.

Five downhole liquid samples were collected from three different depths, -290, -450, and -770 mRSL, on 13-15 February 1990, after the main discharge test. The concentration range was narrow compared to the range for surface samples. For example, chloride concentrations were 15,600±612 ppm, without a clear trend with depth. These concentrations may represent some evapo-concentration related to rock heat boiling during the testing.

Ratios of concentrations among these five downwell samples defined a narrow range. For example, Cl/B = 38.0±2.3, (n = 5). All individual values are higher than 31 (of 33) surface samples, which average 25.4±4.6. The remaining two surface samples had Cl/B = 57.6±3.0, and were the samples with chloride concentrations of 107,000 and 158,000 ppm, referred to earlier. Clearly, reservoir fluids in the vicinity of PIN-3D are highly variable and interpretations must consider that analyses may represent mixtures with (initially) undefined proportions.

EVAPO-CONCENTRATION: The range of apparent concentrations is large, and, for most components, there are 33 data points, enough for reasonable statistics. Figure 2 shows sample concentrations of six components plotted versus days of testing (no compensation for steam losses). All concentrations show general increases, with variability becoming severe after day 20. The similarity of trends suggests continuous boiling from a limited volume of initial liquid, a concept which can be tested.

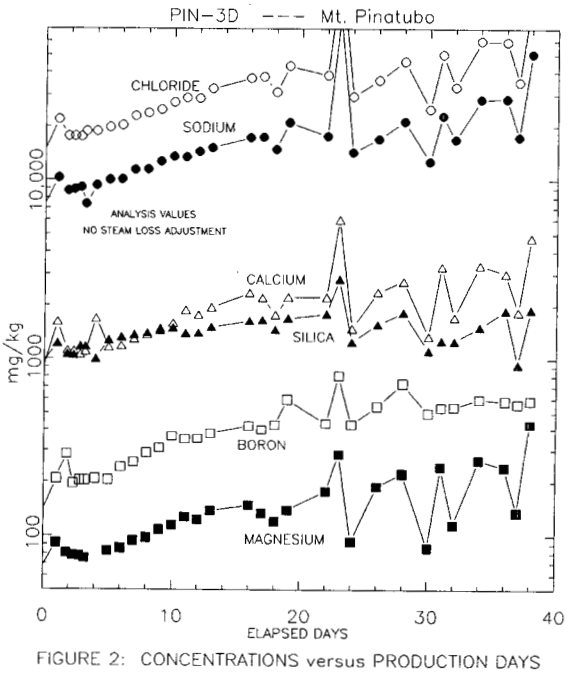

FIGURE 2: CONCENTRATIONS versus PRODUCTION DAYS

When two components (a and b) remain totally dissolved during evapo-concentrations, a graph of their changing concentrations, a versus b, will yield a straight line. The plotted line will be straight in either linear-by-linear graph axes or in logarithmic-by-logarithmic (log-log). In log-log plots, evapo-concentration yields lines with slope values $\delta\log(a)/\delta\log(b) \approx 1$. Hence, plotting several component pairs would yield a set of nearly parallel plots -- if concentration changes were due to evapo-concentration.

Figure 3 shows log-log plots for five components, each plotted versus chloride. Specific values for slopes are: sodium, 0.936; calcium, 0.953; silica, 0.413; boron, 1.099; magnesium, 0.942. The proximity of most slope values to the theoretical unity is strong evidence that evapo-concentration is a dominating process.

However, the differences from unity are more than could be justified by analytical errors if evapo-concentration were the only process operating. Thus, one must strongly suspect that other, non-conservative, processes are also reflected in the data. Slope values less than unity can be due to losses of the non-chloride component. For mid-range chloride concentrations, near 38,000 ppm, losses of initial sodium, calcium, silica, and magnesium are indicated as 4.7, 3.5, 36.0, and 4.3 weight percent, respectively. Loss can be readily suspected for the case for silica, slope 0.413. From a set of computed losses, one might even venture to identify the mineral, or minerals implied to be deposited.

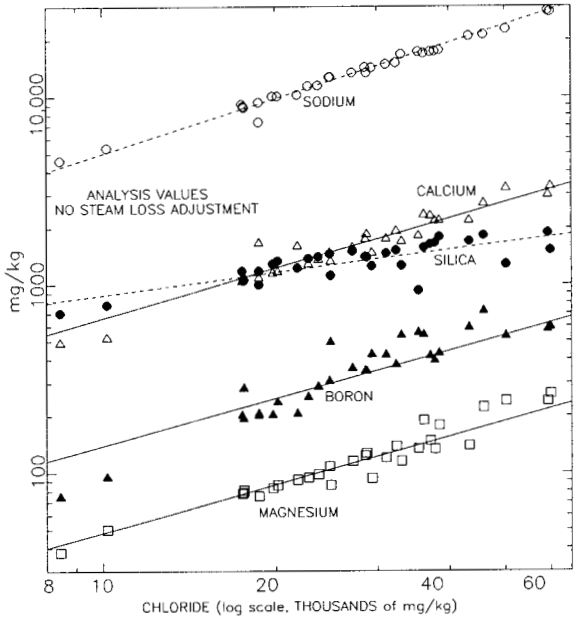

FIGURE 3: TEST FOR EVAPO-CONCENTRATION

The procedure above permits calculations to be made with mathematical, and definable, precision. However, the logical precision requires considering more issues. Specifically, the slope value for boron, about ten percent greater than unity, indicates a gain of about 7.8 weight percent, at a mid-range chloride concentration. This is more than analytical uncertainties and requires a relative addition of boron. Clearly, this requires addition of a distinct fluid which, by implication, also contains sodium, calcium, magnesium, etc. Consequently, the overall apparent "losses" may be due, instead, to the new fluid having lower values of Na/Cl ratios, etc. Since the computed losses, described earlier, explicitly consider evapo-concentration of one initial composition, results would be misleading to some degree. This point is considered later, where some resolution occurs.

Figure 4 shows an expanded view of the boron-chloride relationship with lines connecting sequential data. The first 17 to 20 days of data appear to show a dominating evapo-concentration effect. Subsequent data show scatter mainly above the trend, indicating irregular additions of a boron-rich composition. Whether that composition is relatively richer, or

poorer in other components, including silica, requires additional investigation. Figure 4 does show that a simple evapo-concentration model is appropriate for about the first 20 days of data.

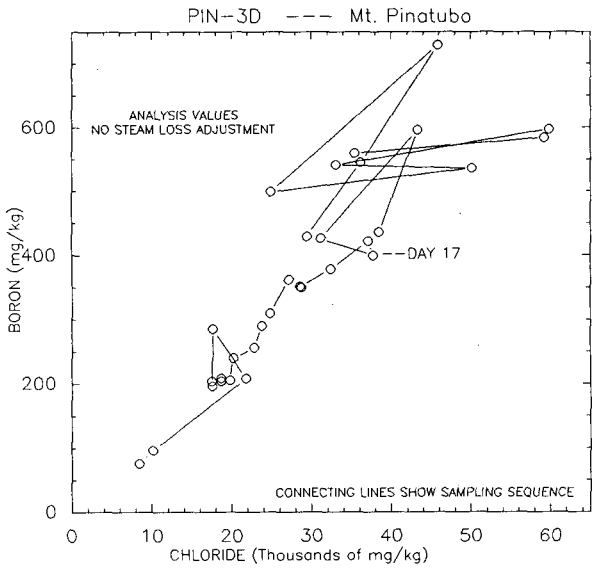

FIGURE 4: CHLORIDE versus BORON

BIAS IN THE QUARTZ GEOTHERMOMETER: Returning to the issue of silica, the effect of evapo-concentration is two-fold. Specifically, the computations for a quartz temperature would be biased. The computation initially proceeds by presuming only adiabatic formation of steam. Loss of additional steam, due to extra boiling related to additions of rock heat, would cause the adiabatic computation to overestimate the quartz temperature. Conversely, loss of silica by deposition, indicated by the low slope value in Figure 3, would tend to cause an underestimate of the true quartz temperature.

Using the apparent silica concentrations to determine pre-boiling (quartz) temperatures does appear mathematically successful for the first few days. Yet, results become increasingly unreasonable after the 5th day of testing. Calculated quartz temperatures range up to 367°C, which greatly exceeds the instrumentally measured wellbore temperatures. They also exceed the temperature of maximum silica solubility, showing that the adiabatic computation method is far outside its range of applicability. *[The specific model used does not include the diminishing solubility of silica above 340°C.]* Thus, despite the low value of silica slope, indicating more than one-third of initial silica is lost by deposition, the effects of evapo-concentration remain clearly potent.

Accordingly, only the earliest silica data may be considered as possibly representative of initial quartz temperatures, and these are somewhat ambiguous. Preliminary discharges on 2-3 December yielded quartz temperatures of 260C. That value is probably low, due to contamination by drilling and injection fluids, also indicated by pH values, near 7, that were never observed in subsequent testing. The value T_{qtz} = 295°C, based on silica concentration measurements for the second day of the extended testing, is reasonable. It may be compared to instrumental measurements of 304°C at -750 mRSL and 225°C at -400 mRSL. This estimate of T_{qtz} does not apply to fluids collected after the 20th day of testing, when irregular mixing became apparent. However, in the absence of other relevant data, it may be the most reasonable estimate.

ADIABATIC STEAM FRACTION AND INITIAL BRINE CONCENTRATIONS: Between a reservoir temperature of 295°C and the 140°C sampling temperature, adiabatic boiling yields about 36 weight percent steam. On the second day of testing, which appears to be the most representative of early conditions, the measured chloride concentration was about 17,600 ppm. This implies a reservoir basis of 11,264 ppm, about 9 percent greater than the estimate of 10,320 ppm, described earlier, based on a regression of chloride versus total discharge enthalpy, with a designated resource temperature of 310°C. Using 295°C in the earlier regression yields 10880 ppm chloride, which may be a better comparison for the two approaches and is only 3.5 percent smaller than the value based on quartz geothermometry.

NON-ADIABATIC STEAM FRACTIONS: Since the log-log plots with chloride indicated a prominent amount of boiling due to additions of rock heat, one may inquire whether the total fluid enthalpy also includes a component due to a separate entry of steam. A reasonable reference composition would be the 20th day of discharge, the last day before onset of irregular additions of undefined fluids. On that day, the chloride concentration reached 37,760 ppm, a factor of 3.35 times the initial reservoir concentration derived in the previous paragraph.

The adiabatic component of evapo-concentration, from 295°C, accounts for a concentration factor of about 1.56 for residual components, such as chloride. The remaining concentration effect, a factor of about 3.35/1.56 = 2.145, corresponds to boil-away of 53.4 percent of the initial liquid, occurring prior to its entering the wellbore, where the adiabatic boiling stage takes place. Enthalpy of a steam/water mixture, 53.4 percent steam at 295°C, would be 2085 j/g. This is much less than the measured enthalpy values at the surface on days 17 through 20, which average 2412±6 j/g, so, a separate steam entry appears operational.

Using 2756 j/g as the enthalpy of the separate steam entry (corresponding to 295°C), with the other, mixed-phase enthalpys, leads to an estimate for the mass fraction of total discharge represented by the separate steam; 48.7 weight percent. Thus, the energy content of PIN-3D fluids have three major inputs; adiabatic heat in initial liquid, rock heat in some steam from initial liquid, and a separate steam component. However, the steam-phase enthalpy value, used above, does not consider the presence of CO_2. Thus, the computed weight percent values must be considered approximate.

GASES An alternative model for steam development could involve boiling in a single feeder fracture, such that all the steam entering the wellbore derived from one initial liquid. The apparent "separate" steam entry would then be merely the effect of differential permeability for steam versus liquid moving through a common path. This alternative can be tested by considering the gas contents in steam and their relationship to the brine components, particularly chloride.

If all the steam were derived from boiling a single initial brine with steam and liquid entering the wellbore at a single common point, then CO_2 content, in the discharging mixture of steam and liquid, would decrease with increasing concentration of chloride. This effect would be prompt and severe. Boil-away of more than a few mass percent of initial liquid would severely purge gases from the residual liquids. Since brine concentrations increase by more than a factor of two between the second and 20th days of production, the nonadiabatic boil-away clearly has been severe. Associated steam production would be essentially gas-free.

However, if CO_2 is carried in steam that enters the wellbore at a different place than the brine (or brine-steam mixture) enters, then CO_2 content in the discharging mixture would not vary systematically with chloride concentration. A separate

steam entry could carry substantial CO_2 to the sampled mixture at the surface, regardless of differential permeability effects, etc., in the fracture(s) where rock heat boiling occurs.

Figure 5 tests for correlations between CO_2 and chloride; an expanded replot of the sodium data is included for comparison. The plot shows CO_2 to be independent of the chloride concentration. Thus, a separate entry for CO_2 is indicated; by implication, it carries the requisite steam.

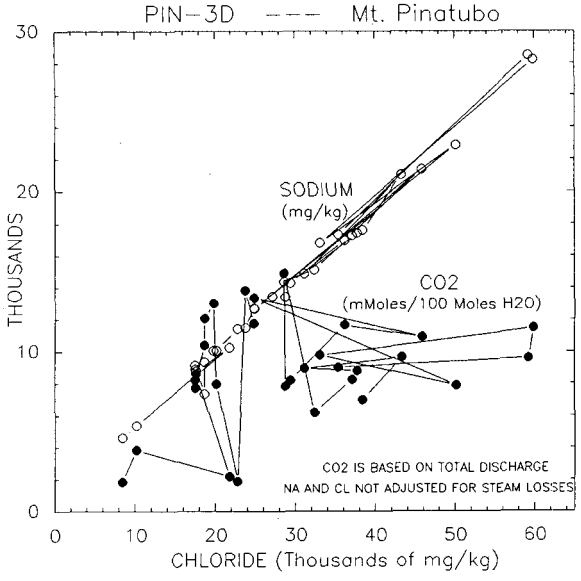

FIGURE 5: CHLORIDE versus SODIUM and CO2

This separate steam entry can also be deduced from the apparent concentrations of CO_2. From Figure 5, the average concentration appears near 10 moles CO_2 per 100 moles H_2O, on a basis of total discharge, about 20 weight percent. However, the solubility limit for CO_2 in water at the temperature and pressure of the PIN-3D production interval is only about 1.8 moles CO_2 per 100 moles H_2O, based on data from Ellis and Golding, (1966). Thus, a substantial vapor phase is indicated, prior to initiation of production. Since there seems no other source of CO_2 except the local rocks, a large magmatic component is indicated. This is in accord with the track of PIN-3D being inside the caldera.

Additional description of this vapor cap and its relationship with an equilibrium liquid phase could be explored. For example, the separate steam entry would be about 40 weight percent CO_2 if no CO_2 were carried by the liquid and its associated steam that issue from the feeder fracture where rock heat boiling occurs. This concentration is far outside normal industrial experience. It emphasizes, further, the magmatic character of the Mt. Pinatubo fluids. This kind of data would be returned to earlier computations, such as the steam enthalpy used for estimating weight percent of separate steam. By iterations, a complete set of internally consistent values may be obtained for most features of the resource.

MULTIPLE MINOR FLUID SOURCES: A minor multiplicity of gas sources is indicated by the imperfect correlation between CO_2 and H_2S shown in Figure 6. If both gases were derived only from a single source of uniform composition, then variations in concentrations would lie along a trend that extended to the graph origin (0,0). Most of the data does trend toward the origin, suggesting that a simple model, described above, has considerable validity. However, multiple offsets of data, above and below the trend toward (0,0), suggest that at least two other minor, distinct inputs are operational. Details in Figure 6 suggest these inputs were sporadic after the fourth day of testing.

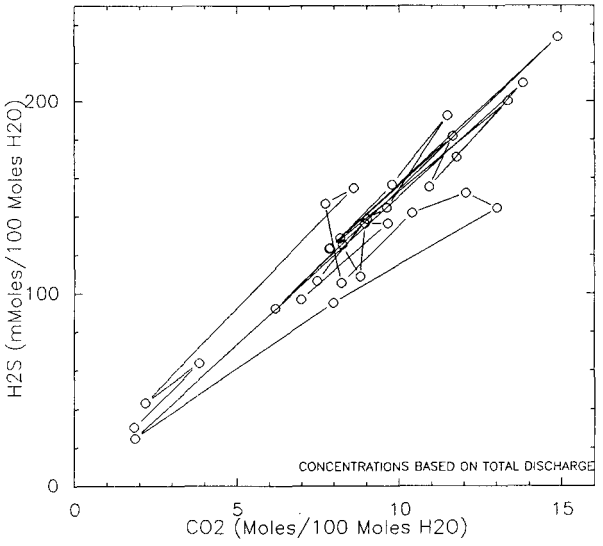

FIGURE 6: CO2 versus H2S

Similar small variations are shown by sodium in Figure 5. The trend lines between later data are parallel to earlier trend lines, but successively offset upwardly, in an *en echelon* pattern. This direction of offset indicates that new fluid input compositions have Na/Cl ratios that are larger than the ratio of the primary (initial) fluid. Returning to the earlier concepts about unit slope for log-log plots of evapo-concentration effects, this direction of offset in the log-log plot would cause the slope to exceed unity. Since the observed net result of all effects on sodium yields a slope value less than unity it may be concluded that three processes are operational; evapo-concentration is the major effect, deposition of sodium (and others) occurs in the rocks, possibly in conjunction with a much more severe deposition of silica tends to depress slope to less than unity, and new liquid compositions are added at irregular times. The new liquids have distinctive proportions of dissolved components.

IMPLICATIONS FOR RESERVOIR ENGINEERING: The small concentration shifts, noted as details in the ratios of Na/Cl, CO_2/H_2S, and Cl/B, may be viewed as deliveries from fractures that intersect the main feeder. Two major alternative mechanisms may be considered. One is the case where fluid from the auxiliary fracture enters the main feeder and mixes during an interval of time when both fluid components have negligible vapor development. Alternatively, the liquid in each fracture may be considered to be stagnant until the boiling front reaches the fracture intersection. Mixing occurs after boiling, and the first parcel of mixed fluid causes a step-change in the measured surface concentration, which is observed.

The concentration shifts, Figures 4, 5, and 6, have more of a step-change character, suggesting that little movement of fluids in fractures occurs prior to their becoming involved with the advancing, boiling front. Additionally, stagnant-until-boil is consistent with the large observed effects of evapo-concentration which requires a continually increasing surface area for heat transfer from rock to fluid.

Although no production interference tests were made in conjunction with the PIN-wells, this conclusion shows that such tests should be interpreted with caution. Most mathematical models of reservoirs carry assumptions about fluid compressibility and what initiates fluid movement. Standard parameters and implied assumptions should always be verified for relevance.

"INITIAL" RESERVOIR COMPOSITION AT PIN-3D:

Composition of reservoir liquid produced initially may be estimated from the chemical analyses of early samples, adjusted for adiabatic boiling based on temperatures in the range of 290 to 300C. The nominal composition is given in Table 1, which applies to the first few days of discharge. After about day 20, other fluid components affected the composition of discharged fluids. Due to undefined, non-adiabatic evapo-concentrations of these new inputs, "reservoir basis" compositions of them cannot be deduced with confidence. The ratios of components can be compared, early versus later production, but the later values must be interpreted as mixtures of liquids with undefined proportions.

TABLE 1: RESERVOIR LIQUID COMPOSITION
PIN-3D; First 20 Days, T = 295 C
(ppm by weight, gas-free)

Sodium	5483	Iron	69.7	Chloride	10940
Potassium	911	Magnesium	4.94	Sulfate	147
Calcium	691	Lithium	8.96	Fluoride	0.95
Silica	656	Rubidium	3.01	Bicarbonate	0.0
Boron	126	Cesium	1.37		
Manganese	98.9	Ammonium	1.05		

ACKNOWLEDGEMENTS

Presentation of these results was made possible through the Geothermal Division, Philippine National Oil Company-Energy Development Corporation and by Mesquite Group, Inc. Special thanks to Paul Brophy for geologic assistance.

REFERENCES

Fournier, R.O. and R.W. Potter, II, 1982, A revised and expanded silica (quartz) geothermometer: Geotherm. Res. Coun. Bul., November, p.3-12.

PNOC-EDC, 1990, Mt. Pinatubo resource assessment: PNOC-EDC Internal Report.

Ellis, A.J. and R.M. Golding, 1963, The solubility of carbon dioxide above 100°C in water and in sodium chloride solutions: Amer. Jour. Sci., v.261, p. 47-60.

PROCEEDINGS, Sixteenth Workshop on Geothermal Reservoir Engineering
Stanford University, Stanford, California, January 23-25, 1991
SGP-TR-134

GEOCHEMICAL CHARACTERISTICS OF ACID FLUIDS IN MT PINATUBO, PHILIPPINES

Marinela M. Buenviaje

Philippine National Oil Company-
Energy Development Corporation
Ft.Bonifacio, Manila, Philippines

ABSTRACT

The surface geochemical characteristics of Mt Pinatubo indicate widespread deep acid fluids as shown by the following : presence of solfataras or sulphur-depositing fumaroles near or at the summit, and recent or active volcanism ; discharge of mixed fluids with significant chloride at middle elevations ; significant amounts of sulphate found in spring discharges at almost all levels (except at lowest levels or near sea level) ; springs with neutral pH and have high amounts of chloride and significant amounts of magnesium and boron ; low Cl/Mg values accompanied by significant amounts of Mg observed at various elevations ; higher proportions of gases, especially CO_2 and significant N_2 ; widespread occurrence of iron hydroxide deposits at almost all elevations ; and all springs discharge immature waters.

A new mixing model is proposed, the Cl-B-Mg ternary diagram, to differentiate the effects on well and spring water chemistry of the following processes: seawater mixing, groundwater dilution and magmatic input.

Seawater mixing is not indicated for Mt Pinatubo springs as shown by crossplots of chloride versus other chemical constituents and the Cl-B-Mg ternary diagram. Neutral alkali chloride waters are present in the area. This is supported by the chemical crossplots, and the Cl-B-Mg plots. In the Cl-B-Mg plot, springs that discharge low pH waters are shown to be manifestations of acid fluids that are localized within a shallow or deep fault zone.

INTRODUCTION

The Mt Pinatubo geothermal area is located in the main northern Philippine island, Luzon. It is approximately 90 kms northwest of Manila.

A preliminary assessment of geothermal energy potential was done through a detailed exploration programme by the Philippine National Oil Company-Energy Development Corporation (PNOC-EDC) from 1982 to 1983 at Mt Pinatubo. The exploration programme involved semi-detailed geologic mapping, geochemical and geophysical surveys.

A three-well deep exploration drilling programme was carried out starting late 1988 at Mt Pinatubo (Fig. 1). All three wells were characterized by low pH values (2.4-3.8), excess enthalpy and low permeability.

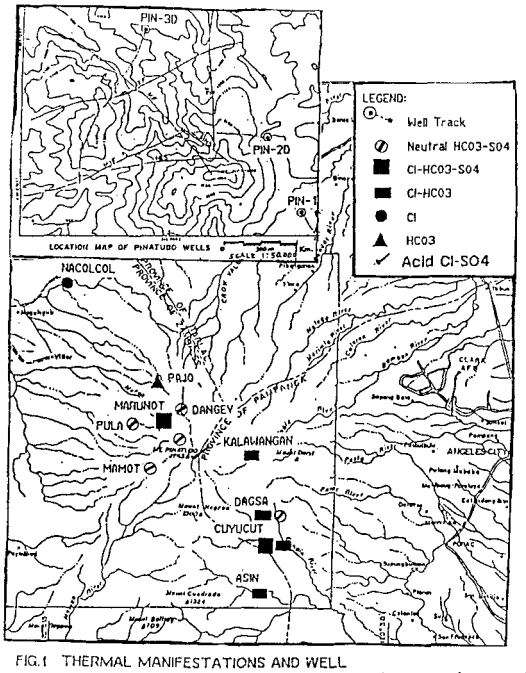

FIG.1 THERMAL MANIFESTATIONS AND WELL LOCATION MAP OF MT. PINATUBO

BACKGROUND : RESULTS OF GEOCHEMICAL INVESTIGATIONS AT MT PINATUBO

Mt Pinatubo is an andesitic strato-volcano. It is the youngest and highest peak (1745 mASL) on a late Tertiary to Quaternary volcanic arc in west Luzon. A breached oval-shaped caldera is enclosing the peak of Mt Pinatubo, an andesitic dome. The caldera is formed by piece-meal subsidence due to the eruption of voluminous pyroclastic materials. The latest activity probably culminated in the growth of the dome. Structures control the location of the thermal features in this area.

The most significant geochemical characteristics of the spring and well fluids in Mt Pinatubo are summarised as follows:

Classification of springs are based on the relative Cl, HCO_3 and SO_4 contents of the water samples (Table 1). Mixed fluids with significant Cl (>20%) are found at middle elevations. Significant bicarbonate contents are found at almost all elevations. Sulphate-rich fluids are found at higher elevations i.e. discharges at greater than 1000 mASL at Mt Pinatubo.

All springs have very low to medium discharge flow rates and are below boiling temperatures. There are solfataras or sulphur-depositing fumaroles near the summit.

Chloride-rich springs such as Dagsa and Cuyucut have significant SO_4, HCO_3, and Mg. This could be due to mixing of chloride-rich fluids from depths with steam condensate fluids flowing along the flanks of the volcano. Such enrichment could also be due to mixing of acid Cl + SO_4 - rich fluids with groundwater.

The only acid spring sample is from the Pinatubo solfatara pool. The latest samples indicate that sampling points are different and show greater meteoric water contribution (M.N.Ramos, pers. comm.). Dilution with meteoric water, as indicated by lower chloride values, is observed for the most recent samples of Dangey, Lower Marunot, Kalawangan and Dagsa springs.

Iron hydroxide deposits are noted in most of the springs at Mt Pinatubo. They are normally thought of as products of weathering (P.R.L. Browne, pers. comm.). Their widespread occurence in Mt Pinatubo are taken to be significant. Inaccuracies in sampling could account for the higher values of iron in a few samples. Acid added to unfiltered water samples would dissolve the iron hydroxide precipitates.

Higher concentrations of iron observed for the three Pinatubo wells are mainly due to acid corrosion of the wellhead assembly in drill pipes. The prevalence of iron hydroxide deposits in the surface could be linked to a significant amount of dissolved iron at depth, however.

Gas samples from the solfatara show significant amounts of H_2S but is predominantly CO_2 with some F, S_2 and Cl.

The origin of the gases discharged from wells and solfataras or fumaroles may be deduced from their chemistry. This is made possible by use of ternary diagrams - plotting relative amounts of N_2, Ar and He or CO_2 (Giggenbach and Goguel, 1989). Higher proportions of N_2 and CO_2 are indicative of magmatic origin (Figs. 2a and 2b). All the Pinatubo well discharge gases are of magmatic or volcanic origin. The solfatara or fumarole gas samples show significant air contamination.

The neutral pH of springs is due to the interaction of acid fluids with the host rocks as it travels to the surface. The very high SO_4 concentration is due to disproportionation of SO_2 into sulphuric acid and hydrogen sulphide, and the oxidation of H_2S in the vadose zone, as shown by the following reactions:

$$SO_2 + H_2 = H_2SO_3$$

$$4H_2SO_3 = 3H_2SO_4 + H_2S$$

Low Cl/Mg values and high Mg values are indicators for acid fluids. Lowest Cl/Mg values are found in Pajo and Upper Marunot.

NEAR SURFACE MIXING RELATIONSHIPS

A series of chemical crossplots (Figs. 3a-3f) of chloride versus other chemical constituents

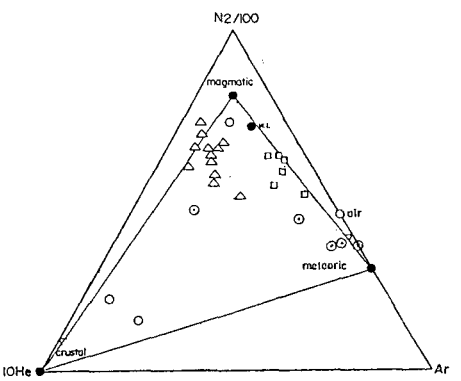

FIG. 2.a RELATIVE N2, He, Ar CONTENTS OF MT. PINATUBO INDICATING MAGMATIC ORIGIN OF GASES

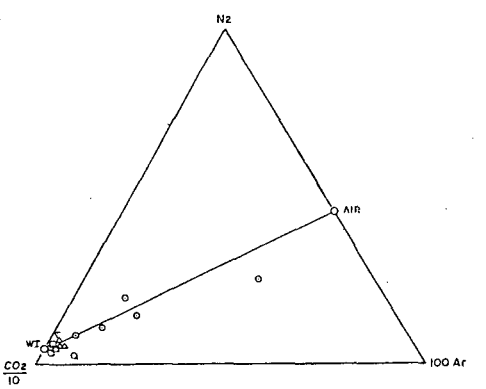

FIG. 2.b RELATIVE N2, CO2 AND Ar CONTENTS OF MT. PINATUBO GAS DISCHARGES

LEGEND:

○ PIN-1 ⊙ PINATUBO SOLFATARA
□ PIN-2D
△ PIN-3D ○WL WHITE ISLAND,N.Z.

Fig 3a Plot of chloride vs sulphate of Mt Pinatubo springs

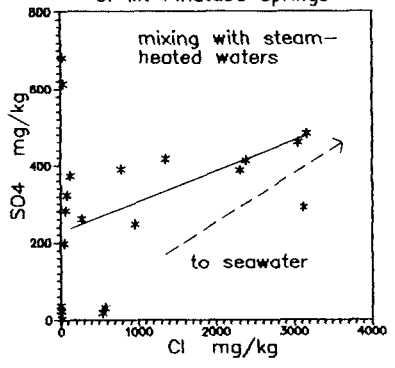

Fig.3b Plot of chloride vs sulphate of Mt Pinatubo springs

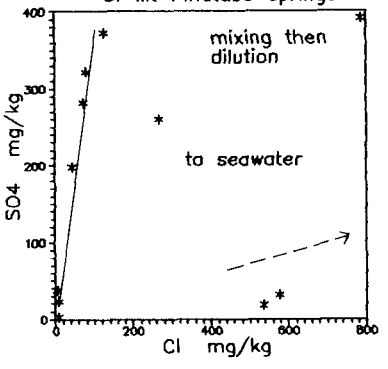

Fig 3c Plot of chloride vs magnesium of Mt Pinatubo springs

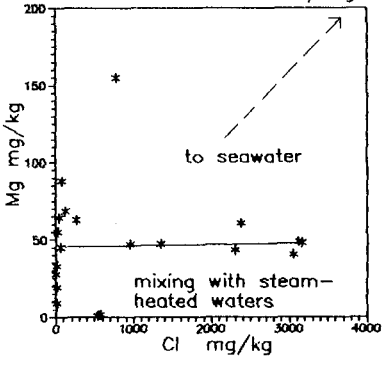

Fig. 3d Plot of chloride vs boron of Mt Pinatubo springs

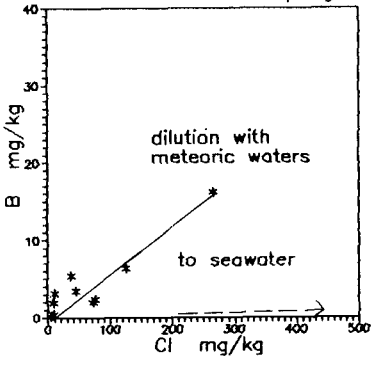

Fig. 3e Plot of chloride vs silica of Mt Pinatubo springs

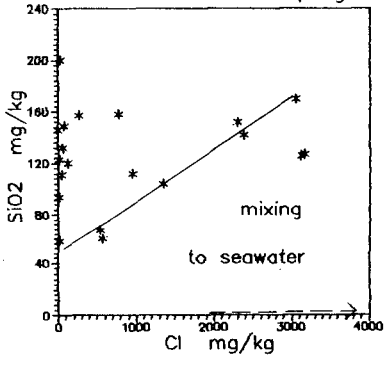

Fig. 3f Plot of chloride vs iron of Mt Pinatubo springs

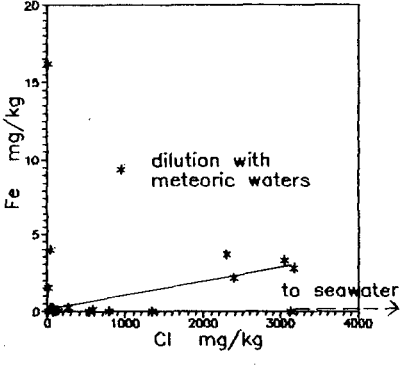

(Arnorrson, 1985) confirm mixing of alkali-chloride fluids with various thermal waters and dilution with meteoric waters in the Mt Pinatubo area. Springs at higher elevations show mixing of steam-heated groundwaters and thermal fluids followed by dilution with meteoric waters (Fig. 3b). Springs at different elevations show mixing of thermal fluids (including steam-heated groundwaters) (Figs. 3a,3c and 3e) or just plain dilution with meteoric waters (Figs. 3d and 3f). Lines to indicate mixing with seawater is precisely drawn in every diagram. Seawater mixing is not indicated for springs since the mixing and dilution lines do not coincide with the line for seawater mixing.

Alkali chloride waters in Mt Pinatubo are diluted and appear at Nacolcol springs. They are mixed with other thermal waters and appear at Asin , Cuyucut and possibly at Dagsa springs. They are diluted and appear at Lower Marunot and Mamot springs.

ORIGIN OF FLUIDS AND DEEP PROCESSES

Very high temperatures allow for the leaching of boron from rocks and boron is volatilized into ascending steam. The Cl-Li-B ternary diagram (Giggenbach and Goguel,1989) shows that Mt Pinatubo well fluids reflect the deep processes and a dilution line can be drawn towards Pinatubo springs

(Fig. 4). Other Philippine wells have variable chloride and boron values (Table 2).

The relative Cl, Li and B contents of the springs, with the exception of Upper Marunot and Dagsa springs, plot them near the chloride corner but no clear distinction is made for seawater mixing from magmatic input.

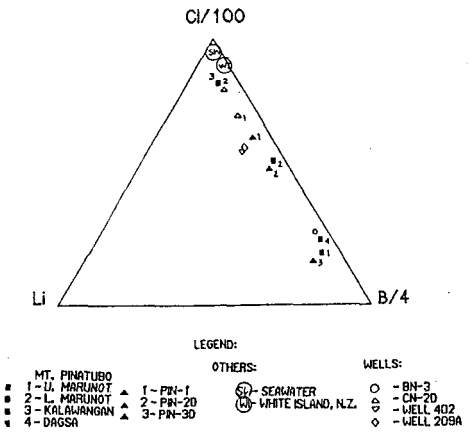

FIG. 4 RELATIVE Cl, LI AND B CONTENTS OF MPGP WATERS

As fluids start to ascend, water-rock interaction occurs, the intensity being dependent on the volume of fluid reacting with the rocks. Most of the spring and well discharge data points plot in areas of geothermal waters (Fig.5). Surprisingly, the highly acidic Pinatubo well fluids do not plot near the Rb corner, which is supposed to imply initial dissolution of crustal rocks in acid waters formed through absoption of magmatic vapour into the deeply circulating ground water (Giggenbach and Goguel, 1989). Most of the fluids show equilibration with rocks either at depth (from well chemistry data points) or at the surface (from spring chemistry data points).

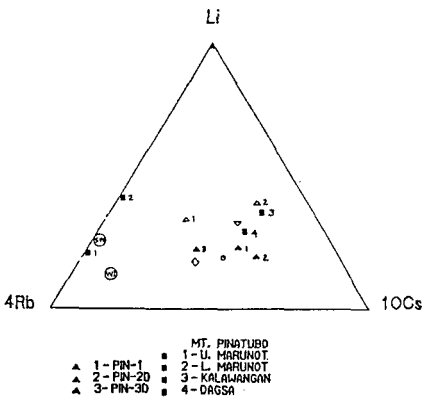

FIG. 5 RELATIVE LI, Rb AND Cs OF MPGP WATERS

RESERVOIR CONDITIONS

When fluids at reservoir depths have equilibrated then the corresponding spring chemistry could be used to determine the minimum temperatures at that depth. This is done by plotting relative Na, K and Mg contents of various spring and well discharges in the area (Fig. 6) (Giggenbach, 1988). PIN-1 (acidic $NaCl-SO_4$ fluid) and PIN-3D (acidic NaCl fluid) plot in the partial equilibrium area together with the acidic well CN-2D, and near neutral pH well 402. The neutral pH surface springs at Mt Pinatubo plot along a mixing line and yield a minimum reservoir temperature estimate of 210°C which is way below the maximum measured downhole temperature of 336°C at PIN-2D. Acidic wells PIN-2D ($Na+K-Cl+SO_4$ fluids) and BN-3 plot near the rock dissolution line in the area for immature waters (Giggenbach, 1988).

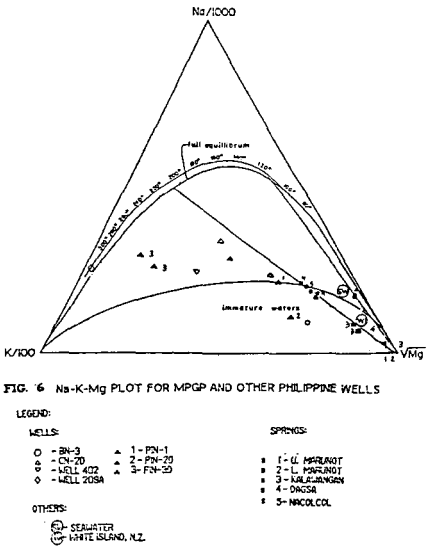

FIG. 6 Na-K-Mg PLOT FOR MPGP AND OTHER PHILIPPINE WELLS

An attempt was made to differentiate the effects on well and spring water chemistry of the following processes: seawater mixing, groundwater dilution and magmatic input. Relative Cl, B and Mg contents of various springs and well waters were plotted along with seawater and solfatara spring samples (Fig. 7). Seawater has significant amounts of Cl and Mg but low boron concentration (Table 1). Volcanic springs have similar levels of Cl and Mg but contain more boron, e.g Pinatubo solfatara spring. High temperature volcanic steam volatilizes boron from rocks and deposits it into shallow aquifers that feed springs.

Neutral pH geothermal systems (Wairakei and Tongonan wells) plot along the common Cl and B axis since their deep well fluids contain trace amount of Mg (Table 2). Brine fluids, (Salton Sea well) plot near the Cl corner along this same axis. Sedimentary-hosted geothermal systems (Ngawha well) (K. Nicholson, pers. comm.) plot near the B corner along

this same axis. Vapour-dominated systems (Kamojang well) also plot near the B corner but has significant Mg due to acidic steam leaching .

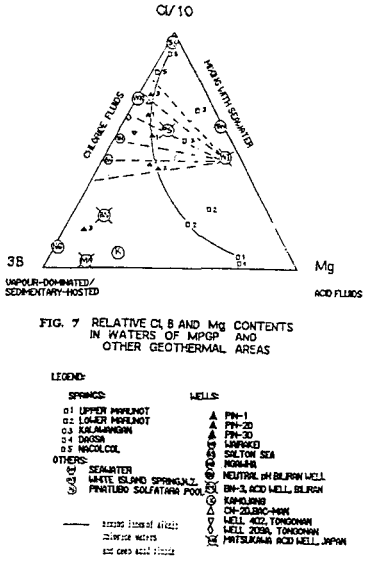

FIG. 7 RELATIVE Cl, B AND Mg CONTENTS IN WATERS OF MPGP AND OTHER GEOTHERMAL AREAS

Increasingly acidic geothermal wells plot away from the common Cl and B axis towards the Mg corner. BN-3 and Matsukawa wells plot quite near the B corner and have low amounts of Cl and Mg. Their acidity may be due to the presence of a higher proportion of gases and downward percolating acid fluids formed in steam-heated near surface aquifers. Pinatubo wells and the Bacman II well CN-2D have relatively greater proportions of Cl and variable amounts of B and Mg. Their chemistry implies deep seated acidity. Their high Cl contents are not due to seawater mixing as they contain significant amounts of boron.

"Path lines" are drawn from the neutral alkali chloride systems in the common Cl-B axis towards the volcanic systems data points. The nearer the well data points to the volcanic systems, the greater the magmatic input. A neutral alkali chloride reservoir possibly exists at the Mt Pinatubo geothermal area as deduced from the position of the well and Pinatubo solfatara data points. This is supported by the presence of a group of neutral pH springs at the lowest elevation, namely, Nacolcol springs.

The rest of the Mt Pinatubo springs show greater Mg concentration at higher elevations. Significant meteoric water component is implied for Upper Marunot and Dagsa springs. Lower Marunot spring waters come from the dilution of PIN-2D type fluids with meteoric water. Kalawangan spring waters lie along a potential "path-line" and together with Cuyucut springs (Fig. 7) are the only indicators for widespread deep acid fluids at Mt Pinatubo.

Curves are drawn between the waters near the Mg corner and the Cl-corner. These curves may represent mixing of alkali chloride waters that feed Nacolcol spring and acid (but have undergone neutralisation due to water-rock interaction) waters that feed Upper Marunot and Dagsa. The Pinatubo wells represent the dominantly acidic waters that have not yet undergone neutralisation by water-rock interactions at depth (Fig. 7).

Springs that discharge acidic waters are shown to be manifestations of acid fluids that are not widespread within the reservoir (Fig. 8). This is well illustrated by the springs of Biliran geothermal project, where, out of 3 wells drilled, one well discharged acidic fluids. Though magmatic input is invoked it is mostly due to acidic steam-heated groundwaters percolating downwards through fault zones.

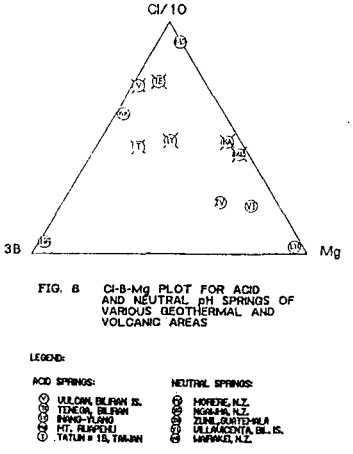

FIG. 8 Cl-B-Mg PLOT FOR ACID AND NEUTRAL pH SPRINGS OF VARIOUS GEOTHERMAL AND VOLCANIC AREAS

The Lake Nyos sample has been used to represent slightly acid CO_2-rich waters in a volcanic setting (Giggenbach and Goguel,1989) and seawater mixing is exemplified by Morere spring, New Zealand.

The trends discussed above are summarised below (Fig. 9). The uncertainties of the mixing model come basically from assuming "representative" data points from various hydrothermal systems.

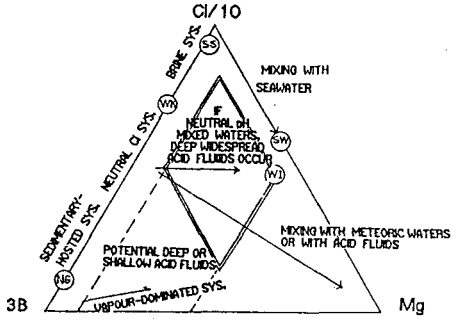

FIG. 9 OBSERVED TRENDS IN THE PROPOSED Cl-B-Mg TERNARY DIAGRAM

CONCLUSIONS: Geochemical Signatures of Widespread Deep Acid Fluids in Mt Pinatubo

The surface geochemical characteristics of widespread deep acid fluids at Mt Pinatubo are summarised as follows:

1. Presence of solfataras or sulphur-depositing fumaroles near or at the summit and recent or active volcanism.

2. Discharge of mixed fluids with significant chloride at elevated grounds.

3. Significant amounts of sulphate found in spring discharges at almost all levels (except at lowest levels or near sea level).

4. Springs with neutral pH and have high amounts of chloride (that is not due to seawater mixing) and significant amounts of magnesium and boron.

5. Low Cl/Mg values accompanied by significant amounts of Mg observed at various elevations.

6. Higher proportions of gases, especially N_2 and CO_2.

7. Widespread occurence of iron hydroxide deposits at almost all levels.

8. Most of the springs are immature waters and a few are partially equilibrated.

Using a Cl-B-Mg diagram, Kalawangan and Cuyucut springs are seen to indicate deep acid fluids at Mt Pinatubo. Mixing lines or curves indicate that neutral alkali waters that feed Nacolcol spring have mixed with widespread acid fluids that have neutralised and are feeding Upper Marunot and Dagsa springs. Acidic springs from other hydrothermal areas are shown to be manifestations of acid fluids that are localized within a shallow or deep fault zone.

ACKNOWLEDGEMENTS

The writer wishes to thank the PNOC-EDC management for the data and facilities used in preparing this report. Special thanks to Profs. K. Nicholson, P.R.L. Browne, J.R.Ruaya and Mr. A.S.J. Baltasar for their advice and review. This report is part of the project for Diploma in Geothermal Energy Technology held at the Geothermal Institute, University of Auckland, New Zealand.

REFERENCES

Arnorrson, S. (1985): The use of mixing models and chemical geothermometers for estimating underground temperatures in geothermal systems. J. Volcanol. and Geotherm. Res.,23 : 299-333.

Giggenbach, W.F. (1988): Geothermal solute equilibria. Derivation of Na-K-Mg-Ca geoindicators. Geochim. Cosmochim. Acta, 52:2749-2765.

Giggenbach, W.F. and R.L. Goguel (1989): "Collection and analysis of geothermal and volcanic water and gas discharges", Report No. CD 2401, 4th ed,DSIR, New Zealand , 81 pp.

TABLE 1 : CHEMISTRY OF MT PINATUBO SPRINGS AND SEAWATER

SOURCE	ELEV. mASL	SAMPLE DATE (yymmdd)	FIELD TEMP. (C)	LAB. pH (25 C)	Li	Na	K	Rb	Cs	Ca	Mg	Fe	Cl	SO4	F	B	SiO2	HCO3
										(in mg/kg)								
PINATUBO	1150	830515	58	1.00	10.5	10134	2276	5.84	2.02	69	1056.0	ND	34053	40600	ND	423.0	605	ND
U. MARUNOT	1075	821012	76	7.75	0.12	58	13.9	0.11	ND	186	55.1	0.25	37	613	ND	5.4	200	259
DANGEY	965	830514	41	7.97	0.41	113	8.3	0.04	0.47	139	88.1	ND	77	322	ND	2.4	149	603
	965	900326	39	7.99	0.27	68	6.1	ND	ND	133	64.3	3.95	44	198	0.39	3.5	111	562
L. MARUNOT	900	821012	47	7.60	0.46	369	27.6	0.16	ND	82	155.0	ND	787	391	ND	23.3	158	64
	900	900403	50	7.94	0.38	157	14.8	0.06	ND	62	62.7	0.27	265	260	0.47	16.2	157	165
MAMOT	900	821007	48	7.77	0.22	74	6.8	ND	ND	163	45.2	0.22	72	282	ND	2.0	132	445
	900	900324	43	7.99	0.44	158	11.4	0.07	0.02	86	68.5	0.07	127	373	0.86	6.4	120	382
KALAWANGAN	675	830511	38	7.87	1.34	785	63.5	0.15	0.17	303	47.4	ND	1347	417	ND	5.4	104	537
	675	900523	40	7.64	1.09	570	49.2	0.13	0.03	114	47.2	9.38	950	247	0.11	11.0	112	456
PULA	600	821014	21	7.27	ND	8	3.8	ND	ND	13	9.2	1.55	9	23	ND	0.4	94	71
PAJO	518	821028	27	7.66	ND	21	4.9	ND	ND	45	27.7	ND	5	37	ND	0.2	146	288
	495	821028	25	8.03	ND	17	5.3	ND	ND	34	19.4	ND	9	3	ND	1.9	123	225
CUYUCUT	325	830313	44	7.99	2.70	1687	123	0.58	0.43	197	43.5	3.65	2304	388	ND	27.7	152	1334
	380	900329	57	8.30	3.19	1720	184	0.51	0.37	26	60.8	2.21	2387	413	0.21	33.5	142	481
DAGSA	300	830314	48	8.10	3.45	2170	148	0.70	0.55	223	40.6	3.29	3049	460	ND	348.0	170	938
	300	900327	44	7.83	0.09	19	3	ND	ND	241	33.1	16.2	10	681	0.32	3.1	58	66
ASIN	295	830513	51	7.81	3.00	2169	158	0.45	0.43	123	48.9	ND	3123	291	ND	16.4	126	1416
	295	900328	54	8.03	3.96	2180	229	0.63	0.46	287	48.3	2.82	3167	483	0.27	8.7	127	1549
NACOLCOL	220	821006	30	6.43	ND	212	2.9	ND	ND	129	0.9	ND	535	18	ND	1.3	67	16
	220	900404	49	7.20	ND	232	3.3	ND	ND	138	1.6	0.13	576	31	0.50	3.2	60	28
SEAWATER	1	831206	29	8.17	0.14	10613	369	0.19	0.09	387	1221.0	0.21	19206	2460	ND	4.6	5	121

TABLE 2: SELECTED WEIRBOX CHEMISTRY OF MT PINATUBO AND OTHER PHILIPPINE WELLS

SOURCE	DATE (yymmdd)	WHP (MPa)	Hd (J/g)	pH (25 C)	Li	Na	K	Ca	Mg	Fe	Cl	F	SO4	HCO3	B	SiO2	H2S
											(in mg/kg)						
PIN-1	891010	0.51	1835	3.61	12.6	7930	889	112	142	80	13300	1.73	1260	ND	186	731	ND
	891014	0.47	1876	3.77	13.0	8036	859	102	177	92	13211	1.66	1367	ND	175	747	ND
	891024	0.34	2231	3.96	10.2	6584	690	109	231	119	10900	2.57	1743	3.9	190	662	ND
PIN-2D	890211	0.97	1531	2.46	5.1	2989	582	34	243	421	5531	2.78	2836	ND	152	1248	6.1
	890212	0.72	1907	2.38	6.7	3302	603	47	283	541	5566	3.32	3143	ND	175	1326	21.8
PIN-3D	900225	0.39	2494	3.23	23.5	17220	3290	2260	170	212	35450	ND	335	ND	331	1883	NA
	900301	0.29	2519	3.25	60.2	30500	10820	6525	451	1340	73740	ND	254	ND	797	1810	0.6
	900313	0.27	2562	3.77	38.3	34550	6780	3640	255	1200	7130	3.19	225	ND	1113	1033	3.8
BN-3	821230	-	1872	3.3	2.1	1246	278	9	84.5	ND	2127	ND	2089	ND	222	1140	ND
CN-2D	820421	-	-	3.78	2.5	2007	173	20	18.2	ND	2553	ND	1416	ND	27	585	ND
	820715	-	1002	3.7	3.2	2601	231	11	8.73	ND	3758	ND	1710	ND	22	651	ND
402	810507	-	-	4.44	17.2	5350	860	119	53	-	9109	-	1340	-	197	612	-
209A	831222	-	-	6.75	24.4	7955	2197	215	0.31	-	14861	-	22	-	292	963	-

- = NOT ANALYSED
ND= NOT DETECTED

PROCEEDINGS, Sixteenth Workshop on Geothermal Reservoir Engineering
Stanford University, Stanford, California, January 23-25, 1991
SGP-TR-134

SIMULATING WELLFLOW OF HIGH-NONCONDENSABLE-GAS GEOFLUIDS USING LABORATORY MEASUREMENTS ON SECONDARY FLUIDS

LAOULACHE, R.N. AND DIPIPPO, R.

MECHANICAL ENGINEERING DEPARTMENT
SOUTHEASTERN MASSACHUSETTS UNIVERSITY
NORTH DARTMOUTH, MA 02747

ABSTRACT

An experimental simulation of an actual steam-water geothermal well based on field data obtained in New Zealand is carried out in a two-phase flow facility using dichlorotetrafluoroethane, known commercially as refrigerant 114. The simulation of steam-water flow is accomplished by a similarity theory which is achieved by using appropriate dimensionless numbers; namely, the Mach, Froude, and Reynolds numbers at the flashing front. The theory is used to scale the flow properties from that of water to that of refrigerant 114 in the two-phase region, and permits the prediction of steam-water characteristics in a flowing well, under much reduced pressure and temperature levels. Two experimental series were conducted to confront the similarity theory with actual measurements from a flowing well with significant noncondensable gases. Experimental results using refrigerant 114 indicate that the pressure distribution along the pipe can be predicted accurately in the two-phase region of a geothermal well.

NOMENCLATURE

a	sonic velocity (m/s)
A	distribution coefficient
C	specific heat (kJ/kg/^{o}C)
D	pipe diameter (m)
F	mass fraction of noncondensable gas
Fr	Froude number
g	acceleration of gravity (m/s^2)
h	enthalpy (kJ/kg)
K	Henry's constant (atm)
$\dot{m}$	mass flow rate (m/sec)
M	molecular weight (g/gmole)
Ma	Mach number
n	number of moles (gmole)
N_D	similarity parameter
P	pressure (bar,a)
Re	Reynolds number
R_a	apparent gas constant (kJ/kg/^{o}C)
T	temperature (K)
v	specific volume (m^3/kg)
x	dryness fraction
X	mole fraction
z	height from flashing front (m)
W	velocity (m/s)
ψ	mass flux (kg/m^{2}s)
μ	dynamic viscosity (Pa.s)

Subscript

a	apparent
c	carbon dioxide CO_2
f	liquid
fg	evaporation/condensation
g	gaseous phase
M	measured
meas	measured
o	stagnation condition
or	orifice
r	refrigerant R-114
ref	reference
res	reservoir
sat	saturation condition
T	total
v	vapor
w	water H_2O

Superscript

*	flashing condition

BACKGROUND

In the mid 1980s the U.S. Department of energy funded a research project at Brown University aimed at developing a reliable, safe, predictive and relatively inexpensive method of simulating the two-phase flow of geothermal fluids in a controlled laboratory environment. The working fluid for the laboratory studies would not be water (due to the high temperatures and pressures) but a fluid that would simulate water (a similarity fluid).

The concept of similitude (or scaling) is well-established for single-phase flows, but is less for two-phase, liquid-vapor flows. This study should not be confused with other studies whose goal is to model actual two-phase flows, particularly in geothermal wells [1-4]. The theoretical basis for the Brown University study, and details of the laboratory setup are given in Refs. [5-6].

The fundamental premise for this effort is depicted schematically in Figure 1. A reliable and predictive similarity theory provides laws for all physical variables pertaining to the problem. These include, in this case, pipe diameters and lengths, fluid flow rates, temperatures and pressures. Expensive, cumbersome, risky and inaccurate field measurements may thus be replaced with relatively inexpensive, controlled, safe and highly accurate laboratory experiments. Having in hand the analytical tools to relate the laboratory results to field results, one may easily design the field equipment (surface piping as well as production and injection wells) for optimum characteristics.

In this paper, we offer a brief summary of the basic similarity theory developed by the Brown University team. The case of geofluids with significant amounts of noncondensable gas is examined through the use of the laws of Henry and Raoult. The experimental facility is described as it

existed at Brown University and the results of a series of measurements designed to prove out the theory are presented.

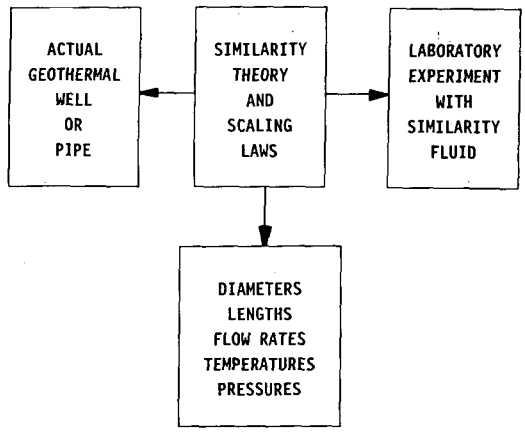

Figure 1. Basic Concept of laboratory simulation of geothermal fluid flow

SUMMARY OF SIMILARITY THEORY

Basic Theory

Many similarity theories have been proposed in two-phase flows [7-10] to simulate water-steam mixtures using fluorinated hydrocarbons. In this work no attempt is made to test these theories since our experimental arrangement required certain reference parameters which differ markedly from other proposed criteria. The reference groups which we identified as the important controlling inlet conditions for pipe flow [11-12] are the Mach, Froude, and Reynolds numbers (Ma^*, Fr^*, Re^*) at the flashing front defined as:

$$Ma^* = W_f^*/a^* \quad (1)$$

$$Fr^* = W_f^*/(g\,D)^{1/2} \quad (2)$$

$$Re^* = \psi\, D/\mu^* \quad (3)$$

$$\text{where } W_f^* = \psi\, v_f^* = (\dot{m}/A)\, v_f^*. \quad (4)$$

The sonic velocity a^* is avaluated under the assumption that the two-phase flow mixture at flashing is homogeneous [13].

In an earlier work [5] we developed a similarity theory to relate reference parameters for R-114 with those of water-steam mixtures. Here we will only summarize the theory. The basic assumptions are the following:

$$1)\ v_f = \text{constant}. \quad (5)$$

$$2)\ h_{fg} = h_g - h_f = \text{constant}. \quad (6)$$

3) Saturated vapor phase obeys the perfect gas equation of state:

$$P\, v_g = R_a\, T, \quad (7a)$$

$$\text{or } P\, v_{fg} = R_a\, T \quad (7b)$$

since in general, $v_g >> v_f$.

These assumptions are valid for water substance over the range 100-300°C and for R-114 in the range of -20 to 70°C.

With the appropriate choice of reference parameters, the theory shows that the temperature, pipe diameter and height correspondences between water substance and R-114 are given by:

$$(T_r/T_w) = (h_{fg,r}\, R_{a,w})/(h_{fg,w}\, R_{a,r}), \quad (8)$$

$$(D_r/D_w) = (T_r\, C_{f,r})/(T_w\, C_{f,w}), \quad (9)$$

$$\text{and } (z_w/z_r) = (D_w/D_r) \quad (10)$$

respectively. At the flashing front, similarity requires that

$$Ma_w^* = Ma_r^*, \quad (11)$$

$$\text{and } Fr_w^*/Fr_r^* = N_{D,w}/N_{D,r}, \quad (12)$$

where

$$N_D = (P\, v_f\, R_a/h_{fg}/C_f)\ e^{(T\, R_a/h_{fg})}. \quad (13)$$

The whole idea can be summarized in the following way. From the stagnation temperature in the reservoir (= flash temperature under adiabatic conditions), the mass flow rate of water, together with the pipe diameter, one can determine the required flash temperature, pipe diameter, and the mass flow rate of R-114 to simulate the steam-water conditions using this similarity theory. Then, the results of tests on the R-114 under controlled laboratory conditions can be used to predict the temperature and pressure of steam-water mixtures in an actual vertical flow. According to eqs.(8-9), to simulate a case where water, flowing at 42 kg/s, flashes at 250°C in a 15 cm pipe, for example, R-114 would have to be flowing at 0.2 kg/s, and flashing at a temperature of 45.4°C in a 2 cm pipe.

If one measures the temperature of R-114, T_r, along the test section, then the temperature T_w for water-steam mixture can be calculated from eq. (8), and the saturation pressure P_w can be found from standard steam tables.

The accuracy of the predicted pressure P_w in the two-phase region can be tested by a comparison with actual pressure measurements from field data.

Noncondensable Gas Effects

Since most geothermal fluids carry noncondensable gases (mostly carbon dioxide, CO_2), it is necessary to investigate this effect. A thermodynamic analysis based on phase equilibrium between water-steam mixtures and CO_2 at any temperature shows that the latter behaves as a solute in a dilute liquid solution of H_2O. If we treat H_2O as an ideal solution, then we can use Henry's law which states that the partial pressure of CO_2 is given by:

$$P_c = K_c\ X_c, \quad (14)$$

where X_c is the mole fraction of CO_2 in the liquid phase of the steam-water mixture:

$$X_c = n_{c,f}\ /\ (n_{c,f} + n_{w,f}). \quad (15)$$

Henry's constant can be found in Ref. [14]. Using the distribution coefficient A [15], the ratio of moles of CO_2 in the liquid phase to that in the vapor phase can be expressed as:

$$(n_{c,f}/n_{c,v}) = A\ (n_{w,f}/n_{w,v}). \quad (16)$$

In the vapor phase:

$$\dot{n}_{c,v} = \dot{m}_{c,v} / M_c \quad (17)$$

$$\dot{n}_{w,v} = \dot{m}_{w,v} / M_w. \quad (18)$$

Of the total mass flow rate $\dot{m}$, the mass flow rates of CO_2 gas and water-steam mixture are:

$$\dot{m}_{c,v} = F\,\dot{m} \quad (19)$$

$$\dot{m}_w = (1 - F)\,\dot{m}, \quad (20)$$

respectively. F is the mass fraction of noncondensable gases. The fraction of $\dot{m}_w$ that is vapor can be determined in terms of the dryness fraction x in the absence of CO_2; that is,

$$\dot{m}_{w,v} = x\,\dot{m}_w. \quad (21)$$

Hence, eq.(15) can be written in terms of eqs.(16-21) as:

$$X_c = [1 + x(1-F)M_c/(A\,F\,M_w)]^{-1}. \quad (22)$$

The dryness fraction x can be calculated from the energy balance between the stagnation point and any section in the two-phase region, for an adiabatic well. Refs. [11,16] show that the kinetic and potential energies per unit mass are negligible in comparison to the latent heat of evaporation. In this case, the dryness fraction is given by:

$$x = (h_o - h_f)/h_{fg}. \quad (23)$$

From Raoult's law, the pressure of liquid water is given by:

$$P_{w,f} = P_{w,sat}\ X_{w,f}, \quad (24)$$

where $X_{w,f} = 1 - X_c$. (25)

The total calculated pressure is

$$P_T = P_{w,f} + P_c. \quad (26)$$

EXPERIMENTAL FACILITY

The experimental work was conducted at Brown University [17] where a facility was designed specifically to study two-phase flow of single substance with phase change, and to simulate flow conditions in geothermal wells. A schematic of this computer-controlled facility is shown in Figure 2. The test section is shown vertical and lies between two isolation butterfly valves (BFV-D and BFD-U) as shown in Figure 3. The working fluid is dichlorotetrafluoroethane (CCl_2F-CCl_2F) known as refrigerant 114 (R-114). The temperature and absolute pressure are measured at the inlet of the test section (stagnation point). Along the test section, the temperature and differential pressure are measured at four stations, 1.219 m apart.

Opening the two butterfly valves initiates the flow in the upward direction under the pressure difference between the accumulator and the condenser. When the gate valve (GV) is slightly open, the fluid flows as single-phase liquid up to and past an orifice plate at the inlet of the test section, and flashes somewhere in the test section to form a two-phase flow. Adjusting the opening of the GV with a computerized servomotor varies the degree of flashing in the test section by changing the back pressure on the orifice plate.

Between the two extreme positions of the GV, a sequence of flows with different topologies can be generated in the test section that would otherwise occur in different positions along a much longer pipe, starting with bubbly flow near flashing that changes ultimately to an annular flow as the GV is progressively opened.

Thus, if we imagine that the fixed test section can be "shifted" in the flow direction, then the set of data can be essentially "pieced" together to represent temperature, and pressure distributions along a very long pipe [11].

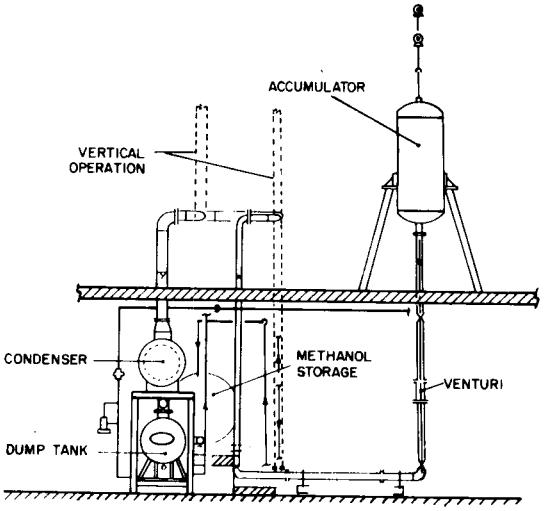

FIGURE 2 VERTICAL SECTION OF THE TEST FACILITY

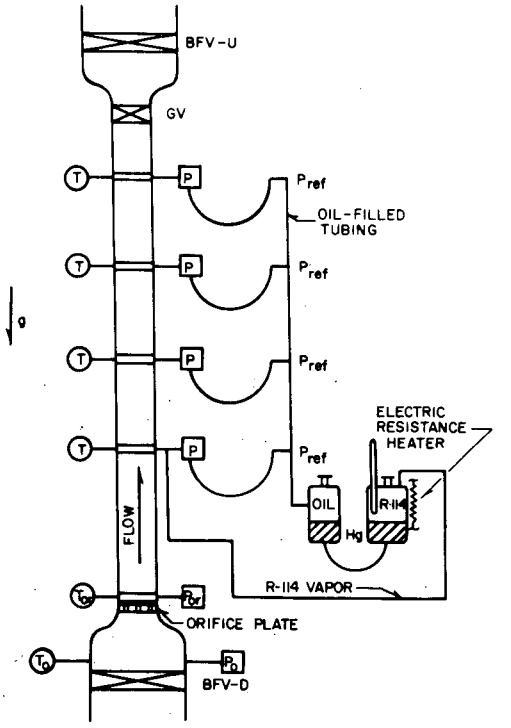

FIGURE 3 VERTICAL TEST SECTION CONFIGURATION

In this experiment a commercially available copper tube was used and it was completely insulated. In order to accurately determine the position of the flash front four additional thermistors, 0.457 m apart, were added along the test section. The first thermistor was at 0.910 m from the stagnation point near the BFV-D.

MEASUREMENTS AND RESULTS

Survey of Well Field Data

We have collected data on wellflow characteristics from a number of wells in New Zealand [18]. They include KA (10,16) (Kawerau); NG (3,9,11,12,13) (Ngahwa); and BR (11,21) (Broadlands/Ohaaki). Geofluid parameters are given in columns 2-4 in Table 1.

TABLE 1

SIMILARITY CONDITIONS FOR SELECTED WELLS

	GEOFLUID					REFRIGERANT-114				
Well No.	D cm	T °C	$\dot{m}$ kg/s	Ma*	Fr*	D cm	T °C	$\dot{m}$ kg/s	Ma*	Fr*
KA-10	15.04	250	42.0	0.105	2.437	2.00	45.4	0.202	0.107	1.037
KA-16	15.04	248	19.0	0.049	1.098	2.01	44.3	0.092	0.049	0.469
NG-3	15.04	228	20.0	0.068	1.117	2.04	33.7	0.104	0.069	0.496
NG-3	15.04	228	24.4	0.083	1.362	2.04	33.7	0.127	0.084	0.605
NG-11	19.88	224	64.4	0.133	1.779	2.71	31.6	0.340	0.134	0.797
NG-11	19.88	224	68.8	0.142	1.895	2.71	31.6	0.362	0.142	0.849
NG-12	19.88	228	13.3	0.026	0.370	2.70	33.7	0.069	0.026	0.164
NG-13	22.05	225	19.4	0.032	0.414	3.00	32.1	0.102	0.032	0.185
NG-13	22.05	225	53.0	0.088	1.131	3.00	32.1	0.280	0.088	0.506
BR-11	19.88	240	62.2	0.102	1.765	2.68	40.1	0.311	0.103	0.765
BR-21	19.88	260	21.9	0.028	0.645	2.61	50.5	0.100	0.028	0.270
BR-21	19.88	260	26.1	0.033	0.769	2.61	50.5	0.120	0.033	0.321

The stagnation temperature of most wells is very high which leads to a relatively high stagnation temperature even under laboratory conditions, as our similarity theory requires (column 8 in Table 1). The instrumentation however was not designed for stagnation temperatures much higher than 30°C for R-114. Unfortunately, field data with low stagnation temperatures were not available. Hence, we settled on one set of data obtained in a well identified as NG-11.

The characteristics of well NG-11 are given in Table 2 and 3. The 1.4 % gas content of the total mass flow rate represents noncondensable gases that are greater than 95 % CO_2 [18]. From the data of Table 3 it appears that the difference between the measured pressure (above the flashing front), and the saturation pressure is due to the partial pressure of carbon dioxide present as a noncondensable gas. To check this observation, let us analyze the two-phase region which consists of a mixture of steam-water and carbon dioxide gas.

TABLE 2

CHARACTERISTICS OF WELL NG-11

Reservoir temperature, T (°C)	224.0
Reservoir pressure, P_{res} (bar,a)	93.0
Stagnation enthalpy (kJ/kg)	965
Mass flow rate, $\dot{m}$(kg/s)	64.4
Noncondensable gas content	
NGC/% totalflow (by mass)	1.4

TABLE 3

PRESSURE AND TEMPERATURE AS A FUNCTION OF DEPTH FOR WELL NG-11

Depth (m)	T_{meas} (°C)	P_{meas} (bar,a)	$P_{H_2O,sat}$ (bar,a)
0	206	20.0	17.65
100	211.5	23.5	19.67
200	215	27.5	21.12
300	218.5	32.0	22.56
400	220	38.0	23.18
500	222.5	44.8	24.20
600	223.5	52.9	24.70
700	224	61.1	25.00

Note: $P_{H_2O,sat}$ was calculated from Steam Tables at the measured temperature.

Table 4 shows the values of parameters which lead to the predicted total pressure P_T. The data clearly indicates that equations (14-26) give an accurate description of the pressure distribution P_M along the pipe. There is strong agreement with the measured pressures between 0-400 m. However, the calculated pressure disagrees with the measured pressure at a depth of 500 m. This means that the flash front lies between 400 and 500 m. Figure 4 shows the temperature profile along the pipe as a function of depth. It can be seen that temperature points at depth greater than 400 m have a steeper slope than points shallower than 400 m. We will assume that flashing occurs at a depth of 400 m. At depths greater than 400 m, the mixture is compressed liquid.

The analysis above shows that the vapor pressure of water can be separated from that of carbon dioxide according to the laws of Henry and Raoult. This is an important result since the similarity theory which is being tested was developed for pure substances in the absence of any noncondensable gases. This means that the pressure similarity is between the saturation pressure of the laboratory fluid (R-114) and the partial pressure of water vapor rather than the total pressure of the water-steam and carbon dioxide mixture.

TABLE 4

PREDICTED PARTIAL VAPOR PRESSURE AND TOTAL PRESSURE AS A FUNCTION OF DEPTH FOR WELL NG-11

Depth (m)	0	100	200	300	400	500
T_{meas} (°C)	206	211.5	215	218.5	220	222.5
K_{CO_2} (atm)	6280	6170	6100	6030	6000	5950
1/A	327	286	262	240	231	217
x 10^2	4.38	3.09	2.25	1.42	1.11	0.53
X_{CO_2} 10^4	4.05	6.57	9.85	17.01	22.60	50.25
P_{CO_2} (bar,a)	2.58	4.11	6.10	10.41	13.76	30.34
P_{H_2O} (bar,a)	17.64	19.66	21.10	22.52	23.13	24.08
P_T (bar,a)	20.22	23.77	27.20	32.93	36.89	54.42
P_M (bar,a)	20.0	23.5	27.5	32.0	38.0	44.80

Note: P_{CO_2} was calculated from Henry's law; P_{H_2O} was found from Raoult's law.

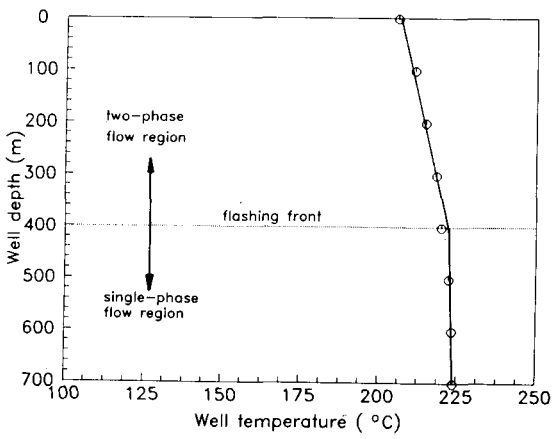

Figure 4. Temperature profile for WELL NG-11

Method of Testing

From the reservoir temperature, mass flow rate, and pipe diameter of well NG-11, we calculated the mass flux, flash Mach, Froude, and Reynolds numbers. This is shown in row 1 of Table 5. Similarity theory requires a constant flashing Mach number, and scaled temperature and diameter for R-114 based on eqs.(8-9). The matching conditions for R-114 are shown in row 2 of Table 5.

TABLE 5

SIMILARITY BETWEEN WATER AND R-114

		T(°K)	$\dot{m}$(kg/s)	D(m)	ψ(kg/m^{2}s)	Ma^*	Fr^*	Re^*x10^{-3}
1.	Water[1]	497.16	64.4	0.1988	2075	0.134	1.779	3461
2.	R-114[2]	304.72	0.34	0.0271	589	0.134	0.797	50.07
3.	R-114 Test (Series 5)	304.36	0.34	0.0254	671	0.156	0.940	53.65
4.	%Uncertainty	±0.13	±0.50			±1.0	±0.51	±0.70
5.	%Deviation Between Rows 2 & 3	0.12	0.0	-6.3	13.9	16.4	17.9	7.1
6.	R-114 Test (Series 6)	304.03	0.292	0.0254	576	0.134	0.801	45.46
7.	% Uncertainty	±0.02	±0.99			±1.0	±1.0	±0.70
8.	%Deviation Between Rows 2 & 6	-0.23	-14.0	-6.3	-2.2	0.0	0.5	-9.2

(1)Data taken from well NG-11; (2)According to similarity theory.

Under laboratory conditions, similarity requires a pipe of 0.0271 m. Due to the difficulty of finding a commercial pipe of exactly 0.0271 m, it was decided to use a 0.0254 m commercially available copper tube.

Using this tube, a series of 27 experiments (called Series 5) were conducted under fixed flashing conditions and mass flow rate, with a very small experimental uncertainty. Row 4 shows the uncertainty (in percent) in holding flashing conditions constant for Series 5. From the data it can be seen that the flash temperature and mass flow rates deviate by 0.12% and 0% from what is required. However, the discrepancy of 6.3% in the diameters resulted in large deviations in the flash Mach number Ma^*, and the Froude number Fr^*, as seen in row 5 of Table 5. In an attempt to compensate for the diameter discrepancy, the mass flux was scaled rather than the mass flow rate. From the data in Table 5, similarity requires a mass flux of 589 kg/(m^{2}s), whereas the actual measured mass flux in the laboratory is 671 kg/(m^{2}s) in Series 5. In a 0.0254 m pipe, a mass flux of 589 kg/(m^{2}s) would require a mass flow rate of 0.30 kg/s instead of 0.34. Thus, a new series of tests (Series 6) was carried out to correct for the discrepancies in Series 5. The measured parameters in Series 6 are shown in row 6 along with the experimental uncertainty in row 7. As can be seen from row 8, Series 6 meets the similarity requirements for mass fluxes rather than mass flow rates.

Laboratory Results versus Field Data

Results of measured temperatures for Series 5 only are shown in Table 6A; measurements of Series 6 are nearly identical, as we will see. Temperature measurements from only the top three probes are considered (Fig. 3) since they are the furthest from the flashing front.

It is interesting to note that the method of "piecing" measurements together is a very convenient way to predict conditions for a long pipe using a much shorter pipe in the laboratory. For example, in row 7, the probe for T_2 is 9.36 m from the flashing front, for a given GV opening, and the measured temperature is 20.4°C. As the GV is opened further, the flashing front moves upstream toward the orifice plate and away from the T_2-probe. But the T_1-probe is now at 9.35 m as shown in row 8. Notice that at essentially the same distance from z^*, the T_1-probe reads 20.43°C, approximately the same as the T_2-probe at the previous GV setting.

Using the measured temperatures T_1, T_2, and T_3 of R-114 from Series 5 and 6, the temperatures and heights of water-steam mixtures are calculated from eqs.(8) and (10) respectively. Values from Series 5 are shown in Table 6B.

TABLE 6A

EXPERIMENTAL TEMPERATURES AND HEIGHTS FOR R114 - SERIES 5

z_1 (m)	z_2 (m)	z_3 (m)	T_1 (°C)	T_2 (°C)	T_3 (°C)
1.22	2.44	3.66	26.89	25.65	24.60
2.21	3.43	4.65	25.88	24.86	23.84
3.14	4.36	5.58	25.10	24.12	23.16
6.26	7.48	8.70	22.65	21.70	20.87
7.10	8.32	9.54	22.00	21.16	20.25
7.79	9.01	10.23	21.52	20.64	19.69
8.14	9.36	10.58	21.27	20.40	19.57
9.35	10.57	11.78	20.43	19.56	18.66
12.02	13.24	14.46	18.51	17.61	16.80
12.11	13.33	14.55	18.42	17.59	16.72
13.19	14.41	15.63	17.65	16.81	15.97
14.63	15.85	17.07	16.66	15.78	14.94
15.45	16.67	17.89	16.07	15.18	14.27
16.16	17.38	18.60	15.55	14.66	13.79
16.73	17.95	19.17	15.13	14.22	13.32
18.14	19.35	20.57	14.09	13.14	12.21
19.11	20.33	21.55	13.33	12.33	11.33
20.21	21.43	22.65	12.43	11.37	10.35
21.83	23.05	24.26	11.05	9.95	8.84
24.36	25.58	26.80	8.89	7.80	6.54
24.69	25.91	27.13	8.59	7.50	6.28
24.81	26.03	27.24	8.49	7.40	6.12
26.93	28.14	29.36	6.43	5.33	3.98
29.17	30.38	31.60	4.18	2.94	1.44
29.28	30.50	31.72	4.06	2.88	1.46
29.40	30.62	31.84	3.95	2.77	1.35
39.63	30.85	32.07	3.72	2.51	1.06

Note: z_1, z_2, z_3 are measured relative to the flashing front ($z^* = 0$).

TABLE 6B

PREDICTED TEMPERATURES AND HEIGHTS FOR STEAM-WATER MIXTURE FROM TABLE 6A BASED ON SIMILARITY THEORY

z_1 (m)	z_2 (m)	z_3 (m)	T_1 (°C)	T_2 (°C)	T_3 (°C)
8.94	17.89	26.84	216.30	214.28	212.57
16.24	25.18	34.13	214.65	212.99	211.33
23.08	32.02	40.97	213.38	211.78	210.22
45.97	54.92	63.86	209.39	207.84	206.48
52.09	61.04	69.99	208.33	206.95	205.47
57.20	66.15	75.10	207.54	206.11	204.56
59.75	68.69	77.64	207.13	205.72	204.36
68.59	77.53	86.48	205.76	204.34	202.88
88.25	97.19	106.14	202.63	201.16	199.84
88.86	97.81	106.76	202.49	201.13	199.71
96.82	105.76	114.71	201.23	199.86	198.49
107.36	116.31	125.26	199.61	198.18	196.81
113.36	122.31	131.76	198.65	197.20	195.72
118.59	127.54	136.48	197.80	196.35	194.92
122.81	131.76	140.71	197.12	195.63	194.17
133.09	142.04	150.99	195.42	193.87	192.36
140.25	149.20	158.15	194.18	192.55	190.92
148.30	157.25	166.20	192.71	190.98	189.32
160.18	169.12	178.07	190.46	188.67	186.86
178.77	187.71	196.66	186.94	185.16	183.11
181.77	190.17	199.12	186.45	184.67	182.68
182.05	191.00	199.94	186.29	184.51	182.42
197.60	206.55	215.50	182.93	181.13	178.93
214.04	222.98	231.93	179.26	177.23	174.79
214.90	223.85	232.80	179.06	177.14	174.82
215.74	224.68	233.63	178.88	176.96	174.64
217.48	226.43	235.38	178.51	176.53	174.17

Note: z_1, z_2, z_3 are measured relative to the flashing front ($z^* = 0$).

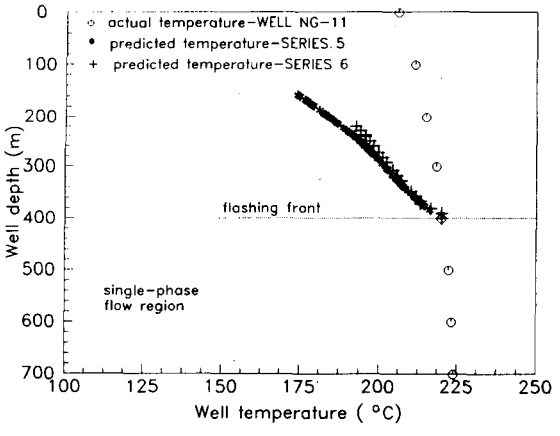

Figure 5. Predicted and actual temperature profiles for WELL-NG 11

DISCUSSION

A comparison of predicted and actual temperatures is shown in Figure 5, with average and maximum relative deviations of 5% and 9% respectively. However, the comparison is more reasonable when we compare pressures.

From the predicted temperatures of steam-water in Table 6B, the partial pressures are calculated from standard steam tables. The result is shown in Figure 6. Two observations should be made. The first one is that the predicted partial pressure at flashing is below the actual pressure by exactly the partial pressure of CO_2 at the flashing front. The second observation is that the predicted pressure gradients for Series 6, away from flashing, is within 3% of that in the actual well as shown in Figure 7. This indicates that if CO_2 were not present, the predicted pressure would be coincident with the actual pressure at the flashing front, and would develop with a pressure gradient deviating by 3% from the actual one. The effect of the presence of CO_2 is to suppress the whole predicted pressure curve by an amount equal to the pressure of CO_2 at flashing. By adding the partial pressure of CO_2 at flashing to the predicted pressure, then the calculated total pressure and the actual pressure in the well will be identical at the flashing front as shown in Figure 8.

From Figure 8, the agreement between the predicted pressure and the actual pressure of water in the well is very good if the predicted and actual pressures are anchored at the flashing front as required by the similarity theory.

It is worth noting that the attempt to correct for the diameter discrepancy By matching the mass flux resulted in a mass flow rate in Series 6, 14% lower than that in Series 5. This effect decreased the initial acceleration pressure gradient at the flash front (Fig. 7), and the pressure became closer to the actual one in the well.

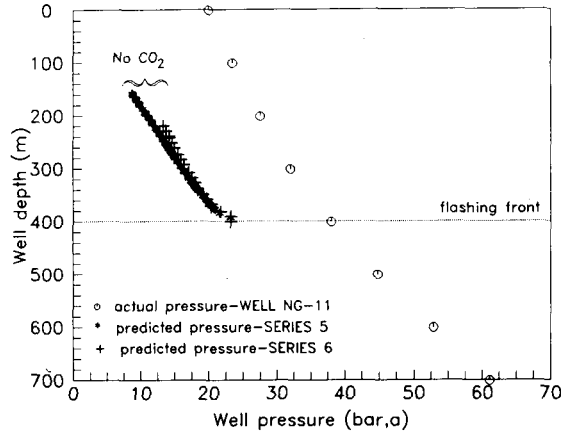

Figure 6. Predicted and actual pressure profiles for WELL-NG 11

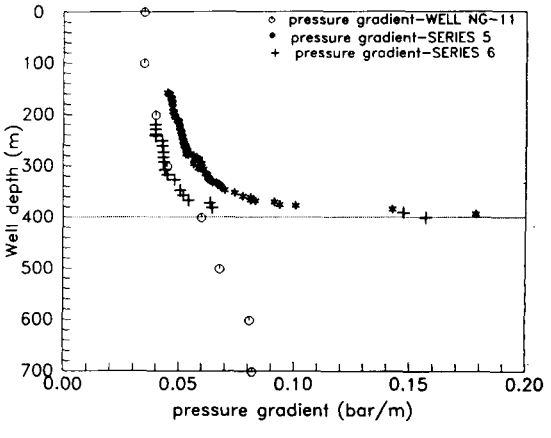

Figure 7. Predicted and actual pressure gradient profiles for WELL NG-11

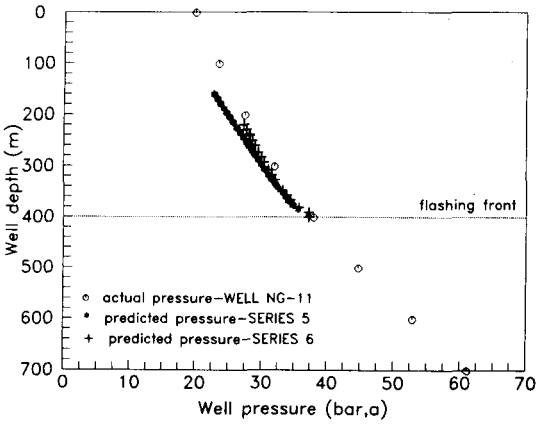

Figure 8. Predicted and actual pressure profiles for WELL-NG 11

CONCLUSION

In this study we showed that a similarity theory can be used successfully in the presence of significant noncondensable gases, to predict the pressure along a vertical pipe of an adiabatic geothermal well. The input field data required for laboratory simulation using R-114 are the mass flow rate of water, the pipe diameter, the stagnation pressure and temperature, and mass fraction of noncondensable gases. From this information, flashing conditions under laboratory conditions are established from similarity theory, and measurements are conducted under those conditions. From the measurements, the partial pressure of water is predicted using similarity theory. The contribution of the partial pressure of CO_2 at flashing is calculated using Henry's law. Hence, the total pressure in the two-phase region, as well as the height above the flashing front can be predicted.

REFERENCES

[1] Barelli, A., Corsi, R., DelPizzo, G., and Scali, C., "A Two-Phase Flow Model for Geothermal Wells in the Presence of Non-Condensable Gas," **Geothermics**, v. 11, no. 3, 1982, pp. 175-191.

[2] Michaelides, E. E., and Shafaie, F. F., "A Numerical Study of Geothermal Well Flow with Salts and Noncondensables present," **Trans. ASME**, v. 108, 1986, pp. 140-145.

[3] Freeston, D. H., and Hadgu, T., "Modelling of Geothermal Wells with Multiple Feed Points: A Preliminary Study,"**Proc. 9th NZ Geoth. Workshop**, 1987, pp. 59-64.

[4] Hadgu, T., and Freeston, D. H., "A Multipurpose Wellbore Simulator," **GRC TRANS.**, v. 14, pt. II, 1990, pp. 1279-1286.

[5] Maeder, P. F., DiPippo, R., Dickinson, D. A., and Nikitopoulos, D. E., "Modelling of Flashing Flows Using Similarity Fluids," **Fundamental Aspects of Gas-Liquid Flows**, Michaelides, E. E., ed., FED-v. 29, 1985, pp. 109-116.

[6] Maeder, P. F., Dickinson, D. A., Nikitopoulos, D. E., and DiPippo, R., "A Facility for the Experimental Investigation of Single Substance Two-Phase Flow," **Fundamental Aspects of Gas-Liquid Flows**, Michalides, E. E., ed., FED-v. 29, 1985, pp. 41-46.

[7] Mayinger, F., "Scaling and Modelling Laws in Two-Phase Flow and Boiling Heat Transfer," **Two-Phase Flow and Heat Transfer**, Vol. 1, Kakac, S., and Veziroglu, T. N., eds., Hemisphere Pub. Corp., Washington, DC, 1976, pp. 129-161.

[8] Ishii, M., and Jones, O. C., Jr., "Derivation and Application of Scaling Criteria for Two-Phase Flows," **Two-Phase Flow and Heat Transfer**, Vol. 1, Kakac, S., and Veziroglu, T. N., eds., Hemisphere Pub. Corp., Washington, DC, 1976, pp. 163-185.

[9] Fridel, L., "Momentum Exchange and Pressure Drop in Two-Phase Flow," **Two-Phase Flow and Heat Transfer**, Vol. 1, Kakac, S., and Veziroglu, T. N., eds., Hemisphere Pub. Corp., Washington, DC, 1976, pp. 239-312.

[10] Kowalczewski, J. J., "Two-Phase Flow in an Unheated and Heated Tubes," Dissertation ETH, Zurich, 1964.

[11] Nikitopoulos, D. E., and Maeder, P. F., "Single-Substance Two-Phase Flow: A Unified Theoretical and Experimental Study," Brown University, Report no. TWOPHASE/3, 1986, Providence, RI.

[12] Dickinson, D. A., and Maeder, P. F., "An Investigation of Single Substance Horizontal Two-Phase Flow," Brown University, Report no. GEOFLO/20, 1984, Providence, RI.

[13] Maeder, P. F., DiPippo, R., Delor, M., and Dickinson, D., "The Physics of Two-Phase Flow: Choked Flow," Brown University, Report no. GEOFLO/10, May 1981, Providence, RI.

[14] Ellis, A. J., and Golding, R. M., "The Solubility of Carbon Dioxide Above 100 °C in Water and in Sodium Chloride Solutions," **American Journal of Science**, v. 261, Jan 1963, pp. 47-60.

[15] Ellis, A. J., "The Solubility of Carbon Dioxide in Water at High Temperatures," **American Journal of Science**, v. 257, Mar 1959, pp. 217-234.

[16] Delhaye, J. M., Giot, M., and Riethmuller, M. L., **Thermohydraulics of Two-Phase Systems for Industrial Design and Nuclear Engineering**, Hemisphere Publishing Corp., 1981, pp. 428.

[17] Laoulache, R. N., Maeder, P. F., and DiPippo, R., "Theoretical and Empirical Study of Single-Substance, Upward Two-Phase Flow in a Constant-Diameter Adiabatic Pipe," Brown University, Report no. TWOPHASE/4, 1987, Providence, RI.

[18] Correspondence between DiPippo, R., Bixley, P. F., and Gudmundsson, J. S. of the Department of Petroleum Engineering, Stanford University, Stanford, CA, 1987.

PROCEEDINGS, Sixteenth Workshop on Geothermal Reservoir Engineering
Stanford University, Stanford, California, January 23-25, 1991
SGP-TR-134

SOME APPROACHES TO ROCK MASS HYDROFRACTURE THEORY

Yuri D.Dyadkin
Department of Mining Thermophysics
Leningrad Mining Institute
Leningrad, USSR

ABSTRACT

A new engineering method has been developed at the Leningrad Mining Institute for defining hot dry rock hydrofracturing parameters. It reflects the structural features of a real jointed rock mass, its gravity-tectonic components of the stress tensor and volume character of deformations, taking into account the inertial effects of hydrodynamics in the non-Darcy zone of radial fluid flow near the injection well, and conversion of the heat energy extracted from hot rock by circulating water partly into filtration-flow additional pressure. Results of calculations are compared to field experiments at Fenton Hill, NM, and are used for the first HDR circulation systems in the USSR.

INTRODUCTION

The study of hydrofracture mechanics became popular in the 1950-60's when hydrofracturing was widely used in the oil and gas industry to improve reservoir permeability. By this time, several theories of hydrofracture essentials had been formed; some are found in the investigations by S.A. Khristianovich, G.I. Barenblatt and Yu.P. Zheltov (1975), by C. Fairhurst and B. Haimson, and others by A. Inglend and A. Green, T. Perkins and L. Kern, P.Fox and A. MacDonald given by Alexeev (1987) and Haimson (1978).

Because of the great difficulties entailed in the attendanthydro-geomechanical problem, the first solutions were obtained for an idealized rock mass as a homogeneous linear elastic medium loaded by constant liquid pressure distributed from a flat fracture and with assumed absence of resistance of the above medium to destruction (e.g., Dyadkin, 1989; Alexeev, 1987; Zheltov, 1975). Application of available calculation methods appeared difficult as noted by Usachev (1986).

Renewed interest in hydrofracture theory occurred in connection with the creation of artificial circulation systems for geothermal energy extraction from hot rock in the USA, Great Britain, Japan, Germany, and France (Dash and Murphy, 1985; Garnish 1987; Tester, et al, 1989). Table 1 lists some of the available water-pressure data from measurement after the pumping unit, P_p, and water flow rate, Q, at various depths, H, and initial rock temperatures, T. The following data from Experiment 2032 by the Los Alamos National Laboratory on hydrofracturing of granodiorite mass by water at H = 3550 m and T = 240 °C at Fenton Hill area in New Mexico were used for the illustration described later (all dimensions in SI): rock density ρ = 2700, Young's modulus E = 5×10^{10}, shear modulus G = 2.65×10^{10}, Poisson ratio υ = 0.257, permeability k = 10^{-18}, total rock pressure q = 91.7×10^{6}, pore liquid pressure P_o = 35.06×10^{6}, vertical stress component $\sigma(z) = q-P_o$, minimum horizontal component of stress tensor $\sigma(x) = 32.15\times10^{6}$, maximum component of horizontal stress $\sigma(y) = 48.2\times10^{6}$, compressive rock strength $[\sigma(c)] = 175\times10^{6}$, uniaxial tension strength $[\sigma(t)] = 15\times10^{6}$, structural weakness coefficient ϕ = 0.5, water density $\rho(w)$ = 1032, water viscosity $\mu(w) = 0.95\times10^{-3}$, temperature extension coefficient $d_w = 1.5\times10^{-4}$, water elasticity modulus $E_w = 0.22\times10^{10}$, injection rate Q_w = 0.111 m/s, length of well open interval h = 22, radius of well cross-section R_w = 0.125, water pressure in well open interval at hydrofracture $P_w = 83\times10^{6}$, water pressure after pumping unit $P_p = 42\times10^{6}$, total hydrofracturing duration $\Sigma(t_z)$ = 62 hr, size of sub-vertical fractured zone ≈ 1150 x 800 x 150, and fracture opening (aperture) δ_o = 2.3 mm.

In the next approach, Haimson (1978) recognized the need to take rock strength into account. This was regarded as a hydro-mechanical task, i.e., the rock mass elasticity deformation and friction forces at viscous liquid flow in fractures were considered simultaneously (Geerstma and Klerk, 1969). Satisfactory

solutions for determining filtration leakage to not appear to exist, although this effect caused great difficulties in the cited geothermal experiments. Investigations by Dyadkin (1985, 1989) showed that several other factors must be taken into account: filtration leakage at fissure development of hydrofracturing in a permeable rock mass overcoming the pore pressure; inertia effects of turbulent flow in the near well zone; rock strength energy criteria; and thermal expansion of the fluid in the rock mass. These factors were not taken into account by other investigators, although they are very important for geothermal hydrofractures.

PROCEDURE DEVELOPMENT

The practicality of the proposed calculation procedure is shown by comparison of the estimated design values with the observed results of field experiments (as listed in Table 1). To avoid repetition of previously published sections of the calculation procedure given in Dyadkin (1985, 1989) for developing a Physical Model for hydrofracturing of the jointed rock mass, it is necessary only to define the procedure for two main parameters: (1) critical pressure at the fracture border P_b and (2) maximum fracture opening δ_o near the well for typical component relations of gravity-tectonic stress field (Haimson, 1978):

$$\sigma_x < \sigma_z < \sigma_y \qquad (1)$$

when the stress difference $\sigma_y - \sigma_x$ "supplies" the difference in anisotropy rock mass destruction resistance in various directions and the hydrofracture develops in vertical plane "yz" on the normal to minimum stress σ_x. Evidently, the critical liquid pressure P_b at the border of the growing vertical fracture totally discharges the rock mass element from compressive stress and at same time overcomes not only pore liquid pressure P_o, but also the rock mass resistivity to breakage ΔP_r under the condition of volume deformation. At the first stage of this investigation, it was assumed that the uniaxial tension strength $[\sigma_t]$ is an indicator of this resistivity. This may result in too large an increase in pressure P_b as the action of compression stress σ_y and σ_z reduces rock resistivity. The greatest slacking effect is considered by the Griffith energy criterium of strength $[\sigma_t]^*$ for plane deformation conditions of "tension- compression". The condition under which this slackening effect is insignificant may be taken as:

$$\sigma_y < 3\,[\sigma_t]_x \qquad (2)$$

The above condition being formulated as $[\sigma_t]^*_x \approx [\sigma_t]_x$. Rock of great strength at small depth corresponds to condition (2). For instance, frozen-rock hydrofractures at depths of 7-10 m are described in Dyadkin (1989). In jointed rock masses at deep horizons and at intensive tectonic stress, condition (2) is not observed and Griffith's criterion value may be found in his equation relating σ_y with $[\sigma_t]_x$, indicated by Baklashov (1988). The solution obtained for the equation is:

$$[\sigma_t]^*_x = \sqrt{a_x^2 + \sigma_y (8\,[\sigma_t]\varphi - \sigma_y)} - a_x \qquad (3)$$

where

$$a_x = 4\,[\sigma_t]_x \phi + \sigma_y \qquad (4)$$

ϕ = coefficient of rock mass structural weakness, which for hard rock, may range from 0.5 to 0.03 (Baklashov,1988; Turchaninov, et al, 1989).

The slackening effect of the second compression stress σ_z may be considered by the VNIMI correction coefficient (Petukhov and Linkov, 1986), illustrating the peculiarities of volume development of deformation:

$$k_v = 1 - \sigma_z / [\sigma_c]\,\phi \qquad (5)$$

The part of liquid pressure to overcome the resistance of rock mass is expressed as

$$\Delta P_{r,v} = [\sigma_t]_x^* \{1 - \sigma_z / [\sigma_c]\phi\} \qquad (6)$$

and condition of hydrofracture at the border of the growing vertical fracture may be shown as

$$P_{b,v} = P_o + \sigma_x + \Delta P_{r,v} \qquad (7)$$

The important influence of the relaxing intensities of the slacking effect under the above conditions is illustrated by LANL Experiment 2032. For these values, it is possible to get $[\sigma_t]^* = 3.55 \times 10^6$ and $k_v = 0.372$. That is, instead of 15 MPa for monolith rock specimen at uniaxial tension strength, the resistance of weakened rock mass under the conditions of vertical hydrofracture deformation will be only $\Delta P_r = 1.32 \times 10^6$.

Figure 1 shows the jointed mass structure for granite, typical for granodiorite and other hard rocks. The main joints system with their azimuth α_n (the angle to maximum stress direction σ_y) at sloping angle β_n. The second joints system crossing of the first and has angles α_s and β_s. These systems, together with sub-horizontal joints, separate the structural blocks with length l_b, width a_b, and thickness t_b. Joints of the first system are partially filled by different second

TABLE 1

Results of LANL field experiments on hydrofracturing of hot granodiorite at Fenton Hill for comparison with LMI calculated data for designing USSR Geothermal Circulation Systems

Number and Date of Experiment Type of rock	Depth (m)	Temp. (°C)	Pump unit parameters Pressure (Mpa)	Flowrate (m^3/s)	Time (hr)	Total Water Volume (m^3)
2016 19 Jun 82 granodiorite	4252	282	46.6	0.093		4883
2020 6-7 Oct 82 granodiorite	3656	245	46.9	0.092		3090
2023 8 Nov 82 granodiorite	3162-4084	270	12.9	0.017		150
2032 11-12 Dec 83	3528-	240	48.0	0.114	61	21200
2042 15-19 May 84	3588	245	41.4	0.026		7600
2061 29 Jun 85	3827-4017	290	31.0	0.011		5230
2066 30Jan-2Feb 86	3914	260	46.2	0.019		3770
Russkie Komarovtsy, Uhzgorod, Ukraine 1988 granodiorite	2240	124	19.0	0.44	19	10500
Cholpon-Ata, Lake Issik-Kul 1988 granite	2400	91	11.0	0.022	50	12000
Tirniaus, Elbrus Mtns 1989 granite	3300	185	28.9	0.044	88	18000
Palanga, Lithuania 1990	4300	141	25.7	0.07	15	3870

mineralizations and define the rock mass fracture permeability k, the greatest structural weakness coefficient ϕ_n; they also define the rock mass fracture porosity m and natural porous liquid pressure P_o. The joints of the second system are considered closed and provide only a small contribution to the rock mass characteristics given above.

In a rock mass containing a vertical hydrofracture, there is the possibility of shear deformation development and displacement of neighboring structural blocks along joints α_s β_s of the second system under irregular loads by injecting liquid pressure from permeable joints α_n β_n of the first system. This kind of hydrofracturing mechanism is possible even without complete discharge of joints α_s β_s from the normal compressive pressure $\sigma_{n,s}$ if the active pressure loading along the block width a_b is enough for Coloun's shear condition and block displacement on the long side l_b along second joints α_s β_o:

$$P_{b,s} = 2\frac{a_b}{l_b}\left([\tau_o]\Psi_s + \sigma_{n,s}tgf\right) \qquad (8)$$

where tgf, $[\tau_o]$ and ϕ_s are friction coefficient, pure shear resistivity, and the coefficient of structural weakness along the second joints

system, the values of which may be approximately estimated by the experimental data of Turchaninov, et al (1989), and $\sigma_{n,s}$ is the compressive stress by normal of secant joints:

$$\sigma_{n,s} = \sin(\beta_s)(\sigma_x \cos(\alpha_s) + \sigma_y \sin(\alpha_s)) + \sigma_z \cos(\beta_s) \quad (9)$$

Evidently, in the case of complete discharge of joints of the main system from normal compressive stress σ_n by injecting liquid pressure P_β, the third version of hydrofracturing mechanics is possible, when the main joints are reopened after overcoming of the weakened contact resistivity :

$$P_{b,n} = P_o + \sigma_{n,t} + [\sigma_t]_n^* (1 - \sigma_a / [\sigma_c]) \phi \quad (10)$$

where

$$[\sigma_t]_n^* = \sqrt{a_n^2 + \sigma_h (\beta [\sigma_t] \varphi_n - \sigma_h)} - a_n \quad (11)$$

$$a_n = 4[\sigma_t]\overline{\varphi} + \sigma_n \quad (12)$$

The values σ_n, σ_a, and σ_n are connected with components of the stress field and the orientation of the joint contacts:

$$\sigma_n = \sin(\beta_n)(\sigma_x \cos(\alpha_n) + \sigma_y \sin(\alpha_n) + \sigma_z \cos(\beta_n)) \quad (13)$$

$$\sigma_a = \cos\beta_n \sqrt{(\sigma_x \sin\alpha_n)^2 + (\sigma_y \cos\alpha_n)^2} - \sigma_z \sin \quad (14)$$

$$\sigma_n = \sqrt{(\sigma_x (\cos\alpha_n \cos\beta_n)^2 + (\sigma_y \cos\alpha_n \sin\beta_n)^2} \quad (15)$$

Like a filtration wedge advancing the hydrofracture border in sedimentary strata with constant (independent of direction) average permeability, injected liquid will flow along the permeable main joints advancing the breaking border and partially discharging rock mass from normal compressive stress. The length of this advancing discharging filtration zone depends on liquid viscosity μ_w and flowrate inside fracture Q_z, its average radius R_z, aperture (opening) near border δ_b, joint permeability (much greater than value of rock mass average level) and pressure difference:

$$l_z = 0.5\,\delta_b \exp((\pi R_z k_n / Q_z \mu_w)(P_{b,n} - P_o)) \quad (16)$$

A specific zone of complete discharge from normal compressive stress exists ahead of the fracture border:

$$l_t = 0.5\,\delta_b \exp((\pi R_z k_n / Q_z \mu_z)(P_{b,n} - P_o - \sigma_n)) \quad (17)$$

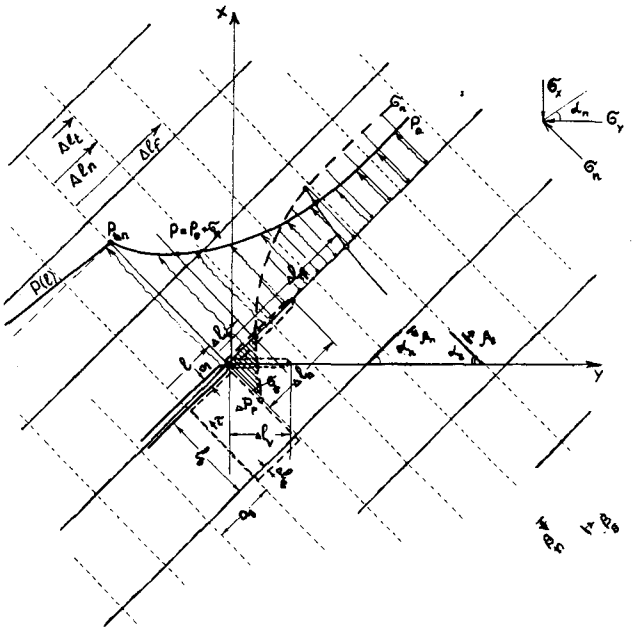

Fig. 1 Distribution of liquid pressure in fracture and in advanced filtration wedge from $P_{\beta,n}$ to P_o and stress level from δ_n to ΔP_r during hydrofracture of jointed rock mass in version of vertical crack propogation Δl_v, joint reopening Δl_n, or structual block shear displacement Δl_s.

Section l_t is a zone of tensile stress development, increasing together with injection liquid pressure, up to the level of $k_v[\sigma_t]_n^*$ before a jump-like break and hydrofracture border moves at value Δl_n.

The most likely hydrofracturing mechanics version corresponds to the minimum value among possible calculated levels: $P_{b,v}$, $P_{b,s}$, and $P_{b,n}$. For instance, in the cases of Table 1, it is noted that for the conditions of the Russkie Komarovtsy project, separate vertical tension fractures seem to be more likely, while at the Cholpon-Ata site, sub-vertical volume shear-fracturing zone is expected, and in the case of the Tirniaus project, the initial data for both of these versions appear to be equally likely.

At the Leningrad Mining Institute, it has been recommended (Dyadkin, 1985) that the definition of the very important parameter, fracture opening (aperture), near the well be adopted from Geerstma and Klerk (1969):

$$\delta_b = 2\sqrt[4]{\frac{(1-\nu)}{G}(\mu_w Q_w R_z)} \quad (18)$$

For the conditions of LANL experiment 2032, equation (18) yields δ_o = 2.27 mm, compared to the value of δ_o = 2.3 mm reported for the experiment by Dash and Murphy (1985) using several different calculating methods. But the regularity of such coincidence is dubious, because in the LANL experiments subvertical fractured zones were formed around the well, cutting across its inclined axis. Equation (18) appears only for the case of hydrofracture along the vertical well axis with rectangular uni-dimensional filtration flow. The same principles of hydrofracturing geometry were solved by Perkins and Kern (1961), Inglend and Green (Alexeev,1987), and Barenblatt (Zheltov,1975), Nordgren (1972), and Geerstma and Haafkens (1979).

The structure of equation (18) does not take into account either of two factors which acquire a special meaning under hydrofracturing of hot hard rock at considerable depth. These factors are: (1) rock strength (or more precisely, their resistivity to break, ΔP_r), and (2) liquid pressure increase ΔP_T as its temperature T_w rises. It is noted that equation (18) considers the filtration process as laminar unidimensional flow. However, for HDR systems, the more typical case is the creation of sub-vertical hydrofractured zones from inclined wells with radially diverging flow of injected liquid as shown from Dash and Murphy (1985), Dyadkin (1989), Garnish (1987) and Tester, et al (1989). For this case and laminar flow Q around the well with cross-sectional radius R, the liquid pressure drop in the fracture aperture. The average radius R can be written as

$$\Delta P_{H,D} = 6\,(Q_w \mu_w/\pi\delta^3)\,\ln(R_f/R_w) \qquad (19)$$

Assuming the suggestion in Geerstma and Klerk (1969) and Geerstma and Haafkens (1979) on aperture opening being constant for the main part of the fracture (its change in the zone near a well is discussed later), we obtain a value for rock mass elastic deformation as being the fracture aperture near the well, δ_{HD}, within the laminar regime of radial flow Q for liquid viscosity μ_w:

$$\delta_{HD} = 1.175\sqrt[4]{\frac{(1-\nu)}{G}\mu_w Q_w R_f \ln\frac{R_f}{R_w}} \qquad (20)$$

Under conditions of the discussed example, we obtain ΔP_{HD} = 0.11x10^6 and δ_{HD} = 2.46 mm. Note that for well radius R_w = 0.125 m , the referred fracture opening and liquid injection flow rate Q_w = 0.111 m/s, the radial speed at the fracture entrance R = R_w and at distances of 1 m and 10 m from the axis will be 57.7, 7.2 and 0.72 m/s ,respectively. At such high speeds near the well, forces of inertia play an important role, Darcy's law is irrelevant, a turbulent flow zone occurs, as fixed, for instance, in experiments on hydrofracture of granites at Falkenberg (Garnish, 1987). The radius of inertia effects zone is calculated by the following equation:

$$R_{in} = \rho_w Q_w^2 / \pi\mu_w Re^* \qquad (21)$$

where the critical Reynold's number Re^* = 1,500 is taken from Pavlov's experimental data (Dyadkin, 1985,1989). Pressure losses in this zone (in our case R_{in} = 25.6 m) can be writen as $k_{in}\,\Delta P_{HD}$, where the coefficient, accounting for the influence of inertia effects, cannot be less than 1:

$$k_{in} = 0.286\sqrt{\frac{R_f Re^* \mu_w}{\rho_w Q_w}}\sqrt[4]{\frac{R_f Re^*}{R_w \ln\frac{R_f}{R_w}}} \geq 1 \qquad (22)$$

and value of rock mass elasticity deformation from fracture that provides the turbulent flow in zone of inertia effects can be defined as

$$\delta_{in} = 0.128\sqrt[4]{\frac{(1-\nu)\,\rho_w^2 Q_w^3}{G R_w \mu_w Re^*}} \qquad (23)$$

Under the discussed conditions we obtain δ_{in} = 2.8 mm and ΔP_{in} = 1.95x10^6, which exceeds ΔP_{HD} by 1.95/0.11 = 17.7 times. This indicates that ignoring flow turbulence in the fracture may lead to serious errors. In our case, with very large value of Q_w = 0.111 m/s and R_f ~ 400 m, equation (22) gives k_{in} = 17.7, which corresponds to the above mentioned correlation. Note that as R_f decreases to the radius of inertia effects zone R_f = R_{in} = 25.6 m, the value of K_{in} decreases to 2.45; at R_f = 10 m k_{in} = 1.3, and for R_f = 7 m, the calculated result of equation (22) appears to be less than 1 and it must be assumed that K_{in} = 1 and $\Delta P_{in} = \Delta P_{HD}$.

It was already noted that equation (18) does not take into account the rock mass mechanical resistance, although for this case, the value of ΔP_b = 1.32x10^6 is quite comparable with ΔP_{in} and much more than ΔP_{HD}.

It is also necessary to take into account the effect of liquid pressure increasing as a result of its being heated by hot rock in the fracture (Dyadkin,1985,1989). This positive pressure effect may be estimated as

$$\Delta P_T = k_p\,\alpha_w\,E_w\,\Delta T \qquad (24)$$

where the coefficient k_p shows what part of the total heat energy obtained by the liquid flow from

rock is being converted into pressure increase, assuming that the major part of this energy is consumed as work of filtration leakage outside the fracture and also goes to elastic and plastic deformation of the rock mass. As a first approach, it is possible to estimate the value of k_p as a ratio of the liquid volume V_w inside the well and fracture V_f to the total volume of injected liquid ΣV_w, including V_w, V_f, and leakage in the advancing filtration wedge ΔV_b and in two equal filtration zones on both sides of fracture $2\Delta V_f$:

$$k_p = \frac{V_w + V_f}{V_w + V_f + \Delta P_b + 2\Delta V_f} \qquad (25)$$

where values of ΔV_b and ΔV_f are defined by the method developed in Dyadkin (1985,1989). For conditions of LANL Experiment 2032, it is possible to find for $V_w + V_f \approx 170$ m^3 and $\Sigma V_w = 21600$ m^3, the approximate value of $k_p = 0.034$. Taking for water $\alpha_w = 1.5\text{x}10^{-4}$ and $E_w = 0.22\text{x}10^{10}$ by equation (24) we obtain for the average temperature difference $\Delta T = 180$ °C, that $\Delta P_T = 2.02\text{x}10^6$, which slightly exceeds ΔP_r and is completely comparable with ΔP_{in}.

The total change of liquid pressure in the fracture can be written as

$$\Delta P_o = k_{in}\Delta P_{HD} + \Delta P_r - \Delta P_T \qquad (26)$$

The interaction of all discussed factors can be taken into account by using the "strength-thermal" coefficient:

$$k_\delta = 1 + \frac{\Delta P_r - \Delta P_T}{k_{in}\Delta P_{HD}} = 1 + \frac{\Delta P_r - \Delta P_T}{\Delta P_{in}} \qquad (27)$$

In our case, at $\Delta P_r = 1.32\text{x}10^6$, $\Delta P_T = 2.02\text{x}10^6$, and $\Delta P_{in} = 1.95\text{x}10^6$, we obtain $K_\delta = 0.641$. Now correcting equation (23) by function (27), we can finally write:

$$\delta_o = \delta_{in}\sqrt[4]{k_\delta} \qquad (28)$$

For this example, we have $\delta_{in} = 2.8$ mm from equation (23) and function $k_\delta = 0.641$, and we obtain $\delta_o = 2.5$ mm.

SUMMARY

Thus, in consequence of the transfer from laminar uni-dimensional to radially divergent flow resulting in turbulence, the pressure increase caused by heating of the liquid in the fracture, and the influence of jointed rock massive mechanical resistivity under volume deformation, together overcoming the compressive stress of the gravity-tectonic field, the computation result of equation (18) changed somewhat (with mutual compensation of subordinate factors), but the calculated values remained rather close to the experimental values.

Naturally, in the case of a massive hydrofracture forming a vertical crack of constant height along the well axis, the value of δ_o should be estimated by equation (18) and for approximate appreciation of above factors, it is possible to use as the correction coefficient the fourth root of k_δ in (18).

Both equation (23) and the coefficient k_p require careful definition in the approximate solution given in equation (28). Continuous experimental examination of thermal-pressure effects in the Leningrad Mining Institute program yielded recent results of $\Delta P_T = 0.16$ MPa/°C in the experiments with impermeable plexiglass. The resulting coefficient has an approximate value of 0.5 as a result of elasticity deformation only.

ACKNOWLEDGEMENTS

The author is very grateful to Paul Kruger for his assistance in the preparation of this paper and to the Stanford Geothermal Program for visit support. Thanks are due to Morton Smith of the Los Alamos National Laboratory for the very useful discussions during the visit.

REFERENCES

Alexeev, V.M., Mathematical Models of Hydrofracture Fissure Spreading, in Physical Processes in Mining, (LMI Press, Leningrad, 1987).

Baklashov, I.V., Deformation and Breaking of Rock Massives, (Nedra, Moscow, 1988).

Dash, Z. and H. Murphy, Estimating Fracture Aperture from Hydraulic Data and Comparison with Theory, LANL-85-20, (Los Alamos, NM, 1985).

Dyadkin, Yu.D., Basic Principles of Geothermal Technology, (LMI Press, Leningrad, 1985).

Dyadkin, Yu.D., Mining of Geothermal Deposits, (Nedra, Moscow, 1989).

Fox, R.W. and A.T. McDonald, Introduction to Fluid Mechanics, (New York, 1978).

Garnish, J.A., edi., Proceedings of the First EEC/US Workshop on Geothermal Hot Dry Rock Technology, Geothermics 14, No.4, 1987.

Geerstma, J. and F. Klerk, A Rapid Method Prediction Width and Extent of Hydraulic Fractures in Rock, J.Petro.Tech., December, 1969.

Geerstma, J. and R. Haafkens, Comparison of the Theories for Predicting Width and Extent of Vertical Hydraulically Induced Fractures, J.Ener.Res.Tech., Trans.ASME 101, March, 1979.

Haimson, B., Hydrofracturing Stress-Measuring Method and Recent Results, Int'l.J.Rock Mech.Min.Sci. 15, No.4, 1978.

Nordgren, R.P., Propagation of Vertical Hydraulic Fracture, Soc.Petro.Engr.J., August, 1972.

Perkins, T.K. and A.R. Kern, Width of Hydraulic Fractures, J.Petro.Tech., September, 1961.

Pjetukhov, I.M. and A.M. Linjkov, Mechanics of Mine Shocks and Bursts, (Nedra, Moscow, 1986).

Tester, T.W., D.W. Brown, and R.M. Potter, Hot Dry Rock Geothermal Energy - A New Agenda for the 21st Century, LA-11514, (Los Alamos, NM, July, 1989).

Turchaninov, I.A., M.A. Iofis, and E.F. Kasparjan, Basic Principles of Rocks, (Nedra, Moscow, 1989).

Usachev, P.M., Seam Hydrofracture, (Nedra, Moscow, 1986).

Zheltov, Yu.P., Mechanics of Oil-Gas Containing Seams, (Nedra, Moscow, 1975).

A Study of Steady-State Steam-Water Counterflow in Porous Media

by
C. Satik, M. Parlar, and Y.C. Yortsos

Paper was withdrawn

Enthalpy Determination Using Flowing Pressure-Temperature Surveys in Two-Phase Wellbores in the Coso Geothermal Field

by

D. H. Kaspereit

No final copy was received by press time

SIXTEENTH ANNUAL WORKSHOP ON
GEOTHERMAL RESERVOIR ENGINEERING
STANFORD UNIVERSITY
January 23-25, 1991

Participants List

Jorge Acuna
Petroleum Eng. Dept,U.S.C
University Park
Los Angeles, CA 90089-1211
(213) 740-0322

Michael C. Adams
University of Utah Research Inst.
391 Chipeta Way, Suite A
Salt Lake City, UT 84108
(801) 524-3435 FAX (801) 524-3453

Dean R. Anderson
State of Hawaii, DBED
Energy Division-Geothermal Prog.
240 Merchant Street, Suite 1060
Honolulu, Hawaii 96813
(808) 586-2353 FAX (808) 586-2355

Emilio U. Antunez
LBL, Earth Science Division
One Cyclotron Road, Bldg 50E
Berkeley, CA 94720
(510) 486-5866

Gudni Axelsson
National Energy Authority
Geothermal Divison
Grensasvegur 9, 108 Reykjavik
ICELAND
354-1-83600 FAX 354-1-688896

Ben Barker
Unocal Geothermal
3576 Unocal Place
Santa Rosa, CA 95406
(707) 545-7600

Terrence G. Barker
S-CUBED
P.O.Box 1620
La Jolla, CA 92038-1620
(619) 453-0060 FAX (619) 755-0474

Elwood L. Baldwin
Baldwin Engineering, Inc.
13604 Midway Road #178
Dallas, TX 75244
(214) 980-0784

Alfredo Battistelli
Aquater
Via Miralbello
San Lorenzo in Campo (PS)
ITALY
721-771-326

Kit Bloomfield
P.G. & E.-West Geysers Power Plant
P.O.Box 456
Healdsburg, CA 95448
(707) 431-3810 FAX (707) 431-4066

Gudmundur S. Bodvarsson
LBL, Earth Science Division
One Cyclotron Road, Bldg 50E
Berkeley, CA 94720
(510) 486-4789 FAX (510) 486-5686

William T. Box, Jr.
Calpine Corp.
P.O. Box 11279
Santa Rosa, CA 95406
(707) 578-2724 FAX (707) 587-2798

Donald W. Brown
Los Alamos National Laboratory
EES-4, MS D443
Los Alamos, NM 87545
(505) 667-1926 FAX (505) 667-8487

Rosemary Vidale Buden
INEL
E G & G MS 2107
P.O.Box 1625
Idaho Falls, ID 83406
(208) 526-1048 FAX (208) 526-0875

Marinela M. Buenviaje
University of Auckland
Lot 8 Block 5, De Leon St.
Remmanville Subd.
Paranaque, Metro Manila
Philippines
815-89-61 FAX (632) 815-2747

Steven Butler
Unocal Geothermal
81-711 Hwy 111
Indio, CA 92201
(619) 342-4723

Sebastian Bwire
Kenya Power and Lighting Company, Inc.
c/o The Pragma Corporation
116 E. Broad St.
Falls Church, VA 22046
(703) 237-9303

Dave Camille
Unocal Geothermal
3576 Unocal Place
Santa Rosa, CA 95406
(707) 545-7600

Raffaele Cataldi
ENEL International
47, Via Cesare Battisti
56125-Pisa
ITALY
(50) 53.57.71 FAX (50) 53.58.76

Jim Combs
Geo Hills Associates
27790 Edgerton Road
Los Altos Hills, CA 94022
(415) 941-5480 FAX (415) 941-5480

John Copp
California Energy Company, Inc.
P.O.Box 1420
Inyokern, CA 93527
(619) 764-2551 FAX (619) 764-2500

John Counsil
Engineering Consultant
1148 Shadyoak Place
Santa Rosa, CA 95404
(707) 538-2288

Barbara Crowley, Vice Chair
California Energy Commission
1516 Ninth Street, MS 33
Sacramento, CA 95814
(916) 324-3316 FAX (916) 327-4620

David V. Duchane
Los Alamos National Laboratory
EES-DOT, MS D443
Los Alamos, NM 87545.
(505) 667-9893 FAX (505) 667-8487

Herman Dykstra
Consultant
4180 Treat Blvd, Ste I
Concord, CA 94518
(510) 676-7464

Kathy Enedy
Pacific Gas & Electric
111 Stony Circle
Santa Rosa, CA 95401
(707) 577-7066

Steve Enedy
NCPA
P.O.Box 663
Middletown, CA 95461
(707) 987-3101 FAX (707) 987-2088

Iraj Ershaghi
Dept. of Petroleum Engineering
University of Southern California
University Park,
Los Angeles, CA 90089-1211
(213) 740-0320

Lynne Fahlquist
USGS
345 Middlefield Rd., MS 910
Menlo Park, CA 94025
(415) 329-5216 FAX (415) 329-5110

David D. Faulder
Idaho National Engineering Laboratory
P.O. Box 1625
Idaho Falls, ID 83415-2107
(208) 526-0674 FAX (208) 526-0875

Shaun Fitzgerald
Cambridge University
Downing Street
Cambridge CB2-3EQ
United Kingdom
0223 333419 FAX 0223 3450

Robert O. Fournier
USGS MS 910
345 Middlefield Rd
Menlo Park, CA 94025
(415) 329 5202 FAX (415) 329-5110

Sabodh K. Garg
S-CUBED
P.O. Box 1620
La Jolla, CA 92038-1620
(619) 453-0060 FAX (619) 755-0474

Colin Goranson
Consultant
1498 Aqua Vista Rd
Richmond, CA
(510) 234-0522 FAX (510) 234-5881

Keshav Goyal
Calpine Corporation
P.O. Box 11279
Santa Rosa, CA 95406-1279
(707) 527-6700 FAX (707) 544-2422

Eduardo Granados
GeothermEx, Inc.
5221 Central Avenue, Suite 201
Richmond, CA 94804
(510) 527-9876

Francois Groff
Department of Petroleum Engineering
Stanford University
Stanford, CA 94305
(415) 494-2461

Richard Gunderson
Unocal Geothermal Division
3576 Unocal Place
P.O. Box 6854
Santa Rosa, CA 95406
(707) 545-7600 FAX (707) 545-8746

Mohinder Gulati
Unocal Geothermal
3576 Unocal Place
Santa Rosa, CA 95406
(707) 545-7600

Tim Haight
Pacific Gas & Electric
77 Beale, Room 2331
San Francisco, CA 94106
(415) 972-7000

Charles B. Haukwa
Kenya Power and Lighting Co., Inc.
c/o Lawrence Berkeley Lab, Bldg 50E
1 Cyclotron Road
Berkeley, CA 94720
(510) 486-7419

Kenneth P. Henderson
Division of Oil & Gas
Dept. of Conservation
1416 Ninth St., Rm 1310
Sacramento, CA 95814
(916) 323-1777 FAX (916) 323-0424

Chuck Hicklin
Pacific Gas & Electric Company
1 California Street, Room F880C
San Francisco, CA 94106
(415) 973-2826 FAX (415) 973-1154

Curt Hildebrand
Unocal Geothermal
3576 Unocal Place
Santa Rosa, CA 95406
(707) 545-7600

Paul Hirtz
Thermochem, Inc.
5347 Skylane Blvd
Santa Rosa, CA 95401
(707) 575-1310 FAX (707) 575-7932

John Holtzapple
Pacific Gas & Electric Co.
77 Beale, Room 2331
San Francisco, CA 94106
(415) 972-7000

John Hornbrook
Department of Petroleum Engineering
Stanford University
Stanford, CA 94305
(415) 324-3374

Glenn D. Horton
Pacific Gas & Electric
111 Stony Circle
Santa Rosa, CA 95401
(707) 577-7062 FAX (707) 577-7067

Stefanie Hummel
Unocal Geothermal
3576 Unocal Place
Santa Rosa, CA 95406
(707) 545-7600

Christy Craig Hunter
California Div. of Oil & Gas
485-B Broadway
El Centro, CA 92243
(619) 353-9900

Eduardo R. Iglesias
I.I.E.
Apdo. Postal 475
Cuernavaca, Mor. Mexico
(73) 18-3811 Ex.3210 FAX (73) 18-2526

Ken Ikeuchi
JMC Geothermal Research & Dev.
72-Sasamori, Ukai, Takizawa-Mura
Iwate 020-01, Japan
81-196-84-4114 FAX 81-196-84-6231

Steve Ingebritsen
U.S. Geological Survey
345 Middlefield Rd
Menlo Park, CA 94025
(415) 329-4422 FAX (415) 329-4422

Joe Iovenitti
Weiss Associates
5500 Shallmound Street
Emeryville, CA 94608
(415) 547-5420

Cathy J. Janik
U.S. Geological Survey
345 Middlefield Rd, MS 910
Menlo Park, CA 94025
(415) 329-5213 FAX (415) 329-5110

Elizabeth Johnson
California Div. of Oil & Gas
50 D Street, Room 300
Santa Rosa, CA 95404
(707) 576-2385

Pete Johnson
State of Calif.-State Lands Commission
245 W. Broadway, Suite 425
Long Beach, CA 90802
(213) 590-5201 FAX (213) 590-5295

Steve Jones
NCPA
P.O. Box 663
Middletown, CA 95461
(707) 987-3101 FAX (707) 987-2088

Dennis Kaspereit
California Energy Co., Inc.
P.O. Box 185
Ridgecrest, CA 93556
(619) 499-2326 FAX (619) 499-2308

Hamid Kazerooni
Sierra Pacific Power Company
P.O. Box 10100
Reno, NV 89520
(702) 689-4390 FAX (702) 689-4202

Christopher Klein
GeothermEx, Inc.
5221 Central Avenue, Suite 201
Richmond, CA 94804
(510) 527-9876

Lawrence E. Kukacka
Brookhaven National Laboratory
Bldg 526
Upton, NY 11973
(516) 282-3065 FAX (516) 282-5598

Mark K. Kumataka
Santa Fe Geothermal, Inc.
P.O. Box 1009
Middletown, CA 95461
(707) 987-2335 FAX (707) 987-2353

Cheng-Hsien Lai
Lawrence Berkeley Laboratory
One Cyclotron Road, Bldg. 50E
Berkeley, CA 94720
(510) 486-4289 FAX (510) 486-5686

Marcelo Lippmann
Lawrence Berkeley Laboratory
One Cyclotron Road, Bldg. 50E
Berkeley, CA 94720
(510) 486-5035 FAX (510) 486-5686

James Lovekin
California Energy Company, Inc.
P.O. Box 1420
Inyokern, CA 93527
(619) 764-2551 FAX (619) 764-2500

E. James Macias
Pacific Gas & Electric
lll Stony Circle
Santa Rosa, CA 95401
(707) 577-7060 FAX (707) 577-7067

John Maney
Unocal Geothermal
3576 Unocal Place
Santa Rosa, CA 95406
(707) 545-7600

H. K. "Pete" McCluer
Consultant
P.O.Box 650
Mt. Auburn, CA 95656
(209) 245 4171 FAX (916) 626-0189

David Meade
Naval Weapons Center
Code 2606 Geothermal Prog. Office
China Lake, CA 93555
(619) 939-3411, Ext.448

Tsvi Meidav
Trans-Pacific Geothermal Corp.
1330 Broadway, Suite 1525
Oakland, CA 94612
(510) 763-7812 FAX (510) 763-2504

Anthony Menzies
GeothermEx, Inc.
5221 Central Avenue, Suite 201
Richmond, CA 94804
(510) 527-9876

Donald E. Michels
Don Michels Associates
P.O. Box 8652
Missoula, Montana 59807
(406) 728-2576 FAX (406) 721-7671

Gerald R. Miller
Pacific Gas & Electric
77 Beale, Room 2331
San Francisco, CA 94106
(415) 972-4104 FAX (415) 972-0871

John E. Mock
U.S. Department of Energy
1000 Independence Avenue
Washington, DC 20585
(202) 586-5340

Phil Mogen
Unocal
P.O. Box 1805
Indio, CA 92202
(619) 342-4723

Phil Molling
Unocal Geothermal Division
3576 Unocal Place
Santa Rosa, CA 95406
(707) 545-7600

George M. Moore
Kenner, Burd, Knutson & Markowitz
Four Embarcadero Center, 25th Floor
San Francisco, CA 94111
(415) 397-3100 FAX (415) 397-3170

Joseph N. Moore
University of Utah Research Inst.
391 Chipeta Way, Suite A
Salt Lake City, UT 84108
(801) 524-3428 FAX (801) 524-3453

Larry Murray
Unocal Geothermal Division
3576 Unocal Place
Santa Rosa, CA 95406
(707) 545-7600

Cuong Phu Nghiem
Dept. of Petroleum Engineering
Stanford University
Stanford, CA 94305
(415) 725-2733

Dennis L. Nielson
University of Utah Research Inst.
391-C Chipeta Way,
Salt Lake City, UT 84108
(801) 524-3438 FAX (801) 524-3453

Gerald Niimi
ThermaSource, Inc.
P.O. Box 1236
Santa Rosa, CA 95402
(707) 523-2960 FAX (707) 523-1029

Harry J. Olson
HNEI, University of Hawaii
811 Olomehani St.
Honolulu, Hawaii 96813
(808) 522-5620 FAX (808) 522-5618

Takashi Okabe
Geothermal Energy Res & Develop.Co.
Kyodo Bldg 11-7, Kabuto-cho
Nihonbashi, Chuo-ku
Tokyo 103, Japan
(03) 3666-5822 FAX (03) 3666-5289

Will Osborn
Mission-East Mesa
P.O. Box 748
Holtville, CA 92250
(619) 356-4613 FAX (619) 356-4619

Peter Persoff
Lawrence Berkeley Laboratory
One Cyclotron Rd, Bldg 50E
Berkeley, CA 94720
(510) 486-5931 FAX (510) 486-5686

Hari Pratomo
Amoseas Indonesia Inc.
c/o Chevron Resources Co
P.O. Box 5049
San Ramon, CA 94583-0949
(510) 842-6830 FAX (510) 842-6900

John W. Pritchett
S-CUBED
P.O. BOX 1620
La Jolla, CA 92038-1620
(619) 453-0060 FAX (619) 755-0474

Karsten Pruess
Lawrence Berkeley Laboratory
One Cyclotron Rd, Bldg. 50E
Berkeley, CA 94720
(510) 486-6732 FAX (510) 486-5686

Ming Qi
Dept. of Petroleum Engineering
Stanford University
Stanford, CA 94305
(415) 725-2733

Marshall Reed
U.S. Department of Energy
1000 Independence Ave, SW
Washington, DC 20585
(202) 586-8076 FAX (202) 586-8153

Joel Renner
INEL
P.O. Box 1625
Idaho Falls, ID 83415-3526
(208) 526-9824 FAX (208) 526-0969

Ken Riedel
Unocal Geothermal
3576 Unocal Place
Santa Rosa, CA 95406
(707) 545-7600

Michael Riley
Dept. of Petroleum Engineering
Stanford University
Stanford, CA 94305
(415) 723-9219

Stu Russell
Russell Associates
2431 Ross
Palo Alto, CA 94303
(415) 326-2260 FAX (415) 325-1701

Fernando Samaniego
UNAM Division de Estudios
de Posgrado,
Facultad de Ingenieria
UNAM 04510 Mexico D.F.
Mexico
(905) 550-8712 FAX (905) 548-0950

Charles Sammis
University of Southern California
Geological Science Dept.
University Park
Los Angeles, CA 90089
(213) 750-5836

R. C. Schroeder
Berkeley Group Inc.
1330 Broadway, Suite 1450
Oakland, CA 94612
(510) 465-1744 FAX (510) 465-1405

Harold R. Sells
Sells Consulting Service
5025 Pacific Grove Dr.
Las Vegas, NV 89130
(702) 645-9771

Mike Shook
Idaho National Engineering Laboratory
P.O. Box 1625
Idaho Falls, ID 83415-2107
(208) 526-6945 FAX (208) 526-0875

Daniel Swenson
Kansas State University
Mechanical Eng. Dept-Durland Hall
Manhattan, KS 66506
(913) 532-5610

G. D. Symons
Energy Technology Atomic Energy Auth.
Bldg 156
Harwell Didcot.Oxon OXll ORA
United Kingdom
0235 821111 FAX 0235 432916

Jefferson W. Tester
Director, MIT Energy Laboratory
77 Massachusetts Avenue, E40-455
Cambridge, MA 02139
(617) 253-3401 FAX (617) 253-8013

Richard Thomas
California Div. of Oil & Gas
1416 9th St.
Sacramento, CA 95814
(916) 323-1787

W. M. Thompson
State of Calif.-State Lands Commission
245 W. Broadway, Suite 425
Long Beach, CA 90802
(213) 590-5201 FAX (213) 590-5295

Alfred Truesdell
Consultant
700 Hermosa Way
Menlo Park, CA 94025
(415) 322-6135 FAX (415) 324-4009

Maria Elena G. Urbino (Macario)
Dept. of Petroleum Engineering
Stanford University
Stanford, CA 94305
(415) 725-2733

Bob Verity
Mesquite Group, Inc.
P.O. Box 1283
221 N. Harbor Bldg, Suite K
Fullerton, CA 92632
(714) 738-8224 FAX (714) 525-2852

Marina Voskanian
State of Calif.-State Lands Commission
245 W. Broadway, Suite 425
Long Beach, CA 90802
(213) 590-5201 FAX (213) 590-5295

Alan Williams
University of California
Inst. of Geoph. and Planetary Physics
Riverside, CA 92521
(714) 787-4503 FAX (714) 787-4509

Kenneth H. Williamson
Unocal Geothermal Division
3576 Unocal Place, P.O. Box 6854
Santa Rosa, CA 95406
(707) 545-7600 FAX (707) 545-8746

Phillip M. Wright
University of Utah Research Inst.
391 Chipeta Way, Suite C
Salt Lake City, UT 84108
(801) 524-3439 FAX (801) 524-3453

Yanis Yortsos
University of Southern California
Petroleum Engineering Program
University Park
Los Angeles, CA 90089-1211
(213) 740-0317

SUBJECT INDEX

Acid fluids: 262, 267
Acid-chloride corrosion
  (see corrosion mitigation): 83, 87
Adsorption: 67, 113
Air injection (see also injection): 64
Airy equation: 69
Amerada pressure gauge: 121
Amorphous silica (see scale formation): 165
Atomic absorption spectroscopy: 91
Atomic absorption method: 12
Back pressure: 24
Bed-of-nails model: 22
BET equation: 113
Bioreactors: 6
Boric acid: 87
Boundary conditions:
  closed: 79, 178, 241
  constant pressure: 79, 224
  impermeable: 155
  linear: 224
  no flow: 98, 135
  unbounded: 241
Brine composition (see fluid flow): 249, 257
British Geological Survey: 33
Brookhaven National Laboratory: 6
Brown University: 275
California Energy Commission (CEC): 1, 3
Calpine Corporation: 5, 76
Camborne School of Mines: 31
Capillary pressure (see also pressure): 203,
  209, 214
Caprock: see reservoir geometry
Cascades: 4
Cerro Prieto geothermal field (Mexico): 84,
  168, 183
Chemical analyses of geothermal waters: 9
  acid titration: 12
  atomic absorption method: 11
  conductivity analysis: 12
  dianthrimide method: 12
  inductively-coupled argon plasma
  spectrophotometry: 12
  ion chromatography: 12
  ion selective electrode: 12
  Mohr-argentometric titration: 12
  molybdate-blue method: 12
  turbidimetric titration: 12
Civil discovery: 55
Civil litigation: 53
CO_2:
  concentration of steam, high: 18
  partial pressures: 118
Coldwater Creek Operator Company
  (CCOC): 5, 15
Compressibility factors of HCFC: 59
Compression effect: 114
Computer codes:
  LBL Reservoir Simulator: 159
  MULKOM: 65, 212
  Multi-Rate Multi-Well: 241
  STAR: 154
  TETRAD: 97, 134
  TOUGH: 65, 212, 241
  WATCH2: 119
Convection: 67
Corrosion mitigation:
  hydrochloric acid buildup: 6
  monitoring techniques: 91
  sampling methods: 90
  wellhead system: 89
Corrosion rate measurements: 94
Coso Geothermal Field: 247
Costs:
  drilling: 36
  HDR: 36, 39
  power plant: 36, 42
Crump algorithm: 67
Darcy's law: 214
Dating:
  hydration: 133
  paleo-magnetic: 133
Decline curve analysis: 75
Department of Scientific and Industrial
  Research (DSIR): 241
Deposition:
  molecular: 167
  particle: 167, 171
Desorption: 113
Dewpoint corrosion: 83, 86
Diffusion: 67
Dispersion (longitudinal): 67
District heating: 2, 144
Dixie Valley (Nevada): 57, 169
Downhole tools: 6
Dynamic relaxation: 21
Electric Power Research Institute (EPRI): 35
Electromagnetic methods: 6
Energy:
  Department of: 2, 3, 108, 275
  Export Trading Company: 5
  Geothermal R & D program: 3
  Technology Advancement Program: 2
  Technology Export Program: 2
Exploitation modeling: 188
Fenton Hill: see Hot dry rock
Fluid flow:
  chemistry: 249, 257
  constant discharge rate: 114
  constant pressure: 114
  cubic law: 203

decline: 79
horizontal: 211
jointed rock: 21, 283
multi-phase, in fractures: 203
non-Darcy: 283
one dimensional steam : 113
radial: 211, 241, 283
simulation of two-phase: 277
single-phase: 241
two-phase: 203, 241, 244, 275
vertical: 211
Fossil liquid-system model: 17
Fractal characterization: 107
Fracture:
aperture: 208
replica: 204
rough-walled: 203
Froude number: 276
Gas:
composition: 247
dissolved: 247
geothermometry: 249
mechanisms for HCl generation: 84
non-condensible: 121, 123, 165, 264, 256, 275
origin: 268
Gas chromatograph: 60
Geochemical response to injection: 81, 232
Geopressured resources: 6
(geothermal heat energy station): 160
Geothermal inflow performance relationship (GIPR): 177
Geothermal systems:
liquid-dominated: 63, 117, 124, 183 , 250
vapor-dominated: 15, 114, 211
Geothermometers:
K-Mg: 119
Mg-Li: 119
Na-K-Ca-Mg: 119
Na-Li: 119
quartz: 211, 264
Geysers geothermal field, U.S.A.
(see also N, NE, NW, S, SE Geysers) : 3, 6, 15, 75, 83, 97, 107
Grashof number: 160
Gravity modeling: 132
Grid:
optimization: 244
orientation: 211
Halogenated alkanes (see also tracers): 57
Hatchobaru, Japan: 170
HCl production: see gas
Heat cycle: 6
Heat deliverability: 177
Heat exchanger wells: 4
Heat-extraction technology: 159
Heat flow: 132 134
Heat mining: 35
Heat pipe: 15
Heat source: 131, 134, 143, 155
Heat transfer: 18, 163, 211
Henry's law: 276
Himalayan Mountain Range: 117
History matching:
Cerro Prieto, Mexico: 186
Zunil, Guatemala: 193
Hot dry rock (HDR): 2, 6, 21, 29, 35
component costs: 39
economic models: 37
Fenton Hill : 6, 23, 283
Hijori, Japan: 33
Leningrad Mining Institute (USSR): 283
MIT economic model: 42
non-thermal: 36
optimizing performance: 49
power plants costs: 42
Roosevelt Hot Springs (RHS), UT: 36, 131
Soultz (France:) 33
stimulation costs: 39
thermal: 36
UK Dept. of Energy R & D Programme: 29
Hydrofracture theory (see also rock stimulation) : 283
Hydrogen chloride generation: 84
Hydrogen sulfide: 88, 91
Idaho National Energy Laboratory (INEL): 5
Immiscible displacement: 212
Impedance: 30
Indonesia: 3
Inductively-coupled argon plasma spectrophotometry: 12
Inflow performance relationship (IPR): 177
Injection: 5
air: 63
proppant (sand): 31
water: 63, 75, 92, 211, 223
Initial-state modeling: 185, 193, 197
Integrated Resource Planning (IRP): 4
International Geothermal Association Secretariat: 2
Isotope:
water composition, stable: 119, 133
Isotopic analyses of geothermal waters: 9
mass spectrometry: 11
uranium method: 11
Jacobian matrix: 242
James "lip method": 120
Japan International Cooperation Agency (JICA): 193, 255
Joint Association Survey (JAS): 39
Jointed rock: 21
Krafla field (Iceland): 84
Langmuir equation: 113
Laplace transformation: 69, 160

Larderello (Italy): 84, 211
Lauwerier model: 160
Lawrence Berkeley Laboratory (LBL): 5, 15, 185, 197
Lawrence Livermore Laboratory: 5
Least Cost Utility Planning (LCUP): 4
Leningrad Mining Institute (USSR): 159, 283
Linear programming: 234
LMI heat-physics model: 159
Local heat source model: 17
Los Alamos National Laboratory (LANL): 2, 35, 283
Los Azufres Geothermal Field (Mexico) : 63
Low Pressure Area (LPA) Injection Project, Geysers: 75
Low temperature geothermal system: 143
Mach number: 276
Magma chamber: 131, 134
Magma Power: 3
Mass-source: 15
Mass spectrometry: 11
Mass-sink: 156
Microearthquake response to injection: 80
Microshocks: 31
Milos, Greece: 169
Mitsubishi Gas Chemical Corporation (MGC): 151
Mitsubishi Materials Corporation (MMC): 151
Mixing models: 268
Mobility ratio: 213
Moderate-temperature resources: 159
Mollier diagram: 78
Mt. Pinatubo, Philippines: 261, 267
Mroczek and McDowell: 170
Nagqu (Tibet, People's Republic of China): 117
National Energy Strategy: 4
Natural state modeling: 151
New Energy and Industrial Technology Development Organization (NEDO): 151
Newton-Raphson technique: 21, 242
Nitrogen (N_2) concentration trend: 65
Northeast Geysers: 83
Northern California Power Agency (NCPA): 5, 75
Northern Geysers: 15
Northwest Geysers: 15
Northwest Power Planning Council: 4
Numerical analysis: 6
Numerical simulation (see initial-state, history matching and exploitation modeling):
  five and nine-point differencing: 214
  space and time discretization effects: 212
  grid orientation effects: 212
Oakridge National Laboratory: 5
Otake, Japan: 170
Pacific Gas & Electric Co. (PG & E): 4
Pacific Northwest: 4
Palinpinon geothermal field (Philippines): 231
Peclet number: 161
Permeability (see also relative permeability):
  anisotropic formation: 154, 225
  distribution: 197, 228
  fracture: 152
  matrix: 77
Permeability-thickness (kh) product: 77, 234
Petrogeothermal reservoir: 159
Philippine National Oil Company (PNOC): 231, 267
Polymerization rate: 167
Polymers: 166
Pressure:
  build-up: 121, 145, 221, 241, 244
  capillary: 203
  cycling: 255
  interwell interference testing: 121, 146, 199, 221
  line-source solution: 224, 225
  log-log analysis: 121
  maintenance: 98
  semilog analysis: 122
  response from injection: 79, 223, 231
  transient analysis: 225, 241
  type curve matching: 121
Pressure-temperature-spinner (P/T/S) logging: 77, 241, 244
Process chemistry (for corrosion mitigation): 87
Pseudo-pressure: 113
Quadratic programming: 234
Quality control: 9
Radioactive decay: 68
Raoult's law: 277
Rayleigh condensation pattern: 16
Rayleigh number: 161
Recharge: 122, 131, 134
Refrigerant 114: 275
Reinjection strategies: 97, 231
Relative permeability:
  calculation: 206
  Corey: 178, 198
  experimental results: 208
  Grant,: 198
  measurement: 203, 206
  straight line: 135
Reservoir model:
  anisotropic line-source: 226
  closed, cylindrical, homogeneous: 177
  double-porosity : 107, 124
  finite element: 23
  fractal statistical: 107
  fractured, liquid-dominated: 63, 124, 183
  fractured network: 67
  fractured petroleum: 108
  fractured porous media: 98

fracture-stimulated: 159
geologic: 131
heat pipe: 16
linear : 123
lumped-parameter: 122, 147
matrix network: 68
medium enthalpy: 117
multiporosity: 107
native state: 131
petrogeothermal: 159
porous medium: 107, 113, 154
shallow, high-temperature: 16
single-phase liquid dominated: 117, 250
three-dimensional, multi-phase: 183
two-phase: 157, 177, 251
three-parallel, hydrofractured: 160
vapor-dominated: 16, 114, 211
Reservoir:
basement: 117
caprock: 194
properties: 24, 161, 180, 219, 224
response to exploitation/production: 63, 98, 123, 148, 186
response to injection: 75, 78
Reservoir engineering:
Iceland: 143
Nagqu (PROC): 117
Roosevelt Hot Springs: 133
Residence time: 165
Reynolds number: 160, 276
Rock deformation model: 21
Rock properties: 154
Rock stimulation: 30, 159, 283
Roosevelt Hot Springs (RHS), Utah: 131
Russkie Komarovtsy (USSR): 159
San Diego Gas & Electric Co. : 4
Salt evolution: 66
Salton Sea: 3,
Sample collection of geothermal waters: 11
Sampling techniques:
isokinetic: 90
nonisokinetic: 90
Scale formation:
calcium carbonate: 117
experiences: 168
fluid scaling tendency: 120
mechanisms: 165
silica: 165
suppression: 173
thickness: 121
Schiltuis equation: 122
Scrubbing of water and caustic steam (see corrosion mitigation): 83, 87
Secondary mineralization: 194
Seismic exploration methods: 6
SGP 1-D Heat Sweep Model: 159
Silica scaling: 165
Silinol group: 166
Similarity theory: 276
Sodium hydroxide: 87
Solubility:
amorphous silica: 165
chalcedony: 165
quartz: 165
Southeast Geysers: 60, 75
Southern California Edison: 4
Southern Geysers: 18
South Coast Air Quality Management District: 5
Space heating: 143
Stanford University Geothermal Program: 5
Steering Committee for Geysers Research: 5
Stehfest algorithm: 67
Subsurface heat exchanger: 30
Successive Over Relaxation (SOR) method: 241
Sumikawa geothermal field (Japan): 151, 221
Supercritical steam: 16
Supercritical waste treatment: 6
Supercritical water oxidation (SCWO): 6
Superheated steam: 16, 85,
Surface thermal features: 267
Svartsengi, Iceland: 170
Technical Advisory Committee: 1
Tejamaniles (Mexico): 63
Temperatures:
response to injection: 81
response to production: 78
stagnation: 278
Ternary diagrams: 269
Thermal breakthrough: 78, 231
Thermal cooldown: 131, 148, 159
Thermal enhancement of oil recovery (TEOR): 6
Thomas algorithm: 242
Tracers:
air: 63
deuterium: 57, 75
halogenated alkanes (HCFC) for vapor-dominated: 57
Iodine-131: 233
Iridium -192
Oxygen-18: 57
Potassium Iodide: 63
radial flow: 67
Sodium fluorescein: 233
tritium: 57, 75
Tracer testing:
continuous injection: 69
finite step injection: 69
Palinpinon, Philippines: 232
Southeast Geysers: 75
Uenotai geothermal field (Japan): 165
UNOCAL: 3, 5, 75
Unocal-NEC-Thermal (U-N-T) project: 75
Univ. of Utah Research Inst. (UURI): 5, 60
Uranium method: 11
U.S. Geological Survey (USGS): 6, 11, 108

Vienna-standard mean ocean water
(V-SMOW): 10
Vogel reference curve: 177
Volatile chloride (see acid-chloride
corrosion): 83
Volatility ratios: 60
Volcanic caldera: 261
Warren-Alquist Act: 1
Wellflow simulation: 275
Well siting: 6
Well spacing: 100
Well testing:
discharge: 199
geysering character: 255
long-term: 146, 195, 199
interference: 199, 221
short-term: 145, 195
Yucca Mountain (Nevada): 108
Zunil geothermal field (Guatemala): 193, 255

AUTHOR INDEX

Adams, M.C.: 57
Antunez, E.U.: 183
Ariki, K.: 151, 221
Artemieva, E.: 159
Axelsson, G.: 143
Battistelli, A.: 117
Beeland, G.: 3
Brown, D.: 21
Buck, C.: 83
Buenviaje, M.M.: 267
Caicedo-A., A: 193
Clark, J.H.: 29
Clemente, V.C.: 261
Copp, J.F.: 247
Crowley, B: 1
D'Amore, F.: 117
Dipippo, R.: 275
Dyadkin, Y.: 159, 283
Enedy, K.: 75
Enedy, S.: 75
Ershaghi, I.: 107
Faulder, D.D.: 97, 131
Garg, S.K.: 151, 221
Gendler, S.: 159
Granados, E.E.: 193
Gutierrez Puente, H.: 63
Herzog, H.J.: 35
Hirtz, P.: 57, 83
Horne, R.N.: 231
Iglesias, E.R.: 177
Iwata, S.: 165
James, M.: 21
Kaspereit, D.H.: 291
Kawano, Y.: 151, 221
Klein, C.W.: 165
Kruger, P.: 159
Kunzman, R.: 83
Laoulache, R.N.: 275
Lin, J.A.: 107
Luzi, C.: 117
Maney, J.: 75
Mariner, R.H.: 9
Martineau, R.: 21
Menzies, A.J.: 183, 193
Merida-I., L.: 193
Meyer, L.: 203
Michels, D.E.: 255, 261
Mock, J.E.: 3
Moore, G.M.: 53
Moore, J.N.: 57
Moreno Ochoa, J.: 63
Moya, S.L.: 177
Nghiem, Cuong Phu: 113
Okabe, T.: 241
Osato, K.: 241
Persoff, P.: 203
Pritchett, J.W.: 151, 221
Pruess, K.: 203, 211
Ramey, Jr., H, J.: 113
Ramirez-Sabag, J.: 67
Ramos, M.N.: 261
Reed, M.J.: 3
Rivera R., J.: 67, 117
Rodriguez, F.: 67
Rossi, R.: 117
Samaniego V., F.: 67
Sammis, C.G.: 107
Sanyal, S.K.: 183, 193
Shook, M.: 97
Smirnova, N.: 159
Suarez Arriaga, M.C.: 63
Swenson, D.: 21
Symons, G.D.: 29
Takasugi, S.: 241
Takeuchi, R.: 165
Tester, J.W.: 35
Tohsaku, N.: 165
Truesdell, A.H.: 15
Urbino, M.E.G.: 231
Williams, A.E.: 247
Wu, F.: 117